ENGINEERING SEMICONDUCTOR NANOCRYSTALS FOR MOLECULAR, CELLULAR, AND IN VIVO IMAGING

A Dissertation
Presented to
The Academic Faculty

By

Andrew Michael Smith

In Partial Fulfillment
of the Requirements for the Degree
Doctor of Philosophy in the
Department of Biomedical Engineering

Georgia Institute of Technology

December, 2008

ENGINEERING SEMICONDUCTOR NANOCRYSTALS FOR MOLECULAR, CELLULAR, AND IN VIVO IMAGING

Approved by:

Dr. Shuming Nie, Advisor
School of Biomedical Engineering
Georgia Institute of Technology

Dr. Gang Bao
School of Biomedical Engineering
Georgia Institute of Technology

Dr. Niren Murthy
School of Biomedical Engineering
Georgia Institute of Technology

Dr. Zhong L. Wang
School of Materials Science and Engineering
Georgia Institute of Technology

Dr. Lily Yang
Department of Surgery
Emory University

Date approved: October 16, 2008

ACKNOWLEDGEMENTS

I dedicate this thesis to my parents, Marge and Winston, and my brother Edward, who have always supported me. I owe to them my values, work ethic, and aspiration to pursue a life of continuous learning. I thank my beautiful and incredibly intelligent girlfriend Mia for being compassionate and patient through the completion of my degree. I am grateful for guidance and inspiration from my friends, family members, and teachers, especially George Petsch, France Dorman, Mark Sommerville, James Powers, Athanassios Sambanis, Joseph Berglund, Schiue-Cheng Tang, Jonathan Beech, and James Mickens. I also thank Matthew Rhyner, Aaron Mohs, Michael Mancini, and Brad Kairdolf, who have taken part in the collaborative efforts of this thesis. Finally, I thank my research advisor, Shuming Nie, an inspiring leader and a brilliant mind who has given me tremendous opportunities over the past six years to learn a broad range of scientific disciplines, the encouragement to work harder than I have ever thought possible, and a vision for my future and the future of science and innovation.

TABLE OF CONTENTS

LIST OF TABLES

LIST OF FIGURES

SUMMARY

Nanotechnology is a new multidisciplinary approach to research that is expected to make critical advances in a diverse range of fields, from quantum computing to biosensing. Biomedicine has already exploited many nanotechnology platforms for the detection and treatment of disease as well as for the fundamental study of cellular biology. A prime example of these successes is the recent implementation of semiconductor quantum dots in a wide range of biological and medical applications. Quantum dots are nearly spherical nanocrystals composed of semiconductor materials that can emit fluorescent light with high intensity and a strong resistance to degradation. In addition, the crystalline, semiconductor nature of these macromolecules engenders unique attributes that cannot be attained from optically labile organic dyes and fluorescent proteins, such as bright infrared fluorescence and efficient broadband excitation. These nanoparticles have shown great promise as sensitive and selective biosensors, contrast agents for cancer imaging, and tracking agents for long-term, real-time monitoring single molecules inside of living cells.

The aim of this work is to understand the fundamental physics of colloidal semiconductor quantum dots, to engineer their optical and structural properties for applications in biology and medicine, and to examine the interaction of these particles with biomolecules and living cells. Toward these goals, new synthetic strategies for colloidal nanocrystals have been developed, implementing a cation exchange method to prepare particles with sizes that are tuned independently from their intense fluorescence, which

may span the visible and near-infrared spectra (500-1000 nm). In addition, a new means of manipulating the optical and electronic properties has been developed through controlled mechanical strain imposed by coherent shell growth. As colloids, these nanocrystals have surfaces which allow the attachment of a diverse array of organic molecules and ligands. The concept of multivalent binding to colloidal surfaces has also been implemented to enable interactions with extremely high affinity. This has led to the development of stable nanocrystals with ultrathin coatings (< 2 nm), 'amphibious' nanocrystals soluble in virtually any liquid, and bioaffinity probes self-assembled through multidentate interactions with polyhistidine-sequences on recombinant proteins.

Despite an intense interest in the integration of biomedicine and nanotechnology, great concern has been raised over the safety of nanoparticles. Very little is known about how exogenous nanoparticles interact with biological molecules and cellular structures, and the eventual fate and potential cytotoxicity of these particles in animals will likely govern the realization of their potential. In this work, semiconductor quantum dots were studied in biological fluids and living cells in order to elucidate their propensity to bind to proteins and cellular structures. Surprisingly it was found that these interactions are strongly dependent on the size of the nanocrystals, and particles that have sizes similar to biological macromolecules are largely inert. This finding allows the nanocrystal size to be used as a parameter to dictate attributes such as cellular transfection and protein adsorption. Finally, the effects of these nanocrystals on cellular function were studied in depth, revealing that the heavy metal composition of quantum dots (e.g. cadmium or mercury) is not a major factor in cytotoxicity. Rather, the colloidal and surface properties of these materials dominate their impact on cells, demonstrating that the rule book for toxicology must be rewritten for nanomaterials.

CHAPTER 1

Introduction

Significant progress in the detection and treatment of disease has recently been led by molecular, systems, and engineering approaches to medicine. Despite increasing survival rates for many diseases, major voids remain in biomedical science that are obstructing the efficient development of treatments and diagnostics, as well as the advancement of the understanding of pathology. Many modern medical tests are currently insufficient in sensitivity to detect cancers and viral infections before they reach their advanced stages. In addition, the resolution and specificity of commonly used medical imaging modalities are frequently inadequate for monitoring diseases. From the perspective of cellular biology, a vast array of molecular biology tools such as PCR and gene array technology are available to study the mechanisms of diseases, but almost no tools are available for studying disease states *in situ* in living cells.

Nanotechnology is a new discipline that may soon provide the tools and theoretical approach for filling many of the technological gaps in medicine. As engineers and physicists studied the properties of materials with smaller and smaller dimensions, biochemists and polymer scientists constructed macromolecules that led these fields to simultaneously converge on the nanometer length scale, roughly 1-100 nm, in the 1970's and 1980's. Many of the fundamental principles governing this size regime had been developed by surface and colloid scientists in the mid-20th century, allowing immediate groundbreaking research and the development of new tools and materials

useful to a diversity of fields. This size range is of particular interest in biology and medicine, as the fundamental building blocks of cells are macromolecules and structures with nanometer-scale dimensions. Thereby, the interface of biology with nanotechnology may allow precise manipulation of biomolecules and cells, in addition to sensitive detection of abnormal disease states.

Among the many useful nanoscience tools already in use in biomedicine, semiconductor quantum dots are unique in their far-reaching potential for the fundamental study of biology, the detection and diagnosis of disease, and as a building block for the construction of complex nanoscale devices for integration with biological systems.[1-3] Quantum dots are nanometer-sized crystals of semiconductor materials (typically 2-8 nm) that emit fluorescent light with great intensity and unparalleled signal stability. These attributes have found immediate use for monitoring individual molecules on cell surfaces in real time for extended periods,[4-8] for sensitive detection of cancer *in vivo*,[9-12] and for sensitive and specific characterization of viruses and cancer antigens in bodily fluids.[13-16] The future applications of these remarkable materials will likely go far beyond these initial proof-of-concept experiments, but first an understanding must be developed for how they interact with biological systems and how their useful physical and optical characteristics can be harnessed.

1.1 Thesis Goals

This thesis aims to provide the theoretical framework and applied engineering strategies for the development of semiconductor quantum dots as advanced functional nanometer-scale tools for the sensitive detection of disease and the study of cellular biology. This goal is approached from three directions. First, an understanding of the pure physics of the optical and electronic properties of quantum dots is developed from a theoretical

level. This is performed by providing an exhaustive review of the physical attributes and applications of quantum dots (Chapter 2), rationally engineering the quantum dot composition and size (Chapter 3), and through the construction of semiconductor heterostructures (Chapter 4). Second, the colloidal and surface properties of these nanocrystals are studied from an applied perspective for the production of particles with enhanced physicochemical attributes for interfacing with biology (Chapter 5), as well as for farther reaching applications in catalysis, optoelectronic devices, and energy conversion (Chapter 6). Finally, the interactions between quantum dot nanocrystals and biological molecules are studied in order to gauge how these particles will behave in living cells and organisms, with particular emphasis on their specific and nonspecific binding, as well as their potential cytotoxic impact (Chapter 7).

1.2 Themes and Significant Findings

The broad scope of the disciplines employed in this thesis is indicative of the multidisciplinary nature of bio-nanotechnology, and underlies the fundamental connections between all fields of science and engineering. Several common themes are frequently encountered throughout this work, including the quantum mechanical theory of quantum confinement, multivalent interactions, redox and acid/base reactions of semiconductor surfaces, and the balance between colloidal surface properties and colloidal stability. These topics serve as the basis for many of the significant findings that are described. The first major finding is the demonstration that cation exchange between ionic nanocrystals may be used to tune the optical properties of these particles, independently from nanoparticle size. This process is controlled through the solubility of the cations and the binding strength between metals and ligands. Second, materials strain is found to vastly impact the optical and electronic properties of quantum dots. This phenomenon has not been appreciated for colloidal materials although it has been

harnessed with great success in bulk materials. Herein it is demonstrated that the optical properties of strained quantum dots can be tuned through the overgrowth of a compressive shell material. Third, implementation of amphiphilic multidentate ligands allows the reaction conditions of nanocrystals to be tuned to yield an amphibious mixture, permitting the dispersion of quantum dots in nearly any liquid medium. The broad solubility of these nanocrystals is shown to be a powerful attribute, and may allow advances not only in biomedicine, but also in solar energy conversion and catalysis.

New technologies have been developed for tuning the interactions between quantum dots and biological systems. First, the surfaces of nanocrystals have been found to largely impact their chemical and colloidal stability in solution, and have been optimized to generate nanoparticles that are essentially biologically inert. Second, conventional surface coatings are subject to a tradeoff between nanoparticle size and stability. However this compromise has been overcome through the high binding strength of multidentate and multivalent interactions, allowing the development of nanoparticles that are both small and ultrastable. Third, the nonspecific binding of nanoparticles is size-dependent, decreasing with size. This attribute has never been observed due to the inherent difficulty in preparing small nanoparticles that are especially resistant to intermolecular binding events, and was made possible with the development of multidentate coatings. Finally, new studies on the cellular toxicity of quantum dots show that these nanoparticles are subject to new rules of toxicology that cannot be explained through conventional mechanisms due to their unique structure. The traditional paradigm of heavy metal toxicity must be reevaluated in light of these studies in order to determine the true limiting properties of nanoparticles that detrimentally impact the health of cells and organisms.

1.3 References

1. Alivisatos, A. P., Gu, W. W., & Larabell, C. Quantum dots as cellular probes. *Annu. Rev. Biomed. Eng.* **7,** 55-76 (2005).

2. Smith, A. M., Duan, H. W., Mohs, A. M., & Nie, S. M. Bioconjugated quantum dots for in vivo molecular and cellular imaging. *Adv. Drug Delivery Rev.* **60,** 1226-1240 (2008).

3. Michalet, X., Pinaud, F. F., Bentolila, L. A., Tsay, J. M., Doose, S., Li, J. J., Sundaresan, G., Wu, A. M., Gambhir, S. S., & Weiss, S. Quantum dots for live cells, in vivo imaging, and diagnostics. *Science* **307,** 538-544 (2005).

4. Ruan, G., Agrawal, A., Marcus, A. I., & Nie, S. M. Imaging and tracking of Tat peptide-conjugated quantum dots in living cells: new insights into nanoparticle uptake, intracellular transport, and vesicle shedding. *J. Am. Chem. Soc.* **129,** 14759-14766 (2007).

5. Howarth, M., Liu, W. H., Puthenveetil, S., Zheng, Y., Marshall, L. F., Schmidt, M. M., Wittrup, D. K., Bawendi, M., & Ting, A. Y. Monovalent, reduced-size quantum dots for imaging receptors on living cells. *Nat. Methods* **5,** 397-399 (2008).

6. Howarth, M., Takao, K., Hayashi, Y., & Ting, A. Y. Targeting quantum dots to surface proteins in living cells with biotin ligase. *Proc. Natl. Acad. Sci. U.S.A.* **102,** 7583-7588 (2005).

7. Lidke, D. S., Nagy, P., Heintzmann, R., Arndt-Jovin, D. J., Post, J. N., Grecco, H. E., Jares-Erijman, E. A., & Jovin, T. M. Quantum dot ligands provide new insights into erbB/HER receptor-mediated signal transduction. *Nat. Biotechnol.* **22,** 198-203 (2004).

8. Dahan, M., Levi, S., Luccardini, C., Rostaing, P., Riveau, B., & Triller, A. Diffusion dynamics of glycine receptors revealed by single-quantum dot tracking. *Science* **302,** 442-445 (2003).

9. Tada, H., Higuchi, H., Wanatabe, T. M., & Ohuchi, N. In vivo real-time tracking of single quantum dots conjugated with monoclonal anti-HER2 antibody in tumors of mice. *Cancer Res.* **67,** 1138-1144 (2007).

10. Gao, X. H., Yang, L. L., Petros, J. A., Marshal, F. F., Simons, J. W., & Nie, S. M. In vivo molecular and cellular imaging with quantum dots. *Curr. Opin. Biotechnol.* **16,** 63-72 (2005).

11. Gao, X. H., Cui, Y. Y., Levenson, R. M., Chung, L. W. K., & Nie, S. M. In vivo cancer targeting and imaging with semiconductor quantum dots. *Nat. Biotechnol.* **22,** 969-976 (2004).

12. Cai, W. B., Shin, D. W., Chen, K., Gheysens, O., Cao, Q. Z., Wang, S. X., Gambhir, S. S., & Chen, X. Y. Peptide-labeled near-infrared quantum dots for imaging tumor vasculature in living subjects. *Nano Lett.* **6,** 669-676 (2006).

13. Agrawal, A., Deo, R., Wang, G. D., Wang, M. D., & Nie, S. M. Nanometer-scale mapping and single-molecule detection with color-coded nanoparticle probes. *Proc. Natl. Acad. Sci. U.S.A.* **105,** 3298-3303 (2008).

14. Han, M. Y., Gao, X. H., Su, J. Z., & Nie, S. Quantum-dot-tagged microbeads for multiplexed optical coding of biomolecules. *Nat. Biotechnol.* **19,** 631-635 (2001).

15. Sukhanova, A. et al. Nanocrystal-encoded fluorescent microbeads for proteomics: antibody profiling and diagnostics of autoimmune diseases. *Nano Lett.* **7,** 2322-2327 (2007).

16. Klostranec, J. M., Xiang, Q., Farcas, G. A., Lee, J. A., Rhee, A., Lafferty, E. I., Perrault, S. D., Kain, K. C., & Chan, W. C. W. Convergence of quantum dot barcodes with microfluidics and signal processing for multiplexed high-throughput infectious disease diagnostics. *Nano Lett.* **7,** 2812-2818 (2007).

CHAPTER 2

Semiconductor Nanocrystals and Biological Applications

Quantum dots are nearly spherical nanocrystals composed of semiconductor materials. The most fundamentally important and useful feature of these particles is their size-dependent absorption and photoluminescence. This effect was discovered in 1982 by the former Soviet scientists Alexander Ekimov and Alexei Efros,[1,2] but had been unwittingly exploited centuries earlier to add pigment to stained glasses. Understanding of the physics of these nanocrystals advanced quickly throughout the 1980's and 1990's, guided primarily by the work of Louis Brus and Paul Alivisatos,[3-9] which was aided by the colloidal synthesis developments of Brus and Moungi Bawendi.[10-12] The applications of these particles were earmarked for electrochemistry, catalysis, solar energy conversion, and light emitting devices, when, in 1998, Alivisatos and Shuming Nie simultaneously published landmark papers demonstrating the utility of these nanoparticles as fluorescence probes for bioimaging.[13,14] This finding immensely expanded interest in quantum dots, culminating in the publication of several thousand papers exploring the interface between semiconductor nanomaterials and biology/medicine over the ensuing decade. In this chapter the physical foundation for this interest is presented. First, the important physical principles of semiconductors materials are detailed (Section 2.1), and the size-dependent properties of nanocrystals are discussed (Section 2.2). The strategies used to chemically synthesize quantum dots are described (Section 2.3), and finally the relevant work in the use of these nanoparticles for biological applications is

reviewed (Section 2.4).

2.1 Semiconductor Physics

The past century has witnessed a tremendous number of theoretical and experimental advances in semiconductor physics, culminating in the production of multitude of useful electronic devices. The recent wave of interest in semiconductor nanostructures like quantum dots indicates that this trend is likely to continue. Appreciation of the novel properties of semiconductor quantum dots and their heralded potential in a diverse range of applications requires a fundamental understanding of the basic concepts central to semiconductor physics. This review of the physics of semiconductors is intended to provide a theoretical context for the research described in this thesis. Thorough explanations of solid state physics,[15] crystallography,[16,17] semiconductor physics,[18,19] quantum mechanics,[20,21] and quantum confinement[1,4,8] can be found in the literature cited herein.

2.1.1 The Electronic Bandgap. Solid state physics and materials science broadly classify solids as conductors, semiconductors, or insulators, depending on the capacity of the materials to conduct electricity at room temperature. The difference between these materials arises from the bandgap energy (E_g), which is the difference in energy between the highest occupied electronic energy level and the lowest unoccupied electronic energy level. In molecular terms, these energy levels constitute the highest occupied molecular orbital (HOMO) and the lowest unoccupied molecular orbital (LUMO), respectively. However in crystals the bonds are delocalized over a large number of atoms, such that the bonding electrons form continuous bands of allowed electronic energy, unlike the discrete energy levels of single small molecules (Figure

2.1).[1] Because of this delocalization effect, the HOMO energy levels from the atoms form the valence band, and the LUMO energy levels form the conduction band (Figure 2.2). The energy difference separating these bands is called the bandgap, a region of forbidden electronic energy within the solid. If an electron is excited, for instance via absorption of a photon of energy greater than the bandgap, or through thermal excitation, the electron enters an antibonding orbital and is free to move in the solid upon application of an electric field, thus generating current. For a metal, the HOMO and LUMO energy levels are either zero or smaller than kT, and thus conduction occurs readily with the application of an electric field. For insulators, this energy gap is large (typically >3 eV)[2], such that conduction does not occur under normal conditions. Between these two extremes, semiconductors have energy gaps that are small enough to allow room temperature conduction, but large enough that the magnitude of conduction can be largely controlled by a host of useful intrinsic and extrinsic factors, such as doping, the presence of a magnetic field, material strain, or incident light. This useful capacity to modulate conduction is the root of the wide-ranging utility of semiconductors, and is responsible for intense development of many electronic devices in the past century.

[1] For this discussion, we will only consider crystalline materials, although amorphous solids have been produced that fall under all three classifications of insulators, semiconductors, and metals.

[2] Thermal excitation of electrons to the conduction band is dictated by Fermi-Dirac statistics, for which the probability of an electron filling the conduction band at temperature T is

$$P \approx e^{-E_g/(2kT)}$$

Therefore, an insulator can be defined by E_g > ~3 eV, for which there are essentially zero excited state electrons in a cubic centimeter of material at room temperature.

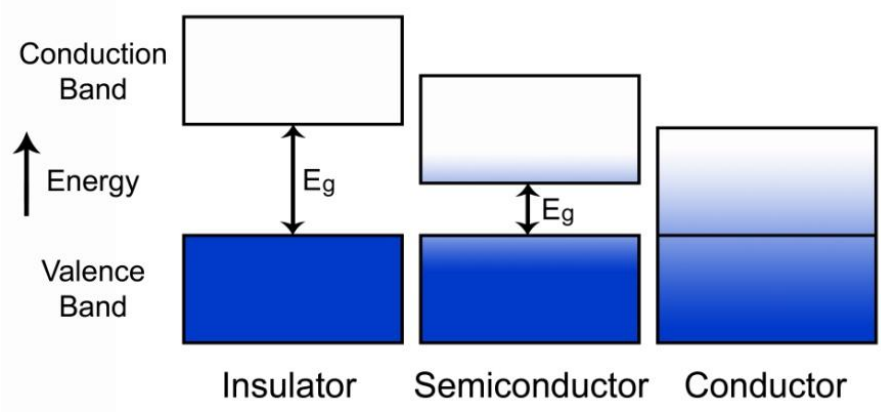

Figure 2.1: Diagram of electronic energy bands in solid-state materials. Occupation of electronic energy levels by electrons is denoted by blue shading, and E_g is the separation between the conduction and valence energy bands.

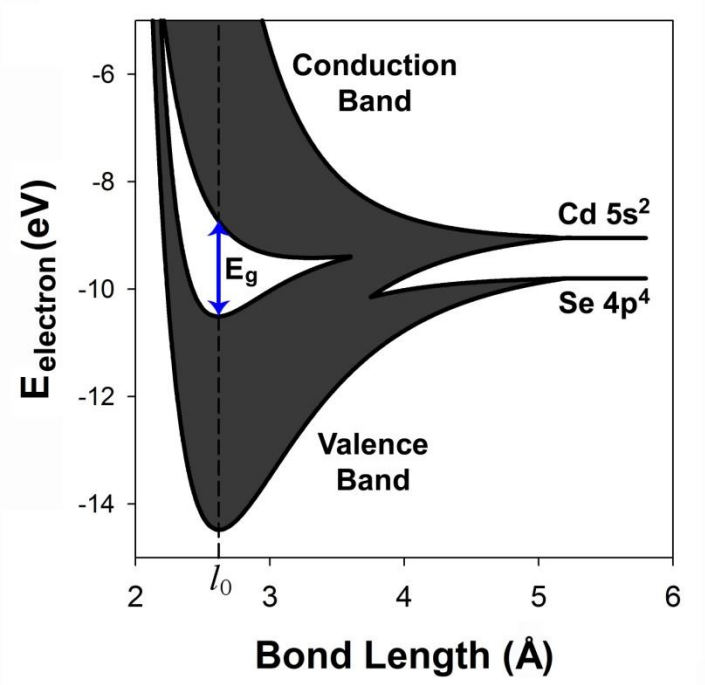

Figure 2.2: Molecular orbital description of bonding in the semiconductor CdSe. The right side of this diagram depicts the valence electron energy levels of individual cadmium (5s) and selenium atoms (4p). When these atoms are assembled together in a lattice, the valence electrons interact, causing the degenerate energy levels of the electrons to split and form wide energy bands. Bonding electrons decrease in energy, contributing to the stability of the crystal. At the equilibrium bond length (l_O, 2.62 Å for CdSe) there is a balance between the attractive forces of the electrons and nuclei and the repulsive forces between nuclei and between electrons. The energy separation between the HOMO and the LUMO is E_g (1.76 eV for CdSe). This simplified diagram

does not depict significant contributions from the d orbitals of either atom or from s orbitals of selenium.

2.1.2 Absorption and Luminescence. The bandgap energy of semiconductors spans a technologically useful range of the electromagnetic spectrum, from the near-ultraviolet, throughout the visible spectrum, and into the infrared. When a photon of light with energy greater than E_g is illuminated on a semiconductor material, the electrons in the material can absorb the photon to transition to a higher electronic energy level, resulting in an excited state electron (Figure 2.3). As previously mentioned, this electron (e^-) is promoted to the antibonding conduction band, and is thus no longer fixed in place in a bond. Excitation of the electron leaves an empty bonding orbital in the valence band, which behaves like a particle of positive charge, called the hole (h^+). With an applied voltage, the electron and hole can migrate in opposite directions to produce a current. If the energy of the excitation photon is significantly greater than the bandgap, the electron and hole will retain excess kinetic energy which will be quickly dissipated to lattice vibrations, stabilizing the energy of the electron and hole at the band edges in a process called relaxation. This relaxation process is highly efficient and rapid due to the nearly continuous electronic energy level spacings in the valence and conduction bands, transferring many small quanta of energy to optical or acoustic phonons (see discussion on indirect bandgaps below). At this point, the charge carriers can recombine and annihilate one another in the process of radiative recombination, or luminescence. The potential energy lost in this process is transferred to a single photon with energy equal to E_g. In this mechanism, it is important to note that a wide range of wavelengths of light are capable of exciting the semiconductor electrons due to the wide electron bands, but luminescence emission occurs at a single wavelength of light.

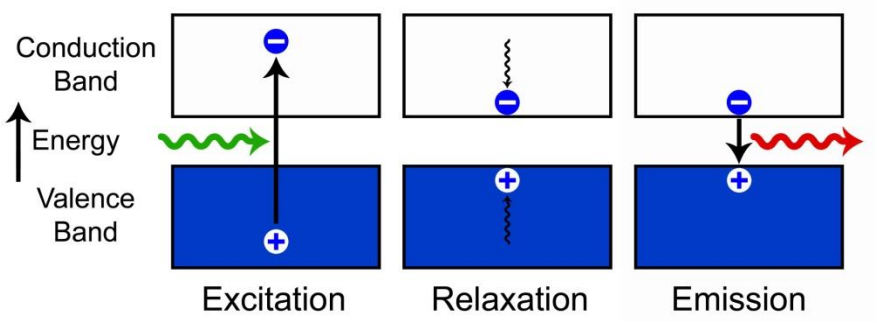

Figure 2.3: Electronic transitions in a semiconductor. On the left, an electron in the valence band absorbs a photon (green), exciting it to the conduction band, and leaving a positively charged hole in the valence band. The electron and hole quickly lose their excess kinetic energies through dissipation to lattice vibrations, settling at the band edges in a process called relaxation. The electron and hole can then radiatively recombine in a process that yields the emission of a single photon (red) with energy equal to the bandgap energy.

2.1.3 Direct and Indirect Bandgaps. In bulk solid state semiconductors, the valence and conduction energy bands are each continua of allowed electronic energy levels, however specific combinations of electronic energy and momentum are forbidden. The relationship between electron energy (E) and crystal momentum ($\hbar k$) is graphically represented in the electronic band structure of a material in an E-k diagram (Figure 2.4). The parameter **k** is the wave vector of the electron in the periodic crystal potential, and its magnitude is inversely related to its wavelength ($k = 2\pi/\lambda$). The crystal momentum is therefore a superposition of the momentum of an electron and the crystal, which is dependent on direction within the crystalline lattice, due to the directional dependence of the periodicity of the crystal potential. Typically, a band structure diagram will depict the energy levels of electronic energy bands along the high symmetry directions of the crystalline lattice. For cubic and wurtzite crystals, these directions are catalogued in Table 2.1 for the first Brillouin zone, which is a primitive cell of the crystalline lattice in reciprocal space and is representative of the symmetry of the entire lattice.

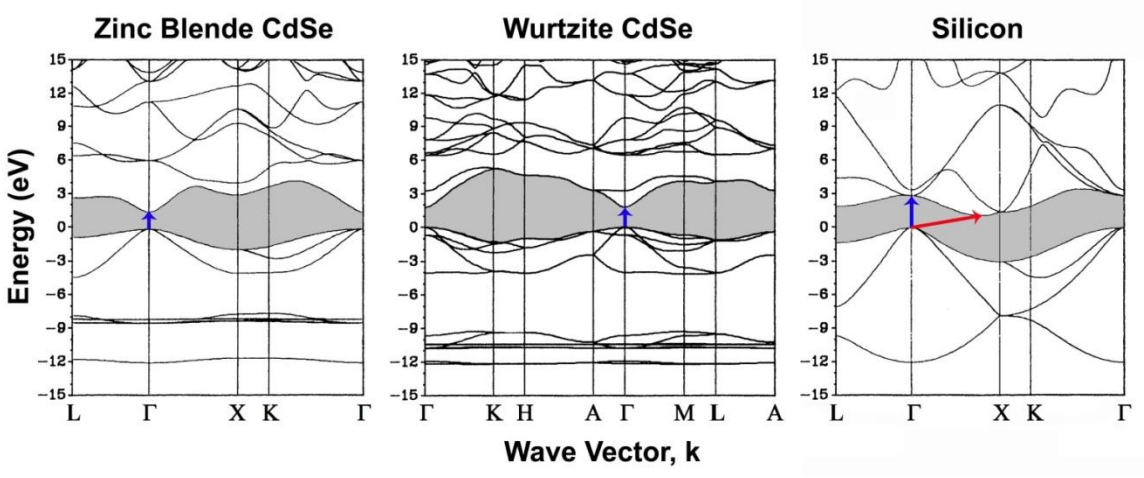

Figure 2.4: Band structures of semiconductors. These E-k diagrams were calculated using the local density approximation, and reproduced from the work of W.Y. Ching.[22,23] Forbidden energy levels within the bandgap are shaded, and the valence band edge is normalized to an energy of 0 eV. Direct band-edge transitions are depicted in blue. The band structure of CdSe is depicted for two crystal structures, zinc blende (left) and wurtzite (middle). Both of these structures are 4-coordinate and the electronic energy levels are therefore similar for both structures. The similarity between these structures is reflected in comparable bandgaps and similar electronic energies at corresponding points in the first Brillouin zone, despite a lower symmetry in the wurtzite structure. The band structure of silicon (diamond lattice structure, right) is also depicted, showing that the conduction band edge is shifted in k-space with respect to the valence band edge. Therefore band-edge transitions can only occur with phonon assistance (red). The smallest direct band gap, indicated in blue, is significantly larger than the indirect bandgap, and determines the major onset of absorption.

Table 2.1: Nomenclature for reciprocal lattice directions of high symmetry in the first Brillouin zone (1BZ) of zinc blende, diamond, and wurtzite crystal structures.

Wurtzite		Zinc Blende/Diamond	
1BZ direction[a]	Lattice direction	1BZ direction[a]	Lattice direction
Γ–Δ–A	[0001]	Γ–Λ–L	[111]
Γ–T–K	[11$\bar{2}$0]	Γ–Σ–K	[110]
Γ–Σ–M	[10$\bar{1}$0]	Γ–Δ–X	[010]
A–S–H	[11$\bar{2}$0]		
K–P–H	[0001]		
M–U–L	[0001]		
A–R–L	[10$\bar{1}$0]		

[a] Directions between 1BZ points (Roman letters; e.g. A, X) along straight lines (Greek or Roman letters; e.g. Δ, P). The zone center is the point Γ.

A direct bandgap semiconductor is one in which the maximum of the valence band energy occurs at the same crystal momentum as the minimum of the conduction band energy. Such is the case for CdSe, depicted in Figure 2.4, for which transitions may occur between the conduction and valence band edges without a change in crystal momentum. However optical transitions that change crystal momentum are complicated by the requirement for conservation of total momentum, as described by the following equations.

$$\text{Absorption: } \hbar k_c - \hbar k_v = \hbar k_{photon} \qquad \textbf{Equation 2.1}$$

$$\text{Emission: } \hbar k_c - \hbar k_v = -\hbar k_{photon} \qquad \textbf{Equation 2.2}$$

Therefore the absorption or emission of a photon by a semiconductor must conserve a change in crystal momentum between the valence band (v) and the conduction band (c). Importantly, the momentum of a photon is generally several orders of magnitude less than that of the crystal momentum (k_c, $k_v >> k_{photon}$), such that this optical transition requires

$$k_c \approx k_v \qquad \textbf{Equation 2.3}$$

Therefore absorption and emission can only readily occur when momentum is internally conserved, that is, for vertical transitions on the E-k diagram. In a direct bandgap semiconductor, this requirement is fulfilled for band-edge absorption and emission, as the relaxed electron and hole both have essentially the same crystal momentum.

A major consequence of this selection rule is that band edge transitions are optically forbidden if the conduction and valence band edges do not coincide in k-space. This is the case for indirect bandgap semiconductors such as silicon (Figure 2.5). For indirect bandgap materials, band-edge absorption and emission are both highly inefficient, justifying why intrinsically direct bandgap semiconductors are ubiquitously used for

optoelectronic devices such as photodetectors and light emitting diodes.[3] Band-edge absorption and radiative recombination may proceed in indirect bandgap materials, but only with assistance from a phonon. A phonon is a quantum of lattice vibration, which may be either optical or acoustical. Phonons are diffracted by the same lattice potential as the electrons, and therefore their wave vectors coincide in k-space. Thus the creation or annihilation of a phonon may allow band-edge absorption or emission to occur, although this transition is of low probability.

$$k_c - k_v = \pm k_{photon} \qquad \textbf{Equation 2.4}$$

The energy of a phonon is typically much smaller than that of a photon, and this inefficient transition may occur with a change in energy essentially equal to the photon energy alone. This indirect transition is analogous to the process of phosphorescence in small molecules, in which a reversal of the spin of an excited state electron results in a triplet excited state with optically forbidden recombination. Although the physical mechanisms are unrelated, both phosphorescent materials and indirect bandgap semiconductors are characterized by very long excited state lifetimes and generally have low radiative emission efficiencies.

2.1.4 Effective Mass. The effective mass approximation independently describes the electrons and holes as if they are free, unbound particles in a vacuum, except their masses are altered by the crystal field. These 'effective' masses can be calculated from the quantum mechanical definition of kinetic energy (E) of a particle of mass m:

$$E = \frac{\hbar^2 k^2}{2m} \qquad \textbf{Equation 2.5}$$

Because the dispersion relationship between E and k is known from the band structure dispersion curve (Figure 2.4), one can readily calculate the mass of an electron for each

[3] Extrinsic, doped semiconductors are also used, but are not discussed in this work.[18,24]

value of E and k. The band edges of semiconductors are the regions of greatest interest, and over a small range of E and k they may be adequately approximated as a parabolic function, such that the effective mass is constant:

$$\frac{1}{m^*} = \frac{1}{\hbar^2}\frac{d^2E}{dk^2} \qquad \textbf{Equation 2.6}$$

Therefore close to the band edges, the electron and hole behave as particles of fixed mass, m_e^* and m_h^*, which are typically expressed as fractions of the mass of a free electron (e.g. $m_e^* = 0.119\ m_o$ and $m_h^* = 0.570\ m_o$ for CdSe, where $m_o \approx 9.11 \times 10^{-31}$ kg). This relation demonstrates that the effective mass of a charge carrier in a semiconductor is related directly to the curvature of the electronic energy band. This approximation is useful for describing the properties of semiconductors, but is only accurate when charge carriers exist only with low kinetic energies, roughly < ~0.5 eV for II-VI semiconductors. For most semiconductors, the curvature of the valence band is much smaller than that of the conduction band, meaning that the hole is substantially heavier than the electron. As a result, electrons have a higher mobility than holes, and as such are often favored as the primary charge carriers in devices. As well, because the wave vector is dependent on the direction within the crystalline lattice, the effective mass is an anisotropic property, and even materials with high crystalline symmetry show anisotropy in charge mobility. It should be noted that in crystalline materials, the delocalization of a large number of electron wavefunctions over a large number of atoms results in negligible atomic reorganization upon excitation, in stark contrast to dyes and other organic pi-conjugated systems, which show much lower charge carrier mobilities.[25]

2.1.5 Excitons. In a semiconductor, the electron and hole generated through excitation are electrostatically attracted to one another. Analogous to a hydrogen atom containing a single proton and electron, this pair of particles is collectively called the exciton, which

has an effective size and binding strength characteristic of the crystal field in which it is dispersed. The binding energy is determined by the following equation

$$E_B = -\frac{\mu e^4}{2\hbar^2(4\pi\varepsilon_o\varepsilon_s)^2} \qquad \textbf{Equation 2.7}$$

where μ is the reduced mass of the optical electron and hole masses, e is the elementary charge, ε_o is the permittivity of vacuum, and ε_s is the static dielectric constant of the semiconductor. The exciton size is dictated by the Bohr exciton radius, which is described as

$$a_B = \frac{\hbar^2 4\pi\varepsilon_o\varepsilon_s}{\mu e^2} \qquad \textbf{Equation 2.8}$$

Therefore, the exciton binding energy and the size are determined solely by the effective masses of the charge carriers and the polarizability of the crystal (i.e. the dielectric constant). The exciton is smaller and more strongly bound when the effective masses are larger and the crystalline matrix is less electrically screening (smaller dielectric constant).

2.1.6 Semiconductor Materials. Solid state semiconductors can have a wide range of materials compositions. The most commonly encountered and often studied semiconductors include three elemental materials (diamond, silicon, and germanium) and an assortment of binary semiconductors, including IV compounds (e.g. SiGe), III-V materials (e.g. InAs), II-VI materials (e.g. CdSe), IV-VI materials (e.g. PbSe), and II-V materials (e.g. Cd_3P_2). Many other binary semiconductors exist, and the compositional variety of these materials expands as they are mixed together as ternary (e.g. $In_xGa_{1-x}As$) and quaternary alloys (e.g. $In_xGa_{1-x}As_yP_{1-y}$). Bandgap engineering is the process of precisely modulating the bandgap of a material through its composition (Figure 2.5). The capacity to independently tune the bandgap of ternary and quaternary alloys without

significantly altering the bond length has been instrumental in producing highly efficient optoelectronic devices and electronics. The materials properties of alloys are often found to vary linearly with composition, in accord with Vegard's Law. This can be expressed mathematically for a ternary alloy $A_xB_{1-x}C$ as

$$a_{A_xB_{1-x}C} = a_{AC}x + a_{BC}(1-x) \qquad \textbf{Equation 2.9}$$

where α is any property of the material, such as the lattice constant or the bandgap energy. Deviations from Vegard's Law can often be modeled with the introduction of a bowing parameter constant, b:

$$a_{A_xB_{1-x}C} = a_{AC}x + a_{BC}(1-x) - bx(1-x) \qquad \textbf{Equation 2.10}$$

Most notably, the optical bowing of the E_g has been described for many ternary semiconductors. This deviation from linearity has allowed the preparation of semiconductor alloys such as $CdSe_yTe_{1-y}$ with a longer wavelength emission (smaller bandgap) than either of the binary materials (Figure 2.5).

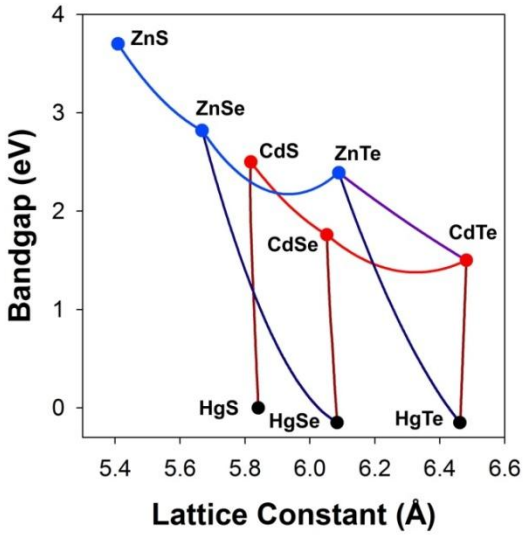

Figure 2.5: Bandgap engineering with II-VI semiconductors. The bandgaps and lattice constants are depicted for cubic zinc chalcogenides (blue), cadmium chalcogenides (red), and mercury chalcogenides (black), and some of their homogeneous alloys (lines). The II-VI oxides are also semiconductors but their intrinsic

use in bandgap engineering is currently complicated by the difficultly of manufacturing oxide alloys and because CdO and HgO crystallize in anomalous lattice structures (rock salt and orthorhombic, respectively). As well, HgO is an indirect semiconductor.

2.1.7 Chemical Trends. The relationship between the chemical identity of a material and its bandgap energy is highly complex and poorly understood. The bandgap energy is indicative of the strength and nature of bonding within the solid material, the atomic numbers of the atoms, and the crystalline lattice structure. The use of band structure modeling has significantly enlightened the current understanding of the origin of the bandgap in semiconductor materials, and some chemical trends have emerged. This section will primarily focus on trends in the II-VI sulfides (ZnS, CdS, HgS), selenides (ZnSe, CdSe, HgSe), and tellurides (ZnTe, CdTe, HgTe), which are direct bandgap structures, and crystallize in the 4-coordinate zinc blende (cubic) or wurtzite (hexagonal) phases under standard conditions. The fundamental understanding of the bonding within these materials (Figure 2.2) revolves around the notion that the valence s-electrons from the metal atom (e.g. Cd-$5s^2$) and the valence p-electrons from the chalcogen (e.g. Se-$4p^4$) are primarily responsible for bonding. These electrons, along with promoted s-electrons from the chalcogen, generate sp^3 hybridized molecular orbitals to yield tetrahedral bonding. As the chalcogens all have greater electronegativity than the metal atoms, the bonding molecular orbitals will have greater electron density on the chalcogens, and thus they are referred to as the anions (S^{-2}, Se^{-2}, Te^{-2}), and the metals are referred to as the cations (Zn^{+2}, Cd^{+2}, Hg^{+2}). However, the proportion of ionic, covalent, and metallic contributions to bonding are different for each distinct compound. The nature of these bonding contributions dictates the electron wavefunctions in the material, and therefore determines the materials properties.

Figure 2.6A demonstrates that the bandgap of II-VI semiconductors decreases as the molecular weight increases when varying the cation or anion independently. Although this is a common trend among nearly all types of semiconductor materials, it is deeply convoluted with many other interrelated factors. This molecular weight relationship manifests itself in the nature of bonding and the bond strength, which increases as the molecular weight decreases due to a decrease in bond length. This decrease in bond length increases the strength of covalent bonds by stabilizing internuclear bonding electrons, and strengthens ionic bonds by increasing the coulombic interaction between ions. As seen in Figure 2.6B, an increase in bond strength results in an increase in the bandgap. From a molecular orbital perspective, this trend is logical because a greater bond strength is indicative of a greater stabilization of the bonding orbitals (HOMO) and, likewise, a greater destabilization of the antibonding orbitals (LUMO), which would result in a wider bandgap. However, the nature of this change in bonding is more complex. From a simplistic perspective, one can calculate the ionicity of these compounds using various thermochemical or theoretical scales (Figure 2.6C) to determine that increasing the atomic weight of the anion consistently decreases the bandgap of the material. This would suggest that the decrease in bandgap as the chalcogen atomic number is increased (S→Se→Te) stems from a decrease in ionicity of the bond. Thereby, when the chalcogen atomic number increases, the difference in energy between the valence electron orbitals of the constituent atoms decreases, thus decreasing the ionicity and closing the HOMO-LUMO gap.

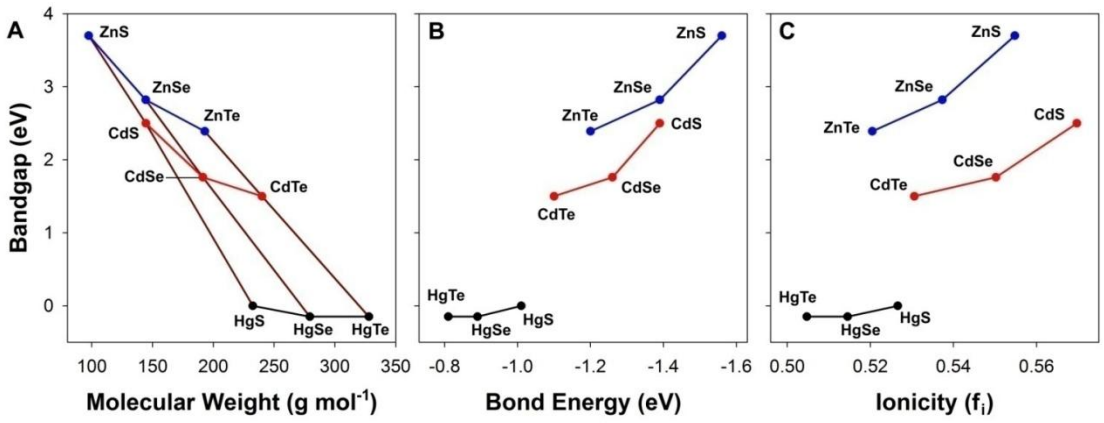

Figure 2.6: Dependence of the bandgap of II-VI semiconductors on the molecular weight, bond energy, and ionicity. The chalcogenides of zinc (blue), cadmium (red), and mercury (black) are depicted. Lines are drawn to guide the eye, and are not indicative of alloyed compositions. (A) The bandgaps of the semiconductors are plotted against their molecular weight. (B) The relationship between the bandgap energy and the energy per bond is depicted. The bond energy was calculated from previously published thermochemical data.[26,27] (C) The relationship between the bandgap and ionicity is depicted. The ionicity was calculated by the method of Pauling,[4] although trends are similar when plotted against the Phillips ionicity or the Szigeti charge.[28-32]

Increasing the atomic number of the cation (Zn→Cd→Hg) results in a greater decrease in the bandgap compared to the effect of the anion (Figure 2.6A), but this effect has no consistent correlation with ionicity of the bond (Figure 2.6C). Figure 2.7A shows the bond energy plotted against molecular weight of the semiconductor, revealing a nearly linear relationship. Therefore it is clear that the disproportionate cationic contribution to the bandgap is not indicative of a significantly greater contribution to the bond strength. Without any evidence of a contribution from the bonding nature or bond strength to this interesting effect, it is apparent that this other factors must be accounted for in this

[4] The Pauling ionicity (f_i) was calculated using the formula

$$f_i = 1 - \frac{N}{M} e^{-\frac{1}{4}(X_A - X_B)^2}$$

where N is the valence for the $A^N B^{8-N}$ material (e.g. 2 for $A^{II}B^{VI}$ or II-VI materials, and 3 for III-V materials), M is the coordination number of the crystal (4 for zinc blende and wurtzite structures), and X is the electronegativity of the isolated atoms A or B, which was calculated from the atomic ionization energies and electron affinities by the method of Milliken.

simple model. *Ab initio* models have shown that d-orbitals of the cations, despite being significantly lower in energy than the valence band maximum, can interact with the p-orbitals of the anions with a net repulsion to increase the valence band maximum.[33,34] This effect would be expected to magnify with increasing cation atomic number due to an increase in the associated d-orbital energy and delocalization, thus correlating with the trend described herein. Therefore this simple cation/conduction band, anion/valence band theory can only superficially predict the properties of some semiconductors, and it ignores relevant contributions of each atom to both bands.

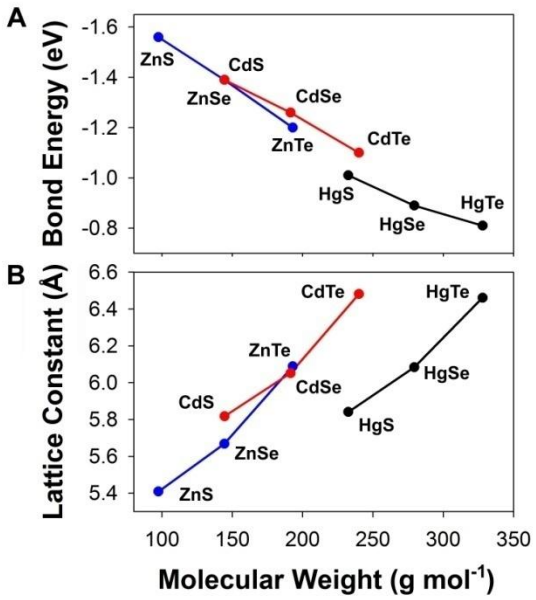

Figure 2.7: Relationship between the bond energy, lattice constant, and molecular weight of II-VI semiconductors. (A) The bond energy and molecular weight are nearly linearly related for all II-VI materials. (B) The lattice constant is highly anomalous for mercury chalcogenides.

It should also be noted that the bandgaps of mercury chalcogenides are almost entirely unaffected by a change in the atomic number of the anion (Figure 2.6). This observation is not only due to the very high energy of the mercury 5d electrons, which attenuates the effects of the HOMO of the anion through strong repulsion, but also because of the

unique chemistry of mercury itself.[35] Mercury is uncharacteristically compact in electron density due to the effects of special relativity (Figure 2.7B). This results in a decrease in the energy of the electron energy levels. As the 6s electrons are abnormally deep, and the 5d electrons increase the anion energy levels, the conduction band of mercury chalcogenides is very low and the valence band is high. In fact, the conduction band and valence bands overlap in energy, resulting in the semimetallic nature of these materials, which have strong conductivity most temperatures.

It is possible to extrapolate these concepts to other semiconductor groups, such as the less ionic III-V materials (e.g. InAs, GaP) and purely covalent IV elemental semiconductors (e.g. Si, Ge), which also crystallize preferentially in four-coordinate lattices. Using the aforementioned logic, it should be no surprise that the more covalent III-V materials have smaller bandgap energies than II-VI materials for comparable bond strengths (Figure 2.8). As well, the bandgaps of purely covalent IV materials are even smaller. Indeed this systematic decrease in ionicity and increase in covalency is readily observed to close the bandgap, as predicted from the II-VI trends. For example, the bond strengths of ZnS, InAs, and α-Sn are nearly identical (~-1.56 eV per bond), but their bandgaps decrease greatly with increasing covalency, from 3.7 eV for ionic ZnS (f_i = 0.555) to -0.413 eV for α-Sn (f_i = 0).

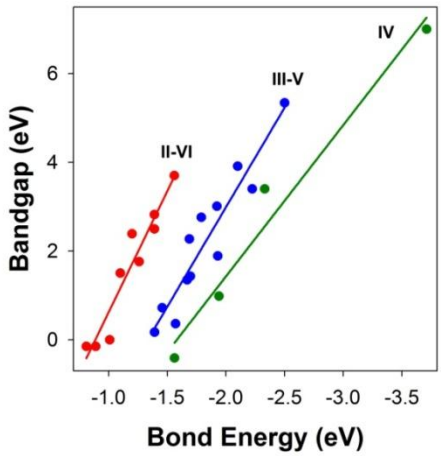

Figure 2.8: Relationship between the bandgap and bond energy for three families of semiconductors. The ionicity of the materials increases in the order IV < III-V < II-VI.

Similar trends are observed within the III-V group compared to the II-VI materials in terms of bandgap dependence on molecular weight, bond strength, and ionicity (Figure 2.9).[36] Like the II-VI materials, the ionic character of the bond is intimately linked to the bandgap. However, unlike the II-VI materials, changing the cation has almost no effect on the bond ionicity, but significantly impacts the bond strength. For this group, the trends are much more linear, as the d-orbitals in the III-V materials are lower in energy, and therefore do not significantly impact the band-edges. A slight deviation from linearity is found for the III-V nitrides, which are highly ionic and have uncharacteristically short bonds (Figure 2.10A). This disparity is due to the lack of repulsive d-orbitals in nitrogen, resulting in a very low valence electron energy, as indicated by a high ionization energy (Figure 2.10B), resulting in a small atomic radius and a high electronegativity, and thus a higher molecular ionicity. Further comparison of these trends with the more ionic IV-VI materials is complicated by the fact that these materials typically crystallize in the 8-coordinate rock salt lattice structure, and only three of these materials (PbS, PbSe, and PbTe) have been extensively studied.

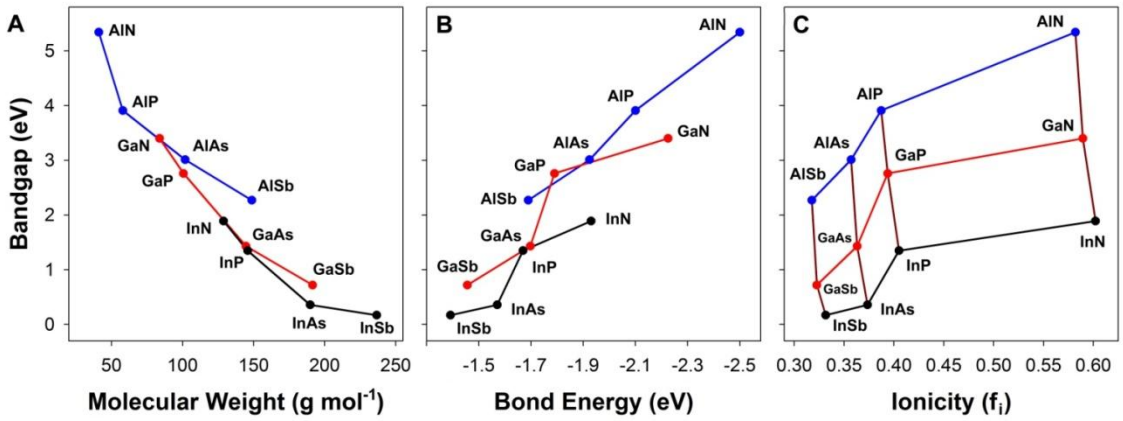

Figure 2.9: Relationship between the bandgap and the molecular weight, bond energy, and ionicity of III-V semiconductors. Lines are drawn between materials with the same cation, and do not indicate alloy compositions. (A) The bandgaps of the semiconductors are plotted against their molecular weight. (B) The relationship between the bandgap energy and the energy per bond. (C) The relationship between the bandgap and ionicity, calculated using the method of Pauling. Importantly, four of these materials are indirect bandgap semiconductors (AlP, AlAs, AlSb, and GaP). All bandgaps correspond to the lowest energy direct transition from the valence band-edge, i.e. the Γ-valley transition (Figure 2.4). Use of the lowest indirect band-edge revealed similar trends (not shown). It is noteworthy that the bandgap of InN is currently under debate.[37,38]

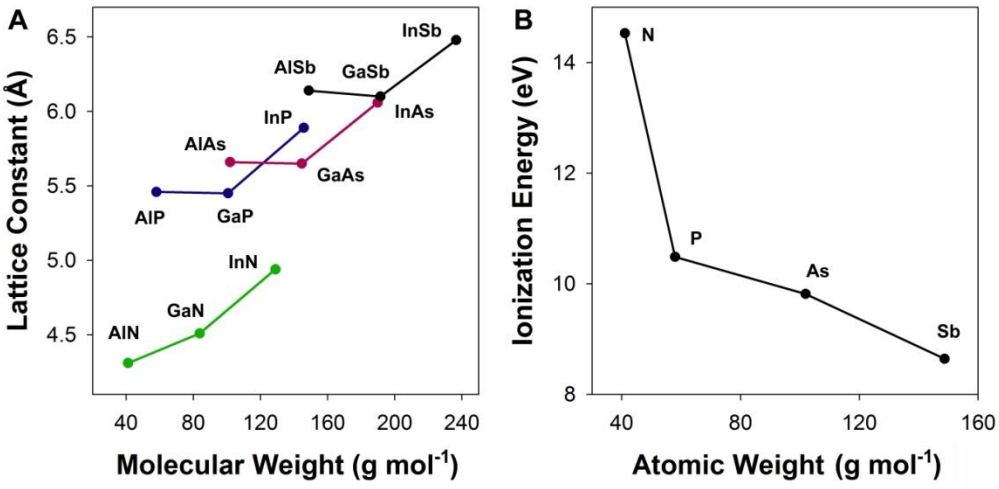

Figure 2.10: The anomalous chemical nature of the III-V nitrides. (A) Relationship between the lattice constants of III-V materials and their molecular weights, demonstrating the abnormally small bond length of the nitrides (green). (B) The ionization energy of nitrogen is much higher than that of the other group V atoms, relative to standard atomic weight.

2.1.8 Band Offsets. The relative energy levels of the valence bands and conduction bands between different semiconductors are known as the band offsets. These are crucial parameters for designing junctions between semiconductors (heterojunctions) for use in electronic devices. These values are notoriously difficult to determine experimentally, varying widely between experimental techniques, and sample preparations, and therefore theoretical estimations have become essential. Figure 2.11 shows the relative band alignments of most of the II-VI and III-V semiconductors calculated from first principles.[34] In practice, real heterojunctions in which the lattice constants are dissimilar (strained heterojunctions), often behave as if they have band offsets vastly different from these predictions, due to interfacial defects that form at the strained interface. In fact, the effects of strain, band offsets, and defect formation are complexly interwoven, and become valuable tools for bandgap engineering on the nanoscale, as examined in Chapter 4.

.

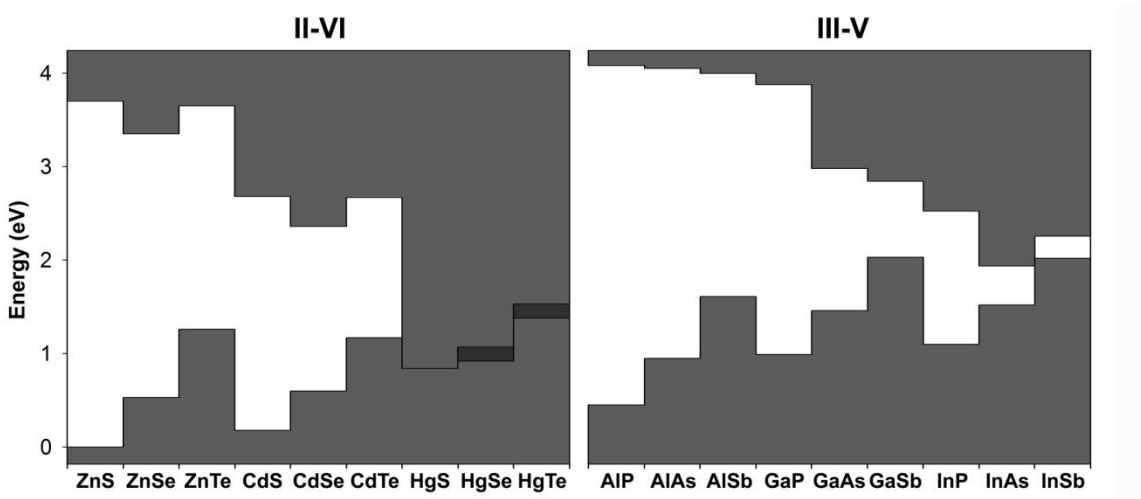

Figure 2.11: Band alignments of II-VI and III-V semiconductors.[34] Materials are organized according to the cation, and the conduction bands and valence bands are shaded. Bandgaps are shown in white and energies are given as relative values. The overlap between the two bands is shown as darker shading for the semimetals HgSe and HgTe. Note that many of the chemical trends described in Section 2.7 are reflected in these calculated band offsets.

2.2 Physics of Semiconductor Nanocrystals

The understanding of a crystalline material as a nearly infinite lattice of atoms bonded together by electrons shared across the atomic network has proven to be a compelling theoretical framework for understanding the properties of semiconductors and predicting their behavior. As described above, the development of continuous electronic bands, the presence of a forbidden bandgap, as well as the theory of effective masses of the charge carriers all depend on the crystal periodicity and electron wavefunctions within the infinite lattice. Therefore it should be no surprise that if this periodicity is disrupted by cutting the crystal, the materials properties will be significantly altered near the exposed lattice facet. If this crystal is cleaved or etched away to a small enough size, it should be expected that the properties of the crystal will be significantly altered from that of the bulk, macroscopic crystal. This is indeed the case, and the optical properties and many physical properties of semiconductors are vastly different for nanocrystals.

2.2.1 Quantum Confinement. The first excited state of a semiconductor is the exciton state, in which an electron-hole pair is coulombically stabilized. The exciton state has a fundamental unit of length dictated by its Bohr radius, which can assume a value less than 1 nm diameter to over 100 nm, depending on the material. Therefore if the dimensions of the semiconductor crystal are on the nanometer scale, the electronic properties of a semiconductor can significantly differ from those of the bulk crystal. When a crystal is shrunk to a size similar to the Bohr diameter, the exciton becomes highly localized in space in the crystal. Similar to the classic example in quantum mechanics of a 'particle in a box,' the lowest energy state of the exciton (particle) will increase if the semiconductor nanocrystal (box) shrinks. This 'quantum confinement effect' results in an increase in energy required to create the exciton and an increase in energy generated when the electron and hole recombine, i.e. an increase in the

bandgap. This effect is illustrated by the characteristic blue-shift of the absorption and luminescence spectra (Figure 2.12) for semiconductors nanocrystals near or smaller than the size of the exciton.

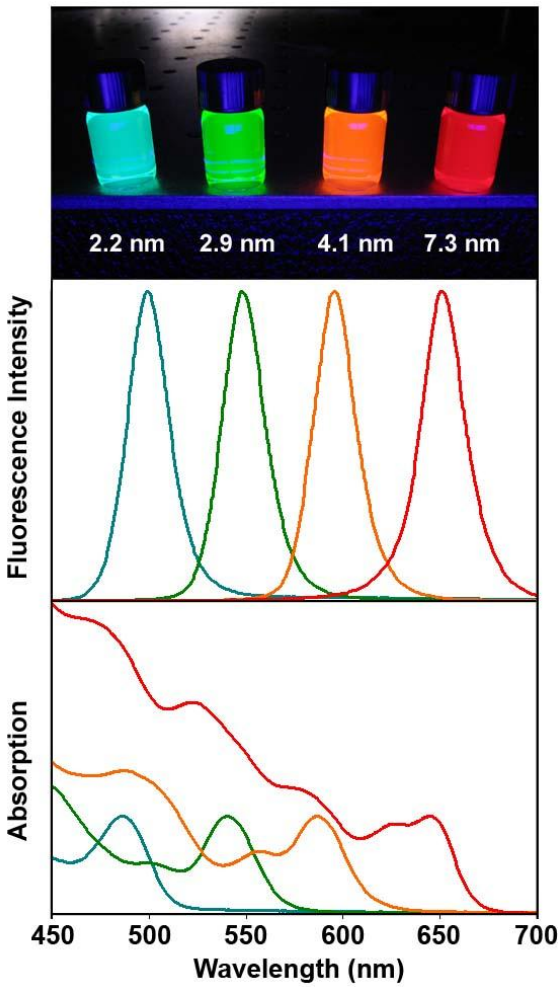

Figure 2.12: Quantum confinement of semiconductor nanocrystals. These CdSe particles are smaller than the Bohr diameter (9.6 nm) and dispersed in chloroform. (A) The dependence of the bandgap energy on nanocrystal size is readily evident from the color of fluorescence upon ultraviolet excitation. Quantum confinement results in a blue-shift (an increase in energy) of the fluorescence wavelength (B) and the absorption spectra (C) compared to bulk CdSe, which has a bandgap of 1.76 eV (704 nm). The discrete, narrow electronic transitions observed in the optical spectra are indicative of highly monodisperse samples.

The quantum confinement effect can also be rationalized from a molecular perspective. When several atoms constituting a semiconductor material bond together, their degenerate energy levels will split in accord with the Pauli exclusion principle. As more and more atoms are added to this cluster, the degeneracy of all of these energy levels continue to split, forming more electronic energy states that occupy a wider range of energies. Therefore both the HOMO and LUMO bands widen and fill in with energy states, causing the separation between these bands to decrease, yielding a smaller bandgap as the cluster grows in size. Before bands of continuous energy have formed, discrete electronic levels exist, which are readily apparent in the discrete electronic transitions observed in the absorption spectra (Figure 2.12C). These transitions are analogous to those observed for individual atoms in the gas phase, which is why semiconductor nanocrystals have been dubbed 'artificial atoms.'

The most important consequence of the quantum confinement effect is the size dependence of the bandgap for nanocrystalline semiconductors. By confining the exciton of a semiconductor, the bandgap may be tuned to a precise energy depending on the dimensionality and degree of confinement.[39-41] If the exciton is confined in one dimension, it is known as a 'quantum well,' which is equivalent to a two-dimensional thin film with pseudo-infinite width. Confinement in two dimensions yields a one-dimensional quantum wire. Confinement in all three dimensions yields a quantum dot, which is quantum mechanically a zero-dimensional particle. Accordingly, the deviation of the optical properties of these confined structures from the bulk optical properties is strongly related to the degree of confinement. That is, when more dimensions are confined, the bandgap of a semiconductor will shift to a greater extent with dot > wire > well (Figure 2.13).

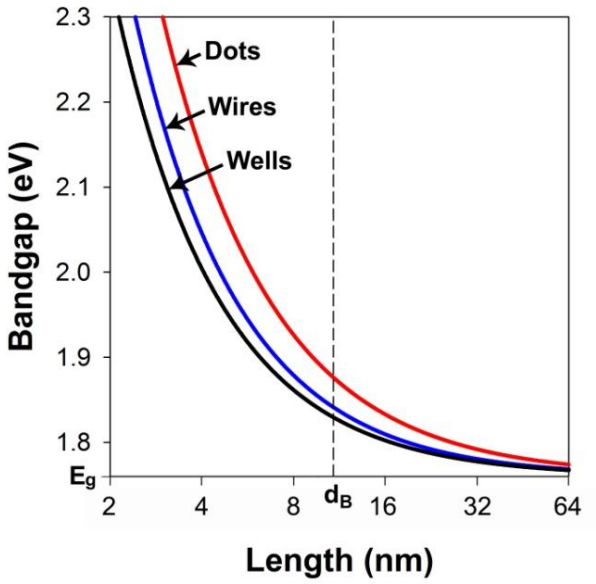

Figure 2.13: Quantum confinement in CdSe quantum wells, wires, and dots. The bandgap of these structures is plotted against the length of the confined dimensions. The bulk energy gap of CdSe (1.76 eV) is noted on the bandgap-axis, and the diameter of the exciton is noted on the length-axis (9.6 nm). Values are a combination of empirical data and theoretical extrapolations.[4,41-45]

2.2.2 Brus Model of Quantum Confinement. The range of bandgap tunability by size is determined largely by the bulk bandgap of the semiconductor and the exciton size of the material (Figure 2.14). A simplistic expression describing this phenomenon was first developed by Brus:[4]

$$\Delta E = \frac{\hbar^2\pi^2}{2r^2\mu} - \frac{1.8e^2}{\varepsilon_\infty r} + \frac{e^2}{r}\overline{\sum_{n=1}^{\infty}\alpha_n\left(\frac{S}{r}\right)^{2n}} \qquad \textbf{Equation 2.11}$$

where ΔE is the change in bandgap due to quantum confinement, r is the radius of the spherical nanocrystal, μ is the reduced effective mass of the electron and hole, e is the elementary charge, ε_∞ is the high-frequency dielectric constant of the semiconductor, S is a position inside the nanocrystal, and α_n is

$$\alpha_n = \frac{\left(\frac{\varepsilon_\infty}{\varepsilon_m} - 1\right)(n+1)}{\varepsilon_\infty\left(\frac{\varepsilon_\infty}{\varepsilon_m}n + n + 1\right)} \qquad \textbf{Equation 2.12}$$

where ϵ_m is the dielectric constant of the medium. The bar over the third term in Equation 2.11 denotes averaging of the sum over the lowest energy S wavefunction Ψ_1 for a particle in a sphere:

$$\Psi_n(r^*) = \frac{C_n}{r^*} \sin\left(\frac{n\pi r^*}{r}\right) \qquad \textbf{Equation 2.13}$$

where $C_1 = 1$. Figure 2.14 shows the size-dependent bandgaps calculated from this model for most of the II-VI materials. The calculated onset of the quantum confinement effect corresponds well with that predicted from the Bohr exciton diameter.

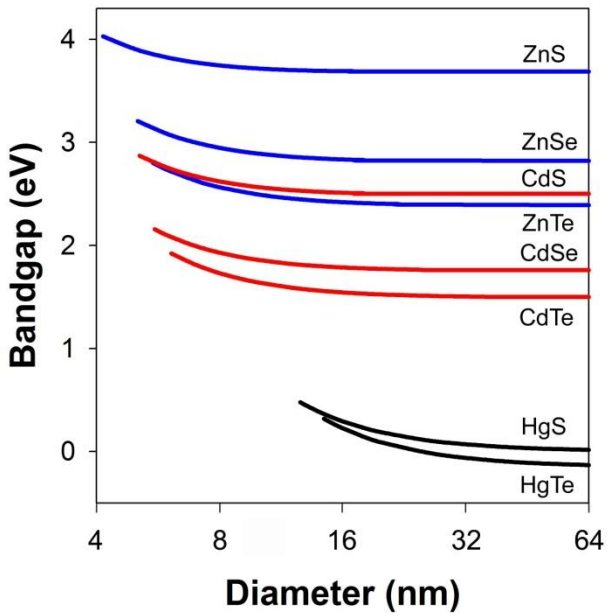

Figure 2.14: Dependence of the bandgap of quantum dots on the material and nanocrystal diameter. The onset of quantum confinement can be observed to vary considerably depending on the exciton diameter. For example, the diameter of the exciton is ~6.6 nm for ZnS and ~91 nm for HgTe. Values were calculated using the method of Brus with bulk effective masses and dielectric constants.

The three terms in Equation 2.11 quantitatively describe the major underlying mechanisms of quantum confinement. The first term accounts for the kinetic energy of the electron and hole within the confined nanocrystal due to localization within the

confining box. This change in energy with size is a consequence of the Heisenberg uncertainty principle, because spatial confinement of the electron and hole reduces the certainty of the momentum, and therefore the kinetic energy becomes less precise, increasing the energy of the lowest energy state. The second term describes the coulombic potential energy, which increases as the oppositely charged electron and hole are forced into a smaller space, which stabilizes the exciton, but in a magnitude smaller than the kinetic energy increase. Both of these terms are analogously accounted for in quantum mechanical descriptions of hydrogenic atoms.[20] The third term deviates from this analogy in order to account for the permittivity of the crystal and its surrounding medium. When the dielectric constant of the crystal is greater than that of the medium, this term is positive, contributing to the solvation confinement of the exciton. This term is very small compared to the first two, and approaches zero as the difference between the dielectric constants of the medium and the crystal approaches zero. For highly confined excitons (quantum dot radius << r_B) the main contribution to quantum confinement is the localization kinetic energy, which increases with r^{-2}, compared to the two other terms which increase with r^{-1}. Notably, this model relies on the effective mass approximation, which fails for values of high kinetic energy (~0.5 eV or above), and thus cannot be used to predict quantum confinement in very small nanocrystals. In addition, the fraction of atoms on the nanocrystal surface increases as the size decreases, which can strongly impact the electronic properties of the crystal.

2.2.3 Optical Properties of Single Quantum Dots and Ensembles. The most striking optical features of quantum dots are the broad absorption spectra containing multiple discrete transitions and the narrow and size-tunable fluorescence emission bands. Because of the size-dependent nature of these optical properties, these discrete transitions can only be observed for homogeneous populations of nanocrystals (Figure

2.12). In fact, the nanocrystal size, size distribution, and presence of distinct size populations may be directly inferred from the onset of absorption, the fluorescence peak width and peak shape, respectively. However, even when an ensemble of quantum dots is composed of nearly monodisperse nanocrystals, the emission spectra are still significantly broadened compared to single isolated quantum dots. Depending on the measurement technique and temperature, the full width at half maximum (FWHM) of fluorescence emission lines of single CdSe nanocrystals have been found to be as narrow as ~0.03 nm (resolution-limited cryogenic spectroscopy)[46] to 12 nm (room temperature),[13] significantly narrower than the most narrow ensemble peaks reported to date (~20 nm FWHM).[47] More interestingly, the emission from single quantum dots is intermittent, which has also been observed for fluorescent dyes and proteins.[48] Many studies have statistically evaluated the blinking nature of single quantum dot fluorescence, consistently showing a power law relationship for the probability densities of on and off times.[49] This 'blinking' can be readily observed under a light microscope, and is thought to arise from ionization of the nanocrystal. In accord with this theory, growing an insulating shell around the nanocrystal to yield a deeper and wider potential well has been show to significantly decrease the off time of the nanocrystal.[48,50,51] The fluorescence emission properties of single quantum dots are currently of great interest due to the recent use of these nanocrystals as probes for optical microscopy. New techniques should shed light on the modulation of the single molecule properties and the intrinsic physics of single molecules compared to their statistically averaged ensembles.

The quantum yield of a fluorescent molecule is the fraction of fluorescent photons emitted per photon absorbed. It has been found that the fluorescence emission from quantum dots may approach unity at room temperature, far above what has been achieved from bulk materials.[52-55] This is largely due to the strong overlap between the

electron and hole wavefunctions in the confined structure, which greatly increases the probability of radiative recombination. In bulk semiconductors, on the other hand, the exciton is not confined in space, and can rapidly dissociate due to its relatively weak binding strength (~1-50 meV), reducing the overlap between the electron and hole wavefunctions, increasing the probability of nonradiative relaxation. However the observation of high quantum yield is remarkable considering the long excited state lifetimes observed in quantum dots (tens to hundreds of nanoseconds) compared to organic dyes (hundreds of picoseconds to several nanoseconds). Longer excited state lifetimes commonly allow the decay of the excited state through less probable nonradiative pathways, and in some instances the lifetime is directly indicative of the spatial overlap between the electron and hole wavefunctions (Chapter 4). The size and structure-dependent excited state lifetime, as well as the nature of the radiative and nonradiative pathways are poorly understood and are areas currently under study.[56]

The optical spectra of monodisperse samples of quantum dots exhibit features that are indicative of the nanocrystal structure. For example, the energy of the first exciton peak, which is the lowest energy absorption transition, is determined by the size of the quantum confined nanocrystal. This relationship has been empirically investigated for many types of semiconductor materials.[43,57,58] The Stokes shift, which is the difference in energy between the first exciton peak of the absorption spectrum and the fluorescence emission peak, is also dependent on the nanocrystal structure, increasing with decreasing size and increasing with structural anisotropy, through physical phenomena that remain poorly understood.[59,60] The molar extinction coefficient is also dependent on the nanocrystal size, and has been empirically catalogued for several semiconductor materials.[43,57] Figure 2.15 demonstrates that the extinction coefficient at the first exciton peak increases exponentially with diameter. This value can vary widely

with material composition for a particular nanocrystal size, which is not surprising since the main contribution to band-edge light extinction by a crystal is from absorption by valence electrons. The concentration of valence electrons in a crystalline sphere is roughly proportional to the density of atoms for materials from the same elemental groups. At energies far above the bandgap, the extinction coefficients can be much larger, due to a larger density of electronic states. As well, semiconductor nanocrystals have also been found to undergo carrier multiplication when excited by light far above the bandgap, leading to the formation of multiple excitons from a single photon of absorbed light, yielding internal quantum efficiencies exceeding 100%, and sometimes over 700%.[61]

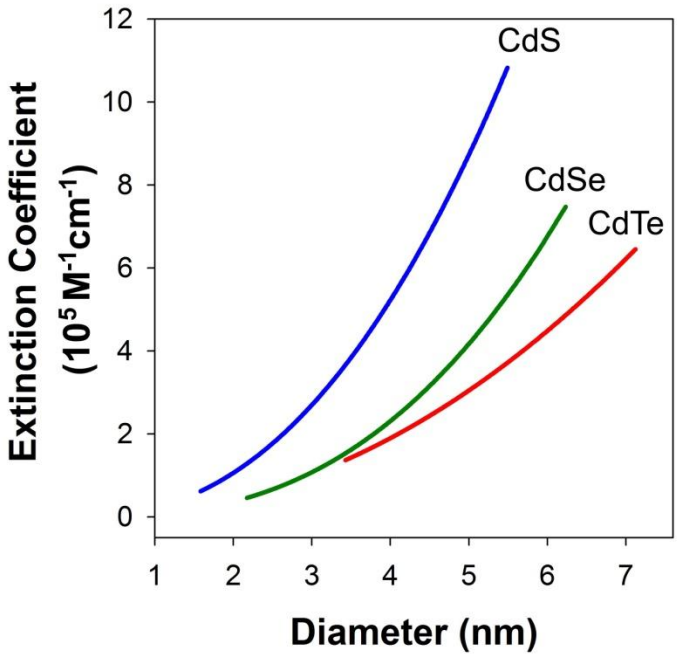

Figure 2.15: Extinction coefficients of CdS, CdSe, and CdTe nanocrystals. Data are plotted from fitted functions to empirical data.[43] Values correspond to the first exciton peaks.

2.2.4 Surface properties of Quantum Dots. The preceding sections explained the dependence of the optical properties of semiconductor nanocrystals on the particle size, which is mostly a factor of the internal structure of the nanocrystal. However as the crystal becomes smaller, the number of atoms on the surface increases, which can also significantly impact the optical properties. The atoms on the surface of a crystal facet are incompletely bonded within the crystal lattice, thus disrupting the crystalline periodicity and leaving a 'dangling orbital' on the atoms pointed outward from the crystal. These orbitals each contain a single electron, and all surface atoms will have 1 or more *unpassivated* orbitals. Most nanocrystals are highly faceted, and therefore each surface contains a periodic array of unpassivated orbitals, with two-dimensional translational symmetry, which may form a band structure similarly to the three-dimensional crystal itself. If these surface energy states contain energy levels within the semiconductor bandgap, they can trap charge carriers at the surface, thereby reducing the overlap between the electron and hole, and lead to nonradiative decay events. Indeed very small nanocrystals are often observed to have multiple fluorescence emission bands, one of which is the bandgap emission, and other ones at lower energy arise from defect sites on the surface. When unpassivated crystalline surfaces are examined microscopically, they are often found to have undergone significant atomic rearrangements in order to reduce the overall energy of the surface facets, typically through contraction of the surface atoms and other ordered displacements. These reconstructions also disrupt the crystal periodicity and introduce new two-dimensional translational symmetry to the nanocrystal, which may yield another source of trap sites. However, in practice, most semiconductor nanocrystals are not used in vacuum, and are either embedded within a solid matrix such as another crystal or a glass, or they are suspended in solution and coated with organic molecules. In these cases, the facets are

passivated by atoms or molecules that bond with the crystal surface atoms to reduce reconstruction and minimize intra-bandgap surface states.

The overwhelming impact of the surface on quantum dot optical properties has now been established over the course of more than two decades of research. The most prominent feature of this relationship is the fact that the fluorescence quantum yield can be significantly controlled through a wide variety of changes to the nanocrystal surface. For example, many III-V quantum dots like InP, are nearly nonfluorescent after synthesis, but can become strongly fluorescent after acid-induced etching of the surface.[62] As well, colloidal nanocrystals passivated with organic molecules such as polymers and basic ligands have fluorescence quantum efficiencies that that are strongly dependent on the nature of the passivating agent.[63-65] Figure 2.16 displays plots of the fluorescence quantum efficiency of CdSe quantum dots mixed with different basic ligands, showing that the emission efficiency is highly dependent on the chemical nature of the basic moiety, as well as the atom in the crystal to which it is bound, either cadmium or selenium. The underlying mechanism for this ligand-tunable quantum yield is poorly understood, and few systematic studies have so far been undertaken. A physical understanding of this phenomenon will likely be aided by *ab initio* computational models of ligand effects on the band structures of small nanocrystals.

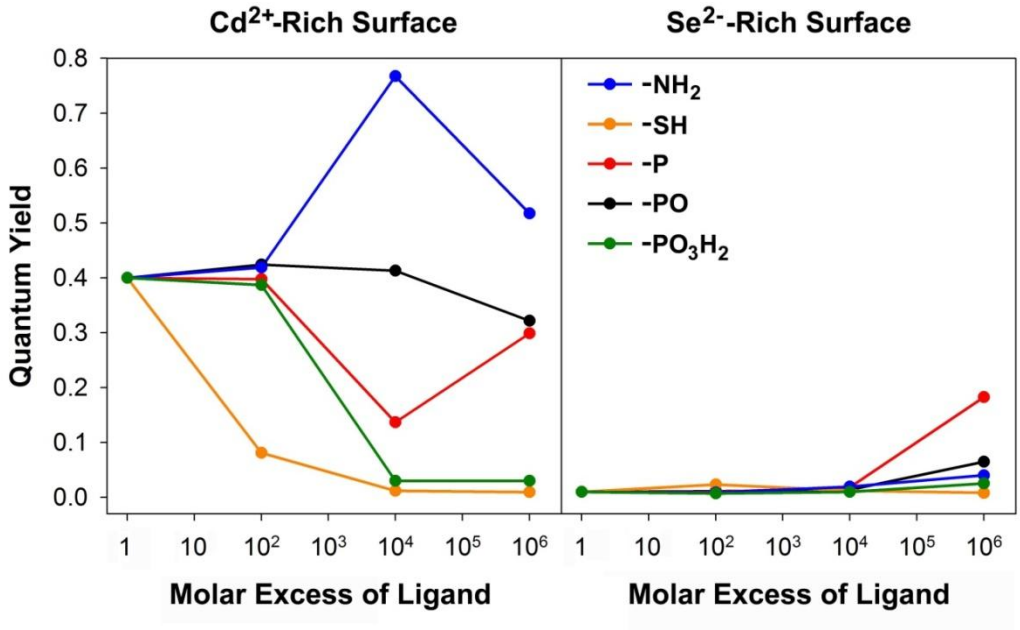

Figure 2.16: Organic ligand effects on the fluorescence quantum yield of CdSe quantum dots. Quantum dots with a diameter of 3.0 nm were synthesized in a trioctylphosphine oxide solvent, and then overcoated with an excess of cadmium or selenium ions. Anion-rich surfaces have previously been found to almost entirely quench quantum dot fluorescence.[66,67] The nanocrystals were purified and mixed with ligands in the ligand:quantum dot molar ratios shown above. Ligands were primary amines (octylamine), thiols (octanethiol), phosphines (trioctylphosphine), phosphine oxides (trioctylphosphine oxide), or phosphonic acids (octylphosphonic acid).

For practical light-emitting applications, it is advantageous to coat quantum dots with an insulating inorganic shell in order to stabilize and maximize the fluorescence. This not only passivates the surface bonds without disrupting the crystal periodicity, but it also buries the semiconductor in a potential energy well, concentrating the charge carriers away from the nanocrystal surface. Thereby surface defect states and trap sites will have a diminished impact on the fluorescence efficiency and fewer environmental factors will influence the emission intensity. In solid state devices, this process is quite simple, as overgrowth of an inorganic shell with a wider bandgap can be easily achieved with complete surface coverage. In colloids, the task is more challenging, but major progress

has resulted in colloidal quantum dots with immensely stable fluorescence efficiency in many solvents and with many changes in local environment. This protection of the charge carriers through a crystalline barrier has proven to be the most crucial part of quantum dot probe development, and is responsible for their high quantum efficiency under oxidizing conditions and substantial photostability. In addition, growth of a shell significantly reduces the off-time of quantum dot blinking, and can be almost entirely eliminated with the overgrowth of a thick shell.[50,51] Details of inorganic capping are outlined in section 2.3.3 and 2.3.4.2.

For many applications it is useful to have a semiconductor nanocrystal surface that can interact with its surroundings. In these cases it is beneficial to maximize the surface area of the material. Figure 2.17 shows the fraction of surface atoms on a CdSe nanocrystal for different shapes and different sizes. It is apparent that spherical quantum dots have the smallest number of total surface atoms and are thermodynamically the most stable shape, thus making them ideal candidates for applications in which fluorescence modulation from external stimuli must be minimized. On the other hand, elongated structures, such as rods and wires, maintain a large fraction of their constituent atoms on their surfaces, making them useful for applications in which the nanocrystal charge carriers can interact with the surrounding environment, such as for oxidation-reduction chemistry, energy transfer, photocatalysis, and sensing applications.

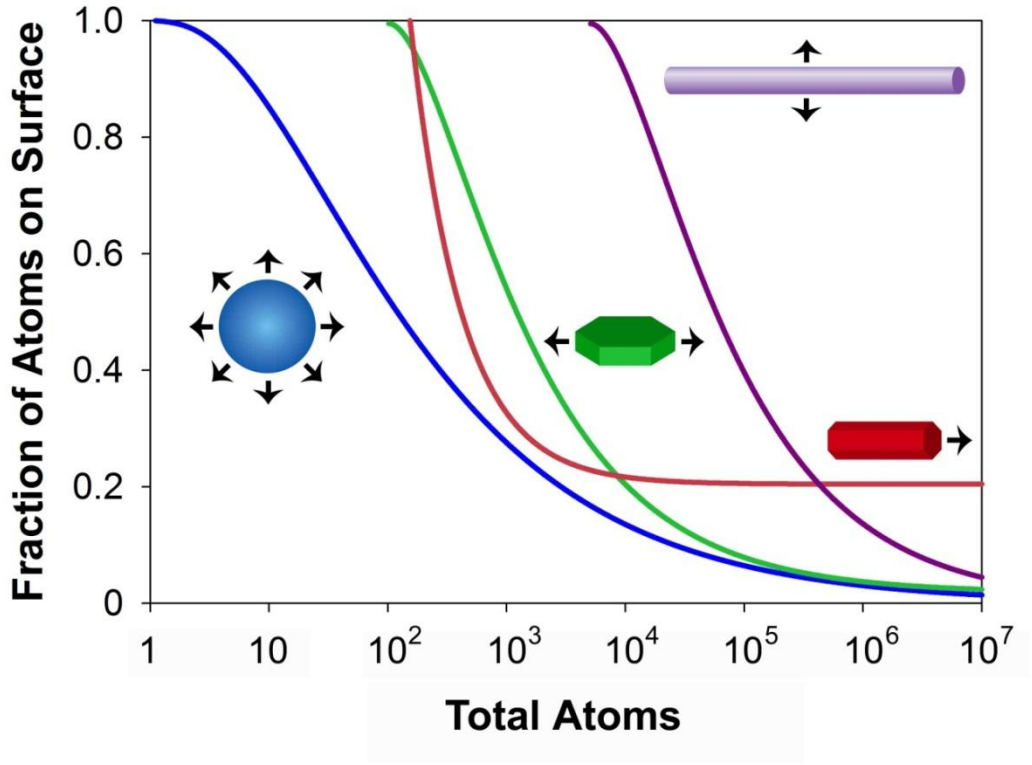

Figure 2.17: Dependence of the fraction of surface atoms on the nanocrystal shape. Values were calculated for wurtzite CdSe, but trends will be similar for other materials. Commonly encountered nanocrystal shapes are depicted, including spherical dots (blue), rods that grow in the axial direction (red, 4 nm width), rods that grow radially (green, 20 nm length), and wires that grow radially (purple, 1 μm length). All anisotropic nanocrystals are modeled as hexagonal cylinders.

Several other interesting materials properties are closely linked with the fraction of surface atoms on the nanocrystal. The melting temperature of semiconductor nanocrystals, and other nanocrystals, decreases as the size decrease, as a larger fraction of atoms of the crystal are on the disordered, incompletely passivated surface.[7] The surface energy differences between different crystal phases have also been used to explain alterations to the pressure-induced phase transitions in high surface-area semiconductor nanocrystals compared to their bulk counterparts.[9,68]

2.2.5 Bandgap engineering. Compared to bulk materials, semiconductor nanocrystals have a diverse range of parameters that can modulate the electronic bandgap, as outlined in Figure 2.18. The bandgap of bulk semiconductors can only be tuned through the material composition. Therefore an immense amount of research over the past century has focused on the properties of semiconductor alloys and semiconductor doping. The discovery of quantum confinement of thin films immensely broadened bandgap engineering, quickly resulting in the production of devices containing quantum confined layers. Although the bandgap can be tuned to a very large degree with one-dimensional quantum confinement in a well, increasing the degree of confinement expands the bandgaps available for a material (Figure 2.13). In addition to size, the shape of the nanocrystal can also be used to tune the bandgap as well as other useful properties, such as the polarization of emitted light. For example, elongated CdSe quantum dots have bandgaps slightly smaller than spherical dots of the same radius, but their light emission is linearly polarized in the direction of the elongated axis.[69,70]

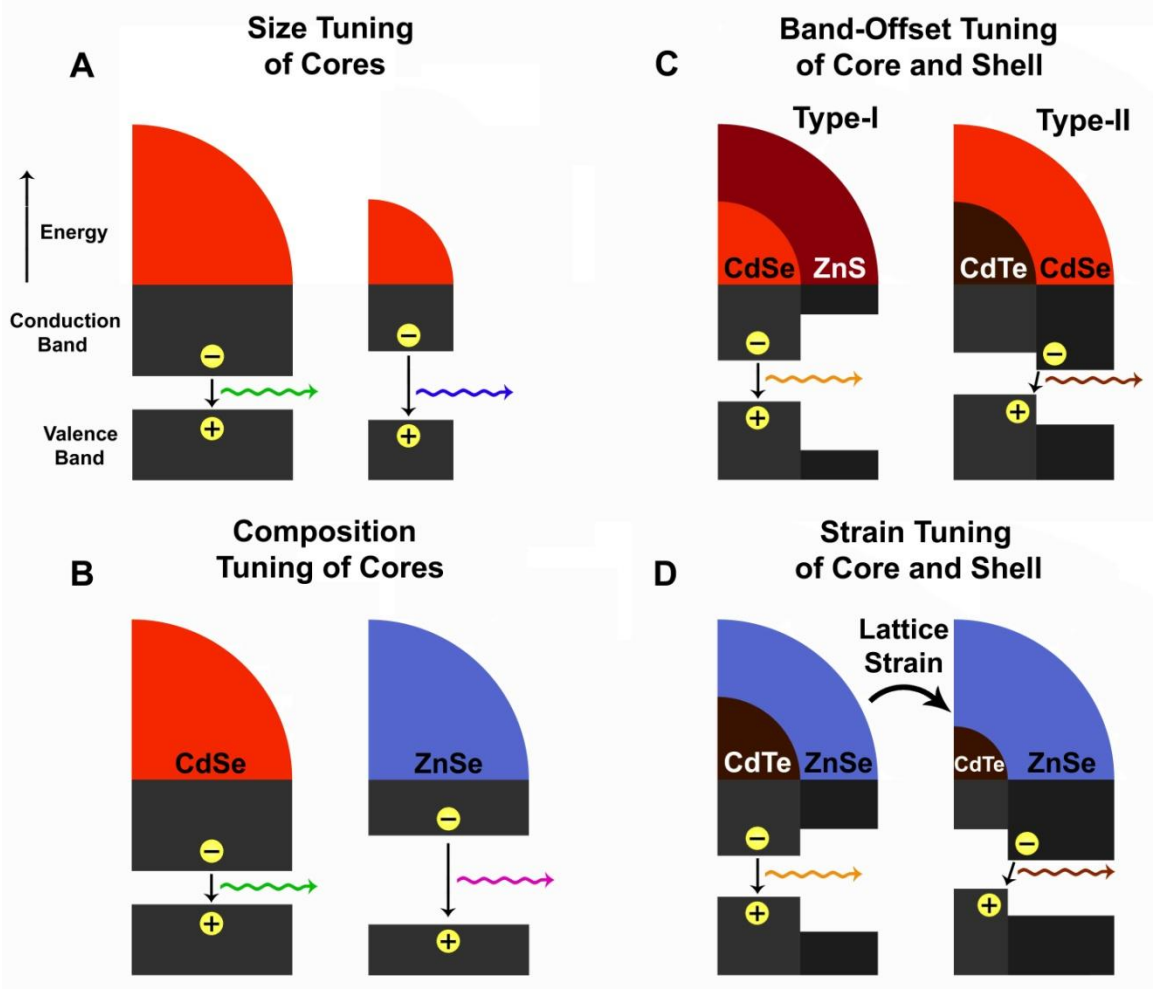

Figure 2.18: Bandgap engineering in semiconductor nanocrystals. The relative sizes of core and (core)shell nanocrystals are represented by cutaways of circles. (A) For semiconductor nanocrystals smaller than the exciton, the bandgap increases with decreasing size. (B) The bandgap of different semiconductor nanocrystals with similar sizes can have vastly different bandgaps, depending mostly on the bulk bandgap. (C) Heterostructures, such as (core)shell structures, can have bandgaps modulated by the band offsets with type-I or type-II band alignments. (D) Heterostructures with a large lattice mismatch can have bandgaps dictated largely by strain-induced changes to the optical properties.

Quantum dot alloying has become area of rigorous research in the past 5 years, since Bailey and Nie reported the first homogeneously alloyed nanocrystals, composed of $CdSe_yTe_{1-y}$.[71] These materials are unique because the alloys emit light at longer wavelengths than either of the constituent binary compounds due to an optical bowing

effect. Since this report, quantum dots have been prepared from the homogeneous alloys $Cd_xZn_{1-x}Se$, $Cd_xZn_{1-x}S$, and $CdSe_yS_{1-y}$.[58,72,73] Chapter 3 describes the optical properties of $Cd_xHg_{1-x}Te$ quantum dots prepared through cation exchange with an immensely wide bandgap range. A chemically related process is impurity doping, in which electron or hole donors are doped into the crystalline structure, creating an intraband defect energy level that allows lower energy light emission from the defect level to the ground state. Although these nanocrystals have been purported to have beneficial properties for biolabeling, the understanding of the optical processes involved with their emission and their synthesis is still at an early stage.[74-79]

Another mechanism of bandgap engineering for semiconductor nanocrystals is through heterostructure synthesis. As previously mentioned, the growth of a wide bandgap shell on a nanocrystal immensely improves the emission efficiency. In these particles, both the electron and hole are sequestered in the core material, which is a type-I configuration. The bandgaps of the heterostructure components can also be chosen so that they are staggered (Figure 2.18C), resulting in spatial separation of the electron and hole, which is a type-II configuration.[80] These nanocrystals have a smaller effective bandgap, which is spatially indirect. In this case, one charge carrier is confined to the core, which is in three-dimensional confinement, whereas the other charge carrier is confined to the two-dimensionally confined shell. It is also possible to confine both of the charge carriers to the shell, resulting in a pseudo-spherical quantum well, or a quantum dot-quantum well.[81] It has also been shown that these structures may be combined in a quantum dot-barrier-quantum well structure that demonstrates dual-color emission.[82] In addition, if the materials constituting these heterostructures have different lattice constants, the band offset and bandgaps can be significantly altered by the interfacial strain (Figure 2.18D). In this case, materials can be specifically chosen for their inherent

band offsets as well as their lattice constants to allow an even wider degree of bandgap control. This effect will be described in detail in Chapter 4.

2.3 Chemical Synthesis of Semiconductor Nanocrystals

2.3.1 Early Quantum Dot Synthesis Methods. The synthesis of quantum confined semiconductor nanocrystals was first described in 1982 by Ekimov,[1,2] who grew nanocrystals and microcrystals of CuCl semiconductors in glass matrices. Simultaneously many groups were exploring the colloidal synthesis of semiconductor materials, prepared through arrested precipitation. First working with cadmium sulfide colloids, a sulfide (ammonium sulfide salt or hydrogen sulfide gas) and a cadmium salt (e.g. cadmium chloride or cadmium sulfate) were mixed in aqueous solution containing a stabilizer, either a small molecular weight ligand (e.g. ethyelenediaminetetraacetic acid) or a polymer (e.g. sodium hexametaphosphate or maleic anhydride/styrene copolymer).[83-86] This stabilizer binds to the surfaces of nano- and micro-crystallites as they nucleate to prevent further growth and to stabilize their dispersion as colloids in solution. In their absence, bulk CdS will quickly precipitate out of solution. Brus first reported in 1983 that when these colloids are sufficiently small, they can exhibit quantum confinement effects.[10,11] Soon thereafter it was reported that the compositional variety and the post-synthetic processibility of colloidal semiconductor nanocrystals could be significantly expanded through syntheses inside reverse micelles[6,87-89] or with the use of molecular thiolate ligands.[90-92]

2.3.2 Coordinating Solvent Synthesis. A major step toward the goal of monodisperse, colloidally dispersible, and highly fluorescent quantum dots was made by Bawendi and coworkers in 1993 with the introduction of nanocrystal synthesis in a high temperature coordinating solvent composed of trioctylphosphine (TOP) and trioctylphosphine oxide

(TOPO).[12] This work demonstrated the production of CdS, CdSe, and CdTe nanocrystals with high crystallinity and monodispersity (<5% root mean square in diameter) over a broad range of sizes. The utility of coordinating solvents[93] and organometallic reagents[6] had previously been established for colloidal nanocrystal synthesis, but this method presented a huge improvement in nanocrystal quality due to a temporal separation of nucleation and growth. In this process organometallic reactants (dimethylcadmium and bis-trimethyoxysilyl chalcogenides) were injected into a hot coordinating solvent, yielding immediate nucleation of nanocrystal seeds. The TOP and TOPO molecules contain basic phosphine functional groups that bond to the crystallite surfaces, limiting growth. The alkyl chains from the coordinating ligands extend away from the nanocrystal surface, producing sterically stable colloids that are dispersible in nonpolar solvents. The injection of a cold (room temperature) precursor solution into the hot solvent immediately reduces the reaction temperature, allowing nanocrystal growth to proceed slowly at a lower temperature, below the temperature threshold for nucleation. This novel demonstration of temporal separation of nucleation and growth was found to be crucial for the production of monodisperse samples, although size-selective precipitations were still necessary to improve the size distribution.

The versatility of this technique has been proven over the ensuing years, resulting in monodisperse, highly crystalline nanocrystals composed of many types of semiconductors, metals, and oxides, and the chemical and colloidal mechanisms have been further elucidated.[94-96] It has also been shown that the highly reactive and toxic organometallic precursors can be replaced with safer oxides and salts (Figure 2.19),[97,98] and that various parameters can be tweaked to allow monodisperse growth of specific sizes of nanocrystals without the need for post-synthesis size-selection.[96,99] It has also been shown that this methodology is not unique to the phosphine and phosphine oxide

ligands used in this seminal study, as a wide variety of aliphatic coordinating ligands (e.g. alkylamines or alkanoic acids) have also been used,[63,100,101] and they can even be largely diluted with non-coordinating solvents (e.g. octadecene or dioctyl ether) in order to save cost and enhance the tunability of sizes through the ligand concentration (Figure 2.20).[99,100] It has also been shown that it is possible to grow nanocrystal structures with a variety of shapes (e.g. rods, tetrapods, arrows) by controlling the reactivity of different crystalline facets through the concentration and chemical nature of the ligands and the concentration of monomers.[95,102,103]

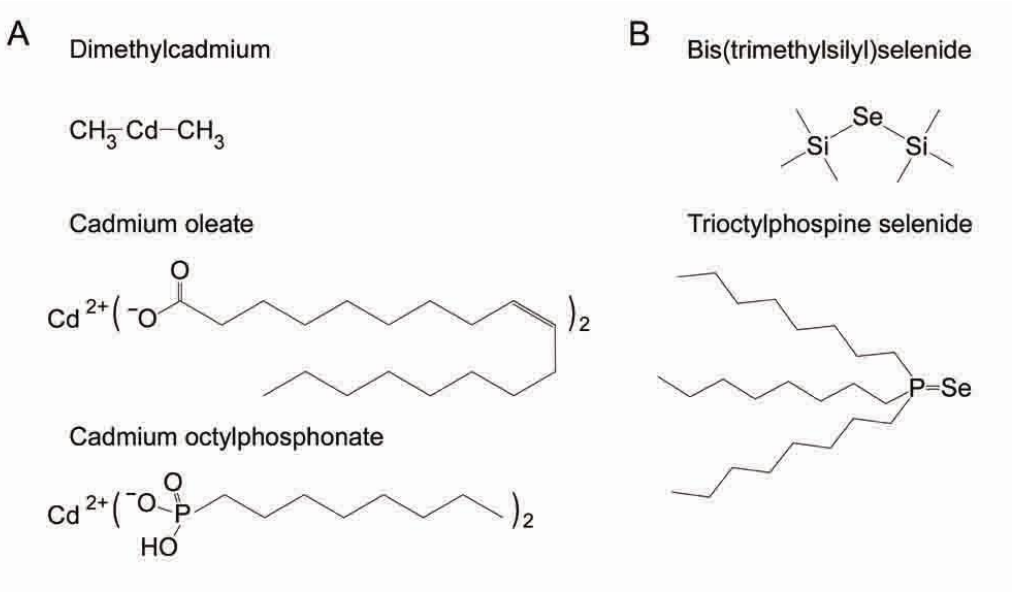

Figure 2.19: Precursors used for high temperature synthesis of CdSe nanocrystals. Cadmium precursors (A) and selenium precursors (B) are shown, which are chemical analogues of those used for zinc, sulfur, and tellurium.

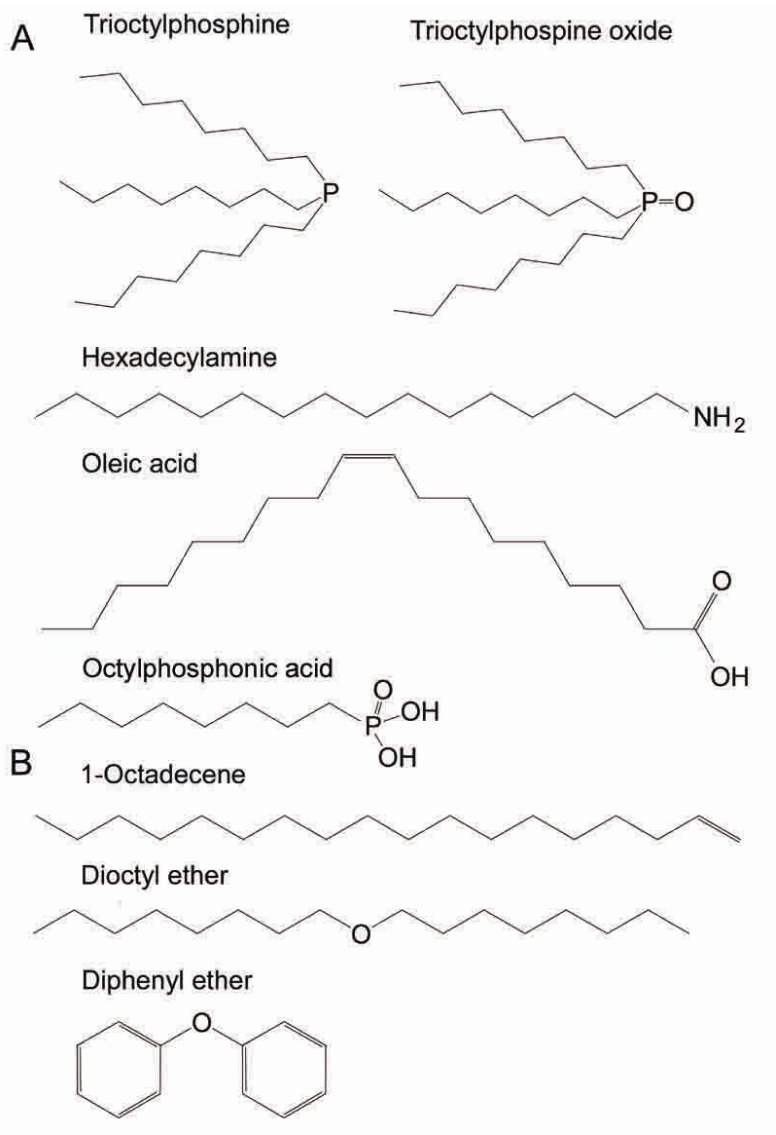

Figure 2.20: Common ligands and solvents used for high temperature nanocrystal synthesis. Coordinating ligands (A) can serve a both ligands for quantum dots and as a high boiling point solvent, and can be diluted with noninteracting high-boiling point solvents (B).

2.3.3 Heterostructure Growth. The next major development in colloidal quantum dot synthesis was the demonstration that the overgrowth of an insulating shell on the surface of a quantum dot tremendously enhances the photoluminescence efficiency. A large body of early work showed that the low room-temperature quantum efficiency of

aqueous quantum dots was likely due to surface defects and trap states, as discussed in section 2.2.4.[104,105] For example, Arnim Henglein and coworkers found that the addition of excess cations to alkaline aqueous solutions of semiconductor colloids (e.g. Cd^{2+} for CdS) resulted in large fluorescence enhancements.[106] This was hypothesized to be the results of surface defect passivation, and a similar trend was found for the addition of alkylamines.[107] It was also reported that when a wider bandgap material (ZnS) was grown on top of semiconductor nanocrystals (CdSe) in reverse micelles, the luminescence efficiency was tremendously enhanced.[108] A seminal report in 1996 by Philippe Guyot-Sionnest and coworkers demonstrated that the quantum yield of (core)shell (CdSe)ZnS nanocrystals prepared at high temperature in a coordinating solvent can reach 50% at room temperature.[109] Bawendi and coworkers improved this synthetic method and analyzed the luminescence dependence of the shell thickness from the perspective of interfacial strain, which will be discussed in detail in Chapter 4.[110]

2.3.4 Engineering of Modern Semiconductor Nanocrystal Bioimaging Probes. A wide variety of synthetic methods for semiconductor nanocrystals have been described over the past decade.[111,112] However the high temperature coordinating solvent syntheses have emerged as the most versatile and the most widely used techniques due to an unmatched combination of monodispersity, crystallinity, size control, shape control, photoluminescence efficiency, and colloidal stability of the resulting nanocrystals. Based on these methods, the production of biologically functional quantum dots has now progressed from a chemical science to a multistep macromolecular engineering process. The most common fabrication scheme involves four steps: 1. Synthesis of the nanocrystal core, most often CdSe, in a high-temperature organic solvent. 2. Growth of an inorganic shell (usually ZnS) epitaxially on the core to protect the optical properties of the quantum dot. 3. Phase transfer of the nanocrystal from organic liquid phase to

aqueous solution. 4. Linkage of biologically active molecules to the nanoparticle surface to render functionality, or linkage of biologically inert polymers to the nanoparticle to minimize biological activity. Each of these four steps will be described in detail.

2.3.4.1 Core synthesis. The synthesis of CdSe nanocrystals has advanced greatly over the past decade, allowing the generation of monodisperse quantum dots that can span the visible spectrum. For this reason, CdSe has become the material of choice for quantum dots, especially for biological applications. In a typical synthesis of CdSe quantum dot cores (Figure 2.21), a room-temperature solution of elemental selenium dissolved in liquid TOP is swiftly injected into hot solution (290-350ºC) of TOPO and hexadecylamine containing a cadmium precursor (cadmium oleate or cadmium phosphonate) under intense stirring in an atmosphere of inert gas (argon or nitrogen). This injection immediately initiates thermodynamically-driven nucleation of tiny CdSe crystallites, as the precursors are introduced at concentrations (typically 10-100 mM) well above the solubility of the resulting semiconductor. This initial nucleation event drastically reduces the concentrations of the monomers, and the cold injection simultaneously reduces the temperature to ~240-290°C, which arrests nucleation seconds later. Because a large amount of the reactants still remain in solution, growth can proceed homogeneously on similarly sized nuclei until a desired size is reached, or until the reactants are depleted. Growth is kinetically controlled by monomer diffusion due to the high viscosity of the solvent (14 cp at the melting point of TOPO, ~50ºC), and through the reaction rate of monomers at the nanocrystal surface, due to strong and possibly anisotropic binding of the coordinating ligands with nanocrystal facets and with the semiconductor precursors. Maintaining a high reaction temperature yields semiconductor nanoparticles that are highly crystalline, containing few lattice defects.

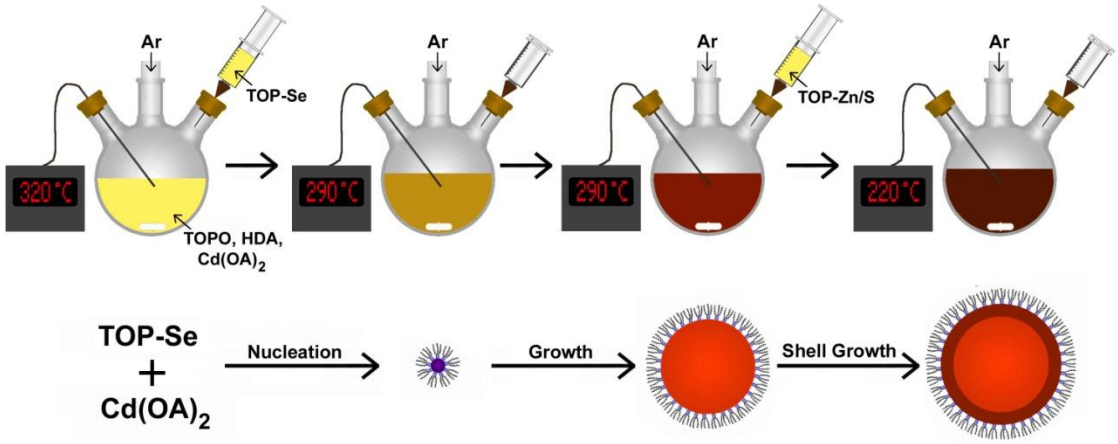

Figure 2.21: Traditional synthesis and capping of (CdSe)ZnS quantum dots in a coordinating solvent. A three-necked flask is commonly used for synthesis in order to allow simultaneous monitoring of reaction temperature through a thermocouple, inert gas flow through a Schlenk line, and convenient injection of reagents. A solution of selenium is swiftly injected into a hot mixture of cadmium oleate dissolved in trioctylphosphine oxide and hexadecylamine, initiating nucleation, and causing a rapid decrease in temperature. The cores grow to a desired size at a temperature low enough that nucleation is arrested. The CdSe cores may then be capped with ZnS at a lower temperature. Often it is desirable to purify the CdSe quantum dots before capping.

The initial step of nucleation is so rapid that it is difficult to study experimentally, but the ensuing growth process is controllable and proceeds much more slowly, and distinct stages of growth have been identified. After nucleation, remaining monomers grow epitaxially on the nuclei, and the nanocrystals reach a size-focusing point, at which the size distribution is the most narrow.[94] Interestingly, the quantum yield of the nanocrystals also reaches a focusing point, at which the nanocrystals in the reaction reach a "bright point," and afterward decrease in photoluminescence efficiency.[96] After the size-focusing point the monomers become depleted, and the size distribution widens again (defocusing) due to Ostwald ripening, which is the dissolution of smaller particles into monomers that deposit on larger particles, which then continue to grow into larger crystals.[94] These phases are highly dependent on the monomer concentration in solution, and many parameters of the synthesis (temperature, initial concentrations of

each of the precursors, solvent composition)[63,96,99,113] may be tuned to adjust the size at which the nanocrystals are focused, at which point it is desirable to quench the reaction to obtain monodisperse particles, usually by decreasing the temperature until crystal growth is negligible.

A vast number of potential parameter combinations have allowed the simple synthesis of CdSe quantum dots with diameters between 2-8 nm, with corresponding emission wavelengths of 450-650 nm, spanning the entire visible spectrum with just one composition (Figure 2.12). By also adjusting the nanocrystal composition (ZnS, CdS, CdSe, CdTe, PbS, PbSe and their alloys), it is now possible to span the wavelength range of 300-4000 nm.[71,80,96,114-117] The resulting quantum dots are coated in coordinating ligands and suspended in a crude mixture of the coordinating solvent and molecular precursors. The nanocrystals are highly hydrophobic, which is a characteristic that allows them to be isolated and purified from the reaction mixture, either through liquid-liquid extraction (usually a mixture of hexane and methanol),[43] or through precipitation from a polar solvent (methanol or acetone) that dissolves the reactants and coordinating ligands but not the quantum dots.[12] The pure core quantum dots are then further processed to generate biological probes.

2.3.4.2 Shell growth. As discussed in section 2.2.4, a semiconductor nanocrystal contains a large number of surface atoms, which can serve as defect sites that quench photoluminescence. The surface atoms of nanocrystals prepared through coordinating solvent syntheses are passivated by organic ligands like TOPO or hexadecylamine, which serve as an electrically insulating monolayer. However the bond strength between the organic ligand and the semiconductor surface atom is much lower than the internal bond strength of the semiconductor lattice, and desorption of ligands makes the

core physically accessible. Through overgrowth of a shell of wider bandgap than the underlying core, strong electronic insulation results in enhanced photoluminescence efficiency, and a stable shell provides a physical barrier to degradation or oxidation. As an example, to passivate CdSe quantum dots with ZnS, the cores are purified to remove unreacted cadmium or selenium precursors, and then resuspended in a coordinating solvent such as hexadecylamine/trioctylphosphine oxide or octadecylamine/octadecene.[63,66,110] Molecular precursors of zinc (diethylzinc or zinc oleate) and sulfur (hexamethyldisilathiane or elemental sulfur) dissolved in TOP or octadecene are then slowly added at elevated temperature. The temperature for growth of ZnS on CdSe is chosen such that it is high enough to favor epitaxial crystalline growth, but is low enough to prevent nucleation of ZnS crystals, and to prevent Ostwald ripening of CdSe cores. Normally this is a temperature around 160-220ºC. The (core)shell (CdSe)ZnS nanocrystals are then purified just like the cores. Although shell growth is a common procedure, uncapped CdSe cores are of also of great interest, especially for energy and charge transfer applications, in which physical access to charge carriers in the core is important.

Structures like (CdSe)ZnS are highly strained due to the difference in lattice constant between the core and shell materials. This interfacial strain can detrimentally impact the fluorescence emission efficiency of quantum dots through the formation of quenching defect sites. In 2004 and 2005, the groups of Peter Reiss, Horst Weller, and Alf Mews reported that the strain-induced quenching can be vastly reduced with the growth of interim layers of intermediate lattice constants.[54,55,118] For example, (CdSe)ZnSe/ZnS and (CdSe)CdS/ZnS were found to have higher photoluminescence quantum yield and photostability than single shell (CdSe)ZnS nanocrystals, and the shells could be grown to larger thicknesses before the emission yield diminished. The exact mechanism of this

phenomenon is poorly understood and will be further explored in Chapter 4. For shell growth, it is important to note that there are many reaction parameters that are not yet fully understood, many of which are known to drastically impact the optical and structural properties of the resulting nanocrystals. For example, Weller reported that CdS grown on spherical CdSe nanocrystals could proceed as a homogeneous concentric sphere or as an elongated rod-like structure with mixed dimensionality of confinement, depending on the relative concentrations of cadmium and sulfur precursors and the temperature.[70] In addition, the lattice structure of the underlying core material can dictate the growth of the shell. For example, Alivisatos reported that CdS shells can grow on pseudo-spherical CdSe nanocrystals as either rods or tetrapods, depending on the symmetry of the crystal structure of the core.[119] This finding was rationalized in terms of the reactivity of the surface facets of zinc blende and wurtzite phases, which is discussed further in Chapter 4. Other recent developments in nanocrystal shell growth have shown that alternating the addition of the precursors may provide more homogeneous shell formation with a decreased probability of shell material nucleation, in a process called successive ion layer adsorption and reaction (SILAR).[66] Further studies to elucidate mechanisms controlling heteroepitaxial growth may allow for the synthesis of nanocrystals with complex structures containing multiple chemical domains and compositional gradients.

2.3.4.3 Phase Transfer. Because quantum dots synthesized in coordinating solvents are coated with alkyl chains that render solubility only in nonpolar organic solvents, phase transfer is an essential and nontrivial step to employ these particles as biological reporters. As an alternative approach, a large variety of aqueous colloidal methods can directly generate quantum dots ready for use in biological environments,[120] but these protocols rarely achieve the level of monodispersity, crystallinity, stability, and

fluorescent efficiency as the quantum dots produced in high-temperature coordinating solvents. Two general strategies have emerged to render hydrophobic quantum dots soluble in aqueous solution (Figure 2.21): ligand exchange, and amphiphilic encapsulation. For ligand exchange, a suspension of TOPO-coated quantum dots may be mixed with a solution containing an excess of a heterobifunctional ligand, which has one functional group that binds to the nanocrystal surface, and another functional group that is hydrophilic. Thereby, hydrophobic TOPO ligands are displaced from the nanocrystal through mass action, as the new bifunctional ligand adsorbs to render water solubility. Using this method, (CdSe)ZnS quantum dots have been coated with mercaptoacetic acid and (3-mercaptopropyl)trimethoxysilane, both of which contain basic thiol groups to bind to the zinc atoms on the nanocrystal surface, yielding quantum dots displaying carboxylic acids or silane monomers, respectively.[13,14] These methods generate quantum dots that are useful for biological assays, but ligand exchange is commonly associated with decreased fluorescent efficiency and a propensity to aggregate and precipitate in biological buffers. More recently it has been shown that these problems can be alleviated by retaining the native nonpolar coordinating ligands on the surface, and covering the hydrophobic nanocrystal with amphiphilic molecules, such as lipids or polymers.[121-123] These methods yield water-soluble quantum dots that are stable for long periods of time due to a protective bilayer encapsulating the nanocrystal through hydrophobic interactions. No matter what method is used to suspend the nanocrystal in aqueous buffers, they should be purified from residual ligands and excess amphiphiles before use in biological assays, using ultracentrifugation, dialysis, or filtration. Also, when choosing a water solubilization method, it should be noted that many biological and physical properties of the nanoparticle may be affected by the surface coating, and the overall physical dimensions of the nanoparticles are highly dependent on the thickness of the coating. Typically the

nanoparticles are much larger when encapsulated in amphiphiles, compared with those coated with a monolayer of ligand. These themes are further examined in Chapters 5 and 6.

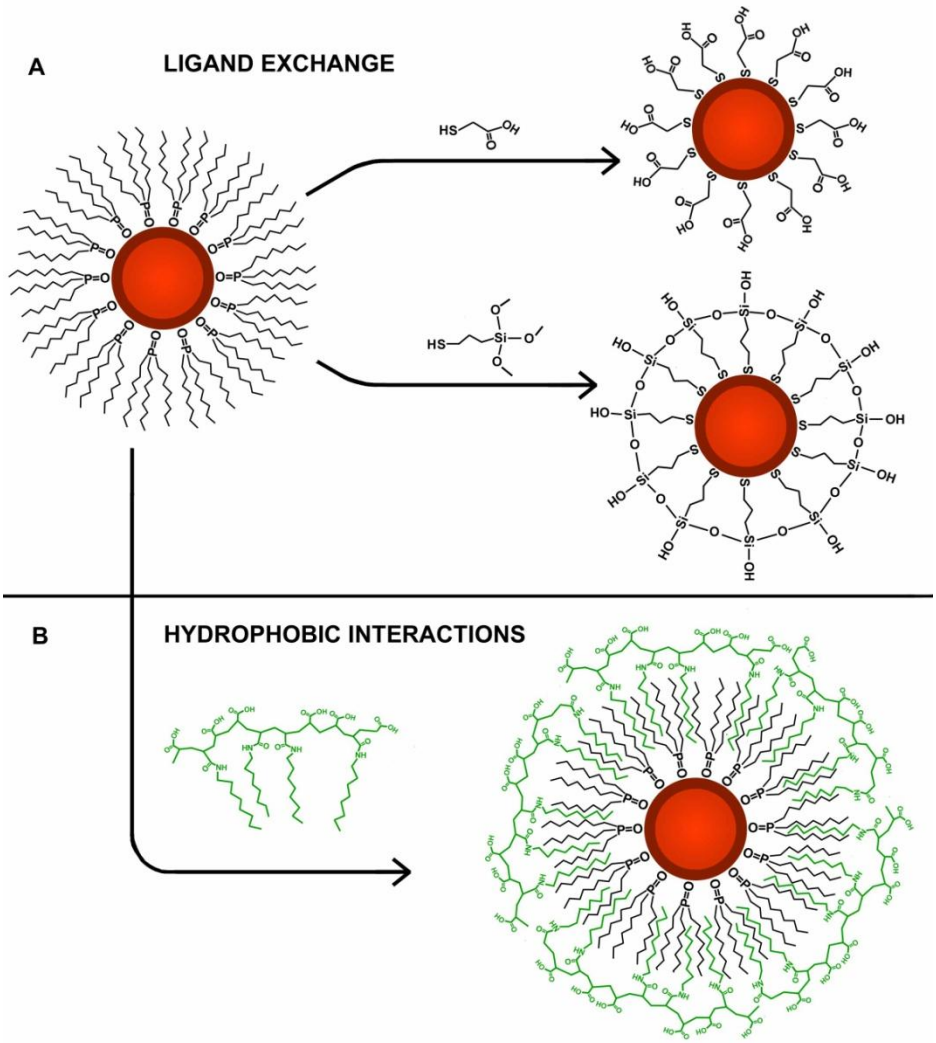

Figure 2.22: Transfer of hydrophobic nanocrystals to aqueous solution. The two general mechanisms of ligand exchange (A) with mercaptoacetic acid or (3-mercaptopropyl)trimethoxysilane and hydrophobic encapsulation (B) with octylamine-modified polyacrylic acid are discussed in the text.

2.3.4.4 Bioconjugation. The use of quantum dots to observe molecular events in biology has become one of their most intriguing applications. Biological specificity can be

rendered by coupling to peptides, proteins, aptamers, nucleotides, polysaccharides, or small molecule ligands. Methods used to modify aqueous nanocrystals with bioaffinity molecules fall under several broad categories, with applicability dictated by the specific nanocrystal surface coating (Figure 2.22). Nanocrystals with accessible surface atoms can directly interact with biomolecules that contain chelating or strongly basic residues. This method has been used to successful tag quantum dots coated with hydrophilic thiol ligands using peptides and nucleotides with reduced thiols,[124-126] and recombinant proteins containing histidine tags.[127-130] The use of histidine tags is a powerful and versatile technique that is further discussed in Chapter 7. These methods are generally not applicable for nanocrystals coated with thick hydrophobic bilayers, which have sterically inaccessible surface facets. The most commonly used coupling scheme is the covalent coupling between functional groups of the organic surface coating and functional groups on proteins or other biomolecules. This typically involves amide bond formation between carboxylic acid groups on the quantum dot and primary amines on proteins using carbodiimide chemistry, or the formation of a thioether between maleimide-activated primary amines on a quantum dot and a reduced thiol on a biomolecule.[131] Although the former method is more widely applicable due to the ubiquity of primary amines in biomolecules, the later method is more specific, resulting in more predictable crosslinking geometries and reduced aggregation, especially for antibody-quantum dot coupling.

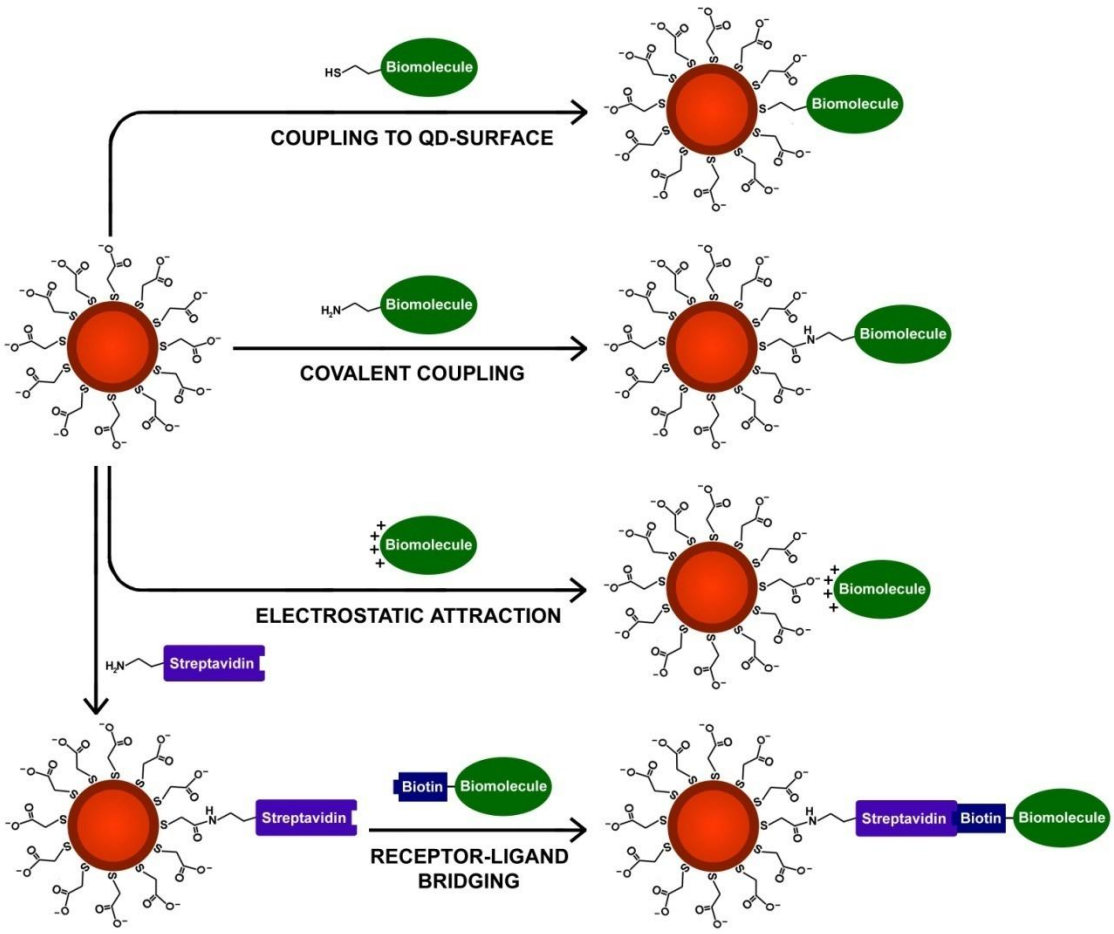

Figure 2.23: Bioconjugation methods used for aqueous semiconductor nanocrystals. Methods are discussed in the text.

The most commonly used water solubilization methods result in quantum dots covered with carboxylic acid functional groups, and thus these colloids are regarded as negatively charged colloids in neutral or basic buffers.[13,122] This net negative charge can induce electrostatic association with positively charged molecules, a technique that has been used to coat quantum dots with cationic avidin proteins and recombinant maltose-binding proteins fused with positively charged peptides.[132,133] However this method is generally not advisable due to common occurrences of aggregation and the instability of electrostatic interactions under high salt conditions. Bioconjugation may also be approached through a more modular direction using high-affinity streptavidin-biotin

binding. Quantum dot-streptavidin conjugates are convenient for indirect binding to a broad range of biotinylated biomolecules, which are widely available commercially.[122] Biocompatible quantum dots are now commercially available, conjugated to a variety of functional biological molecules, like streptavidin, biotin, or monoclonal antibodies. Currently, bioconjugation methods are a major limiting step in the production of quantum dots for bioimaging applications due to the poor efficiency, specificity, reproducibility, scalability, and versatility of most coupling schemes, and due to the inability to control the stoichiometry and geometry of binding.[134] More complex and specific bioconjugation methods are currently in development, including nickel-NTA-histidine interactions, SNAP-tagging, HALO-tagging, and crosslinking to glycosylated residues on proteins, which should alleviate these problems.[131,135] It should be noted that many applications require fluorescent nanocrystals without a biological function. In these instances, it is useful to modify the surfaces of these colloids to minimize nonspecific binding interactions, using bioinert molecules such as polyethylene glycol.

2.4 Biological Applications of Semiconductor Nanocrystals

The integration of nanotechnology with biology and medicine is expected to radically advance our understanding of life and pathology, and improve our ability to detect and cure diseases.[122,123,131,136-158] Semiconductor quantum dots are one of the prime examples of this great expectation, and their use as fluorescent probes has already shown promise for detecting biomolecules, observing biological events, and detecting diseases. The potential of quantum dots stems from the unique optical properties of these nanocrystals outlined earlier in this chapter, especially the bright and tunable narrow-band fluorescence emission, tremendous photostability, and broad absorption spectra, which are unmatched by any other current probes. Modern quantum dot bioimaging agents have developed considerably in the past decade, and a variety of

complex macromolecular architectures have been utilized, as outlined in Figure 2.23. These light-emitting nanoparticles meet many of the needs of biologists and physicians studying the most infrequent events biology that require ultrasensitive detection, for which there is currently a dearth of useful tools. The striking ability to detect quantum dots with great sensitivity, even down to the single molecule level, should soon make great strides in the detection of low concentration cancer biomarkers and viruses, the development of high-throughput screening assays, the observation of events inside of living cells in real time, molecular profiling of cancer tissue, laparoscopic imaging of diseases, and image-guided surgery.

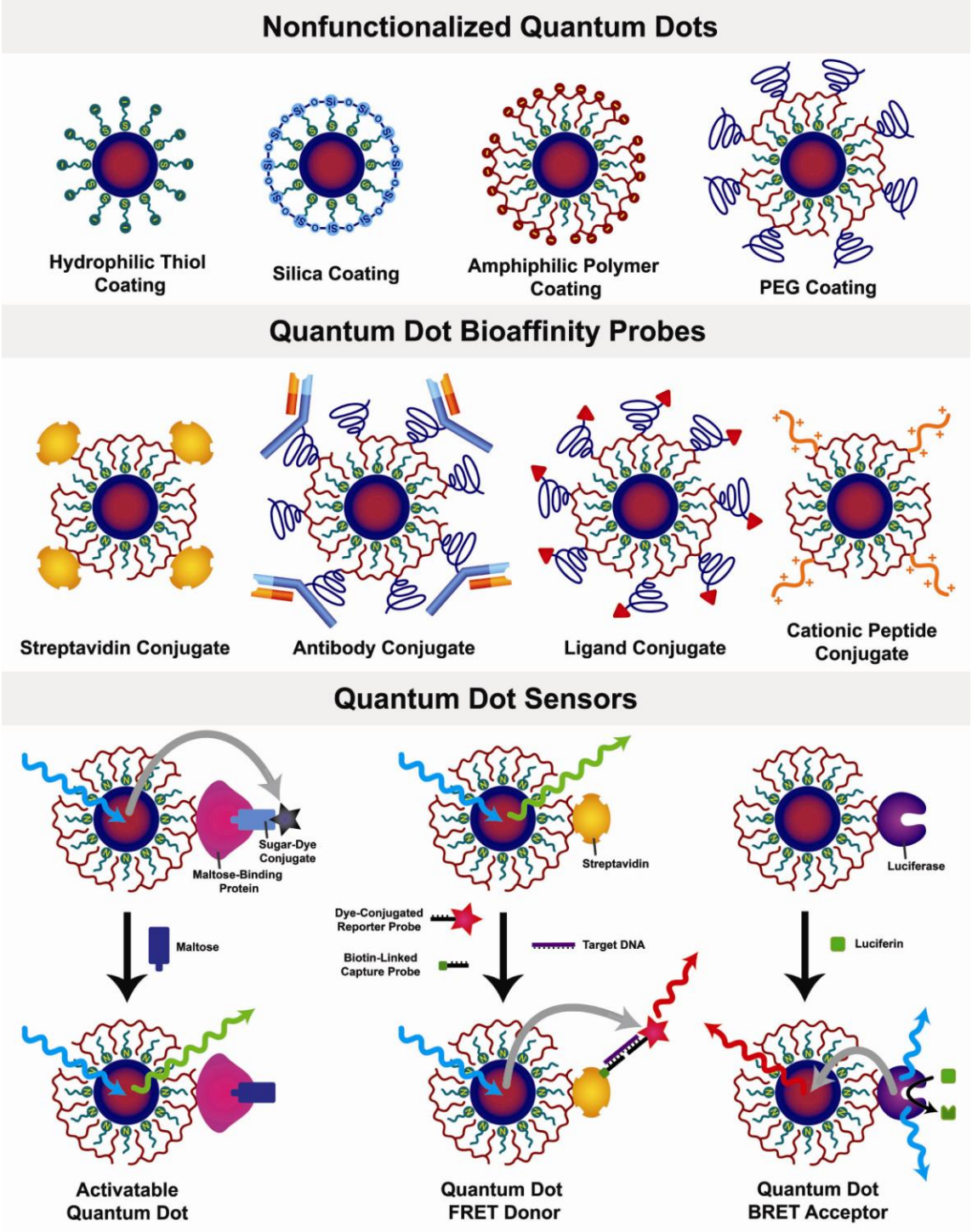

Figure 2.24: Schematic diagrams of nonfunctionalized and bioconjugated quantum dot probes for sensing and imaging applications. From left to right, biologically nonfunctional quantum dots (top) can be coated with a monolayer of hydrophilic thiols or a cross-linked silica shell, or they can be encapsulated in micelles using amphiphilic polymers based on polyacrylic acid or polyethylene glycol. Quantum

dot bioaffinity probes (middle) can be prepared by conjugation to streptavidin for modular and high affinity coupling with biotinylated molecules, coupling to antibodies for detection of specific antigens, attachment to small molecule ligands, peptides, or aptamers, or coupling to cationic peptides like the HIV-1 Tat peptide for high efficiency induction of endocytosis. Quantum dot biosensors (bottom) have also been prepared for FRET-based sensing of proteins, FRET-mediated sensing of DNA, or BRET-induced quantum dot bioluminescence. These sensors are described in detail in the text.

2.4.1 Comparison Between Semiconductor Quantum Dots and Conventional Fluorophores. Organic dyes and fluorescent proteins have been used in nearly all conceivable detection scenarios throughout biology, from single molecule imaging inside living cells to macroscopic animal imaging. The fundamental optical advantages of fluorescent quantum dots over these conventional light emitters arise from their crystalline semiconductor nature, which yields a large density of electronic states with negligible atomic reorganization. Most importantly, the brightness of a quantum dot is several orders of magnitude greater than that of an organic dye or fluorescent protein. Many dyes and quantum dots have similar quantum efficiencies (~20-80% in water), but the molar extinction coefficients of quantum dots are much larger, generally 1-5 x 10^6 M^{-1} cm^{-1}, compared to 5-10 x 10^4 M^{-1} cm^{-1} for dyes.[43] This brightness is useful for the detection of single quantum dots with lower excitation intensities and with higher temporal resolution compared to organic dyes. In addition, recently it has been shown that quantum rods and tetrapods can have even larger extinction coefficients, greater than 10^8 M^{-1} cm^{-1},[119] theoretically 1000 times brighter than most organic fluorophores. The two-photon cross-sections of quantum dots are also extremely large, 100-20,000 times that of organic dyes.[159] The effective brightness of quantum dots is also a result of the width of their absorption bands compared to organic dyes (Figure 2.24), allowing excitation at short wavelengths that do not overlap with the emission bands for the detection of a greater fraction of emitted light than what is possible for organic dyes. As

well, because the emission bands are narrow (typically 25-35 nm FWHM) and Gaussian, quantum dots are ideal candidates for multiplexing applications for the simultaneous detection of multiple analytes and for spectral encoding.

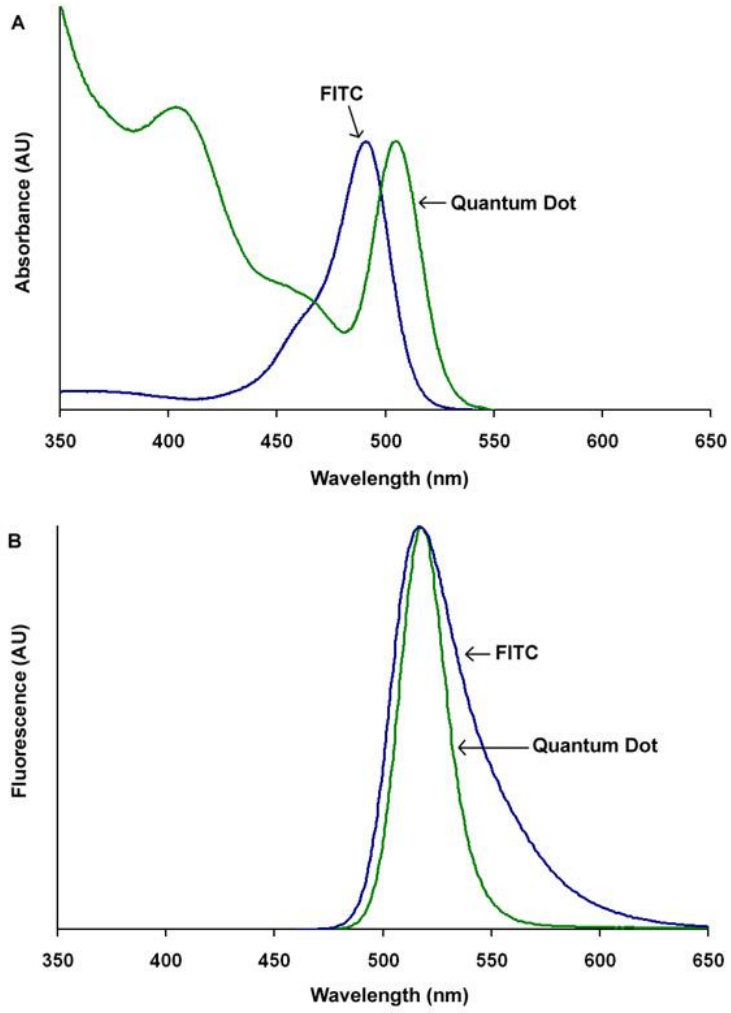

Figure 2.25: Comparison of the spectral features of organic dyes and quantum dots. Absorption (A) and fluorescence (B) spectra are shown for the organic dye fluoresceine isothiocyanate (FITC; blue) and a CdSe nanocrystal (~2.4 nm diameter; green) with a similar fluorescence maximum.

The photostability of quantum dot emission is one of the most important properties for long term observation of signals necessary for the study of events in living cells. Most

studies have shown that quantum dots are hundreds to thousands of times more stable against photodegradation than organic dyes.[13,14,51] This remarkable advantage stems from the capacity to grow an insulating inorganic shell on the quantum dot, as discussed in section 2.2.4, which can protect the optical elements from oxidative degradation. Embedding organic fluorophores in beads leads to a similar stabilization in fluorescence emission, but the resulting particles generally have other associated disadvantages, such as a vast increase in size and a propensity for nonspecific binding. The excited state lifetime is also much larger for quantum dots compared to organic dyes (Section 2.2.3), which can allow an even greater level of detection sensitivity through time-gated spectroscopy due to the short fluorescence lifetimes of intrinsic biological fluorophores.[160] Quantum dots are also superior in their optical and chemical versatility, as their emission wavelength can be tuned with great precision merely by adjusting the size or composition of the nanocrystal. Because various colors of semiconductor nanocrystals can be coated with the same organic ligands and polymers, they can all be conjugated to biological molecules using the same chemistry. In contrast, preparing dyes with new wavelengths of emission requires the development of an entirely new chemical species with possibly different functional groups for conjugation, and the development of new fluorescent proteins requires difficult and consuming protein engineering. Importantly, quantum dot fluorescence can be engineered to span the near-infrared spectrum, a spectral region of great sensitivity in biological environments for which no stable or bright organic dyes exist.

The most important disadvantage of quantum dots compared to organic dyes and proteins is their colloidal nature. These particles are often 5-30 nm in hydrodynamic diameter when dispersed in water, making them comparable to the size of large proteins. As such, they do not have the diffusive molecular nature of organic dyes, and

cannot natively perform some of their most useful tasks, such as plasma membrane translocation, and high efficiency energy transfer. However this colloidal nature is an advantage under some circumstances. For example, quantum dots are highly electron-dense and are therefore innately discernable via electron microscopy, which is not possible for small organic dyes.[161,162] In addition, because of their large surface areas, multiple bioaffinity molecules may be attached to a single quantum dot, which could have enhanced affinity through multivalent interactions. As well, stable polymeric coatings on quantum dots can render them stable under harsh biological conditions, such as low-pH endosomes and oxidative peroxisomes, which could degrade conventional dyes. From a biocompatibility perspective, most conventional quantum dots contain highly toxic elements, such as cadmium, mercury, or lead. Although many organic dyes are also known to be highly cytotoxic, the potential cellular and organismal toxicity specific to semiconductor nanocrystals must be carefully addressed before some of their hypothetical applications are pursued (Section 2.4.5 and Chapter 7).

2.4.2 *In Vitro* Diagnostic Assays. Screening of blood, urine, and other bodily fluids for the presence of biomolecules has become a routine and vital part of modern medicine. Especially relevant today are screening assays for viral antigens and cancer markers, which have become commonly used diagnostic techniques, yet are limited by the lack of specific soluble markers and sensitive means to detect them at low concentration. Although many cancer biomarkers have been identified, including proteins, specific DNA or mRNA sequences, and circulating tumor cells, the specificity of only one of these markers for cancer is generally poor, as exemplified by the prostate specific antigen (PSA) screening test for the detection of prostate cancer.[163] Indeed, specific cancer diagnosis from serum samples alone may only be possible with a multiplexed approach to assess a large number of biomarkers.[164] On the other hand, viral antigens are often

quite specific for particular strains of viral infections, but may only be present in copy numbers too low to be detected. Quantum dots could not only serve to improve the sensitivity of biomarker detection, but they could also allow the detection of hundreds to thousands of molecules simultaneously. Experimental groundwork has already begun to demonstrate the feasibility of these expectations, as quantum dots have found to be superior to conventional fluorescent probes in many types of clinical assays.

2.4.2.1 Protein Immunoassays. The ability to detect viral infections and screen for cancer in its earliest stages necessitates highly sensitive assays to detect viral antigens and biomarkers of carcinogenesis. The current gold standards for detecting low copy number proteins are enzyme-linked immunosorbent assays (ELISA), which have a limit of detection in the pM range. Although these assays are used clinically, they are labor-intensive, time-consuming, prohibitive of multiplexing, and expensive. In this regard, the high sensitivity of quantum dot detection could possibly increase the clinical relevance and routine use of diagnosis based on low-copy number proteins. Quantum dots have been successfully used as substitutes for organic fluorophores and colorimetric reagents in a variety of immunoassays for the detection of specific proteins, yet they have not demonstrated an increase in sensitivity (100 pM).[165,166] Increasing the sensitivity of these probes may only be a matter of optimizing bioconjugation parameters and assay conditions, although the multiplexing capabilities of these probes have already been demonstrated. Hedi Mattoussi and coworkers simultaneously detected four toxins using four different quantum dots, emitting between 510 nm and 610 nm, in a sandwich immunoassay configuration with a single excitation source.[167] Although there was spectral overlap of the emission peaks, deconvolution of the spectra revealed fluorescence contributions from all four toxins. This assay was far from quantitative, however, and it is apparent that fine-tuning of antibody cross-reactivity will be required to

make multiplexed immunoassays useful. Similarly, Savvas Makrides and coworkers demonstrated the ease of simultaneously detecting two proteins with two spectrally distinct quantum dots in a Western blot assay.[168]

2.4.2.2 Protein Biosensors. Biosensors are a new class of probe developed for biomarker detection on a real-time, continuous basis in a complex mixture. Assays resulting from these new probes could be invaluable for cancer biomarker detection and viral infection diagnosis because of their high speed, ease of use, and low cost, enabling quick point-of-care screening. Quantum dots are optically ideal for biosensor applications due to their resistance to photobleaching, allowing for continuous monitoring of signal. Fluorescence resonance energy transfer (FRET) has been the most common mechanism used to render quantum dots switchable from a quenched "off" state to a fluorescent "on" state. FRET is the nonradiative energy transfer from an excited donor fluorophore to an acceptor. The acceptor can be any molecule (such as a dye or another nanoparticle) that absorbs radiation at the wavelength of the emission of the donor (the quantum dot). Mattoussi and coworkers used quantum dots conjugated to maltose binding proteins as an *in situ* biosensor for detection of the sugar maltose (Figure 2.23, bottom left).[130] By initially incubating the quantum dot with an energy-accepting dye that is conjugated to a sugar recognized by the receptor, excitation of the quantum dot (blue) yields little fluorescence, as the energy is nonradiatively transferred (grey) to the dye with ~60% efficiency. Upon addition of maltose, the quencher-sugar conjugate is displaced, restoring fluorescence (green) in a concentration-dependent manner. Quantum dot biosensors have also been assembled that do not require binding and dissociation to modulate quenching and emission. However before this work can be translated into clinical tools, these probes must be optimized for higher detection sensitivity, which will require higher quenching efficiencies.

2.4.2.3 Nucleic Acid Detection. Early detection and diagnosis of cancer and viral infections could be greatly improved with genomic screening of individuals for hereditary predispositions to certain types of cancers, by detecting mutated genes and other nucleic acid biomarkers for cancer in bodily fluids, and by detecting low-copy number viral genes. The current gold standard for sensitive detection of nucleic acids is polymerase chain reaction (PCR) combined with a variety of molecular fluorophore assays, commonly resulting in a detection limit in the fM range. However, like ELISAs, the clinical utility of nucleic acid analysis for cancer diagnosis is precluded by its time and labor consumption and poor multiplexing capabilities. Many types of new technologies have been developed recently for the rapid and sensitive detection of nucleic acids, most notably RT-PCR and nanoparticle-based biobarcodes,[169] each of which have a limit of detection in the tens of molecules. However quantum dots could have an advantage in this already technologically crowded field because of their multiplexing potential. Alivisatos and coworkers reported the detection of specific single nucleotide polymorphisms of the human p53 tumor suppressor gene using quantum dots in a microarray assay format,[170] although the level of sensitivity (2 nM) was far from current standards. Importantly, this work demonstrated the capacity to simultaneously detect two different DNA sequences using two different quantum dots.

Recently Tza-Huei Wang developed a quantum dot biosensor for DNA, analogous to the aforementioned protein biosensor (Figure 2.23, bottom middle).[171] By mixing the ssDNA to be detected with (a) an acceptor fluorophore conjugated to a DNA fragment complementary to one end of the target DNA and (b) a biotinylated DNA fragment complementary to the opposite end of the target DNA, these nucleotides hybridize to yield a biotin-DNA-fluorophore conjugate. Upon mixing this conjugate with streptavidin-coated quantum dots, nanocrystal fluorescence (green) is quenched via nonradiative

energy transfer (grey) to the fluorophore conjugate. This dye acceptor then becomes fluorescent (red), specifically and quantitatively indicating the presence of the target DNA. Because quantum dots have broadband absorption compared to organic dyes, excitation of the nanocrystal construct at a short wavelength does not directly excite the dye, thereby allowing extremely low background signals. This allows the highly sensitive and quantitative detection of as few as 50 DNA copies with sufficient specificity to differentiate single nucleotide differences. However this strategy is not ideal for high-throughput analysis of multiple biomarkers because sensitive detection required the analysis of single quantum dots, followed by statistical data analysis.

2.4.2.4 High-Throughput Multiplexing. Rather than using single quantum dots for identification of single biomarkers, it has been proposed that different colors of quantum dots can be combined into a larger structure, such as a microbead, to yield an "optical barcode." With the combination of 6 quantum dot emission colors and 10 quantum dot intensity levels for each color, one million different codes are theoretically possible. A vast assortment of biomarkers may be optically encoded by conjugation to these beads, opening the door to the multiplexed identification of many biomolecules for high-throughput screening of biological samples. Pioneering work was reported by Nie and coworkers in 2001, in which 1.2 μm polystyrene beads were encoded with three colors of quantum dots (red, green, and blue) and different intensity levels.[172] The beads were then conjugated to DNA, resulting in different nucleic acids being distinguished by their spectrally distinct optical codes. These encoded probes were incubated with their complementary DNA sequences, which were also labeled with a fluorescent dye as a target signal. The hybridized DNA was detected through colocalization of the target signal and the probe optical code, *via* single-bead spectroscopy, using only one

excitation source. The bead code identified the sequence, while the intensity of the target signal corresponded to the presence and abundance of the target DNA sequence.

The high-throughput potential of this report was realized in 2003 with the use of a similar system to detect DNA sequences that differed by only one nucleotide (single nucleotide polymorphisms).[173] In this work, 194 samples of 10 different DNA sequences from specific alleles of the human cytochrome P450 gene family were correctly identified by hybridization to encoded probes. High-throughput analysis was achieved by the use of flow cytometry to identify spectral codes, rather than single-bead spectroscopy. This identification would have been considerably more difficult with organic fluorophores due to the fact that their emission peaks overlap, obscuring the distinct codes, and because multiple excitation sources would be required. Further studies on such nano-barcoding technologies have shown that in comparison to standard planar chips, bead-based multiplexing has the advantages of greater sensitivity, higher statistical analysis, faster assaying time, and the flexibility to add new probes at lower costs.[174-177] It is foreseeable that once encoded libraries have been developed for identification of nucleic acid sequences and proteins, solution-based multiplexing of quantum dot-encoded beads could quickly produce a vast amount of genomic and protein expression data. This could not only be used to discover new biomarkers for disease, but it could also open the door to simple and fast genotyping of patients and cancer classification for personalized medical treatment.

2.4.3 Cellular Labeling. Fluorescent dyes have been indispensible tools for cellular labeling since the introduction of immunohistochemistry in 1942.[178] In 1994, the recombinant expression of green fluorescent protein opened new doors for highly specific fluorescent detection and monitoring of protein expression and localization.[179]

Despite the many discoveries that have resulted from these techniques, organic dyes and fluorescent proteins are extremely limited in their optical capabilities, especially in their capacity for analyte quantification, multiplexing, single molecule detection, and continuous monitoring of stable signals. This is especially true for applications in pathological evaluation of fixed tissues and for monitoring single molecules in living cells.

2.4.3.1 Labeling of fixed cells and tissues. The feasibility of using quantum dots for biomarker detection in fixed cellular monolayers was first demonstrated by Alivisatos and coworkers in 1998.[14] By labeling nuclear antigens with green silica-coated quantum dots and F-actin filaments with red quantum dots in fixed mouse fibroblasts, these two spatially distinct intracellular antigens were simultaneously detected. This article and others[13,122] have demonstrated that quantum dots are brighter and dramatically more photostable than organic fluorophores when used for cellular labeling. Many different cellular antigens in fixed cells and tissues have been labeled using quantum dots, including specific genomic sequences,[180,181] mRNA,[182] plasma membrane proteins,[122,183] cytoplasmic proteins,[14,122] and nuclear proteins,[14,122] and it is apparent that they can function as both primary and secondary antibody stains. In addition, high resolution actin filament imaging has been demonstrated using quantum dots,[122] and the fluorescence can be correlated directly to electron micrograph contrast due to the high electron density of semiconductor nanocrystals.[161,162] It is now clear that quantum dots are superior to organic dyes for fixed cell labeling.

With this knowledge, it is evident that one of the most promising applications for cellular labeling with quantum dots is for the evaluation of pathological tissue specimens for cancer diagnosis. Pathological evaluation of biopsies of primary tumors and their distal metastases is the most important cancer diagnostic technique in practice. After

microscopic examination of the tissue, a pathologist predicts a grade and stage of tumor progression, so that the cancer can be classified to give a prognosis and appropriate treatment regimen. However evaluation is based primarily on qualitative morphological assessment of the tissue sections, sometimes with fluorescent staining of the tissue for specific cancer biomarkers. This field is highly subjective, and diagnoses of identical tissue sections may vary between pathologists. A more objective and quantitative approach based on biomarker detection would increase diagnostic accuracy. Quantum dots are ideal candidates for quantitative staining of tissues for biomarkers because of their optical multiplexing capacity and because they have already been proven to be outstanding probes for fluorescent detection of proteins and nucleic acids in cells. However the translation from fixed cell labeling to labeling of formaldehyde-fixed, paraffin-embedded tissue sections of tumor biopsies is not simple due to the high autofluorescence and the loss of antigen presentation associated with the embedding and fixation processes. Nevertheless, early tissue section labeling experiments with quantum dots have shown success for detecting biomarkers rat neural tissue,[184] human skin basal cell carcinomas,[183] and human tonsil tissue.[185] More recently, the multiplexing, quantitative capacity of quantum dot labeling has been realized in fixed, embedded prostate cancer specimens,[131,144,186] breast tumor specimens,[144,187] and in coronary arteries and aortas.[188] The recent advances in immunohistochemistry (IHC) for protein detection and fluorescence *in situ* hybridization (ISH)[180,181] for nucleic acid detection using quantum dot probes could revolutionize clinical evaluation of cancer biopsies because of the large number of biomarkers that could be detected simultaneously.

2.4.3.2 Live Cell Imaging. Despite advances in the labeling of fixed cells and tissues with semiconductor quantum dots, only limited progress has been made in developing

quantum dot probes for imaging inside living cells. A major problem is the lack of efficient methods for delivering single quantum dots into the cytoplasm of a living cell. A common observation is that quantum dots tend to aggregate inside cells, and are often trapped in endocytotic vesicles such as endosomes and lysosomes.

2.4.3.2.1 Imaging and Tracking of Membrane Receptors. Quantum dot bioconjugates have been found to be powerful imaging agents for specific recognition and tracking of plasma membrane antigens on living cells. In 2002 Thomas Jovin and coworkers coupled red-light emitting (CdSe)ZnS nanocrystals to epidermal growth factor, a small protein with a specific affinity for the erbB/HER membrane receptor.[189] After addition of these conjugates to cultured human cancer cells, receptor-bound quantum dots could be identified at the single-molecule level. The bright, stable fluorescence emitted from these quantum dots allowed the continuous observation of protein diffusion on the cellular membrane, and could even be visualized after the proteins were internalized. Maxime Dahan and coworkers similarly reported that quantum dots conjugated to an antibody fragment specific for glycine receptors on the membranes of living neurons allowed tracking of single receptors.[190] These conjugates showed superior photostability, lateral resolution, and sensitivity relative to organic dyes. These applications have inspired the use quantum dots for monitoring other plasma membrane proteins such as integrins,[191,192] tyrosine kinases,[193,194] G-protein coupled receptors,[195] and membrane lipids associated with apoptosis.[196,197] As well, detailed procedures have recently been published for receptor labeling and visualization of receptor dynamics with quantum dots,[198,199] and new techniques to label plasma membrane proteins using versatile molecular biology methods with minimized receptor crosslinking have been developed.[134,200,201]

2.4.3.2.2 Intracellular Delivery of Quantum Dots. A variety of techniques have been explored to label cells internally with quantum dots using passive uptake, receptor-mediated internalization, chemical transfection, and mechanical delivery. Quantum dots have been loaded passively into cells by exploiting the innate capacity of many cell types to uptake their extracellular space through endocytosis.[202-204] It has been found that the efficiency of this process may be dramatically enhanced by coupling the nanocrystals to membrane receptors. This is likely due to the avidity-induced increase in local concentration of the nanoparticles at the surface of the cell, as well as an active enhancement caused by receptor-induced internalization.[189,203,205] However, these methods lead to sequestration of aggregated nanoparticles in vesicles, showing strong colocalization with membrane dyes. Although these quantum dots cannot diffuse to specific intracellular targets, this is a simple way to label cells, and an easy method to fluorescently image the process of endocytosis. Nonspecific endocytosis was also utilized by Alivisatos and coworkers to fluorescently monitor the motility of cells on a quantum dot-coated substrate.[204] The path traversed by each cell became dark, and the cells increased in fluorescence as they took up more quantum dots. Chemical transfection methods were originally developed for the intracellular delivery of a wide variety of drugs and biomolecules, enhancing plasma membrane translocation with the use of cationic lipids or peptides.[206-210] The efficacy of these carriers for the intracellular deliver of quantum dots is discussed below. Mechanical delivery methods include microinjection of nanoparticles into individual cells, and electroporation of cells in the presence of the quantum dots. Microinjection has been reported to deliver quantum dots homogeneously into the cytoplasms of cells,[121,210] however this method is of low statistical value, as careful manipulation of single cells forbids the use of large sample sizes. Electroporation makes use of the increased permeability of cellular membranes under pulsed electric fields to deliver nanoparticles, but this method has been reported

to result in aggregation of quantum dots in the cytoplasm,[210] and generally results in widespread cell death.

Despite the current technical challenges, quantum dots are quickly gaining popularity as intracellular probes due to their intense, stable fluorescence, and recent reports have demonstrated that intracellular targeting is not far off. In 2004, Sangeeta Bhatia and coworkers demonstrated that quantum dots conjugated to organelle-targeting peptides could specifically stain either cellular mitochondria or nuclei following microinjection into fibroblast cytoplasms.[210] Similarly, Faqing Chen and coworkers targeted peptide-quantum dot conjugates to cellular nuclei, using electroporation to overcome the plasma membrane barrier.[206] These schemes have resulted in organelle-level resolution of intracellular targets for living cells, yielding fluorescent contrast of vesicles, mitochondria, and nuclei, but not the ability to visualize single molecules. Recently Dahan and coworkers demonstrated the capacity to image individual kinesin motors in HeLa cells using quantum dots delivered into the cytoplasm via osmotic lysis of pinocytotic vesicles.[211] By incubating the cells in a hypertonic solution containing the nanoparticles, water efflux resulted in membrane invagination and pinocytosis, trapping extracellular quantum dots in endosomal vesicles. Then a brief incubation in hypotonic medium induced intracellular water influx, rupturing the newly formed vesicles, and releasing single quantum dots into the cytosol. All of the nanoparticles were observed to undergo random Brownian motion in the cytoplasm. However if these quantum dots were first conjugated to kinesin motor proteins, a significant population of the nanocrystals exhibited directional motion. The velocity of the directed motion and its processivity (average time before cessation of directed motion) were remarkably close to those observed for the motion of these conjugates on purified microtubules *in vitro*. Although this work managed to overcome the plasma membrane diffusion barrier, it highlighted a

different problem fundamental to intracellular imaging of living cells, which is the impossibility of removing probes that have not found their target. In this report, the behavior of the quantum dots was sufficient to distinguish target-bound quantum dots from those that were not bound to their target, but this will not be the case for the majority of other protein targets. Without the ability to wash away unbound probes like what is possible in the intracellular labeling of fixed, permeabilized cells, the need for activateable probes that are 'off' until they reach their intended target is apparent. However quantum dots have already found a niche for quantitative monitoring of motor protein transport and for tracking the fate of internalized receptors, allowing the study of downstream signaling pathways in real time with high signal-to-noise and high temporal and spatial resolution.[189,193,194,212,213]

2.4.3.2.2 Cell-Penetrating Quantum Dots. Cell-penetrating peptides are a class of chemical transfectants that have garnered widespread interest due to the high transfection efficiency of their conjugated cargo, versatility of conjugation, and low toxicity. Although the mechanism of delivery is still a matter of some debate,[214-220] quantum dots have been successfully delivered to cells using cell-penetrating peptides such as polyarginine and HIV-1 Tat.[208,212,221] Nie and coworkers recently used Tat peptide-conjugated quantum dots to examine the cellular uptake and intracellular transport of nanoparticles in live cells, and confirmed previous reports of a macropinocytosis internalization mechanism.[222] The engulfed nanocrystals were found to be tethered to the inner surfaces of vesicles, and were actively transported by molecular motors (such as dyneins) along microtubules to the microtubule organizing center (MTOC).[223] In addition, the nanoparticle conjugates attach to filopodia, and were observed to bud off from fliopodial tips as quantum dot-loaded vesicles. These results provide new insights into the mechanism of Tat peptide mediated delivery, and are also

important to the development of nanoparticle probes for intracellular targeting and imaging.

Another class of quantum dot probe can mediate cellular internalization and endosomal disruption through the 'proton-sponge effect.[224-226] Although the mechanism of this effect is also unclear, polymers and nanoparticles containing a large number of conjugate bases with buffering capacity in the pH 5-6 range are known to disrupt endosomal organelles in living cells. This may be caused by a buffering of influxed protons in acidic endosomes, which causes an osmotic influx of water that ruptures the vesicles. Recently Nie and coworkers coated quantum dots with an endosomolytic hyperbranched copolymer ligand composed of polyethylenimine grafted to polyethylene glycol.[227] The resulting quantum dots were highly stable in acidic solution,[228] and escape from vesicles was found to be mediated by the grafting ratio of PEG, which showed an inverse relationship with cytotoxicity. In further developments, it was found that these polymeric coatings can be engineered to balance the electrostatic charge and the proton absorbing capacity to allow coulombic adsorption of silencing RNA and release from endosomes.[229] These proton-sponge conjugates were found to have gene silencing efficiencies 10-20 times greater than commercial siRNA delivery agents, and also allowed fluorescence and electron microscopic imaging.

Dusica Maysinger and coworkers recently reported that very small quantum dots (2.2 nm) coated with small molecule ligands (cysteamine) spontaneously translocate to the nuclei of murine microglial cells following cellular uptake through passive endocytosis.[230] In contrast, larger nanocrystals (5.5 nm) and small quantum dots bound to albumin were located in the cytosol only. This is fascinating because these particles could not only escape from endocytotic vesicles, but they were also subjected to an unknown type of

active machinery that attracted the quantum dots to the nucleus. Igor Nabiev studied a similar trend of size-dependent quantum dot segregation in human macrophages, and found that small nanoparticles may target nuclear histones and nucleoli after active transport across the nuclear membrane.[231] They found that the size cut-off for this effect was around 3.0 nm. Larger nanocrystals eventually ended up in vesicles in the MTOC region, although some quantum dots were found to be free in the cytoplasm. This group proposed that the proton-sponge effect was also responsible for endosomal escape, as their small carboxyl-coated quantum dots could buffer in the pH 5-7 range. These insights are important for the design and development of nanoparticle agents for intracellular imaging and therapeutic applications.

2.4.4 *In Vivo* Animal Imaging. Compared to the study of living cells in culture, different challenges arise with the increase in complexity to a multicellular organism, and with the accompanying increase in size. Unlike monolayers of cultured cells and thin tissue sections, tissue thickness becomes a major concern because biological tissue attenuates most signals used for imaging. Optical imaging, especially fluorescence imaging, has been used in living animal models, but it is still limited by the poor transmission of visible light through biological tissue. It has been suggested that there is a near-infrared optical window in most biological tissue that is the key to deep-tissue optical imaging.[232] The rationale is that Rayleigh scattering decreases with increasing wavelength, and the major chromophores in mammals, hemoglobin and water, have local minima in absorption in this window. Few organic dyes are available that emit brightly in this spectral region, and they suffer from the same photobleaching problems as their visible counterparts, although this has not prevented their successful use as contrast agents for living organisms.[233] One of the most distinct advantages of quantum dots for imaging in living tissue is that their emission wavelengths can be tuned

throughout the near-infrared spectrum by adjusting their composition and size, resulting in photostable fluorophores that are stable in biological buffers.[155]

2.4.4.1 Biodistribution of Quantum Dots. For most *in vivo* imaging applications using nanoparticle contrast agents, systemic delivery into the bloodstream will be the primary mode of administration. For this reason, the interactions of the nanoparticles with the components of plasma, the specific and nonspecific adsorption to blood cells and vascular endothelium, and the temporal biodistribution are of great interest. Soon after exposure to blood, quantum dots may be adsorbed by various proteins which could significantly alter their physicochemical properties and bioaffinity. It is also feasible that they could modulate hemostasis or initiate an immune response.[234,235] The number of papers published on quantum dot pharmacokinetics and biodistribution is limited, but several common trends have been observed. It has been consistently reported that quantum dots are taken up nonspecifically by the reticuloendothelial system (RES), including the liver and spleen, and the lymphatic system.[234,236,237] For example, Byron Ballou and coworkers reported that (CdSe)ZnS nanocrystals coated with an amphiphilic polymer were rapidly removed from the bloodstream into organs of the RES, and remained there for at least 4 months with detectable fluorescence.[234] Electron microscopy revealed that these quantum dots retained their morphology, suggesting nanocrystals with robust organic coatings are stable *in vivo* for very long periods of time without degradation into their potentially toxic elemental components. Further work by Warren Chan and coworkers demonstrated that within hours after administration, nearly 100% of albumin-coated quantum dots were removed from circulation and sequestered in the liver, where they were primarily accumulated in Kupffer cells, the resident macrophages of the liver.[237] These findings are not intrinsic to quantum dots, but are likely dependent on the size of the nanoparticles and their surface properties, and recent

publications have focused on this insight. John Frangioni and coworkers demonstrated that the renal clearance of quantum dots is closely related to the hydrodynamic diameter of the nanoparticle and the renal filtration threshold (~5-6 nm).[238] It is also vital for the nanoparticle surface to resist protein adsorption, which could significantly increase the hydrodynamic size above that of the renal threshold and promote phagocytosis. However it is unlikely that even small quantum dots could be entirely eliminated from the kidneys, as it has also been found that smaller quantum dots (~9 nm) may directly extravasate out of blood vessels, into interstitial fluid.[239]

2.4.4.2 *In Vivo* Vascular Imaging. One of the most immediately successful applications of quantum dots *in vivo* has been their use as contrast agents for the two major circulatory systems of mammals, the cardiovascular system and the lymphatic system. In 2003, Watt Webb and coworkers demonstrated that green-light emitting quantum dots remained fluorescent and detectable in capillaries of adipose tissue and skin of a living mouse following intravenous injection.[240] This work was aided by the use of near-infrared two-photon excitation for deeper penetration of excitation light, and by the extremely large two-photon cross-sections of semiconductor nanocrystals.[159] In other work, Bawendi and Frangioni used near-infrared quantum dots to image the coronary vasculature of a rat heart,[241] and Phil Campbell and coworkers imaged the blood vessels of chicken embryos with a variety of near-infrared and visible quantum dots.[242] The latter report showed that quantum dots were markedly brighter than traditionally used FITC-dextran conjugates, and resulted in a higher uniformity in image contrast across vessel lumena. Frederick Haselton and coworkers recently demonstrated the potential for quantum dots to serve as molecular imaging agents for vascular imaging.[243] Spectrally distinct nanoparticles were conjugated to three different cell adhesion molecules (CAMs), and intravenously injected in a diabetic rat model. Fluorescence angiography

of the retinal vasculature revealed CAM-specific increases in fluorescence, and allowed imaging of the inflammation-specific behavior of individual leukocytes, as they freely floated in the vessels, rolled along the endothelium, and underwent leukostasis. The unique spectral properties of quantum dots allowed the authors to simultaneously image up to four spectrally distinct quantum dot tags.

For imaging of the lymphatic system, the overall size of the probe is an important parameter for determining biodistribution and clearance. For example, Bawendi and Frangioni intradermally injected ~16-19 nm near-infrared quantum dots in mice and pigs.[155] The nanoparticles translocated to sentinel lymph nodes, likely due to a combination of passive flow in lymphatic vessels, and active migration of dendritic cells that engulfed the nanoparticles. Fluorescence contrast of these nodes could be observed up to 1 cm beneath the skin surface. However, if these quantum dots were formulated to have a smaller overall hydrodynamic size (~9 nm), they could migrate further into the lymphatic system, with up to 5 nodes showing fluorescence.[239] This technique could have great clinical impact due to the quick speed of lymphatic drainage and the ease of identification of lymph nodes, enabling surgeons to fluorescently identify and excise nodes draining from primary metastatic tumors for the staging of cancer. This technique has been used to identify lymph nodes downstream from the lungs,[236,244] esophagus,[245] and from subcutaneous tumors.[246] Recently the multiplexing capabilities of quantum dots have been exploited for mapping lymphatic drainage networks.[247] By injection of quantum dots of different color at different intradermal locations, these nanoparticles could be fluorescently observed to drain to common nodes,[248] or up to 5 different nodes in real time. A current problem is that a major fraction of the nanoparticles remain at the site of injection for an unknown length of time.[249]

2.4.4.2 *In Vivo* Tracking of Quantum Dot Loaded Cells. Cells can be loaded with quantum dots and other tracking agents *in vitro*, and then administered to an organism, providing a means to identify the original cells and their progeny within the organism. This was first demonstrated on a small organism scale by microinjecting quantum dots into the cytoplasms of single frog embryos.[121] As the embryos grew, the cells divided, and each cell that descended from the original labeled cell retained a portion of the fluorescent cytoplasm, which could be fluorescently imaged in real time under continuous illumination. In reports by both Kenji Yamamoto[250] and Sanford Simon,[209] cells loaded with quantum dots were injected intravenously into mice, and their distributions in the animals were later determined through tissue dissection, followed by fluorescence imaging. Also Nie and coworkers loaded human cancer cells with quantum dots, and injected these cells subcutaneously in an immune-compromised mouse. The cancer cells divided to form a solid tumor, which could be visualized fluorescently through the skin of the mouse.[123] Amy Rosen and coworkers recently reported that human mesenchymal stem cells loaded with quantum dots could be implanted into an extracellular matrix patch for use as a regenerative implant for canine hearts with a surgically-induced defect.[251] Eight weeks following implantation, it was found that the nanocrystals remained fluorescent within the cells, and could be used to track the locations and fates of these cells. This group also directly injected quantum dot-labeled stem cells into the canine myocardium, and used the fluorescence signals in cardiac tissue sections to elaborately reconstruct the locations of these cells in the heart. With reports that cells may be labeled with quantum dots at a high degree of specificity,[207,208] it is foreseeable that multiple types of cells may be simultaneously monitored in living organisms, and also identified using their distinct optical codes.[252]

2.4.4.3 *In Vivo* Tumor Imaging. Imaging of tumors presents a unique challenge not only because of the urgent need for sensitive and specific contrast agents of cancer, but also because of the unique biological attributes inherent to cancerous tissue. Blood vessels are abnormally formed during tumor-induced angiogenesis, having erratic architectures and wide endothelial pores. These pores are large enough to allow the extravasation of large macromolecules up to ~400 nm in size, which accumulate in the tumor microenvironment due to a lack of effective lymphatic drainage.[253-256] This 'enhanced permeability and retention' effect (EPR effect) has inspired the development of a variety of nanotherapeutics and nanoparticulates for the treatment and imaging of cancer. Because cancer cells are effectively exposed to the constituents of the bloodstream, their surface receptors may also be used as active targets of bioaffinity molecules. In the case of imaging probes, active targeting of cancer antigens (molecular imaging) has become an area of tremendous interest to the field of medicine because of the potential to detect early stage cancers and their metastases. Semiconductor nanocrystals hold great promise for these applications mainly due to their intense fluorescent signals and multiplexing capabilities, which could allow a high degree of sensitivity and selectivity in cancer imaging with multiple antigens.

The first steps toward this goal were undertaken in 2002 by Bhatia and coworkers, who conjugated quantum dots to peptides with affinity for various tumor cells and their vasculatures, and intravenously injected them into tumor-bearing mice.[126] Microscopic fluorescence imaging of tissue sections from the mice demonstrated that the nanoparticles specifically homed to tumor vasculature. In 2004 Nie and coworkers demonstrated that tumor targeting with quantum dots could generate tumor contrast on the scale of whole-animal imaging. These nanocrystals were conjugated to an antibody against the prostate-specific membrane antigen (PSMA), and were intravenously

injected into mice bearing subcutaneous human prostate cancers.[123] Tumor fluorescence was significantly greater for the actively targeted conjugates compared to nonconjugated nanocrystal, which also accumulated passively though the EPR effect. Using similar methods, Ququan Wang and coworkers were able to actively target and image mouse models of human liver cancer using quantum dots conjugated to an antibody against alpha-fetoprotein,[257] and the group of Xiaoyuan Chen showed that labeling quantum dots with RGD peptides significantly increased their uptake in human glioblastoma tumors.[258] In this later case, further microscopic analysis showed that almost all of the tumor contrast was likely due to the presence of large aggregates in their samples (150nm and above), which could bind to the tumor neovasculature through strong multivalent interactions.[259] Recent reports that quantum dots conjugated to luciferase enzymes can emit fluorescence without an external source of excitation may lead to greatly enhanced molecular sensitivity and depth penetration.[260] The mechanism behind this technology is a result of bioluminescence resonance energy transfer (BRET) (Figure 2.23, bottom right). The enzyme luciferase catalyzes the bioluminescent oxidation of exogenously administered luciferins, and conjugation of the enzyme to quantum dots results in nonradiative excitation of the quantum dot through BRET, inducing their fluorescence.

The development of clinically relevant nanocrystalline contrast agents for *in vivo* imaging is certain to encounter many roadblocks in the near future (see Section 2.4.5), however quantum dots can already be used as powerful imaging agents for the study of the complex anatomy and pathophysiology of cancer in animal models. The group of Rakesh Jain demonstrated that quantum dots greatly enhance current intravital microscopy techniques for the imaging of tumor microenvironment.[261] The authors used quantum dots as fluorescent contrast agents for blood vessels using two-photon

excitation, and simultaneously captured images of extracellular matrix from autofluorescent collagen, and perivascular cell contrast from fluorescent protein expression. The use of quantum dots allowed stark contrast between the tumor constituents due to their intense brightness, tunable wavelengths, and reduced propensity to extravasate into the tumor, compared to organic dye conjugates. In this work, the authors also used quantum dot-tagged beads with variable sizes to model the size-dependent distribution of various nanotherapeutics in tumors. Also in this report, primary bone marrow lineage-negative cells, which are thought to be progenitors for neovascular endothelium, were labeled *ex vivo* with quantum dots and imaged *in vivo* as they flowed and adhered to tumor blood vessels following intravenous administration. More recently, Hideo Higuchi and coworkers used semiconductor nanocrystals to study the biological processes involved in active targeting of nanoparticles. The authors used quantum dots labeled with an antibody against human epidermal growth factor receptor 2 (HER2) to target human breast cancer in a mouse model.[262] Through intravital fluorescence microscopy of the tumor following systemic nanoparticle administration, the authors could distinctly observe individual nanoparticles as they circulated in the bloodstream, extravasated into the tumor, diffused in extracellular matrix, bound to their receptors on tumor cells, and then translocated into the perinuclear region of the cells. The combination of sensitive quantum dot probes with powerful techniques like intravital microscopy and *in vivo* animal imaging could soon lead to major breakthroughs in the current understanding of tumor biology, improve early detection schemes, and guide the rational design of nanoparticle therapeutics.

2.4.5 Quantum Dot Toxicity. Great concern has been raised over the use of quantum dots in living cells and animals due to their composition of heavy metal ions. Presently the most commonly used quantum dots contain divalent cadmium, a nephrotoxin in its

ionic form. However the toxic nanocrystalline core is epitaxially shielded in a biologically inert zinc sulfide shell that is resistant to degradation, and further encapsulated in a stable organic polymer. Although this strong sequestration limit the acute bioavailability of cadmium, slow leaching of the toxic elements over time may yield a cytotoxic response if the nanocrystals accumulate permanently in cells and organs. In addition, secondary cytotoxic effects may occur, such as the catalytic formation of reactive oxygen species or the adsorption of vital cellular proteins and organelles. *In vivo*, quantum dots larger than the renal filtration threshold accumulate indefinitely in the reticuloendothelial system following intravenous administration. The eventual fate of these nanoparticles is of vital importance, but so far has yet to be elucidated.

2.4.5.1 Toxicity Due to Cadmium *in Vivo*. The only long-term study to date on the biodistribution of semiconductor nanocrystals showed that the concentration of cadmium in the liver and kidneys gradually increased over the course of 28 days following intravenous administration to mice, as determined via elemental analysis.[263] Throughout this time period, 100% of the injected dose was found to remain in the mice, 40% of which accumulated in the liver, consistent with RES uptake. However over the course of this study, the cadmium in the kidneys increased gradually from 1.5 to 9.2% of the total injected dose. From this study, it was not apparent if the cadmium was in the form of a free ion, or remained in the nanocrystalline form, although fluorescence microscopy revealed the presence of intact quantum dots in the liver and kidneys. The redistribution of the cadmium over time may signify the degradation of quantum dots *in vivo,* since the natural accumulation site of Cd^{2+} ions are the liver and kidneys.[205,264-266] In acute exposures, free cadmium may redistribute to the kidneys via hepatic production of metallothionein.[205] Although the quantum dots used in this study were robustly

prepared, with a stable polymer shell, these findings indicate the possibility of quantum dot degradation *in vivo*, which merits further, more detailed mechanistic studies.

2.4.5.2 Cytotoxicity Due to Cadmium *in vitro*. A majority of studies evaluating the cytotoxic effects of quantum dots toward cultured cells have attempted to correlate the release of cadmium from the nanocrystal with cytotoxic manifestations. This is reasonable, due to the well documented cytotoxicity of cadmium ions. It is well established that cadmium ions can be released from cadmium chalcogenide nanocrystals through oxidative degradation,[83,106,267] and these metal ions may bind to sulfhydryl groups on intracellular proteins, which may impair their functionality.[268] Several groups have attempted to make this correlation quantitative through fluorometric assays for free cadmium and spectroscopic determination of heavy metals.[205,269,270] For example, Bhatia and coworkers facilitated cadmium release from quantum dots through oxidative and photochemical etching, resulting in overt toxicity in primary rat hepatocytes.[205] In addition it was found that nanocrystal surface modifications that are known to attenuate oxidative etching, such as ZnS shell overgrowth or adsorption by albumin, were successful in abating this toxic effect, which has since been verified by several reports.[268,271] Although the current literature on the toxicity of cadmium-containing nanocrystals is far from conclusive, the development of heavy metal-free quantum dots may be useful for advancing this field in the event that metal toxicity is insurmountable.[78,79] Further studies are reported in Chapter 7.

2.4.5.3 A Critical Analysis of *in Vitro* Cytotoxicity Data. A significant number of reports have recently explored the cytotoxicity of quantum dots toward cultured cells, but it is difficult to draw firm conclusions due to a widespread inconsistency in (a) semiconductor nanocrystal compositions, (b) nanoparticle surface coatings and (c) experimental

conditions, such as the duration of the nanoparticle exposure, use of comparable or even relevant cell lines, media choice (i.e. with or without serum), and even the units of concentration (mg/ml versus nM). Nonetheless, literature data has shown a strong association between quantum dot cytotoxicity and the chemical and colloidal stability of these nanoparticles, which can be separated into three categories. (1) Core CdTe quantum dots that are synthesized in aqueous solution and stabilized by small thiolate ligands (e.g. mercaptoacetic acid). These quantum dots have been widely used due to their ease of synthesis, low cost, and immediate solubility in biological buffers. However, because these nanocrystals are protected by only a weakly bound ligand, they are highly susceptible to degradation and aggregation, and their cytotoxicity toward cells in culture has been well established.[270,272] (2) (Core)shell (CdSe)ZnS quantum dots synthesized in nonpolar solvents and transferred to water using thiolate ligands. CdSe is less prone to oxidation than CdTe, and ZnS is even more inert, and therefore these quantum dots are much more chemically stable. With direct comparison to CdTe nanocrystals, these particles are significantly less toxic, although high concentrations have been found to induce toxic responses from cells.[147] Because these quantum dots are coated with a ZnS shell, the origin of this cytotoxicity is still unclear, whether it is from degradation of the shell, leading to cadmium release, or if it is caused by other effects. When coated with small ligands, these quantum dots have similar surface chemistries compared to aqueous CdTe nanocrystals, burdened by significant ligand desorption which will render the nanocrystal colloidally unstable.[64] This propensity to aggregate may contribute to cytotoxicity, even if free cadmium is not released. Importantly for the comparison between (CdSe)ZnS nanocrystals and their cadmium-only counterparts (CdTe or CdSe core quantum dots), thiolate ligands bind more strongly to zinc than to cadmium, which may contribute to colloidal stability. (3) (Core)shell (CdSe)ZnS quantum dots synthesized in nonpolar solvents and transferred to water via encapsulation in an

amphiphilic polymer or cross-linked silica. These quantum dots are significantly more stable colloidally, chemically and optically when compared to their counterparts coated in small ligands.[228] For this reason, they have been found to be nearly biologically inert in both living cells and living animals.[123,155,86,206, 80,234,240,268,273] Only when exposed to harsh conditions or when directly injected into cells at immensely high concentrations have these quantum dots been found to elicit toxic or inflammatory responses.[121,271]

2.4.5.4 Alternative Cytotoxic Mechanisms *in Vitro*. It is feasible that a significant amount of toxicological data obtained for quantum dots thus far has been overwhelmingly influenced by the colloidal nature of these nanoparticles. The tendency for nanoparticles to aggregate, precipitate on cells in culture, nonspecifically adsorb to biomolecules, and catalyze the formation of reactive oxygen species (ROS) may be just as important as heavy metal toxicity contributions to toxicity. For example, Wolfgang Parak and coworkers found that (CdSe)ZnS quantum dots coated with an amphiphilic polymer induced the detachment of human breast cancer cells from their cell culture substrate.[268] This effect was found to also occur for biologically inert gold nanoparticles coated with the same polymer, thus ruling out the possibility of heavy metal atom poisoning. Microscopic examination of the cells revealed that the nanoparticles precipitated on the cells, causing physical harm. Indeed, carbon nanotubes, which are entirely composed of elementally harmless carbon, have been found to be capable of impaling cells and causing major problems in the lungs of mammals.[274] Nonspecific adsorption to intracellular proteins may also impair cellular function, especially for small quantum dots (3 nm and below), which can invade the cellular nucleus,[230,275] bind histones and nucleosomes,[155] and damage DNA *in vitro*.[276,277] Quantum dots are also known to catalyze the formation of ROS,[272,278] particularly when exposed to ultraviolet radiation. Francoise Winnik and coworkers exposed cultured cells to CdTe nanocrystals and

determined that the cytotoxic response could only be explained through the effects of ROS generation, as there was no dose-dependent relationship with intracellular Cd^{2+} release, as determined with a cadmium-reactive dye.[270] Protection of the surface of a quantum dot with a ZnS shell may greatly reduce ROS production.[279,280] Despite a recent surge of interest in the cytotoxicity of nanoparticles, there is still much to learn about the cytological and physiological mediators of nanoparticle toxicology.

2.4.6 Outlook. The applications of quantum dots in biomedicine span a broad range of length scales and address an assortment of clinical and biological sensing needs. Despite the many assets of these probes, many challenges must be overcome in order to harness their great potential originally outlined by Nie and Alivisatos in 1998. (1) The optical properties of these particles must be engineered with a greater focus on the near-infrared. Currently aqueous quantum dots with near-infrared emission have much lower quantum yield, photostability, and chemical stability than their visible light counterparts, and their emission bands are disproportionately broad, which limits their multiplexing capabilities. These needs are addressed in Chapters 3 and 4. (2) The colloidal and surface properties of these nanoparticles must be optimized in order to maximize their stability, minimize nonspecific binding, and minimize their size. Chapter 5 and 6 consider these needs. (3) Current quantum dot probes are prone to nonspecific binding and methods for bioconjugation for inducing bioaffinity are poorly developed. The interactions governing these properties must be more thoroughly understood and optimized for the production of versatile, successful optical imaging agents, especially for reducing RES uptake *in vivo* and increasing the efficiency of *in vivo* targeting. These needs are discussed further in Chapters 5 and 7. (4) A greater fundamental understanding must be achieved for the interactions between nanoparticles and biological systems, most importantly in terms of their mechanisms of cytotoxicity and

interactions with blood components. The complexity of these interactions will likely require many years to be fully revealed, but many new insights are discussed in Chapter 7. In the future, the major goal for bio-nanotechnology is to develop complex biological probes and agents that can be used to monitor and specifically manipulate biological systems, most importantly for medical applications. The nanocrystal probes designed from quantum dot backbones have already reached an impressive level of layered complexity, and probes with multimodal imaging and drug delivery capabilities are in early development. [229,281-294] Increasing the precision, dimensionality, and multimodality of these particles may generate great advances throughout biomedical fields. Although the most intuitive biomedical applications of nanotechnology are for cancer detection, profiling and treatment, explorations of underutilized applications in cardiovascular disease and infectious disease detection and treatment are certainly merited.

2.5 References

1. Efros, A. L. & Efros, A. L. Interband absorption of light in a semiconductor sphere. *Sov. Phys. Semiconduct.* **16,** 772-775 (1982).

2. Ekimov, A. I. & Onushchenko, A. A. Quantum size effect in the optical-spectra of semiconductor micro-crystals. *Sov. Phys. Semiconduct.* **16,** 775-778 (1982).

3. Brus, L. E. A Simple-Model for the Ionization-Potential, Electron-Affinity, and Aqueous Redox Potentials of Small Semiconductor Crystallites. *J. Chem. Phys.* **79,** 5566-5571 (1983).

4. Brus, L. E. Electron-electron and electron-hole interactions in small semiconductor crystallites - the size dependence of the lowest excited electronic state. *J. Chem. Phys.* **80,** 4403-4409 (1984).

5. Brus, L. Electronic Wave-Functions in Semiconductor Clusters - Experiment and Theory. *J. Phys. Chem.* **90,** 2555-2560 (1986).

6. Steigerwald, M. L., Alivisatos, A. P., Gibson, J. M., Harris, T. D., Kortan, R., Muller, A. J., Thayer, A. M., Duncan, T. M., Douglass, D. C., & Brus, L. E. Surface derivatization and isolation of semiconductor cluster molecules. *J. Am. Chem. Soc.* **110,** 3046-3050 (1988).

7. Goldstein, A. N., Echer, C. M., & Alivisatos, A. P. Melting in semiconductor nanocrystals. *Science* **256,** 1425-1427 (1992).

8. Alivisatos, A. P. Perspectives on the physical chemistry of semiconductor nanocrystals. *J. Phys. Chem.* **100,** 13226-13239 (1996).

9. Tolbert, S. H. & Alivisatos, A. P. High-pressure structural transformations in semiconductor nanocrystals. *Annu. Rev. Phys. Chem.* **46,** 595-625 (1995).

10. Rossetti, R., Ellison, J. L., Gibson, J. M., & Brus, L. E. Size effects in the excited electronic states of small colloidal CdS crystallites. *J. Chem. Phys.* **80,** 4464-4469 (1984).

11. Rossetti, R., Nakahara, S., & Brus, L. E. Quantum size effects in the redox potentials, resonance Raman spectra, and electronic spectra of CdS crystallites in aqueous solution. *J. Chem. Phys.* **79,** 1086-1088 (1983).

12. Murray, C. B., Norris, D. J., & Bawendi, M. G. Synthesis and characterization of nearly monodisperse CdE (E = S, Se, Te) semiconductor nanocrystallites. *J. Am. Chem. Soc.* **115,** 8706-8715 (1993).

13. Chan, W. C. W. & Nie, S. M. Quantum dot bioconjugates for ultrasensitive nonisotopic detection. *Science* **281,** 2016-2018 (1998).

14. Bruchez, M., Moronne, M., Gin, P., Weiss, S., & Alivisatos, A. P. Semiconductor nanocrystals as fluorescent biological labels. *Science* **281,** 2013-2016 (1998).

15. Rogalski, M. S. & Palmer, S. B. *Solid State Physics*. Gordon & Breach, Amsterdam, Netherlands (2000).

16. Verma, A. R. *Crystallography for Solid State Physics*. Wiley, New York, NY (1982).

17. Tilley, R. J. D. *Crystals and Crystal Structures*. Wiley, Hoboken, NJ (2006).

18. Yu, P. Y. & Cardona, M. *Fundamentals of Semiconductors: Physics and Materials Properties*. Springer, New York, NY (2001).

19. Adachi, S. *Properties of Group-IV, III-V and II-VI Semiconductors*. John Wiley & Sons, West Sussex, England (2005).

20. Atkins, P. *Physical Chemistry*. W.H. Freeman Co., New York, NY (2000).

21. Rogalski, M. S. & Palmer, S. B. *Quantum Physics*. Gordon & Breach, Amsterdam, Netherlands (1999).

22. Xu, Y. N. & Ching, W. Y. Electronic, optical, and structural properties of some wurtzite crystals. *Phys. Rev. B* **48,** 4335-4351 (1993).

23. Huang, M. Z. & Ching, W. Y. Calculation of optical excitations in cubic semiconductors. I. Electronic structure and linear response. *Phys. Rev. B* **47,** 9449-9463 (1993).

24. Bhattacharya, P. *Semiconductor Optoelectronic Devices*. Prentice-Hall, Upper Saddle River, NJ (1997).

25. Dimitrakopoulos, C. D. & Mascaro, D. J. Organic thin-film transistors: a review of recent advances. *IBM J. Res. Dev.* **45,** 11-27 (2001).

26. Manca, P. A relationship between the binding energy and the band-gap energy in semiconductors of diamond or zinc-blende structure. *J. Phys. Chem. Solids* **20,** 268-273 (1961).

27. Batsanov, S. S. Ionization, atomization, and bond energies as functions of distances in inorganic molecules and crystals. *Russ. J. Inorg. Chem.* **52,** 1223-1229 (2007).

28. Phillips, J. C. Ionicity of the chemical bond in crystals. *Rev. Mod. Phys.* **42,** 317-356 (1970).

29. Koh, A. K. Correlations in alkaline-earth chalcogenides and II-VI and III-V semiconductors with radius ratio. *J. Phys. Chem. Solids* **58,** 467-473 (1997).

30. Catlow, C. R. A. & Stoneham, A. M. Ionicity in solids. *J. Phys. C* **16,** 4321-4338 (1983).

31. Szigeti, B. Polarisability and dielectric constant of ionic crystals. *Trans. Faraday Soc.* **45,** 155-166 (1949).

32. Berding, M. A. & Sher, A. Polarity in semiconductor compounds. *Phys. Rev. B* **36,** 7433-7436 (1987).

33. Zhang, S. B., Wei, S. H., & Zunger, A. d-Band excitations in II-VI semiconductors: a broken-symmetry approach to the core hole. *Phys. Rev. B* **52,** 13975-13982 (1995).

34. Wei, S. H. & Zunger, A. Calculated natural band offsets of all II-VI and III-V semiconductors: Chemical trends and the role of cation d orbitals. *Appl. Phys. Lett.* **72,** 2011-2013 (1998).

35. Delin, A. & Kluner, T. Excitation spectra and ground-state properties from density-functional theory for the inverted band-structure systems *b*-HgS, HgSe, and HgTe. *Phys. Rev. B* **66,** 035117 (2002).

36. Vurgaftman, I., Meyer, J. R., & Ram-Mohan, L. R. Band parameters for III-V compound semiconductors and their alloys. *J. Appl. Phys.* **89,** 5815-5875 (2001).

37. Monemar, B., Paskov, P. P., & Kasic, A. Optical properties of InN - the bandgap question. *Superlattices Microstruct.* **38,** 38-56 (2005).

38. Litimein, F., Bouhafs, B., & Ruterana, P. Full-potential study of d-electrons effects on the electronic structure of wurtzite and zinc-blende InN. *Phys. Status Solidi A* **203,** 35-41 (2006).

39. Li, J. B. & Wang, L. W. Comparison between quantum confinement effects of quantum wires and dots. *Chem. Mater.* **16,** 4012-4015 (2004).

40. D'Andrea, A. & Del Sole, R. Excitons in semiconductor confined systems. *Solid State Commun.* **74,** 1121-1124 (1990).

41. Buhro, W. E. & Colvin, V. L. Semiconductor nanocrystals - Shape matters. *Nat. Mater.* **2,** 138-139 (2003).

42. Wang, Q. B. & Seo, D. K. Synthesis of deep-red-emitting CdSe quantum dots and general non-inverse-square behavior of quantum confinement in CdSe quantum dots. *Chem. Mater.* **18,** 5764-5767 (2006).

43. Yu, W. W., Qu, L. H., Guo, W. H., & Peng, X. G. Experimental determination of the extinction coefficient of CdTe, CdSe, and CdS nanocrystals. *Chem. Mater.* **15,** 2854-2860 (2003).

44. Shabaev, A. & Efros, A. L. 1D exciton spectroscopy of semiconductor nanorods. *Nano Lett.* **4,** 1821-1825 (2004).

45. Iotti, R. C. & Andreani, L. C. Crossover from strong to weak confinement for excitons in shallow or narrow quantum wells. *Phys. Rev. B* **56,** 3922-3932 (1997).

46. Empedocles, S. A., Norris, D. J., & Bawendi, M. Photoluminescence spectroscopy of single CdSe nanocrystallite quantum dots. *Phys. Rev. Lett.* **77,** 3873-3876 (1996).

47. Wu, D., Kordesch, M. E., & Van Patten, P. G. A new class of capping ligands for CdSe nanocrystal synthesis. *Chem. Mater.* **17,** 6436-6441 (2005).

48. Nirmal, M., Dabboussi, B. O., Bawendi, M., Macklin, J. J., Trautman, J. K., Harris, T. D., & Brus, L. E. Fluorescence intermittency in single cadmium selenide nanocrystals. *Nature* **383,** 802-804 (1996).

49. Tang, J. & Marcus, R. A. Mechanisms of fluorescence blinking in semiconductor nanocrystal quantum dots. *J. Chem. Phys.* **123,** (2005).

50. Mahler, B., Spinicelli, P., Buil, S., Quelin, X., Hermier, J. P., & Dubertret, B. Towards non-blinking colloidal quantum dots. *Nat. Mater.* **2008,** (2008).

51. Chen, Y. F., Vela, J., Htoon, H., Casson, J. L., Werder, D. J., Bussian, D. A., Klimov, V. I., & Hollingsworth, J. A. "Giant" multishell CdSe nanocrystal quantum dots with suppressed blinking. *J. Am. Chem. Soc.* **130,** 5026-5027 (2008).

52. Nirmal, M. & Brus, L. Luminescence photophysics in semiconductor nanocrystals. *Acc. Chem. Res.* **32,** 407-414 (1999).

53. McBride, J., Treadway, J., Feldman, L. C., Pennycook, S. J., & Rosenthal, S. J. Structural basis for near unity quantum yield core/shell nanostructures. *Nano Lett.* **6,** 1496-1501 (2006).

54. Xie, R. G., Kolb, U., Li, J. X., Basche, T., & Mews, A. Synthesis and characterization of highly luminescent CdSe-Core CdS/$Zn_{0.5}Cd_{0.5}$S/ZnS multishell nanocrystals. *J. Am. Chem. Soc.* **127,** 7480-7488 (2005).

55. Talapin, D. V., Mekis, I., Gotzinger, S., Kornowski, A., Benson, O., & Weller, H. CdSe/CdS/ZnS and CdSe/ZnSe/ZnS core-shell-shell nanocrystals. *J. Phys. Chem. B* **108,** 18826-18831 (2004).

56. Fisher, B. R., Eisler, H. J., Stott, N. E., & Bawendi, M. Emission intensity dependence and single-exponential behavior in single colloidal quantum dot fluorescence lifetimes. *J. Phys. Chem. B* **108,** 143-148 (2004).

57. Moreels, L., Lambert, K., De Muynck, D., Vanhaecke, F., Poelman, D., Martins, J. C., Allan, G., & Hens, Z. Composition and size-dependent extinction coefficient of colloidal PbSe quantum dots. *Chem. Mater.* **19,** 6101-6106 (2007).

58. Swafford, L. A., Weigand, L. A., Bowers, M. J., McBride, J. R., Rapaport, J. L., Watt, T. L., Dixit, S. K., Feldman, L. C., & Rosenthal, S. J. Homogeneously alloyed CdS_xSe_{1-x} nanocrystals: Synthesis, characterization, and composition/size-dependent band gap. *J. Am. Chem. Soc.* **128,** 12299-12306 (2006).

59. Bagga, A., Chattopadhyay, P. K., & Ghosh, S. Origin of Stokes shift in InAs and CdSe quantum dots: Exchange splitting of excitonic states. *Phys. Rev. B* **74,** (2006).

60. Wang, X. Y., Qu, L. H., Zhang, J. Y., Peng, X. G., & Xiao, M. Surface-related emission in highly luminescent CdSe quantum dots. *Nano Lett.* **3,** 1103-1106 (2003).

61. Klimov, V. I. Spectral and dynamical properties of multilexcitons in semiconductor nanocrystals. *Annu. Rev. Phys. Chem.* **58,** 635-673 (2007).

62. Talapin, D. V., Gaponik, N., Borchert, H., Rogach, A. L., Haase, M., & Weller, H. Etching of colloidal InP nanocrystals with fluorides: Photochemical nature of the process resulting in high photoluminescence efficiency. *J. Phys. Chem. B* **106,** 12659-12663 (2002).

63. Talapin, D. V., Rogach, A. L., Kornowski, A., Haase, M., & Weller, H. Highly luminescent monodisperse CdSe and CdSe/ZnS nanocrystals synthesized in a hexadecylamine-trioctylphosphine oxide-trioctylphospine mixture. *Nano Lett.* **1,** 207-211 (2001).

64. Aldana, J., Wang, Y., & Peng, X. Photochemical instability of CdSe nanocrystals coated by hydrophilic thiols. *J. Am. Chem. Soc.* **123,** 8844-8850 (2001).

65. Wuister, S., Donega, C., & Meijerink, A. Influence of thiol capping on the exciton luminescence and decay kinetics of CdTe and CdSe quantum. *J. Phys. Chem. B* **108,** 17393-17397 (2004).

66. Li, J. J., Wang, Y. A., Guo, W. Z., Keay, J. C., Mishima, T. D., Johnson, M. B., & Peng, X. G. Large-scale synthesis of nearly monodisperse CdSe/CdS core/shell nanocrystals using air-stable reagents via successive ion layer adsorption and reaction. *J. Am. Chem. Soc.* **125,** 12567-12575 (2003).

67. Jasieniak, J. J. & Mulvaney, P. From Cd-rich to Se-rich - the manipulation of CdSe nanocrystal surface stoichiometry. *J. Am. Chem. Soc.* **129,** 2841-2848 (2007).

68. Tolbert, S. H. & Alivisatos, A. P. Size dependence of a first order solid-solid phase transition: the wurtzite to rock salt transformation in CdSe nanocrystals. *Science* **265,** 373-376 (1994).

69. Hu, J. T., Li, L. S., Yang, W. D., Manna, L., Wang, L. W., & Alivisatos, A. P. Linearly polarized emission from colloidal semiconductor quantum rods. *Science* **292,** 2060-2063 (2001).

70. Talapin, D. V., Koeppe, R., Gotzinger, S., Kornowski, A., Lupton, J. M., Rogach, A. L., Benson, O., Feldmann, J., & Weller, H. Highly emissive colloidal CdSe/CdS heterostructures of mixed dimensionality. *Nano Lett.* **3,** 1677-1681 (2003).

71. Bailey, R. E. & Nie, S. M. Alloyed semiconductor quantum dots: Tuning the optical properties without changing the particle size. *J. Am. Chem. Soc.* **125,** 7100-7106 (2003).

72. Talapin, D. V., Poznyak, S. K., Gaponik, N. P., Rogach, A. L., & Eychmuller, A. Synthesis of surface-modified colloidal semiconductor nanocrystals and study of photoinduced charge separation and transport in nanocrystal-polymer composites. *Physica E* **14,** 237-241 (2002).

73. Zhong, X., Zhang, Z., Liu, S., Han, M., & Knoll, W. Embryonic nuclei-induced alloying process for the reproducible synthesis of blue-emitting $Zn_xCd_{1-x}Se$ nanocrystals with long-time thermal stability in size distribution and emission wavelength. *J. Phys. Chem. B* **108,** 15552-15559 (2004).

74. Erwin, S. C., Zu, L., Haftel, M. I., Efros, A. L., Kennedy, T. A., & Norris, D. J. Doping semiconductor nanocrystals. *Nature* **436,** 91-94 (2005).

75. Yang, Y. A., Chen, O., Angerhofer, A., & Cao, Y. C. Radial-position-controlled doping in CdS/ZnS core/shell nanocrystals. *J. Am. Chem. Soc.* **128,** 12428-12429 (2006).

76. Mikulec, F. V., Kuno, M., Bennati, M., Hall, D. A., Griffin, R. G., & Bawendi, M. G. Organometallic synthesis and spectroscopic characterization of manganese-doped CdSe nanocrystals. *J. Am. Chem. Soc.* **122,** 2532-2540 (2000).

77. Zu, L. J., Norris, D. J., Kennedy, T. A., Erwin, S. C., & Efros, A. L. Impact of ripening on manganese-doped ZnSe nanocrystals. *Nano Lett.* **6,** 334-340 (2006).

78. Pradhan, N., Battaglia, D. M., Liu, Y. C., & Peng, X. G. Efficient, stable, small, and water-soluble doped ZnSe nanocrystal emitters as non-cadmium biomedical labels. *Nano Lett.* **7,** 312-317 (2007).

79. Pradhan, N. & Peng, X. G. Efficient and color-tunable Mn-doped ZnSe nanocrystal emitters: Control of optical performance via greener synthetic chemistry. *J. Am. Chem. Soc.* **129,** 3339-3347 (2007).

80. Kim, S., Fisher, B., Eisler, H. J., & Bawendi, M. Type-II quantum dots: CdTe/CdSe(core/shell) and CdSe/ZnTe(core/shell) heterostructures. *J. Am. Chem. Soc.* **125,** 11466-11467 (2003).

81. Battaglia, D., Li, J. J., Wang, Y. J., & Peng, X. G. Colloidal two-dimensional systems: CdSe quantum shells and wells. *Angew. Chem. Int. Ed.* **42,** 5035-5039 (2003).

82. Battaglia, D., Blackman, B., & Peng, X. G. Coupled and decoupled dual quantum systems in one semiconductor nanocrystal. *J. Am. Chem. Soc.* **127,** 10889-10897 (2005).

83. Kalyanasundaram, K., Borgarello, E., Duonghong, D., & Gratzel, M. Cleavage of water by visible-light irridiation of colloidal CdS solutions: inhibition of photocorrosion by RuO_2. *Angew. Chem. Int. Ed.* **20,** 987-988 (1981).

84. Duonghong, D., Ramsden, J., & Gratzel, M. Dynamics of interfacial electron-transfer processes in colloidal semiconductor systems. *J. Am. Chem. Soc.* **104,** 2977-2985 (1982).

85. Rossetti, R. & Brus, L. E. Electron-hole recombination emission as a probe of surface chemistry in aqueous CdS colloids. *J. Phys. Chem.* **86,** 4470-4472 (1982).

86. Kuczynski, J. & Thomas, J. K. Photochemistry at the surface of colloidal cadmium sulfide. *Chem. Phys. Lett.* **88,** 445-447 (1982).

87. Meyer, M., Wallberg, C., Kurihara, K., & Fendler, J. H. Photosensitized charge separation and hydrogen production in reversed micelle entrapped platinized colloidal cadmium sulphide. *J. Chem. Soc., Chem. Commun.* 90-91 (1984).

88. Lianos, P. & Thomas, J. K. Cadmium sulfide of small dimensions produced in inverted micelles. *Chem. Phys. Lett.* **125,** 299-302 (1986).

89. Lianos, P. & Thomas, J. K. Small CdS particles in inverted micelles. *J. Colloid Interface Sci.* **117,** 505-512 (1987).

90. Rajh, T., Micic, O. I., & Nozik, A. J. Synthesis and characterization of surface-modified colloidal CdTe quantum dots. *J. Phys. Chem.* **97,** 11999-12003 (1993).

91. Rogach, A. L., Katsikas, L., Kornowski, A., Su, D. S., Eychmuller, A., & Weller, H. Synthesis and characterization of thiol-stabilized CdTe nanocrystals. *Ber. Bunsen-Ges. Phys. Chem.* **100,** 1772-1778 (1996).

92. Rogach, A. L., Katsikas, L., Kornowski, A., Su, D., Eychmuller, A., & Weller, H. Synthesis, morphology and optical properties of thiol-stabilized CdTe nanoclusters in aqueous solution. *Ber. Bunsen-Ges. Phys. Chem.* **101,** 1668-1670 (1997).

93. Olshavsky, M. A., Goldstein, A. N., & Alivisatos, A. P. Organometallic synthesis of GaAs crystallites exhibiting quantum confinement. *J. Am. Chem. Soc.* **112,** 9438-9439 (1990).

94. Peng, X. G., Wickham, J., & Alivisatos, A. P. Kinetics of II-VI and III-V colloidal semiconductor nanocrystal growth: "Focusing" of size distributions. *J. Am. Chem. Soc.* **120,** 5343-5344 (1998).

95. Peng, X. G., Manna, L., Yang, W. D., Wickham, J., Scher, E., Kadavanich, A., & Alivisatos, A. P. Shape control of CdSe nanocrystals. *Nature* **404,** 59-61 (2000).

96. Qu, L. H. & Peng, X. G. Control of photoluminescence properties of CdSe nanocrystals in growth. *J. Am. Chem. Soc.* **124,** 2049-2055 (2002).

97. Peng, Z. A. & Peng, X. G. Formation of high-quality CdTe, CdSe, and CdS nanocrystals using CdO as precursor. *J. Am. Chem. Soc.* **123,** 183-184 (2001).

98. Qu, L. H., Peng, Z. A., & Peng, X. G. Alternative routes toward high quality CdSe nanocrystals. *Nano Lett.* **1,** 333-337 (2001).

99. Yu, M. W. & Peng, X. G. Formation of high-quality CdS and other II-VI semiconductor nanocrystals in noncoordinating solvents: Tunable reactivity of monomers. *Angew. Chem. Int. Ed.* **41,** 2368-2371 (2002).

100. Murray, C. B., Sun, S. H., Gaschler, W., Doyle, H., Betley, T. A., & Kagan, C. R. Colloidal synthesis of nanocrystals and nanocrystal superlattices. *IBM J. Res. Dev.* **45,** 47-56 (2001).

101. Hines, M. A. & Guyot-Sionnest, P. Bright UV-blue luminescent colloidal ZnSe nanocrystals. *J. Phys. Chem. B* **102,** 3655-3657 (1998).

102. Milliron, D. J., Hughes, S. M., Cui, Y., Manna, L., Li, J. B., Wang, L. W., & Alivisatos, A. P. Colloidal nanocrystal heterostructures with linear and branched topology. *Nature* **430,** 190-195 (2004).

103. Yin, Y. & Alivisatos, A. P. Colloidal nanocrystal synthesis and the organic-inorganic interface. *Nature* **437,** 664-670 (2005).

104. Ramsden, J. J. & Gratzel, M. Photoluminescence of small cadmium sulphide particles. *J. Chem. Soc., Faraday Trans.* **80,** 919-933 (1984).

105. Kamat, P. V., Dimitrijevic, N. M., & Fessenden, R. W. Photoelectrochemistry in particulate systems. 6. Electron-transfer reactions of small CdS colloids in acetonitrile. *J. Phys. Chem.* **91,** 396-401 (1984).

106. Spanhel, L., Haase, M., Weller, H., & Henglein, A. Photochemistry of colloidal semiconductors. 20. Surface modification and stability of strong luminescing CdS particles. *J. Am. Chem. Soc.* **109,** 5649-5655 (1987).

107. Dannhauser, T., O'Neil, M., Johansson, K., Whitten, D., & McLendon, G. Photophysics of quantized colloidal semiconductors dramatic luminescence enhancement by binding of simple amines. *J. Phys. Chem.* **90,** (1986).

108. Kortan, A. R., Hull, R., Opila, R. L., Bawendi, M. G., Steigerwald, M. L., Carroll, P. J., & Brus, L. E. Nucleation and growth of CdSe on ZnS quantum crystallite seeds, and vice versa, in inverse micelle media. *J. Am. Chem. Soc.* **112,** 1327-1332 (1990).

109. Hines, M. A. & Guyot-Sionnest, P. Synthesis and characterization of strongly luminescing ZnS-capped CdSe nanocrystals. *J. Phys. Chem.* **100,** 468-471 (1996).

110. Dabbousi, B. O., Rodriguez-Viejo, J., Mikulec, F. V., Heine, J. R., Mattoussi, H., Ober, R., Jensen, K. F., & Bawendi, M. G. (CdSe)ZnS core-shell quantum dots: Synthesis and characterization of a size series of highly luminescent nanocrystallites. *J. Phys. Chem. B* **101,** 9463-9475 (1997).

111. Alivisatos, A. P. Semiconductor clusters, nanocrystals, and quantum dots. *Science* **271,** 933-937 (1996).

112. Crouch, D., Norager, S., O'Brien, P., Park, J. H., & Pickett, N. New synthetic routes for quantum dots. *Philos. Trans. R. Soc. London A* **361,** 297-310 (2003).

113. Donega, C. D., Hickey, S. G., Wuister, S. F., Vanmaekelbergh, D., & Meijerink, A. Single-step synthesis to control the photoluminescence quantum yield and size dispersion of CdSe nanocrystals. *J. Phys. Chem. B* **107,** 489-496 (2003).

114. Zhong, X. H., Feng, Y. Y., Knoll, W., & Han, M. Y. Alloyed $Zn_xCd_{1-x}S$ nanocrystals with highly narrow luminescence spectral width. *J. Am. Chem. Soc.* **125,** 13559-13563 (2003).

115. Hines, M. A. & Scholes, G. D. Colloidal PbS nanocrystals with size-tunable near-infrared emission: Observation of post-synthesis self-narrowing of the particle size distribution. *Adv. Mater.* **15,** 1844-1849 (2003).

116. Pietryga, J., Schaller, R., Werder, D., Stewart, M., Klimov, V., & Hollingsworth, J. Pushing the band gap envelope: Mid-infrared emitting colloidal PbSe quantum dots. *J. Am. Chem. Soc.* **126,** 11752-11753 (2004).

117. Li, S., Pradhan, N., Wang, Y., & Peng, X. High quality ZnSe and ZnS nanocrystals formed by activating zinc carboxylate precursors. *Nano Lett.* **4,** 2261-2264 (2004).

118. Bleuse, J., Carayon, S., & Reiss, P. Optical properties of core/multishell CdSe/Zn(S,Se) nanocrystals. *Physica E* **21,** 331-335 (2004).

119. Talapin, D. V., Nelson, J. H., Shevchenko, E. V., Aloni, S., Sadtler, B., & Alivisatos, A. P. Seeded growth of highly luminescent CdSe/CdS nanoheterostructures with rod and tetrapod morphologies. *Nano Lett.* **7,** 2951-2959 (2007).

120. Gaponik, N., Talapin, D. V., Rogach, A. L., Hoppe, K., Shevchenko, E. V., Kornowski, A., Eychmuller, A., & Weller, H. Thiol-capping of CdTe nanocrystals: An alternative to organometallic synthetic routes. *J. Phys. Chem. B* **106,** 7177-7185 (2002).

121. Dubertret, B., Skourides, P., Norris, D. J., Noireaux, V., Brivanlou, A. H., & Libchaber, A. In vivo imaging of quantum dots encapsulated in phospholipid micelles. *Science* **298,** 1759-1762 (2002).

122. Wu, X. Y., Liu, H. J., Liu, J. Q., Haley, K. N., Treadway, J. A., Larson, J. P., Ge, N. F., Peale, F., & Bruchez, M. P. Immunofluorescent labeling of cancer marker Her2 and other cellular targets with semiconductor quantum dots. *Nat. Biotechnol.* **21,** 41-46 (2003).

123. Gao, X. H., Cui, Y. Y., Levenson, R. M., Chung, L. W. K., & Nie, S. M. In vivo cancer targeting and imaging with semiconductor quantum dots. *Nat. Biotechnol.* **22,** 969-976 (2004).

124. Gao, X. H., Chan, W. C. W., & Nie, S. M. Quantum-dot nanocrystals for ultrasensitive biological labeling and multicolor optical encoding. *J. Biomed. Opt.* **7,** 532-537 (2002).

125. Mitchell, G. P., Mirkin, C. A., & Letsinger, R. L. Programmed assembly of DNA functionalized quantum dots. *J. Am. Chem. Soc.* **121,** 8122-8123 (1999).

126. Akerman, M. E., Chan, W. C. W., Laakkonen, P., Bhatia, S. N., & Ruoslahti, E. Nanocrystal targeting in vivo. *Proc. Natl. Acad. Sci. U.S.A.* **99,** 12617-12621 (2002).

127. Goldman, E. R., Medintz, I. L., Hayhurst, A., Anderson, G. P., Mauro, J. M., Iverson, B. L., Georgiou, G., & Mattoussi, H. Self-assembled luminescent CdSe-ZnS quantum dot bioconjugates prepared using engineered poly-histidine terminated proteins. *Anal. Chim. Acta* **534,** 63-67 (2005).

128. Clapp, A. R., Medintz, I. L., Mauro, J. M., Fisher, B. R., Bawendi, M. G., & Mattoussi, H. Fluorescence resonance energy transfer between quantum dot donors and dye-labeled protein acceptors. *J. Am. Chem. Soc.* **126,** 301-310 (2004).

129. Ding, S. Y., Rumbles, G., Jones, M., Tucker, M. P., Nedeljkovic, J., Simon, M. N., Wall, J. S., & Himmel, M. E. Bioconjugation of (CdSe)ZnS quantum dots using a genetically engineered multiple polyhistidine tagged cohesin/dockerin protein polymer. *Macromol. Mater. Eng.* **289,** 622-628 (2004).

130. Medintz, I. L., Clapp, A. R., Mattoussi, H., Goldman, E. R., Fisher, B., & Mauro, J. M. Self-assembled nanoscale biosensors based on quantum dot FRET donors. *Nat. Mater.* **2,** 630-638 (2003).

131. Xing, Y. et al. Bioconjugated quantum dots for multiplexed and quantitative immunohistochemistry. *Nat. Protoc.* **2,** 1152-1165 (2007).

132. Mattoussi, H., Mauro, J. M., Goldman, E. R., Anderson, G. P., Sundar, V. C., Mikulec, F. V., & Bawendi, M. G. Self-assembly of CdSe-ZnS quantum dot bioconjugates using an engineered recombinant protein. *J. Am. Chem. Soc.* **122,** 12142-12150 (2000).

133. Goldman, E. R., Balighian, E. D., Mattoussi, H., Kuno, M. K., Mauro, J. M., Tran, P. T., & Anderson, G. P. Avidin: A natural bridge for quantum dot-antibody conjugates. *J. Am. Chem. Soc.* **124,** 6378-6382 (2002).

134. Howarth, M., Liu, W. H., Puthenveetil, S., Zheng, Y., Marshall, L. F., Schmidt, M. M., Wittrup, D. K., Bawendi, M., & Ting, A. Y. Monovalent, reduced-size quantum dots for imaging receptors on living cells. *Nat. Methods* **5,** 397-399 (2008).

135. Zhang, Y., So, M. K., Loening, A. M., Yao, H. Q., Gambhir, S. S., & Rao, J. H. HaloTag protein-mediated site-specific conjugation of bioluminescent proteins to quantum dots. *Angew. Chem. Int. Ed.* **45,** 4936-4940 (2006).

136. Alivisatos, A. P. The use of nanocrystals in biological detection. *Nat. Biotechnol.* **22,** 47-52 (2004).

137. Ferrari, M. Cancer nanotechnology: Opportunities and challenges. *Nat. Rev. Cancer* **5,** 161-171 (2005).

138. Niemeyer, C. M. Nanoparticles, proteins, and nucleic acids: Biotechnology meets materials science. *Angew. Chem. Int. Ed.* **40,** 4128-4158 (2001).

139. Cao, Y. W. C., Jin, R. C., & Mirkin, C. A. Nanoparticles with Raman spectroscopic fingerprints for DNA and RNA detection. *Science* **297,** 1536-1540 (2002).

140. Gao, X. H., Yang, L. L., Petros, J. A., Marshal, F. F., Simons, J. W., & Nie, S. M. In vivo molecular and cellular imaging with quantum dots. *Curr. Opin. Biotechnol.* **16,** 63-72 (2005).

141. Michalet, X., Pinaud, F. F., Bentolila, L. A., Tsay, J. M., Doose, S., Li, J. J., Sundaresan, G., Wu, A. M., Gambhir, S. S., & Weiss, S. Quantum dots for live cells, in vivo imaging, and diagnostics. *Science* **307,** 538-544 (2005).

142. Nie, S. M., Xing, Y., Kim, G. J., & Simons, J. W. Nanotechnology applications in cancer. *Annu. Rev. Biomed. Eng.* **9,** 257-288 (2007).

143. Rosi, N. L. & Mirkin, C. A. Nanostructures in biodiagnostics. *Chem. Rev.* **105,** 1547-1562 (2005).

144. Yezhelyev, M. V., Gao, X., Xing, Y., Al-Hajj, A., Nie, S. M., & O'Regan, R. M. Emerging use of nanoparticles in diagnosis and treatment of breast cancer. *Lancet Oncol.* **7,** 657-667 (2006).

145. Liu, Z., Cai, W. B., He, L. N., Nakayama, N., Chen, K., Sun, X. M., Chen, X. Y., & Dai, H. J. In vivo biodistribution and highly efficient tumour targeting of carbon nanotubes in mice. *Nat. Nanotech.* **2,** 47-52 (2007).

146. Lee, E. S., Na, K., & Bae, Y. H. Polymeric micelle for tumor pH and folate-mediated targeting. *J. Controlled Release* **91,** 103-113 (2003).

147. Weissleder, R., Kelly, K., Sun, E. Y., Shtatland, T., & Josephson, L. Cell-specific targeting of nanoparticles by multivalent attachment of small molecules. *Nat. Biotechnol.* **23,** 1418-1423 (2005).

148. Hood, J. D., Bednarski, M., Frausto, R., Guccione, S., Reisfeld, R. A., Xiang, R., & Cheresh, D. A. Tumor regression by targeted gene delivery to the neovasculature. *Science* **296,** 2404-2407 (2002).

149. Duncan, R. Polymer conjugates as anticancer nanomedicines. *Nat. Rev. Cancer* **6,** 688-701 (2006).

150. Couvreur, P. & Vauthier, C. Nanotechnology: Intelligent design to treat complex disease. *Pharm. Res.* **23,** 1417-1450 (2006).

151. Moghimi, S. M., Hunter, A. C., & Murray, J. C. Long-circulating and target-specific nanoparticles: Theory to practice. *Pharmacol. Rev.* **53,** 283-318 (2001).

152. Torchilin, V. P. Micellar nanocarriers: Pharmaceutical perspectives. *Pharm. Res.* **24,** 1-16 (2007).

153. McCarthy, J. R., Kelly, K. A., Sun, E. Y., & Weissleder, R. Targeted delivery of multifunctional magnetic nanoparticles. *Nanomedicine* **2,** 153-167 (2007).

154. Harisinghani, M. G., Barentsz, J., Hahn, P. F., Deserno, W. M., Tabatabaei, S., van de Kaa, C. H., de la Rosette, J., & Weissleder, R. Noninvasive detection of clinically occult lymph-node metastases in prostate cancer. *N. Engl. J. Med.* **348,** 2491-2499 (2003).

155. Kim, S. et al. Near-infrared fluorescent type II quantum dots for sentinel lymph node mapping. *Nat. Biotechnol.* **22,** 93-97 (2004).

156. Rhyner, M. N., Smith, A. M., Gao, X. H., Mao, H., Yang, L., & Nie, S. M. Quantum dots and multifunctional nanoparticles: new contrast agents for tumor Imaging. *Nanomedicine* **1,** 209-217 (2006).

157. Woodle, M. C. & Lu, P. Y. Nanoparticles deliver RNAi therapy. *NanoToday* **8,** 34-41 (2005).

158. Medarova, Z., Pham, W., Farrar, C., Petkova, V., & Moore, A. In vivo imaging of siRNA delivery and silencing in tumors. *Nat. Med.* **13,** 372-377 (2007).

159. Rubart, M. Two-photon microscopy of cells and tissue. *Circ. Res.* **95,** 1154-1166 (2004).

160. Dahan, M., Laurence, T., Pinaud, F., Chemla, D., Alivisatos, A., Sauer, M., & Weiss, S. Time-gated biological imaging by use of colloidal quantum dots. *Opt. Lett.* **26,** 825-827 (2001).

161. Nisman, R., Dellaire, G., Ren, Y., Li, R., & Bazett-Jones, D. P. Application of quantum dots as probes for correlative fluorescence, conventional, and energy-filtered transmission electron microscopy. *J. Histochem. Cytochem.* **52,** 13-18 (2004).

162. Giepmans, B. N. G., Deerinck, T. J., Smarr, B. L., Jones, Y. Z., & Ellisman, M. H. Correlated light and electron microscopic imaging of multiple endogenous proteins using quantum dots. *Nat. Methods* **2,** 743-749 (2005).

163. Hernandez, J. & Thompson, I. Prostate-specific antigen: A review of the validation of the most commonly used cancer biomarker. *Cancer* **101,** 894-904 (2004).

164. Goessl, C. Noninvasive molecular detection of cancer - the bench and the bedside. *Curr. Med. Chem.* **10,** 691-706 (2003).

165. Goldman, E. R., Anderson, G. P., Tran, P. T., Mattoussi, H., Charles, P. T., & Mauro, J. M. Conjugation of luminescent quantum dots with antibodies using an engineered adaptor protein to provide new reagents for fluoroimmunoassays. *Anal. Chem.* **74,** 841-847 (2002).

166. Bakalova, R., Zhelev, Z., Ohba, H., & Baba, Y. Quantum dot-based western blot technology for ultrasensitive detection of tracer proteins. *J. Am. Chem. Soc.* **127,** 9328-9329 (2005).

167. Goldman, E. R., Clapp, A. R., Anderson, G. P., Uyeda, H. T., Mauro, J. M., Medintz, I. L., & Mattoussi, H. Multiplexed toxin analysis using four colors of quantum dot fluororeagents. *Anal. Chem.* **76,** 684-688 (2004).

168. Makrides, S., Gasbarro, C., & Bello, J. Bioconjugation of quantum dot luminescent probes for Western blot analysis. *BioTechniques* **39,** 501-506 (2005).

169. Penn, S. G., He, L., & Natan, M. J. Nanoparticles for bioanalysis. *Curr. Opin. Chem. Biol.* **7,** 609-615 (2003).

170. Gerion, D., Chen, F. Q., Kannan, B., Fu, A. H., Parak, W. J., Chen, D. J., Majumdar, A., & Alivisatos, A. P. Room-temperature single-nucleotide polymorphism and multiallele DNA detection using fluorescent nanocrystals and microarrays. *Anal. Chem.* **75,** 4766-4772 (2003).

171. Zhang, C. Y., Yeh, H. C., Kuroki, M. T., & Wang, T. H. Single-quantum-dot-based DNA nanosensor. *Nat. Mater.* **4,** 826-831 (2005).

172. Han, M. Y., Gao, X. H., Su, J. Z., & Nie, S. Quantum-dot-tagged microbeads for multiplexed optical coding of biomolecules. *Nat. Biotechnol.* **19,** 631-635 (2001).

173. Xu, H. X. et al. Multiplexed SNP genotyping using the Qbead (TM) system: a quantum dot-encoded microsphere-based assay. *Nucleic Acids Res.* **31,** e43 (2003).

174. Rosenthal, S. J. Bar-coding biomolecules with fluorescent nanocrystals. *Nat. Biotechnol.* **19,** 621-622 (2001).

175. Eastman, P. S. et al. Qdot nanobarcodes for multiplexed gene expression analysis. *Nano Lett.* **6,** 1059-1064 (2006).

176. Klostranec, J. M., Xiang, Q., Farcas, G. A., Lee, J. A., Rhee, A., Lafferty, E. I., Perrault, S. D., Kain, K. C., & Chan, W. C. W. Convergence of quantum dot barcodes with microfluidics and signal processing for multiplexed high-throughput infectious disease diagnostics. *Nano Lett.* **7,** 2812-2818 (2007).

177. Sukhanova, A. et al. Nanocrystal-encoded fluorescent microbeads for proteomics: antibody profiling and diagnostics of autoimmune diseases. *Nano Lett.* **7,** 2322-2327 (2007).

178. Coons, A. H., Creech, H. J., & Jones, R. N. The demonstration of pneumococcal antigen in tissues by the use of fluorescent antibody. *J. Immunol.* **45,** 159-170 (1942).

179. Chalfie, M., Tu, Y., Euskirchen, G., Ward, W. W., & Prasher, D. C. Green fluorescent protein as a marker for gene expression. *Science* **263,** 802-805 (1994).

180. Pathak, S., Choi, S. K., Arnheim, N., & Thompson, M. E. Hydroxylated quantum dots as luminescent probes for in situ hybridization. *J. Am. Chem. Soc.* **123,** 4103-4104 (2001).

181. Xiao, Y. & Barker, P. E. Semiconductor nanocrystal probes for human metaphase chromosomes. *Nucleic Acids Res.* **32,** e28 (2004).

182. Matsuno, A., Itoh, J., Takekoshi, S., Nagashima, T., & Osamura, R. Y. Three-dimensional imaging of the intracellular localization of growth hormone and prolactin and their mRNA using nanocrystal (quantum dot) and confocal laser scanning microscopy techniques. *J. Histochem. Cytochem.* **53,** 833-838 (2005).

183. Sukhanova, A., Devy, M., Venteo, L., Kaplan, H., Artemyev, M., Oleinikov, V., Klinov, D., Pluot, M., Cohen, J. H. M., & Nabiev, I. Biocompatible fluorescent nanocrystals for immunolabeling of membrane proteins and cells. *Anal. Biochem.* **324,** 60-67 (2004).

184. Ness, J. M., Akhtar, R. S., Latham, C. B., & Roth, K. A. Combined tyramide signal amplification and quantum dots for sensitive and photostable immunofluorescence detection. *J. Histochem. Cytochem.* **51,** 981-987 (2003).

185. Sukhanova, A., Venteo, L., Devy, J., Artemyev, M., Oleinikov, V., Pluot, M., & Nabiev, I. Highly stable fluorescent nanocrystals as a novel class of labels for immunohistochemical analysis of paraffin-embedded tissue sections. *Lab. Invest.* **82,** 1259-1261 (2002).

186. Xing, Y., Smith, A. M., Agrawal, A., Ruan, G., & Nie, S. M. Molecular profiling of single cancer cells and clinical tissue specimens with semiconductor quantum dots. *Int. J. Nanomedicine* **1,** 473-481 (2006).

187. Yezhelyev, M. V. et al. In situ molecular profiling of breast cancer biomarkers with multicolor quantum dots. *Adv. Mater.* **19,** 3146-3151 (2007).

188. Ferrara, D. E., Weiss, D., Carnell, P. H., Vito, R. P., Vega, D., Gao, X. H., Nie, S. M., & Taylor, W. R. Quantitative 3D fluorescence technique for the analysis of en face preparations of arterial walls using quantum dot nanocrystals and two-photon excitation laser scanning microscopy. *Am. J. Physiol. Regul. Integr. Comp. Physiol.* **290,** R114-R123 (2006).

189. Lidke, D. S., Nagy, P., Heintzmann, R., Arndt-Jovin, D. J., Post, J. N., Grecco, H. E., Jares-Erijman, E. A., & Jovin, T. M. Quantum dot ligands provide new insights into erbB/HER receptor-mediated signal transduction. *Nat. Biotechnol.* **22,** 198-203 (2004).

190. Dahan, M., Levi, S., Luccardini, C., Rostaing, P., Riveau, B., & Triller, A. Diffusion dynamics of glycine receptors revealed by single-quantum dot tracking. *Science* **302,** 442-445 (2003).

191. Lieleg, O., Lopez-Garcia, M., Semmrich, C., Auernheimer, J., Kessler, H., & Bausch, A. R. Specific integrin Labeling in living Celts using functionalized nanocrystals. *Small* **3,** 1560-1565 (2007).

192. Chen, H. F., Titushkin, I., Stroscio, M., & Cho, M. Altered membrane dynamics of quantum dot-conjugated integrins during osteogenic differentiation of human bone marrow derived progenitor cells. *Biophys. J.* **92,** 1399-1408 (2007).

193. Echarte, M. M., Bruno, L., Arndt-Jovin, D. J., Jovin, T. M., & Pietrasanta, L. I. Quantitative single particle tracking of NGF-receptor complexes: Transport is bidirectional but biased by longer retrograde run lengths. *FEBS Lett.* **581,** 2905-2913 (2007).

194. Rajan, S. S. & Vu, T. Q. Quantum dots monitor TrkA receptor dynamics in the interior of neural PC12 cells. *Nano Lett.* **6,** 2049-2059 (2006).

195. Young, S. H. & Rozengurt, E. Qdot Nanocrystal Conjugates conjugated to bombesin or ANG II label the cognate G protein-coupled receptor in living cells. *Am. J. Physiol. Cell. Physiol.* **290,** C728-C732 (2006).

196. Le Gac, S., Vermes, I., & van den Berg, A. Quantum dots based probes conjugated to annexin V for photostable apoptosis detection and imaging. *Nano Lett.* **6,** 1863-1869 (2006).

197. Koeppel, F., Jaiswal, J. K., & Simon, S. M. Quantum dot-based sensor for improved detection of apoptotic cells. *Nanomedicine* **2,** 71-78 (2007).

198. Jaiswal, J. K., Goldman, E. R., Mattoussi, H., & Simon, S. M. Use of quantum dots for live cell imaging. *Nat. Methods* **1,** 73-78 (2004).

199. Courty, S., Bouzigues, C., Luccardini, C., Ehrensperger, M. V., Bonneau, S., & Dahan, M., in *Methods in Enzymology*, edited by J. Inglese Elsevier, Inc., Amsterdam (2006), Vol. 414, pp. 211-228.

200. Howarth, M., Takao, K., Hayashi, Y., & Ting, A. Y. Targeting quantum dots to surface proteins in living cells with biotin ligase. *Proc Natl Acad Sci U S A* **102,** 7583-7588 (2005).

201. Bonasio, R., Carman, C. V., Kim, E., Sage, P. T., Love, K. R., Mempel, T. R., Springer, T. A., & von Andrian, U. H. Specific and covalent labeling of a membrane protein with organic fluorochromes and quantum dots. *Proc. Natl. Acad. Sci. U.S.A.* **104,** 14753-14758 (2007).

202. Hanaki, K., Momo, A., Oku, T., Komoto, A., Maenosono, S., Yamaguchi, Y., & Yamamoto, K. Semiconductor quantum dot/albumin complex is a long-life and highly photostable endosome marker. *Biochem. Biophys. Res. Commun.* **302,** 496-501 (2003).

203. Jaiswal, J. K., Mattoussi, H., Mauro, J. M., & Simon, S. M. Long-term multiple color imaging of live cells using quantum dot bioconjugates. *Nat. Biotechnol.* **21,** 47-51 (2003).

204. Parak, W. J., Boudreau, R., Le Gros, M., Gerion, D., Zanchet, D., Micheel, C. M., Williams, S. C., Alivisatos, A. P., & Larabell, C. Cell motility and metastatic potential studies based on quantum dot imaging of phagokinetic tracks. *Adv. Mater.* **14,** 882-885 (2002).

205. Derfus, A. M., Chan, W. C. W., & Bhatia, S. N. Probing the cytotoxicity of semiconductor quantum dots. *Nano Lett.* **4,** 11-18 (2004).

206. Chen, F. & Gerion, D. Fluorescent CdSe/ZnS nanocrystal-peptide conjugates for long-term, nontoxic imaging and nuclear targeting in living cells. *Nano Lett.* **4,** 1827-1832 (2004).

207. Mattheakis, L., Dias, J., Choi, Y., Gong, J., Bruchez, M., Liu, J., & Wang, E. Optical coding of mammalian cells using semiconductor quantum dots. *Anal. Biochem.* **327,** 200-208 (2004).

208. Lagerholm, B., Wang, M., Ernst, L., Ly, D., Liu, H., Bruchez, M., & Waggoner, A. Multicolor coding of cells with cationic peptide coated quantum dots. *Nano Lett.* **4,** 2019-2022 (2004).

209. Voura, E., Jaiswal, J., Mattoussi, H., & Simon, S. Tracking metastatic tumor cell extravasation with quantum dot nanocrystals and fluorescence emission-scanning microscopy. *Nat. Med.* **10,** 993-998 (2004).

210. Derfus, A. M., Chan, W. C. W., & Bhatia, S. N. Intracellular delivery of quantum dots for live cell labeling and organelle tracking. *Adv. Mater.* **16,** 961-966 (2004).

211. Courty, S., Luccardini, C., Bellaiche, Y., Cappello, G., & Dahan, M. Tracking individual kinesin motors in living cells using single quantum-dot imaging. *Nano Lett.* **6,** 1491-1495 (2006).

212. Nan, X. L., Sims, P. A., Chen, P., & Xie, X. S. Observation of individual microtubule motor steps in living cells with endocytosed quantum dots. *J. Phys. Chem. B* **109,** 24220-24224 (2005).

213. Cambi, A., Lidke, D. S., Arndt-Jovin, D. J., Figdor, C. G., & Jovin, T. M. Ligand-conjugated quantum dots monitor antigen uptake and processing by dendritic cells. *Nano Lett.* **7,** 970-977 (2007).

214. Langel, U. *Cell-Penetrating Peptides: Processes and Applications*. CRC Press, Boca Raton, FL, (2002).

215. Brooks, H., Lebleu, B., & Vives, E. Tat peptide-mediated cellular delivery: back to basics. *Adv. Drug Delivery Rev.* **57,** 559-577 (2005).

216. Wadia, J. S. & Dowdy, S. F. Transmembrane delivery of protein and peptide drugs by TAT-mediated transduction in the treatment of cancer. *Adv. Drug Delivery Rev.* **57,** 579-596 (2005).

217. Gupta, B., Levchenko, T. S., & Torchilin, V. P. Intracellular delivery of large molecules and small particles by cell-penetrating proteins and peptides. *Adv. Drug Delivery Rev.* **57,** 637-651 (2005).

218. Futaki, S. Membrane-permeable arginine-rich peptides and the translocation mechanisms. *Adv. Drug Delivery Rev.* **57,** 547-558 (2005).

219. Zorko, M. & Langel, U. Cell-penetrating peptides: mechanism and kinetics of cargo delivery. *Adv. Drug Delivery Rev.* **57,** 529-545 (2005).

220. Conner, S. D. & Schmid, S. L. Regulated portals of entry into the cell. *Nature* **422,** 37-44 (2003).

221. Delehanty, J. B., Medintz, I. L., Pons, T., Brunel, F. M., Dawson, P. E., & Mattoussi, H. Self-assembled quantum dot-peptide bioconjugates for selective intracellular delivery. *Bioconjug. Chem.* **17,** 920-927 (2006).

222. Ruan, G., Agrawal, A., Marcus, A. I., & Nie, S. M. Imaging and tracking of Tat peptide-conjugated quantum dots in living cells: new insights into nanoparticle uptake, intracellular transport, and vesicle shedding. *J. Am. Chem. Soc.* **129,** 14759-14766 (2007).

223. Gonczy, P., Pichler, S., Kirkham, M., & Hyman, A. A. Cytoplasmic dynein is required for distinct aspects of MTOC positioning, including centrosome separation, in the one cell stage Caenorhabditis elegans embryo. *J. Cell Biol.* **147,** 135-150 (1999).

224. Neu, M., Fischer, D., & Kissel, T. Recent advances in rational gene transfer vector design based on poly(ethylene imine) and its derivatives. *J. Gene Med.* **7,** 992-1009 (2005).

225. Boussif, O., Lezoualch, F., Zanta, M. A., Mergny, M. D., Scherman, D., Demeneix, B., & Behr, J. P. A Versatile Vector For Gene And Oligonucleotide Transfer Into Cells In Culture And In-Vivo - Polyethylenimine. *Proc. Natl. Acad. Sci. U.S.A.* **92,** 7297-7301 (1995).

226. Pack, D. W., Hoffman, A. S., Pun, S., & Stayton, P. S. Design and development of polymers for gene delivery. *Nat. Rev. Drug Discovery* **4,** 581-593 (2005).

227. Duan, H. W. & Nie, S. M. Cell-penetrating quantum dots based on multivalent and endosome-disrupting surface coatings. *J. Am. Chem. Soc.* **129,** 3333-3338 (2007).

228. Smith, A. M., Duan, H. W., Rhyner, M. N., Ruan, G., & Nie, S. M. A systematic examination of surface coatings on the optical and chemical properties of semiconductor quantum dots. *Phys. Chem. Chem. Phys.* **8,** 3895-3903 (2006).

229. Gao, X. H., Yezhelyev, M. V., Qi, L., O'Regan, R. M., & Nie, S. M. Proton-sponge-coated quantum dots for siRNA delivery and imaging. *J. Am. Chem. Soc.* **130,** 9006-9012 (2008).

230. Lovric, J., Bazzi, H. S., Cuie, Y., Fortin, G. R. A., Winnik, F. M., & Maysinger, D. Differences in subcellular distribution and toxicity of green and red emitting CdTe quantum dots. *J. Mol. Med.* **83,** 377-385 (2005).

231. Nabiev, I. et al. Nonfunctionalized Nanocrystals Can Exploit a Cell's Active Transport Machinery Delivering Them to Specific Nuclear and Cytoplasmic Compartments. *Nano Lett.* (2007).

232. Weissleder, R. A clearer vision for in vivo imaging. *Nat. Biotechnol.* **19,** 316-317 (2001).

233. Frangioni, J. V. In vivo near-infrared fluorescence imaging. *Curr. Opin. Chem. Biol.* **7,** 626-634 (2003).

234. Ballou, B., Lagerholm, B. C., Ernst, L. A., Bruchez, M. P., & Waggoner, A. S. Noninvasive imaging of quantum dots in mice. *Bioconjug. Chem.* **15,** 79-86 (2004).

235. Dobrovolskaia, M. A. & Mcneil, S. E. Immunological properties of engineered nanomaterials. *Nat. Nanotech.* **2,** 469-478 (2007).

236. Soltesz, E., Kim, S., Laurence, R., DeGrand, A., Parungo, C., Dor, D., Cohn, L., Bawendi, M., Frangioni, J., & Mihaljevic, T. Intraoperative sentinel lymph node mapping of the lung using near-infrared fluorescent quantum dots. *Ann. Thorac. Surg.* **79,** 269-277 (2005).

237. Fischer, H. C., Liu, L. C., Pang, K. S., & Chan, W. C. W. Pharmacokinetics of nanoscale quantum dots: In vivo distribution, sequestration, and clearance in the rat. *Adv. Funct. Mater.* **16,** 1299-1305 (2006).

238. Choi, H. S., Liu, W., Misra, P., Tanaka, E., Zimmer, J. P., Ipe, B. I., Bawendi, M. G., & Frangioni, J. V. Renal clearance of quantum dots. *Nat. Biotechnol.* **25,** 1165-1170 (2007).

239. Zimmer, J. P., Kim, S. W., Ohnishi, S., Tanaka, E., Frangioni, J. V., & Bawendi, M. G. Size series of small indium arsenide-zinc selenide core-shell nanocrystals and their application to in vivo imaging. *J. Am. Chem. Soc.* **128,** 2526-2527 (2006).

240. Larson, D. R., Zipfel, W. R., Williams, R. M., Clark, S. W., Bruchez, M. P., Wise, F. W., & Webb, W. W. Water-soluble quantum dots for multiphoton fluorescence imaging in vivo. *Science* **300,** 1434-1436 (2003).

241. Lim, Y. T., Kim, S., Nakayama, A., Stott, N. E., Bawendi, M. G., & Frangioni, J. V. Selection of quantum dot wavelengths for biomedical assays and imaging. *Mol. Imaging* **2,** 50-64 (2003).

242. Smith, J. D., Fisher, G. W., Waggoner, A. S., & Campbell, P. G. The use of quantum dots for analysis of chick CAM vasculature. *Microvasc. Res.* **73,** 75-83 (2007).

243. Jayagopal, A., Russ, P. K., & Haselton, F. R. Surface engineering of quantum dots for in vivo vascular Imaging. *Bioconjug. Chem.* **18,** 1424-1433 (2007).

244. Parungo, C., Colson, Y., Kim, S., Kim, S., Cohn, L., Bawendi, M., & Frangioni, J. Sentinel lymph node mapping of the pleural space. *Chest* **127,** 1799-1804 (2005).

245. Parungo, C. et al. Intraoperative identification of esophageal sentinel lymph nodes with near-infrared fluorescence imaging. *J. Thorac. Cardiovasc. Surg.* **129,** 844-850 (2005).

246. Ballou, B., Ernst, L. A., Andreko, S., Harper, T., Fitzpatrick, J. A. J., Waggoner, A. S., & Bruchez, M. P. Sentinel lymph node imaging using quantum dots in mouse tumor models. *Bioconjug. Chem.* **18,** 389-396 (2007).

247. Kobayashi, H., Hama, Y., Koyama, Y., Barrett, T., Regino, C. A. S., Urano, Y., & Choyke, P. L. Simultaneous multicolor imaging of five different lymphatic basins using quantum dots. *Nano Lett.* **7,** 1711-1716 (2007).

248. Hama, Y., Koyama, Y., Urano, Y., Choyke, P. L., & Kobayashi, H. Simultaneous two-color spectral fluorescence lymphangiography with near infrared quantum dots to map two lymphatic flows from the breast and the upper extremity. *Breast Cancer Res. Treat.* **103,** 23-28 (2007).

249. Gopee, N. V., Roberts, D. W., Webb, P., Cozart, C. R., Siitonen, P. H., Warbritton, A. R., Yu, W. W., Colvin, V. L., Walker, N. J., & Howard, P. C. Migration of intradermally injected quantum dots to sentinel organs in mice. *Toxicol. Sci.* **98,** 249-257 (2007).

250. Hoshino, A., Hanaki, K., Suzuki, K., & Yamamoto, K. Applications of T-lymphoma labeled with fluorescent quantum dots to cell tracing markers in mouse body. *Biochem. Biophys. Res. Commun.* **314,** 46-53 (2004).

251. Rosen, A. B. et al. Finding fluorescent needles in the cardiac haystack: Tracking human mesenchymal stem cells labeled with quantum dots for quantitative in vivo three-dimensional fluorescence analysis. *Stem Cells* **25,** 2128-2138 (2007).

252. Lin, S. et al. Quantum dot imaging for embryonic stem cells. *BMC Biotechnol.* **7,** 67 (2007).

253. Jain, R. K. Delivery of molecular medicine to solid tumors: lessons from in vivo imaging of gene expression and function. *J. Controlled Release* **74,** 7-25 (2001).

254. Jain, R. K. Transport of molecules, particles, and cells in solid tumors. *Annu. Rev. Biomed. Eng.* **1,** 241-263 (1999).

255. Maeda, H., Wu, J., Sawa, T., Matsumura, Y., & Hori, K. Tumor vascular permeability and the EPR effect in macromolecular therapeutics: a review. *J. Controlled Release* **65,** 271-284 (2000).

256. Matsumura, Y. & Maeda, H. A New Concept for Macromolecular Therapeutics in Cancer-Chemotherapy - Mechanism of Tumoritropic Accumulation of Proteins and the Antitumor Agent Smancs. *Cancer Res.* **46,** 6387-6392 (1986).

257. Yu, X. F. et al. Immunofluorescence detection with quantum dot bioconjugates for hepatoma in vivo. *J. Biomed. Opt.* **12,** 014008 (2007).

258. Cai, W. B., Shin, D. W., Chen, K., Gheysens, O., Cao, Q. Z., Wang, S. X., Gambhir, S. S., & Chen, X. Y. Peptide-labeled near-infrared quantum dots for imaging tumor vasculature in living subjects. *Nano Lett.* **6,** 669-676 (2006).

259. Smith, B. R., Cheng, Z., De, A., Koh, A. L., Sinclair, R., & Gambhir, S. S. Real-time intravital imaging of RGD-quantum dot binding to luminal endothelium in mouse tumor neovasculature. *Nano Lett.* **8,** 2599-2606 (2008).

260. So, M. K., Xu, C. J., Loening, A. M., Gambhir, S. S., & Rao, J. H. Self-illuminating quantum dot conjugates for in vivo imaging. *Nat. Biotechnol.* **24,** 339-343 (2006).

261. Stroh, M. et al. Quantum dots spectrally distinguish multiple species within the tumor milieu in vivo. *Nat. Med.* **11,** 678-682 (2005).

262. Tada, H., Higuchi, H., Wanatabe, T. M., & Ohuchi, N. In vivo real-time tracking of single quantum dots conjugated with monoclonal anti-HER2 antibody in tumors of mice. *Cancer Res.* **67,** 1138-1144 (2007).

263. Yang, R. H., Chang, L. W., Wu, J. P., Tsai, M. H., Wang, H. J., Kuo, Y. C., Yeh, T. K., Yang, C. S., & Lin, P. Persistent tissue kinetics and redistribution of nanoparticles, quantum dot 705, in mice: ICP-MS quantitative assessment. *Environ. Health Perspect.* **115,** 1339-1343 (2007).

264. Ikeda, M., Watanabe, T., Zhang, Z. W., Moon, C. S., & Shimbo, S. The integrity of the liver among people environmentally exposed to cadmium at various levels. *Int. Arch. Occup. Environ. Health* **69,** 379-385 (1997).

265. Omarova, A. & Phillips, C. J. C. A meta-analysis of literature data relating to the relationships between cadmium intake and toxicity indicators in humans. *Environ. Res.* **103,** 432-440 (2007).

266. Rikans, L. E. & Tetsuo, Y. Mechanisms of cadmium-mediated acute hepatotoxicity. *J. Biochem. Mol. Toxicol.* **14,** 110-117 (2000).

267. Mancini, M. C., Kairdolf, B. A., Smith, A. M., & Nie, S. M. Oxidative quenching and degradation of polymer-encapsulated quantum dots: new insights into the

long-term fate and toxicity of nanocrystals in vivo. *J. Am. Chem. Soc.* **130,** 10836-10837 (2008).

268. Kirchner, C., Liedl, T., Kudera, S., Pellegrino, T., Javier, A. M., Gaub, H. E., Stolzle, S., Fertig, N., & Parak, W. J. Cytotoxicity of colloidal CdSe and CdSe/ZnS nanoparticles. *Nano Lett.* **5,** 331-338 (2005).

269. Chang, E., Thekkek, N., Yu, W. W., Colvin, V. L., & Drezek, R. Evaluation of quantum dot cytotoxicity based on intracellular uptake. *Small* **2,** 1412-1417 (2006).

270. Cho, S. J., Maysinger, D., Jain, M., Roder, B., Hackbarth, S., & Winnik, F. M. Long-term exposure to CdTe quantum dots causes functional impairments in live cells. *Langmuir* **23,** 1974-1980 (2007).

271. Maysinger, D., Behrendt, M., Lalancette-Herbert, M., & Kriz, J. Real-time imaging of astrocyte response to quantum dots: In vivo screening model system for biocompatibility of nanoparticles. *Nano Lett.* **7,** 2513-2520 (2007).

272. Lovric, J., Cho, S. J., Winnik, F. M., & Maysinger, D. Unmodified cadmium telluride quantum dots induce reactive oxygen species formation leading to multiple organelle damage and cell death. *Chem. Biol.* **12,** 1227-1234 (2005).

273. Zhang, T. T., Stilwell, J. L., Gerion, D., Ding, L. H., Elboudwarej, O., Cooke, P. A., Gray, J. W., Alivisatos, A. P., & Chen, F. F. Cellular effect of high doses of silica-coated quantum dot profiled with high throughput gene expression analysis and high content cellomics measurements. *Nano Lett.* **6,** 800-808 (2006).

274. Lam, C. W., James, J. T., McCluskey, R., Arepalli, S., & Hunter, R. L. A review of carbon nanotube toxicity and assessment of potential occupational and environmental health risks. *Crit. Rev. Toxicol.* **36,** 189-217 (2006).

275. Nabiev, I. et al. Nonfunctionalized nanocrystals can exploit a cell's active transport machinery delivering them to specific nuclear and cytoplasmic compartments. *Nano Lett.* **7,** 3452-3461 (2007).

276. Green, M. & Howman, E. Semiconductor quantum dots and free radical induced DNA nicking. *Chem. Commun.*121-123 (2005).

277. Liang, J. G., He, Z. K., Zhang, S. S., Huang, S., Ai, X. P., Yang, H. X., & Han, H. Y. Study on DNA damage induced by CdSe quantum dots using nucleic acid molecular "light switches" as probe. *Talanta* **71,** 1675-1678 (2007).

278. Zhang, Y., He, J., Wang, P. N., Chen, J. Y., Lu, Z. J., Lu, D. R., Guo, J., Wang, C. C., & Yang, W. L. Time-dependent photoluminescence blue shift of the quantum dots in living cells: Effect of oxidation by singlet oxygen. *J. Am. Chem. Soc.* **128,** 13396-13401 (2006).

279. Ipe, B. I., Lehnig, M., & Niemeyer, C. M. On the generation of free radical species from quantum dots. *Small* **1,** 706-709 (2005).

280. Chan, W. H., Shiao, N. H., & Lu, P. Z. CdSe quantum dots induce apoptosis in human neuroblastoma cells via mitochondrial-dependent pathways and inhibition of survival signals. *Toxicol. Lett.* **167,** 191-200 (2006).

281. Mulder, W. J. M., Koole, R., Brandwijk, R. J., Storm, G., Chin, P. T. K., Strijkers, G. J., Donega, C. D., Nicolay, K., & Griffioen, A. W. Quantum dots with a paramagnetic coating as a bimodal molecular imaging probe. *Nano Lett.* **6,** 1-6 (2006).

282. Bakalova, R., Zhelev, Z., Aoki, I., Ohba, H., Imai, Y., & Kanno, I. Silica-shelled single quantum dot micelles as imaging probes with dual or multimodality. *Anal. Chem.* **78,** 5925-5932 (2006).

283. van Tilborg, G. A. F., Mulder, W. J. M., Chin, P. T. K., Storm, G., Reutelingsperger, C. P., Nicolay, K., & Strijkers, G. J. Annexin A5-conjugated quantum dots with a paramagnetic lipidic coating for the multimodal detection of apoptotic cells. *Bioconjug. Chem.* **17,** 865-868 (2006).

284. Cai, W. B. & Chen, X. Nanoplatforms for targeted molecular imaging in living subjects. *Small* **3,** 1840-1854 (2007).

285. Cai, W. B., Chen, K., Li, Z., Gambhir, S. S., & Chen, X. Dual-functional probe for PET and near-infrared fluorescence imaging of tumor vasculature. *J. Nucl. Med.* **48,** 1862-1870 (2007).

286. Santra, S., Yang, H. S., Holloway, P. H., Stanley, J. T., & Mericle, R. A. Synthesis of water-dispersible fluorescent, radio-opaque, and paramagnetic CdS : Mn/ZnS quantum dots: A multifunctional probe for bioimaging. *J. Am. Chem. Soc.* **127,** 1656-1657 (2005).

287. Wang, S., Jarrett, B. R., Kauzlarich, S. M., & Louie, A. Y. Core/shell quantum dots with high relaxivity and photoluminescence for multimodality imaging. *J. Am. Chem. Soc.* **129,** 3848-3856 (2007).

288. Gu, H. W., Zheng, R. K., Zhang, X. X., & Xu, B. Facile one-pot synthesis of bifunctional heterodimers of nanoparticles: A conjugate of quantum dot and magnetic nanoparticles. *J. Am. Chem. Soc.* **126,** 5664-5665 (2004).

289. Gu, H. W., Yang, Z. M., Gao, J. H., Chang, C. K., & Xu, B. Heterodimers of nanoparticles: Formation at a liquid-liquid interface and particle-specific surface modification by functional molecules. *J. Am. Chem. Soc.* **127,** 34-35 (2005).

290. Manabe, N., Hoshino, A., Liang, Y. Q., Goto, T., Kato, N., & Yamamoto, K. Quantum dot as a drug tracer in vivo. *IEEE Trans. Nanobioscience* **5,** 263-267 (2006).

291. Bagalkot, V., Zhang, L., Levy-Nissenbaum, E., Jon, S., Kantoff, P. W., Langer, R., & Farokhzad, O. C. Quantum dot - aptamer conjugates for synchronous cancer imaging, therapy, and sensing of drug delivery based on bi-fluorescence resonance energy transfer. *Nano Lett.* **7,** 3065-3070 (2007).

292. Chen, A. A., Derfus, A. M., Khetani, S. R., & Bhatia, S. N. Quantum dots to monitor RNAi delivery and improve gene silencing. *Nucleic Acids Res.* **33,** e190 (2005).

293. Tan, W. B., Jiang, S., & Zhang, Y. Quantum-dot based nanoparticles for targeted silencing of HER2/neu gene via RNA interference. *Biomaterials* **28,** 1565-1571 (2007).

294. Derfus, A. M., Chen, A. A., Min, D. H., Ruoslahti, E., & Bhatia, S. N. Targeted quantum dot conjugates for siRNA delivery. *Bioconjug. Chem.* **18,** 1391-1396 (2007).

CHAPTER 3

Quantum Dot Bandgap Engineering through Mercury Cation Exchange

The field of colloidal nanocrystal synthesis has progressed considerably in the past decade, yielding precise control over nanocrystal structure and properties. Liquid suspensions of semiconductor, metal, and oxide nanocrystals can now be prepared with a wide range of sizes, shapes, and heterostructures. For colloidal quantum dots, fluorescence emission can be tuned over a broad wavelength range, spanning the ultraviolet through the infrared, however several major challenges still remain. First, although the precise manipulation of fluorescence emission wavelengths through nanocrystal size is well established, many applications exist in which it is desirable to implement similarly sized nanocrystals with distinct optical properties. To this end, ternary alloy nanocrystals have been developed (e.g. $CdSe_xTe_{1-x}$ and CdS_xSe_{1-x}), yet these particles must be prepared in a kinetically controlled reaction in which it is not yet possible to control both size and composition independently.[1-3] Second, a variety of quantum dots have been prepared that emit light in the near-infrared spectrum (e.g. InAs, CdTe/CdSe), for which biological tissue is relatively transparent and only weakly autofluorescent, however these nanocrystal do not have adequate quantum efficiency, photostability, or oxidation resistance compared to their visible light counterparts (CdSe/ZnS).[4-7]

To address both of these issues, this chapter describes the preparation of highly fluorescent $Cd_xHg_{1-x}Te$ quantum dots, which have independently tunable sizes and emission wavelengths, as well as bright near-infrared fluorescence emission. The synthetic methods developed to produce these materials employ spontaneous cation exchange of Hg^{2+} ions with the crystalline lattice of pre-synthesized CdTe nanocrystals. Thereby, the nanocrystal size is first selected in the well-developed synthesis of binary CdTe quantum dots, and the wavelength of emission is selected by the extent of mercury exchange in a subsequent step. Several methods were developed to study the cation exchange mechanism, using quantum dots in polar protic solvents, polar aprotic solvents, and nonpolar solvents, resulting in the capacity to tune the thermodynamics of exchange in diffusion-limited or reaction-limited regimes. The process of cation exchange has recently become a subject of intense research interest due to the capacity to spontaneously generate new nanocrystalline materials from preformed lattices.[8-13] The mechanism of this process is poorly understood, but the methods described herein shed light on this process. In addition these mercury exchange principles are broadly applicable and may also be use to tune the bandgaps of $Cd_xHg_{1-x}Se$, $Cd_xHg_{1-x}S$, and $Zn_xHg_{1-x}Se$ nanocrystals. The $Cd_xHg_{1-x}Te$ nanocrystals can emit light over the range of 500-1000 nm with 30-90 nm full-width-at-half-maximum (FWHM), and after capping with a shell with a graded composition, these nanocrystals are highly photostable with a quantum yield of ~80%.

3.1 Synthesis Methods

3.1.1 Nanocrystal Synthesis. CdTe synthesis was performed in a high temperature solvent containing basic coordinating ligands. Cadmium oxide (25.7 mg, 0.2 mmol), tetradecylphosphonic acid (122 mg, 0.44 mmol), and dioctyl ether (DOE, 2 mL) were added to a three-necked flask and heated to 250°C under argon until complete

dissolution of CdO. After cooling to room temperature, oleylamine (1 g, 3.74 mmol) and additional DOE (6.5 mL) were added. The solution was heated to reflux under vacuum (~20 Pa, ~65°C) for 1 hour and then heated to 300°C under argon flow. A second solution, containing tellurium (12.76 mg, 0.1 mmol), trioctylphosphine (TOP, 2 mL), and DOE (3 mL), previously dissolved at ~280°C and then cooled to room temperature, was injected into the cadmium precursor solution, and the growth temperature was set to 265°C. Using this method, highly monodisperse nanocrystals were grown between 2.0 and 3.5 nm diameter after reaction times between 20 seconds and 10 minutes. To grow larger nanocrystals, additional cadmium and tellurium precursors were sequentially injected dropwise into the reaction solution, starting at 4 minutes after the first injection. The 0.02 M tellurium solution used for the first injection was also used for subsequent injections, and a 0.02 M cadmium oleate solution in DOE was used as a cadmium precursor. After reaching the desired size, the reaction mixture was cooled to room temperature, diluted with 85 mL hexane, and centrifuged to remove most of the excess cadmium precursor. The nanocrystals were isolated using at least six hexane-methanol extractions. On the final extraction, the nanocrystals were condensed to ~ 1 mL through the addition of methanol. These nanocrystals were then diluted to ~20 mL with chloroform, bubbled with argon for 30 minutes and stored at 4°C in the dark. Quantum dot size was determined from the published correlation with the first exciton peak wavelength,[14] and verified via TEM. The CdSe, CdS, and ZnSe nanocrystals were prepared and purified using similar protocols, adapted from previous reports.[15-19]

3.1.2 Phase Transfer Methods. To transfer purified nonpolar CdTe quantum dots to water or dimethyl sulfoxide (DMSO) using thioglycerol, a solution of quantum dots in chloroform (~20 μM) was mixed with an excess of thioglycerol (~0.2 M). The mixture immediately became opaque, and the solution was repeatedly sonicated and vortexed

for ~15 minutes. The nanocrystals were isolated via centrifugation, washed with acetone, and then dried under vacuum. After resuspension in a solution of 1 mM thioglycerol in deionized water (pH 11), the nanocrystals were sonicated, centrifuged at 7000g for 15 minutes to remove aggregates, and finally passed through a 0.2 μm filter. Quantum dots prepared through this method were brightly fluorescent and stable for months. For phase transfer to DMSO, the nanocrystals were resuspended in DMSO containing 1 mM thioglycerol, rather than an aqueous solution.

For phase transfer from aqueous solution to nonpolar solution, an extraction procedure from water to 1-octanethiol was implemented. On a small scale, 1 mL of aqueous quantum dots was mixed with 3 mL methanol, and 1 mL of 1-octanethiol was added. This solution was repeatedly vortexed and sonicated for ~5 minutes. Chloroform (1 mL) was then added to separate the emulsion, drawing the quantum dots to the bottom nonpolar phase. This phase was isolated via centrifugation and 50 mg of TOP was added in order to further stabilize the nanocrystals, which were purified through extractions between decane-methanol phases. Precipitation of these labile nanocrystals should be avoided in order to minimize aggregation. This optimized protocol resulted in highly monodisperse nanocrystals with optical properties that were essentially unchanged from those in water. Deviations from this optimization can lead to significant etching of the labile HgTe shell. A similar method was used to transfer quantum dots from DMSO to nonpolar solution, which did not require the use of a methanol emulsifier because of the relatively low surface tension between DMSO and octanethiol. Briefly, a DMSO solution of quantum dots was mixed 1:1 by volume with octanethiol, and then vortexed and sonicated for 5 minutes. The octanethiol phase was isolated by centrifugation and the quantum dots were precipitated with the addition of a 20-fold excess of a 2:1 mixture of methanol:acetone containing a small amount of

trioctylphosphine to maintain colloidal stability. The nanocrystals were then resuspended in chloroform.

3.1.3 Mercury Exchange. In aqueous solution, nanocrystals were diluted to ~20 μM with basic thioglycerol buffer, and a freshly prepared solution of mercury perchlorate (1 mM) in deionized water was added. The nanocrystals were immediately vortexed, and allowed to equilibrate for 1 month before analysis. In DMSO, a similar protocol was used, except the mercury precursor was prepared by dissolving mercury acetate in a solution of thioglycerol in DMSO. The thioglycerol:mercury ratio was 3:1, and thioglycerol was diluted in DMSO prior to introduction of mercury in order to prevent reduction to metallic mercury. In nonpolar solution, a 1:1:2 mixture of oleic acid, oleylamine, and hexane was prepared and allowed to cool to room temperature after exothermic mixing. A solution of 20 μM quantum dots was then diluted 1:1 with this ligand solution, and a mercury acetate solution in octylamine was added. The solution was immediately mixed and monitored via UV-Vis absorption spectroscopy until the desired absorption was observed. At this point, the excess mercury was extracted in a mixture of 1:2:3 decane:hexane:methanol. The nanocrystals were extracted 4 times, and each time a small amount of the ligand mixture was added in order to maintain colloidal stability. Notably, these nanocrystals were labile toward strong ligands such as thiols.

3.1.4 Elemental Analysis. Prior to elemental analysis of alloyed nanocrystals, quantum dots in aqueous solution were first isolated and purified using a centrifugal filtration device (Millipore, 5 kDa molecular weight cutoff). The concentration of metals in the eluant was tested to verify the dissociation of cadmium ions from quantum dots that underwent cation exchange. The nanocrystals were etched and dissolved in aqueous

solution with the addition of a small amount of nitric acid. For hydrophobic quantum dots in nonpolar solutions, the particles were isolated with the addition of an excess of acetone. After resuspension in chloroform, a small amount of oleylamine was added to maintain colloidal stability (~0.01 mg/mL). The quantum dots were similarly precipitated two more times to ensure complete removal of unbound metals, which were almost entirely found in the first supernatant. Following the final precipitation, the pellet was washed with acetone and methanol, redispersed in a small amount of chloroform and transferred to a glass vial. The chloroform was removed under vacuum, and the quantum dot film was dissolved in aqua regia at 80°C for ~ 4 hours. The solution was then diluted in deionized water and analyzed for cadmium, mercury, tellurium, and selenium using inductively coupled plasma mass spectrometry (ICP-MS, VG PlasmaQuad 3).

3.1.5 Shell Growth. The methods and calculations used for shell growth are described in depth in Chapter 4. Briefly, purified $Cd_xHg_{1-x}Te$ nanocrystals prepared through cation exchange in DMSO were diluted in oleylamine in an inert atmosphere, and heated to 130°C. A single monolayer of CdTe was grown on the surface using organometallic reagents, and the temperature was increased to 170°C. A single monolayer of CdSe was then grown on the quantum dots, and the temperature was increased to 220°C, at which point 3 monolayers of CdS were deposited. The nanocrystals were annealed at this temperature for 2 hours, and then cooled to room temperature and isolated via precipitation from acetone.

3.2 Synthesis Strategy

The process of mercury cation exchange was originally described by Horst Weller and coworkers for the production of $Cd_xHg_{1-x}S$ quantum dot alloys from CdS nanocrystals.[20-23] This same group later extended these techniques to prepare brightly fluorescent $Cd_xHg_{1-x}Te$ quantum dots through the mechanism illustrated in Figure 3.1.[24,25] CdTe nanocrystals (~2-2.5 nm diameter) were synthesized from the reaction between cadmium perchlorate and sodium hydrogen telluride in basic water in the presence of thioglycerol. After purification, the thioglycerol stabilized quantum dots were mixed with mercury perchlorate, inducing partial exchange of the Cd^{2+} ions on the surface of the nanocrystals for Hg^{2+} ions, resulting in CdTe cores with HgTe shells. The spontaneity of this reaction was hypothesized to be due to the much higher solubility of Cd^{2+} ions in aqueous solution compared to Hg^{2+} ions, and due to the nearly identical bond lengths of these materials (see section 3.6 for discussion). HgTe has a much smaller bandgap than CdTe, resulting in a red-shift of the absorption band and the emission wavelength with mercury exchange (Figure 3.2). This structure cannot be accurately described as a quantum dot, as the charge carriers necessarily reside primarily in the shell region, where the electronic energy levels are the smallest. However, the nanocrystal is also too small to be described as a quantum well, as the charge carriers are not entirely confined in the shell. That is, the small size of the entire nanocrystal permits a large degree of quantum tunneling from the shell into the core center, and there is no tangential confinement of the charge carriers in the shell because the circumference is much smaller than the Bohr exciton diameter of HgTe (91 nm). Because of this intermediate quantum confinement regime, these nanocrystals have been dubbed quantum dot-quantum wells.

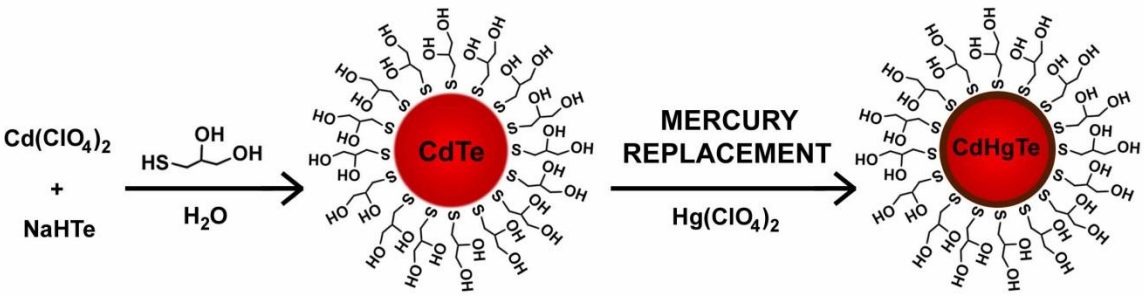

Figure 3.1: Synthesis scheme for $Cd_xHg_{1-x}Te$ quantum dot-quantum wells, as originally described by Weller and coworkers.[24] See text for details.

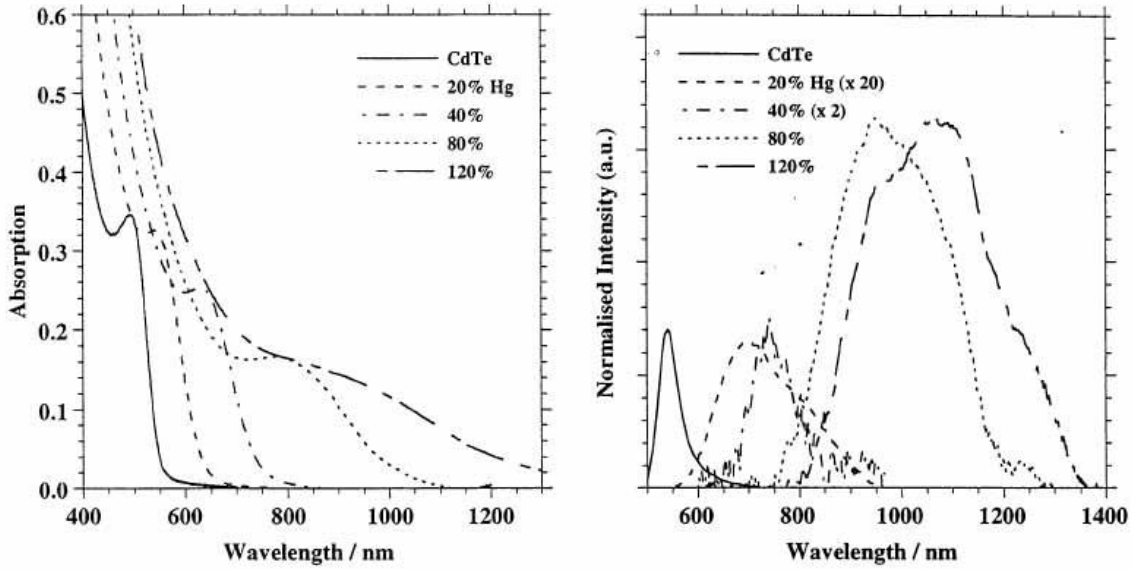

Figure 3.2: Red-shift of CdTe emission with mercury cation exchange of aqueous nanocrystals. The absorption band edges (left) and fluorescence emission (right) shift with increasing mercury content, indicated as the percentage mercury added compared to cadmium present. This figure is reproduced from the work of Weller and coworkers.[24]

From Figure 3.2 it is apparent that the nanocrystals prepared from this method have broad emission bands and indistinct absorption features. Clearly, the mercury exchange method is successful in yielding a strong red-shift in emission and bright near-infrared fluorescence, however the spectral properties are far from ideal. To improve this

method, the work described in this chapter is predicated on the idea that these poor spectral features are solely the result of the poor crystallinity of these nanocrystals. That is, this original report implemented aqueous nanocrystals that were prepared at room temperature. Such low temperature techniques do not result in a high degree of crystallinity compared to higher temperature methods, in which kinetic reaction constraints can be overcome to yield low energy crystals with few defects. Thereby, if these poor-quality quantum dots can be replaced with high quality quantum dots prepared at high temperature, the optical properties should be drastically improved, thus expanding the utility of the nanocrystals for biological labeling applications. In addition, it is virtually impossible to prepare nanocrystals larger than ~3.0 nm with a high degree of monodispersity using this original aqueous method. Utilization of a high temperature synthesis with precise size control will also alleviate this limitation.

Figure 3.3 depicts the new scheme used for the cation exchange of mercury with high quality CdTe nanocrystals, as well as the post-synthetic processes implemented to yield brightly fluorescent quantum dots for biological labeling. CdTe nanocrystals are first prepared in a high boiling point coordinating solvent, and grown to a desired size (2-10 nm diameter). The highly crystalline quantum dots are coated with a monolayer of alkylamine ligands (e.g. hexadecylamine), and are only soluble in nonpolar solvents. In order to perform mercury exchange using the traditional protocol, the hydrophobic ligands are first replaced with thioglycerol, and the nanocrystals are suspended in water. Mercury exchange is then performed, and the nanocrystals are then transferred back to the nonpolar solvent. It is also possible to perform this mercury exchange process directly in nonpolar solvents. These telluride nanocrystals are inherently labile toward oxidation, so after alloying, a shell of wide bandgap material (CdSe and CdS) is grown on the core at high temperature in order to protect the optical properties. It should be

noted that the generation of a highly crystalline, coherently epitaxial shell can only be reproducibly performed in nonpolar coordinating solvents at high temperature. Therefore this step would not be possible with the traditional aqueous approaches. After this final step, these quantum dots may be transferred to water using a variety of methods, such as the amphiphilic polymer approach depicted in the figure.

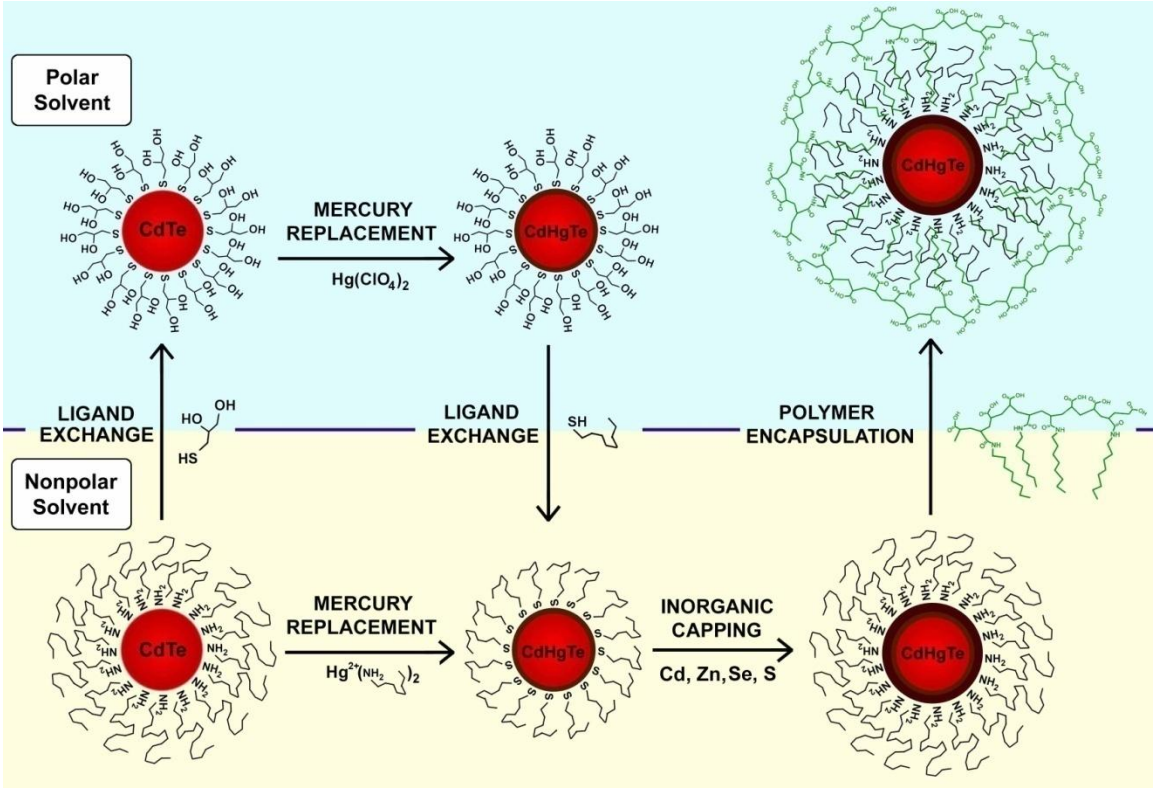

Figure 3.3: Schematic depiction of the multiphase synthesis procedure for monodisperse, brightly fluorescent $Cd_xHg_{1-x}Te$ nanocrystals. The mercury exchange process is performed on crystalline, size-controlled CdTe nanocrystals produced in nonpolar solvents, and the quantum dot-quantum wells are capped at high temperature before phase transfer to water for use in bioimaging.

3.3 Optical Properties of $Cd_xHg_{1-x}Te$ Nanocrystals

CdTe nanocrystals produced at high temperature were highly crystalline compared to their aqueous low temperature synthesis counterparts. Figure 3.4 depicts a high-

resolution transmission electron micrograph (HRTEM) of ~3.8 nm nanocrystals, showing a high degree of monodispersity, as well as crystalline planes that extend throughout a majority of the particles. Such evidence of crystallinity is never apparent from aqueous preparations of CdTe nanocrystal. The X-ray diffraction spectra of these nanocrystals corroborate this assertion of high crystallinity (see Chapter 4), which is also verified by the high quantum yield (40-80%). Using the synthetic scheme in Figure 3.3, these nanocrystals were transferred to water using thioglycerol, and mercury exchange was performed using the same methods developed by Weller and coworkers. The resulting optical properties were vastly improved, showing discrete band-edge fluorescence emission with narrow peaks (compare Figure 3.2 and Figure 3.5A). In addition, the absorption spectral features are maintained with the addition of various amounts of mercury. These nanocrystals can be initially prepared with a wide range of homogeneous sizes (Figure 3.5A-C), allowing the study of $Cd_xHg_{1-x}Te$ alloy optical properties with respect to both size and composition, with high spectral resolution of electronic transitions. The quantum mechanical properties of HgTe nanocrystals and their alloys are of particular interest to physicists because of the extremely large exciton Bohr radius of this material, which allows the preparation of nanocrystals in the strong confinement regime (both holes and electrons confined) without necessitating the use of extremely small nanocrystallites, for which surface effects may dominate.[26]

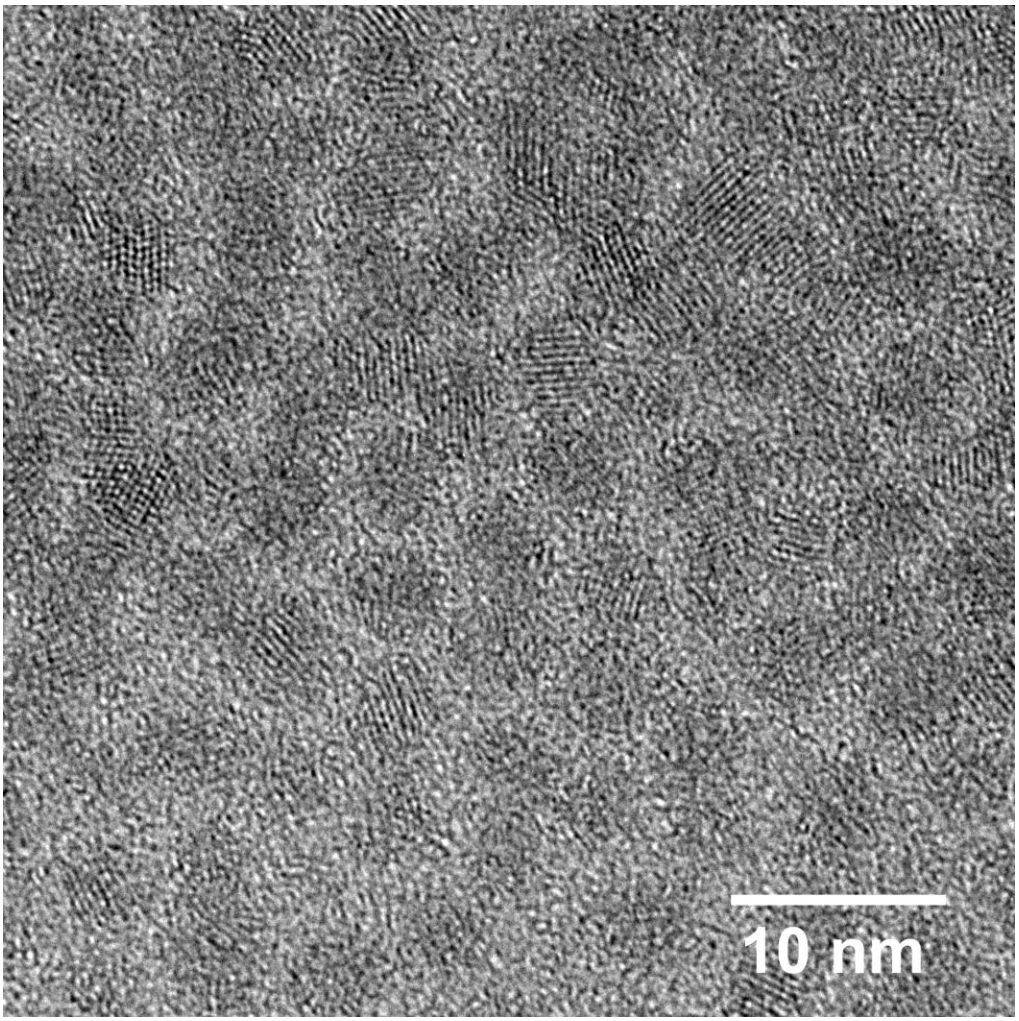

Figure 3.4: HRTEM of ~3.8 nm CdTe nanocrystals prepared at high temperature in a coordinating solvent, showing monodispersity and high crystallinity.

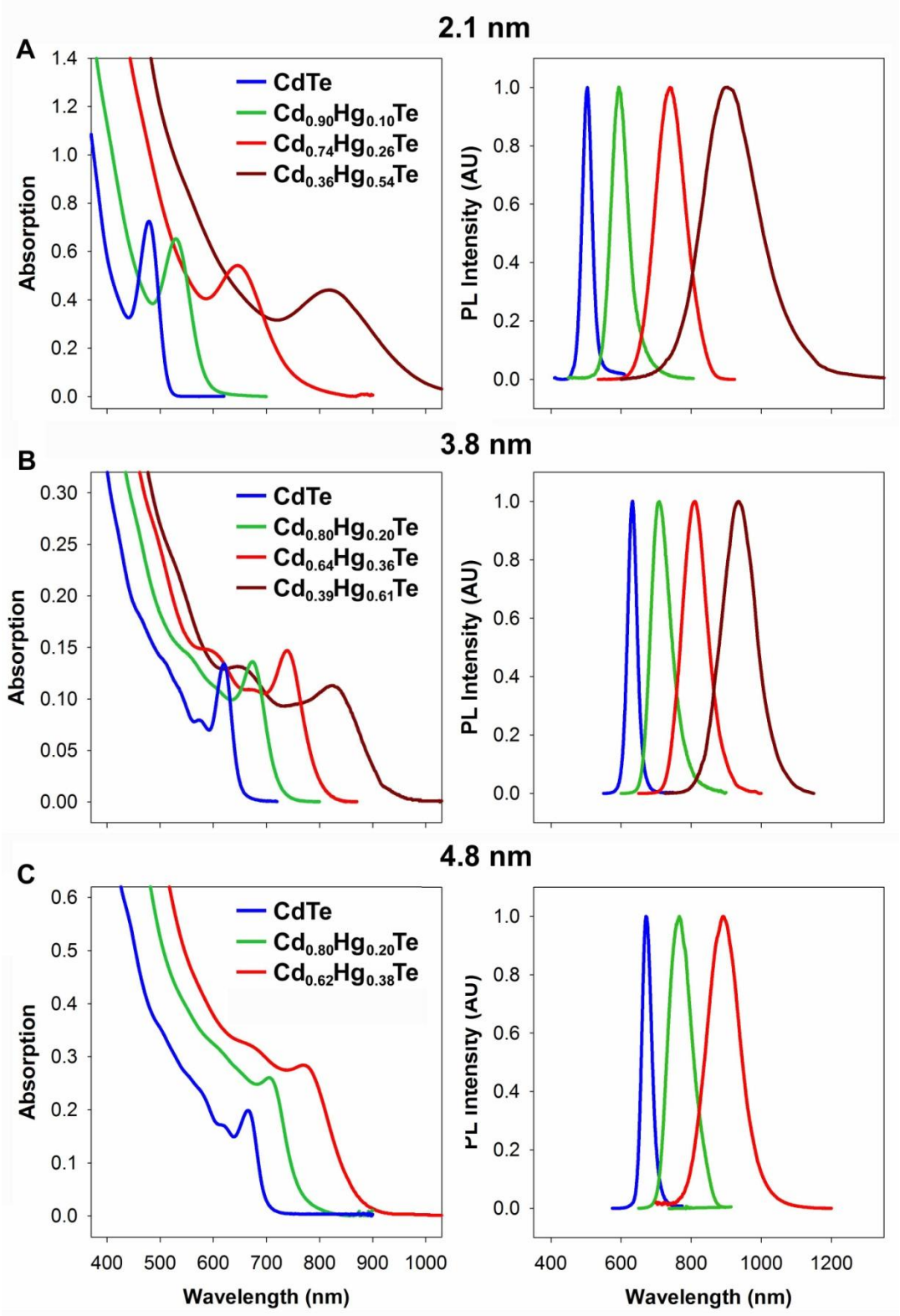

Figure 3.5: Mercury cation exchange of CdTe nanocrystals, showing absorption (left) and fluorescence spectra (right). The core sizes are 2.1 nm (A), 3.8 nm (B), and 4.8 nm (C), and mercury exchange was performed in aqueous solution.

It is important to note that after mercury cation exchange, the 2.1 nm $Cd_xHg_{1-x}Te$ nanocrystals can have a wavelength of emission as long as ~930 nm with the multiphase approach (Figure 3.5A), whereas similar CdTe nanocrystals prepared in the aqueous procedure can emit at wavelengths longer than 1050 nm (Figure 3.2). The addition of more mercury could not further shift this emission wavelength, suggesting that either all of the cadmium was depleted from the quantum dot, or that the remaining cadmium was inert toward exchange. Elemental analysis revealed that ~36% of the cadmium still remained in the quantum dot. Therefore it is likely that this material remained in the interior of the structure, sequestered away from the surface of the nanocrystal where exchange can occur. The CdTe nanocrystals prepared in aqueous solution may allow a greater extent of exchange due to their lower crystallinity, as the presence of multiple crystalline domains within individual nanocrystals can increase the surface energy of the particles.

To further study the efficiency of cation exchange, 2.1 nm and 3.8 nm CdTe nanocrystals were mixed with different ratios of mercury, purified, and analyzed via elemental analysis and TEM. TEM revealed that the nanocrystals were essentially identical in size, before and after mercury exchange (Figure 3.6). It was further revealed that cation exchange occurred efficiently and stoichiometrically at low mercury concentrations, which leveled off at high concentrations, reaching a maximum exchange efficiency of 62% for the 2.1 nm nanocrystals and 57% for the 3.8 nm nanocrystals (Figure 3.7). These values correspond to an exchange depth of ~1.3 monolayer into the 2.1 nm nanocrystals and ~1.4 monolayers for the 3.8 nm nanocrystals. This suggests that the mercury can displace cadmium ions from the crystal beyond the first monolayer of the crystalline facets, penetrating into the core. However, this process is limited, as

further equilibration and even heating did not significantly increase the mercury incorporation beyond these values.

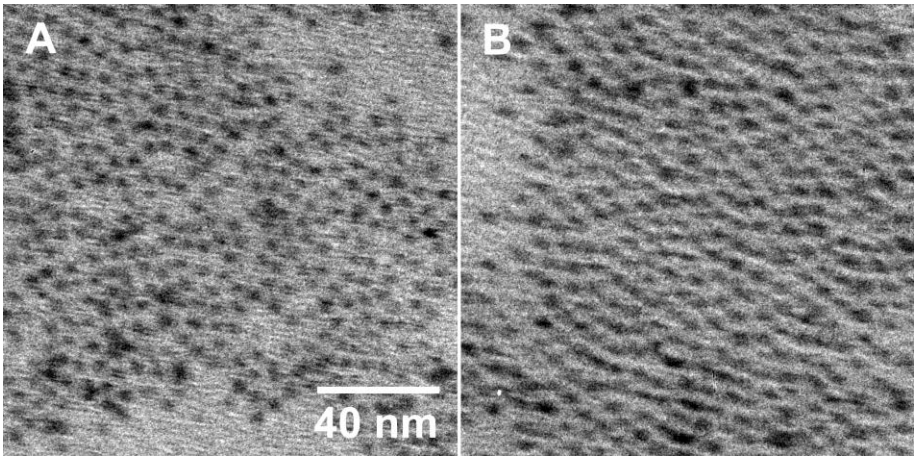

Figure 3.6: TEMs of 3.8 nm nanocrystals composed of CdTe (A) or $Cd_{0.39}Hg_{0.61}Te$ (B). The same quantum dots were used in Chapter 4 for further experiments, and panel A is reproduced in Figure 4.11.

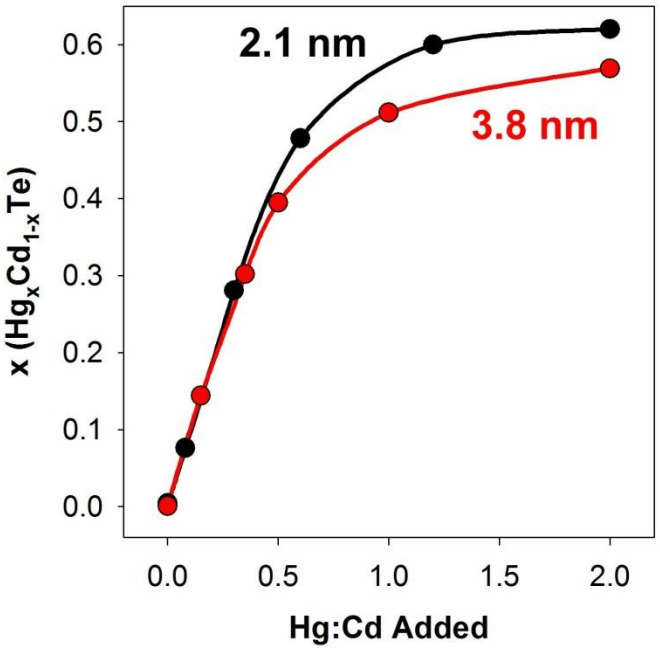

Figure 3.7: Efficiency of mercury cation exchange for two sizes of CdTe nanocrystals in aqueous solution. ICP-MS elemental analysis of the 2.1 nm and 3.8 nm nanocrystals was determined after equilibration with mercury perchlorate for 1 month and purification.

The dependence of the optical properties of these nanocrystals on the ternary alloy composition is depicted in Figure 3.8. The optical absorption bandgap decreased linearly with increasing mercury content for both the 2.1 nm and 3.8 nm nanocrystals, suggesting a behavior similar to a quantum dot, rather than a quantum well structure. However the Stokes shift increased significantly with increasing mercury content, a phenomenon that has never before been reported. The Stokes shift is known to depend on the nanocrystal size and shape (see Chapter 2). As both of these nanocrystals were quasi-spherical and did not change in size with composition, the composition is likely to be the cause of this shift. As a general rule, within the quantum confinement regime the Stokes shift increases with decreasing quantum dot size. Because the Bohr exciton diameter of CdTe (13 nm) is significantly smaller than that of HgTe (91 nm), the degree of confinement increases as the composition shifts toward HgTe, causing the Stokes shift to increase. As well, a change in dimensionality of quantum confinement may also play a role in the Stokes shift, as the quantum dot-quantum well behaves more like a quantum well as the core size increases. As stated previously, there is an upper limit to the cation exchange efficiency that cannot be surmounted for each nanocrystal size. However, the linear trend of the optical bandgap with composition can be used to extrapolate to pure HgTe quantum dots. Surprisingly, the linear trends of both the 2.1 nm nanocrystals and the 3.8 nm nanocrystals extrapolate to an optical absorption of 1040 nm, despite the difference in nanocrystal size. This unexpected finding suggests that the dimensionality of confinement does play an important role in these nanocrystals, as the 3.8 nm quantum dots have a weaker relationship with composition than their 2.1 nm counterparts. Clearly, the properties of these mixed-dimensionality structures can neither be sufficiently described as individual quantum dots nor as quantum wells.

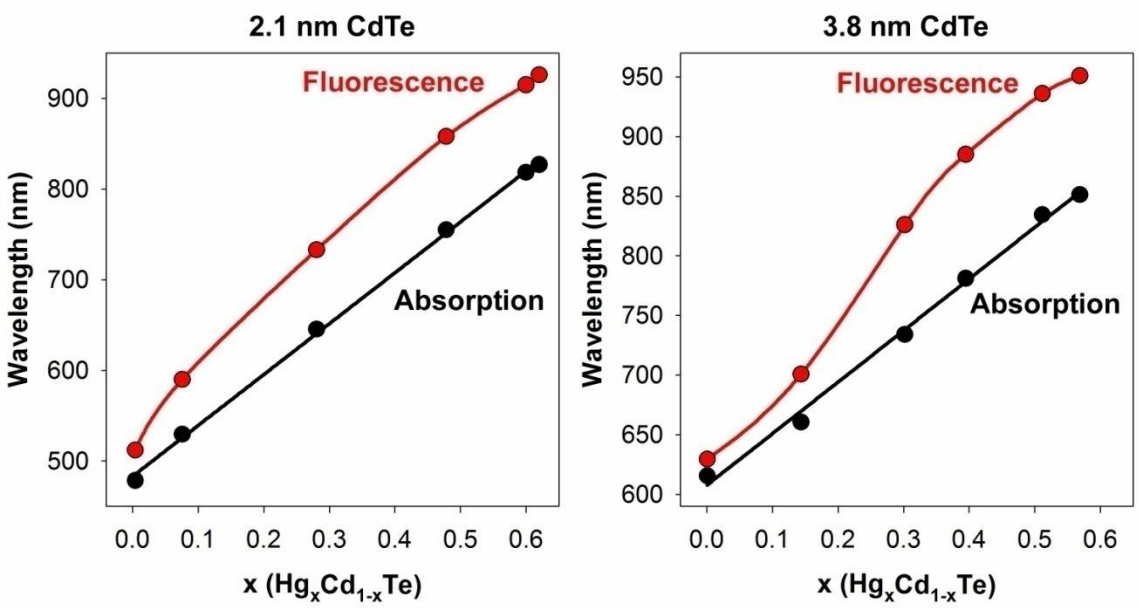

Figure 3.8: Dependence of the absorption band edge and fluorescence maxima of $Cd_xHg_{1-x}Te$ quantum dot-quantum wells. Absorption data are fitted to linear trends, whereas lines connecting fluorescence data are not fitted, but added merely to guide the eye.

Despite high quantum dot crystallinity and monodispersity, the fluorescence emission bands of the $Cd_xHg_{1-x}Te$ quantum dots widened substantially with increasing mercury content (Figures 3.5). This broadening was partially a result of plotting the data in terms of wavelength rather than energy. Replotting the data as transitions in energy diminished this broadening effect (Figure 3.9), but a substantial broadening is still present with alloying. This broadening has both homogeneous and inhomogeneous contributions. First, the process of alloying is an inherently inhomogeneous process due to the non-zero polydispersity of the nanocrystal samples and the variety of surface facets and atoms present on each nanocrystal within the ensemble. Thereby, smaller nanocrystals within the ensemble have higher surface energy, which will kinetically favor cation exchange over larger nanocrystals in the ensemble, broadening the distribution of alloy compositions. Second, the optical transitions of HgTe are known to be inherently

wider than those of CdTe in bulk materials, suggesting an inevitable homogeneous broadening effect with increasing HgTe composition.[27,28] These effects are demonstrated in Figure 3.10, showing 3 different sizes of $Cd_xHg_{1-x}Te$ alloy quantum dots with 3 different alloy compositions, all with the same emission wavelength. Increasing the composition of mercury and decreasing the nanocrystal size results in much broader optical transitions, which are also reflected in the absorption spectra. Comparisons like this would not be possible if it were not for the new synthetic scheme developed herein.

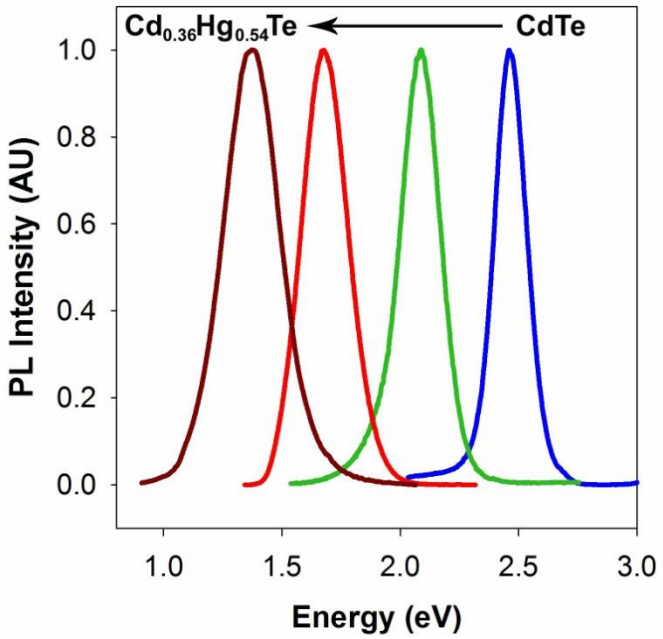

Figure 3.9: Fluorescence emission spectra of 3.8 nm $Cd_xHg_{1-x}Te$ nanocrystals, replotted from Figure 3.5B in terms of energy, rather than wavelength.

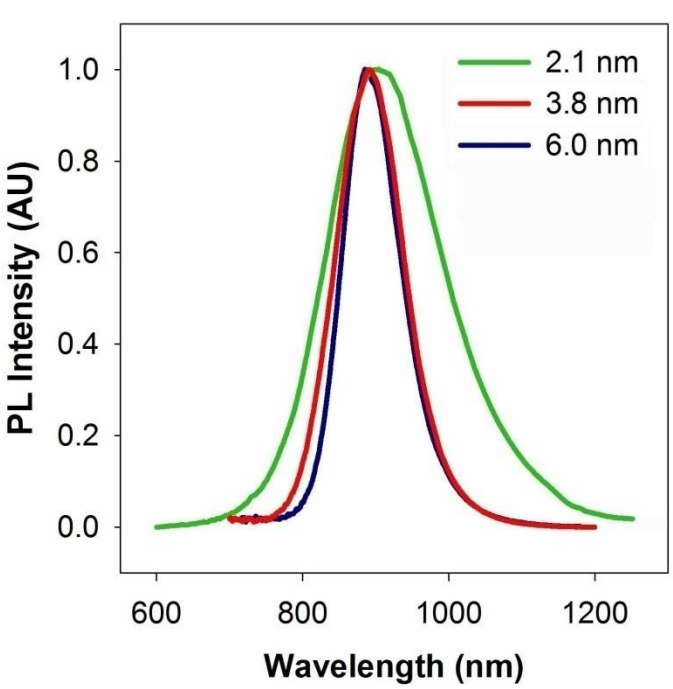

Figure 3.10: Fluorescence bandwidth dependence on composition and size for $Cd_xHg_{1-x}Te$ nanocrystals.

3.4 Solvent Impact on Mercury Cation Exchange

A multiphase procedure was developed and optimized for mercury exchange of CdTe nanocrystals in polar and nonpolar solvents (Figure 3.3). Thioglycerol-coated CdTe nanocrystals were strongly susceptible to mercury exchange using conventional protocols in aqueous solution. These nanocrystals could also be suspended in polar aprotic solvents such as DMSO or DMF for mercury cation exchange. However the exchange was found to be dramatically slower in these solvents, and less homogeneous, as indicated by wider optical peaks. This is likely due to the high viscosity of these solvents, which decreases the efficiency of mixing and solute equilibration. To extend this concept to nonpolar solvents, quantum dots were coated with alkanethiols (octanethiol) to simulate the aqueous conditions, and mixed with a solution of mercury acetate in octylamine. Surprisingly, mercury exchange was entirely inhibited under these conditions, resulting in a maximum red-shift of ~5 nm, compared to

the ~400 nm shifts observed in aqueous solution. This effect was even found to occur when the solvent was highly inviscid (chloroform or hexane), thus implicating a chemical reactivity induced inhibition of cation exchange. In the absence of thiols, mercury exchange was entirely uncontrollable, as mercury instantly reacted with the nanocrystals, resulting in heterogeneous alloying marked by broad optical transitions.

A wide variety of nonpolar coordinating ligands were tested in order to control the activity of the mercury ions and the reactivity of the nanocrystal surfaces. It was found that a 1:1 mixture of oleic acid:oleylamine resulted in highly homogeneous nanocrystal alloying. However, the mechanism by which exchange occurred was found to be different than the mechanism in aqueous solution. In aqueous solutions containing thiolate ligands, the incorporation of mercury occurred homogeneously in a dose-dependent fashion. However in nonpolar solvents with weaker ligands, adding small amounts of mercury resulted in inhomogeneous cation exchange, and optical spectra showed a complete loss of optical transitions (Figure 3.11). This process was unrecoverable, as the addition of more mercury could not improve the inhomogeneous optical spectra. On the other hand, the initial addition of a large excess of mercury (more than the amount of cadmium in the nanocrystal) resulted in highly homogeneous exchange that proceeded quickly until the maximum amount of exchange was achieved. These observations suggest that the rate of exchange is controlled through the rate of diffusion in nonpolar solvents, and through the chemical reaction rate in aqueous solution. That is, thioglycerol strongly binds to both Hg^{2+} ions in solution and to Cd^{2+} atoms on the nanocrystal surface, and therefore the rate limiting step for exchange is the reaction rate between the strongly bound mercury ion and the nanocrystal surface. However in nonpolar solution containing weaker ligands like amines and carboxyls, the reaction rate between the mercury ions and the surface of the nanocrystal is so high that a small amount of

mercury reacts almost instantaneously upon introduction, causing inhomogeneous alloying due to a reaction rate that is far greater than the diffusion rate. Such a kinetically controlled exchange process is undesirable from a production perspective, and therefore attempts were made to terminate mercury exchange at specific time-points after the addition of excess Hg^{2+}. It was found that quick extraction of the excess mercury precursor could effectively terminate cation exchange by separation of the precursor to a separate phase (e.g. methanol), and the partially exchanged nanocrystals could be purified to yield stable colloids at room temperature. However, these nanocrystals were labile toward strongly binding ligands, such as thiols and phosphonic acids, resulting in an etching of the mercury, indicated by a blue-shift of the optical spectra and a decrease in oscillator strength of all of the optical transitions.

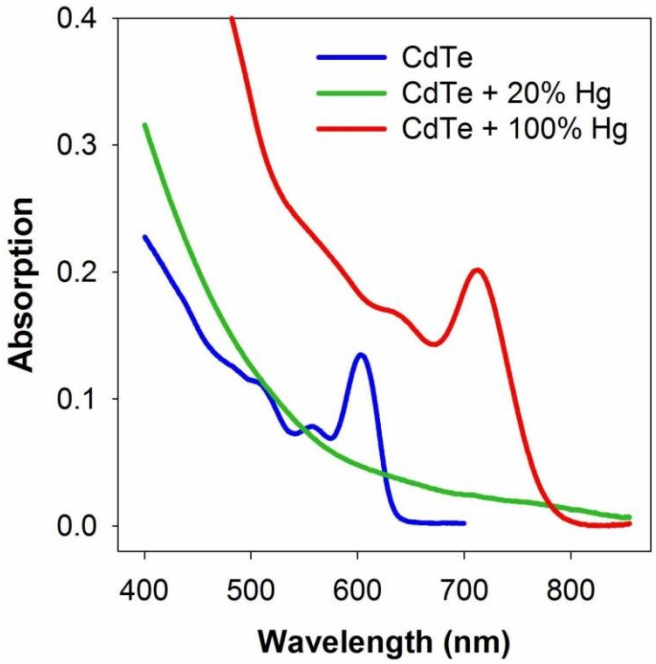

Figure 3.11: Optical spectra of homogeneous and inhomogeneous mercury cation exchange in nonpolar solvents. 3.8 nm CdTe cores were mixed with mercury in quantities much smaller than the amount of cadmium (20%) or equal to the total amount of cadmium (100%). The cation exchange process is homogeneous only in the presence of a large excess of mercury, resulting in nanocrystals with discrete optical transitions.

3.5 Mercury Exchange with Other II-VI Materials

In order to determine if the mercury exchange methods developed herein are widely applicable to other materials, ~3.8 nm CdTe, CdSe, CdS, and ZnSe were prepared in coordinating solvents at high temperature, and then subjected to mercury cation exchange in the oleic acid-oleylamine ligand mixture that was optimized for CdTe. The optical spectra of all of these materials demonstrate red-shifts in both fluorescence and absorption (Figure 3.12), which is in accord with an alloying process with mercury, which would reduce the bandgap of all of these materials. With the exception of $Zn_xHg_{1-x}Se$, the mercury alloys were brightly fluorescent and displayed discrete electronic transitions in their absorption spectra. Elemental analysis revealed that exchange was less efficient for these materials, reaching a maximum of ~30% conversion for $Cd_xHg_{1-x}Se$. This corresponds to one half of a monolayer, meaning that the mercury may only have exchanged with specific facets of these nanocrystals, or it may only exchange with the first atomic layer of atoms, which corresponds to one half of a monolayer for polar facets.

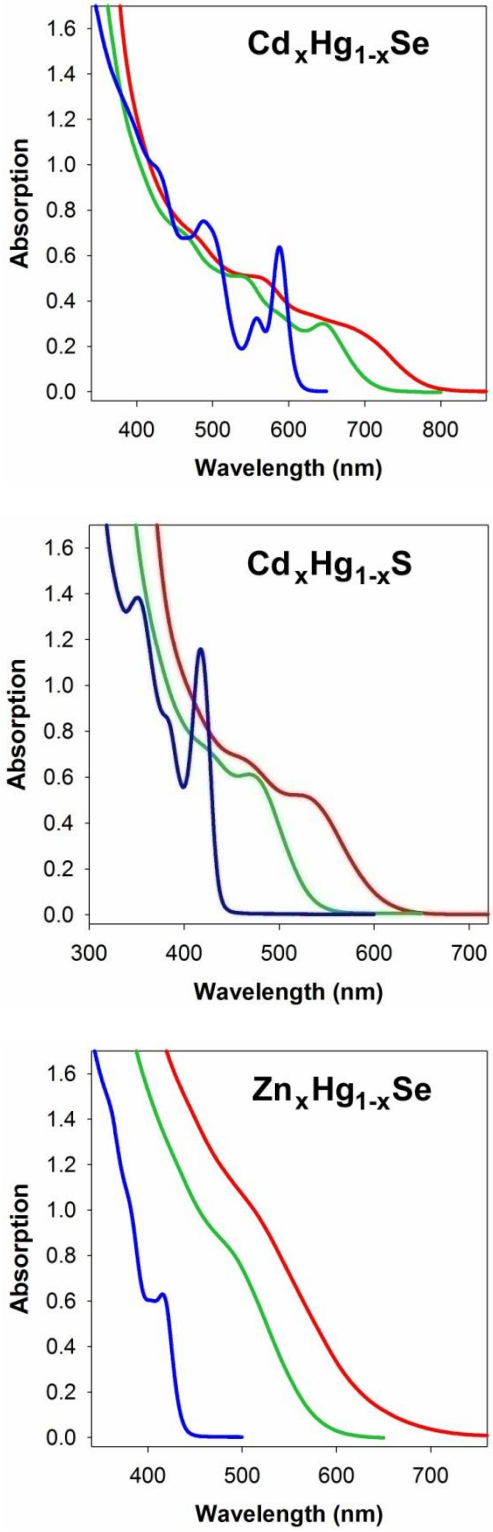

Figure 3.12: Spectra of $Cd_xHg_{1-x}Se$, $Cd_xHg_{1-x}S$, and $Cd_xZn_{1-x}Se$ nanocrystals prepared through cation exchange in a nonpolar solution.

3.6 Cation Exchange Mechanism

The mechanism of aqueous mercury cation exchange originally postulated by Weller and coworkers for the spontaneous formation of $Cd_xHg_{1-x}S$ and $Cd_xHg_{1-x}Te$ alloys from pure binary cadmium chalcogenide nanocrystals was related to the solubility of the individual binary compounds in water.[21,24] That is,

$$CdTe(s) \longrightarrow Cd^{2+}(aq) + Te^{2-}(aq) \qquad k_{sp} = 10^{-41.5} \qquad \textbf{Equation 3.1}$$

$$HgTe(s) \longrightarrow Hg^{2+}(aq) + Te^{2-}(aq) \qquad k_{sp} = 10^{-69.6} \qquad \textbf{Equation 3.2}$$

Clearly, both CdTe and HgTe are nearly insoluble in water, however the solubility of CdTe is roughly 10^{28} times greater than that of HgTe. In addition, CdTe and HgTe have nearly identical lattice constants, allowing unstrained exchange of cations. However, the results of this thesis show that these hypotheses are incomplete. These exchange reactions do not take place in pure aqueous solution, as strongly binding thiol ligands are crucial components of these mixtures for the stabilization of the metal ions and the colloidal stability of the nanocrystals. Thereby the stability of the ligand-metal complexes must also be a factor, as thiols bind much more strongly to mercury ions than to cadmium cations.[29-33]

$$Cd^{2+}(aq) + 2MAA^{2-}(aq) \longrightarrow Cd(MAA)_2(aq) \qquad k = 10^{15.63} \qquad \textbf{Equation 3.3}$$

$$Hg^{2+}(aq) + 2MAA^{2-}(aq) \longrightarrow Hg(MAA)_2(aq) \qquad k = 10^{44.3} \qquad \textbf{Equation 3.4}$$

where MAA^{2-} is fully deprotonated mercaptoacetic acid ($^{-}S\text{-}CH_2\text{-}COO^{-}$). The use of this ligand is relevant, as we have found that MAA and thioglycerol can be used interchangeably in these reactions in aqueous solution. In addition, these reactions

were all performed in basic solution above the pK_a of the MAA thiol (pH ~11). However we have also tested these reactions at higher acidity, and they proceed similarly at all pH levels down to ~5, at which point the nanocrystals are no longer colloidally stable due to protonation of the thiol ligand. This is in accord with similar relative affinities between divalent cadmium and mercury for the different protonated species of the MAA ligands. The higher affinity of the thiol ligands for mercury ions compared to cadmium ions is experimentally verified with the addition of a very minute amount of mercury perchlorate to a solution of CdTe quantum dots in the absence of excess thiol ligands, which entirely precipitates the nanocrystals from solution. The nanocrystals may be resuspended with the addition of a small amount of extra ligand.

Equations 3.3 and 3.4 demonstrate that thiolate ligands have a much higher affinity for mercury than for cadmium, and the balanced equation reads

$$\mathrm{CdTe(s)} + \mathrm{Hg(MAA)_2(aq)} \longrightarrow \mathrm{HgTe(s)} + \mathrm{Cd(MAA)_2(aq)} \qquad k = 0.269 \qquad \textbf{Equation 3.5}$$

This equation suggests that cation exchange is favorable only for the introduction of CdTe into HgTe. However this mechanism is incomplete, as thiolate ligands also bind to the mercury ions on the surface facets of the nanocrystal. Ligand binding energies on nanocrystal facets have not yet been elucidated for these materials and ligands, but it has been estimated that the cadmium-thiolate bond on a CdSe nanocrystal surface is roughly 1/2 the strength of the bond between divalent cadmium and mercaptoacetic acid.[34] Thereby making the assumption that both of these binding strengths decrease by half for both mercury and cadmium surface atoms, the ligand binding equilibrium may be described as

$$[\mathrm{CdTe}]\text{-}\mathrm{Cd}^{1+}(\mathrm{s}) + \mathrm{MAA}^{2-}(\mathrm{aq}) \longrightarrow [\mathrm{CdTe}]\text{-}\mathrm{Cd}(\mathrm{MAA})^{1-}(\mathrm{s}) \qquad k = 10^{5.7}$$ **Equation 3.6**

$$[\mathrm{HgTe}]\text{-}\mathrm{Hg}^{1+}(\mathrm{s}) + \mathrm{MAA}^{2-}(\mathrm{aq}) \longrightarrow [\mathrm{HgTe}]\text{-}\mathrm{Hg}(\mathrm{MAA})^{1-}(\mathrm{s}) \qquad k = 10^{22.2}$$ **Equation 3.7**

Therefore, binding of thiolate ligands to HgTe nanocrystals is much more energetically favorable than binding to CdTe nanocrystals, resulting in the balanced equation

$$[\mathrm{CdTe}]\text{-}\mathrm{Cd}(\mathrm{MAA})^{1-}(\mathrm{s}) + \mathrm{Hg}(\mathrm{MAA})_2(\mathrm{aq}) \rightarrow [\mathrm{HgTe}]\text{-}\mathrm{Hg}(\mathrm{MAA})^{1-}(\mathrm{s}) + \mathrm{Cd}(\mathrm{MAA})_2(\mathrm{aq}), \; k = 8.5 \times 10^{15}$$ **Equation 3.8**

Therefore, it is the relatively affinity of the thiol ligands for the metal ion and nanocrystal surface, as well as the solubility of the free metal ions, that drives cation exchange. This theory predicts that such a mechanism may be modulated merely through the relative binding strengths of the ligands.

Strong evidence for the ligand-impact on cation exchange comes from the different core materials. Out of CdTe, CdSe, CdS, and ZnSe, only CdTe was found to be capable of exchanging with mercury in aqueous solution in the presence of thiolate ligands. The relative solubilities of the cadmium chalcogenides and mercury chalcogenides are similar, independent of the chalcogen composition, but the solubility of ZnSe is ~10^{39} greater than HgSe, which would be expected to favor cation exchange even more. However, thiolate ligands bind much more strongly to the surfaces of CdSe, CdS, and ZnSe quantum dots than they do to CdTe due to smaller bond lengths within the crystal, which prevents the displacement of cadmium atoms by mercury atoms.

Simple differences in solubility are therefore insufficient to thoroughly explain the cation exchange mechanism. The delicate balance of thermodynamic forces controlling ion

exchange can be largely influenced by the relative ligand binding strengths between the different exchange ions. Thereby one may exchange the ions of a crystal with a material that actually is thermodynamically less stable. That is, HgTe has a weaker bond strength than CdTe (-0.81 eV compared to -1.10 eV). Therefore the energy of a HgTe crystal is higher, and thus CdTe is a more thermodynamically stable material. However, it is possible to 'pull' the cadmium ions out of the lattice with a ligand that binds selectively to one ion or the other. That is, the total energy of a mercury ion bound to the nanocrystal surface and to a thiolate ligand is actually less than the energy of a cadmium ion due to the weak solubility of the mercury ion and its strong binding strength toward thiolates.

The observation that the relative ligand binding strength is the dominant factor for mercury exchange is also revealed in nonpolar solutions, for which the solubilities of both divalent cadmium and mercury are essentially zero, with very little energetic drive induced by solubility product disparities. Compared to thiolate ligands, fully protonated thiol ligands bind more weakly to mercury ions and cadmium ions, as well as to the surfaces of II-VI nanocrystals. However, performing mercury exchange on CdTe in a solvent of hexane containing protonated thiols results in negligible exchange over the course of several weeks. This suggests that the binding strength of the ligand is not sufficient to overcome the thermodynamic stability of CdTe compared to HgTe without a driving force of solubility disparity. However, the use of amine ligands did favor the mercury cation exchange process. Amine ligands bind more strongly to cadmium ions than to mercury ions due to the hard base nature of the small amine ligand and softer acidity of the more polarizable mercury ions. This is the opposite of the binding trend of thiols and thiolate ligands, which are soft bases, favoring reactions with mercury over cadmium. This causes an energetic favorability of cadmium ion dissociation from the nanocrystal lattice, and a replacement with mercury.

The results herein show that it is possible to manipulate the direction of cation exchange by both solubility of the materials and ligand nature. Solubility effects are only relevant in aqueous solution, in which the solvent may strongly interact with the ions to generate a strong disparity in relative hydration. In noninteracting solvents, the effects of ligand nature dominate, allowing the possibility of replacing ions of a stable crystal structure with a less stable crystal structure merely through the relatively binding strengths of the ligands. Alivisatos and coworkers have recently shown that similar factors control silver ion exchange with CdSe nanocrystals, and cation exchange can be driven in either direction through an appropriate choice of ligand and an appropriate cation concentration.[8]

3.7 Graded Shell Growth

CdTe nanocrystals are labile toward oxidation due to the high oxidation state of tellurides (see discussion in Chapter 7.4). In addition, the fluorescence quantum efficiencies of $Cd_xHg_{1-x}Te$ alloys with very low mercury content are extremely low (<2 %), likely due to a surface defect behavior of small deposits of HgTe on the nanocrystal surface, which can trap the electron and hole in spatially segregated regions on the nanocrystal surface. Thereby, in order for these nanocrystals to be useful as near-infrared fluorescence probes for biological detection, it will be necessary to grow a wider bandgap shell on the cores. The methodology of (core)shell heterostructure growth on colloids is the subject of Chapter 4, but the results of this process are discussed here.

$Cd_xHg_{1-x}Te$ nanocrystals were capped with a graded CdTe/CdSe/CdSe shell in a solvent of oleylamine at a temperature that was slightly less than the Ostwald ripening temperature. This temperature was found to be similar to that of CdTe, which is around

150°C for 3.8 nm nanocrystals. Interestingly, between room temperature and this high temperature, there were no changes in the optical spectra of these alloy nanocrystals, suggesting an absence of atomic diffusion in the quantum dot-quantum well structures, unlike that which was observed for (CdSe)ZnSe quantum dots.[35] For shell growth, a monolayer of CdTe was first grown epitaxially on the surface to serve as a buffer layer to prevent mercury from leaching out of the quantum dot at higher temperatures used for growth of thicker shells. Without this layer, a large blue-shift was observed with capping, indicative of mercury depletion. After this thin shell of CdTe was grown, a second shell of CdSe was grown on this layer in order to reduce the lattice mismatch between the core and shell materials, and in order to increase the thermal stability of the nanocrystal so that it could be capped at higher temperatures (220°C) necessary for the deposition of sulfides such as CdS. At this elevated temperature, a highly homogeneous shell of 3 monolayers of CdS was grown on these nanostructures. The relative band alignments of the bulk materials are depicted in Figure 3.13 in order to show the graded bandgap from the core to the shell material. This grading allows a smooth transition in lattice parameter in order to prevent defect formation, and still allows the growth of a wide bandgap shell.

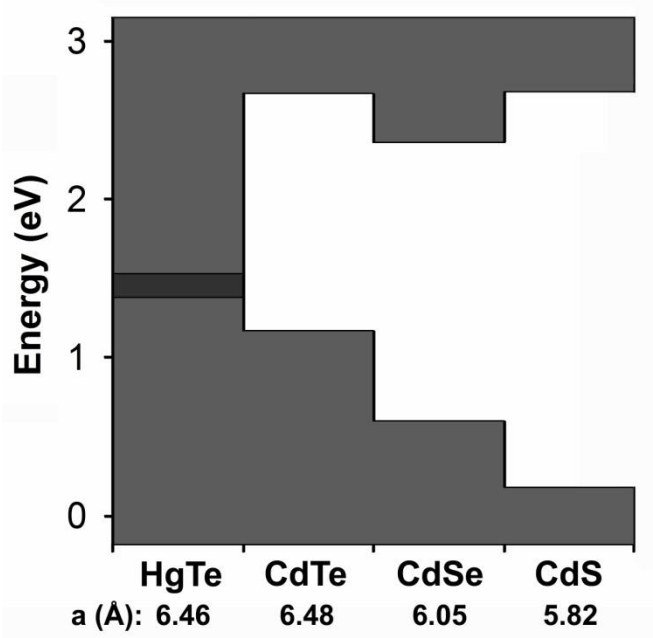

Figure 3.13: Bulk band offsets of HgTe, CdTe, CdSe, and CdS. The valence bands and conduction bands are shaded, and the lattice constants for zinc blende materials are provided beneath each material. The bands of HgTe are inverted, such that valence band edge is higher in energy than the conduction band edge, depicted as darker shading.

Figure 3.14 shows HRTEMs of capped quantum dots prepared from 3.8 nm $Cd_{0.39}Hg_{0.61}Te$ cores. Panels A and B depict $(Cd_xHg_{1-x}Te)CdTe/CdS$ quantum dots grown without a buffer layer, which appear to be much broader in size distribution compared to the $(Cd_xHg_{1-x}Te)CdTe/CdSe/CdS$ quantum dots with a buffer layer (panels C and D). However, measurements of these particles show that both nanocrystal samples had nearly the exact same size distribution (~14.5% relative standard deviation), which is essentially the same as that of the cores. The difference in morphologies of these particles is a result of the dimensionality of shell growth. With the CdSe buffer layer, the shells grew spherically, likely due to the improved capacity of the highly strained CdS shell to grow on CdSe compared to the highly lattice mismatched CdTe material. The average size of these nanocrystals was 9.21 $\pm$ 1.35 nm in diameter. Without the buffer layer, the nanocrystals preferentially grew in the

[111] zinc blende lattice direction (panels A and B) with an aspect ratio of ~1.5 (10.35 ± 1.51 nm length, 6.92 ± 1.00 nm width). These growth modes are discussed further in Chapter 4. Figure 3.15 depicts the fluorescence emission spectra of these multishell nanocrystals during shell growth, showing a very small red-shift in fluorescence induced by epitaxy (64 meV), a phenomenon consistent with a type-I band alignment (Chapter 4). Shell growth tremendously stabilized the near-infrared light emission from these nanocrystals, yielding exceptionally high quantum yields of ~80%, high photostability toward ultraviolet excitation, and a shelf life of over a year at ambient conditions under room light.

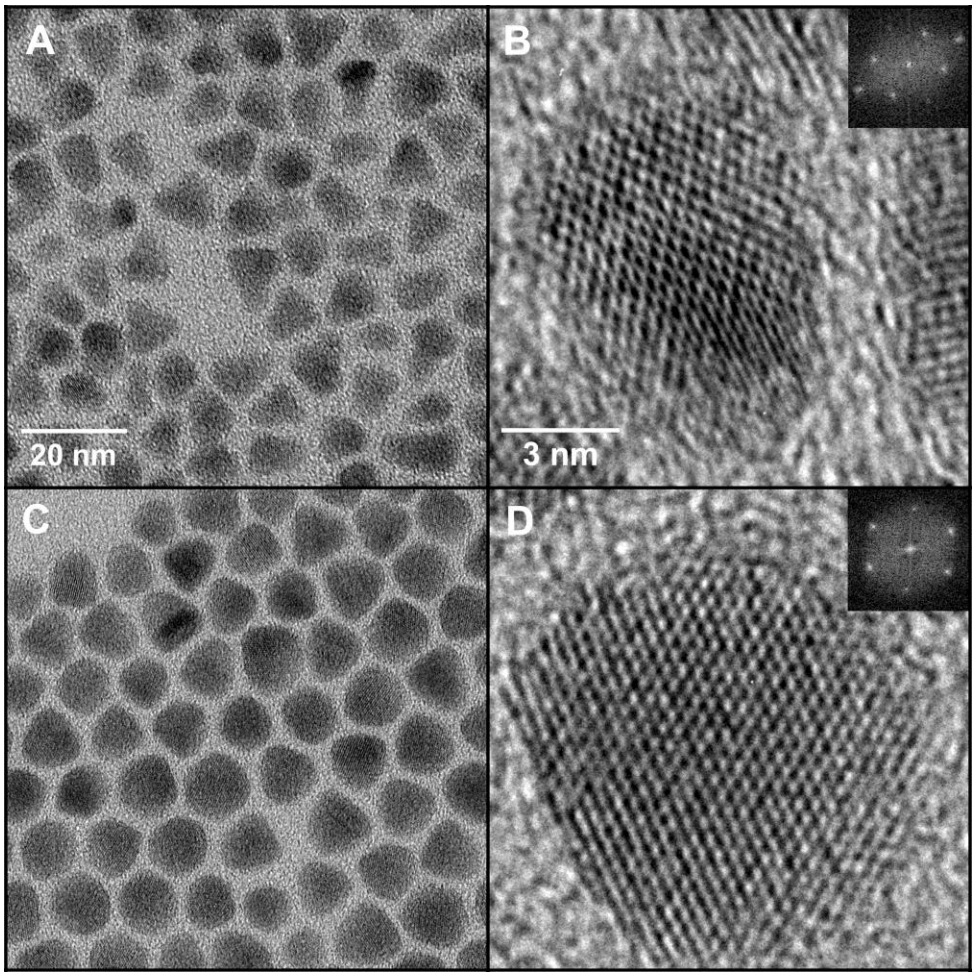

Figure 3.14: HRTEM images of ($Cd_xHg_{1-x}Te$)CdTe/CdS (A, B) and ($Cd_xHg_{1-x}Te$) CdTe/CdSe/CdS nanocrystals (C, D), showing uniform spherical growth when an interim CdSe shell was used for improved lattice matching between the core and shell materials. A large fraction of the quantum dots without the CdSe layer were oriented with their zinc blende (110) planes parallel to the TEM grid (B), suggesting preferential growth in the [111] direction. Most quantum dots with a CdSe layer showed preferential orientation with their (111) planes parallel to the TEM grid, suggesting growth axially outward from the [111] direction. Incorporation of all 5 elements into these structures was confirmed via energy dispersive X-ray (data not shown)

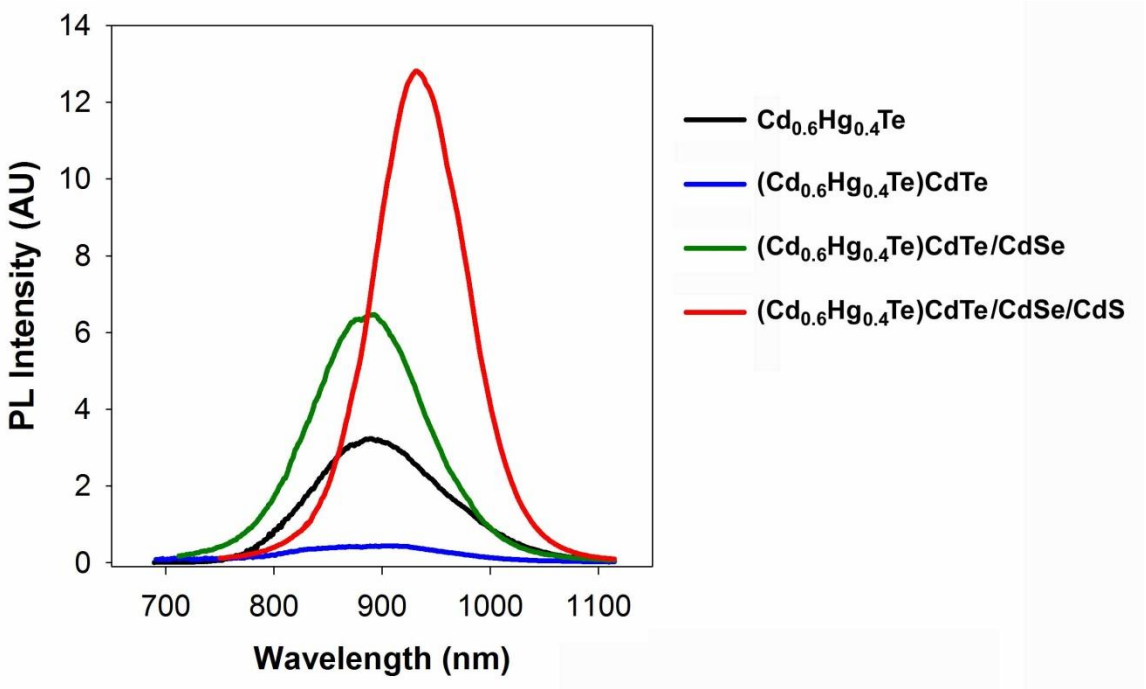

Figure 3.15: Fluorescence emission spectra of ($Cd_xHg_{1-x}Te$)CdTe/CdSe/CdS nanocrystals after various stages of capping.

3.8 Outlook

In summary, it has been shown that $Cd_xHg_{1-x}Te$ nanocrystals and other mercury alloys are efficient near-infrared fluorophores with excellent spectral properties. The development of novel processing mechanisms for cation exchange in nonpolar solution has allowed the preparation of highly uniform nanocrystals with homogeneous alloy compositions, tunable sizes, high optical purity and superior quantum yield compared to those previously prepared in aqueous solution. The fluorescence bands may be tuned

though the near-infrared with high quantum yield and relatively narrow bands, and the nanocrystal size may be tuned independently from the bandgap. In addition, the results herein provide great insight into the thermodynamics and ligand control of the cation exchange process, which is becoming a widely used technique for preparing novel types of nanomaterials. For experiments requiring highly photostable near-infrared probes, the shell growth experiments performed herein have generated highly stable, bright fluorophores with a quantum yield of 80%. Development of $Cd_xHg_{1-x}Se$ and $Cd_xHg_{1-x}S$ materials should improve these results even further and lead to new classes of stable, bright labels for near-infrared fluorescence imaging.

3.9 References

1. Bailey, R. E. & Nie, S. M. Alloyed semiconductor quantum dots: Tuning the optical properties without changing the particle size. *J. Am. Chem. Soc.* **125,** 7100-7106 (2003).

2. Zhong, X. H., Feng, Y. Y., Knoll, W., & Han, M. Y. Alloyed $Zn_xCd_{1-x}S$ nanocrystals with highly narrow luminescence spectral width. *J. Am. Chem. Soc.* **125,** 13559-13563 (2003).

3. Swafford, L. A., Weigand, L. A., Bowers, M. J., McBride, J. R., Rapaport, J. L., Watt, T. L., Dixit, S. K., Feldman, L. C., & Rosenthal, S. J. Homogeneously alloyed CdS_xSe_{1-x} nanocrystals: Synthesis, characterization, and composition/size-dependent band gap. *J. Am. Chem. Soc.* **128,** 12299-12306 (2006).

4. Aharoni, A., Mokari, T., Popov, I., & Banin, U. Synthesis of InAs/CdSe/ZnSe core/shell1/shell2 structures with bright and stable near-infrared fluorescence. *J. Am. Chem. Soc.* **128,** 257-264 (2006).

5. Kim, S., Fisher, B., Eisler, H. J., & Bawendi, M. Type-II quantum dots: CdTe/CdSe(core/shell) and CdSe/ZnTe(core/shell) heterostructures. *J. Am. Chem. Soc.* **125,** 11466-11467 (2003).

6. Zimmer, J. P., Kim, S. W., Ohnishi, S., Tanaka, E., Frangioni, J. V., & Bawendi, M. G. Size series of small indium arsenide-zinc selenide core-shell nanocrystals and their application to in vivo imaging. *J. Am. Chem. Soc.* **128,** 2526-2527 (2006).

7. Kim, S. W., Zimmer, J. P., Ohnishi, S., Tracy, J. B., Frangioni, J. V., & Bawendi, M. G. Engineering $InAs_xP_{1-x}$/InP/ZnSe III-V alloyed core/shell quantum dots for the near-infrared. *J. Am. Chem. Soc.* **127,** 10526-10532 (2005).

8. Son, D. H., Hughes, S. M., Yin, Y. D., & Alivisatos, A. P. Cation exchange reactions in ionic nanocrystals. *Science* **306,** 1009-1012 (2004).

9. Jeong, U., Xia, Y., & Yin, Y. D. Large-scale synthesis of single-crystal CdSe nanowires through a cation-exchange route. *Chem. Phys. Lett.* **416,** 246-250 (2005).

10. Wark, S. E., Hsia, C. H., & Son, D. H. Effects of ion solvation and volume change of reaction on the equilibrium and morphology in cation-exchange reaction of nanocrystals. *J. Am. Chem. Soc.* **130,** 9550-9555 (2008).

11. Zhu, W., Wang, W., & Shi, J. A reverse cation-exchange route to hollow PbSe nanospheres evolving from Se/Ag_2Se core/shell colloids. *J. Phys. Chem. B* **110,** 9785-9790 (2006).

12. Camargo, P. H. C., Lee, Y. H., Jeong, U., Zou, Z., & Xia, Y. Cation exchange: a simple and versatile route to inorganic colloidal spheres with the same size but different compositions and properties. *Langmuir* **23,** 2985-2992 (2007).

13. Dloczik, L. & Konenkamp, R. Nanostructure transfer in semiconductors by ion exchange. *Nano Lett.* **3,** 651-653 (2003).

14. Yu, W. W., Qu, L. H., Guo, W. H., & Peng, X. G. Experimental determination of the extinction coefficient of CdTe, CdSe, and CdS nanocrystals. *Chem. Mater.* **15,** 2854-2860 (2003).

15. Qu, L. H. & Peng, X. G. Control of photoluminescence properties of CdSe nanocrystals in growth. *J. Am. Chem. Soc.* **124,** 2049-2055 (2002).

16. Yu, M. W. & Peng, X. G. Formation of high-quality CdS and other II-VI semiconductor nanocrystals in noncoordinating solvents: Tunable reactivity of monomers. *Angew. Chem. Int. Ed.* **41,** 2368-2371 (2002).

17. Peng, Z. A. & Peng, X. G. Formation of high-quality CdTe, CdSe, and CdS nanocrystals using CdO as precursor. *J. Am. Chem. Soc.* **123,** 183-184 (2001).

18. Mohamed, M. B., Tonti, D., Al-Salman, A., Chemseddine, A., & Chergui, M. Synthesis of high quality zinc blende CdSe nanocrystals. *J. Phys. Chem. B* **109,** 10533-10537 (2005).

19. Hines, M. A. & Guyot-Sionnest, P. Bright UV-blue luminescent colloidal ZnSe nanocrystals. *J. Phys. Chem. B* **102,** 3655-3657 (1998).

20. Hasselbarth, A., Eychmuller, A., Eichberger, R., Giersig, M., Mews, A., & Weller, H. Chemistry and photophysics of mixed CdS/HgS colloids. *J. Phys. Chem.* **97,** 5333-5340 (1993).

21. Eychmuller, A., Mews, A., & Weller, H. A quantum dot quantum well: CdS/HgS/CdS. *Chem. Phys. Lett.* **208,** 59-62 (1993).

22. Mews, A., Eychmuller, A., Giersig, M., Schooss, D., & Weller, H. Preparation, characterization, and photophysics of the quantum-dot quantum-well system CdS/HgS/CdS. *J. Phys. Chem.* **98,** 934-941 (1994).

23. Schooss, D., Mews, A., Eychmuller, A., & Weller, H. Quantum-dot quantum-well CdS/HgS/CdS - Theory and experiment. *Phys. Rev. B* **49,** 17072-17078 (1994).

24. Harrison, M. T., Kershaw, S. V., Burt, M. G., Eychmuller, A., Weller, H., & Rogach, A. L. Wet chemical synthesis and spectroscopic study of CdHgTe nanocrystals with strong near-infrared luminescence. *Mater. Sci. Eng. B* **69,** 355-360 (2000).

25. Rogach, A. L., Harrison, M. T., Kershaw, S. V., Kornowski, A., Burt, M. G., Eychmuller, A., & Weller, H. Colloidally prepared CdHgTe and HgTe quantum dots with strong near-infrared luminescence. *Phys. Status Solidi B* **224,** 153-158 (2001).

26. Wise, F. W. Lead salt quantum dots: The limit of strong quantum confinement. *Acc. Chem. Res.* **33,** 773-780 (2000).

27. Hara, K., Machimura, H., Usui, M., Munekata, H., Kukimoto, H., & Yoshino, J. Growth and characterization of wide bandgap $Zn_{1-x}Hg_xSe$. *J. Cryst. Growth* **150,** 725-728 (1995).

28. Monterrat, E., Ulmer, L., Magnea, N., Mariette, H., Pautrat, J. L., Kheng, K., & Fuchs, F. Optical spectroscopy of CdHgTe/CdTe quantum wells and superlattices. *Semicond. Sci. Technol.* **8,** (1993).

29. Turyan, I. & Mandler, D. Electrochemical study of the Cd(II)/Cd(Hg) system in 2-mercaptoacetic acid solutions. *Electrochim. Acta* **40,** 1093-1100 (1995).

30. Aguilar, M., Alegret, S., & Casassas, E. Complex formation between Cd(II) and 2-mercaptopropionic acid in 3.0 M $NaClO_4$ at 25°C. *J. Inorg. Nucl. Chem.* **39,** 733-737 (1977).

31. Aguilar, M., Alegret, S., & Casassas, E. Solubility equilibria in the system Cd(II)-2-mercaptopropionic acid at 25°C. *J. Inorg. Nucl. Chem.* **40,** 1903-1905 (1978).

32. Matsui, H. & Ohtaki, H. A potentiometric study on complex formation of cadmium(II) ion with 2-mercaptoacetic and 2-mercaptopropionic acids. *Polyhedron* **2,** 631-633 (1983).

33. Mittal, M. L., Saxena, R. S., & Pandey, A. V. Metal complexes of 2-dimethylaminoethanethiol hydrochloride. *J. Inorg. Nucl. Chem.* **35,** 1691-1693 (1973).

34. Aldana, J., Lavelle, N., Wang, Y. J., & Peng, X. G. Size-dependent dissociation pH of thiolate ligands from cadmium chalcogenide nanocrystals. *J. Am. Chem. Soc.* **127,** 2496-2504 (2005).

35. Zhong, X. H., Han, M. Y., Dong, Z., White, T. J., & Knoll, W. Composition-tunable $Zn_xCd_{1-x}Se$ nanocrystals with high luminescence and stability. *J. Am. Chem. Soc.* **125,** 8589-8594 (2003).

CHAPTER 4

Quantum Dot Shell Growth and the Impact of Strain

Heterostructures containing domains of different material compositions have played a major role in technological advances in the past century. Improvements have been made in optoelectronics, microelectronics, and many electrical devices due to a better understanding of heterojunctions like quantum well superlattices, Shottkey barriers, and p-n junctions. However further progress has been limited by the general inflexibility of bandgap engineering and the detrimental impact of lattice strain on the quality of crystalline interfaces. These problems may be resolved in the near future with the use of nano-heterostructures, which have unprecedented bandgap control and a unique relationship with strain. Structures such as quantum confined semiconductor nanowires and nanobelts with conducting leads are the likely predecessors for the nano-architectures of future devices and electronics. Compared to these solid-state structures prepared through bulk epitaxy, colloidally prepared nanostructures have generated entirely new classes of complex heterojunctions between chemically dissimilar domains, with finely tuned bandgaps and high crystallinity. Colloidal systems also have the advantage of diffusive compatibility with biological systems for applications like nanoscopic manipulation of diseased tissue and *in situ* monitoring of biological events.

Lattice strain is a structural parameter that has been exploited in microelectronic devices with great success, but its role in colloidal nanocrystals is still poorly understood. This chapter describes the development of highly strained colloidal nanocrystals which are

lattice-mismatched heterostructures grown by epitaxial deposition of a compressive shell (ZnS, ZnSe, ZnTe, CdS, or CdSe) onto a soft and small nanocrystalline core (CdTe). This combination of a “squeezed” core and a “stretched” shell causes dramatic changes in both the conduction and valence band energies. As a result, strain can be used as a parameter for bandgap engineering in colloidal nanocrystals by modulating the spatial overlap between electrons and holes. Rationally designed (core)shell structures with specific compositions and domain sizes can result in a segregation of the electrons and holes in separate domains, yielding extended excited state lifetimes and giant spectral shifting. This attribute is most apparent in (CdTe)ZnSe nanocrystals, which exhibit narrow light emission with high quantum yield across a broad range of visible and near-infrared wavelengths (500 nm to 1050 nm).

4.1 Lattice Strain in Nanocrystals

The impact of strain on materials is fundamentally important to a broad range of fields, from optoelectronics to biomechanics. Recent studies have explored the complex relationship between nanomaterials and strain, demonstrating that nanostructures with novel properties can be generated through lattice strain,[1,2] and that nanomaterials respond differently to strain compared to their bulk counterparts.[3-5] As discussed in previous chapters, semiconductor quantum dots are typically prepared as (core)shell nanocrystals with interfacial strain. The fluorescence efficiency of these materials is believed to be detrimentally affected by the lattice mismatch between the core and shell materials,[6-9] but other effects of epitaxial strain have been largely unexplored.

4.1.1 Strain and Relaxation. Strained epitaxy is the coherent growth of a material on a substrate with a different bond length. Thermodynamically this process is unfavorable on a bulk substrate due to the contraction or expansion of the bond length that must

occur in the epitaxial layer (epilayer). This change in bond length reduces the bond strength in the epilayer, and if it is grown above a critical thickness, this energy will become large enough to induce a crystalline defect in the epilayer. Some crystalline defects, such as misfit dislocations (Figure 4.1), allow the epilayer to relax its conformation to its lowest energy bond length. Considerable effort has been made to theoretical predict and experimental determine the critical thickness for strained layers. In general, it is crucial to minimize the formation of defects, which can form luminescence-quenching traps and scatter charge carriers, which reduces current.

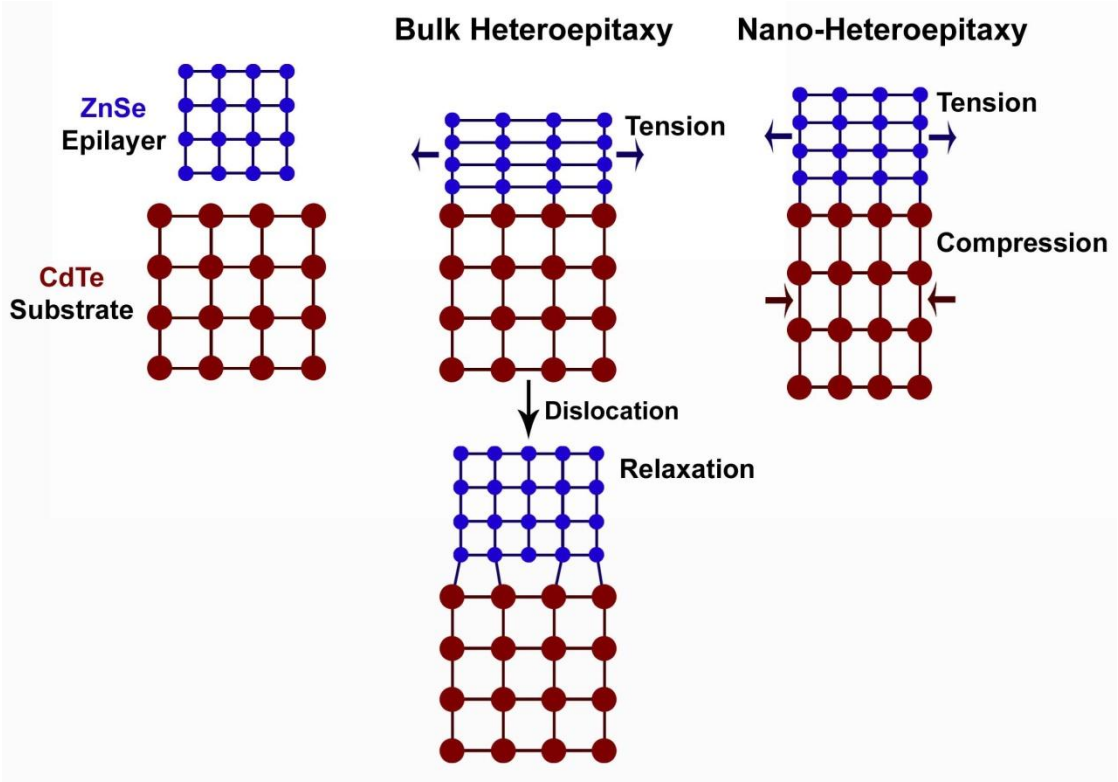

Figure 4.1: Epitaxial crystal growth on bulk substrates and on nanocrystal substrates. (A) Exaggerated crystal domains of CdTe and ZnSe have a large mismatch in lattice constant. (B) Epitaxial growth of ZnSe on a bulk CdTe substrate necessitates a warping of the ZnSe crystal structure, resulting in tensile strain parallel to the interface and compressive strain in the perpendicular direction. The formation of misfit dislocations relaxes this structure to alleviate strain in the epilayer. (C) Epitaxial growth of ZnSe on a CdTe nanocrystal deforms the core substrate, allowing sharing of the total strain. The core will be compressed by epitaxial growth and the shell will be stretched. The interfacial strain is shared over a relatively larger surface area, resulting in a higher tolerance to strain before defect formation.

Compared to bulk epitaxy, strain is expected to manifest itself uniquely in colloids because the epitaxial layer and its substrate can strain each other in a coupled interactive manner. This "double straining" effect changes the properties of both the epitaxial layer and the substrate. The experimental data and theoretical calculations herein reveal that a very high level of strain can be tolerated in small nanocrystals, compared to what is achievable in bulk materials. Small nanocrystals (<5 nm) have a high surface area-to-volume ratio and highly curved surfaces, allowing the stress from a lattice-mismatched epitaxial shell to be distributed over a large fraction of the constituent atoms. For larger nanocrystals and bulk substrates, the total number of atoms is larger, and the epitaxial stress is imposed on a surface that contains a smaller fraction of the constituent atoms, favoring the formation of strain-relaxing crystalline defects rather than homogenous strain (Figure 4.1).

4.1.2 Strain Effects on Optical and Electronic Properties of Semiconductors. In crystalline solids, a stress-induced change in the lattice parameter will alter the intrinsic inter-atomic distance, which modifies the energy levels of bonding electrons (Figure 4.2). In a crystalline semiconductor, this deformation significantly changes its electronic and optical properties such as the absorption and emission band edges.[10-12] The strain-induced change in bandgap is represented by the deformation potential, a, defined as

$$a = \frac{\partial E_{g,o}}{\partial(\ln V)} \qquad \textbf{Equation 4.1}$$

where $E_{g,o}$ is the bandgap of the unstrained semiconductor and $\partial(\ln V)$ is the fractional volume change. For zinc blende II-VI and III-V semiconductors, the electronic energy gap increases with applied compressive force, and decreases under tensile strain, an effect that has been experimentally observed and theoretically predicted.[10,13] This can be rationalized in terms of the bonding contributions to the valence and conduction band

energies (section 2.1.7). The valence band contains bonding electrons, and the unstrained bond length is a result of minimization of the average energy of these electrons. Therefore compressing the lattice or inducing tensile stretching results in an increase in energy of the valence band edge. The conduction band, however, is composed of antibonding electronic energy levels, which will be stabilized through expansion of the lattice and destabilized with lattice contraction. Thereby, the conduction band edge energy increases with compression and decreases with expansion. Importantly, the conduction band shifts to a greater extent than the valence band due to a lower density of electronic states. Together, these effects yield a negative deformation potential (a <0).

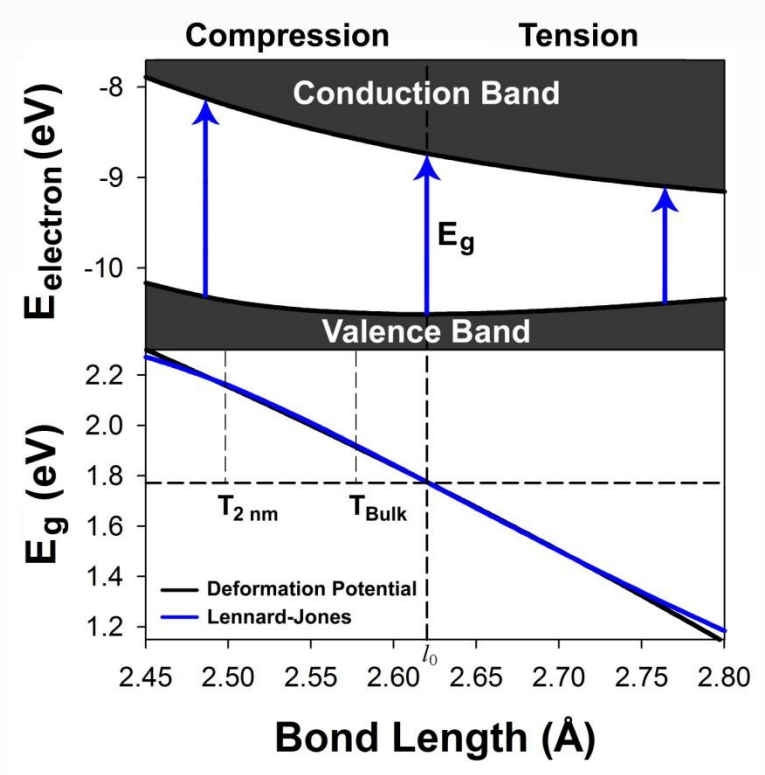

Figure 4.2: Dependence of the bandgap on strain for bulk CdSe. The top plot shows the dependence of the CdSe band structure on bond length, with the valence and conduction bands shaded, and the equilibrium bond length indicated as a dotted line (l_O = 2.62 Å). This curve is a magnified section of Figure 2.2, calculated using Lennard-Jones parameters. Compression of the crystal decreases the bond length, which increases the energy of the valence band and the conduction band, increasing the

bandgap energy. Tension increases the energy of the valence band but decreases the energy of the conduction bad, reducing the bandgap. The bottom curves graphically display this bandgap-bond length relationship, showing calculations from the Lennard-Jones parameters (blue line) and the linear deformation potential theory (black curve a = -2.9 eV). Dotted lines show the unstrained bond length and the unstrained bandgap energy (1.76 eV). The deformation potential is generally only valid for small changes in the bond length (<~5%), due to the unavoidable phase transitions that occur with compression. Bulk wurtzite CdSe transforms to the rock salt phase at a pressure of ~3 GPa (depicted as T_{Bulk}). This transition pressure increases as the dimensions of the crystal decrease on the nanometer scale (section 2.2.4), and CdSe quantum dots can have a transition pressure as high as 4.9 GPa for 2 nm nanocrystals ($T_{2\ nm}$).[14,15] The rock salt phase of CdSe has an indirect bandgap, and the deformation potential is no longer valid.

The effect of strain-induced bandgap modulation has been under intense study in optoelectronics, as materials strain is inherent in the epitaxial growth of lattice-mismatched heterostructures, leading to the development of lasers and light emitting diodes consisting of semiconductor films that are strained by their growth substrates.[16,17] By straining thin layers within the quantum confinement regime, the interplay between quantum confinement and lattice strain can yield a high level of control in bandgap engineering. This control may be broadened by replacing the quantum wells with zero-dimensional quantum dots, which are more strongly confined, and may be spontaneously deposited on a lattice-mismatched substrate in the Stranski-Krastanov growth mode.[16] These self-assembled quantum dots can be prepared with reproducible sizes and uniform patterns. However, their fabrication costs are high, and these quantum dots are island-like, rarely forming zero-dimensional spherical morphologies. In contrast, colloidal syntheses of quantum dots have demonstrated an exquisite degree of control over both size and shape, with excellent monodispersity, high quantum yields (approaching unity), and much lower costs. Because of these advantages, recent work has started to integrate these particle suspensions into solid-phase devices.[18,19]

4.2 Colloidal Synthesis Methods for Strained (Core)Shell Nanocrystals

The synthesis of colloidal (core)shell semiconductor nanocrystals is based on the high temperature coordinating solvent methods described in Chapters 2 and 3. Different sizes of CdSe and CdTe cores (1.8 – 8 nm) were prepared using techniques described in Chapter 3, and then coated with a shell according to modifications of literature methods outlined herein.[6,7,20,21]

4.2.1 Purification of Core Nanocrystals. Core nanocrystals prepared in a coordinating solvent were diluted ~1:5 in hexane and centrifuged to remove insoluble cadmium precursors. For purification, precipitations were avoided in order to prevent colloidal destabilization of CdTe nanocrystals. Instead, cores were isolated from excess surfactants and unreacted precursors through multiple rounds (at least 7) of hexane-methanol extractions. On the final extraction, the nanocrystals were concentrated to 50-300 μM with the addition of excess methanol. These hexane solutions of nanocrystals were diluted to ~30 μM, centrifuged to remove potential aggregates, bubbled with argon to remove oxygen and water, and stored at ~4°C for at least 2 days. During this time a small amount of white precipitate typically formed, which was likely unreacted cadmium oleate or a cadmium phosphonates, and was removed via centrifugation prior to shell growth. Elemental analysis of core nanocrystals prepared using the methods in Chapter 3 and purified by this method showed a nearly 1:1 ratio of Cd:chalcogen for nanocrystals larger than 3 nm, and a ~1.2:1 ratio for nanocrystals as small as 1.8 nm. After purification, the fluorescence quantum yield was generally 40-80% for CdSe and CdTe nanocrystals smaller than 6 nm.

4.2.2 Shell Growth. Hexane solutions of purified quantum dots were diluted in oleylamine to roughly half of the concentration of their original reaction solution, typically

in 10 mL reaction volumes. The reaction vessel was then attached to a Schlenk line and degassed at room temperature to remove hexane. The solution was then refluxed under vacuum (~20 Pa) at ~100°C for an additional 40-60 minutes to ensure complete removal of oxygen, water, hexane, and other low boiling point impurities. The solution was then purged three times with argon, and the temperature was increased to the initial capping temperature (T_{ML1}). This temperature was empirically optimized to be as high as possible, to maximize the reactivity of the shell precursors, but low enough to inhibit the competing process of Ostwald ripening. The onset of Ostwald ripening was determined by heating the nanocrystals in oleylamine to 100°C for 10 minutes, measuring the absorption and emission spectra of the quantum dots to look for possible signs of ripening, and then ramping the temperature in 10°C increments and repeating this process. Note that the temperatures used for CdTe are significantly lower than those typically used for shell growth on CdSe cores, mainly due to the greater ripening propensity of CdTe compared to CdSe. A summary of the important experimental parameters for (CdTe)ZnSe nanocrystals is provided in Table 4.1.

Table 4.1: Experimental Parameters for Synthesis of (CdTe)ZnSe Nanocrystals.

CdTe size	[QD]	T_{OW}	T_{ML1}	T_{ML2}	T_{ML3-4}	T_{ML5-6}	T_{ML7-9}
1.8 nm	28 μM	150ºC	140ºC	190ºC	225ºC	250ºC	n.a.
3.8 nm	6.0 μM	170ºC	150ºC	225ºC	225ºC	250ºC	260ºC
5.2 nm	4.0 μM	210ºC	190ºC	225ºC	225ºC	250ºC	n.a.
6.2 nm	3.0 μM	230ºC	225ºC	225ºC	225ºC	250ºC	n.a.

Notes: [QD] is the quantum dot concentration used for shell growth; T_{OW} is the temperature for onset of Ostwald ripening of the CdTe cores; and $T_{ML\#}$ is the growth temperature used for various shell monolayers. Growth of shells thicker than 6 ML was only performed on 3.8-nm CdTe cores.

A variety of alternative shell precursors were tested for this work. Carboxylate salts of cadmium and zinc required a much higher reaction temperature compared to their organometallic counterparts. With fatty acid salts of zinc and cadmium, the smallest CdTe cores could not be capped without suffering from significant Ostwald ripening at the high temperatures required for efficient shell deposition. However larger cores (>4 nm) could be efficiently capped with these precursors. Several chalcogenide precursors were also tested, including commonly used organosilicon compounds (e.g. hexamethyldisilathiane) and elemental chalcogens in the absence of phosphines. These reagents were generally too reactive to prevent homogeneous nucleation of shell materials. Phosphine-chalcogenides, however, were found to yield an excellent balance of resistance to nucleation and a high reactivity toward epitaxial growth.

A modified version of the successive ion layer adsorption and reaction (SILAR) procedure was used to deposit epitaxial shells, described herein for (CdTe)ZnSe structures.[21] At the initial capping temperature (T_{ML1}), a solution of cation precursor (0.1 M diethylzinc or dimethylcadmium dissolved in TOP) containing the amount required to constitute a 0.25 ML shell was slowly injected. After 10 minutes, which was experimentally determined to be a sufficient period of time to prevent homogenous nucleation of the shell material, the anion precursor (0.1 M sulfur, selenium, or tellurium, dissolved in TOP) was injected. After this second injection, shell growth was allowed to proceed for a period of time dependent on the initial growth temperature and the shell composition. For example, for the growth of ZnSe on CdTe, the following reaction times were used: 4 hours for 150ºC, 2 hour for 170ºC, and 30 minutes for 210-225ºC. For other shell materials, however, it was found that the shell growth rate was strongly dependent on the reactivity of the precursors. Both diethylzinc and dimethylcadmium were highly reactive at all of the temperatures used in this work, as these reactions were

limited by the deposition rate of the chalcogen. Generally, tellurium and selenium reacted efficiently at low temperatures (e.g. 2 hours reaction time at 170°C), but initial growth of CdS and ZnS required extended times, up to 8 hours before completion on 1.8 nm cores at 140ºC. After the first two injections at T_{ML1}, a second pair of injections was performed to grow 1 ML of total shell on the cores, using the same reaction time for the first 0.5 ML.

Once this thin layer of shell material was deposited on the nanocrystals, indicated by spectral red-shifting, the temperature threshold of these nanocrystals toward ripening was significantly enhanced. This is due to a combination of the increase in overall size of the nanocrystals, the greater bond strength and thermal stability of the shell materials used in this study (CdS, CdSe, ZnSe, ZnS, ZnTe) compared to the cores (CdTe), as well as the greater strength of bonding of the amine and phosphine ligands to the shell material, compared to CdTe. Thereby, after the deposition of just 1 monolayer, the temperature of the reaction could be increased drastically without optical signs of ripening. In this manner, the growth temperature was increased to a point at which the reaction was much more efficient, and shorter reaction times could be used to complete shell growth. The deposition of ZnSe on CdTe was optimized for all of the sizes tested, however the deposition of the other shell materials (ZnS, ZnTe, CdS, CdSe) was only optimized for 3.8 nm quantum dot cores, although the extrapolation of this technique to other core sizes should like be straightforward by employing the methodology described herein. For this procedure, 0.25 monolayer increments were used so that the surface stoichiometry of anions and cations would be similar for each 0.5 ML shell growth cycle. When performed with 0.5 ML increments, like the SILAR procedure originally described by Peng and coworkers, there was a significant decrease in quantum yield after each

anion injection, thus obscuring the relative changes in fluorescence emission efficiency, which is in accord with previous findings.[21,22]

4.2.3 Shell Thickness Calculations. To calculate the amount of shell precursors required to constitute a precise number of monolayers, an approach was employed that is similar to epitaxial overgrowth of thin films on bulk substrates. Specifically, with the deposition of a thin epilayer on a nanocrystal core, it is assumed that the material deposits layer-by-layer as a coherent, epitaxial structure. Thereby, the core serves as a 'substrate' to which the shell material must conform in order to undergo heteroepitaxial growth. This rationale is strongly supported by the data provided herein, showing that the overgrowth of a thin shell (1-2 ML) of lattice-mismatched material (e.g. ZnSe) only marginally alters the crystalline lattice of the core material. Instead, the shell material adopts the lattice constant of the core material during initial growth, and extensive deformation of the core only occurs once a shell of substantial thickness is deposited. Therefore, the calculation of the epilayer material quantity can be considered from the perspective of homoepitaxial growth of CdTe on a CdTe substrate, using the bulk density of CdTe and a judiciously chosen monolayer thickness. In this way, the molar quantity of precursors added to grow a specific number of shell monolayers should be the same for all types of materials grown as epitaxial shells, theoretically differing only in the event of defect formation, and the concomitant relaxation of the heterostructure. From this perspective of heteroepitaxy, it is evident that one cannot accurately predict the size of a (core)shell nanocrystal with a predetermined number of monolayers of shell growth unless the strain within both the core and the shell materials are taken into consideration. Initially, the shell material will adopt the lattice constants of the core material, and thus appear larger than expected, if one presumes that the shell material will adopt its bulk lattice constants. This effect will eventually wane as the compressive

shell reaches a thickness large enough to compress the core. It should be noted that the 'ideal' calculation method for the deposition of a shell would to be to determine the exact number of unpassivated orbitals on the surface atoms on the quantum dot, and to add this specific number of elemental precursors to constitute 1.0 monolayer of shell (or 0.5 monolayers if the surface facets are polar), and then repeat the process for the next monolayer. However, exact determination of these values is not yet feasible, although theoretically calculated values strongly correlate with the approach used herein.

The volume of shell material comprising m monolayers can be calculated as:

$$V_{shell} = \frac{4}{3}\pi\left[(r_c + m \times d_{ML})^3 - r_c^3\right] \qquad \textbf{Equation 4.2}$$

where V_{shell} is the volume of shell material per quantum dot, r_c is the radius of the quantum dot core (assuming a spherical geometry), and d_{ML} is the thickness of one monolayer of shell. Here we use d_{ML} = 0.324 nm, the (200) interplanar spacing for zinc blende CdTe. This value was selected based on the preferential growth of the shells outward from the [111] axis. Note that the choice of other interplanar distances, such as the (220) separation distance, could also be justified, although the application of the SILAR growth mechanism is theoretically incompatible with nonpolar facets. The amount of shell material to add can then be calculated using the following formula:

$$n_{shell} = \frac{V_{shell} \times D_{core} \times N_A \times n_{QD}}{MW_{core}} \qquad \textbf{Equation 4.3}$$

where n_{shell} is the number of moles of each precursor required to deposit m monolayers of shell material, D_{core} is the density of the core material (D_{CdTe} = 5.85 g cm^{-3}), N_A is Avogadro's number, n_{QD} is the number of moles of quantum dots in solution, and MW_{core} is the molecular weight of the core material. The molar quantities of precursors added for different shell thicknesses on a 3.8 nm core are summarized in Table 4.2 in Section 4.4.1.

4.3 Optical Properties of Strained (Core)Shell Quantum Dots

The optical properties of (core)shell semiconductor nanocrystals are currently a subject of intense study from both theoretical and experimental perspectives. Overgrowth of a coherent epitaxial shell of a material on a quantum dot core of different composition leads to an expansion of the lattice domain size, a red-shift in optical spectra, and a non-linear modulation of fluorescence quantum yield with shell growth. The nature of this behavior is currently poorly understood, and is the subject of this section.

4.3.1. Type-I and Type-II Quantum Dots. The original justification for heteroepitaxial shell growth on semiconductor quantum dots was for electronic insulation,[6,23-26] serving a similar purpose as cladding layers on waveguides and barrier layers in quantum well structures. Using this logic, it was reasoned that if a wider bandgap material is grown on a core quantum dot, like (CdSe)ZnS heterostructures, the resulting electronic insulation would protect the charge carriers from quenching defects on the nanocrystal surface. This concept was successfully demonstrated by several groups, resulting in hugely enhanced fluorescence from quantum dots, even reaching near-unity quantum yield at room temperature.[6,8,24,27,28] In such a quantum dot, both the electron and hole are confined to the core, yet small red-shifts (~5-10 nm) in the absorption and fluorescence band edges are observed with shell growth. This was explained through the finite potential well of the shell material, which allows a small degree of charge carrier tunneling into the shell, effectively increasing the size of the exciton and reducing the quantum confinement.

In 2003 Bawendi and coworkers demonstrated that the electron and hole could be segregated in either the core or shell regions, depending on the band alignments of the core and shell materials, such as for (CdTe)CdSe quantum dots.[29] The staggered band

offsets of these structures only insulated one of the charge carriers in the core, sequestering the other charge carrier in the shell material. Thereby, the confinement dimensionality of such a structure is mixed, as one of the charge carriers is confined to the core in zero dimensions (a quantum dot), and the other is confined to the shell as a two-dimensional structure (a quantum well). These materials can have longer wavelengths of emission than either of the constituent materials of the heterostructure by allowing the bandgap to close at the interface (Figure 4.3). In comparison with type-I materials that confine both charge carriers to the core, these type-II quantum dots demonstrate large spectral shifting with shell growth, a loss of discrete band-edge electronic transitions, and an increase in excited state lifetime due to a decrease in the overlap integral between the electron and hole wavefunctions. It is also interesting to note that several groups have studied 'quasi-type-II' structures, in which one of the charge carriers is strongly confined to one region of the structure and the other one is significantly delocalized over the entire heterostructure. These materials have optical properties intermediate between those of type-I and type-II structures.

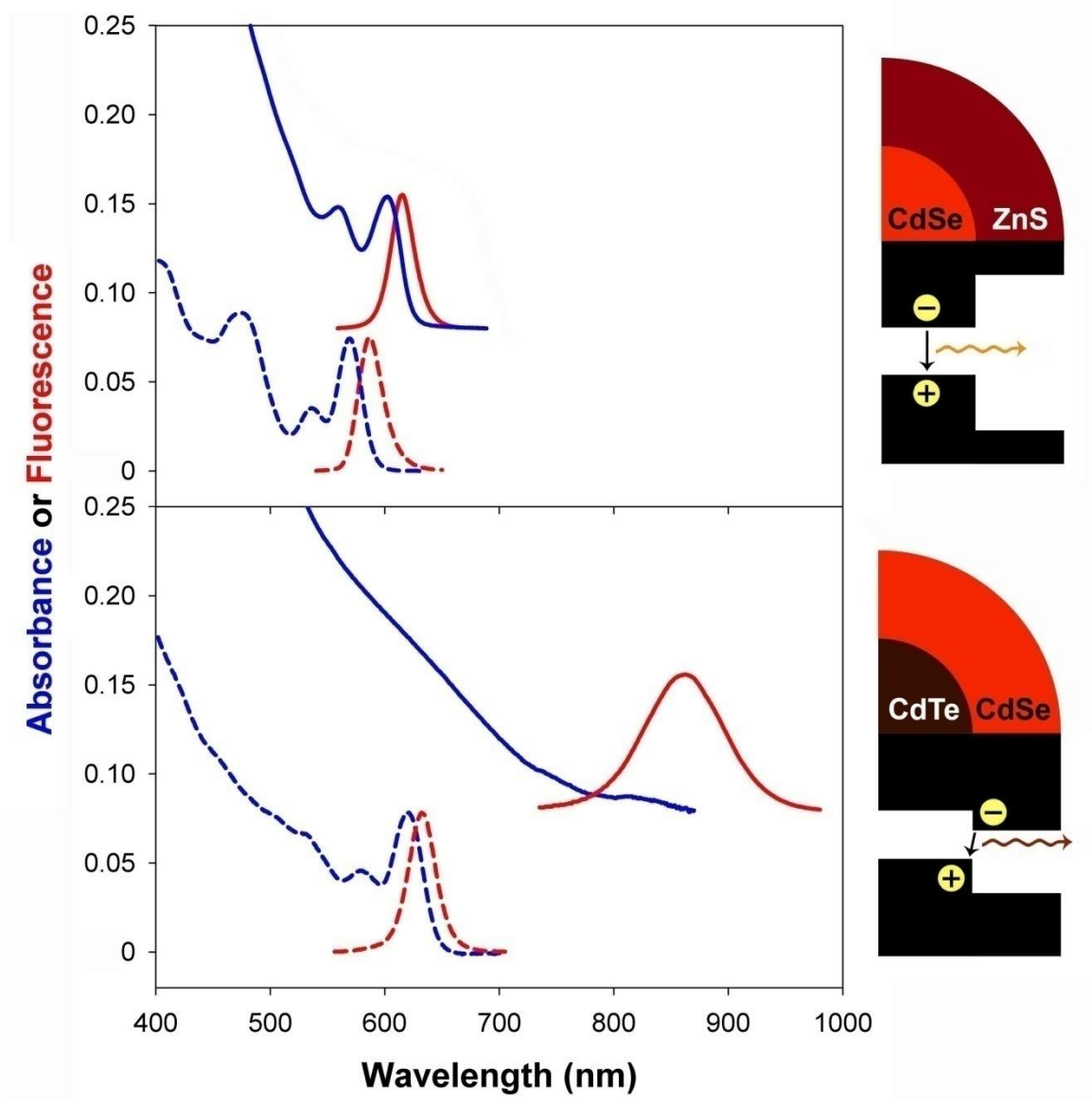

Figure 4.3: Optical properties of type-I and type-II (core)shell quantum dots. Absorption spectra (blue) and fluorescence spectra (red) are shown for cores (dotted lines) and (core)shell structures (solid lines), along with energy band diagrams (right). In type-I quantum dots such as (CdSe)ZnS (top), the core material valence band is higher in energy than the shell and the conduction band energy is lower in energy, confining both of the charge carriers to the core. Thereby, shell overgrowth only marginally changes the bandgap, and the absorption and fluorescence spectra are similar to those of the core, but with an enhanced stability and fluorescence efficiency. In type-II quantum dots such as (CdTe)CdSe (bottom), the energy bands are staggered such that the charge carriers are spatially segregated, allowing only indirect band-edge transitions. Shell overgrowth decreases the bandgap, allowing electronic transitions at lower energy, thus red-shifting the absorption and fluorescence spectra. Discrete transitions are attenuated from the absorption spectra and the band edge oscillator strength diminishes.

4.3.2 Optical Mechanisms in Strain-Tunable (CdTe)ZnSe Quantum Dots. As illustrated in Figure 4.4, lattice strain can induce significant bandgap energy changes when a shell material is coherently grown on a small and compressible nanocrystalline core. In the bulk state, heterostructures of CdTe and ZnSe have valence and conduction bands that are aligned to localize both the electrons and holes in CdTe (type-I behavior). On the nanometer scale, however, epitaxial growth of a ZnSe shell strongly compresses a CdTe nanocrystal because the lattice parameter of ZnSe (5.668 Å) is considerably smaller than that of CdTe (6.482 Å). Because the deformation potential of these semiconductors is negative and the conduction band shifts to a much larger degree than the valence band,[30] compression of CdTe (a_{CdTe} = -3.70 eV) induced by shell growth increases the energy of the conduction band. At the same time, the shell material (a_{ZnSe} = -4.99 eV) is under tensile strain, resulting in a decrease of its conduction band energy. These two strain effects work in a concerted fashion (double straining) to alter the energy band offsets, converting standard type-I quantum dots into type-II heterostructures, resulting in a spatial separation of the electrons and holes. As the shell grows in thickness, the core conduction band energy rises due to increased compressive strain from the shell, while the shell's conduction band energy decreases due to a reduction in quantum confinement.

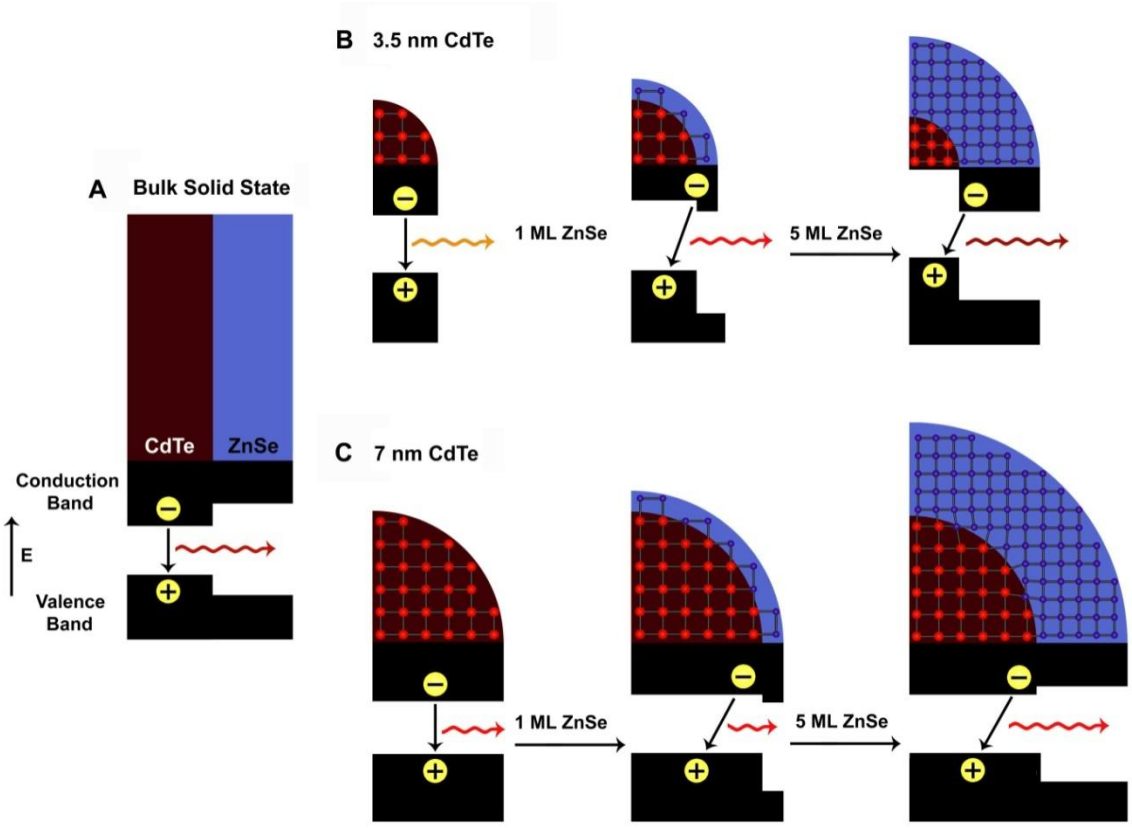

Figure 4.4: Mechanism of strain-tuning of the optical properties of (CdTe)ZnSe heterostructures. (A) As a bulk heterostructure, the interface between CdTe and ZnSe yields a type-I band alignment, with the conduction band energy minimum and valence band energy maximum both located in the CdTe domain. The bulk bandgap is 1.50 eV for CdTe and 2.82 eV for ZnSe. (B) The charge carriers in a small CdTe quantum dot (3.5 nm) are quantum-confined, thus increasing the bandgap energy (~2.0 eV). With overgrowth of a thin shell of ZnSe (1 monolayer, ML), the core is slightly compressed due to the smaller lattice parameter of ZnSe (5.668 Å) compared to CdTe (6.482 Å), increasing the energy of the CdTe conduction band. The shell material is under large tensile strain due to coherent growth on the CdTe substrate, resulting in a significant reduction of the conduction band in the shell. Because of these simultaneous shifts of the core and shell, there is only a very small difference in energy between the conduction bands of the core and shell, causing the electron wavefunctions to spread across the entire nanocrystal. Quantum confinement and strain have a smaller impact on the valence bands, and the hole remains in the core, leading to a quasi-type-II structure, in which the hole is strongly confined, but the electron is delocalized over the entire quantum dot. Overgrowth of a larger shell (5 ML) further increases the core conduction band energy and decreases the conduction band energy in the shell. Thus the band offsets become staggered, shifting the electron almost entirely into the shell material, resulting in a type-II alignment. (C) With a larger CdTe core (7 nm), the quantum confinement effect is reduced, decreasing the bandgap (~1.7 eV). Overgrowth of a thin shell of ZnSe strongly strains the shell, with little effect on the core due to the large core domain size compared to the shell. The electron is weakly delocalized over the entire nanocrystal, again yielding a quasi-type-II band structure. However, growth of a larger shell (5 ML) exceeds the critical thickness, and can only be accommodated by

the formation of defects that relax the strain between the two materials. Therefore the core and shell materials are under little strain, returning their band offsets close to their bulk values.

4.3.3 Absorption and Fluorescence in Highly Strained (CdTe)ZnSe. With increasing epitaxial shell growth of ZnSe on CdTe, the optical absorption and fluorescence emission spectra are dramatically shifted toward longer wavelengths (lower energies) (Figure 4.5), beyond the band-edge energy of bulk CdTe (1.50 eV) and ZnSe (2.82 eV). Several lines of evidence suggest that this red shift is due to a transformation to type-II band alignment: (i) a gradual reduction of distinct optical absorption features; (ii) a decrease in the band-edge oscillator strength, and (iii) a significant increase in excited state lifetimes (Figure 4.6). These changes are caused by spatial separation of holes into the core and electrons into the shell, resulting in a decrease in the electron-hole overlap integral.

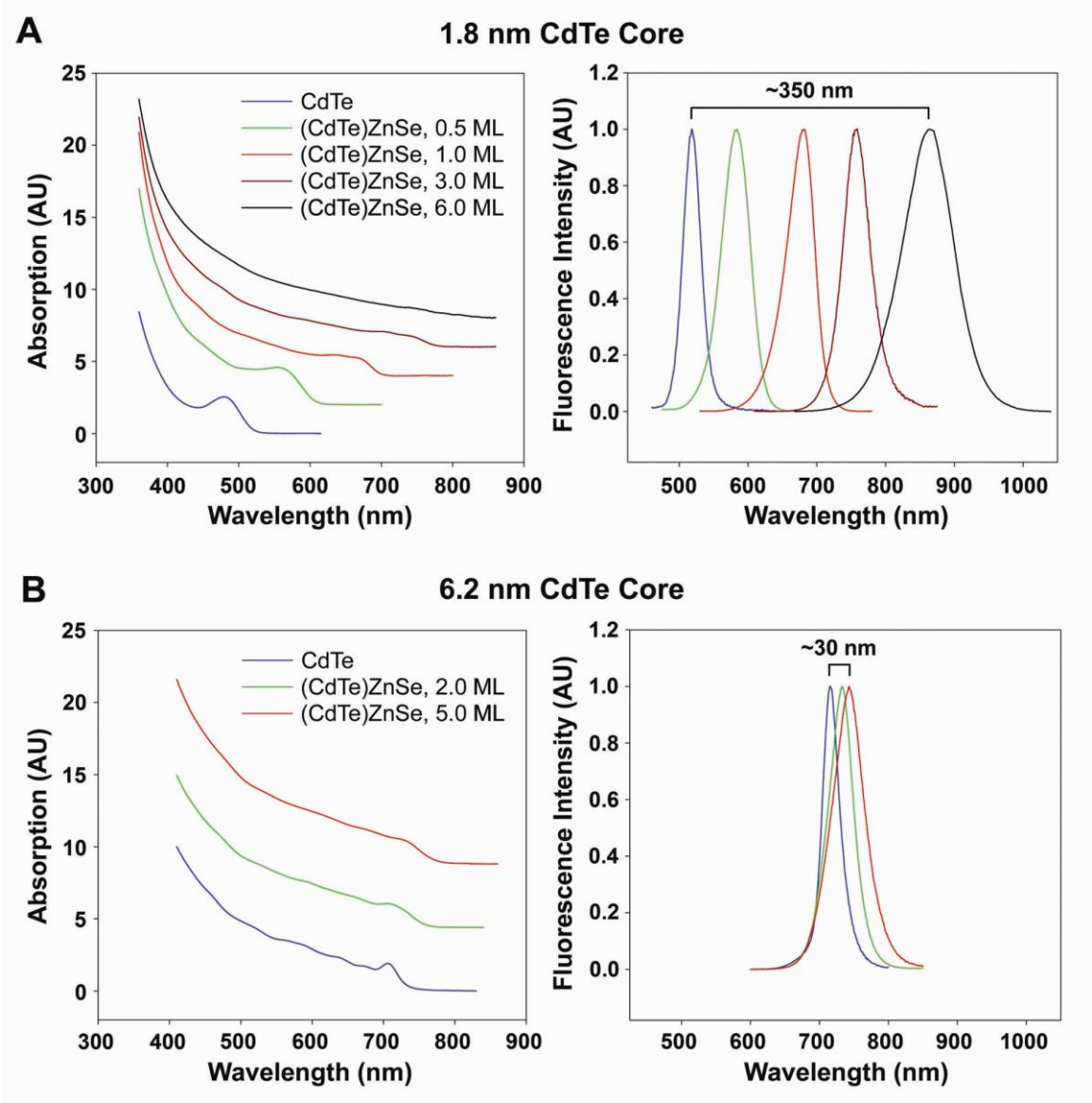

Figure 4.5: Optical spectra of strain-tunable (CdTe)ZnSe nanocrystals. Absorption (left) and fluorescence emission (right) spectra of (core)shell nanocrystals with (A) 1.8 nm CdTe cores and (B) 6.2 nm cores, capped with different thicknesses of ZnSe. The bandgap shift is strikingly more pronounced for smaller nanocrystals.

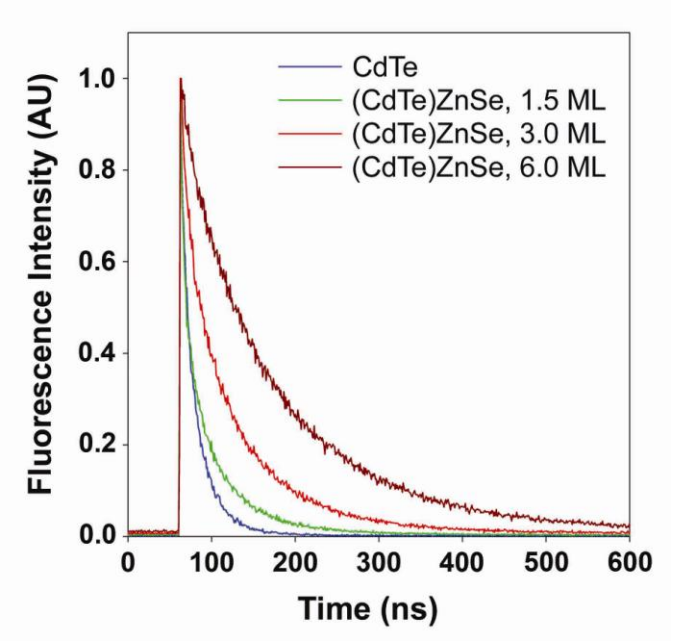

Figure 4.6: Time-resolved fluorescence decay curves of 3.8 nm CdTe cores capped with ZnSe shells of different thicknesses. The excited state lifetimes were calculated to be 18.4 (core), 35.5 (1.5 ML), 59.8 (3.0 ML), and 115.0 ns (6.0 ML).

The largest spectral shifts are observed with *very small* cores, such as 1.8 nm CdTe, allowing tuning from the green to the near-infrared spectra. In contrast, larger CdTe cores cannot be effectively compressed through epitaxy, and their emission spectra are much less tunable by lattice strain. The strain-tunable spectral ranges are shown in Figure 4.7 for different sized CdTe cores. It is remarkable that quantum dots with small cores can be tuned to emit beyond the spectral ranges of large dots, at both the blue and red sides of the emission spectra. This novel phenomenon has not been observed for other types of quantum dots and cannot be explained by conventional factors (see section 4.6). Depending on the core size and shell thickness, these quantum dots can be tuned to emit between 500 nm and 1050 nm with a quantum efficiency between 25-60%. The fluorescence peak width is consistently between 40 and 90 nm (full-width-at-half-maximum or FWHM) in the near infrared (700 – 900 nm).

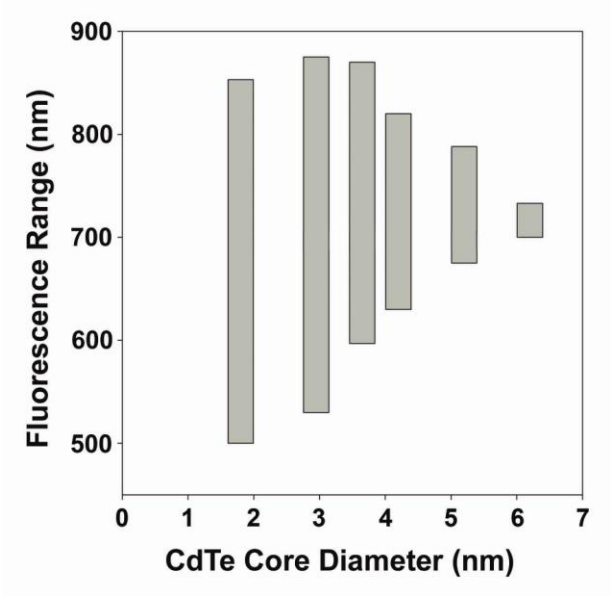

Figure 4.7: Strain-tunable spectral ranges for different CdTe core sizes. Ranges were measured by the fluorescence emission peaks with 0-5 monolayers of shell growth.

An interesting finding is that the strain-induced spectral changes are gradual and do not exhibit an abrupt transformation as might be expected for a switch from type-I to type-II. For core sizes less than 4 nm diameter, data indicate that the transition to type-II behavior is “complete” after capping with 2-3 monolayers (ML) of shell material, as defined by the complete disappearance of the first exciton absorption peak. Between 0 and 2-3 ML, however, the behavior of these nanocrystals is ‘quasi-type-II,’ with the hole confined to the core and the electron only weakly confined, being largely delocalized across the entire nanocrystal.[31]

4.3.4 Multilayered Structures. To further understand the separation of electrons and holes in these strained nanostructures, systematic capping experiments were performed in which interim shell layers provide specific energy barriers to either the hole or the

electron (Figure 4.8). Capping CdTe with a CdSe shell is known to generate type-II quantum dots with the electron located in the shell, due to the lower conduction band energy level of CdSe compared to CdTe. In contrast, capping CdTe with a ZnTe shell or an interim layer of ZnTe provides a large barrier to electron diffusion out of the nanocrystal core, but little impediment to hole diffusion out of the core. As expected, capping CdTe with CdSe yields a type-II quantum dot with a substantial decrease of the band gap, whereas ZnTe capping only slightly changes the band gap. By using one monolayer of these materials as a barrier to hole or electron diffusion, overgrowth of ZnSe leads to a type-II structure only when grown with the CdSe interim layer. Very little red-shift is observed for quantum dots with an interim layer of ZnTe, confirming that electron diffusion into the shell is essential for the strain-induced type-II structure to function. Hole confinement to the core is also supported by the high quantum efficiency of these (core)shell quantum dot, as surface hole traps are more detrimental to the optical properties of quantum dots than are electron traps.[29,32-34]

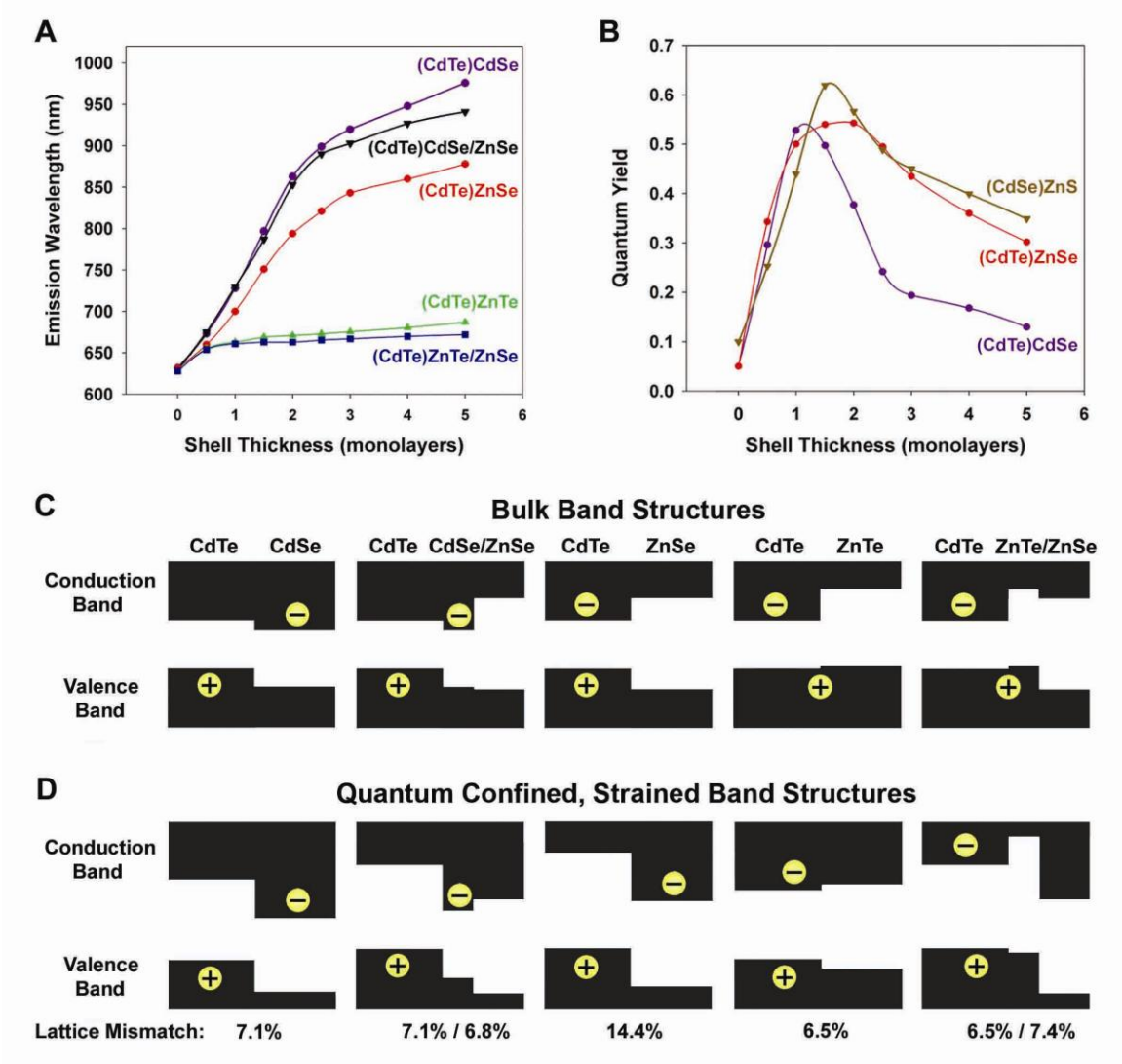

Figure 4.8: Comparison of emission wavelengths and quantum yields for different (core)shell and multilayered structures. (A) Emission wavelengths of 3.8 nm CdTe cores capped with CdSe (purple), ZnSe (red), or ZnTe (green), or one monolayer of CdSe followed by ZnSe (CdSe/ZnSe; black), or one monolayer of ZnTe followed by ZnSe (ZnTe/ZnSe; blue). (B) Quantum yields of 3.8 nm CdTe cores capped with ZnSe (red), or CdSe (purple), or 3.8 nm CdSe cores capped with ZnS (brown). (C) Diagrams of bulk band offsets for (core)shell materials in (A). (D) Diagrams of band structures of quantum confined, strained nanocrystals calculated using model-solid theory and a continuum elasticity model for the impact of strain (see Section 4.5). The bandgaps have been shifted down in energy relative to the bulk values for clarity.

4.3.5 Quantum Efficiency and Strain. It is remarkable that the highly strained (CdTe)ZnSe heterostructures (14.4% lattice mismatch) are able to maintain excellent

photoluminescence properties. We attribute the high quantum yield to the high crystallinity of the initial CdTe cores (quantum yield up to 80%), and the homogeneity of shell growth at high temperatures (shell growth was incomplete and nonuniform below 200°C). Also, the lattice compressibility is considerably higher for CdTe (bulk modulus B_u = 42.4 GPa) and ZnSe (B_u = 62.4 GPa) as compared to the commonly used quantum dot materials of CdSe (B_u = 53.1 GPa) and ZnS (B_u = 77.1 GPa).[35] Thus, the ability of CdTe and ZnSe to elastically compress when subject to a large stress, rather than relaxing to form defect trap sites, allows these quantum dots to maintain a high quantum yield after 2 ML of shell growth (Figure 4.8B), unlike similarly strained (CdSe)ZnS QDs (12% lattice mismatch), which reach a peak in quantum yield after roughly 1.5 ML of shell growth. This difference is likely due to the inability of the less elastic CdSe and ZnS to withstand strain without forming defects. Using the softer CdTe core, CdS and ZnS shells (11.4% and 19.8% lattice mismatches, respectively) could be successfully grown with high quantum yields maintained even after 3 ML of shell growth (Figures 4.9 and 4.10).

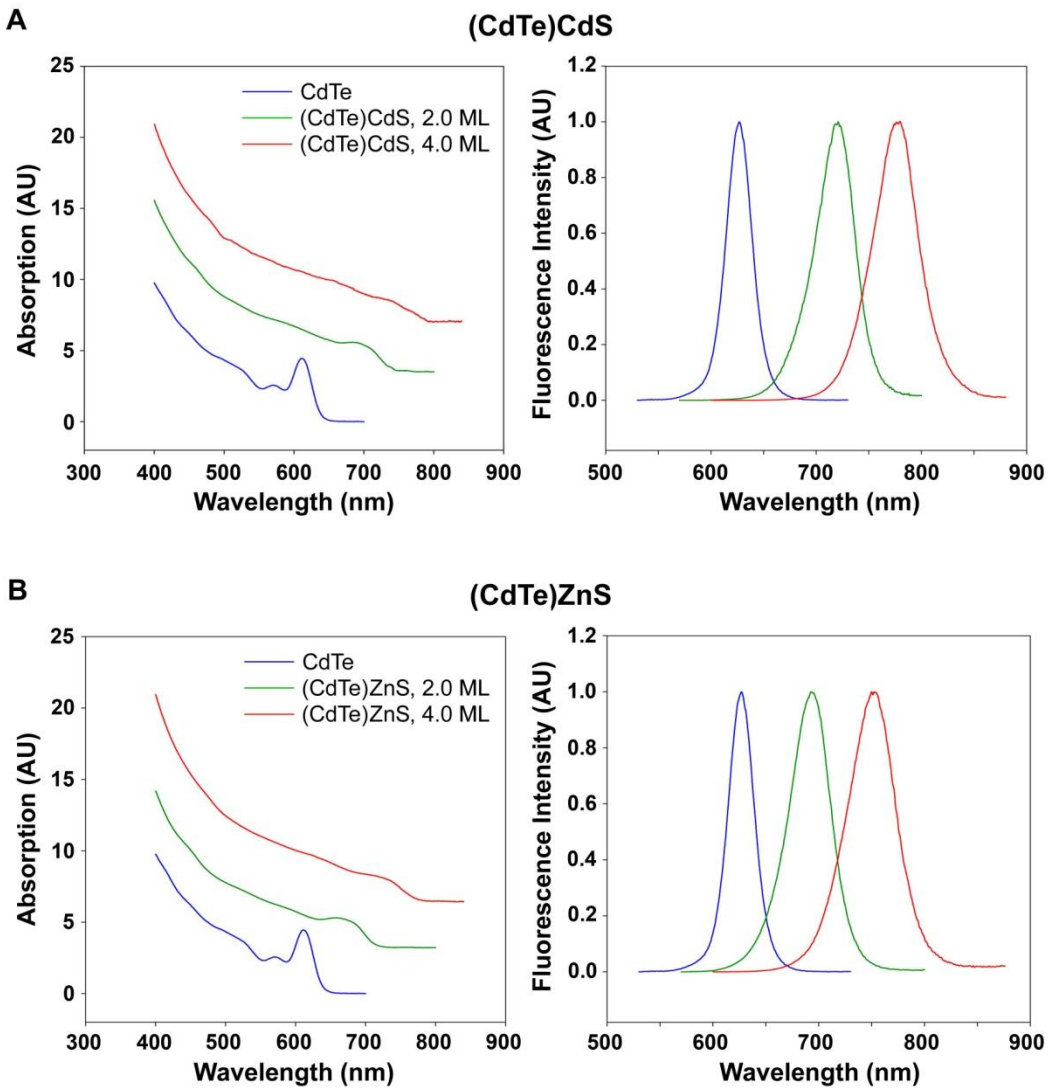

Figure 4.9: Optical characteristics of (A) (CdTe)CdS and (B) (CdTe)ZnS quantum dots. Absorption and emission spectra are shown for (core)shell nanocrystals with 0, 2, or 4 monolayers of shell.

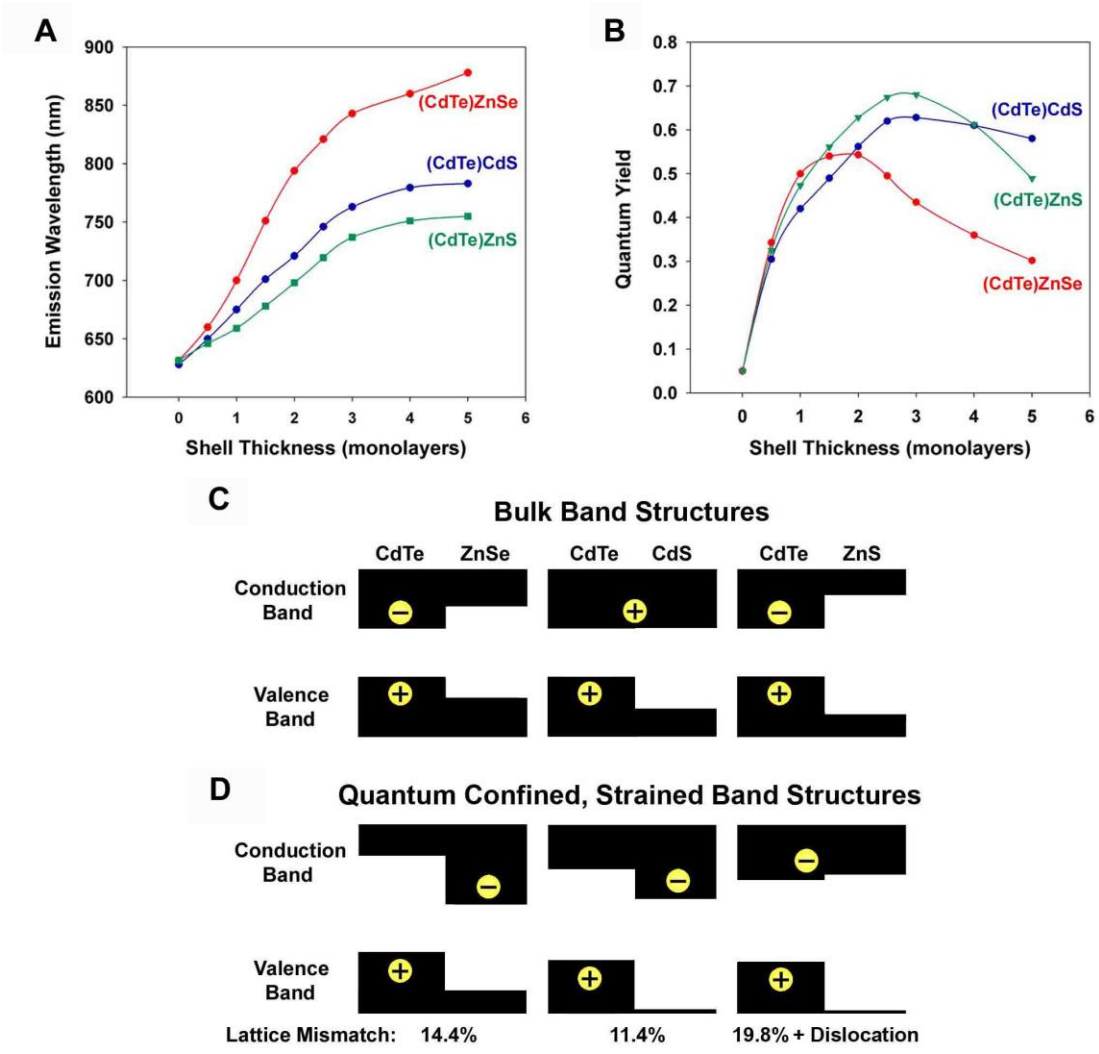

Figure 4.10: Comparison of optical tunability and fluorescence quantum yields for CdTe cores coated with different shell materials and thicknesses. (A) Emission wavelengths of 3.8 nm CdTe cores capped with ZnSe (red), CdS (blue), or ZnS (green). (B) Fluorescence quantum yields of the same nanocrystals. Data for ZnSe shells are replotted from Figure 4.8. (C) Diagrams of bulk band offsets for (core)shell nanocrystals in (A) and (B). (D) Diagrams of band offsets for (core)shell nanocrystals, accounting for the impacts of quantum confinement and strain, calculated by using model-solid theory and a continuum elasticity model. In this model, it was found that the (CdTe)ZnS (core)shell quantum dots are not coherent beyond ~3 monolayers of shell growth, and therefore a single dislocation loop and its associated strain relaxation were included in the band structure calculation.

The concept of strain-induced defect formation has been the predominant paradigm for understanding the photoluminescence efficiency of (core)shell quantum dots,[6] but this

concept does not account for the low quantum efficiencies of type-II quantum dots.[29] Alfred Mews and coworkers reported that type-II (ZnTe)CdSe quantum dots have a quantum yield of 15-20%, which decreases after growth of 1.5 ML, despite a lattice mismatch of only 0.6%.[36] In the work reported herein, Figure 4.8 shows that type-II (CdTe)CdSe QDs (7.1% lattice mismatch) reach a peak in fluorescence efficiency after only 1 ML of shell growth, whereas highly strained (CdTe)ZnS quantum dots (~20% lattice mismatch) reach a peak fluorescence efficiency after 2.5-3 ML of shell growth (Figure 4.10). The separation of charge carriers in type-II quantum dots can result in a decreased probability of radiative recombination, and the extended excited state lifetimes may increase the probability of nonradiative recombination events. In addition, one of the charge carriers in type-II quantum dots is confined to the shell region, and this carrier thus has an increased probability of being trapped in a surface defect site, a major factor governing the photoluminescence efficiency of quantum dots.

4.4 Structural Characterization of Strained Heterostructures

4.4.1 Size Determination via Electron Microscopy. Transmission electron microscopy (TEM) of (CdTe)ZnSe quantum dots indicate that shell growth is coherent and homogeneous, despite a large difference in lattice constants. Figure 4.11 shows TEM images of these quantum dots at various points throughout the shell growth process. The CdTe core nanocrystals are slightly elongated prolate spheroids, with an aspect ratio of ~1.4, whereas all of the (core)shell structures up to 9 monolayers are quasi-spherical. There is no indication of independent nucleation of shell materials, and a high monodispersity is observed for up to 6 monolayers of growth (Figure 4.12), after which the polydispersity significantly increases (>15% relative standard deviation in diameter). Table 4.2 compares the measured diameters of the nanocrystals with the 'ideal'

diameters calculated from the amount of shell precursors added during shell growth. Theoretical sizes are calculated for pseudomorphic growth on spheres or as concentric cylinders around a cylindrical core, with and without strain. The empirically measured sizes match a shell growth mode between spherical and cylindrical geometries, a finding that is also supported by high resolution transmission electron microscopy and X-ray diffraction (see below).

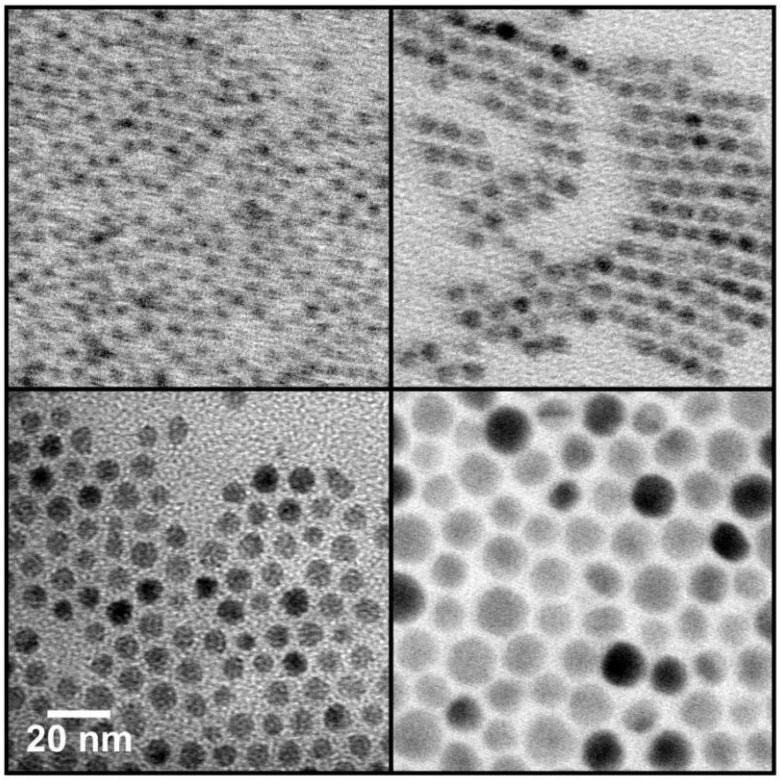

Figure 4.11: Transmission electron micrographs of (CdTe)ZnSe quantum dots with various shell thicknesses. 3.8 nm CdTe quantum dots (top left) are shown in addition to (CdTe)ZnSe quantum dots with 2 (top right), 6 (bottom left), or 9 (bottom right) monolayers of shell. Optical spectra of these nanocrystals are displayed in Figure 4.13.

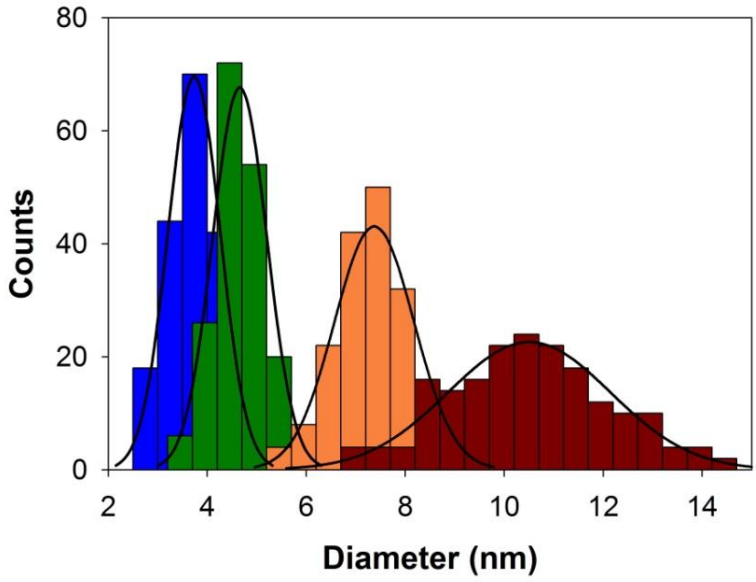

Figure 4.12: Size distributions for (CdTe)ZnSe quantum dots depicted in TEMs in Figure 4.11. Average sizes are 3.75 ± 0.53 nm for CdTe cores (blue), 4.66 ± 0.55 nm for 2 ML shell (green), 7.37 ± 0.81 nm for 6 ML shell (orange), and 10.51 ± 1.64 nm for 9 ML shell (red). For each sample, ~180 particles were measured, and reported as mean diameter ± standard deviation.

Table 4.2: Summary of Shell Thickness Data

Shell thickness	n_{ZnSe} / n_{QD}	d_{obs} (nm)	$d_{T\text{-}S}$ (nm) relaxed	$d_{T\text{-}S}$ (nm) strained	$d_{T\text{-}C}$ (nm) relaxed	$d_{T\text{-}C}$ (nm) strained
0 (core)	n.a.	3.75	n.a.	n.a.	n.a.	n.a.
2 ML	595	4.66	4.74	5.04	4.22	4.60
6 ML	3071	7.37	6.85	7.31	7.08	7.79
9 ML	6446	10.51	8.50	9.20	9.71	10.91

Notes: Shell growth of ZnSe on ~3.8 nm CdTe cores was performed as described in Section 4.2. The molar amount of each ion precursor added is tabulate as the number of moles of ZnSe per mole of nanocrystal (n_{ZnSe} / n_{QD}). The resulting nanocrystal diameter is shown, determined via TEM (d_{obs}). Four types of theoretically calculated diameters (d_T), are presented, assuming either spherical growth ($d_{T\text{-}S}$) or growth in the radial direction along a cylindrical core ($d_{T\text{-}C}$). These results were calculated for either relaxed structures without strain or coherently strained structures. The observed sizes indicate that shell growth proceeds coherently in a manner that is intermediate between spherical and cylindrical.

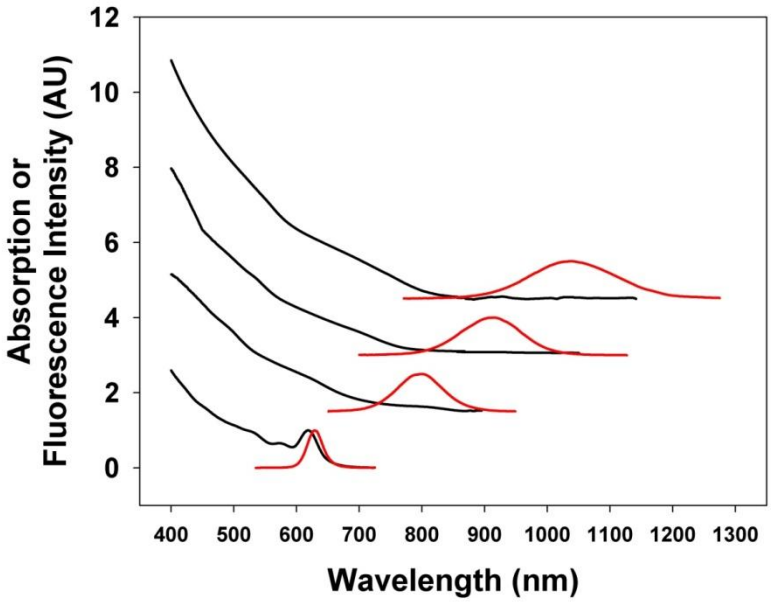

Figure 4.13: Absorption (black) and fluorescence emission (red) spectra for (CdTe)ZnSe quantum dots described in Figure 4.11. From bottom to top, the 3.8 nm CdTe cores are capped with 0, 2, 6, or 9 monolayers of ZnSe shell.

4.4.2 Structural Analysis via High Resolution Electron Microscopy. High-resolution TEM reveals the coherent crystallinity of these quantum dots, with lattice planes extending throughout the entire nanocrystal (Figure 4.14). We have also observed lattice warping and electron-density differences, as expected for strained core-shell structures (Figure 4.15). However, other than low-energy stacking faults, no major crystalline defects are observed, consistent with the high quantum yield and band-edge emission observed throughout shell growth (Figure 4.13). Figure 4.14 depicts high-resolution TEMs of (CdTe)ZnS quantum dots with zero or 6 monolayers of shell. The small CdTe core nanocrystals only measure ~6 unit cells in any direction, and thus the crystallographic orientation of only a small number of nanocrystals in a specific field of view can be identified. However, these nanocrystals can be unambiguously confirmed to be in the zinc blende phase due to the distinctive patterns of the (110) zinc blende

plane (see Fourier transform in Figure 4.14A and discussion in section 4.4.3). However the crystal structure of the (core)shell nanocrystals cannot be confirmed due to preferential orientation of the nanocrystals on the TEM grid. Nearly all nanocrystals (>95%) with shells larger than 2 monolayers are oriented with the zinc blende (111) plane parallel to the TEM grid. This preferential growth is attributed to the anisotropy of the underlying zinc blende CdTe cores, which are found to be slightly elongated in the [111] direction, with an aspect ratio of ~1.4. A prevalence of wurtzite stacking faults in this direction also adds a fundamental degree of anisotropy in the underlying crystalline lattice (see Section 4.4.3). Importantly, the lattice mismatch between the wurtzite structures of the core and shell materials is slightly larger in the *a*-direction compared to the *c*-direction, and the compressibility of wurtzite II-VI materials is higher in directions perpendicular to the *c*-axis.[35] This suggests that that shell growth may be favored to propagate in the radial direction outward along the cylindrically shaped nanocrystals. This mode of shell growth contrasts with that observed for most CdSe nanocrystals, which typically favor growth in the *c*-direction of wurtzite structures, commonly attributed to the high reactivity of the *c*-terminal facet and closer lattice match in this direction.[8,37,38]

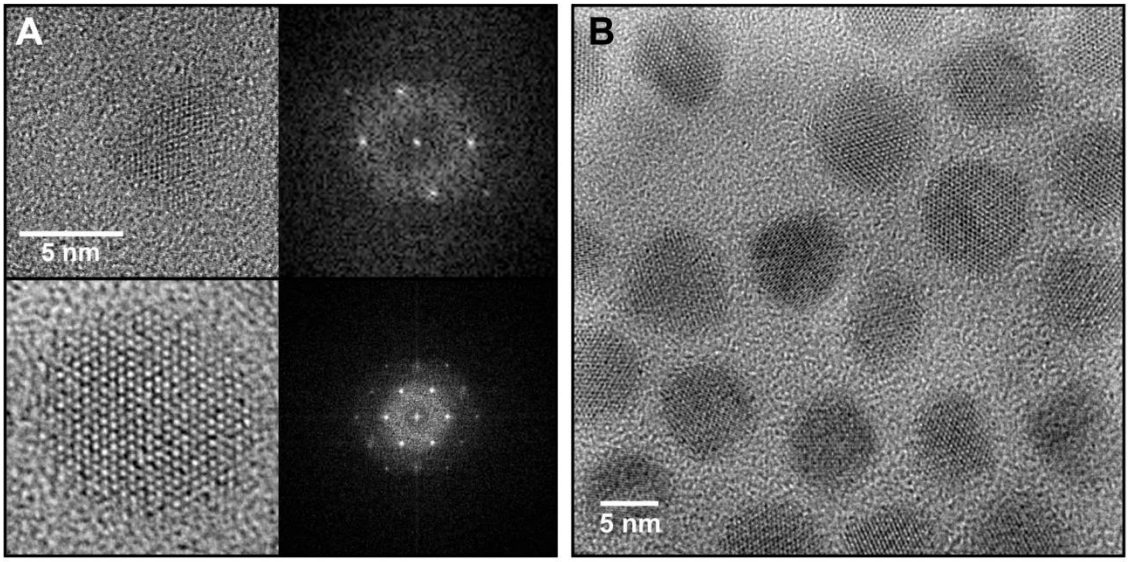

Figure 4.14: High resolution transmission electron micrographs of (CdTe)ZnSe nanocrystals. (A) Micrographs and fast-Fourier transforms of 3.8 nm CdTe quantum dots (top) and (CdTe)ZnSe quantum dots with 6 monolayers of shell (bottom). (B) Micrograph of (CdTe)ZnSe quantum dots with 6 monolayers of shell.

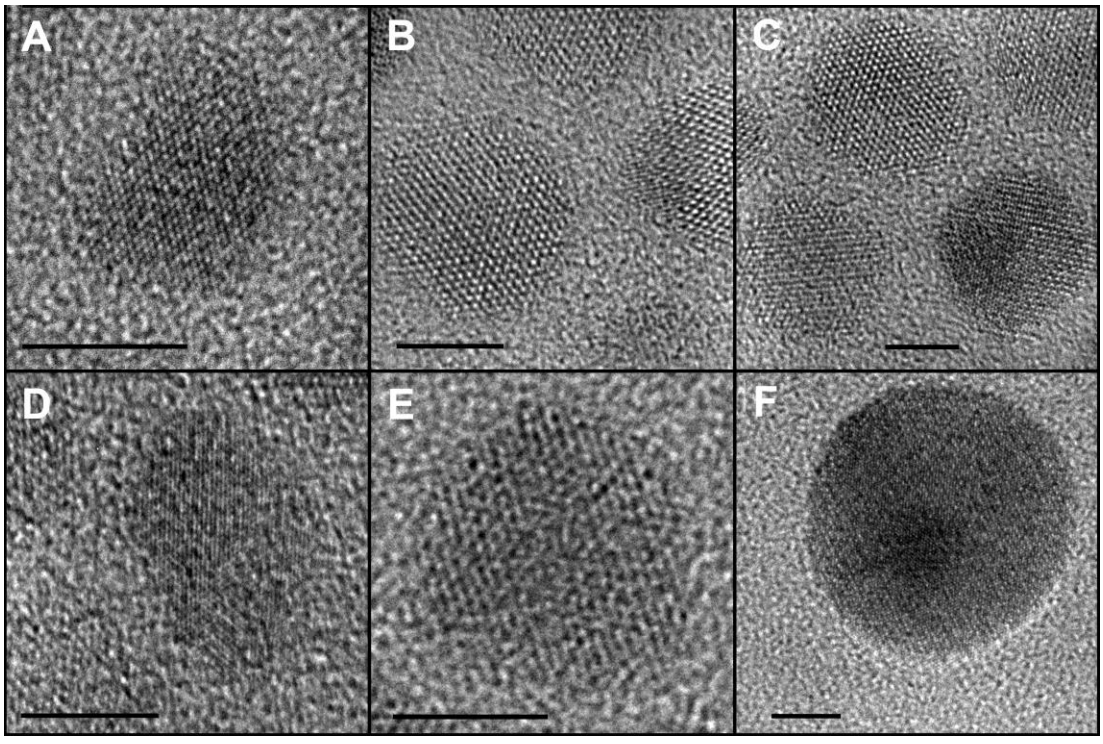

Figure 4.15: (Core)shell (CdTe)ZnSe quantum dots exhibiting lattice warping and localized differences in electron density. Shell thicknesses were 3 monolayers (a), 6 monolayers (b-e), or ~10 monolayers (f). Scale bars represent 5 nm.

4.4.3 Powder X-Ray Diffraction. Powder X-ray diffraction (XRD) data (Figure 4.16) show that these nanocrystals grow homogeneously as uniform crystalline domains. The CdTe cores show a zinc-blende diffraction pattern, which shifts to smaller bond lengths with shell growth. After 6 monolayers of shell growth, the lattice constant has shrunk by 5.1% relative to zinc blende CdTe, indicating an expansion of the ZnSe shell lattice by 8.5% compared to bulk. Further increasing the shell thickness to 9 ML nearly doubles the total nanocrystal volume, but only slightly changes the lattice parameters. The diffraction peaks become narrower due to the larger crystalline domains produced, with no evidence of pure ZnSe or CdTe domains. Combined with the quasi-spherical morphology of these particles observed in TEMs, this data suggests that crystal growth is coherent and homogeneous, despite the large strain between the core and the shell materials. The XRD spectra show patterns of a hexagonal lattice with shell growth, indicated by splitting of the (111) reflection and the development of a peak between the (220) and (311) reflections. This observation is further analyzed through simulations below.

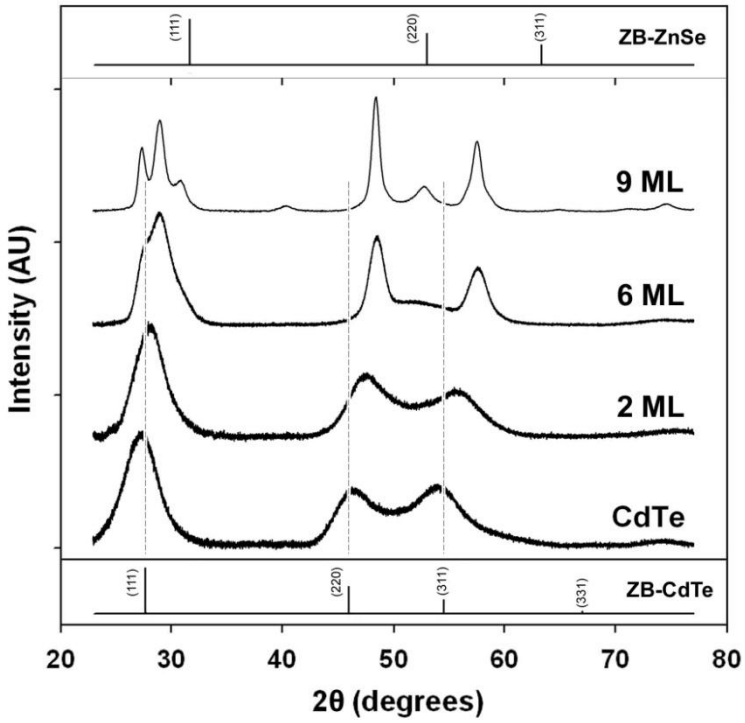

Figure 4.16: Powder X-ray diffraction (XRD) of (CdTe)ZnSe nanocrystals. XRD patterns for 3.8 nm CdTe and (CdTe)ZnSe quantum dots with 2, 6, or 9 monolayers of shell are shown. Bulk diffraction peaks for zinc blende (ZB) ZnSe (top) and CdTe (bottom) are indexed. Vertical dotted lines correspond to the major diffraction peaks of bulk CdTe.

4.5.3.1 Comparison of zinc blende and wurtzite crystal structures. II-VI materials are polymorphic, crystallizing in either the zinc blende (cubic) or wurtzite (hexagonal) phases in bulk and as nanostructures.[39-44] These two crystalline phases are structurally quite similar, which is reflected in a miniscule difference in lattice energy between the two structures (<10 meV per atom) and a high frequency of zinc blende-wurtzite polytypism.[39,44] For both of these phases, the atoms are bonded in a tetrahedral geometry, which may be slightly skewed for a nonideal wurtzite structure. The major energetic differences between these two structures arise from the orientation of 6-membered rings of atomic subunits in a 'chair' conformation in the zinc blende [111] direction compared to a 'boat' conformation in the wurtzite [0001] direction. The

eclipsed conformation of the wurtzite structure allows additional long-range electrostatic attraction between anions and cations in the [0001] direction, indicated by a slightly higher Madelung constant (0.2% larger), causing more ionic materials (e.g. ZnO, ZnS) to favor this structure over zinc blende. This conformational difference can be observed most readily in the zinc blende $[1\bar{1}0]$ direction and the wurtzite $[11\bar{2}0]$ directions (Figure 4.17B). This slight anisotropy in bonding also contributes to anisotropy in electronic and optical properties of the wurtzite structure.

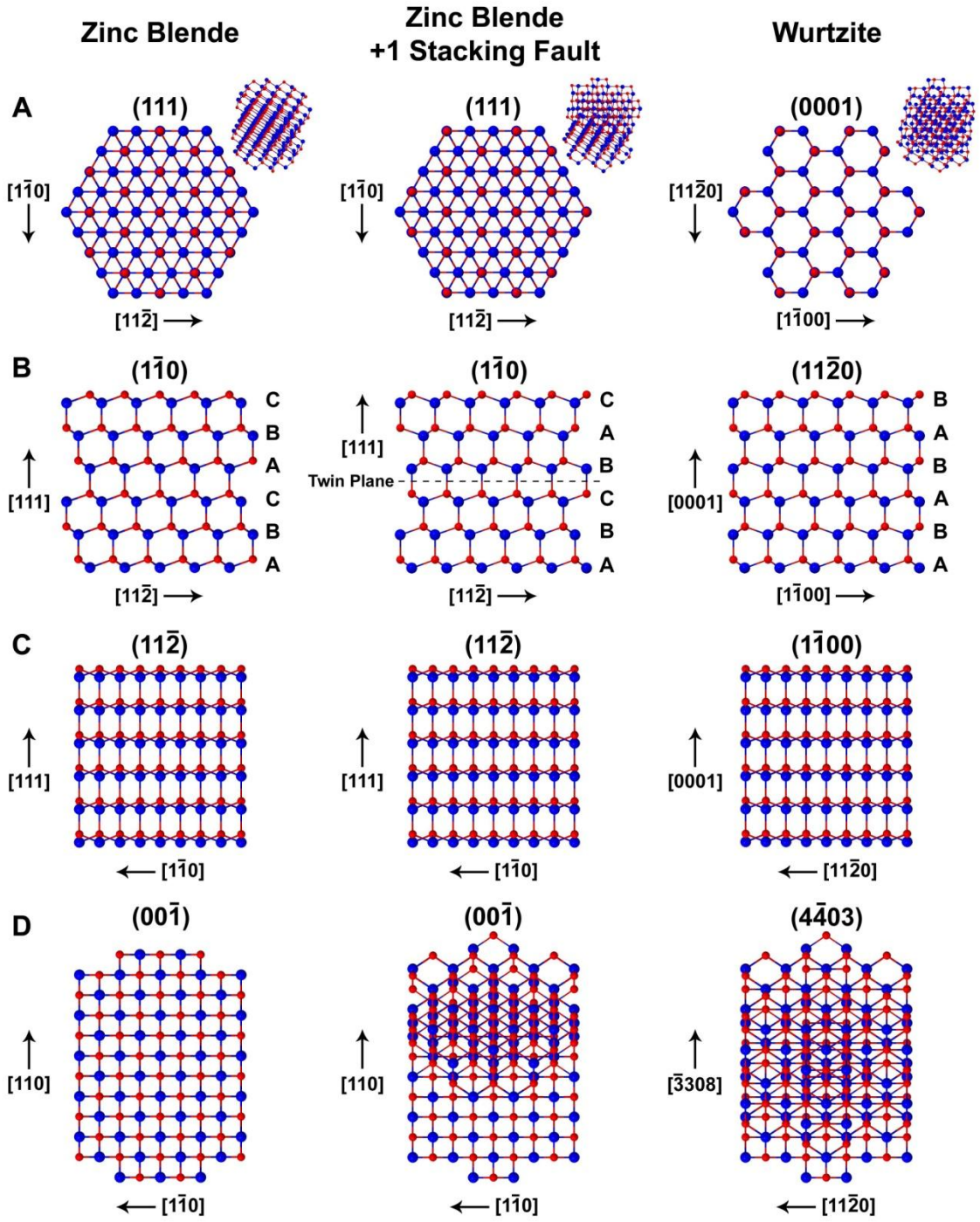

Figure 4.17: Zinc blende and wurtzite lattice structures and polytypes. Lattice structures are shown for segments of the high symmetry directions of zinc blende (left), showing the equivalent direction with the addition of a single wurtzite stacking fault (middle) and for the pure wurtzite structure (right). Anions are red and cations are blue. (A) Lattice structures viewed down the [111] and [0001] axes, with small scale structures showing the overall size and symmetry of the models depicted in this figure. (B) Lattice

structures viewed down the $[1\bar{1}0]$ and $[11\bar{2}0]$ directions, showing the 'chair' and 'boat' conformations of the zinc blende and wurtzite phases, respectively. A single wurtzite lattice fault introduces a twin plane in the center of the zinc blende structure. (C) Lattice structures viewed down the $[11\bar{2}]$ and $[1\bar{1}00]$ directions. (D) Lattice structures viewed down the $[00\bar{1}]$ and $[4\bar{4}03]$ directions, showing complete disruption of the lattice symmetry with the addition of a single stacking fault.

The structural difference between these two phases is due to the stacking order of lattice planes in the zinc blende [111] direction, which is structurally equivalent to the wurtzite [0001] direction. In the zinc blende lattice, unique planes are stacked in the order ABCABC…, whereas the wurtzite structure only has two equivalent (0001) planes with ABABAB… ordering (Figure 4.17B). Because of the equivalence between these two lattice directions, polytypism between these two structure is manifested in stacking faults in the [111] zinc blende direction or the wurtzite [0001] direction. The zinc blende structure has a much higher degree of symmetry than the wurtzite structure, and introducing just one wurtzite stacking fault in a zinc blende structure significantly disrupts this symmetry. For example, the zinc blende structure has four equivalent [111] directions arranged tetrahedrally and the wurtzite structure has only one analogous [0001] direction. Introducing one wurtzite stacking fault in the middle of a zinc blende CdTe nanocrystal completely eliminates the 4-fold symmetry of the [111] axes, resulting in the production of a unique anisotropy with a single [111] axis (Table 4.3). In addition, this single stacking fault causes a complete loss of the three cubically oriented [100] axes (Figure 4.17D) and a loss of 3 of the 6 [110] axes. Despite this loss of crystal symmetry, a large number of the original facets still remain, and controlling the surface energy of different exposed facets has been found to be one mechanism to control the phase of II-VI nanostructures.[20,45,46]

Table 4.3: Comparison of lattice direction symmetry and equivalency for zinc blende and wurtzite crystal structures

Zinc Blende					Wurtzite			
Plane	Polarity[a]	N[b]	N_{1SF}[b]	BD ($\times d^{-2}$)[c]	Plane	Polarity[a]	N[b]	BD ($\times d^{-2}$)[c]
(111)	Polar	4	1	0.433	(0001)	Polar	1	0.433
$(1\bar{1}0)$	Nonpolar	6	3	0.530	$(11\bar{2}0)$	Nonpolar	3	1.061
$(11\bar{2})$	Nonpolar	12	3	0.612	$(1\bar{1}00)$	Nonpolar	3	0.459
$(00\bar{1})$	Polar	3	0	0.750				

[a] Polarity refers to the electrostatic polarity of the facet terminated by the specified plane.
[b] N is the number of equivalent plane directions, and 1SF indicates the presence of one wurtzite stacking fault.
[c] BD is bond density, the surface density of unpassivated orbitals in facets terminated by the specified planes. Units are in inverse area for square bond lengths (d^2).

4.5.3.2 Simulation of Diffraction Patterns. From the preceding discussion, it is evident that although the hexagonal wurtzite and cubic zinc blende phases are quite similar in molecular bonding, their structures strongly differ in symmetry. Introducing even a small number of wurtzite stacking faults to a zinc blende crystal would be expected to significantly disrupt the high symmetry of the cubic unit cell, however the overall hexagonal symmetry of the wurtzite phase is not significantly perturbed by the addition of zinc blende stacking faults. Crystal symmetry is strongly linked with diffraction techniques, so powder XRD spectra (Figure 4.16) can be analyzed to reveal the crystal phase and possible presence of stacking faults in the highly strained (CdTe)ZnSe nanocrystals.

To this end, XRD spectra were simulated using the Debye formula (Appendix A), as shown in Figure 4.18.[6,42,43] Twenty zinc blende crystal lattice structures were constructed with randomly distributed wurtzite stacking faults in the [111] direction with a specific frequency (0-100%), and then atoms were removed from these structures that fell outside of a hexagonal prism with specific dimensions. Core CdTe quantum dots were simulated as ~850 atom hexagonal cylinders, and (core)shell structures were simulated by extending the lattices of these cores using zinc and selenium atoms. The Debye equation was then solved for these structures using the DISCUS software package,[47] and the spectra were averaged to simulate a distribution of stacking faults. Only ten spectra were averaged for the 6 monolayer and 9 monolayer samples due to the long processing times required for such large structures. Thermal effects were incorporated through Debye-Waller factors, however it should be noted that strain would be expected to impact thermal fluctuations of atoms, but in ways that are not immediately predictable. No surface relaxations were incorporated in the simulations. The parameters for nanocrystal modeling are listed in Table 4.4.

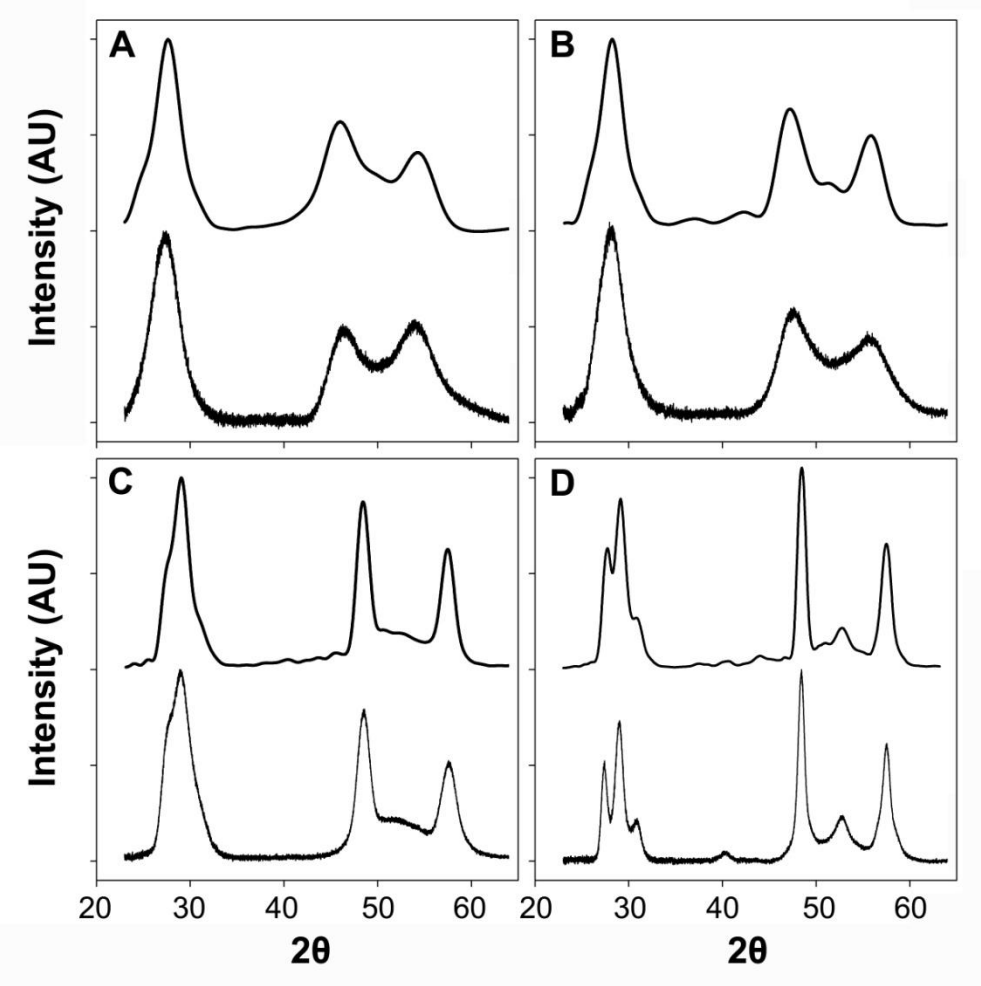

Figure 4.18: Simulations of XRD data. Simulations are displayed above the experimental data, which are reproduced from Figure 4.16. The dimensions, lattice constants, and frequencies of stacking faults for each crystal structure are itemized in Table 4.4. Core nanocrystals (A) were used as a substrate upon which coherent layers of ZnSe were extended to simulate a (core)shell structure with 2 (B), 6 (C), or 9 (D) shell monolayers. Inclusion of 30-40% wurtzite stacking faults in the [111] direction was found to be essential for accurately modeling the scattering between the (220) and (311) peaks, and is supported by microscopic evidence (Figure 4.19).

Table 4.4: Parameters for nanocrystal models used for XRD simulations

Sample	SF%	Height (nm)	Width (nm)	Lattice Constant, a (Å)
CdTe core	32%	4.2	3.0	6.49
CdTe/ZnSe, 2 ML	33%	4.7	4.3	6.40
CdTe/ZnSe, 6 ML	38%	6.6	7.2	6.19
CdTe/ZnSe, 9 ML	35%	7.2	10.9	6.17

Notes: The percentage of wurtzite stacking faults in the zinc blende [111] direction is indicated as SF%. Each nanocrystal was modeled as a hexagonal prism with height and width indicated in the table.

Simulations of the diffraction patterns of these structures reveal that the aforementioned increase in hexagonal patterning to the XRD spectra with shell growth are not indicative of a phase change. Instead, these changes reflect a high prevalence of stacking faults in the [111] zinc blende direction. The presence of these faults in (CdTe)ZnSe quantum dots is shown microscopically in Figure 4.19. The structural simulation data demonstrate that all of the (core)shell nanocrystals characterized in Figure 4.16 are predominantly zinc blende, with 30-40% of the (111) lattice planes stacked in the hexagonal geometry. Therefore, the increasing hexagonal nature of the diffraction patterns is caused solely by the narrowing of the diffraction peaks with coherent shell growth, which reveals the underlying cubic-hexagonal polytypism that is obscured by the wide diffraction peaks of small cores.

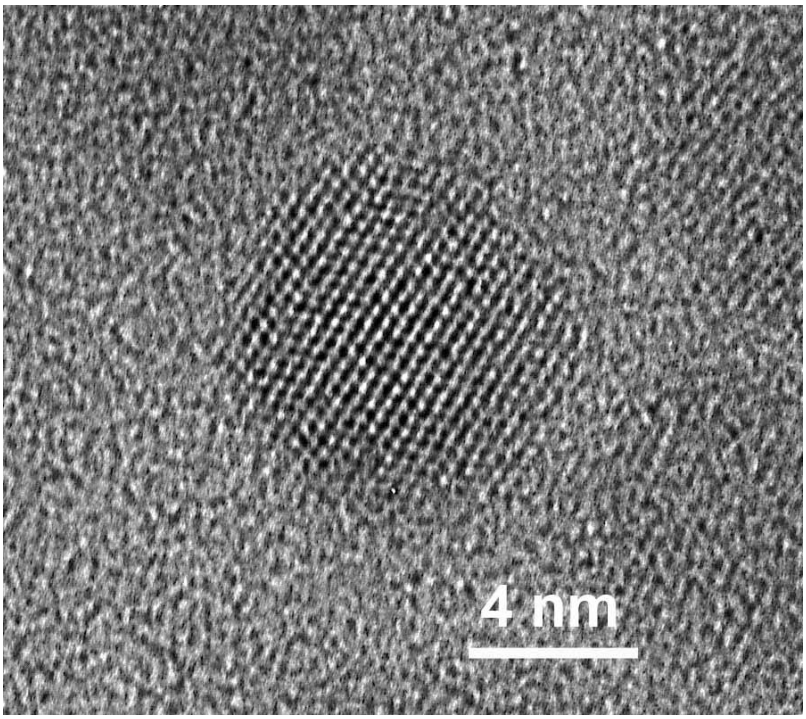

Figure 4.19: High-resolution transmission electron micrograph of 3.8 nm CdTe quantum dot coated with 6 monolayers of ZnSe. This nanocrystal is oriented with its {110} plane parallel to the TEM grid, which occurs infrequently for these nanocrystals, as discussed in the main text. Multiple stacking faults along the [111] zinc blende direction are evident in the visible twinning.

The structures that most accurately simulate the experimental data show an anisotropy of shell growth, with preferential deposition on lattice planes perpendicular to the [111] axis, in accord with TEM size data (Table 4.2) and high resolution TEM structural analysis (Figure 4.14). This is indicated qualitatively in the disproportionately narrow widths and high intensities of the peaks for the nanocrystal reflections perpendicular to the [111] axis for nanocrystals with thicker shells. Deviations between the simulations and experimental data were significantly impacted by imperfect background subtraction of the experimental spectra, especially for the smallest nanocrystals. In addition, there is an inherent tradeoff between spectral resolution and numerical computation time, which

manifests itself in artifactually wider peaks for larger nanocrystals. This finite resolution diminishes the curvature of peaks in Figure 4.18D, an effect which could be eliminated with higher resolution computations, but which is computationally forbidding. Previous studies also suggest that the larger polydispersity of the 9 ML nanocrystals (Figure 4.12) narrows the diffraction peaks and lengthens the tails.[48]

4.5 Modeling of Strain and Band Structures

4.5.1 Continuum Elasticity Modeling. To gain further insight into the mechanism of strain tuning, a continuum elasticity model was implemented for coherently grown epitaxial ZnSe shells on CdTe cores (Appendix B).[49] Figure 4.20 demonstrates that the shell induces a radial compression of the core, resulting in isotropic, compressive strain. The shell lattice is under tensile strain in the tangential directions surrounding the core, and is compressively strained in the radial direction. The strain in the shell decays with increasing distance from the interface, but does not decay fully to zero. This result demonstrates that thick shells are unable to compress the core to more than a critical value, leaving a significant amount of elastic strain in the shell. Based on the lattice constants experimentally observed from XRD and TEM, however, the compression of the core should be much larger. This discrepancy is most likely due to the nonspherical growth in the shell occurring perpendicular to the [111] direction, causing the heterostructure to more closely resemble concentric cylinders rather than concentric spheres. Modeling this system as cylinders redistributes much of the strain to the shell, and more strongly correlates with the experimentally observed lattice parameters.

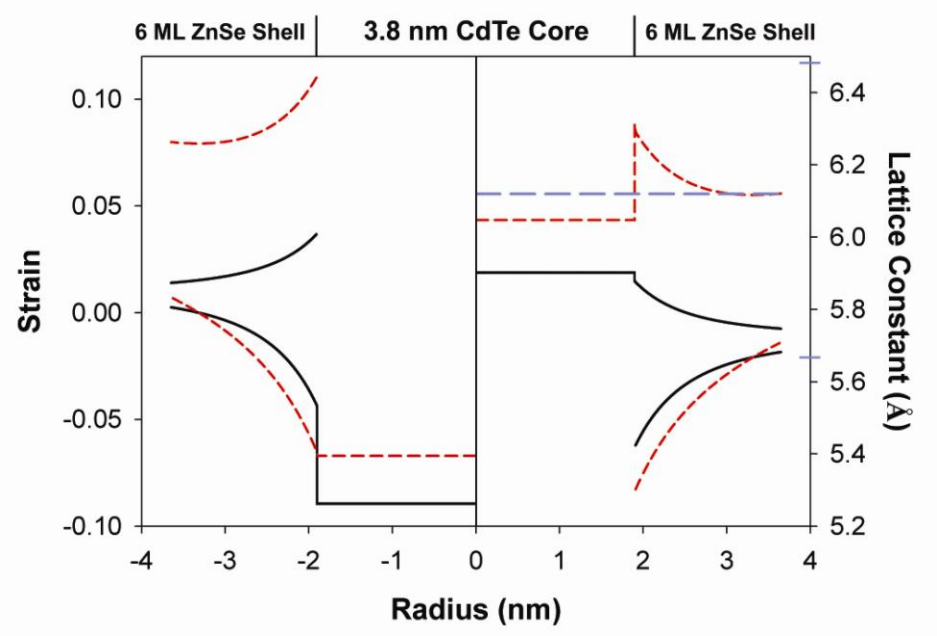

Figure 4.20: Continuum elasticity simulation data for high-strain (CdTe)ZnSe nanocrystals. Left: strain distribution in a 3.8 nm-diameter CdTe nanocrystal coated with a 6 monolayer ZnSe shell, modeled as concentric spheres (solid black line) or concentric cylinders (hatched red line). Strain in the core is isotropically compressive, while strain in the shell is tangentially tensile (top line) and radially compressive (bottom line). Right: calculated lattice constants corresponding to spherical and cylindrical strain profiles, compared to the experimentally observed lattice constants (blue hatched line). Blue axis indicators correspond to unstrained CdTe (6.482 Å) and ZnSe (5.668 Å).

This continuum elasticity model can be used to predict the critical shell thickness for which the formation of a dislocation loop is energetically more favorable than coherent, epitaxial growth. This was calculated by determining the shell thickness for which the energy of the coherent, elastically strained state is equal to the energy of the incoherent state, with the latter arising from energy due to both the defect and the residual elastic energy from strain. A circular dislocation loop is a type of misfit dislocation (Figure 4.1) that can encircle the interface between the core and shell material to release strain, and is expected to be the lowest energy incoherent defect state for such a strained heterostructure. Figure 4.21 depicts this critical thickness for different core sizes, demonstrating that CdTe cores with a diameter less than ~3.5 nm can tolerate strained,

coherent growth of shells with essentially any thickness. It should be noted that this critical thickness is the absolute minimum shell thickness that results in defect formation. There may be a significant activation energy for dislocation formation, and the nucleation of a such a defect is kinetically controlled and will likely only occur after overgrowth of a shell thicker than the critical thickness.

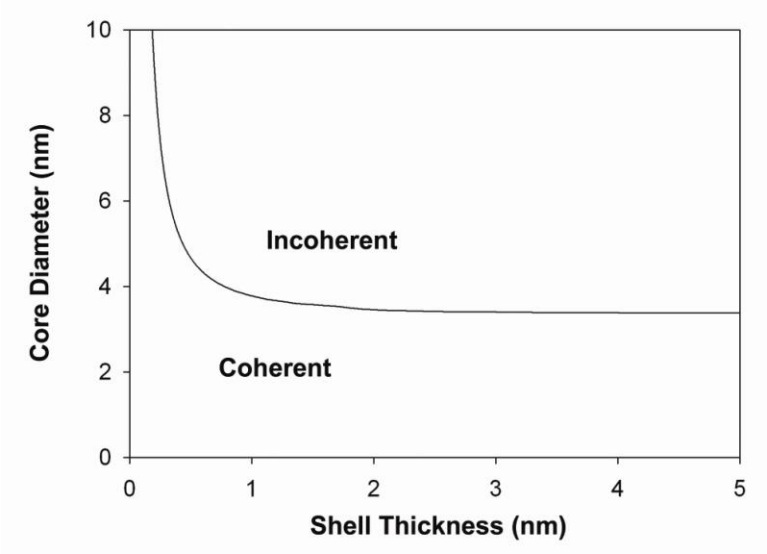

Figure 4.21: Critical shell thickness for (CdTe)ZnSe quantum dots. The minimum shell thickness for which the formation of a dislocation loop is energetically more favorable than coherent growth is indicated by a solid line for different core sizes. For shell thicknesses greater than the critical thickness, defect formation is favored to relax the structure to incoherent growth.

4.5.2 Band Structure Calculations. Using the theoretically derived lattice deformations, the "model-solid theory" was used to calculate the band offsets and bandgaps of the various (core)shell structures.[50] With knowledge of the bandgap of the core from optical spectroscopy before capping, the relative energy shifts of the conduction and valence band edges due to quantum confinement were calculated to a first approximation from the relationship

$$\Delta E_{e,h} \propto m_{e,h}^{-1} \qquad \textbf{Equation 4.4}$$

in which the change in energy of the conduction (valence) band edge due to quantum confinement, ΔE_e (ΔE_h), is inversely proportional to the bulk effective mass of the electron (hole).[51] Determination of the band edges of the shell is more difficult, but can be approximated to a surprisingly accurate degree by assuming the shell to behave as a two-dimensional quantum well. This approximation is theoretically acceptable if the perimeter of the sphere is larger than the exciton Bohr diameter of the shell material, such that the radial direction is not quantum confined. The dependence of the bandgap of an unstrained quantum well on its width has been empirically determined and calculated theoretically for many different II-VI materials, and can be found in the literature. Once the bandgaps, band offsets, and material strain of the core and shell materials are known, the model-solid approach of Van de Walle and Martin[50] can be used to approximate the bandgap of the entire heterostructure using published parameters for the materials of interest.[4-6] There are several advantages and disadvantages to this approach for the determination of band structure. This method is robust and purely analytical, requiring very little computational power to implement. The reliance on empirical data adds credibility, and no correction factor needs to be used for the bandgaps, unlike for local density approximations, although theoretically calculated bandgaps and band offsets could just as easily be used instead. The use of a continuum elastic model of nanocrystals is likely to be less accurate than atomistic elasticity models, especially in regions with abrupt changes in strain, such as in the direct vicinity of nano-heterostructure interfaces, but this approach has been shown to agree strongly with more complex models.[52] However, the model-solid approach does not account for quantum tunneling, which is believed to be an important characteristic of the wave nature of charge carriers for influencing the optical properties of

heterostructures, especially for nanocrystals with highly localized charge carriers. It is possible that the accuracy of this model could be increased with the inclusion of a term accounting for the finite well depths of the charge carriers. The nonspherical, anisotropic growth of the nanocrystals described herein, and the anisotropy and possible size-dependence of the materials parameters of these semiconductors, are other sources of error when comparing with this model. Nevertheless, these methods show strong correlation with experimental data, allowing the prediction of bandgaps of these structures at various stages of shell epitaxial growth (Figure 4.22).

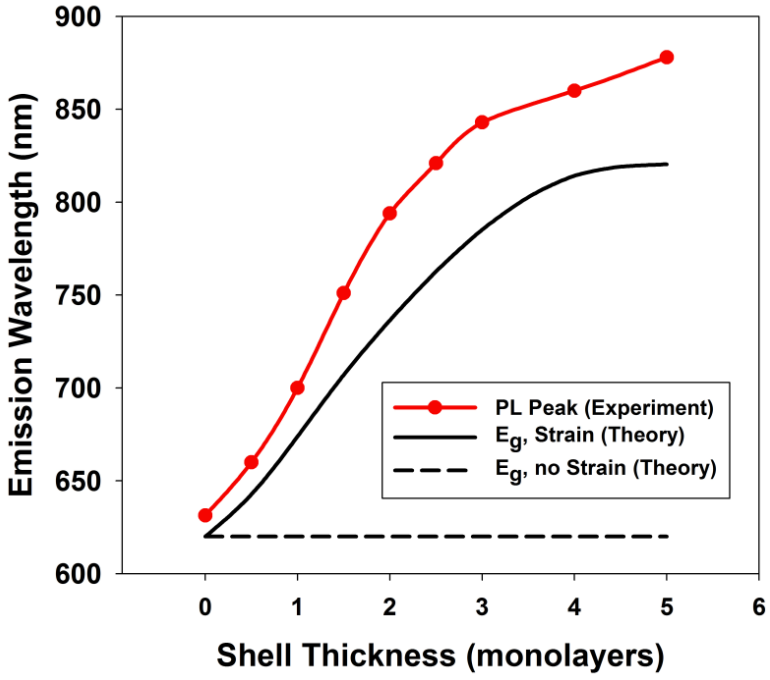

Figure 4.22: Comparison of experimentally determined photoluminescence (PL) emission wavelengths with predicted bandgap values from the continuum elasticity-model solid theory calculations. Experimental data is from 3.8 nm CdTe quantum dots coated with 0 to 5 monolayers of ZnSe shell (reproduced from Figure 4.8). Theoretical data implements concentric cylinders, with strain (black solid line) or without strain (black hatched line). When accounting for quantum confinement of the materials, the quantum dots are type-I when the effects due to strain are ignored. This is not surprising, due to the type-I alignment of the band offsets for the bulk heterostructure. With strain, the bandgap decreases due to the formation of a type-II structure. The disparity between the experimental PL peak and the predicted energy gap is due to a

combination of the Stokes shift between the absorption band edge and the PL peak, and due to the various shortcomings of this semi-empirical model, as outlined in the text.

4.5.3 Size Dependence of Materials Parameters. For these modeling calculations, bulk material parameters are used because no general trends have yet emerged regarding the dependence of elastic moduli on particle size. For some materials, the compressibilities change with grain size, most commonly showing a softening effect with decreasing size.[15,53] In other instances, however, compressibility values are found to be unchanged in nanoparticles compared to the bulk.[53,54] For II-VI semiconductors, it has been reported that CdS quantum dots have similar compressibilities compared to the bulk,[54] whereas CdSe quantum dots are more compressible than the bulk material.[15] Quantum confinement by itself may induce structural modifications in semiconductor nanocrystals,[55] and these nanocrystals may be subject to compressive or tensile forces depending on the nature of their passivating ligands.[56] For the strain-tunable quantum dots in this work, the elasticities of nanoscale ZnSe and CdTe have not been determined as a function of particle size. If the elasticities of the core and shell materials decrease evenly, the total elastic strain energy in these dots would be reduced. This energy reduction is not expected to alter crystalline deformation or lead to major net changes in our bandgap calculations. To further examine the case in which only one of the materials becomes more elastic, a theoretical model was implemented using smaller elastic moduli (20% smaller than bulk) for either the core or shell materials. This softening effect marginally modifies the magnitude of the strain-induced band shifting (by less than 3%). It is also important to note that the observed crystalline polytypism may slightly affect the calculated bandgaps. Shengbai Zhang and coworkers calculated a bandgap 1.50 eV for zinc blende CdTe and a bandgap of 1.547 eV for wurtzite.[44] For

ZnSe, experimental data of the bandgaps also reveal a very small difference of 2.82 eV for zinc blende, and 2.8474 eV for wurtzite.[39]

4.6 Other Structural and Quantum Mechanical Mechanisms

4.6.1 Quantum Confinement. Some of the optical properties of (CdTe)ZnSe nanocrystals may be superficially explained simply from the perspective of quantum confinement of electronic energy states. As the dimensions of the heterostructure decrease from bulk to that of the core-shell quantum dot, the corresponding widening of the bandgap may occur asymmetrically between the bands of the core and shell, thus altering the band offsets between the materials. If this is the case, when the ZnSe shell thickness increases, its conduction band edge will decrease in energy, below that of the conduction band of the highly confined CdTe core, thus increasing electron density in the shell, and yielding a type-II structure. This rationale has been proposed as a mechanism for modulating between type-I and type-II character in (ZnSe)CdSe and (CdS)ZnSe core/shell quantum dots by adjusting the shell thickness.[57,58] However this is not an adequate explanation for the (CdTe)ZnSe system because the bulk conduction band offsets (ΔE_c=0.68 eV) and valence band offsets (ΔE_v=0.64 eV) are similar, and despite large differences in electron and hole effective masses, the relative bandshifts should not be tremendously different. Moreover, if this were the case, CdS would be an even better shell material for generating type-II quantum dots with CdTe cores, due to the near-zero conduction band offset between these materials in bulk, and because the effective masses of its charge carriers are comparable to those of ZnSe.[35] (CdTe)CdS quantum dots indeed do demonstrate quasi-type-II character after thick shells are grown (≥ 5 monolayers), however the magnitude of spectral shifting is much less than that of (CdTe)ZnSe (Figure 4.10). Quantum confinement-induced modifications of band offsets do, indeed play an important role in the highly strained nanocrystals described herein,

but they are small compared to the role of strain (Figure 4.22). It should be noted that a large amount of the previous work on (core)shell structure modeling to explain type-I and type-II quantum dot modulation from the sole perspective of quantum confinement has been significantly biased by the inaccuracy of effective masses for small nanocrystals and thin shells. Although effective mass approximations of band alignments are useful for explaining broad trends, they are insufficient to accurately predict precise changes in band alignments for nanocrystals, which makes the pseudo-empirical approach used herein even more widely useful.

4.6.2 Interfacial Alloying. The study of interfacial alloying of bulk heterostructures is a challenging task, and very few tools exist for such analyses for nanocrystals. Alloying of the (CdTe)ZnSe quantum dots at the core/shell interface could possibly generate a type-II structure. That is, diffusion of either zinc or selenium from the shell into the core could result in ZnTe/CdSe or CdTe/CdSe/ZnTe interfaces, respectively, which are both type-II heterostructures in bulk. Indeed, Cd(Te,Se) quantum dots grown via self-assembly on a ZnSe substrate using molecular beam epitaxy show two emission bands, one attributed to Cd(Te,Se) type-I quantum dot emission, and another to lower energy type-II behavior, believed to be due to a ZnSeTe/ZnSe interface.[59] However this alloying mechanism is unsatisfactory, due to the fact that this band shift is highly dependent on the size of the quantum dot core (Figure 4.7), and type-II character is not evident for core-shell quantum dots with cores larger than ~5 nm diameter (Figure 4.5 and 4.7). In addition, alloying and interatomic diffusion within the crystal should be driven mostly by entropic factors, and therefore should occur more readily at high temperatures. Instead, most of the band-shifting that is observed occurs at low temperatures, when thin shells are grown on the quantum dot cores, prior to increasing the temperature to expedite capping on these more stable (core)shell structures. CdTe cores with thin 1 ML shell of ZnSe

can be heated to over 260°C without observation of changes in the optical spectra. As well, this type-II nature does not develop until thicker shells are grown on the quantum dots (2-3 monolayers), whereas type-II quantum dots would be predicted to have formed with only thin shells within this model because (CdTe)CdSe has strong type-II characteristics after 1 monolayer of shell growth.

Also supporting this argument against the occurrence of interfacial alloying is that most other (core)shell quantum dots such as (CdSe)ZnS and (CdSe)CdS have not been observed to undergo significant interatomic rearrangements, even at elevated temperatures.[6,23] The only report of alloy formation after the synthesis of a (core)shell structure demonstrated that this process for (CdSe)ZnSe nanocrystals is temperature-dependent, and a very high temperature is required to overcome the activation energy for interatomic diffusion.[60] In the literature, cations have been shown to be the more mobile species in II-VI crystals, as the anions generally retain their lattice within the structure.[1,60-65] A great deal of evidence now points toward the possibility of various types of cationic exchange mechanisms within nanocrystals, but very little evidence of anionic diffusion. To test the possibility of cation diffusion-alloying in the nanocrystals prepared herein, (CdTe)ZnTe quantum dots were prepared with 2 ML of shell. These nanocrystals were composed of two different cations, Cd and Zn, but only one anion, Te. Therefore, if cationic diffusion does occur, one would expect the formation of a $Cd_xZn_{1-x}Te$ alloy quantum dot, or a (CdTe)$Cd_xZn_{1-x}Te$/ZnTe (core)/shell/shell quantum dot, both of which would result in a blue-shift in the optical spectra of the quantum dot due to the significantly larger bandgap of ZnTe (2.39 eV) compared to CdTe (1.50 eV). The core quantum dots had a photoluminescence peak at ~630 nm, which shifts to 672 nm after capping at 225°C. When these nanocrystals were heated to 290°C for 3 hours, no major changes were observed in the fluorescence emission spectra and absorption spectra.

This structure was thermally very stable, showing no signs of alloying at any point, unlike the previous reports of temperature-dependent cationic alloying in (CdSe)ZnSe quantum dots. (CdTe)CdSe quantum dots similarly showed no changes indicative of alloy formation at high temperature. Because the possibilities of cationic diffusion and anionic diffusion can be ruled out independently, it is unrealistic to presume that both of these could occur simultaneously.

4.6.3 Direct-to-Indirect Bandgap Transition. In another possible scenario, the strain within the CdTe (6.482 Å lattice constant) core caused by the compressive ZnSe (5.668 Å lattice constant) shell might be able to induce an indirect bandgap in the CdTe quantum dot, as previously observed for small InP quantum dots that transition from direct to indirect semiconductors under hydrostatic compression.[66,67] This is caused by the opposite response of the Γ and X conduction band edges to pressure due to directional differences in charge distribution in zinc blende crystals. Bulk CdTe and ZnSe do not exhibit a direct-to-indirect crossover for pressures up to their first phase transition. In addition, this possibility is unlikely because the band shifts of the photoluminescence and absorption spectra are gradual with shell growth, which would not reflect a pressure-induced direct-to-indirect semiconductor transition, in which the direct band-edge commonly disappears suddenly, leading to the appearance of an indirect edge and very low photoluminescence efficiency.

4.7 Outlook

The insights into the unique impact of strain on nanocrystals described herein are valuable from both a theoretical and applied perspective. The finding that epitaxial strain plays a large role in modifying the bandgaps of heterostructures of semiconductor nanocrystals addresses many of the poorly understood attributes of these particles, such

as the consistent red-shift with epitaxial overgrowth, the dependence of quantum efficiency on shell thickness, the interrelationship between quantum confinement and strain, and the crossover between coherent and incoherent growth modes. Furthermore, nearly all (core)shell nanocrystals and other types of nano-heterostructures are subject to varying degrees of lattice strain because of the structural mismatch between two different materials. It should be noted that a previous publication by Chen *et al*. described the production of (CdSe)CdS and the modulation of optical properties through lattice strain.[9] However, the experimental results that they observed were not caused by lattice strain but arose from the continuous growth of CdSe cores (not CdS shells) under their experimental conditions, and the theoretical application of strain was erroneous.

It is an interesting and powerful notion that epitaxial strain in a freestanding colloid can induce a stable modification of molecular bond lengths. The modification of molecular bond lengths significantly impacts the electronic and energetic properties of a molecule or crystal, and divulges great insight into the underlying atomistic physics of the system. For example, sp^3 hybridized alkanes can be strained to modify their bond lengths and angles through the synthesis of strained ring systems, however these structures are not continuously tunable, requiring demanding chemistry to design structures with slightly different characteristics. In addition, inducing bond length alterations in crystalline materials has traditionally relied on the use of high pressure in solid state systems or the controlled mechanical warping of bulk structures. The fact that colloidal systems may allow bond-length altered crystals to be suspended in liquid without external perturbations could yield a tremendous degree of flexibility in the study these systems. The shell materials of these colloids 'lock' the core material into a nonequilibrium lattice through coherent epitaxy, and the theoretical models used herein show that the core material can be under an effective pressure as high as 3 GPa. The inherent utility of

generating a strained, freestanding solid has already been demonstrated by Mark Eriksson and coworkers, who produced tensile-strained silicon films that were nearly defect-free due to the high tolerance of nanometer-scale crystals to elastic strain sharing with an epitaxial layer.[5] Extension of this concept to small crystals suspended as colloids in liquid phase should further enhance the applications of such strained-systems.

Although (CdTe)ZnSe nanocrystals are the focus of this work, the theories and methods described herein are widely applicable, and are not unique to this specific system. Of the materials examined, this specific (core)shell structure exhibited the largest dependence on strain. The basis for this finding is that CdTe is the most compressible of all the II-VI and III-V materials except for mercury telluride, and its deformation potential is also high.[30,26] This means that the lattice of CdTe is readily compressed, and upon compression, its electronic energy bands shift to a large degree. ZnSe also has a high deformation potential but has a much higher bulk modulus; its role as a less deformable, highly mismatched shell material is likely crucial in generating the unique optical properties reported. Other colloidal semiconductor nanocrystals with similar bulk materials parameters could be employed for strain tuning, especially III-V antimonides (AlSb, GaSb, and InSb) and other II-VI tellurides (ZnTe and HgTe). Extension of these concepts to multidimensional anisotropic systems with more chemical domains may lead to the capacity to prepare multifunctional nanoscopic devices and tools for solar energy conversion, biological tagging and imaging.

4.8 References

1. Robinson, R. D., Sadtler, B., Demchenko, D. O., Erdonmez, C. K., Wang, L. W., & Alivisatos, A. P. Spontaneous superlattice formation in nanorods through partial cation exchange. *Science* **317,** 355-358 (2007).

2. Lee, J. et al. Bandgap modulation of carbon nanotubes by encapsulated metallofullerenes. *Nature* **415,** 1005-1008 (2002).

3. Suhr, J., Victor, P., Sreekala, L. C. S., Zhang, X., Nalamasu, O., & Ajayan, P. M. Fatigue resistance of aligned carbon nanotube arrays under cyclic compression. *Nat. Nanotech.* **2,** 417-421 (2007).

4. Hall, A. R., Falvo, M. R., Superfine, R., & Washburn, S. Electromechanical response of single-walled carbon nanotubes to torsional strain in a self-contained device. *Nat. Nanotech.* **2,** 413-416 (2007).

5. Roberts, M. M., Klein, L. J., Savage, D. E., Slinker, K. A., Friesen, M., Celler, G., Eriksson, M. A., & Lagally, M. G. Elastically relaxed free-standing strained-silicon nanomembranes. *Nat. Mater.* **5,** 388-393 (2006).

6. Dabbousi, B. O., Rodriguez-Viejo, J., Mikulec, F. V., Heine, J. R., Mattoussi, H., Ober, R., Jensen, K. F., & Bawendi, M. G. (CdSe)ZnS core-shell quantum dots: Synthesis and characterization of a size series of highly luminescent nanocrystallites. *J. Phys. Chem. B* **101,** 9463-9475 (1997).

7. Manna, L., Scher, E. C., Li, L. S., & Alivisatos, A. P. Epitaxial growth and photochemical annealing of graded CdS/ZnS shells on colloidal CdSe nanorods. *J. Am. Chem. Soc.* **124,** 7136-7145 (2002).

8. McBride, J., Treadway, J., Feldman, L. C., Pennycook, S. J., & Rosenthal, S. J. Structural basis for near unity quantum yield core/shell nanostructures. *Nano Lett.* **6,** 1496-1501 (2006).

9. Chen, X. B., Lou, Y. B., Samia, A. C., & Burda, C. Coherency strain effects on the optical response of core/shell heteronanostructures. *Nano Lett.* **3,** 799-803 (2003).

10. Maki, H., Testuya, S., & Ishibashi, K. Direct observation of the deformation and the band gap change from an individual single-walled carbon nanotube under uniaxial strrain. *Nano Lett.* **7,** 890-895 (2007).

11. Li, Y. H., Gong, X. G., & Wei, S. H. Ab initio all-electron calculation of absolute volume deformation potentials of IV-IV, III-V, and II-VI semiconductors: The chemical trends. *Phys. Rev. B* **73,** 245206 (2006).

12. Li, J. B. & Wang, L. W. Deformation potentials of CdSe quantum dots. *Appl. Phys. Lett.* **85,** 2929-2931 (2004).

13. Persson, J., Hakanson, U., Johansson, M. K. J., Samuelson, L., & Pistol, M. E. Strain effects on individual quantum dots: Dependence of cap layer thickness. *Phys. Rev. B* **72,** 085302 (2005).

14. Tolbert, S. H. & Alivisatos, A. P. Size dependence of a first order solid-solid phase transition: the wurtzite to rock salt transformation in CdSe nanocrystals. *Science* **265,** 373-376 (1994).

15. Tolbert, S. H. & Alivisatos, A. P. High-pressure structural transformations in semiconductor nanocrystals. *Annu. Rev. Phys. Chem.* **46,** 595-625 (1995).

16. Brunner, K. Si/Ge nanostructures. *Rep. Prog. Phys.* **65,** 27-72 (2002).

17. Lamberti, C. The use of synchrotron radiation techniques in the characterization of strained semiconductor heterostructures and thin films. *Surf. Sci. Rep.* **53,** 1-197 (2004).

18. Mueller, A. H., Petruska, M. A., Achermann, M., Werder, D. J., Akhadov, E. A., Koleske, D. D., Hoffbauer, M. A., & Klimov, V. I. Multicolor light-emitting diodes based on semiconductor nanocrystals encapsulated in GaN charge injection layers. *Nano Lett.* **5,** 1039-1044 (2005).

19. Tan, Z. N., Zhang, F., Zhu, T., Xu, J., Wang, A. Y., Dixon, D., Li, L. S., Zhang, Q., Mohney, S. E., & Ruzylo, J. Bright and color-saturated emission from blue light-emitting diodes based on solution-processed colloidal nanocrystal quantum dots. *Nano Lett.* **7,** 3803-3807 (2007).

20. Yu, W. W., Wang, Y. A., & Peng, X. G. Formation and stability of size-, shape-, and structure-controlled CdTe nanocrystals: Ligand effects on monomers and nanocrystals. *Chem. Mater.* **15,** 4300-4308 (2003).

21. Li, J. J., Wang, Y. A., Guo, W. Z., Keay, J. C., Mishima, T. D., Johnson, M. B., & Peng, X. G. Large-scale synthesis of nearly monodisperse CdSe/CdS core/shell nanocrystals using air-stable reagents via successive ion layer adsorption and reaction. *J. Am. Chem. Soc.* **125,** 12567-12575 (2003).

22. Jasieniak, J. J. & Mulvaney, P. From Cd-rich to Se-rich - the manipulation of CdSe nanocrystal surface stoichiometry. *J. Am. Chem. Soc.* **129,** 2841-2848 (2007).

23. Peng, X. G., Schlamp, M. C., Kadavanich, A. V., & Alivisatos, A. P. Epitaxial growth of highly luminescent CdSe/CdS core/shell nanocrystals with photostability and electronic accessibility. *J. Am. Chem. Soc.* **119,** 7019-7029 (1997).

24. Hines, M. A. & Guyot-Sionnest, P. Synthesis and characterization of strongly luminescing ZnS-capped CdSe nanocrystals. *J. Phys. Chem.* **100,** 468-471 (1996).

25. Spanhel, L., Haase, M., Weller, H., & Henglein, A. Photochemistry of colloidal semiconductors. 20. Surface modification and stability of strong luminescing CdS particles. *J. Am. Chem. Soc.* **109,** 5649-5655 (1987).

26. Eychmuller, A., Mews, A., & Weller, H. A quantum-dot quantum-well - CdS/HgS/CdS. *Chem. Phys. Lett.* **208,** 59-62 (1993).

27. Talapin, D. V., Mekis, I., Gotzinger, S., Kornowski, A., Benson, O., & Weller, H. CdSe/CdS/ZnS and CdSe/ZnSe/ZnS core-shell-shell nanocrystals. *J. Phys. Chem. B* **108,** 18826-18831 (2004).

28. Xie, R. G., Kolb, U., Li, J. X., Basche, T., & Mews, A. Synthesis and characterization of highly luminescent CdSe-Core $CdS/Zn_{0.5}Cd_{0.5}S/ZnS$ multishell nanocrystals. *J. Am. Chem. Soc.* **127,** 7480-7488 (2005).

29. Kim, S., Fisher, B., Eisler, H. J., & Bawendi, M. Type-II quantum dots: CdTe/CdSe(core/shell) and CdSe/ZnTe(core/shell) heterostructures. *J. Am. Chem. Soc.* **125,** 11466-11467 (2003).

30. Wei, S. H. & Zunger, A. Predicted band-gap pressure coefficients of all diamond and zinc-blende semiconductors: Chemical trends. *Phys. Rev. B* **60,** 5404-5411 (1999).

31. Piryatinski, A., Ivanov, S. A., Tretiak, S., & Klimov, V. I. Effect of quantum and dielectric confinement on the exciton-exciton interaction energy in type II core/shell semiconductor nanocrystals. *Nano Lett.* **7,** 108-115 (2007).

32. Xie, R., Zhong, X., & Basche, T. Synthesis, characterization, and spectroscopy of type-II core/shell semiconductor nanocrystals with ZnTe cores. *Adv. Mater.* **17,** 2741-2745 (2005).

33. Chen, C. Y., Cheng, C. T., Yu, J. K., Pu, S. C., Cheng, Y. M., Chou, P. T., Chou, Y. H., & Chiu, H. T. Spectroscopy and femtosecond dynamics of type-II CdSe/ZnTe core-shell semiconductor synthesized via the CdO precursor. *J. Phys. Chem. B* **108,** 10687-10691 (2004).

34. Jeong, S., Achermann, M., Nanda, J., Lvanov, S., Klimov, V. I., & Hollingsworth, J. A. Effect of the thiol-thiolate equilibrium on the photophysical properties of aqueous CdSe/ZnS nanocrystal quantum dots. *J. Am. Chem. Soc.* **127,** 10126-10127 (2005).

35. Adachi, S. *Properties of Group-IV, III-V and II-VI Semiconductors*. John Wiley & Sons, Wes Sussex, England (2005).

36. Xie, R. G., Zhong, X. H., & Basche, T. Synthesis, characterization, and spectroscopy of type-II core/shell semiconductor nanocrystals with ZnTe cores. *Adv. Mater.* **17,** 2741-2745 (2005).

37. Talapin, D. V., Koeppe, R., Gotzinger, S., Kornowski, A., Lupton, J. M., Rogach, A. L., Benson, O., Feldmann, J., & Weller, H. Highly emissive colloidal

CdSe/CdS heterostructures of mixed dimensionality. *Nano Lett.* **3,** 1677-1681 (2003).

38. Manna, L., Wang, L. W., Cingolani, R., & Alivisatos, A. P. First-principles modeling of unpassivated and surfactant-passivated bulk facets of wurtzite CdSe: A model system for studying the anisotropic growth of CdSe nanocrystals. *J. Phys. Chem. B* **109,** 6183-6192 (2005).

39. Yeh, C. Y., Lu, Z. W., Froyen, S., & Zunger, A. Zinc-blende - wurtzite polytypism in semiconductors. *Phys. Rev. B* **46,** 10086-10097 (1992).

40. Ito, T. Simple criterion for wurtzite-zinc-blende polytypism in semiconductors. *Jpn. J. Appl. Phys.* **37,** L1217-L1220 (1998).

41. Lawaetz, P. Stability of the wurtzite structure. *Phys. Rev. B* **5,** 4039-4045 (1972).

42. Bawendi, M. G., Kortan, A. R., Steigerwald, M. L., & Brus, L. E. X-ray structural characterization of larger CdSe semiconductor clusters. *J. Chem. Phys.* **91,** 7282-7290 (1989).

43. Murray, C. B., Norris, D. J., & Bawendi, M. G. Synthesis and characterization of nearly monodisperse CdE (E = S, Se, Te) semiconductor nanocrystallites. *J. Am. Chem. Soc.* **115,** 8706-8715 (1993).

44. Wei, S. H. & Zhang, S. B. Structure stability and carrier localization in CdX (X = S, Se, Te) semiconductors. *Phys. Rev. B* **62,** 6944-6947 (2000).

45. Carbone, L., Kudera, S., Carlino, E., Parak, W. J., Giannini, C., Cingolani, R., & Manna, L. Multiple wurtzite twinning in CdTe nanocrystals induced by methylphosphonic acid. *J. Am. Chem. Soc.* **128,** 748-755 (2006).

46. Talapin, D. V., Nelson, J. H., Shevchenko, E. V., Aloni, S., Sadtler, B., & Alivisatos, A. P. Seeded growth of highly luminescent CdSe/CdS nanoheterostructures with rod and tetrapod morphologies. *Nano Lett.* **7,** 2951-2959 (2007).

47. Proffen, T. & Neder, R. B. DISCUS: a program for diffuse scattering and defect-structure simulation. *J. Appl. Crystallogr.* **30,** (1997).

48. Langford, J. I., Louer, D., & Scardi, P. Effect of a crystallite size distribution on X-ray diffraction line profiles and whole-powder-pattern fitting. *J. Appl. Crystallogr.* **33,** 964-974 (2000).

49. Balasubramanian, S., Ceder, G., & Kolenbrander, K. D. Three-dimensional epitaxy: Thermodynamic stability range of coherent germanium nanocrystallites in silicon. *J. Appl. Phys.* **79,** 4132-4136 (1996).

50. Van de Walle, C. G. Band Lineups and Deformation Potentials in the Model-Solid Theory. *Phys. Rev. B* **39,** 1871-1883 (1989).

51. Efros, A. L. & Efros, A. L. Interband absorption of light in a semiconductor sphere. *Sov. Phys. Semiconduct.* **16,** 772-775 (1982).

52. He, L. X., Bester, G., & Zunger, A. Strain-induced interfacial hole localization in self-assembled quantum dots: Compressive InAs/GaAs versus tensile InAs/InSb. *Phys. Rev. B* **70,** 235316 (2004).

53. Zhang, J. Z., Zhao, Y. S., & Palosz, B. Comparative studies of compressibility between nanocrystalline and bulk nickel. *Appl. Phys. Lett.* **90,** (2007).

54. Goldstein, A. N., Echer, C. M., & Alivisatos, A. P. Melting in semiconductor nanocrystals. *Science* **256,** 1425-1427 (1992).

55. Zhang, X. Y., Sharma, P., & Johnson, H. T. Quantum confinement induced strain in quantum dots. *Phys. Rev. B* **75,** (2007).

56. Meulenberg, R. W., Jennings, T., & Strouse, G. F. Compressive and tensile stress in colloidal CdSe semiconductor quantum dots. *Phys. Rev. B* **70,** (2004).

57. Balet, L. P., Ivanov, S. A., Piryatinski, A., Achermann, M., & Klimov, V. I. Inverted core/shell nanocrystals continuously tunable between type-I and type-II localization regimes. *Nano Lett.* **4,** 1485-1488 (2004).

58. Ivanov, S. A., Piryatinski, A., Nanda, J., Tretiak, S., Zavadil, K. R., Wallace, W. O., Werder, D., & Klimov, V. I. Type-II core/shell CdS/ZnSe nanocrystals: synthesis, electronic structures, and spectroscopic properties. *J. Am. Chem. Soc.* **128,** 11708-11719 (2007).

59. Toropov, A. A., Sedova, I. V., Lyublinskaya, O. G., Sorokin, S. V., Sitnikova, A. A., Ivanov, S. V., Bergman, J. P., Monemar, B., Donatini, F., & Dang, L. S. Coexistence of type-I and type-II band lineups in Cd(Te,Se)/ZnSe quantum-dot structures. *Appl. Phys. Lett.* **89,** 123110-123112 (2006).

60. Zhong, X. H., Han, M. Y., Dong, Z., White, T. J., & Knoll, W. Composition-tunable $Zn_xCd_{1-x}Se$ nanocrystals with high luminescence and stability. *J. Am. Chem. Soc.* **125,** 8589-8594 (2003).

61. Shaw, D. Diffusion mechanisms in II-VI materials. *J. Cryst. Growth* **86,** 778-796 (1988).

62. Chan, E. M., Marcus, M. A., Fakra, S., ElNaggar, M., Mathies, R. A., & Alivisatos, A. P. Millisecond kinetics of nanocrystal cation exchange using microfluidic X-ray absorption spectroscopy. *J. Phys. Chem. A* **111,** 12210-12215 (2007).

63. Son, D. H., Hughes, S. M., Yin, Y. D., & Alivisatos, A. P. Cation exchange reactions in ionic nanocrystals. *Science* **306,** 1009-1012 (2004).

64. Jeong, U., Xia, Y., & Yin, Y. D. Large-scale synthesis of single-crystal CdSe nanowires through a cation-exchange route. *Chem. Phys. Lett.* **416,** 246-250 (2005).

65. Camargo, P. H. C., Lee, Y. H., Jeong, U., Zou, Z., & Xia, Y. Cation exchange: a simple and versatile route to inorganic colloidal spheres with the same size but different compositions and properties. *Langmuir* **23,** 2985-2992 (2007).

66. Hatami, F., Masselink, W. T., Schrottke, L., Tomm, J. W., Talalaev, V., Kristukat, C., & Goni, A. R. InP quantum dots embedded in GaP: Optical properties and carrier dynamics. *Phys. Rev. B* **67,** 085306-085313 (2003).

67. Lee, C. J., Mizel, A., Banin, U., Cohen, M. L., & Alivisatos, A. P. Observation of pressure-induced direct-to-indirect band gap transition in InP nanocrystals. *J. Chem. Phys.* **113,** 2016-2020 (2000).

CHAPTER 5

Quantum Dot Surface Modification and Size Minimization

The colloidal and surface properties of quantum dots play a major role in their interaction with biological systems and strongly impact their properties as imaging agents for molecular, cellular, and *in vivo* animal imaging. Chapters 2-4 in this thesis describe the engineering of quantum dot optical properties through complex chemical syntheses, resulting in highly ordered, uniform, colloidal particles. However these state-of-the-art synthesis protocols are performed in nonpolar coordinating solvents, yielding nonpolar colloids insoluble in biological buffers. Phase transfer of these nanoparticles to aqueous solution has been a major limiting factor in the successful exploitation of the unparalleled optical properties of these nanocrystals. The phase transfer methods are either based on the displacement of native nonpolar ligands with small-molecule coordinating ligands or the micellar encapsulation of hydrophobic quantum dots in amphiphilic polymers or lipids (Figure 2.21). However it is still not clear how these different surface coating molecules affect the optical, colloidal, and chemical properties of the solubilized quantum dots. This chapter reports the systematic evaluation of the effects of surface coating chemistry on the hydrodynamic size, fluorescence quantum yield, photostability, and chemical stability of water-soluble quantum dots. A trade-off between minimum size and overall stability is observed, and is overcome through the rational design of a multidentate, multifunctional ligand.

5.1 Comparison of Ligand and Polymer Coatings

For colloidal nanocrystals, two independent interfaces play crucial roles in dictating nanoparticle properties (Figure 5.1). The nanocrystal-organic surfactant interface plays an important role in nanocrystal structure and optical and electronic properties. The interface between the organic molecules stabilizing the quantum dot dispersion and the surrounding medium largely influences the colloidal properties of the nanoparticles, such as the hydrodynamic size, charge and intermolecular/interparticle interactions. These interfaces can be intimately linked, particularly if a single molecule is responsible for both surfaces. For example, hydrophilic thiols bind to quantum dot surface atoms and simultaneously stabilize quantum dot dispersions in polar solvents, and as such, are responsible for the surface-related optical properties of the quantum dot and also for surface charge and possible aggregation. On the other hand, quantum dots with hydrophobic organic ligands can be encapsulated in a variety of surfactants for stabilization in polar solvents, allowing the optical properties to be dictated by the original underlying ligands, and the colloidal properties can be independently tuned by the encapsulating surfactant. Herein, hydrophobic quantum dots are modified with a variety of hydrophilic ligands and polymers to study the relationship between these two interfaces.

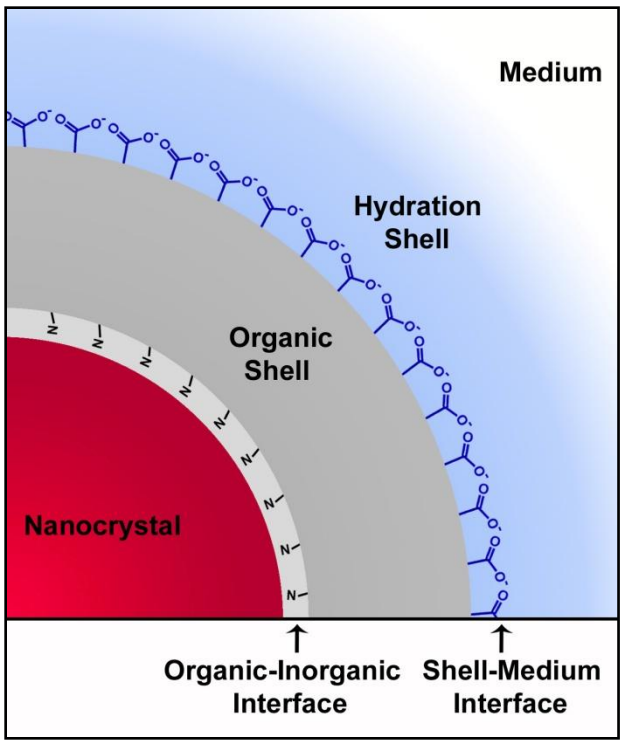

Figure 5.1: Schematic of a quantum dot dispersed in aqueous medium. The inorganic quantum dot surface is directly bonded to organic coordinating molecules. These ligands, and any surrounding polymeric coating, dictate the thickness of the organic shell, which provides a protective barrier from aqueous solutes. The outward facing organic molecules influence the colloidal properties of the quantum dots, such as surface charge and hydration shell-dependent hydrodynamic size.

Five different water solubilization schemes were optimized for this work (Figure 5.2). Using bifunctional ligands (monodentate and polydentate), polymeric encapsulation (graft, diblock polymers and lipids), and different surface colloidal stabilizations (anionic, cationic, and neutral polymers), the colloidal, interfacial, and optical properties could be modulated to produce distinct and useful properties. For each of these preparations, a variety of phase transfer methods were tested to maximize quantum dot quality and encapsulation efficiency, ranging from extractions to solvent evaporations and dialysis. Some of these techniques are modifications of those reported in the literature.[1-6] Ligand exchange using hydrophilic thiols, like

mercaptopropionic acid, is still the most widely used phase transfer technique for quantum dots, owing to its simplicity, speed, and the consistent production of single, isolated hydrophilic nanocrystals.[1] However the resulting particles are notoriously prone to aggregation over time due to the lability of the thiol-quantum dot bond.[7,8] Ligand exchange using multidentate polyethylenimine was previously reported to result in nanocrystals soluble in a variety of polar solvents like water and ethanol.[2] Three different strategies were implemented for encapsulation of quantum dots in amphiphilic polymers, each of which allowed the retention of the hydrophobic ligands on the nanocrystal surface. Amphipol encapsulation was first reported by Bruchez and coworkers,[9] and later studied in greater depth by Parak and coworkers.[5] Lipid-PEG encapsulation of nanocrystals was reported by Benoit Dubertret and coworkers,[3] and block copolymer encapsulation of hydrophobic nanoparticles was reported by Nie[6] and Andrew Taton.,[10] each of which resulted in highly stable colloidal dispersions. In assessing each of these coating and encapsulation strategies, it is hypothesized that thicker organic shells and polymeric surface coatings will enhance stability.

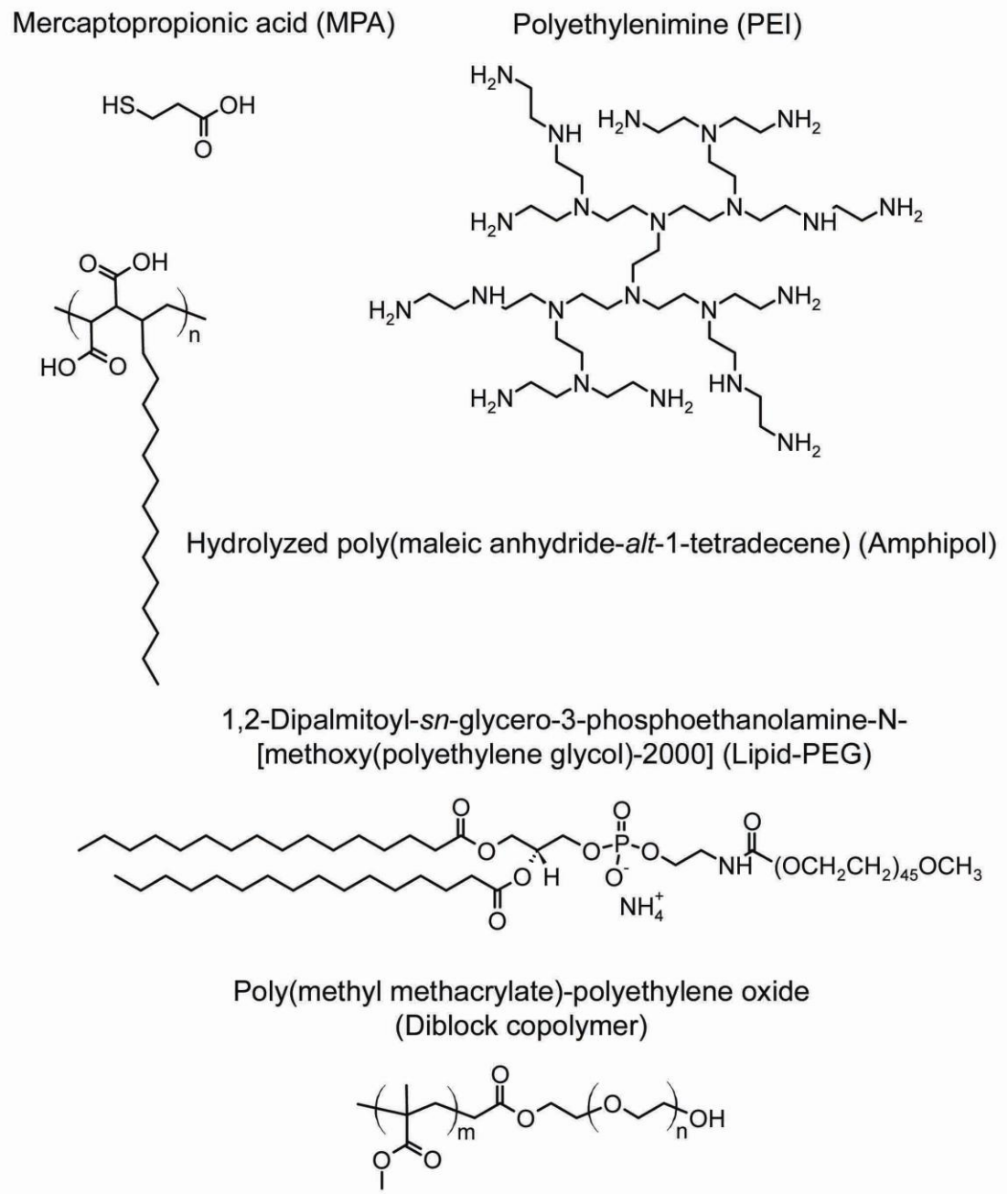

Figure 5.2: Small molecules, multidentate ligands, and amphiphilic polymers used for quantum dot coating. Formal chemical names are given, along with abbreviation in parentheses.

5.1.1 Experimental Methods for Ligand Exchange and Polymer Coating. Cadmium selenide quantum dots (4.5 nm) were synthesized in a coordinating solvent and capped with a shell of CdS (2 monolayers) and then ZnS (2 monolayers) in a solvent of

octadecylamine (ODA) / octadecene (ODE), following procedures outlined in Chapters 3 and 4.[11-14] These (CdSe)CdS/ZnS particles have been shown to be highly luminescent and have greater photostability than CdSe cores, (CdSe)CdS (core)shells, and (CdSe)ZnS quantum dots, presumably due to improved lattice matching between the highly strained CdSe core and ZnS shell with interim layers of CdS.[12,13,15,16] These nanocrystals were stored as a crude mixture at 4ºC and purified using repeated extractions in hexane/methanol, followed by precipitations with acetone prior to use. The quantum dots were transferred to water using 5 different ligands or polymers, and each phase-transfer protocol was independently optimized to maximize colloidal stability and quantum yield.

5.1.1.1 Mercaptopropionic Acid-Coated Quantum Dots: A large excess of mercaptopropionic acid (MPA; 300 µL) was added to a 1 µM solution of quantum dots in chloroform (1 mL) and stirred overnight at room temperature. The nanocrystals were isolated from the opaque suspension via centrifugation, and the pellet was washed twice with chloroform to remove excess ODA. After resuspension in a 1.1 mM aqueous solution of MPA (pH 10), the nanocrystals were incubated at room temperature for 24 hours to finalize ligand exchange. The particles were centrifuged at 14,000g for 15 minutes to remove aggregates, dialyzed repeatedly against 50 mM borate buffer (pH 8.5), and then stored at 4ºC in the dark.

5.1.1.2 Polyethylenimine-Coated Quantum Dots: Polyethylenimine (PEI; M_n 10,000 Da) was mixed with a nanocrystal dispersion in chloroform, and the solvent was slowly evaporated. The resulting dried film was dissolved in deionized water and the solution was centrifuged to yield a clear supernatant containing a white precipitate,

probably composed of displaced ODA. Unbound PEI was removed via repeated dialysis against deionized water, and then 500 mM borate buffer was added to a final concentration of 50 mM.

5.1.1.3 Amphipol Encapsulated Quantum Dots: Poly(maleic anhydride-*alt*-1-tetradecene) (Amphipol; M_n 7300 Da) was hydrolyzed at 80ºC in water (5% w/v) for 24 hours and then lyophilized, yielding an amphiphilic polycarboxylate. This protonated polymer was dissolved in chloroform and mixed with quantum dots at a quantum dot:polymer chain ratio of 500:1. The solvent was slowly evaporated under a slight vacuum. The dried film was resuspended in borate buffer, centrifuged (14,000g, 15 minutes) to remove aggregates, and purified from excess polymer via ultracentrifugation (540,000g, 1 hour). To PEGylate the carboxylic acids on these nanocrystals, the particles were mixed with monoamine-terminated polyethylene glycol (amino-PEG; 2000 Da) at a quantum dot:PEG ratio of 1:3000, and then excess *N*-(3-dimethylaminopropyl)-*N*'-ethylcarbodiimide hydrochloride (EDC) was added (quantum dot:EDC = 1:5000). After 24 hours at room temperature, excess EDC was quenched with the addition of 1-thioglycerol, and the quantum dots were purified via ultracentrifugation.

5.1.1.4 Lipid Encapsulated Quantum Dots: Quantum dots and 1,2-dipalmitoyl-*sn*-glycero-3-phosphoethanolamine-*N*-[methoxy(polyethylene glycol)-2000] (Lipid-PEG) were mixed in a 1:5000 molar ratio in chloroform, and the solvent was slowly evaporated under a slight vacuum. The nanoparticles were resuspended in deionized water and purified via ultracentrifugation as described above.

5.1.1.5 Amphiphilic Diblock Copolymer Coated Quantum Dots: Quantum dots and poly(methyl methacrylate)-polyethylene oxide diblock copolymer (PMMA-PEO; 20,300 KDa; 43% PMMA, 57% PEO) were dissolved in THF, mixed, and then dialyzed repeatedly against deionized water using a low molecular weight cutoff membrane (2000 Da). The resulting aqueous solution was then subjected to several cycles of centrifugation (14,000g, 15 minutes), and then ultracentrifugation (540,000g, 1 hour) to remove aggregates and excess polymer. Finally, the nanoparticles were resuspended in borate buffer.

5.1.2 Optical and Colloidal Characterization. The inorganic (CdSe)CdS/ZnS nanocrystals synthesized herein had a roughly spherical shape with a 6.5 nm diameter and a fluorescent emission peak at 630 nm (Figure 5.3), 24 nm full-width-at-half-maximum, and nearly 80% quantum yield in chloroform. After phase transfer to water, the spectral positions and features were generally unchanged, but the quantum efficiences were strongly dependent on the coating method (Table 5.1).

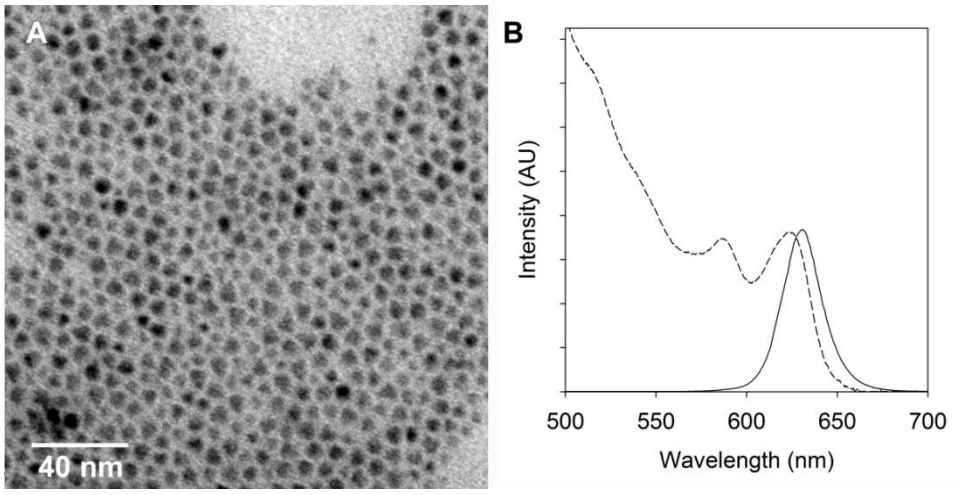

Figure 5.3: TEM (A) and optical spectra (B) for the quantum dots used in stability assays. Fluorescence spectra (solid line) and absorption spectra (dotted line) are plotted in arbitrary units of intensity (AU).

Table 5.1: Quantum yield, hydrodynamic diameter, and zeta potential of quantum dots with various ligands and coatings.

Quantum Dot Coating	Quantum Yield[a]	Hydrodynamic Diameter (nm)[b]	Zeta Potential (mV)[c]
Octadecylamine (in hexane)	79.3%	~7	n.a.
Mercaptopropionic acid	63.4%	6-8	-35.4 ± 1.8
Polyethylenimine	43.0%	10-12	17.9 ± 0.9
Amphipol	64.1%	~18	-34.7 ± 2.1
Lipid-PEG	52.8%	~30	-5.07 ± 1.09
Diblock copolymer	20.9%	~35	-17.4 ± 0.7

[a] Relative to the organic dye Atto 610
[b] Determined via dynamic light scattering
[c] Reported as zeta potential ± standard deviation

Dynamic light scattering (DLS) data, transmission electron micrographs, and proposed self-assembly schematics are depicted in Figures 5.4 to 5.8 for comparison of the five different encapsulation and coating strategies. Zeta potential values and average hydrodynamic sizes are summarized in Table 5.1. Whereas DLS and zeta potential data are reproducible and fairly quantitative, each type of quantum dot coating behaves differently when spread on a TEM grid and also seems to interact differently with the phosphotungstic acid stain, probably due to differences in surface charge and polymer characteristics. Therefore TEM is only used as a qualitative method for evaluating nanoparticle structure. Quantum dots coated with MPA are the smallest overall (6-8 nm hydrodynamic diameter) due to stabilization by a single monolayer of hydrophilic ligand. They are also negatively charged due to deprotonation of MPA at neutral and basic pH, and are highly clustered when spread on a TEM grid (Figure 5.4). Quantum dots coated with PEI are larger by DLS measurements (10-12 nm), suggesting that the multidentate polymeric coating

contributes significantly to its size. These hydrodynamic dimensions agree well with a previous report of quantum dots encapsulated in PEI (Figure 5.5).[2] PEI-coated nanocrystals are highly positive in charge, even in basic solution, which is not surprising, considering PEI contains primary, secondary, and tertiary amines capable of buffering over a wide pH range.[17,18]

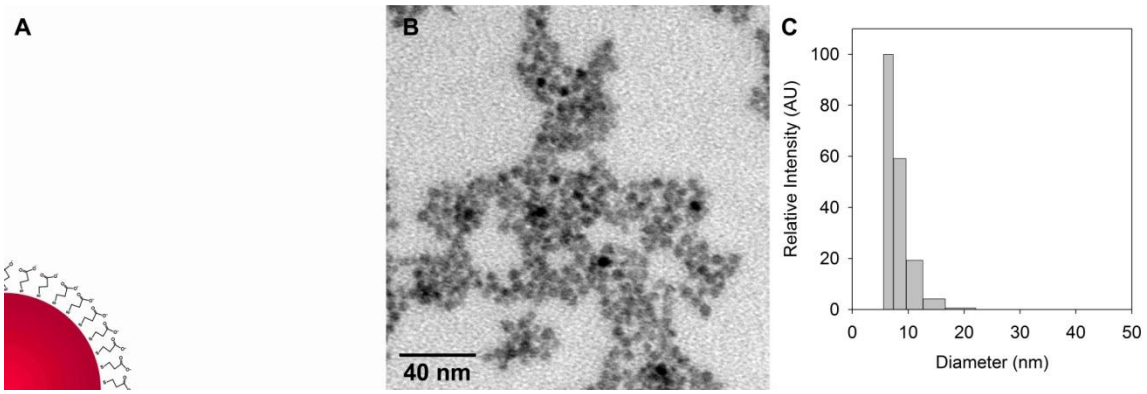

Figure 5.4: Structural schematic (A), TEM (B), and DLS spectrum for MPA-coated quantum dots.

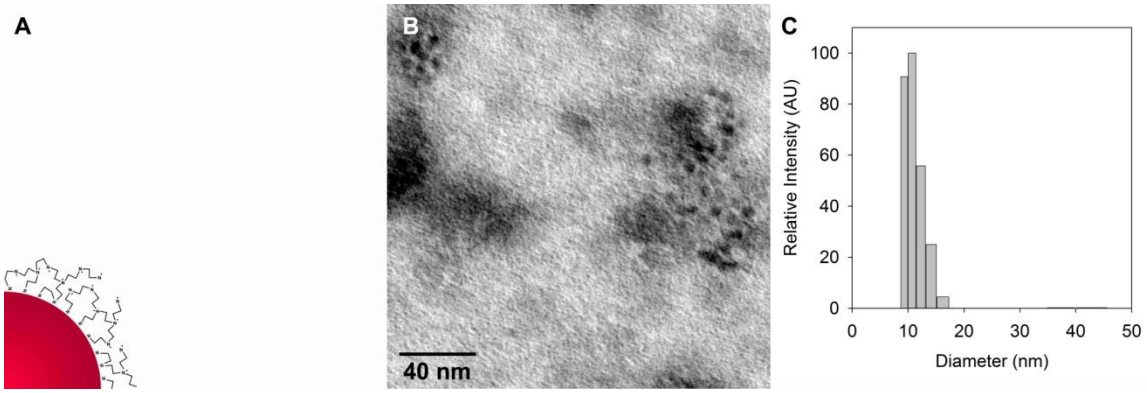

Figure 5.5: Structural schematic (A), TEM stained with phosphotungstic acid(B), and DLS spectrum for PEI-coated quantum dots.

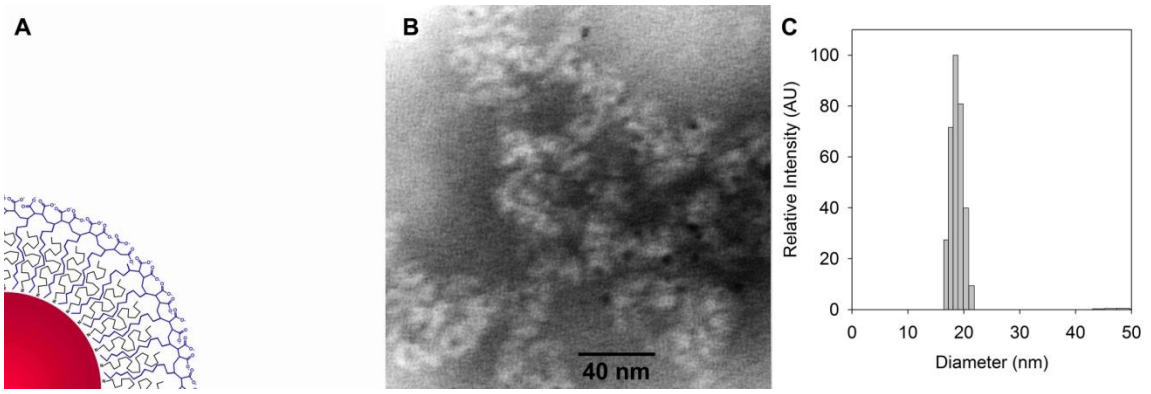

Figure 5.6: Structural schematic (A), TEM stained with phosphotungstic acid(B), and DLS spectrum for amphipol-coated quantum dots.

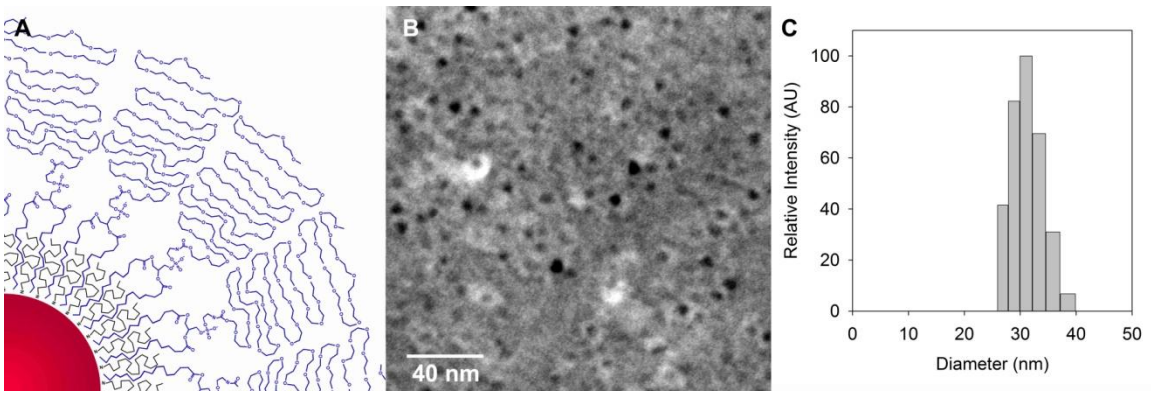

Figure 5.7: Structural schematic (A), TEM stained with phosphotungstic acid(B), and DLS spectrum for lipid-PEG-coated quantum dots.

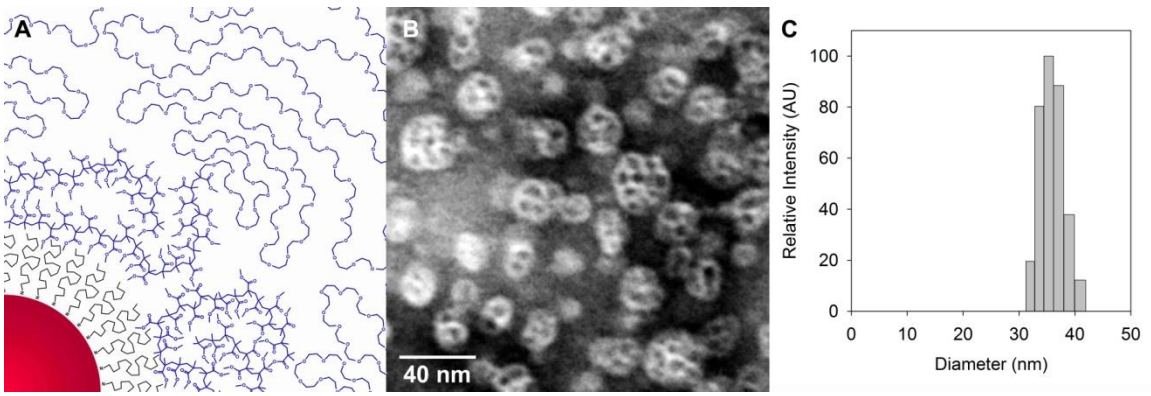

Figure 5.8: Structural schematic (A), TEM stained with phosphotungstic acid(B), and DLS spectrum for diblock copolymer-coated quantum dots.

Compared to quantum dots coated with monodentate and polydentate ligands, all of the quantum dots encapsulated in amphiphilic polymers are measured to be significantly larger via DLS and are surrounded by visible shells of low electron density in TEM micrographs. There is a correlation between the size of the quantum dots on TEM grids and their size from DLS measurements, but this relationship is not quantitative, most likely due to the fact that nanoparticles and their surrounding polymers adopt different conformations when spread and dried as thin films, compared to those in aqueous solution. This is also undoubtedly a result of the fundamental difference between nanoparticle hydrodynamic size measured by DLS and the electron density observed in TEM. Quantum dots coated with amphipol are roughly 18 nm in diameter by DLS measurements, and negatively charged (Figure 5.6). Quantum dots coated with lipid-PEG are significantly larger (30 nm) and nearly neutral (Figure 5.7). Coating quantum dots with the amphiphilic diblock copolymer generates even larger particles (~35 nm), encapsulating clusters of 2-10 nanocrystals within single nanoparticles, with thick polymeric shells in electron micrographs (Figure 5.8). These nanoparticles have a slight negative charge, presumably due to a terminal hydroxyl group on the PEG, unlike the terminal methoxy group of the lipid-PEG quantum dots.

5.1.3 Optical and Structural Stability Assays. II-VI semiconductors are labile toward oxidation due to the high oxidation potential of reduced chalcogens. Thereby, II-VI nanocrystals may be etched and fully dissolved in solution with oxidizing agents or acids, an effect which is catalyzed by illumination at wavelengths shorter than the band edge absorption. An example of these chemical reactions is

$$[\mathrm{CdSe}]_n + 2\mathrm{O}_2 \rightarrow [\mathrm{CdSe}]_{n-1} + \mathrm{Cd}^{2+} + \mathrm{SeO}_4^{2-} \qquad \textbf{Equation 5.1}$$

These degradation mechanisms are further studied in Chapter 7.

5.1.3.1 Photochemical oxidation. Quantum dots were photocatalytically etched by soluble oxygen. Quantum dots in borate buffer (74 nM, 800 µL) were transferred to a 1 mL glass cuvette, resulting in a dead volume of 200 µL of air. Similar to previously reported photooxidation experiments,[7,12,19,20] cuvettes were sealed and positioned in front of a 6-watt ultraviolet lamp (UVGL-58, UVP) with 254 nm illumination and spatially homogeneous photon flux, as verified using a power meter. UVC illumination in the presence of oxygen caused all quantum dot samples to gradually decrease in fluorescence quantum efficiency, and both the fluorescence and absorption spectra blue-shifted, indicating oxidative etching of the surfaces of the quantum dots (Figure 5.9). However shortly after the onset of illumination, quantum dots coated with MPA and PEI increased in quantum yield (by a factor of 4-10%), probably due to a photoenhancement effect that has been commonly described in the literature.[21,22] Interestingly, none of the amphiphilic polymer-encapsulated quantum dots underwent detectable photoactivation, suggesting that the differences in phase transfer techniques were related to this phenomenon. Quantum yield is highly sensitive to the surface of the nanocrystal, especially with respect to ligand chemistry, and the original hydrophobic capping ligands on MPA and PEI-coated quantum dots were displaced for hydrophilic ones. This photoenhancement effect may be due to a surface rearrangement of ligands and/or photocatalytic annealing of surface atoms to repair defects and recombination centers that formed during a disordered ligand exchange.

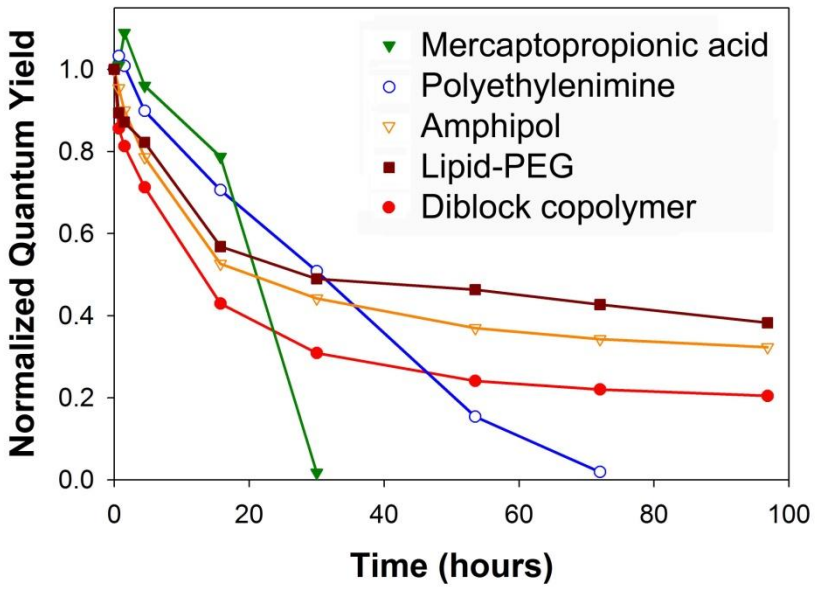

Figure 5.9: Photooxidation of quantum dots in aqueous solution. All nanocrystal solutions were originally the same concentration, and quantum yield was measured periodically during exposure to ultraviolet light. Before plotting, the quantum yield for each quantum dot type was normalized to its initial value. At the 30 hour time point, MPA-coated quantum dots had precipitated from solution. Example spectra of a blue-shift in emission are given in Figure 5.10.

All quantum dot samples decreased substantially in quantum yield over the ~97 hour assay. Within 30 hours of UV exposure, MPA-coated quantum dots precipitated, which is in accord with previous reports of photooxidation of the thiol ligand, resulting in colloidal instability and aggregation.[7] PEI-coated quantum dots did not precipitate, but instead photodegraded and dissolved after a substantial blue-shift in emission (Figure 5.10). Amphiphilic polymer-encapsulated quantum dots also photobleached and blue-shifted in fluorescence, but at a much slower rate than MPA- and PEI-coated nanocrystals. This can be attributed to the hydrophobic bilayer surrounding each nanocrystal, which serves as a steric barrier to oxygen diffusion. PEI coated quantum dots were also surrounded by a polymer but it was apparently porous enough to allow oxygen diffusion to the nanocrystal surface, despite strong multivalent attachment. The amphiphilic polymer-stabilized quantum dots appeared

to undergo two separate phases of oxidation, beginning with an initial steep and nearly linear decline in quantum yield, which then levelled out to a very slow decline in quantum yield. PEI-coated quantum dots, on the other hand, demonstrated a nearly continuous, linear decline in quantum yield until complete photooxidation occurred. It is possible that the two phases observed for polymer encapsulated quantum dots were caused by the presence of two subpopulations of particles in solution, one that was weakly protected from soluble oxygen, and another that was strongly protected. Quantum dots with defects in their polymeric shells could be innately more susceptible to photooxidation due to a higher local concentration of oxygen. However this rationale is not likely the cause of this biphasic trend, as the photoluminescence spectra were homogeneous and displayed a similar peak width throughout degradation. Alternatively, it is possible that depletion of soluble oxygen decreased the rate of photooxidation. This is also unlikely, as quantum dot solutions were purposely prepared to be very dilute, and the amount of soluble oxygen was sufficient to quickly and completely photodegrade PEI-coated quantum dots. The most plausible explanation for this reduction in etching speed is due to trapping of organic ligands, polymers, and inorganic degradation products in the quantum dot micelle microenvironment as the degradation continued over time. This would result in a larger steric barrier to oxidation over time, unlike MPA- and PEI-coated quantum dots, which have no physical means of encapsulating this organic and inorganic debris.

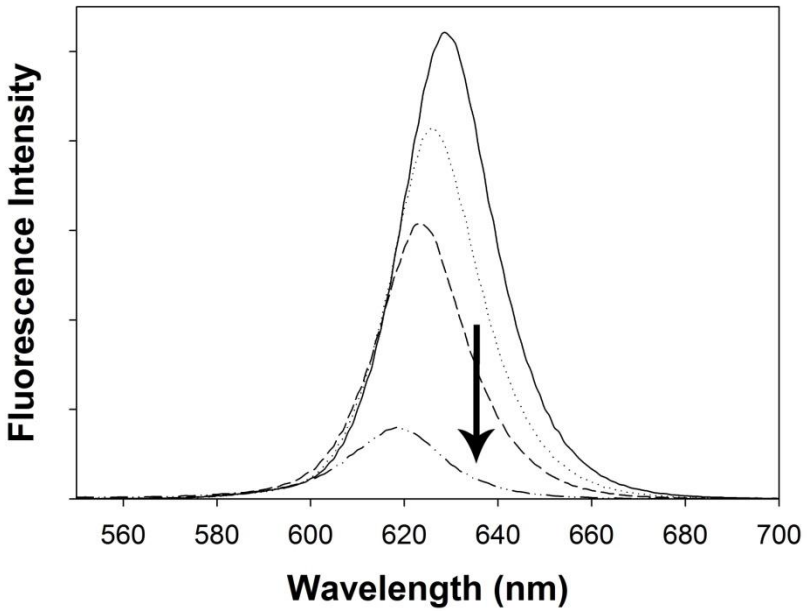

Figure 5.10: Fluorescence spectra of PEI-coated quantum dots during the photooxidation experiment. Over time, the nanocrystals decreased in quantum yield and the fluorescence maximum blue-shifted. The arrow indicates increasing time.

It should be noted that all of these quantum dots were exceptionally photostable under illumination conditions commonly used for biological experiments. Extremely high photon fluxes per nanoparticle and UVC excitation are unrealistic experimental conditions for nearly all biological assays implementing fluorescent probes, and were only used to obtain long-term stability information over a reasonable period of time. Indeed, these quantum dots demonstrated exceptional photostability in a microscopic setup with 125 mW laser excitation at 488 nm (data not shown).

5.1.3.2 Chemical Oxidation. Quantum dots were etched in aqueous solution in the absence of light using hydrogen peroxide. A solution of quantum dots (900 µL, 370 nM) in 50 mM borate buffer was transferred to a cuvette, 100 µL of 3% H_2O_2 (w/v) was added, the cuvette was sealed to prevent solvent evaporation, and absorption spectra were obtained periodically. The trends observed for photooxidation were

also observed for hydrogen peroxide-mediated oxidation (Figure 5.11). For these experiments, optical density was found to be a more appropriate measure of quantum dot etching than quantum yield, as the quantum efficiency of PEI and MPA-coated quantum dots sharply declined following exposure to hydrogen peroxide. MPA-coated quantum dots again quickly precipitated due to oxidation of the hydrophilic thiol ligands. These quantum dots could be resuspended with the addition of excess MPA ligand and adjustment of the pH to ~11. However, over time, these quantum dots again precipitated due to oxidation of the ligands caused by residual hydrogen peroxide. PEI-coated quantum dots rapidly oxidized and completely dissolved in solution, yielding a clear, colorless liquid (Figure 5.12). Quantum dots coated in amphiphilic polymers were much more resistant to oxidation, especially ones coated with lipid-PEG or the amphiphilic diblock copolymer, which retained bright fluorescence and only demonstrated modest etching. In contrast, amphipol-encapsulated quantum dots were more prone to chemical oxidation, and eventually completely dissolved. This experiment uncovered a chemical instability of amphipol-coated quantum dots that would have otherwise gone unnoticed from photooxidation experiments. This disparity between photooxidation and H_2O_2-mediated oxidation suggests that the limiting factor for oxidation of alkylated polycarboxylate-encapsulated quantum dots is the local concentration of oxidant around the quantum dot surface, rather than the photocatalytic rate.

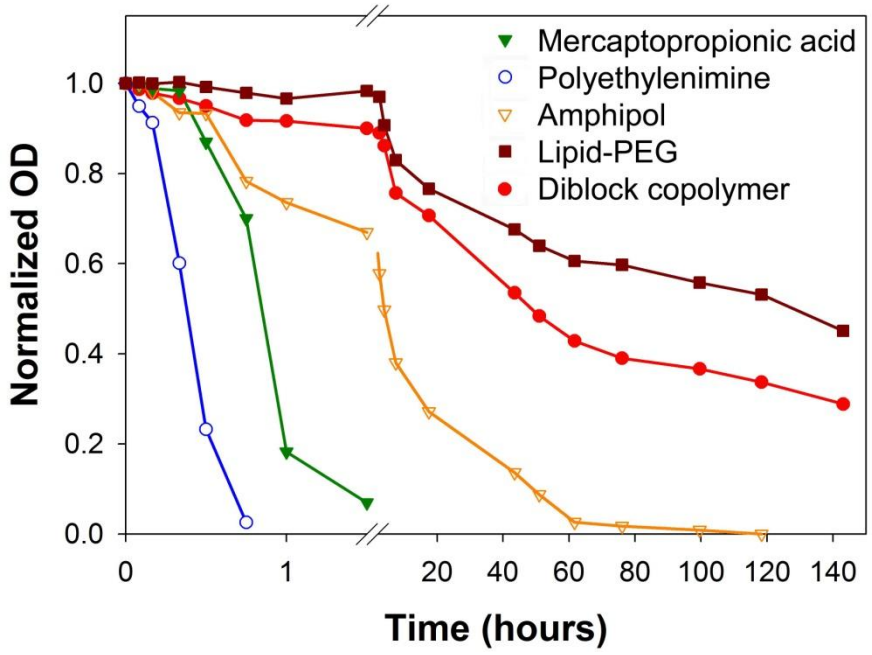

Figure 5.11: Hydrogen peroxide-mediated degradation of quantum dots in aqueous solution. All quantum dots were initially the same concentration, and a decrease in optical density (OD) at 622 nm correlates with a blue-shift in the absorption edge and gradual etching.

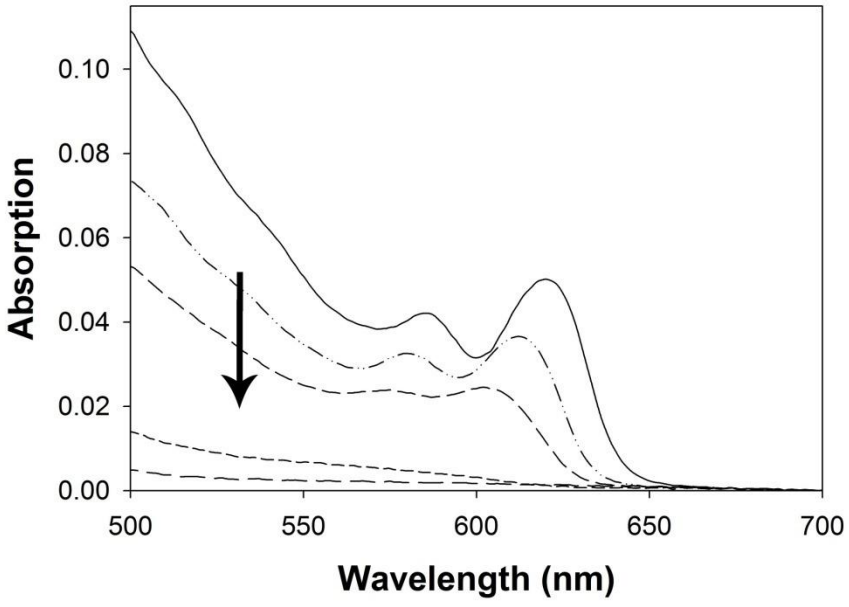

Figure 5.12: Absorption spectra of PEI-coated quantum dots during hydrogen peroxide-mediated oxidation. A blue-shift of the absorption onset and decrease in optical density are indicative of gradual etching. Increasing time is indicated by the arrow.

To determine if this lability toward oxidation was due to the lack of a surrounding PEG layer that could provide a diffusion barrier to chemical etchants, amphipol-encapsulated quantum dots were covalently modified with 2000 Da PEG, in an attempt to react all surface carboxylates. Nearly complete neutralization of surface charge and an increase of hydrodynamic radius (33 nm) suggested that this reaction was successful (Figure 5.13). This modification, however, made negligible impact on oxidation rate (Figure 5.14), so other factors must have been responsible for this instability toward oxidation (see Section 5.1.4).

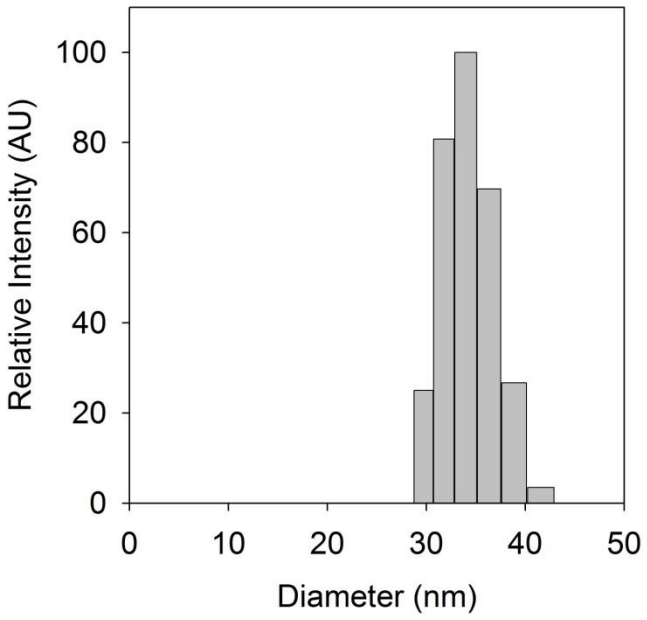

Figure 5.13: Dynamic light scattering data for amphipol quantum dots modified with 2000 Da PEG. The zeta potential before conjugation was -34.7 ± 2.1 mV, and -6.49 ± 0.41 mV after modification.

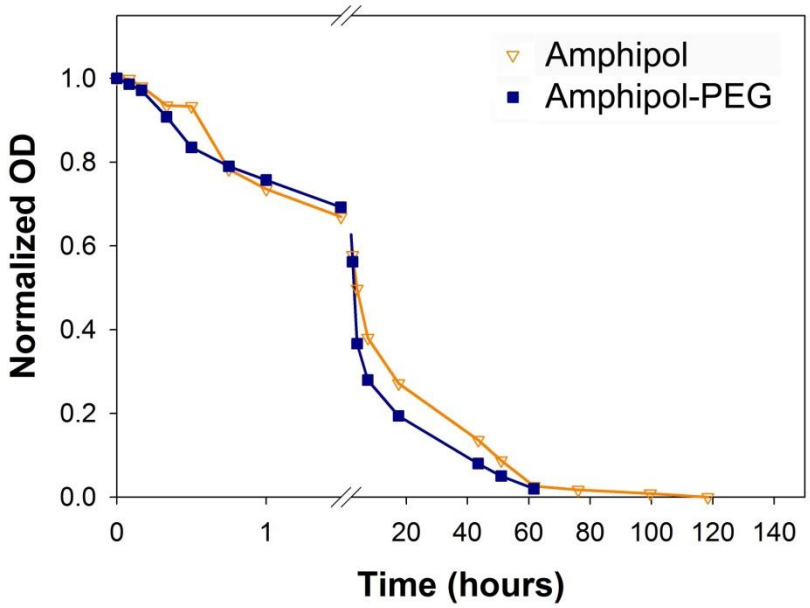

Figure 5.14: Comparison of hydrogen peroxide-mediated etching of quantum dots encapsulated in amphipol, before and after coupling to PEG.

The quick oxidation of PEI-coated quantum dots again demonstrated that polymeric or multidentate encapsulation alone is not sufficient for strong protection of the nanocrystal surface, and a dense packing of organic molecules, which is possible with hydrophobic bilayers, may be necessary to prevent solutes from reaching the crystal facets. Both PEI-coated quantum dots and quantum dots encapsulated by amphiphilic polymers were coordinated directly to amine-containing ligands. The only major difference between the two strategies is the absence of a hydrophobic bilayer on the PEI-coated quantum dots. The presence of amines and oxygen has been shown to etch the surfaces of cadmium selenide[23] and lead sulfide nanocrystals,[24] sometimes at specific facets. It is possible that an excess of amines could enhance chemical oxidation and photocatalytic oxidation. As PEI-coated quantum dots are not only passivated by amines, but are also stabilized colloidally by

amines, there must be a local excess of these basic functional groups surrounding the quantum dot surface that could serve to catalyze oxidation.

5.1.3.3 Acid Etching. Quantum dots were acid-etched in borate buffer. The nanocrystals were diluted to 370 nM, and 900 µL of this solution was transferred to a cuvette. Then 100 µL of 1 M HCl in water was added, and the resulting pH was verified to be 1. The cuvette was sealed to prevent solvent evaporation, and absorption spectra were obtained periodically. All of the quantum dots tested were stable in neutral and basic aqueous solution, however strong acids can dissolve semiconductors, and have been used for controlled surface etching.[25] Dissolution of quantum dots in 0.1 M hydrochloric acid resulted in degradation of all quantum dots tested over time except for PEI-coated nanocrystals (Figure 5.15 and 5.16). Quantum dots coated in anionically stabilized MPA or amphipol immediately aggregated and slowly precipitated. MPA-coated quantum dots could be resuspended by increasing the pH to ~11 with sodium hydroxide. Quantum dots encapsulated in amphipols could also be resuspended, but permanent aggregation was evident, as mild centrifugation generated quantum dot-containing pellets. Modification of these amphipol-coated nanocrystals with PEG increased their stability toward acid treatment, but these quantum dots also eventually precipitated. Lipid-encapsulated and diblock copolymer-coated quantum dots were much more resistant to acid etching, but slowly degraded and eventually lost their fluorescence.

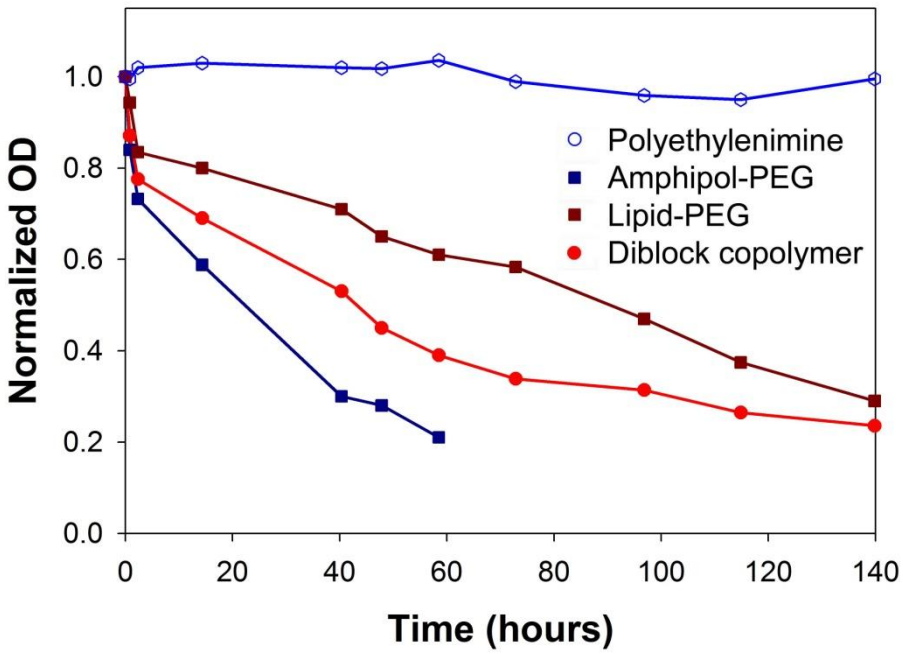

Figure 5.15: Acid-induced etching of quantum dots. Quantum dots were suspended in an aqueous solution of pH 1 and monitored via absorption spectrophometry. Quantum dots coated with MPA or amphipol are not shown because they immediately aggregated. All quantum dot types degraded except for PEI-coated quantum dots. After 60 minutes, PEGylated quantum dots coated with amphipol precipitated.

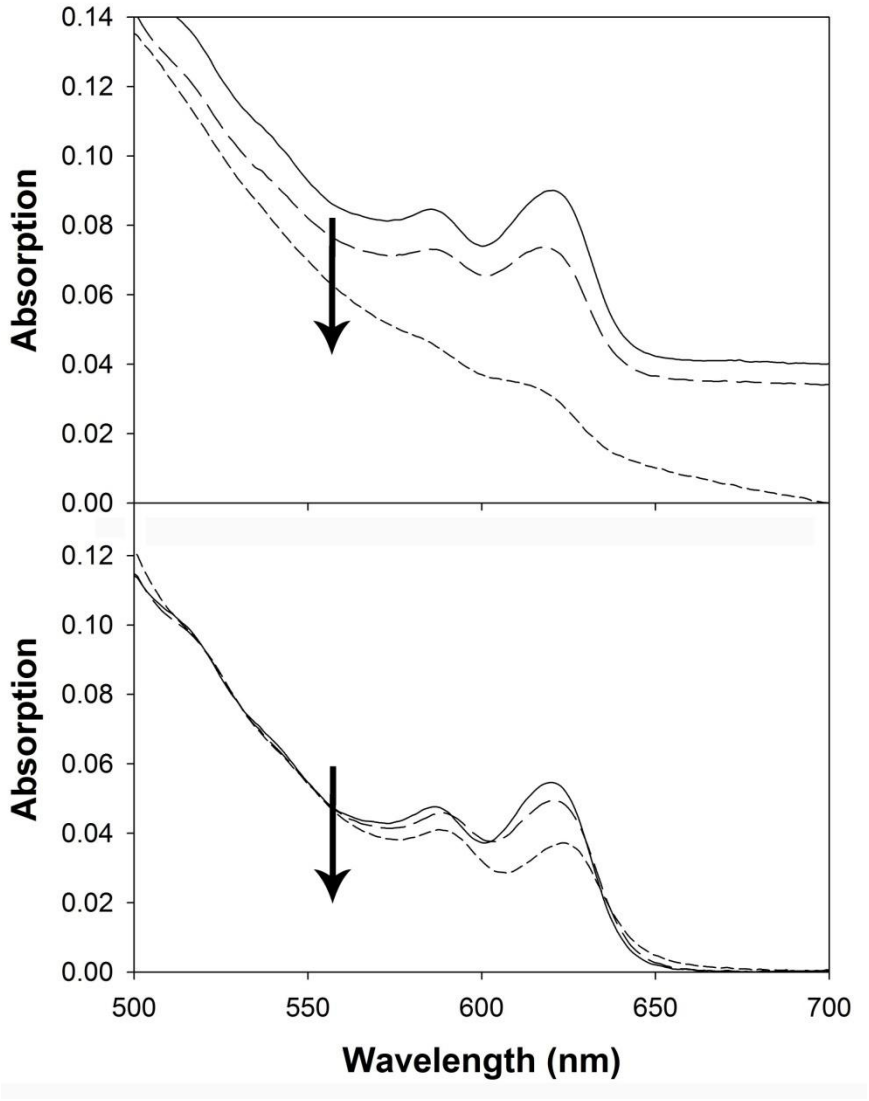

Figure 5.16: Absorption spectra of quantum dots during acid-mediated degradation. Very little shift of the absorption onset occurs over the course of the 140 hour assay for quantum dots coated in diblock copolymer (top), but the first exciton peak decreases slightly in intensity. The nanocrystals slowly lose their colloidal stability, as evident from the increase in scattering in the lowest graph above. For lipid-coated quantum dots (bottom), the first exciton peak decreases in intensity and slightly red-shifts during exposure to acid. The arrows indicate increasing time.

Quantum dots coated in PEI were completely resistant to acid etching, maintaining the same absorption spectra and quantum yield throughout the entire 140 hour assay at pH 1. It is not surprising that these nanocrystals were colloidally stable in acidic

solution, since they were stabilized by cationic charges on their surface. However their degree of chemical stability toward acid was unexpected, and merits further study. This interesting phenomenon may be due to a localized buffering of hydronium ions near the nanocrystal surface, thus increasing the local pH. It has already been shown that PEI functions as a proton "sponge," an effect that has been useful in the release of materials from acidic cellular lysosomes.[18]

5.1.4 Self-Assembly and Nanoparticle Interface Theory. In nonpolar organic solvents, substantial coverage of the quantum dot surface by passivating ligands is important for maintaining the optical properties of the underlying nanocrystal and for preserving colloidal stability. This effect is exemplified by nonsolvent precipitations of quantum dots from solution, which leaches ligands off of the quantum dot surface, effectively decreasing quantum yield and decreasing solubility in nonpolar solvents.[11,26] Likewise in aqueous solution, complete surface coverage of the inorganic nanocrystal by organic molecules is crucial for stability. For example, during phase transfer of ODA-coated quantum dots to water via ligand exchange with MPA, if ligand exchange is incomplete, residual ODA can destabilize the aqueous dispersion. For this reason, this exchange process was allowed to occur over the course of several days. Alternatively, elevated temperatures can be used to push ligand exchange to completion.

Complete surface coverage is not only important for colloidal stabilization and to prevent aggregation, but it is also crucial for protecting the underlying semiconductor material. Without a diffusion barrier to oxygen and other etching agents, quantum dots can quickly degrade. Through optimization of the density and thickness of an organic shell, quantum dots optical properties can be greatly enhanced. Peng and

coworkers demonstrated that hydrophilic thiol-coated CdSe nanocrystals are significantly more resistant to photooxidation when the organic ligand is longer, presumably due to a greater diffusion barrier to oxygen.[7] Likewise, even if the organic coating is thick, instability may arise if it forms an incomplete, or porous, interface. This may explain the relative instability of amphipol-coated quantum dots compared to lipid-PEG quantum dots. Both encapsulations were performed under nearly identical conditions, and after PEG-modification of the amphipol, both quantum dot types should be chemically and colloidally similar, with ODA ligands encapsulated in 12-carbon saturated alkyl chains, surrounded by 2000 MW mPEG for steric stabilization in solution. Indeed these quantum dots were very similar in zeta potential and dynamic light scattering measurements, yet the nanocrystals that were originally encapsulated in the amphipol were substantially less stable toward soluble etching agents. This may be due to the presence of an incomplete or irregular interface on the surface of the quantum dot due to the bulky size of this graft-like polymer. Lipids with only two alkyl chains can more easily fill in small gaps in the hydrophilic bilayer during self-assembly, forming a complete monolayer, whereas small gaps between larger polymer chains (~25 alkyl chains per polymer chain for the amphipol) will likely go unfilled due to the lack of a sterically suitable surfactant.

It is possible that these pores for small molecules may be sealed with cross-linking molecules, which has previously been shown to enhance the stability of colloids. Cross-linked hydrophilic thiols on the surface of quantum dots[27] and cross-linked dendron-encapsulated quantum dots[19] were significantly more stable compared to their non-cross-linked counterparts. Also coating quantum dots with inorganic, amorphous silica has been shown to generate highly stable quantum dots, partially

due to the high degree of surface cross-links.[28-31] It is important to note that for biological applications, protection of the quantum dot surface is not only important for probe stability, but it is also vital to prevent leakage of cytotoxic semiconductor materials from the inorganic core.[32]

5.1.5 Selection of Surface Coatings for Specific Applications. In this section, it was demonstrated that the optical and colloidal properties of semiconductor quantum dots can be widely tuned by varying the surface properties of the organic coating on the nanoparticle. Although none of these encapsulation strategies will likely to be universally optimal for all biological applications, general trends are evident that should inform the use of quantum dot surface coatings for specific biomedical applications. For applications that require the minimization of hydrodynamic radius (e.g. energy transfer studies), hydrophilic ligands may be the most useful, even if the resulting particles are significantly less stable than those encapsulated in amphiphilic polymers. Experiments relying on sustained fluorescence in the presence of oxidizing agents (e.g. peroxosomal staining in living cells) may require quantum dots protected with a hydrophobic bilayer. Assays stability under acidic conditions (e.g. lysosomal staining) may be best suited for quantum dots coated with cationic PEI or neutral PEG.

5.2 Quantum Dot Size Minimization

In Section 5.1, it was demonstrated that the stability of hydrophilic quantum dots toward oxidation is directly related to the thickness of the organic shell. That is, quantum dots coated in a polymeric micelle were significantly more stable against photooxidation and chemical oxidation than those coated with small ligands or multidentate ligands. This finding is logical from the perspective of diffusion rates of soluble etchants across a

sterically hindered interface. However, this finding is highly undesirable for applications in biology and medicine, which often require the use of small probes with strong chemical- and photo-stability. Recent reports have highlighted the unique applications of such small-sized quantum dots, which can extravasate from blood vessels (< ~9 nm diameter),[33] filter from the bloodstream through the kidneys (≤ 5.5 nm diameter),[34] translocate to cellular nuclei (≤ ~3.0 nm),[35,36] and efficiently accept or donate both energy and charge.[37-40] These applications have driven considerable effort to address this problem, especially with the use of functionalized dihydrolipoic acid,[41,42] dithiocarbamates,[43] and cross-linked ligand coatings.[19,44] However, these size-reduced quantum dots have found only limited utility in live cell and *in vivo* applications, either because of their insufficient fluorescence, lack of stability, or because their hydrodynamic sizes are still larger than 10 nm.

Here we report a rational strategy for engineering the hydrodynamic size and stability of quantum dots. This problem is approached from both the limit of highly stable but large micelle-encapsulated quantum dots and from the limit of small but highly unstable ligand-coated quantum dots. First, the hydrodynamic size of quantum dots coated in stable micelles was minimized. Second, the stability of quantum dots coated with small hydrophilic ligands was optimized. From these studies, it was found that the optimum compromise between stability and size can be reached with the use of multivalent ligands, allowing a shell thickness as small as 1.5-2 nm.

5.2.1. Size Minimization of Quantum Dot Micelles. From the previous studies on stability of (CdSe)CdS/ZnS quantum dots toward chemical oxidation and photooxidation (Figures 5.9 and 5.11), it was found that the stability of micelle-encapsulated quantum dots was greatest for lipid-PEG encapsulation. The small di-alkane chains of the lipids

can efficiently intercalate with the alkane chains on the surface of the hydrophobic quantum dots to produce a dense polymeric shell, impermeable toward dissolved etchants. Thereby, these polymers are the most reasonable starting point for minimizing the size of quantum dot micelles. The lipids and polymers used in this process are depicted in Figure 5.17.

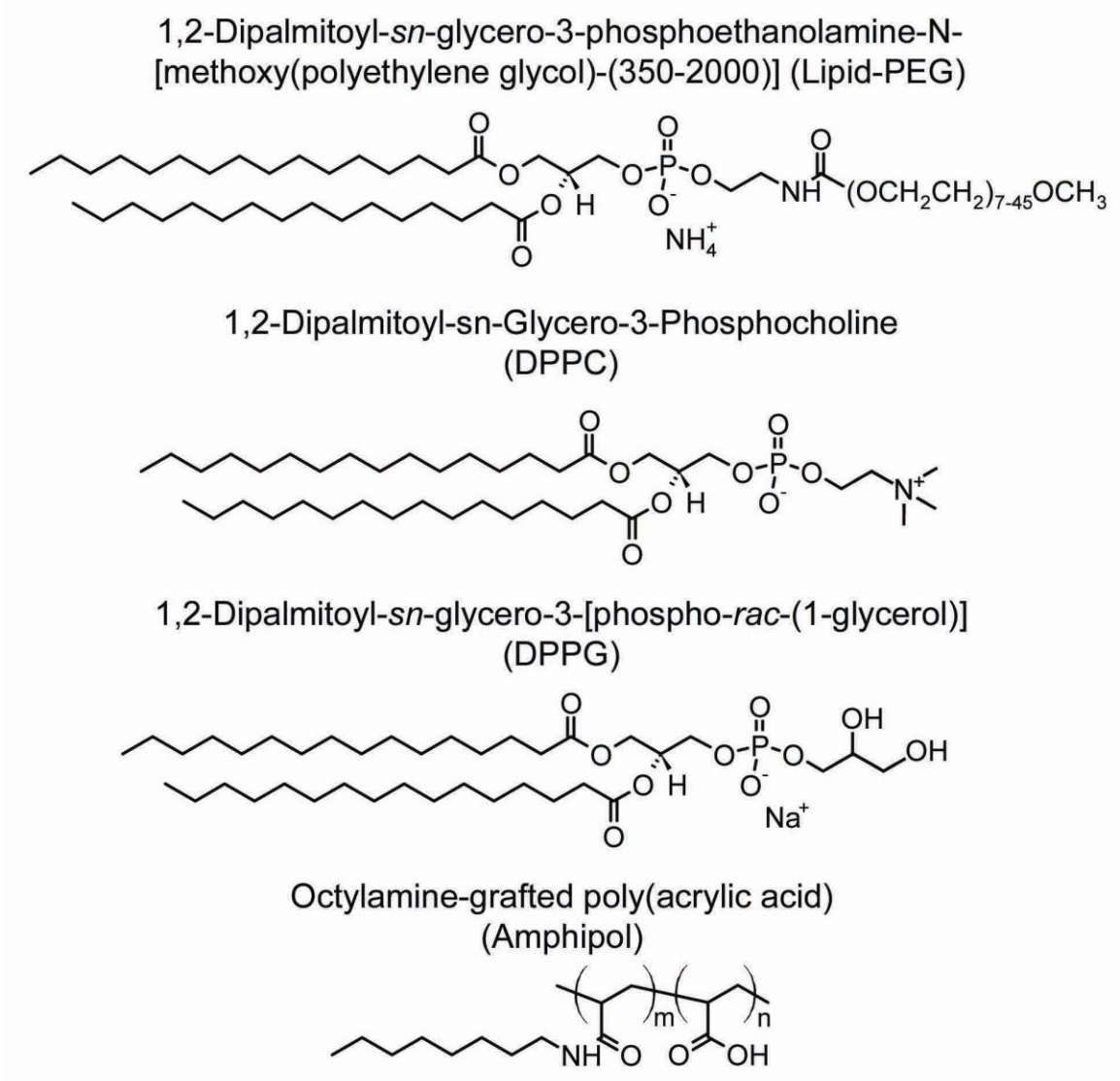

Figure 5.17: Structure of lipids and polymers used for size minimization of quantum dot micelles.

The first parameters optimized for lipid encapsulation of 6.5 nm (CdSe)CdS/ZnS quantum dots were the chain-lengths of PEG on the lipids and the degree of dilution of these nonpolar lipids with small molecular weight lipids (DPPC). The quantum dots coated with 100% lipid-PEG-2000 were hydrodynamically ~30 nm in water (Table 5.1). Significantly smaller micelles were produced when 80% (molar amount) of these lipids were replaced with molecular cationic DPPC lipids (Figure 5.18), yielding a hydrodynamic diameter of ~26 nm. This decrease in size is likely a consequence of the PEG chains altering their conformation on the particle surface, becoming more mushroom-like with the lower surface density of PEG chains, rather than behaving as upright brush-like polymers on the surface.[45,46] Reducing the quantity of lipid-PEG below 20% resulted in significant destabilization of the micelles toward ultracentrifugation. The length of the PEG chain could be reduced to as small as 350 Da without significantly decreasing the colloidal stability of the particles, resulting in nanoparticles as small as 15-16 nm diameter (Figure 5.18).

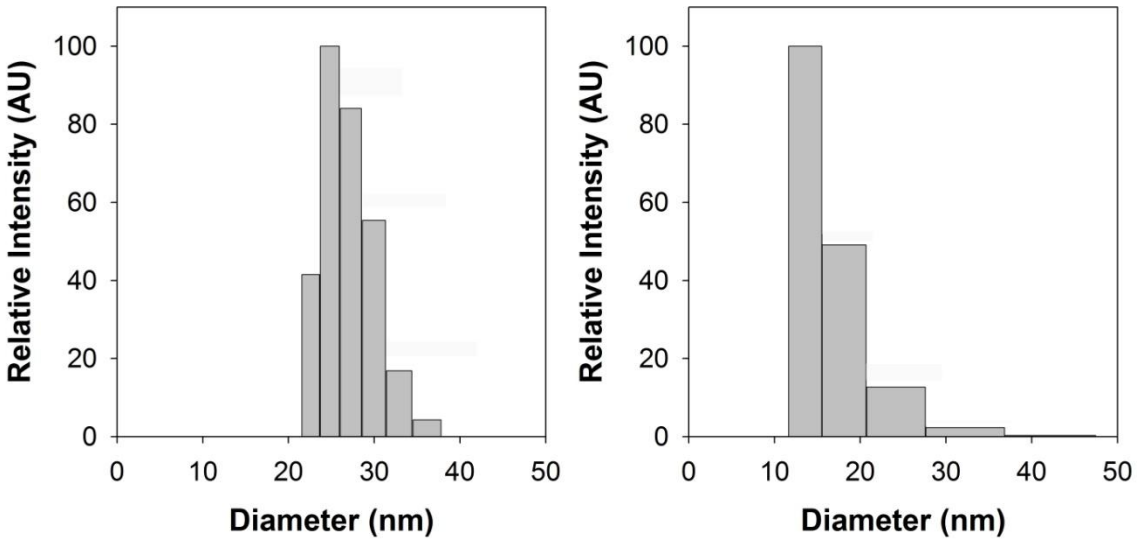

Figure 5.18: Dynamic light scattering of aqueous quantum dots coated in 20% lipid-PEG-2000 + 80% DPPC (left) or 100% lipid-PEG-350.

The two approaches of diluting the surface density of PEG and decreasing the lipid molecular weight on the micelle-encapsulated quantum dots were then combined to produce a size-minimized quantum dot micelle. However dilution of the lipid-PEG-350 with DPPC resulted in significant destabilization of the resulting micelles, possibly due to interaction of the amine groups of DPPC with the nanocrystal surface and the poor water solubility of this lipid. Nevertheless, lipid-PEG-350 could be diluted up to 70% with a lipid-glycerol analogue (DPPG) with a slight negative charge (Figure 5.17). However this dilution only marginally decreased the overall hydrodynamic size of the quantum dots (Figure 5.19). An attempt was made to decrease the size of the hydrophobic layers by using octylamine ligands on the quantum dot surface, which would decrease the length of the nonpolar alkyl chains from 18 to 8. However, the size of the resulting micelles was essentially unchanged (data not shown), suggesting that the size of lipid-encapsulated quantum dots is mostly dictated by the lipid, and not the underlying hydrophobic nanocrystal. Accordingly, lipids containing shorter hydrophobic domains were tested for encapsulation of quantum dots, but chain lengths shorter than 12 carbon units resulted in widespread destabilization of the colloids in water.

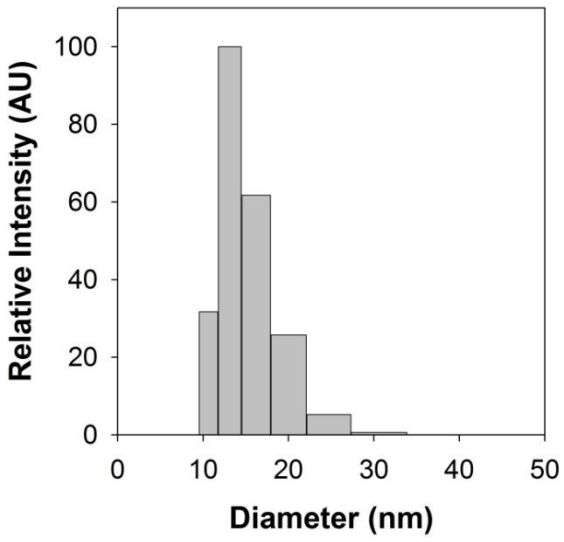

Figure 5.19: Dynamic light scattering of quantum dots coated in 30% lipid-PEG-350 + 70% DPPG.

Optimization of the lipid coating for size minimization of quantum dots resulted in a hydrodynamic diameter as small as ~14 nm in water, which corresponds to a 3.75 nm shell thickness. Although lipids were found to be the most stable of the micellar coatings for quantum dot protection, the self-assembly process for these micelles in water is less efficient than those with amphipol ligands, which have multiple hydrophobic and hydrophilic domains that allow multiple stable attachment points to the nanocrystal surface. Thereby, it may be possible to also optimize these coatings for minimized size. As the hydrophilic domains of these polymers are already size-optimized, containing just a thin shell of carboxylate functional groups, the only region to optimize is the hydrophobic domain. To this end, quantum dots were coated with a mixture of octylamine and trioctylphosphine ligands, and then coated with 40% octylamine-modified polyacrylic acid (Figure 5.17). The hydrophobic bilayer on these quantum dots is thus composed of interdigitated alkane chains of 8-carbon lengths, which is predicted to be significantly smaller for these than those from the previous optimization, which implemented 14-18 carbon units. The resulting aqueous quantum dots were significantly smaller than those with larger hydrophobic domains, and also maintained their uniformity in size (compare Figure 5.20 with Figure 5.6). The final size for these nanocrystals was ~13 nm, which corresponds to a shell thickness of 3.25 nm.

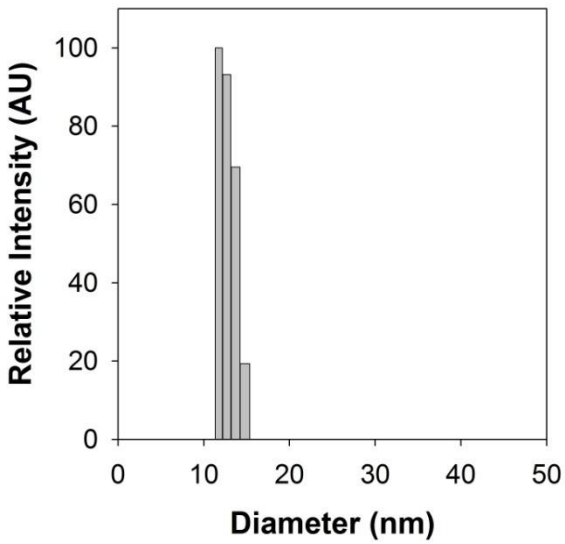

Figure 5.20: Dynamic light scattering data for 6.5 nm quantum dots with 8-carbon ligands, coated with octylamine-modified polyacrylic acid.

5.2.2. Size Minimization of Quantum Dots using Multivalent Ligands. It is evident from the preceding section that in order to produce small quantum dots (<10 nm), it will be necessary to eliminate the surrounding hydrophobic bilayer. The minimum stable coating thickness in such a micellar structure is 3.25 nm, resulting in a 6.5 nm increase in hydrodynamic size over the size of the inorganic core. Although the hydrophobic bilayer is the origin of the ultrastability of micelle-encapsulated quantum dots (section 5.1), it is feasible that this bilayer assembly can be eliminated with a stable polymeric backbone that attaches directly to the quantum dot surface (Figure 5.21). Herein a new strategy is introduced to minimize the hydrodynamic size of quantum dots based on the use of multifunctional and multidentate polymer ligands. A significant finding is that a mixed composition of thiol (-SH) and amine ($-NH_2$) coordinating groups grafted to a linear polymer chain can lead to a highly compact quantum dot with long-term colloidal stability, a strong resistance to photobleaching, and high fluorescence quantum yield. In contrast to the standing brush-like conformations of PEGylated ligands and monovalent

thiols, these multidentate polymer ligands can wrap around the nanocrystal in a closed "flat" conformation. This structure is highly stable from a thermodynamic perspective, and is thus responsible for the excellent colloidal and optical properties observed. This technology is developed for coating CdTe nanocrystals, but the methodology herein is widely applicable across a broad range of materials.[1] This new class of coating yields bright and stable quantum dots with small hydrodynamic sizes between 5.6 nm to 9.7 nm, with fluorescence emission tunable from the visible (515 nm) to the near infrared (720 nm).

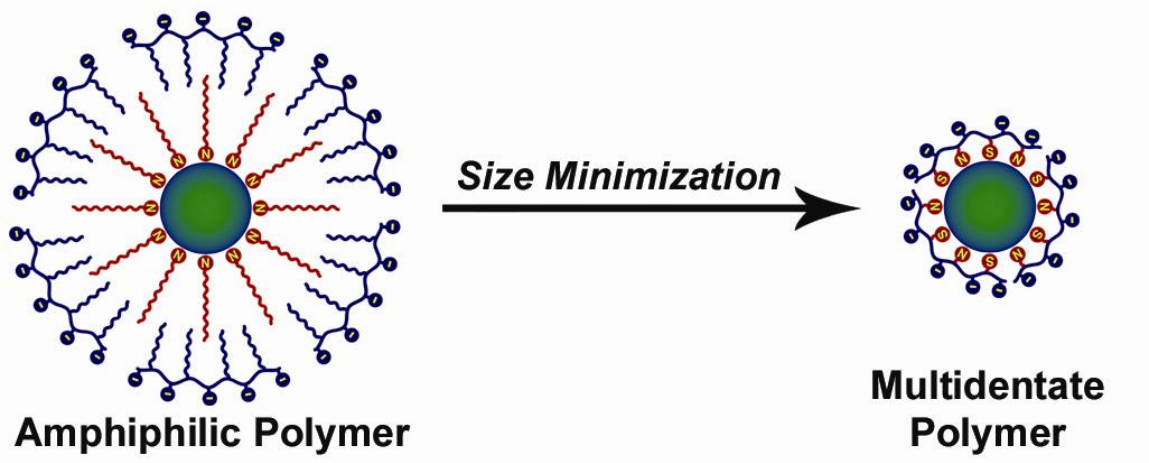

Figure 5.21: Basis for the size minimization process. The hydrophobic bilayer surrounding quantum dots in traditional amphiphilic polymer encapsulation strategies (left) is supplanted with a single layer of a multidentate polymer ligand. This multidentate polymer effectively fuses the hydrophobic quantum dot ligands (red) directly to the hydrophilic coating surface (blue), eliminating the hydrophobic bilayer.

[1] CdTe was chosen for this study due to its well developed synthetic chemistry, its wide range of biologically useful emission spectra (~500-730 nm), and because its propensity to oxidize provides an opportunity for improvement in stabilization. Importantly, very small colloidal quantum dots can be similarly prepared with a variety of compositions (CdS, CdSe, CdTe, ZnSe, PbS, InP, InAs). However these nanocrystals must be coated with an inorganic insulating shell prior to phase transfer, due to the quenching effect of thiolate ligands. CdTe has the distinct advantage of bright fluorescence when stabilized with hydrophilic thiols, without the need for an inorganic shell that would yield an additional increase in the overall particle size.

5.2.2.1 Methods for Polymer Synthesis and Quantum Dot Coating. Figure 5.22 depicts the synthesis of a linear multidentate polymer ligand. Roughly 35% of the carboxylic acids of polyacrylic acid (PAA, MW ~1800) were covalently modified with cysteamine and *N*-Fmoc-ethylenediamine using diisopropylcarbodiimide (DIC) and *N*-hydroxysuccinimide (NHS). After deprotection of the amine with piperidine and purification, each polymer molecule contained approximately 3.5 active thiols and 3.0 active amines, as determined via Ellman's reagent and fluorescamine assays. For coating quantum dots, this balanced composition of amines and thiols was found to provide superior monodispersity, photostability, and fluorescence quantum yield compared to either amines or thiols alone. Further studies are still needed to understand the underlying mechanisms for this effect. The CdTe quantum dots were prepared in a high temperature organic solvent using hydrophobic ligands (e.g. alkylamines, see Chapter 3), and it was necessary to first exchange the native ligands with hydrophilic thioglycerol due to the insolubility of the polymer in nonpolar solvents. These polar monovalent ligands were then replaced with the multidentate ligand.

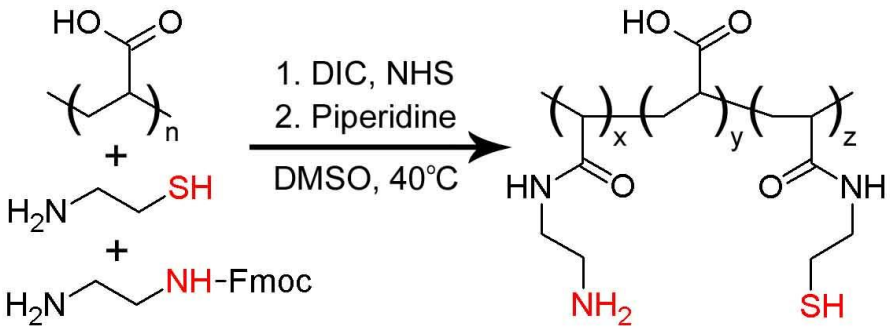

Figure 5.22: Synthesis of multidentate thiolated, aminated polyacrylic acid. The coordinating moieties, thiols and amines, are highlighted in red.

5.2.2.1.1 Polymer Synthesis. PAA (1 g, 13.9 mmol carboxylic acids) was mixed with 25 mL DMSO in a 150 mL three-necked flask. After stirring for 24 hours at 35°C, freshly prepared anhydrous solutions of cysteamine (187 mg, 2.43 mmol) and Fmoc-ethylenediamine (686 mg, 2.43 mmol), each dissolved in 6 mL DMSO, were added. The solution was protected from light and bubbled with argon for 30 minutes at 35°C. After the addition of an anhydrous solution of NHS (1.12 mg, 9.71 mmol) in 6 mL DMSO, DIC (736 mg, 5.83 mmol) was slowly added over the course of 40 minutes during vigorous stirring. Bubbling was continued for 30 minutes, and then the reaction was allowed to proceed for 7 days at 40°C in the dark. Piperidine (18 mL) was then added, and the solution was stirred for four hours to deprotect the primary amines. β-Mercaptoethanol (501 mg, 6.41 mmol) was added to quench the reaction, and the solution was stirred for 2 hours at 40°C, then cooled to room temperature and filtered. The mixture was condensed to ~4 mL at 45°C under vacuum (~40 Pa), and the polymer was precipitated with the addition of a 2:1 mixture of ice-cold acetone:chloroform, and isolated via centrifugation. The polymer was dissolved in ~5 mL anhydrous dimethylformamide, filtered, and precipitated again with acetone-chloroform. This process was repeated three times, and the polymer was finally washed with acetone, dried under vacuum, and stored under argon. This modified polymer was a white powder, soluble in water, DMSO, dimethylformamide, or methanol, but insoluble in acetone, unlike PAA. If stored under air, this polymer darkened and became yellow-brown over the course of a few weeks, and also became increasingly difficult to dissolve in various solvents. This aging process coincided with a significant decrease in the number of active thiols per polymer, determined as described below, and is therefore likely due to the formation of interpolymer disulfide crosslinks.

5.2.2.1.2 Determination of Reactive Amines and Thiols. The modified polymer was assayed for reactive amines and thiols using fluorescamine and 5,5′-dithiobis(2-nitrobenzoic acid) (Ellman's reagent), respectively. For amine determination, a 10 mg/mL solution of fluorescamine in DMSO was freshly prepared, and glycine standards (100 nM – 1 mM) were prepared in deionized water. The assay was initiated by mixing 411.3 µL water, 50 µL sample or standard, 25 µL of 1 M sodium borate buffer (pH 8.5), and 13.7 µL fluorescamine solution. After 20 minutes of reaction in the dark, the fluorescence intensity at 470 nm, with 380 nm excitation, was measured. The polymer was assayed immediately after dissolution at 10 µg/mL in 20 mM sodium hydroxide. For thiol determination, a 2 mM stock solution of Ellman's reagent in 50 mM sodium acetate buffer (pH 4.7), and L-cysteine standards (10 µM – 100 mM) in deionized water were freshly prepared at 4°C. The assay was initiated by mixing 850 µL water, 10 µL sample or standard, 100 µL of 1 M Tris buffer (pH 8.5), and 50 µL Ellman's reagent solution. After 10 minutes of reaction, the optical density at 412 nm was measured. The polymer was assayed immediately after dissolution in 20 mM sodium hydroxide at 500 µg/mL. Standard curves allowed the determination of the molar amount of thiol or amine per gram of polymer. These values were converted to moles of functional group per polymer chain using the molecular weight of the modified polymer (~2200 Da), determined via gel filtration chromatography, which correlated strongly with theoretical calculations.

5.2.2.1.3 Ligand Exchange with Thioglycerol. Purified CdTe quantum dots (2.5 nm) in chloroform (7 mL, ~150 µM) were added to a three-necked flask connected to a Schlenk line. Under intense stirring, neat 1-thioglycerol was added dropwise until the first visible sign of flocculation. Then 4 mL of DMSO was added dropwise. An excess of 1-thioglycerol (3 mL) was then added, and chloroform was removed under vacuum at 25°C. After stirring for an additional 2 hours at 25°C under argon, the quantum dots

were precipitated with the addition of an ice-cold mixture of acetone:chloroform (1:1, 193 mL total). Following centrifugation, the pellet was washed with acetone and dried under vacuum. It was noted that the fluorescence maximum and the first exciton peak blue-shifted if this ligand exchange procedure was performed in the presence of air and a large excess of 1-thiglycerol. The extent of blue-shifting was found to be time dependent (Figure 5.22) and was substantially reduced when the reaction was performed under inert gas. This blue-shift was deemed to be the result of controlled oxidative etching of the quantum dots, rather than alternative mechanisms (e.g. formation of a $CdTe_xS_{1-x}$ alloy or core-shell structure) for several reasons. (1) This hypsochromic shift was strongly correlated with a substantial decrease in the extinction coefficient of the first exciton peak (Figure 5.23). In fact, after ~2 days of reaction, there was essentially no absorption at wavelengths greater than 320 nm, likely due to complete dissolution of the quantum dots. Because this etching process was uniform, the quantum dots maintained a discrete first exciton peak, allowing exact calculation of extinction coefficients of ultrasmall quantum dots with the reasonable assumption that the total number of quantum dots remained fixed. (2) This blue-shift of the optical spectra was associated with a decrease in photoluminescence efficiency, an increase in Stokes shift, and an increase in deep trap emission (Figure 5.22), common features of ultrasmall quantum dots (< ~ 2nm) (3) Small quantum dots (2.5 nm) at high concentration could easily be detected via TEM and DLS, but after a substantial blue-shift, neither of these techniques revealed the presence of nanoparticles. This suggests that the resulting nanoparticles were below the size limit for TEM contrast, and that their scattering intensity was reduced below their detection limit via DLS. (4) Finally, elemental analysis (inductively coupled plasma – mass spectrometry) of the quantum dot supernatant after precipitation revealed the presence of both free cadmium and tellurium only after extended etching times.

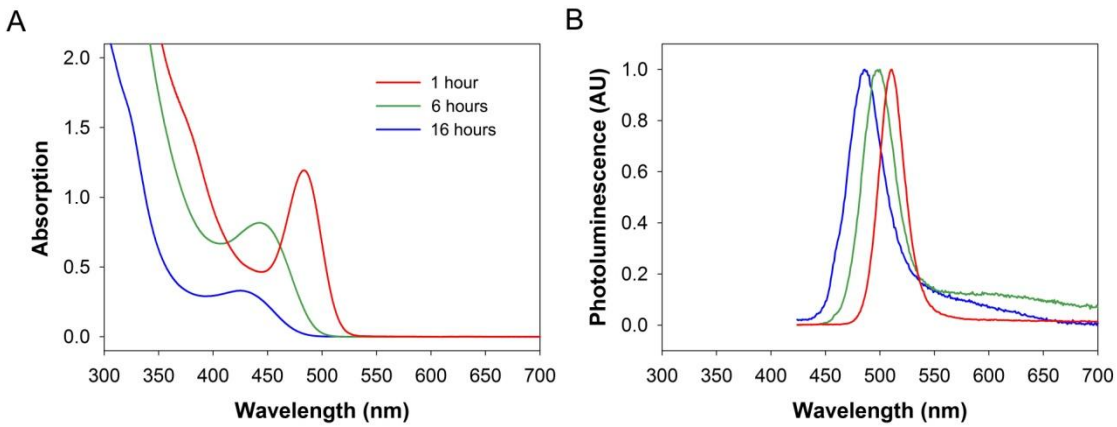

Figure 5.23: Ligand-induced etching of CdTe nanocrystals. Absorption spectra (A) and fluorescence spectra (B) show a blue-shift over time.

5.2.2.1.4 Coating with the Multidentate Polymer Ligand. Two techniques were employed to coat 1-thioglycerol quantum dots with the modified polymer. In the first method, CdTe quantum dots were suspended in basic water (50 mM sodium hydroxide), centrifuged at 7000g for 10 minutes, and then filtered to remove aggregated nanocrystals. Various amounts of polymer dissolved in basic water were added to the quantum dots, which were then gently mixed. In the second method, quantum dots coated with 1-thioglycerol were suspended in DMSO and centrifuged at 7000g for 10 minutes to remove possible nanocrystal aggregates. The nanocrystals were diluted to ~5-20 μM for smaller sizes (2.5-3.5 nm), or ~2-5 μM for larger nanocrystals. The nanocrystal solution was then degassed extensively at room temperature and charged with argon. An anhydrous DMSO solution of the polymer (~5 mg/mL) was added under vigorous stirring. The solution was then heated to 60°C for 90 minutes for smaller quantum dots (2.5-3.5 nm), or 70-75°C for 120 minutes for larger nanocrystals. In the absence of the polymer, the nanocrystals aggregated and precipitated from solution during heating. Indeed, the multidentate polymer greatly enhanced the thermal stability of these nanocrystals, as there was no evidence of Ostwald ripening of 2.5 nm cores up to ~130°C. After cooling

the quantum dots to room temperature, ice-cold aqueous sodium hydroxide (50 mM, twice the volume of DMSO) was slowly added, and the solution was stirred for 2 hours. The quantum dots were then extensively dialyzed against basic water for 2-3 days using 25 kDa molecular weight cutoff dialysis tubing (Spectra/Por). Figure 5.24 depicts the optical properties of these quantum dots and their hydrodynamic sizes at the different stages of this coating procedure.

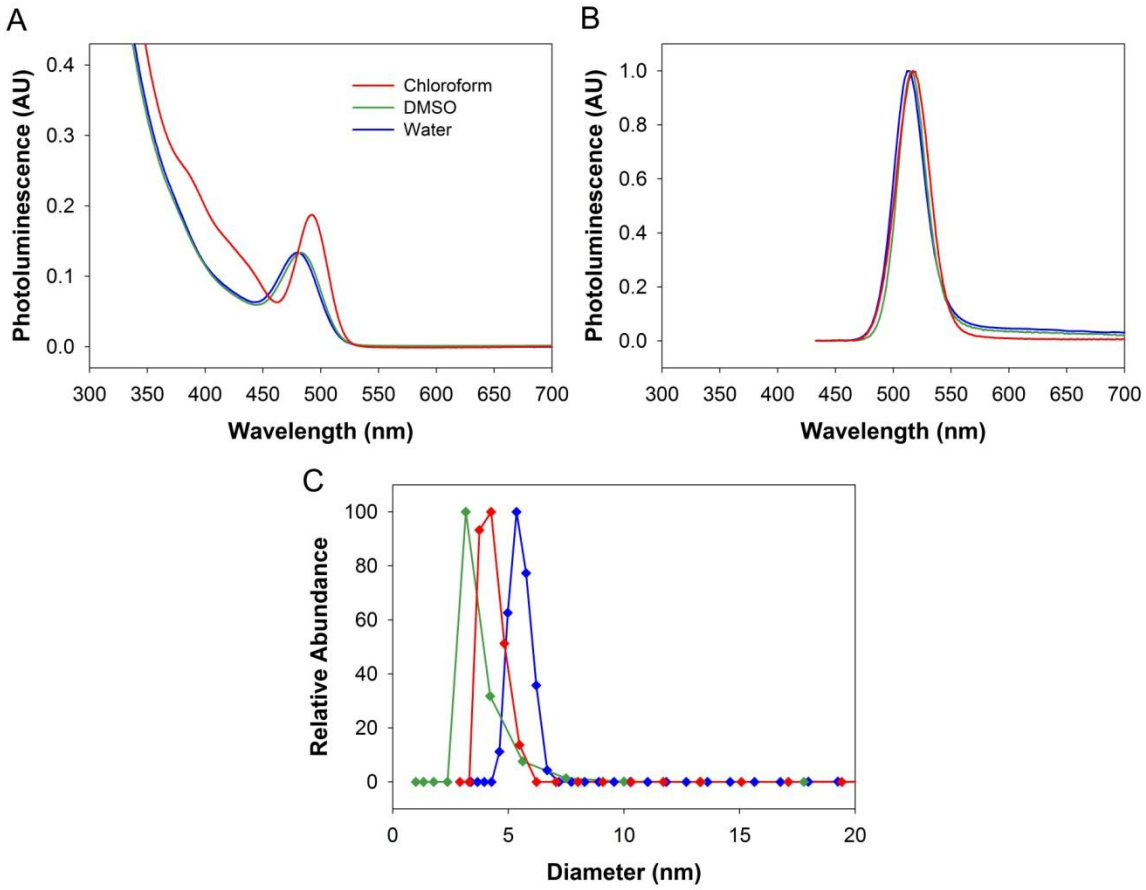

Figure 5.24: Absorption (A), photoluminescence (B), and dynamic light scattering spectra (C) of 2.5 nm CdTe quantum dots in chloroform, DMSO after ligand exchange with 1-thioglycerol, and in water after coating with the multidentate polymer. Note that a small amount of deep trap emission arises upon coating with 1-thioglycerol, and remains after exchange with the polymer. Photoluminescence spectra were obtained with 420 nm excitation.

5.2.2.1.5 Calculation of Molar Capping Ratio. The amount of polymer added per quantum dot was standardized with respect to the number of surface atoms on the quantum dot. This relationship was used in order to shed light on the mechanism of interaction between the quantum dots and the polymer, and to simplify the extrapolation of the polymer coating procedure to other nanocrystalline materials, without the need for extensive optimization. The molar capping ratio (MCR) was reported as the number of thiol and amine groups per surface atom. Therefore

$$MCR = \frac{n_{SH}+n_{NH2}}{n_{Cd}+n_{Te}} \qquad \textbf{Equation 5.2}$$

where n_{SH} and n_{NH2} are the numbers of thiols and amines on the polymer ligand, respectively, and n_{Cd} and n_{Te} are the number of cadmium and tellurium surface atoms on the quantum dot surfaces. For example, a 2.5 nm CdTe quantum dot has ~95 total surface atoms (the calculation of the number of surface atoms per quantum dot is described below), and one polymer chain contains roughly 6.5 basic groups (3.5 thiols and 3.0 amines). Therefore, the optimal capping ratio (OCR) value of 1.5x denotes the addition of ~22 polymer chains per quantum dot, or roughly 48 mg of polymer per μmol of quantum dot. Indeed, this is a very small amount of polymer for such a large number of quantum dots. With elevated temperature this reaction is highly efficient, as nearly all of the polymer binds to the quantum dots (no detectable free amines were found in the dialysate during purification).

5.2.2.1.6 Calculation of Surface Atoms per Nanocrystal. Determination of surface atom density on nanocrystals can be difficult, and imprecise, especially for very small particles that cannot be easily characterized microscopically. Nevertheless, reasonable accuracy can be obtained by using theoretical calculations informed by empirical data. In this work, the CdTe nanocrystals that were prepared (2.5-6 nm diameter) were found to be in

the zinc blende crystal structure (see Chapter 4), allowing the use of the bulk density and interplanar distances of zinc blende CdTe in these calculations. It is likely that a variety of crystalline facets are exposed on individual nanocrystals, each with a range of planar densities of atoms. It is also likely that there is a distribution of different facets exposed across an assembly of nanocrystals. Therefore one may obtain an effective average number of surface atoms per nanocrystal by averaging the surface densities of commonly exposed facets in zinc blende nanocrystals over the calculated surface area of the nanocrystal. In this work we chose to use the commonly observed (111), (100), and (110) zinc blende planes, which are representative of the lattice structure, with both polar and nonpolar surfaces. For this calculation, we defined a surface atom as an atom (either Cd^{2+} or Te^{2-}) located on a nanocrystal facet with one or more unpassivated orbitals. Some facets, such as Cd^{2+}-terminated {111} faces, have closely underlying Te^{2-} atoms that are less than 1 Å beneath the surface plane. These atoms reside in the voids between Cd^{2+} atoms, and thus are likely to be sterically accessible from the surface, but because they are completely passivated, they were not included in this definition.

First we calculated the average distance between parallel planes of atoms for zinc blende CdTe (Table 5.2). This average interplanar distance, d, is therefore the distance between the plane of surface atoms and the next underlying plane of atoms. In the [100] and [110] directions, all adjacent planes are equidistant, whereas this distance varies between neighboring planes in the [111] direction, and thus we calculated an “average” interplanar distance. We also calculated the planar density of atoms on each facet, although this data was not directly used in our calculation.

Table 5.2: Characteristics of three lattice planes of the zinc blende CdTe crystal structure.

Lattice plane	d (nm)[a]	Polarity	D_{SA} (atoms nm^{-2})[b]	B / A[c]
(111)	0.187	Polar	5.50	1
(100)	0.162	Polar	4.76	2
(110)	0.229	Nonpolar	6.73	1

[a] d is the average interplanar distance.
[b] D_{SA} is the atomic density on the specified lattice facet.
[c] B / SA is the number of bonds per surface atom.

Next we calculated the effective volume of surface atoms within each quantum dot. We assumed a spherical geometry, and used the interplanar distance d as the thickness of one monolayer of surface atoms in each nanocrystal. In this calculation, the surface volume was used, rather than the surface area, in order to yield a more realistic determination of surface atoms in very small nanocrystals (< 2 nm). For these high surface area nanocrystals, use of the surface area generally resulted in a surface atom number that was larger than the total number of atoms in each nanocrystal. Therefore

$$V_{SA} = \frac{4}{3}\pi\left[r^3-(r-d)^3\right] \qquad \textbf{Equation 5.3}$$

where V_{SA} is the volume of surface atoms per quantum dot, r is the nanocrystal radius, and d is the average interplanar distance from Table 5.1.

It was assumed that this spherical shell of surface atoms was the same density as bulk zinc blende CdTe, and therefore the number of surface atoms per nanocrystal could be calculate as

$$n_{SA} = 2\,\frac{V_{SA}\times D_{CdTe}\times N_A}{MW_{CdTe}} \qquad \textbf{Equation 5.4}$$

where n_{SA} is the number of surface atoms per nanocrystal, D_{CdTe} is the bulk density of zinc blende CdTe (5.85 g cm^{-3}), N_A is Avogadro's number, MW is the molecular weight of CdTe, and 2 is a factor accounting for 2 atoms per molecule of CdTe. Table 5.3 displays the calculated number of surface atoms on a single, spherical CdTe quantum dot that is hypothetically terminated solely by {111}, {100}, or {110} planes for various nanocrystal sizes. These values may be averaged, depending on available empirical information. For instance, HRTEM analysis of some of our larger CdTe nanocrystal samples revealed that the {110} planes were frequently parallel to the TEM grid. Therefore it is likely that these nanocrystals were faceted along this plane, allowing them to adopt this orientation on their substrate during solvent evaporation.[23] In this case, more weight can be given to these facets in the averaging calculation. For these calculations, we could obtain very little structural information about these very small nanocrystals, and therefore we simply averaged these three representative values together.

Table 5.3: Total number of atoms and total number of surface atoms in various sizes of CdTe nanocrystals.

d_{QD} (nm)	Atoms / QD	SA / QD, (111)	SA / QD, (100)	SA / QD, (110)	SA / QD, Average
2.5	240	92.6	81.9	109	94.6
3	415	137	121	163	140
4	984	251	220	301	258
6	3322	584	510	705	599

Note: The surface atom (SA) count is listed for each surface facet of interest, as well as its numerical average. This later value was used to calculate the molar capping ratio, described above.

Several methods have been reported in the literature to determine the number of surface atoms on nanocrystals without the use of complex energy-minimization computations.[47,48] We compared several different calculation methods based on a quasi-spherical particles, as well as methods we developed to predict the number of surface atoms on different polyhedral shapes with various lattice facets. For all of these methods, we obtained strongly correlated results. A substantial difference (greater than 15%) was only observed in comparison with empirically unrealistic shapes with 8 sides or less (cubes or tetrahedrons). The specific method used for this work was chosen for its simplicity and its ease of quickly incorporating empirical knowledge of known facets.

We note two factors that could yield errors in this calculation and complicate the interpretation of the MCR value, with respect to the interaction between the nanocrystal surface atoms and the multidentate ligand. (1) Nanocrystals of various sizes have been theoretically and experimentally shown to have reconstructed surface atoms that may minimize the total energy of the crystal.[49-52] Because of the very high fraction of atoms that reside on the surfaces of the small nanocrystals used in this study (~39% for 2.5 nm quantum dots), surface reconstruction is likely. (2) Many lattice directions, such as the (100) direction, are terminated by atoms with two unpassivated orbitals, which could theoretically bind to two ligands. Atoms with more than one exposed binding site are even more likely to be present on the smallest quantum dots, which have such highly curved surfaces that a surface 'facet' may not even be an appropriate term for their description.

5.2.2.2 Compact Assembly of Multidentate Ligands on Quantum Dots. Figure 5.25 depicts the methods used to encapsulate CdTe quantum dots in the multidentate polymeric ligand. Because the PAA-based polymer was highly hydrophilic, there was no

way to efficiently coat hydrophobic quantum dots unless the native nonpolar ligands were first displaced with a polar ligand (thioglycerol). This allowed the dissolution of the quantum dots in a polar solvent, in which thioglycerol could be replaced with the tightly binding multidentate ligand. Performing this process in water, however, resulted in large nanocrystals with extensive aggregation, likely due to crosslinking of the quantum dots through the multidentate ligand (Figure 5.26). Instead, it was found that robust, compactly coated quantum dots could only be produced after heating (60-70°C) for 1-2 hours in an aprotic solvent (DMSO) under inert conditions (Figure 5.25). This observation is in accord with the 'loops, trains, and trails' model of polymer surface adsorption.[53-55] Although it is thermodynamically favorable for the linear polymer to maximize its adsorption (train domains), self-assembly of this highly ordered structure does not readily occur at room temperature . The kinetics for the closure of loops and trails are slow, and thus elevated temperatures are needed to expedite this process.

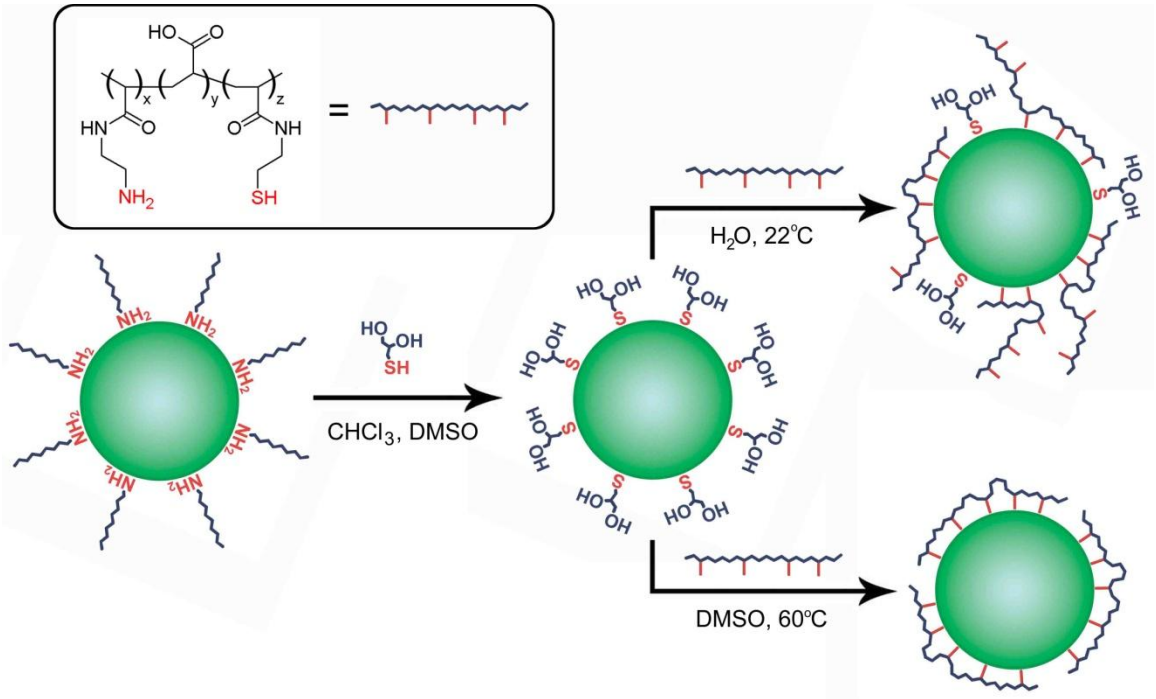

Figure 5.25: Methods used for self-assembly of the multidentate ligand on the quantum dot surface.

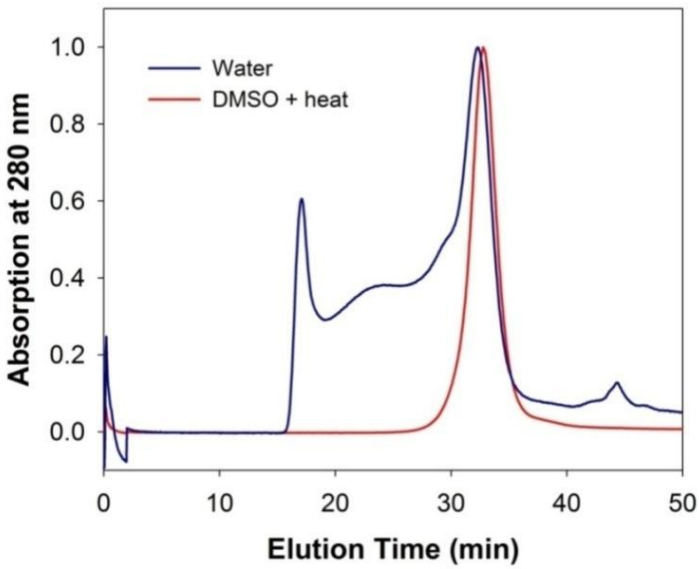

Figure 5.26: Comparison of gel filtration chromatograms[2] of 6.0 nm CdTe quantum dots coated with the multidentate polymer, using the aqueous method and the aprotic solvent method of Figure 5.25. The MCR value was 0.75. The quantum dots coated in DMSO were purified extensively prior to testing and demonstrated a highly narrow size distribution. The quantum dots coated in water were tested 3 weeks after mixing, and were not purified in order to prevent destabilization of a wide size range of labile aggregates.

Figure 5.27 compares the optical properties and hydrodynamic sizes of CdTe quantum dots (2.5 nm) coated with a traditional amphiphilic polymer (octylamine-modified polyacrylic acid) or the mixed thiol/amine multidentate ligand. Although the amphiphilic polymer and the multidentate ligand were prepared from the same molecular-weight polyacrylic acid backbone, the quantum dots coated with the multidentate ligand are considerably smaller in size and also much brighter in fluorescence. Dynamic light scattering measurements show that the multidentate polymer coating is only 1.5-2 nm in thickness, and a lack of aggregation is verified via TEM (Figure 5.28). This compact shell matches the geometric predictions of a polymer conformation with a high degree of

[2] Details of gel filtration chromatography are given in Appendix C.

adsorption on the quantum dot surface, enabled by its high affinity and low molecular weight. In comparison, the coating thicknesses are on the order of 4-7 nm for amphiphilic polymers and even some monovalent molecular ligands.[56,57] It is also worth noting that the CdTe quantum dot is not protected with an electronically insulating inorganic shell (e.g. ZnS or CdS) and its fluorescence is retained with the multidentate polymer, but nearly completely quenched by the amphiphilic polymer.

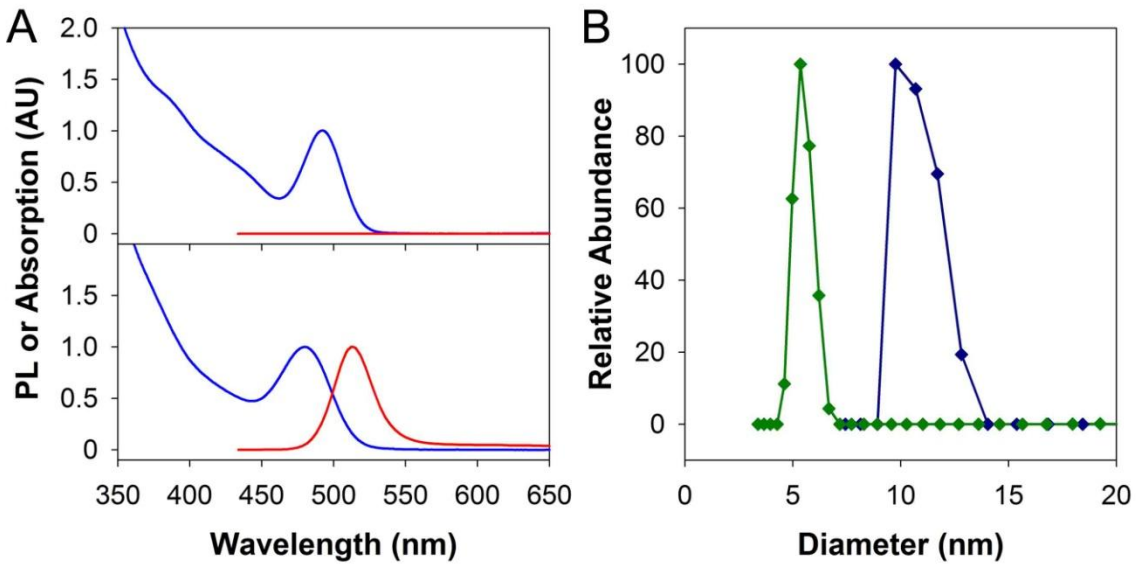

Figure 5.27: Comparison of optical and hydrodynamic properties of CdTe quantum dots (2.5 nm) solubilized in water with an amphiphilic polymer (octylamine-modified polyacrylic acid) or a multidentate polymer ligand. (A) Absorption (blue curves) and fluorescence emission (red curves) spectra of CdTe quantum dots with amphiphilic polymer (top) or multidentate polymer (bottom) coatings. (B) Dynamic light scattering size data of quantum dots with amphiphilic polymer (blue curve) and multidentate polymer (green curve) coatings. PL = photoluminescence, AU = arbitrary units. All samples were dissolved in phosphate buffered saline.

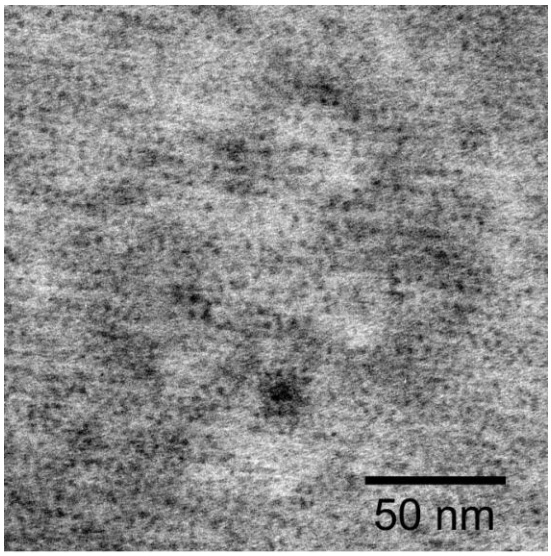

Figure 5.28: TEM of 2.5 nm CdTe quantum dots coated with the multidentate polymer in water.

5.2.3 Molar Capping Ratio. As shown in Figure 5.29, the fluorescence quantum yield, monodispersity and photostability of these polymer-coated quantum dots are strongly dependent on the molar capping ratio (MCR), which is calculated by dividing the sum of basic groups (amine or thiol) on the polymer by the sum of cadmium and tellurium atoms on the quantum dot surface (Equation 5.2). When the MCR values are below 1.0, the amount of polymer is insufficient to completely coat 2.5-nm CdTe quantum dots, resulting in polydisperse nanocrystals. Polydispersity was quantitatively assessed from the polydispersity index (PDI) in gel filtration chromatograms, as shown in Figure 5.30. When the MCR values are above 2.0, the excess polymer leads to better monodispersity and colloidal stability, but a reduced fluorescence quantum yield. Between these two limits is the optimal capping ratio (OCR) of approximately 1.5 (Figure 5.29A), yielding small, monodisperse nanocrystals (PDI < 1.5) with bright fluorescence (~50% quantum yield) and exceptional photostability (Figure 5.29B).

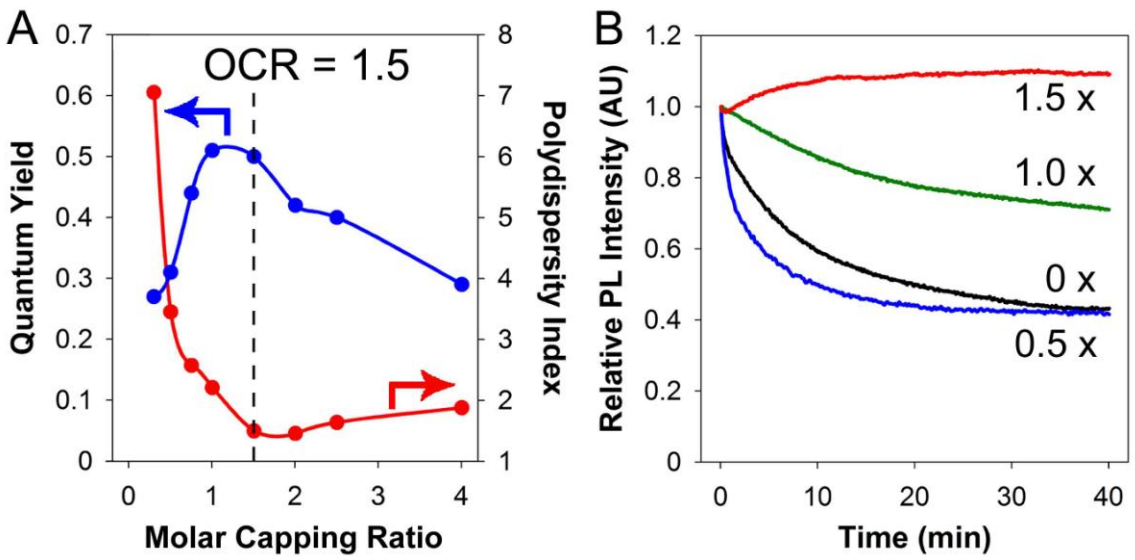

Figure 5.29: Effects of polymer capping ratios on quantum dot properties. (A) Fluorescence quantum yield (blue curve) and polydispersity index (red curve) of 2.5 nm CdTe quantum dots as a function of molar capping ratio. Polydispersity indices were calculated from gel filtration chromatograms, some of which are depicted in Figure 5.30.[3] (B) Photostability data[4] at various capping ratios (MCR = 1.5, 1.0, or 0.5) and in the absence of polymer (MCR = 0).

[3] Polydispersity index (PDI) was calculated from chromatograms using conventional techniques for polymer characterization, with the formula PDI = M_w / M_n. The PDI for pure protein solutions was typically 1.25-1.35.

[4] Photoluminescence stability was measured using a spectrofluorometer from Photon Technology International with a xenon lamp excitation source and photomultiplier tube detector. Emission spectra were recorded (400-620 nm) from 200 nM solutions of quantum dots with continuous high intensity 390 nm excitation (16 nm excitation spectrometer slit widths).

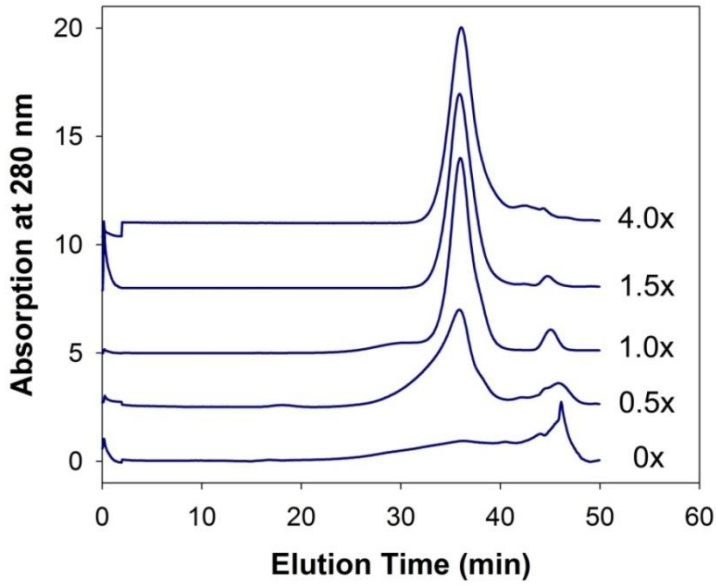

Figure 5.30: Gel filtration chromatograms of 2.5 nm CdTe quantum dots coated with different amounts of the multidentate polymer, in phosphate buffered saline. The coating procedure was performed at 60°C in DMSO. The amount of polymer added is indicated by the MCR values on the right. Note the presence of higher molecular weight aggregates (shorter retention times) for MCR values below the optimal capping ratio (1.5x). The 0x nanocrystals were not heated, but instead were dialyzed against borate buffer for 30 minutes prior to injection into the column. All other nanocrystal samples were dialyzed for 2 hours.

The OCR is dependent on the size of the quantum dot, and its value changes to 1.0 for 3.0 nm cores, and to 0.5 for 4.0 nm cores. This trend is indicative of the size-dependent differences in nanocrystal surface curvature, the intrinsic degree of flexibility of the polymer, and the increasing availability of more than one free orbital per surface atom with decreasing nanocrystal size, as discussed further in Section 5.2.2.1.6. The OCR can be semi-quantitatively determined using the aqueous ligand coating procedure (Figure 5.31). In this method, the multidentate ligand is added to thioglycerol-coated quantum dots at room temperature. Addition of a small excess of polymer above the OCR value results in complete precipitation of the nanocrystals from solution, and the

quantum yield dependence on the MCR was found to be similar for the aqueous and nonaqueous coating procedures.

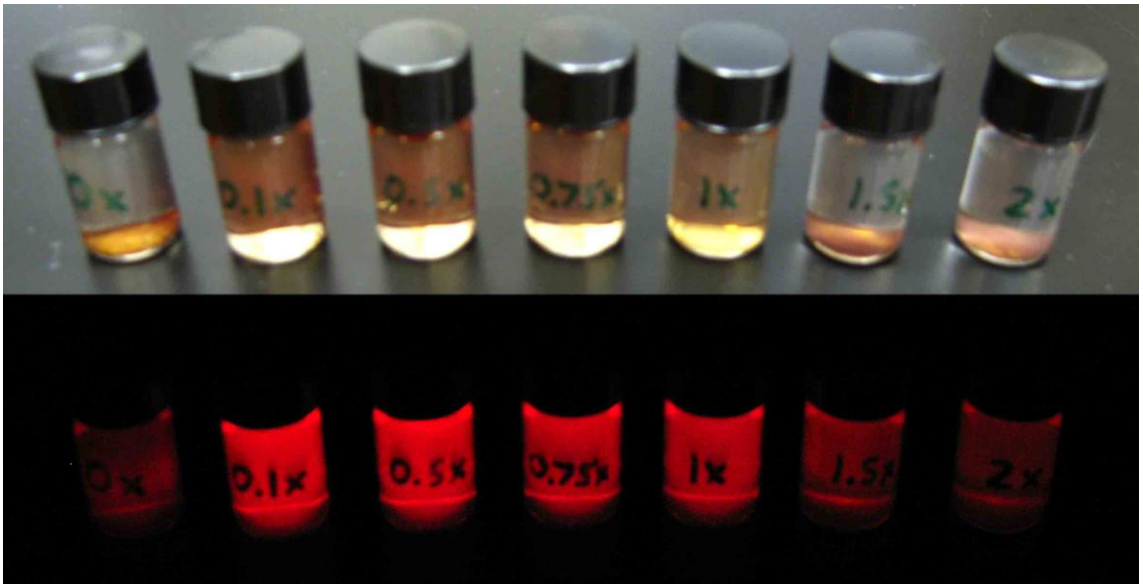

Figure 5.31: Photographs of 4 nm thioglycerol-stabilized CdTe nanocrystals in water, 6 months after addition of various amounts of the polythiol polymer. Molar capping ratios are indicated on the vials, and are, from left to right, 0, 0.1, 0.5, 0.75, 1, 1.5, and 2. The OCR is 0.5.

5.2.2.4 Minimum Size. The smallest nanoparticles that could be prepared were 5.5 nm in hydrodynamic diameter, encapsulating a 2.5 nm core. This 2.5 nm core size is also the smallest size that can be reliably prepared using the coordinating solvent synthesis described herein. In order to prepare smaller nanocrystals, these particles were oxidatively etched in a slow, controlled process (Figure 5.23) to yield monodisperse nanocrystals with a diameter of 1-2 nm. However, after coating with the multidentate polymer, these nanocrystals were actually larger in size (Figure 5.32), with a diameter of 6-6.5 nm, which is incidentally similar to the length of the fully outstretched polymer (~6.3 nm). We attribute this interesting effect to the extremely high surface curvature of these

nanocrystals, which is not conducive to multivalent interactions with a linear polymer. Although cores smaller than 2.5 nm were colloidally stable after coating with the polymer, they were found to have significant deep trap emission, and were prone to photobleaching.

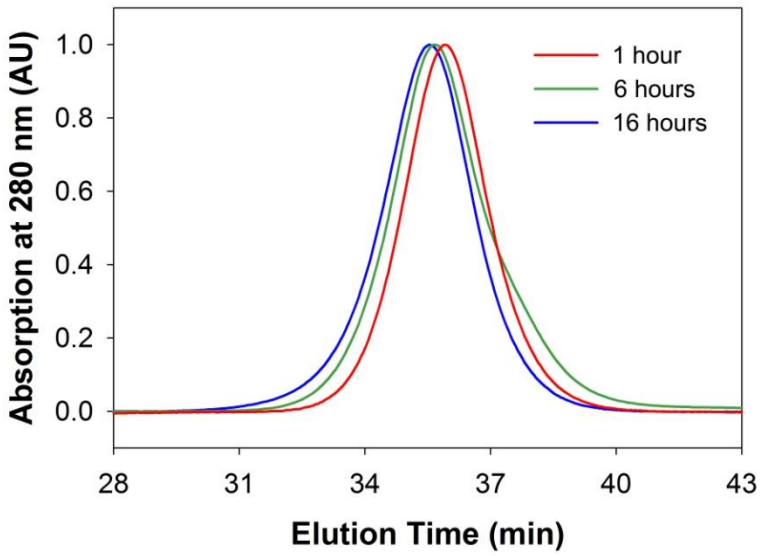

Figure 5.32: Gel filtration chromatograms of CdTe quantum dots (2.5 nm) that were etched (Section 5.2.2.1.3) in DMSO and coated with the multidentate ligand. With etching, the nanocrystals shrink in crystalline size, but after coating with the multidentate polymer, a small increase in hydrodynamic diameter is apparent.

5.2.2.5 Stability. The multidentate polymer-coated quantum dots are stable at room temperature for more than one year after purification, with no significant changes in gel filtration chromatograms. The quantum yield is retained under these conditions when stored in the dark, but gradually decays to ~20% with continual exposure to room light. In comparison, purified CdTe quantum dots coated with monovalent ligands generally precipitate within 2 days at room temperature, and are even unstable when stored in excess ligand. In addition, CdTe nanocrystals coated in amphiphilic polymers

completely oxidize over the course of 1-2 weeks when stored at room temperature. The quantum dots coated with multidentate ligands could undergo dialysis for more than one week without deleterious effects, whereas quantum dots coated with monovalent ligands generally aggregate within 2-3 hours. These nanocrystals can also withstand ultracentrifugation, and spread evenly on TEM grids when cast from aqueous solutions (Figure 5.27), unlike their aggregation-prone counterparts coated in monovalent ligands. Indeed this multidentate polymer combines the compact size of the monovalent ligand coatings, the antioxidant properties of reduced thiols, and the colloidal stability of amphiphilic micellar coatings.

5.2.2.6 Size Comparison with Proteins. In order to assess the relevance of these new quantum dots for bioimaging applications, their hydrodynamic sizes were compared directly with proteins. Figure 5.33 shows a size comparison of gel filtration chromatograms of multidentate polymer-coated quantum dots (four emission colors) with globular protein standards. The results demonstrate that the green-emitting quantum dots (515 nm) have a hydrodynamic size slightly larger than fluorescent proteins (MW = 27-30 kDa), while the yellow-emitting quantum dots (562 nm) dots are slightly smaller than serum albumin (MW = 66 kDa). Even the near-infrared emitting dots (720 nm) are similar to antibodies (MW = 150 kDa) in hydrodynamic size.

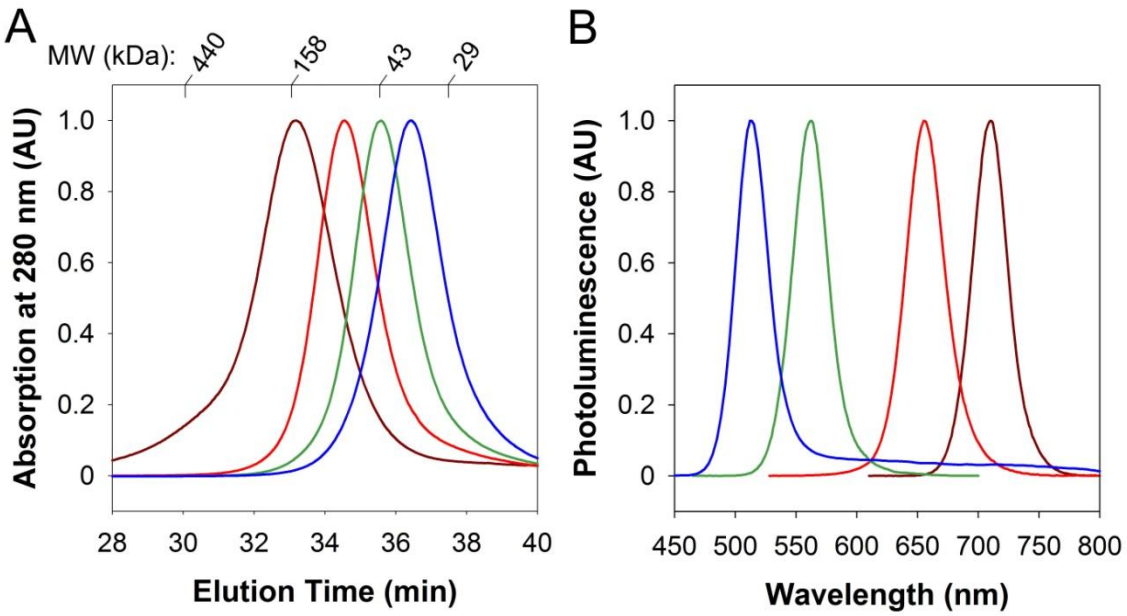

Figure 5.33: (A) Gel filtration chromatograms of multidentate polymer coated CdTe quantum dots showing direct size comparison with protein standards ferritin (440 kDa), aldolase (158 kDa), ovalbumin (43 kDa), and carbonic anhydrase (29 kDa). (B) Fluorescence emission spectra from the corresponding quantum dots. The quantum dot hydrodynamic sizes are 5.6 nm (2.5 nm core, blue), 6.6 nm (3.1 nm core, green), 7.8 nm (4.0 nm core, red), and 9.7 nm (6.0 nm core, brown).

5.2.2.7 Outlook. In summary, a low molecular weight, linear polymer containing multiple thiols and amines can be used as a tightly binding multidentate ligand to prepare ultrastable cadmium telluride quantum dots. Importantly, this multidentate ligand approach results in tremendously enhanced optical stability compared to monovalent ligand approaches, and a vastly smaller size compared to traditional micellar approaches. The hydrodynamic thickness of only 1.5-2 nm approaches the theoretical minimum value that could be possible with only a molecular monolayer of ligand and hydration shell. These optimizations can be directly applied to a broad range of semiconductor materials and core/shell structures (e.g. CdS, ZnSe, CdSe/ZnS, and CdTe/CdS). These new quantum dots are a new generation of bright and stable nanocrystal probes with hydrodynamic sizes similar to proteins (5.6 nm to 9.7 nm) with

tunable fluorescence emission from the visible (515 nm) to the near infrared (720 nm), attributes that will be widely valuable for bioimaging applications. The size-minimized quantum dots reported here could ultimately allow molecular and cellular optical imaging at the level of single particles and single molecules (Chapter 7).

5.3 References

1. Chan, W. C. W. & Nie, S. M. Quantum dot bioconjugates for ultrasensitive nonisotopic detection. *Science* **281,** 2016-2018 (1998).

2. Nann, T. Phase-transfer of CdSe@ZnS quantum dots using amphiphilic hyperbranched polyethylenimine. *Chem. Commun.*1735-1736 (2005).

3. Dubertret, B., Skourides, P., Norris, D. J., Noireaux, V., Brivanlou, A. H., & Libchaber, A. In vivo imaging of quantum dots encapsulated in phospholipid micelles. *Science* **298,** 1759-1762 (2002).

4. Wu, X., Liu, H., Haley, K., Ng, C., Burt, A., & Bruchez, M. *Development of quantum dot probes for multiplexed breast cancer analysis*. Claremont Resort, Berkeley, CA (2001).

5. Pellegrino, T., Manna, L., Kudera, S., Liedl, T., Koktysh, D., Rogach, A. L., Keller, S., Radler, J., Natile, G., & Parak, W. J. Hydrophobic nanocrystals coated with an amphiphilic polymer shell: A general route to water soluble nanocrystals. *Nano Lett.* **4,** 703-707 (2004).

6. Gao, X. H., Cui, Y. Y., Levenson, R. M., Chung, L. W. K., & Nie, S. M. In vivo cancer targeting and imaging with semiconductor quantum dots. *Nat. Biotechnol.* **22,** 969-976 (2004).

7. Aldana, J., Wang, Y., & Peng, X. Photochemical instability of CdSe nanocrystals coated by hydrophilic thiols. *J. Am. Chem. Soc.* **123,** 8844-8850 (2001).

8. Aldana, J., Lavelle, N., Wang, Y. J., & Peng, X. G. Size-dependent dissociation pH of thiolate ligands from cadmium chalcogenide nanocrystals. *J. Am. Chem. Soc.* **127,** 2496-2504 (2005).

9. Wu, X. Y., Liu, H. J., Liu, J. Q., Haley, K. N., Treadway, J. A., Larson, J. P., Ge, N. F., Peale, F., & Bruchez, M. P. Immunofluorescent labeling of cancer marker Her2 and other cellular targets with semiconductor quantum dots. *Nat. Biotechnol.* **21,** 41-46 (2003).

10. Kim, B. S., Qiu, J. M., Wang, J. P., & Taton, T. A. Magnetomicelles: Composite nanostructures from magnetic nanoparticles and cross-linked amphiphilic block copolymers. *Nano Lett.* **5,** 1987-1991 (2005).

11. Qu, L. H. & Peng, X. G. Control of photoluminescence properties of CdSe nanocrystals in growth. *J. Am. Chem. Soc.* **124,** 2049-2055 (2002).

12. Talapin, D. V., Mekis, I., Gotzinger, S., Kornowski, A., Benson, O., & Weller, H. CdSe/CdS/ZnS and CdSe/ZnSe/ZnS core-shell-shell nanocrystals. *J. Phys. Chem. B* **108,** 18826-18831 (2004).

13. Xie, R. G., Kolb, U., Li, J. X., Basche, T., & Mews, A. Synthesis and characterization of highly luminescent CdSe-Core $CdS/Zn_{0.5}Cd_{0.5}S/ZnS$ multishell nanocrystals. *J. Am. Chem. Soc.* **127,** 7480-7488 (2005).

14. Li, J. J., Wang, Y. A., Guo, W. Z., Keay, J. C., Mishima, T. D., Johnson, M. B., & Peng, X. G. Large-scale synthesis of nearly monodisperse CdSe/CdS core/shell nanocrystals using air-stable reagents via successive ion layer adsorption and reaction. *J. Am. Chem. Soc.* **125,** 12567-12575 (2003).

15. Manna, L., Scher, E. C., Li, L. S., & Alivisatos, A. P. Epitaxial growth and photochemical annealing of graded CdS/ZnS shells on colloidal CdSe nanorods. *J. Am. Chem. Soc.* **124,** 7136-7145 (2002).

16. Bleuse, J., Carayon, S., & Reiss, P. Optical properties of core/multishell CdSe/Zn(S,Se) nanocrystals. *Physica E* **21,** 331-335 (2004).

17. Cook, S. E., Park, I. K., Kim, E. M., Jeong, H. J., Park, T. G., Choi, Y. J., Akaike, T., & Cho, C. S. Galactosylated polyethylenimine-graft-poly(vinyl pyrrolidone) as ahepatocyte-targeting gene carrier. *J. Controlled Release* **105,** 151-163 (2005).

18. Kulkarni, R. P., Mishra, S., Fraser, S. E., & Davis, M. E. Single cell kinetics of intracellular, nonviral, nucleic acid delivery vehicle acidification and trafficking. *Bioconjug. Chem.* **16,** 986-994 (2005).

19. Guo, W., Li, J. J., Wang, Y. A., & Peng, X. G. Luminescent CdSe/CdS core/shell nanocrystals in dendron boxes: Superior chemical, photochemical and thermal stability. *J. Am. Chem. Soc.* **125,** 3901-3909 (2003).

20. Guo, W. Z., Li, J. J., Wang, Y. A., & Peng, X. G. Conjugation chemistry and bioapplications of semiconductor box nanocrystals prepared via dendrimer bridging. *Chem. Mater.* **15,** 3125-3133 (2003).

21. Uematsu, T., Maenosono, S., & Yamaguchi, Y. Photoinduced fluorescence enhancement in mono- and multilayer films of CdSe/ZnS quantum dots: Dependence on intensity and wavelength of excitation light. *J. Phys. Chem. B* **109,** 8613-8618 (2005).

22. Jones, M., Nedeljkovic, J., Ellingson, R. J., Nozik, A. J., & Rumbles, G. Photoenhancement of luminescence in colloidal CdSe quantum dot solutions. *J. Phys. Chem. B* **107,** 11346-11352 (2003).

23. Li, R. F., Lee, J., Yang, B. C., Horspool, D. N., Aindow, M., & Papadimitrakopoulos, F. Amine-assisted facetted etching of CdSe nanocrystals. *J. Am. Chem. Soc.* **127,** 2524-2532 (2005).

24. Hines, M. A. & Scholes, G. D. Colloidal PbS nanocrystals with size-tunable near-infrared emission: Observation of post-synthesis self-narrowing of the particle size distribution. *Adv. Mater.* **15,** 1844-1849 (2003).

25. Micic, O. I., Cheong, H. M., Fu, H., Zunger, A., Sprague, J. R., Mascarenhas, A., & Nozik, A. J. Size-dependent spectroscopy of InP quantum dots. *J. Phys. Chem. B* **101,** 4904-4912 (1997).

26. Talapin, D. V., Rogach, A. L., Kornowski, A., Haase, M., & Weller, H. Highly luminescent monodisperse CdSe and CdSe/ZnS nanocrystals synthesized in a hexadecylamine-trioctylphosphine oxide-trioctylphospine mixture. *Nano Lett.* **1,** 207-211 (2001).

27. Jiang, W., Mardyani, S., Fischer, H., & Chan, W. C. W. Design and characterization of lysine cross-linked mereapto-acid biocompatible quantum dots. *Chem. Mater.* **18,** 872-878 (2006).

28. Selvan, S. T., Tan, T. T., & Ying, J. Y. Robust, non-cytotoxic, silica-coated CdSe quantum dots with efficient photoluminescence. *Adv. Mater.* **17,** 1620-+ (2005).

29. Gerion, D., Pinaud, F., Williams, S. C., Parak, W. J., Zanchet, D., Weiss, S., & Alivisatos, A. P. Synthesis and properties of biocompatible water-soluble silica-coated CdSe/ZnS semiconductor quantum dots. *J. Phys. Chem. B* **105,** 8861-8871 (2001).

30. Wolcott, A., Gerion, D., Visconte, M., Sun, J., Schwartzberg, A., Chen, S. W., & Zhang, J. Z. Silica-coated CdTe quantum dots functionalized with thiols for bioconjugation to IgG proteins. *J. Phys. Chem. B* **110,** 5779-5789 (2006).

31. Correa-Duarte, M. A., Giersig, M., & Liz-Marzan, L. M. Stabilization of CdS semiconductor nanoparticles against photodegradation by a silica coating procedure. *Chem. Phys. Lett.* **286,** 497-501 (1998).

32. Derfus, A. M., Chan, W. C. W., & Bhatia, S. N. Probing the cytotoxicity of semiconductor quantum dots. *Nano Lett.* **4,** 11-18 (2004).

33. Zimmer, J. P., Kim, S. W., Ohnishi, S., Tanaka, E., Frangioni, J. V., & Bawendi, M. G. Size series of small indium arsenide-zinc selenide core-shell nanocrystals and their application to in vivo imaging. *J. Am. Chem. Soc.* **128,** 2526-2527 (2006).

34. Choi, H. S., Liu, W., Misra, P., Tanaka, E., Zimmer, J. P., Ipe, B. I., Bawendi, M. G., & Frangioni, J. V. Renal clearance of quantum dots. *Nat. Biotechnol.* **25,** 1165-1170 (2007).

35. Lovric, J., Bazzi, H. S., Cuie, Y., Fortin, G. R. A., Winnik, F. M., & Maysinger, D. Differences in subcellular distribution and toxicity of green and red emitting CdTe quantum dots. *J. Mol. Med.* **83,** 377-385 (2005).

36. Nabiev, I. et al. Nonfunctionalized nanocrystals can exploit a cell's active transport machinery delivering them to specific nuclear and cytoplasmic compartments. *Nano Lett.* **7,** 3452-3461 (2007).

37. Clapp, A. R., Medintz, I. L., & Mattoussi, H. Forster resonance energy transfer investigations using quantum-dot fluorophores. *ChemPhysChem* **7,** 47-57 (2006).

38. Xu, J., Wang, J., Mitchell, M., Mukherjee, P., Jeffries-El, M., Petrich, J. W., & Lin, Z. Q. Organic-inorganic nanocomposites via directly grafting conjugated polymers onto quantum dots. *J. Am. Chem. Soc.* **129,** 12828-12833 (2007).

39. Vinayakan, R., Shanmugapriya, T., Nair, P. V., Ramamurthy, P., & Thomas, K. G. An approach for optimizing the shell thickness of core-shell quantum dots using photoinduced charge transfer. *J. Phys. Chem. C* **111,** 10146-10149 (2007).

40. Dennis, A. M. & Bao, G. Quantum dot-fluorescent protein pairs as novel fluorescence resonance energy transfer probes. *Nano Lett.* **8,** 1439-1445 (2008).

41. Susumu, K., Uyeda, H. T., Medintz, I. L., Pons, T., Delehanty, J. B., & Mattoussi, H. Enhancing the stability and biological functionalities of quantum dots via compact multifunctional ligands. *J. Am. Chem. Soc.* **129,** 13987-13996 (2007).

42. Liu, W., Howarth, M., Greytak, A. B., Zheng, Y., Nocera, D. G., Ting, A. Y., & Bawendi, M. G. Compact biocompatible quantum dots functionalized for cellular imaging. *J. Am. Chem. Soc.* **130,** 1274-1284 (2008).

43. Dubois, F., Mahler, B., Dubertret, B., Doris, E., & Mioskowski, C. A versatile strategy for quantum dot ligand exchange. *J. Am. Chem. Soc.* **129,** 482-483 (2007).

44. Kim, S. W., Kim, S., Tracy, J. B., Jasanoff, A., & Bawendi, M. G. Phosphine oxide polymer for water-soluble nanoparticles. *J. Am. Chem. Soc.* **127,** 4556-4557 (2005).

45. Levin, C. S., Bishnoi, S. W., Grady, N. K., & Halas, N. J. Determining the conformation of thiolated poly(ethylene glycol) on Au nanoshells by surface-enhanced Raman scattering spectroscopic assay. *Anal. Chem.* **78,** 3277-3281 (2006).

46. Marsh, D., Bartucci, R., & Sportelli, L. Lipid membranes with grafted polymers: physicochemical aspects. *Biochim. Biophys. Acta* **1615,** 33-59 (2003).

47. Kirchner, C., Liedl, T., Kudera, S., Pellegrino, T., Javier, A. M., Gaub, H. E., Stolzle, S., Fertig, N., & Parak, W. J. Cytotoxicity of colloidal CdSe and CdSe/ZnS nanoparticles. *Nano Lett.* **5,** 331-338 (2005).

48. Katari, J. E. B., Colvin, V. L., & Alivisatos, A. P. X-Ray photoelectron-spectroscopy of CdSe nanocrystals with applications to studies of the nanocrystal surface. *J. Phys. Chem.* **98,** 4109-4117 (1994).

49. Aruguete, D. M., Marcus, M. A., Li, L. S., Williamson, A., Fakra, S., Gygi, F., Galli, G. A., & Alivisatos, A. P. Surface structure of CdSe nanorods revealed by combined X-ray absorption fine structure measurements and ab initio calculations. *J. Phys. Chem. C* **111,** 75-79 (2007).

50. Puzder, A., Williamson, A. J., Zaitseva, N., Galli, G., Manna, L., & Alivisatos, A. P. The effect of organic ligand binding on the growth of CdSe nanoparticles probed by Ab initio calculations. *Nano Lett.* **4,** 2361-2365 (2004).

51. Rempel, J. Y., Trout, B. L., Bawendi, M. G., & Jensen, K. F. Properties of the CdSe(0001), (0001), and (1120) single crystal surfaces: Relaxation,

reconstruction, and adatom and admolecule adsorption. *J. Phys. Chem. B* **109,** 19320-19328 (2005).

52. Ding, Y. & Wang, Z. L. Profile imaging of reconstructed polar and non-polar surfaces of ZnO. *Surf. Sci.* **601,** 425-433 (2007).

53. Wang, X. S., Dykstra, T. E., Salvador, M. R., Manners, I., Scholes, G. D., & Winnik, M. A. Surface passivation of luminescent colloidal quantum dots with poly(dimethylaminoethyl methacrylate) through a ligand exchange process. *J. Am. Chem. Soc.* **126,** 7784-7785 (2004).

54. Wang, M. F., Felorzabihi, N., Guerin, G., Haley, J. C., Scholes, G. D., & Winnik, M. A. Water-soluble CdSe quantum dots passivated by a multidentate diblock copolymer. *Macromolecules* **40,** 6377-6384 (2007).

55. Chakraborty, A. K. & Golumbfskie, A. J. Polymer adsorption-driven self-assembly of nanostructures. *Annu. Rev. Phys. Chem.* **52,** 537-573 (2001).

56. Pons, T., Uyeda, H. T., Medintz, I. L., & Mattoussi, H. Hydrodynamic dimensions, electrophoretic mobility, and stability of hydrophilic quantum dots. *J. Phys. Chem. B* **110,** 20308-20316 (2006).

57. Smith, A. M., Duan, H. W., Rhyner, M. N., Ruan, G., & Nie, S. M. A systematic examination of surface coatings on the optical and chemical properties of semiconductor quantum dots. *Phys. Chem. Chem. Phys.* **8,** 3895-3903 (2006).

CHAPTER 6

Amphiphilic Multidentate Ligand Coatings for Amphibious Nanocrystals and Reaction Control

The use of multidentate ligands as coatings for nanocrystals has recently been a subject of intense interest.[1-9] As demonstrated in Chapter 5, multidentate coordination can enhance the stability of labile nanocrystals due to binding constants that can grow almost exponentially with valency. Analogously, metal ion chelates are significantly more stable than monodentate ligand complexes, and the binding interactions between multivalent ligands and cellular receptors are vastly stronger than equivalent monovalent interactions.[10] The current theoretical understanding of these interactions is well developed, yet the extension of these concepts to atomic interactions between ligands and crystal surfaces has not yet been explored. For example, in comparison to metal ion chelates, multidentate ligands bind to nanocrystals through surfaces of metal ions, with facet dependent geometries. In comparison to ligand-receptor interactions, the interactions between coordinating ligands and nanocrystal surfaces occur on a scale that is an order of magnitude smaller (Angstroms rather than nanometers), for which fixed binding geometries and steric hindrance would be expected to be overwhelming factors. Insight can be drawn from the extensive study of the conformation of polymers adsorbed to solid substrates,[11] yet still there is a dearth of understanding of these interactions at the nanoscale, especially with respect to the highly curved surfaces of nanocrystals and the role of specific chemistries. A major limiting factor in the study of such

phenomena has been the availability of a suitable experimental system, as the assembly of multidentate ligands on nanocrystals is nontrivial (see Chapter 5).

In this chapter it is demonstrated that a wide variety of nanocrystals can be coated with amphiphilic multivalent ligands *in situ* during synthesis. These nanocrystals show tremendous colloidal stability and their thermal stability is also vastly enhanced compared to their monovalent ligand counterparts. This work describes the first use of amphiphilic multidentate ligands for nanocrystal synthesis, and reveals two major findings. First, the amphiphilic character of the multidentate ligand causes the nanocrystals to behave as amphibious colloids, soluble in nearly any solvent. Second, the multidentate coordinating capacity of these ligands induces a unique control over nanocrystal assembly. Both of these attributes are extremely valuable from a fundamental perspective, yielding a greater understanding of the multidentate nature of binding on small nanocrystals, allowing a means to study controlled nanocrystal synthesis, and providing an unmatched capacity to study the solvent-dependent characteristics of various nanocrystals. In addition, the scope of applications for these nanocrystals is immense, showing immediate utility for biological labelling, multi-solvent catalysis, and device incorporation.

6.1 Nanocrystal Synthesis Methods

6.1.1 Amphipol syntheses. The synthesis of hydrophobically modified polyacrylic acid (PAA, MW 1773 Da) was based on previously described procedures.[12,13] As an example, the preparation of 40% octylamine-modified PAA (PAA-$OA_{0.4}$) is described in detail. PAA (5 g, 69.39 mmol carboxylic acid) was dissolved overnight in 1-methyl-2-pyrrolidone (MPD, 150 mL) at 50ºC. A solution of octylamine (3.587 g, 27.75 mmol) in

MPD (~15 mL) was slowly added to the PAA solution, which was then vigorously stirred for approximately 1 hour at 50ºC. A solution of *N*-hydroxysuccinimide (6.389 g, 55.51 mmol) in MPD (~15 mL) was then added dropwise, and the reaction mixture was bubbled with ultrahigh purity argon for 30 minutes. During bubbling, a solution of *N,N'*-dicyclohexylcarbodiimide (6.872 g, 33.31 mmol) in MPD (~15 mL) was added dropwise over the course of 20 minutes, and bubbling was continued for an additional 20 minutes. The reaction was allowed to proceed for 48 hours under argon flow at 50ºC, during which the insoluble dicyclohexylurea reaction byproduct precipitated. After cooling the reaction to 4ºC, the reaction was filtered, and then diluted to 1.5 L with water, and the pH was adjusted to ~11 with 12.5 M sodium hydroxide. The polymer was then precipitated by adjusting the pH of the solution to ~3.5 with 5 M HCl, and filtered. For purification, the following procedure was repeated three times. The polymer was dissolved in basic water, filtered, precipitated with acid and collected via filtration. After the final precipitation, the polymer was washed with water and lyophilized to yield a white powder. The polymer was then dissolved in chloroform, filtered, and dried under vacuum to yield a yellow solid. Synthesis of polymers with different modification ratios or with different hydrophobic domains was performed by adjusting the reactant ratios and the chain lengths of the alkylamines. For modification at ratios greater than 50%, the reaction was generally performed in two sequential steps, and the DCC product was removed via filtration prior to performing the second half of the modification. The hydrolysis of poly(maleic anhydride-*alt*-1-tetradecene) was described in Chapter 5.

6.1.2 General synthesis strategy. All nanocrystal syntheses were performed using standard air-free techniques with a Schlenk line and glove box or bag. For most nanocrystals prepared for this work, a metal salt (metal acetate or acetyacetonate) was

added to a 100 mL vial containing amphipols and 8 mL polyethylene glycol (PEG). Generally the metal ion concentration was 12.5 mM, and the ratio of amphipol carboxylic acids to metal was 3:1 – 20:1, depending on the desired nanocrystal size (higher concentrations yielded smaller nanocrystal sizes). The mixture was then degassed thoroughly at room temperature during heavy stirring, and then heated to 70°C under vacuum for an additional hour. Evacuation was allowed to occur very slowly in order to prevent a large amount of sudsing. The solution was then charged with argon, and heated to a temperature at which the metal ion precursor reacted with the amphipol to form a stable chelate. Then additional reactants were added and the solution was heated to the reaction temperature.

Swift injections of precursors was not required to achieve monodisperse nanocrystals. Samples were obtained from the reaction by removing small aliquots, which were diluted in various solvents while the reaction mixture was still warm. Different PEG molecular weights resulted in similar nanocrystals size and monodispersity, although high molecular weights (>2000 Da) were avoided due to their viscosity and very low molecular weights (<250 Da) yielded less efficient micellization. Temperatures above 300ºC were avoided, as the reaction solution tended to irreversibly darken. Metal halides were generally incompatible with these reactions. Metal oxides were compatible, but required a much higher temperature to form a complex with the multidentate polymer. All of the amphipol-metal ion complexes were insoluble in water until nanocrystal nucleation, allowing a convenient means to qualitatively monitor of the progress of the reaction. Nanocrystals were purified in water using ultracentrifugation, size-exclusion chromatography, or dialysis. In nonpolar solvents, nanocrystals were purified by spontaneous precipitation, as described in the text. These particles may also be purified through other various chromatographic or extraction methods.

6.1.3 Synthesis of CdTe. For a typical synthesis of CdTe nanocrystals, cadmium(II) acetate hydrate (0.2 mmol), amphipols (1.6 mmol carboxylic acids), and dihydroxy-PEG (8 mL, 400 MW) were added to a 50 mL flask and evacuated at room temperature to ~20 Pa. Caution should be used when slowly degassing this extremely sudsy mixture to prevent contamination of the Schlenk line. While under vacuum, the temperature was slowly ramped to 70ºC, resulting in vigorous bubbling. After 1 hour of evacuation, the solution was clear, with a slight yellow hue. The reaction was then charged with argon and the temperature was raised to 150ºC. Tributylphosphine-telluride precursor was then added, consisting of tellurium (0.1 mmol), tributylphosphine (0.8 mmol), and PEG (4 mL), and the reaction temperature was increased to 280ºC. Although it was found that these CdTe quantum dots were highly fluorescent, in some solvents the emission quenched when exposed to both oxygen and light. This has been commonly reported for CdTe quantum dots,[14-16] but can be largely attenuated with the addition of a small amount of low molecular weight thiol (e.g. thioglycerol or mercaptoacetic acid) or other antioxidant. For the growth of CdS or CdSe shells, the amount of tellurium injected was decreased from 0.1 mmol to 0.06 mmol and aliquots were taken to determine the size and concentration of the CdTe cores. Twenty minutes after the initial injection, 0.06 mmol of either sulfur or selenium was added dropwise to the reaction, and the reaction was allowed to proceed for 2-4 hours at 260ºC. Elemental sulfur dissolved in PEG-500 (0.05 M), and tributylphosphine-selenide dissolved in PEG-500 (0.05 M) were used as reactants.

6.1.4 Synthesis of PbSe. The synthesis of PbSe nanocrystals was similar to that of CdTe nanocrystals, except lead acetate trihydrate was used in the place of cadmium acetate hydrate. Tributylphosphine-selenide was used as the selenium precursor, and

the reaction was performed between 200- 265ºC, depending on the concentration of amphipol.

6.15 Synthesis of Iron Oxide. Iron(III) acetylacetonate (0.03532 g, 0.1 mmol), amphipols (0.3 mmol), 1,2-hexadecanediol (0.35 mmol), dodecylamine (0.3 mmol), and dihydroxy-PEG (8 mL) were mixed in a 100 mL flask and evacuated at room temperature to ~20 Pa. The temperature was slowly increased to 130ºC, at which point vigorous bubbling began. The reaction mixture became clear and amber-colored as the iron-amphipol complex formed. The temperature was then raised to 280ºC for 3 hours to yield iron oxide nanocrystals. The presence of amines was found to decrease the nucleation temperature and improve size control.

6.16 Synthesis of Metal Nanocrystals. For the synthesis of metal nanocrystals, dihydroxy PEG allowed the reduction of metals salts in the absence of an additional reducing agent, possibly due to similar mechanisms as polyol syntheses of metal nanocrystals.[17] For these nanocrystals, the reactions were similar to those described in sections 6.1.2-6.1.5, except the amphipol was first dissolved in PEG through heating (200°C) and cooled to room temperature prior to introduction of the metal salt, which was in lower concentration (1-6 mM). Silver nanocrystals were prepared using silver(I) acetate at a growth temperature of 120-150ºC. Palladium nanocrystals were prepared using palladium(II) acetylacetonate at a growth temperature of 120-150ºC. Gold nanocrystals were prepared using gold(III) acetate at a growth temperature of 60-100ºC. In order to produce homogeneous and stable metal nanocrystals, it was vital to first dissolve the metal salt in the reaction mixture before heating. The dissolution of gold acetate was aided with the addition of chloroform, which could then be removed under vacuum, resulting in a clear solution at 40°C after several hours.

6.2 Spontaneous Generation of Hydrophilic and Hydrophobic Coatings in an Amphibious Bath

Recent research has led to high-quality and monodispersed colloidal nanocrystals by using a number of synthetic methods including reactions in reverse micelles, arrested precipitation in aqueous solution, and organic-phase high temperature syntheses using hydrophobic coordinating ligands (see Chapters 2 and 3). The nanocrystals synthesized by these methods have shown various degrees of crystallinity, monodispersity, size-tunability, stability, and processibility. However, a major limitation is that the resulting nanoparticles are soluble only in the reaction solution or in chemically similar media.[18,19] For example, nanocrystals synthesized in trioctylphosphine oxide or other organic solvents are only soluble in nonaqueous media, whereas nanocrystals prepared in aqueous solution are not compatible with nonpolar solvents that are often used for fabrication of composite materials, device incorporation, and catalytic reactions.[20]

Here we report a new strategy to couple the synthesis and encapsulation of high-quality nanocrystals to yield nearly universal solubility. This method is based on the use of an 'amphibious bath' consisting of amphiphilic multidentate ligands in a noncoordinating solvent (such as low-molecular weight polyethylene glycol or PEG). The multidentate ligands (amphipols[21,22]) are linear polymer chains with aliphatic sidechains and carboxylic acid functional groups, and are found to act as both a ligand for metal ion precursors and a nanoparticle surface stabilizer. A major finding is that the resulting nanocrystals are instantly soluble in both polar and nonpolar solvents (such as water, acetone, DMF, and chloroform). This amphibious bath method is applicable to a wide variety of technologically important nanocrystals including photoluminescent

semiconductors (II-VI and IV-VI quantum dots), catalytic metals (palladium), noble metals (gold and silver), and superparamagnetic materials (iron oxide). This work broadly improves the applicability of nanocrystals in biolabeling, catalysis, and device fabrication.

As depicted in Figure 6.1, the multidentate polymer serves as a coordinating ligand for metal ion precursors, replacing traditionally used monovalent ligands such as oleic acid or stearic acid. At elevated temperatures (100-280°C), these polymeric carboxylate precursors react with similar chemistry as their monovalent fatty acid analogues.[23,24] Upon nanocrystal nucleation, these multidentate polymers strongly bind to the nanocrystal surface during growth to yield monodisperse, highly stable colloids. As synthesized, the nanocrystals are nonpolar due to directional coordination of the amphiphilic ligand on the crystal surface, allowing solubility in nonpolar solvents. However, metal ions are consumed during nanocrystal growth, releasing free polymer molecules into the reaction solution. When exposed to polar solvents, the multidentate polymer spontaneously encapsulates and solubilises the nanocrystals through the formation of hydrophilic micelles. This strategy is fundamentally different from previous approaches in which nanocrystals with amphibious attributes are coated with amphiphilic polymers such as polyethyleneimine,[25] or poly[2-(dimethylamino)ethyl] methacrylate.[26] The previous work involved surface modification of pre-synthesized nanocrystals and required removal of the reaction solvent prior to redispersion in a new solvent.

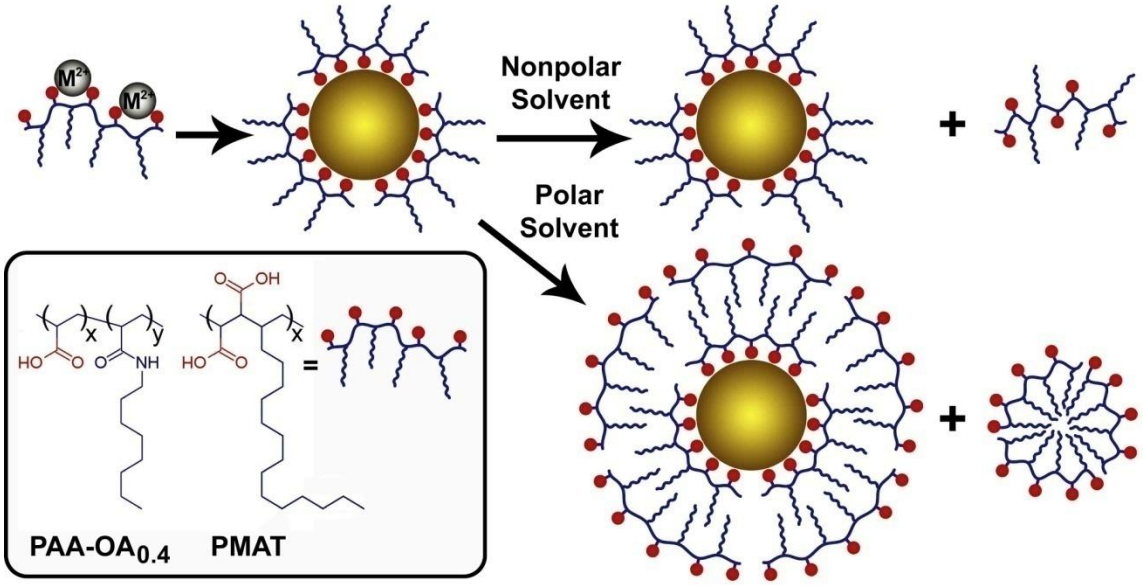

Figure 6.1: Schematic showing the use of amphiphilic multidentate ligands to prepare nanocrystals that are instantly soluble in both polar and nonpolar solvents. The resulting nanocrystals are coated with the multidentate polymer, and are soluble in organic solvents. Upon exposure to water or other highly polar solvents, these nanocrystals are spontaneously solubilized by a second layer of the excess multidentate polymer, without any additional materials or steps. The inset shows the structures of two multidentate polymer ligands: octylamine-grafted polyacrylic acid (x = 0.6, y = 0.4, PAA-$OA_{0.4}$) and hydrolyzed poly(maleic anhydride-*alt*-1-tetradecene) (PMAT).

6.2.1 Colloidal Characterization. Figure 6.2 shows solutions of fluorescent CdTe nanocrystals synthesized in an amphibious bath, demonstrating solubility in a broad range of solvents. It should be stressed that these nanocrystals do not contain a mixture of hydrophilic and hydrophobic surface groups, and are not amphiphilic by themselves. Rather, this broad solubility arises from the amphibious nature of the reaction mixture toward both polar and nonpolar solvents. The nanocrystals purified in nonpolar solvents are no longer soluble in polar solvents unless excess amphipols are again added to the solution. Similarly, once the nanocrystals are solubilised in a polar solvent, they lose their solubility in nonpolar solvents, even if the polar solvent is removed and excess amphipol is added. This indicates that the hydrophilic coating generated in polar solvents is very stable and is essentially irreversible. As a result, the

nanocrystals do not aggregate and remain monodispersed, as judged by light scattering and electron microscopy measurements (below), and by the narrow surface plasmon absorption peaks of noble metal nanocrystals (see below).

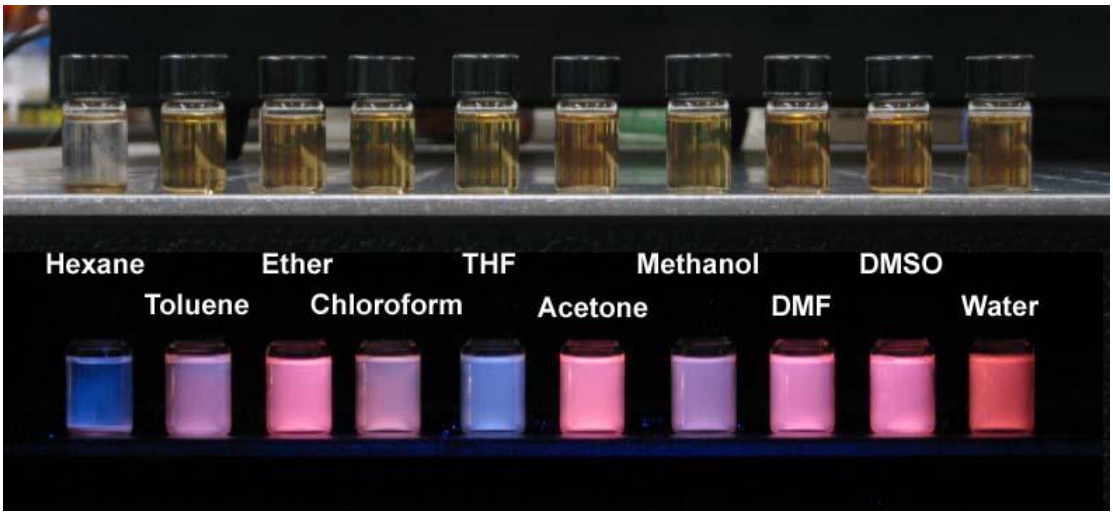

Figure 6.2: Photographs of CdTe nanocrystals synthesized in an amphibious bath instantly dissolved in a broad range of polar and nonpolar solvents. The top photograph shows the solutions under room light and the bottom photograph is with ultraviolet illumination. When the nanocrystal fluorescence is quenched, the amphibious mixture shows a blue hue (see the hexane and THF vials). The precipitation of the nanocrystals from hexane is discussed in the text.

In order to further understand the surface coatings of these nanocrystals, they have been directly compared with analogous nanocrystals synthesized with monovalent ligands. CdTe nanocrystals were prepared with a first exciton peak at 550 nm, using both the amphibious reaction bath and a conventional organic ligand method.[16] Theoretically the inorganic nanocrystals comprising these two samples should be essentially the same (3.2 nm diameter) due to their nearly identical optical properties.[27] First these two colloids were characterized in hexane using dynamic light scattering (DLS). Figure 6.3 reveals a slightly larger hydrodynamic size for the polymer-coated nanocrystals (6.8 nm) compared to the ones coated with monovalent ligands (5.2 nm).

This difference is due to the steric bulkiness of the amphipol ligand and its larger radius of gyration compared to a small monovalent ligand. In fact, the hydrodynamic thickness value of ~1.8 nm is consistent with the theoretical prediction of a 'loops-trains-tails' binding conformation for a monolayer of this multidentate polymer on the nanocrystal surface.[1,11] Next, these same nanocrystals were characterized in water. To prepare aqueous dispersions of the conventional CdTe nanocrystals, these nonpolar colloids were encapsulated in micelles composed of the same amphipol that was used for the amphibious nanocrystal synthesis (PAA-$OA_{0.4}$). Previous research has shown that the resulting hydrophilic nanocrystals are surrounded by a stable hydrophobic bilayer.[19,28,29] Once in water, both of these nanocrystals are similar in size (12-13 nm), as determined by DLS and size-exclusion chromatography (Figure 6.3B). They also have nearly identical electrostatic charges with a zeta potential of about -35 mV at pH 8.5. Therefore in water, these nanocrystals have similar structures. The thickness of this anionic micellar shell is 4-5 nm, which matches previous measurements of hydrophobic bilayers on nanocrystals.[19,28,30]

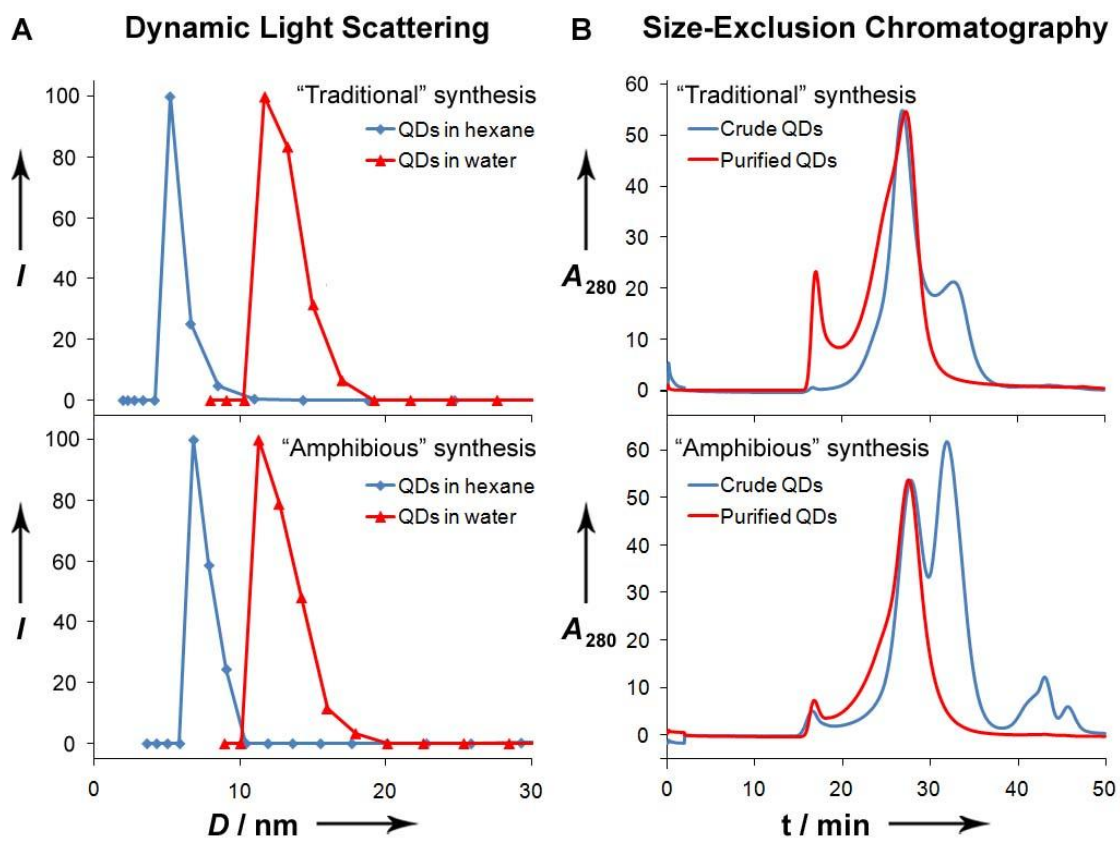

Figure 6.3: Size characterization of CdTe quantum dots (QDs) in hexane and water. (A) Dynamic light scattering measurements of purified CdTe in hexane (red) or water (blue), prepared using traditional multistep syntheses (top) or the one-step amphibious synthesis (bottom). (B) Size-exclusion chromatograms of aqueous solutions of traditional CdTe QDs encapsulated in a micelle (top) or amphibious nanocrystals (bottom). Chromatograms were obtained on crude reaction mixtures (blue) and nanocrystals isolated via ultracentrifugation (red). Empty amphipol micelles elute at ~32 minutes and PEG elutes at ~42 minutes.

6.2.2 Polymer Shell Characterization. The self-generated polymeric encapsulation layer was further examined by electron microscopy. Transmission electron microscopy (TEM) reveals smaller overall dimensions of the CdTe nanocrystals (Figure 6.4), compared to their hydrodynamic sizes. This is expected, due to the inability of electron microscopy to resolve surface-associated solvent molecules, and due to compaction of the shell that occurs during the drying process. TEM also confirms that the size of the

conventional ligand-coated CdTe nanocrystals matches predictions from their first exciton peak. However the nanocrystals prepared in the one-step amphibious reaction bath are again observed to be larger in size, due to a dense polymeric coating. It is difficult to resolve the interface between the polymeric shell and the nanocrystal surface on such small nanocrystals, but it is more evident on larger nanocrystals. Although the growth of very large CdTe nanocrystals is strongly inhibited by the multidentate ligands, further growth can proceed for PbSe nanocrystals. Figure 6.5 displays images of 22.5 nm aqueous PbSe nanocrystals using both Z-contrast scanning TEM (STEM) and scanning electron microscopy (SEM). Image contrast from STEM is weighted toward electron-dense regions like the nanocrystal core, whereas SEM can resolve surface features like the organic polymer shell. Nearly every individual nanocrystal is found to be coated with a uniform shell with an average dry thickness of 1.6 nm (Figure 6.5). Some closely packed particles are observed to have organic shells with webbing that connects to adjacent particles, which may indicate interaction between the hydrophobic bilayers upon drying. These structural studies further support the conclusion that a simple single-pot process can be used to synthesize highly ordered micelle-encapsulated nanocrystals that before could only be prepared using a complex and laborious multistep process consisting of nanocrystal synthesis, purification, and encapsulation.

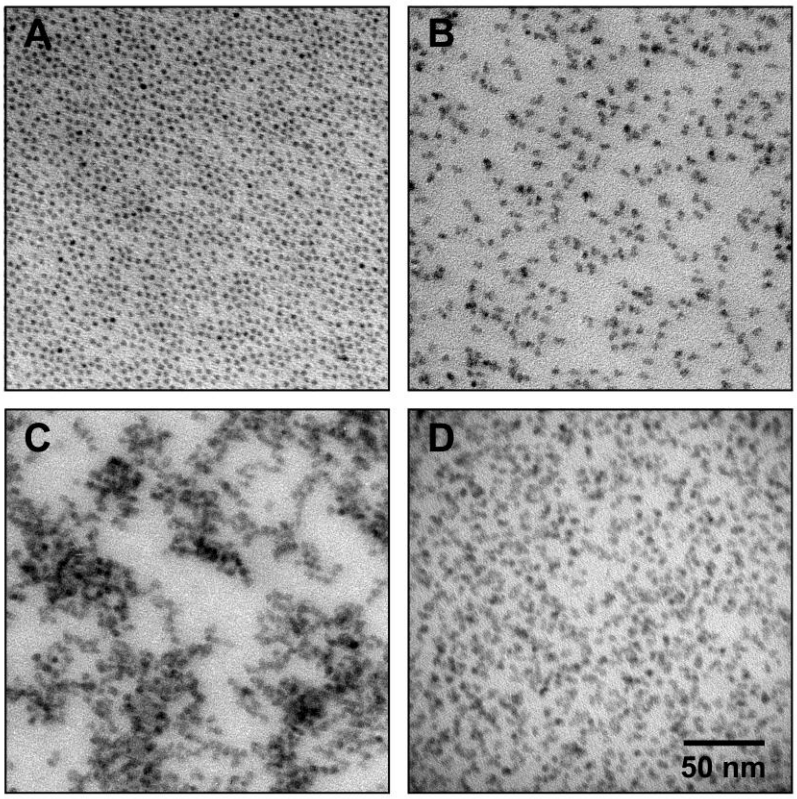

Figure 6.4: Electron micrographs of purified CdTe nanocrystals cast from a hexane solution, prepared using traditional coordinating ligands (A), or the 'amphibious' reaction (B). Also depicted are 'amphibious' nanocrystals cast from an aqueous solution before (C) and after purification (D). There was no significant aggregation evident in any of the solvents tested.

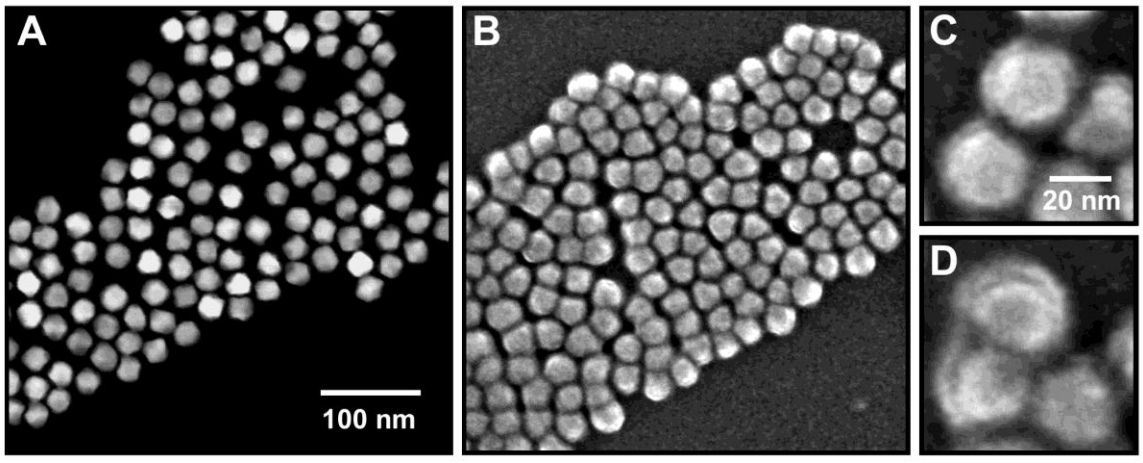

Figure 6.5: Electron micrographs of PbSe nanocrystals grown in the presence of amphipols, diluted in water, purified, and deposited on a TEM grid. (A) Z-contrast STEM revealed that the nanocrystals are quasi-spherical and highly faceted, with an

average diameter of 22.5 ± 1.7 nm. (B) The same grid was imaged via SEM, showing a size of 25.7 ± 2.5 nm. The scale is identical to that of (a). (C) Magnified SEM image, demonstrating an electron-dense core and organic shell. (D) A rare example of nanocrystals in which the polymer shells are seemingly fused together. The scale is identical to that of (c).

6.2.3 Reaction Mechanism. This phenomenon of spontaneous encapsulation is related to the nature of the amphiphilic coordinating ligand, as well as the reaction solvent. The contributions of both of these reaction components were independently evaluated, as summarized in Table 6.1. The multidentate, amphiphilic structure of the amphipol is crucial for attaining the dual functionality of coordination and encapsulation. Traditional hydrophobic coordinating ligands used in high-temperature nanocrystal reactions, such as oleic acid, can be used to prepare stable, monodisperse colloids in nonpolar solvents. However these ligands are poor surfactants, and cannot stabilize nanocrystals in polar solvents. Achieving efficient encapsulation from a coordinating ligand requires a balanced ratio of coordinating groups to hydrophobic groups. That is, too many coordinating groups yield poor encapsulation efficiency, whereas ligands containing too many hydrophobic domains cannot stabilize the nanocrystals during growth. In general, alkylation ratios of 30-60% work well for aliphatic chain lengths from 8 to 14 carbons. Interestingly, spatial or structural ordering of these domains is not necessary, as amphipols with ordered structures (PMAT, Figure 6.1) and randomly grafted structures (PAA-$OA_{0.4}$) yield nearly identical particles. On the other hand, the use of a linear, graft-like polymer backbone is crucial for the success of this procedure, as it allows directional orientation of the hydrophilic and hydrophobic domains while preventing crosslinking. Performing this same procedure with a di-carboxy PEG ligand resulted in complete precipitation of the nanocrystals after nucleation due to ligand-induced crosslinking.

Table 6.1: Solubility data of CdTe nanocrystals synthesized with multidentate ligands (amphipol) or traditional monovalent ligands (oleic acid) in three different solvents (ODE, DOE, or PEG).

Ligand	Solvent	Spontaneous precipitation	Chloroform solubility[a]	Acetone solubility[a]	Methanol solubility[a]	% Polar Extraction[b]
Oleic acid	ODE	No	~100%	0%	0%[d]	0%
	DOE	No	~100%	0%	0%	0%
	PEG	Yes/No[c]	~100%	0%	0%	0%
Amphipol	ODE	No	~100%	24.7%	0%[d]	0%
	DOE	No	~100%	72.2%	0%	0%
	PEG	Yes/No[c]	~100%	98%	98%	~100%

[a] Solubility was assessed as the fraction of nanocrystals stable in solution after dilution of the crude reaction mixture 1:10 in the solvent, and centrifugation at 7000g for 10 minutes.
[b] Extraction percentage between hexane and methanol phases.
[c] Spontaneous precipitation only occurs for dimethoxy-PEG, a liquid at room temperature (<~500 Da).
[d] ODE is immiscible with methanol.

The capacity to self-generate a micellar surface coating is highly sensitive to the chemical nature of the reaction solvent. Traditional nonpolar solvents, like dioctyl ether (DOE) and octadecene (ODE) prevent micellar encapsulation of nanocrystals. The use of PEG as a reaction solvent is important because of its 'amphibious' nature (that is, soluble in both polar and nonpolar solvents). The only solubility exception for the nanocrystals is hexane (Figure 6.2), in which PEG is insoluble. However once PEG is removed from the nanocrystals (see below), they become soluble in aliphatic hydrocarbons. It is thus surprising that the nanocrystals are instantly soluble in diethyl ether, a solvent in which PEG does not disperse. This feature is a result of the strong surfactant character of amphipol, which can solubilize a large amount of PEG in ether, even when present in small quantities.

Another interesting finding is that the terminal groups on PEG (methoxy or hydroxy) can influence the colloidal properties of the nanocrystals, even though they do not directly interact with the nanocrystal surface. When the nanocrystals are synthesized in PEG terminated solely by methoxy groups, they spontaneously precipitate out of the reaction mixture when the temperature is cooled below ~50°C. This observation of temperature-controlled precipitation and dispersion could be exploited to bypass the expensive and laborious purification procedures in large-scale synthesis of various nanocrystals. In contrast to methoxy terminal groups, both monohydroxy- and dihydroxy-terminated PEG solvents result in soluble colloid nanocrystals at room temperature (25°C). As noted above, PEG does not interact with the nanocrystals because (a) the growth kinetics of CdTe nanocrystals are nearly identical when using ODE, DOE, dimethoxy-PEG, monomethoxy-PEG, or dihydroxy-PEG, and (b) the use of a PEG solvent does not increase the hydrophilicity of nanocrystals prepared with monovalent ligands (Table 6.1). It is thus clear that the strongly binding amphipol ligand is responsible for the amphibious character of the nanocrystals, and PEG is an 'adjuvant' that enhances this effect.

6.2.4 Materials Compositions. The amphibious reaction bath method is broadly applicable to a wide range of nanocrystalline materials (Figure 6.6). Amphibious nanocrystals can be prepared with compositions of noble metals (gold and silver) that demonstrate discrete surface plasmon bands in various solvents (Figure 6.7). Amphibious quantum dots with intense, size-tunable photoluminescence (Figures 6.2 and 6.8) can be used directly in either biological buffers or in devices and composites. In addition, we have prepared catalytic palladium and superparamagnetic iron oxide nanocrystals (Figures 6.9 and 6.10). Energy dispersive X-ray confirmed the compositions of all of these nanocrystals (data not shown). Preliminary studies have

shown that the palladium nanocrystals are highly catalytic for cross-coupling reactions between arylboronic acids and aryl halides in both polar and nonpolar solvents. All of these nanocrystals are stable at room temperature for at least 3-4 months after purification in both polar and nonpolar solvents, with no major changes in light scattering measurements and electron micrographs. This remarkable stability is attributable to the strong binding between the multidentate ligand and the nanocrystal surface, as well as the stable micellar coating of amphipols in polar solvents. Indeed, amphipols have previously been used to stabilize nonpolar nanocrystals[19,28,29] and integral membrane proteins[21] in aqueous solution through hydrophobic interactions. Previous studies have found that this hydrophobic binding is essentially irreversible.[19,31]

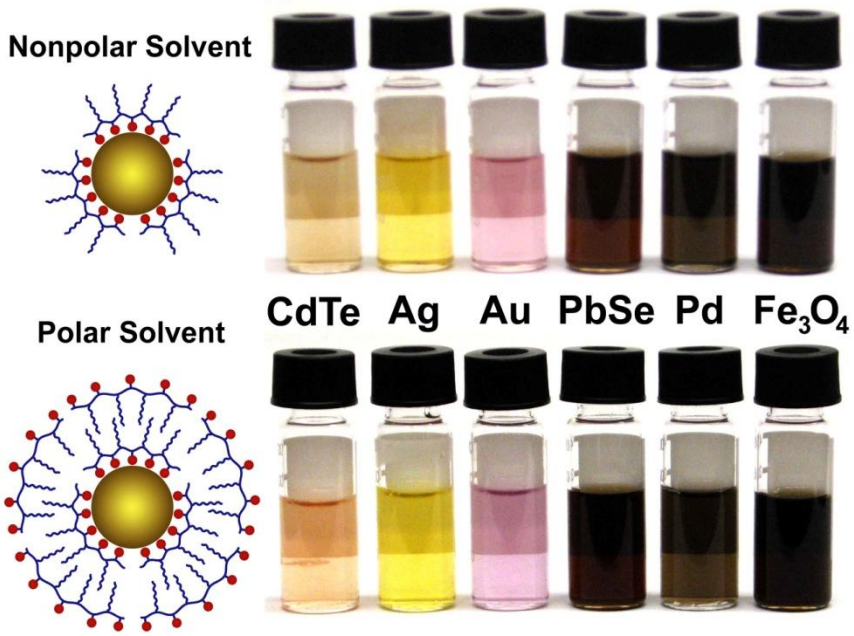

Figure 6.6: Metal, metal oxide, and semiconductor nanocrystals that are synthesized in an amphibious bath and are instantly soluble in both polar and nonpolar solvents. Shown on the left are schematic structures of self-generated hydrophobic and hydrophilic coatings on the nanocrystal surface.

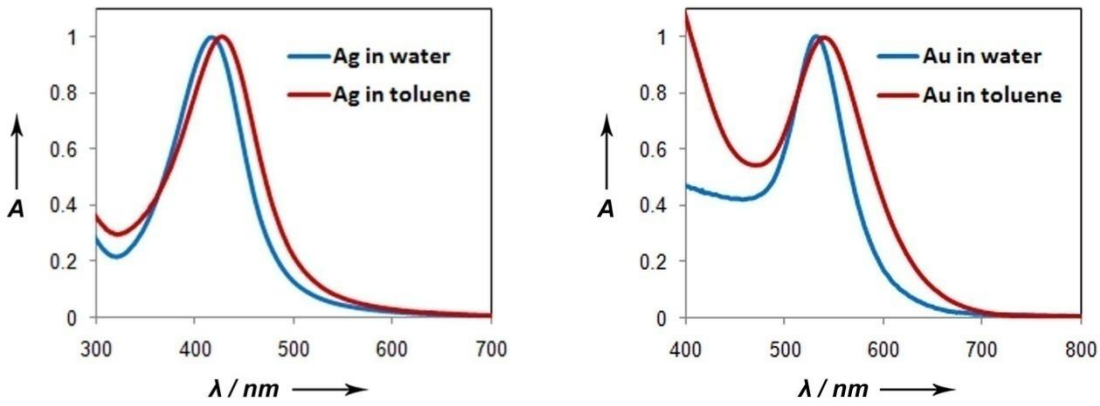

Figure 6.7: Left: Absorption spectra of amphibious silver nanocrystals dispersed in water or toluene. Right: Absorption spectra of amphibious gold nanocrystals dispersed in water or toluene.

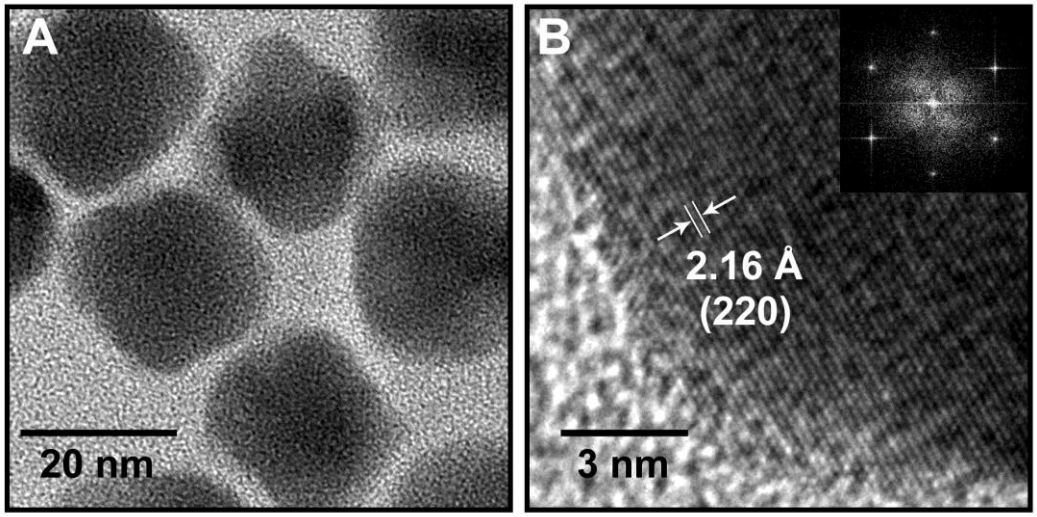

Figure 6.8: Additional lead selenide structural characterization. PbSe nanocrystals were grown in the amphibious bath to a size of 22.5 ± 1.7 nm, diluted in water, purified, and cast on a TEM grid. (A) High-resolution transmission electron micrographs of the nanocrystals. (B) Representative nanocrystal at high magnification with inset showing a fast Fourier transform of the nanocrystal image. The nanocrystal is oriented with its rock salt (111) plane parallel to the TEM grid and is significantly faceted along the nonpolar {110} faces.

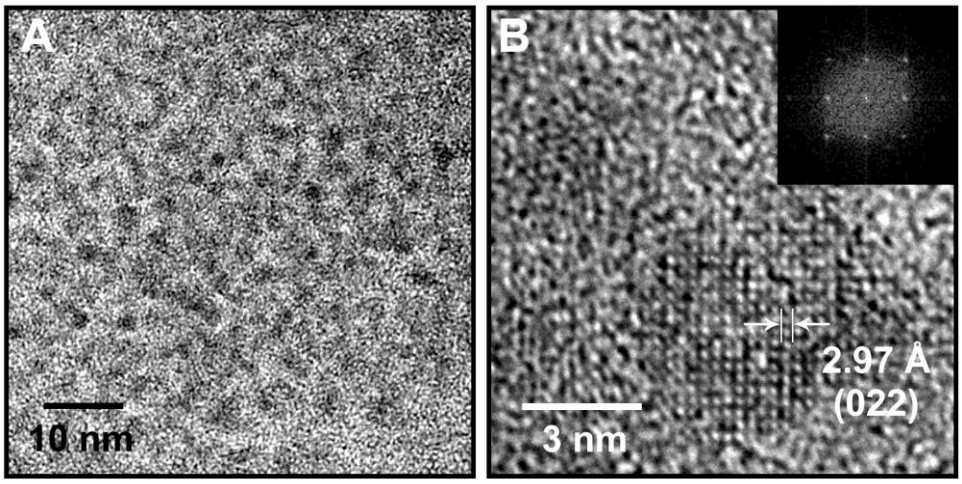

Figure 6.9: Iron oxide structural characterization. Iron oxide nanocrystals were grown in the amphibious bath to a size of 3.03 ± 0.53 nm, diluted in water, purified, and cast on a TEM grid. (A) High-resolution transmission electron micrographs of the nanocrystals. (B) Nanocrystal at high magnification with inset showing a fast Fourier transform of the nanocrystal image. The nanocrystal is oriented with its face-centered cubic (100) plane parallel to the TEM grid.

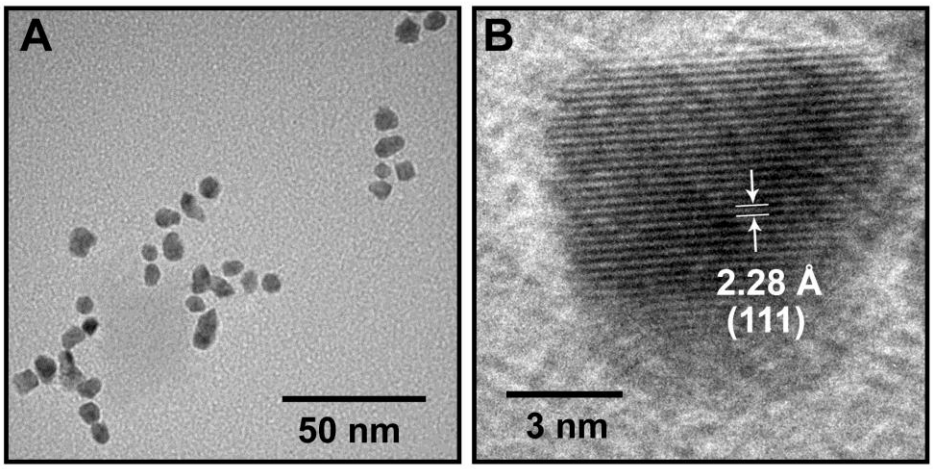

Figure 6.10: Palladium structural characterization. Slightly elongated Pd nanocrystals in the amphibious bath were diluted in water, purified, and cast on a TEM grid. (A) High-resolution transmission electron micrographs of the nanocrystals. The nanocrystals were highly faceted and slightly elongated, with short axis length 6.01 ± 1.00 nm and long axis length 8.43 ± 1.95 nm. (B) Nanocrystal at high magnification, showing faceting in the (111) direction

6.2.5 Applications of Amphibious Nanocrystals. We have developed a new synthesis strategy for a large variety of nanocrystals that are instantly soluble and stable in both polar and nonpolar solvents. A new finding is that multidentate ligands (amphipols) can serve as both coordinating ligands for metal atoms and nanocrystals, as well as micellization agents for nanocrystal encapsulation. To our knowledge, such a highly ordered self-assembly process using a single surfactant for both coordination and hydrophobic encapsulation in a single step has never before been reported. The high temperatures used for crystal growth result in monodisperse and highly crystalline particles, with reaction yields typically greater than 90%. The growth of larger nanocrystals revealed the high faceting of the nanocrystals, which is highly desirable for applications in catalysis, sensing, and energy transfer. For applications in nonpolar solvents, these nanocrystals may be spontaneously purified from their reaction solvent, and for use in aqueous solution, greater than 99% of these nanocrystals are stable after dilution in water as carboxyl-functionalized colloids. The long-term stability of these nanocrystals is tremendous due to the strong multidentate coordination by the amphipols and the strong hydrophobic interactions of the micelles in polar solutions, both of which are stabilized through multiple anchor points on the surface. The nanocrystals that were produced herein have great potential for applications in biological environments, homogeneous catalysis, device incorporation, and for the study of the solvent-dependent characteristics of nanocrystalline materials (Figure 6.11).

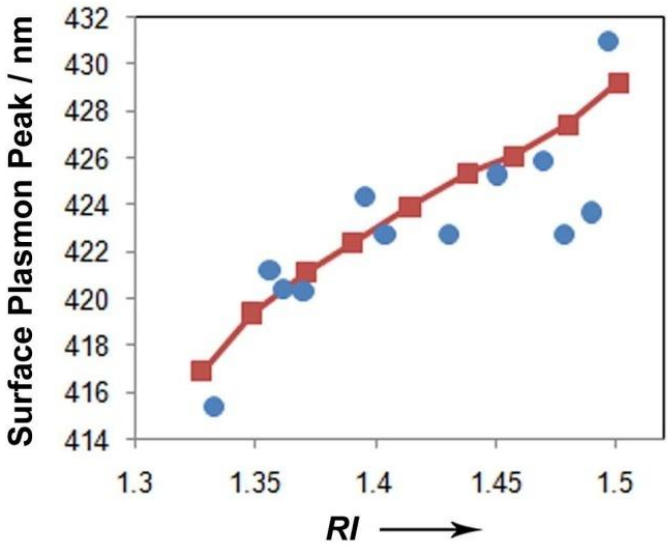

Figure 6.11: An example of simplified examination of the solvent-dependent properties of nanocrystals through the amphibious reaction bath procedure. The surface plasmon peak of amphibious silver nanocrystals is plotted against the refractive index of the solvent. Mixtures of benzene-methanol (red squares), as well as 12 other noninteracting solvents (blue circles), were tested.

6.3 Control of Nanocrystal Growth, Nucleation, and Structure with Multidentate Ligands

This amphibious bath synthesis is an evolution of the high temperature coordinating solvent nanocrystal reactions (Chapters 2 and 3).[32] It has been previously shown that the concentration of coordinating ligands (e.g. oleic acid) can dictate the final size of the nanocrystals.[23] As shown in this section, the replacement of molecular ligands with polymeric, multidentate ligands results in a unique size-dependence on the ligand concentration, with sizes tunable over a much broader range. Interestingly, these multidentate ligands tightly bind to metal precursors and to the nanocrystal surfaces through carboxylate-metal chelation, with both steric and diffusional barriers to uncontrolled nucleation and growth. Because of these unique physicochemical features, the dependence of the nanocrystal size on the ligand concentration is not only amplified, allowing tuning over a broader size range, but it is also inverted, which has never before

been reported for semiconductor nanocrystals. We postulate that this inversion is due to the close spatial proximity of metal ions on the polymeric backbone, forming reactant 'multimers' that react as a single unit of monomers. The synthesis of CdTe quantum dots using this strategy results in size-controlled, monodisperse nanocrystals with homogeneous nucleation and growth (Figure 6.12), whereas the analogous reactions using traditional monovalent ligands is uncontrollable and heterogeneous.

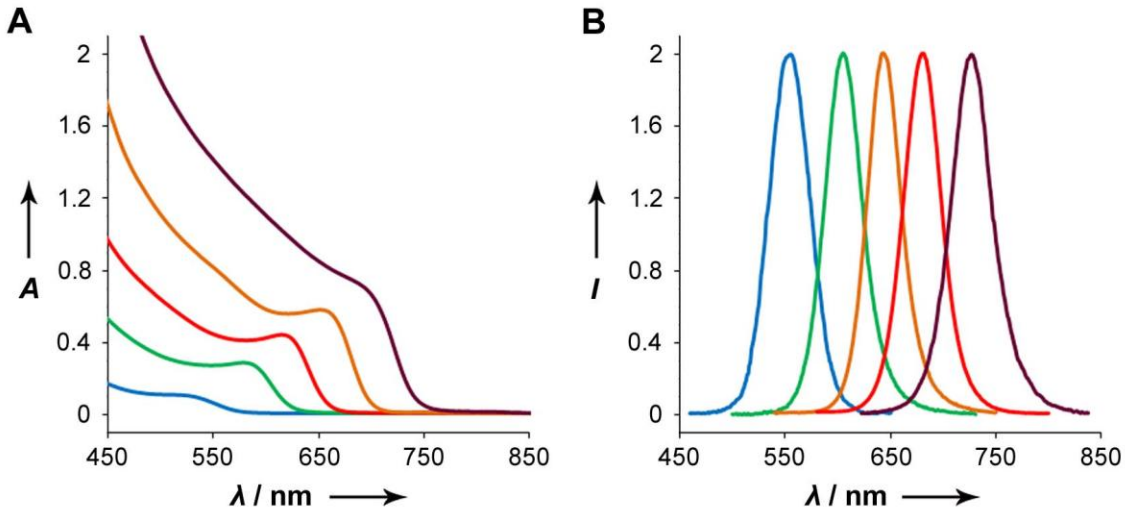

Figure 6.12: Optical absorption (A) and fluorescence emission spectra (B) of CdTe nanocrystals in the size range of 2.5 – 7 nm (diameter) synthesized in the presence of multidentate amphiphilic ligands (a mixture of amphipol and PEG).

6.3.1 Reaction Kinetics. Recent reports in the literature have described the tuning of nanocrystal size through the initial concentration of coordinating ligands in high temperature syntheses. This effect has been found to occur for a variety of nanocrystal materials, including CdS, CdSe, PbS, and InP.[23,33,34] The hypothesis is that a greater initial concentration of ligands decreases the activity of precursors, thus decreasing the rate of nucleation when the reactants are mixed at high temperature. Therefore after an initial burst of nucleation, a higher concentration of ligand will result in fewer nuclei, and a larger amount of free precursors in solution will be available to grow on the small

nuclei to achieve larger sizes. We have verified this hypothesis for CdSe nanocrystals (Figure 6.13, left) prepared using cadmium oleate and tributylphosphine selenide in an octadecene solvent. However when we attempted to apply these same principles to prepare CdTe nanocrystals, the reaction showed a negligible and poorly reproducible amount of tunability in size with respect to oleic acid concentration, and even a slight reversal of the ligand-precursor trend (Figure 6.13, middle). These nanocrystals rapidly nucleated with relatively large sizes (5-7 nm diameter) and broad size distributions, indicated by wide fluorescence emission peaks.

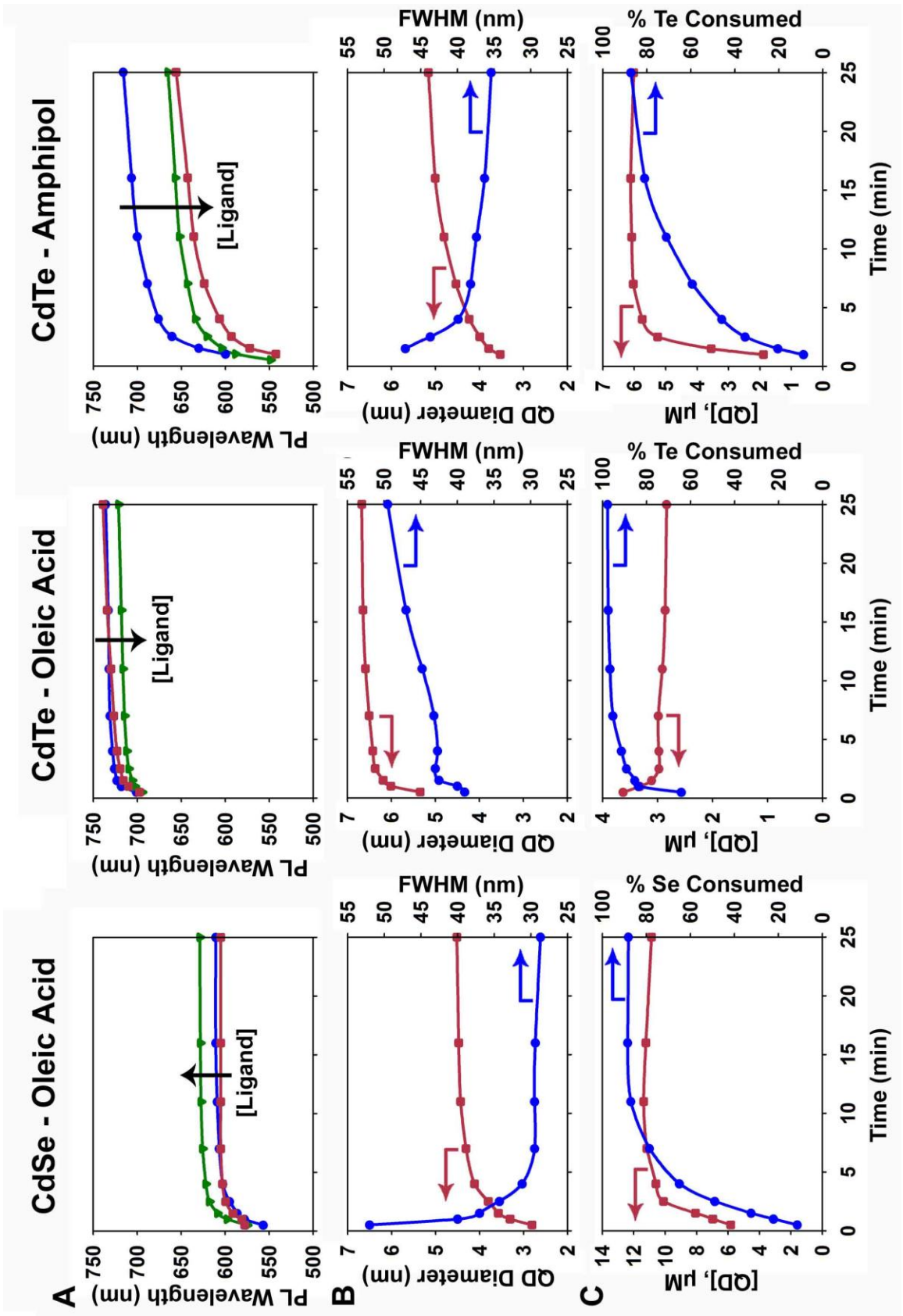

Figure 6.13: Kinetic evaluation of CdSe and CdTe nanocrystal synthesis reactions. Three reaction systems were monitored: CdSe with oleic acid ligands (left), CdTe with oleic acid ligands (middle), and CdTe with amphipol ligands (right) (A) The peak wavelength of photoluminescence was monitored over time after injection of the chalcogenide precursor. Ligand concentrations were calculated as COOH:Cd ratios, and were 4:1 (red), 8:1 (green), and 60:1 for the oleic acid ligands or 20:1 for the amphipol ligands (blue). (B) Quantum dot (QD) diameter (red) was calculated from the wavelength of the first exciton peak, which was determined from the second derivative of the absorption spectrum (Figure 6.14). The full-width-at-half-maximum (FWHM, blue) of the emission spectra is indicative of nanocrystal polydispersity. (C) Quantum dot concentrations, [QD], were calculated from the absorption values and known extinction coefficients (red), allowing the calculation of chalcogen consumption (blue). All reactions in (B) and (C) were performed with a COOH:Cd ratio of 4:1. Note that all of the x-and y-axes are identical, except for [QD] in (C). The amphipol used was PAA-$OA_{0.4}$. All reactions were performed in an ODE solvent, although similar trends were found to occur in DOE and PEG solvents.

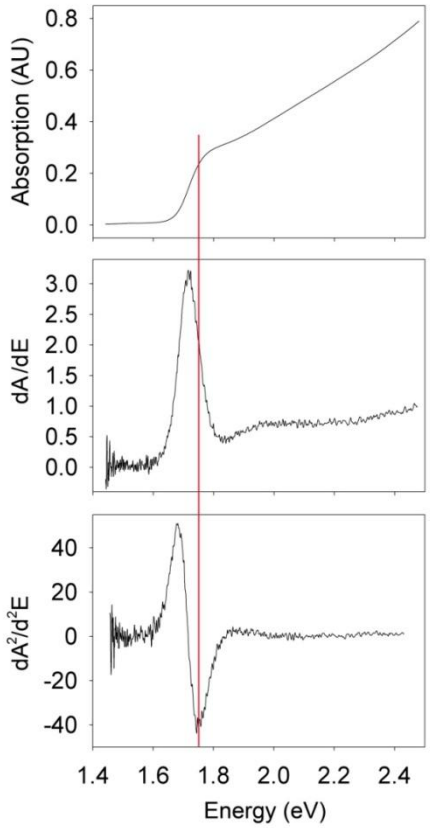

Figure 6.14: Extraction of the first exciton peak from absorption spectra of CdTe nanocrystals, using the second derivative method. The first exciton peak can even be extracted from relatively polydisperse samples, as shown here for CdTe quantum dots with a 706 nm first exciton peak. This allows fairly precise determination of nanocrystal size and concentration.

When the reactions of CdSe and CdTe are compared in detail, the mechanism for the differences becomes clear. Upon introduction of a selenium precursor, CdSe nanocrystals slowly nucleate over the course of the first 2-3 minutes. After this initial nucleation process, the remaining precursors grow on the nascent nuclei and focus in size to narrow the size distribution, as the consumption of precursors is slow and controlled in both the nucleation step and the following growth step. On the other hand, when tellurium is introduced into a reaction, its reactivity is so high that nucleation is instant, and nearly all of the reactants are consumed in seconds, leaving no precursors to focus the size distribution. Interestingly, immediately after injection, it was found that the number of total CdTe nanocrystals in the reaction quickly decreased from the initial value, indicating either occurrences of nanoparticle fusion or Ostwald ripening (TEM evidence suggests fusion to be the main effect, see below). After the number of nanocrystals in solution stabilized, there was a brief phase of size-focusing, indicated by a narrowing of the emission bandwidth. However because the distribution was initially highly heterogeneous and the reactants were quickly depleted, there was little improvement in the overall monodispersity before Ostwald ripening controlled the reaction, increasing the polydispersity. Altering the concentration of oleic acid had little impact because this reaction was overwhelmingly controlled by the high reactivity of tellurium, rather than the reactivity of cadmium.

When oleic acid was replaced with multidentate amphipols in this reaction, CdTe nanocrystals could be widely controlled in both size and size distribution (Figure 6.13, right). In fact, the kinetics of nucleation and growth of these nanocrystals strongly resembled those of CdSe (Figure 6.13, left), with nucleation occurring homogenously over the course of a few minutes without evidence of nanoparticle fusion or ripening. It was found that the consumption of tellurium was slow and controlled, and that the

nanocrystals focused in size with much narrower size distributions than could be achieved with oleic acid. Remarkably, the impact of the ligand concentration on the final focused size of the nanocrystals was amplified, allowing tuning over a broader range of sizes (Figure 6.13A). Indeed, by altering the ligand concentration and the reaction time, we could easily obtain nanocrystals from 2.5-8.0 nm in diameter (Figure 6.12), with emission from the green visible region to the near-infrared. The CdTe quantum dots prepared using this strategy reproducibly yield peak widths with full-width-at-half-maximum (FWHM) values around 35-37 nm, although ones as narrow as 33 nm have been achieved. For the monovalent ligand reaction, the most narrow size distribution occurred several seconds after injection, at around 38 nm FWHM. This monovalent reaction was purposely chosen to simulate the differences between monovalent and multivalent ligands, but it is not, itself, optimal for the synthesis of CdTe nanocrystals. It should be noted that other synthesis strategies using monovalent ligands have produced quantum dots with FWHM as narrow as 27 nm, but in our experience, 29-32 nm is typical for the most monodisperse CdTe.

It is an important finding that the dependence of the nanocrystal size on the multivalent ligand concentration follows the opposite trend of conventional size tuning. That is, a higher initial concentration of ligand results in *smaller* quantum dots. Initially we postulated that this may be due to a lower reaction completion when the nanocrystals focused in size, but it was found that 70-90% of the reactants were consumed for all ligand concentrations tested. Instead, we propose a multidentate sequestering mechanism for this unique attribute (Figure 6.15). The multidentate carboxylic acid ligands can react almost stoichiometrically with the cadmium precursors to yield nearly a 2:1 carboxylic acid:cadmium ratio. Under these conditions, there are ~7-8 cadmium atoms per polymer chain in solution when using the PAA-$OA_{0.4}$ ligand (containing an

average of 15 carboxylic acids). Each cadmium-polymer chains reacts as a single cadmium 'multimer' during the nucleation process, as opposed to monomers of monovalent cadmium. When the ligand:cadmium ratio increases, the number of cadmium atoms per polymer chain decreases stochastically, and therefore more cadmium multimers exist in solution, which may independently react with tellurium to yield nuclei. Therefore, as the ligand concentration increases, more nuclei form, and the size of the focused nanocrystals decreases. The kinetic analysis of the reaction (Figure 16.3) shows that these nanocrystals do not fuse together, as the nucleation process is slow and controlled. This is due to the high binding strength of the multidentate ligands on the nanocrystal surfaces and due to the associated high steric hindrance of the polymer, only allowing surface access to small monomers and multimers. This ligand-concentration effect would be expected to yield a continuous trend with ligand concentration until each cadmium atom is chelated by a single polymer chain. Experimentally, we found this trend to be valid for carboxylic acid:cadmium ratios up to ~12:1. Beyond this ratio, there was only a small dependence of the ligand concentration on the final size, and the trend reverted back to the conventional dependence, as the nanocrystals increased in size with increasing ligand concentration. This phase of the synthesis can be explained by the traditional mechanisms of an increase in polymer concentration resulting in decreased reactant activity, described earlier.

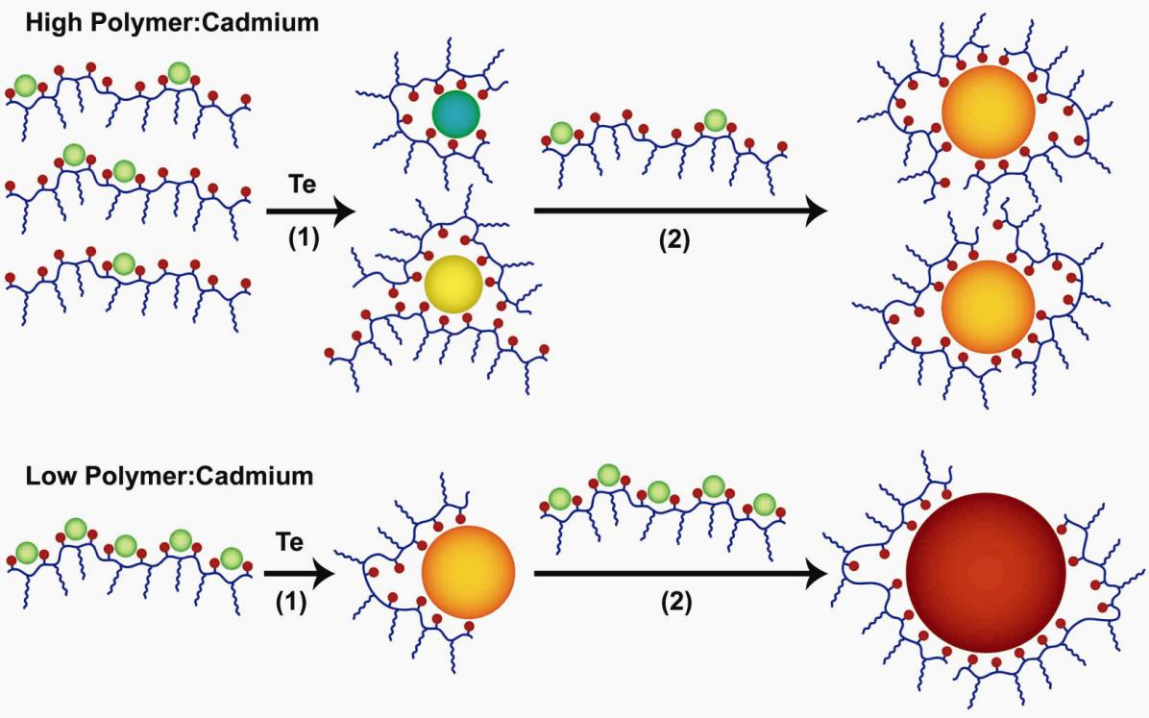

Figure 6.15: Control of reaction kinetics with multidentate ligands. This schematic describes the reaction control of CdTe, but the mechanisms for other nanocrystals may be similar. Green circles represent metal ions, which fuse to form larger nanocrystals. For high polymer concentrations (top), only one or two cadmium atoms are bound to each polymer chain prior to nucleation. Nucleation is initiated at high temperature with the addition of tellurium (1), resulting in the formation of small crystallites. These small crystallites are tightly bound through multidentate coordination to single polymer ligands, and cannot fuse together due to strong steric hindrance, but can grow slowly through reaction with small tellurium atoms and unreacted cadmium monomers (2). When the concentration of polymer is low (bottom), the polymer chains are nearly saturated with cadmium ions, containing up to 7-8 per chain. The induction of nucleation with the addition of tellurium (1) causes the cadmium 'multimers' to react as one nucleation site, bound to a single polymer, resulting in larger initial nuclei. Fewer nuclei exist in solution due to their sequestration in single reacting multimers, and thus the remaining tellurium and unreacted multimers grow on the nascent nuclei to much larger sizes (2). In addition, the low polymer concentration decreases multidentate interactions, increasing the activity of the nanocrystal surface reactivity.

Importantly, the investigation of this mechanism for nanocrystal growth would not be possible if it were not for the slow, homogeneous nucleation process afforded by the use of amphipol ligands. Traditional methodology for the production of monodisperse nanocrystals has called for the temporal separation of nucleation and growth, as

originally described by La Mer and Dinegar.[35] Indeed, it has been found in traditional high temperature organometallic reactions for the production of nanocrystals that a cold injection of precursors instantly produces similarly sized nanocrystallites, upon which homogeneous growth can proceed to generate monodisperse nanocrystals.[32] However it is clear from the kinetics of the reactions of CdSe nanocrystals prepared with oleate ligands and CdTe nanocrystals prepared with amphipol ligands that this effect may not always be predominant. In these reactions, nucleation proceeds over the course of several minutes and still results in monodisperse nanocrystals. This attribute is due to the relatively fast rate of monomer nucleation compared to the slow rate of monomer deposition on nascent nanocrystals. This disproportionately low reactivity of monomers toward growth is due to the strong binding of the ligand on the nanocrystal surface that reduces the reactivity of the surface facets, as well as the steric hindrance provided by the polymer that resists access to the nanocrystal surface. These effects yield uniform reactant consumption and allow nucleation and growth to briefly coincide while still resulting in homogeneous nanocrystals, much like the synthesis of iron oxide nanocrystals.[36] This finding opens the door to the synthesis of homogeneous nanocrystals without an injection event, which is a useful attribute for industrial scale reactions in which instantaneous and homogenous mixing of solutions is difficult and dangerous. As well, for most nanocrystal synthesis, size polydispersity is marred by Ostwald ripening in later phases of growth when most of the precursors have been consumed. However for the amphipol ligands, the onset of Ostwald ripening is significantly delayed, only commencing after one or two hours. This is likely due to the strong, multivalent binding of the polymer to the growing nanocrystals. Indeed, the multivalent binding strength of these polymers, combined with the sterically controlled reactivity and strong passivation of nanocrystals surfaces are complexly intertwined.

6.3.2 Lattice Structure and Morphology. As discussed extensively in Chapter 4, cadmium telluride is polymorphic and polytypic in bulk and in nanostructures, demonstrating both zinc blende and wurtzite phases. Although zinc blende is the most common phase for this material in bulk, CdTe nanocrystals can assume both lattice structures, and may be tuned between these two structures through a choice in ligand chemistry.[16] CdTe nanocrystals prepared with oleic acid ligands were previously reported to be wurtzite, however this is in direct conflict with our high-resolution transmission electron microscopy (HRTEM) analysis of these nanocrystals (Figure 6.15A). Previous studies only implemented X-ray diffraction techniques, which can be difficult to interpret without in depth modeling of stacking faults, and can be obscured by polydispersity.[16] In contrast, HRTEM can be used to visualize and identify specific lattice planes, some of which can be used to unambiguously classify lattice structures, as discussed in Chapter 5. The {110} lattice planes were frequently observed, with very infrequent wurtzite stacking faults, suggesting a strong zinc blende character to these quantum dots.

When first nucleated, CdTe nanocrystals assumed spherical shapes in the presence of oleic acid ligands, but later showed signs of nanocrystal fusion, with multiple crystalline domains coinciding on the same nanocrystal. As well, these nanocrystals grow in irregular shapes, with seemingly no preference for axes of elongation. In contrast, the nanocrystals grown in the presence of the multidentate polymer were found to be homogeneous in size and in crystallinity at all points throughout a 2 hour reaction. In addition, nanocrystals grown with the polydentate polymer were unambiguously identified to assume the zinc blende lattice structure via HRTEM. Because of the large mass fraction of amorphous polymer associated with these nanocrystals, and due to their small sizes, x-ray diffraction was not attempted, as our experience has shown that

distinguishing the zinc blende from wurtzite lattice structures in small nanocrystals is impractical unless a highly crystalline sample can be obtained (Chapter 5).

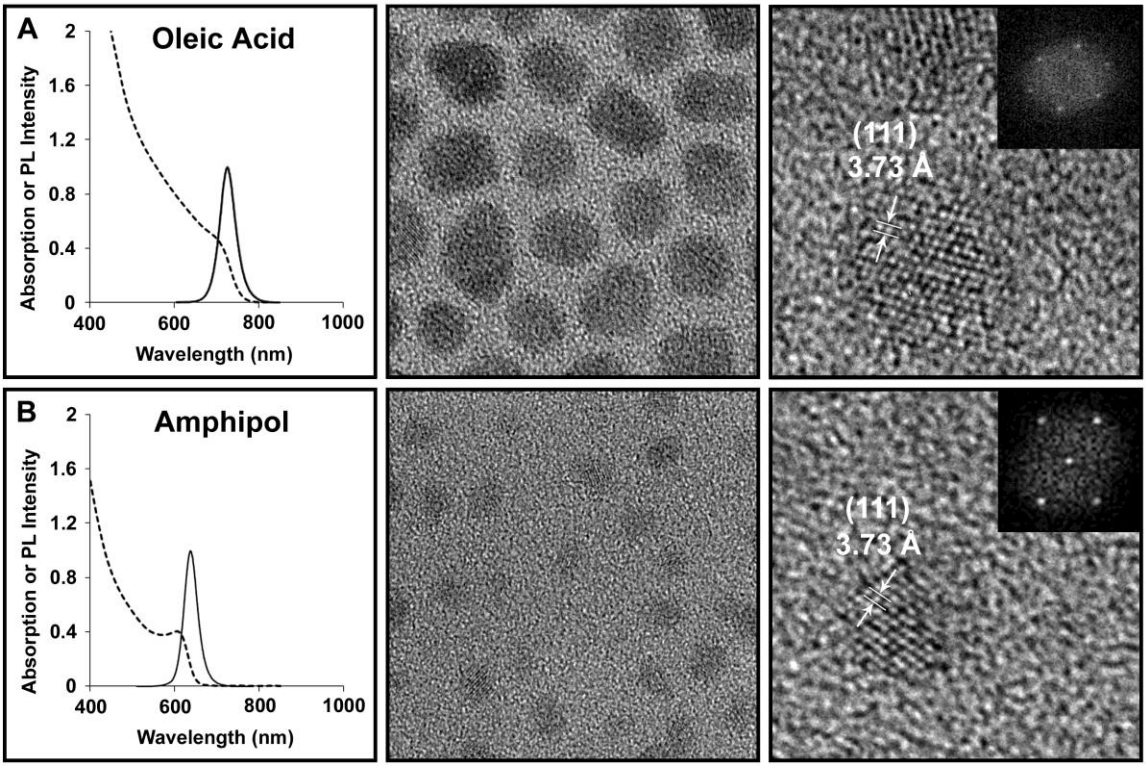

Figure 6.16: Characterization of CdTe nanocrystals prepared using monovalent ligands (A) or multidentate amphipols (B). Left: Absorption (dotted line) and emission spectra (solid line) of quantum dot, plotted in arbitrary units. Middle: High-resolution transmission electron micrographs of the nanocrystals. The dimensions of each box are 50 nm x 50 nm. Right: Representative nanocrystal shown at high magnification with and inset showing a fast Fourier transform of the nanocrystal image. The dimensions of each box are 14 nm x 14 nm. Both nanocrystals are oriented with their zinc blende (110) planes parallel to the TEM grid.

6.3.3 (Core)Shell Nanocrystal Synthesis. Due to the high binding strength of the multidentate polymer to the nanocrystal surfaces, it is reasonable to speculate that these nanocrystals may not be amenable to postsynthetic surface modification. Specifically, inorganic shells are typically grown on quantum dots in order to protect their optical properties and to improve their chemical stability toward oxidation (Chapter 4) and to

generate a variety of useful heterostructures. To this end, CdTe nanocrystals were grown in the presence of amphipol ligands and capped with CdS or CdSe, yielding a strong red-shift in optical spectra, indicative of the type-II nature of the band structure. Generally in these syntheses, an excess of the cationic precursor is used in order to afford a surface rich in cations for strong interaction with the carboxylate polymer. Because there is an excess of cadmium in solution, a shell may be grown merely by the addition of elemental sulfur or selenium to the synthesis reaction after core growth at 280ºC. EDX analysis of the purified nanocrystals demonstrated that these elements were successfully incorporated into the nanomaterials (data not shown). Injection of sulfur (1:1 S:Te) red-shifted the emission peak from ~630 nm to ~700 nm, whereas selenium (1:1 Se:Te) red-shifted the emission to ~830 nm (Figures 6.15 and 6.16). As well, HRTEM analysis revealed that the nanocrystals grew significantly as the zinc blende lattice constants contracted (Figure 6.16). Elemental analysis of these nanoparticles in water also revealed an important aspect of their synthesis. Even after purification, if these nanocrystals were synthesized in the presence of a large excess of cadmium, excess cadmium remained bound to the nanoparticles. The elemental ratio of Cd:Te in CdTe quantum dots purified in water was ~2:1 when prepared with a 3-fold excess of Cd. It was found that this excess cadmium could be eliminated if the quantum dots were prepared with a ratio less than 2:1, or if the remaining cadmium was consumed during shell growth. For the use of these nanocrystals as water-soluble probes in living cells or animals, it is important to consume all of the cation precursors in order to avert leaching of toxic metal ions.

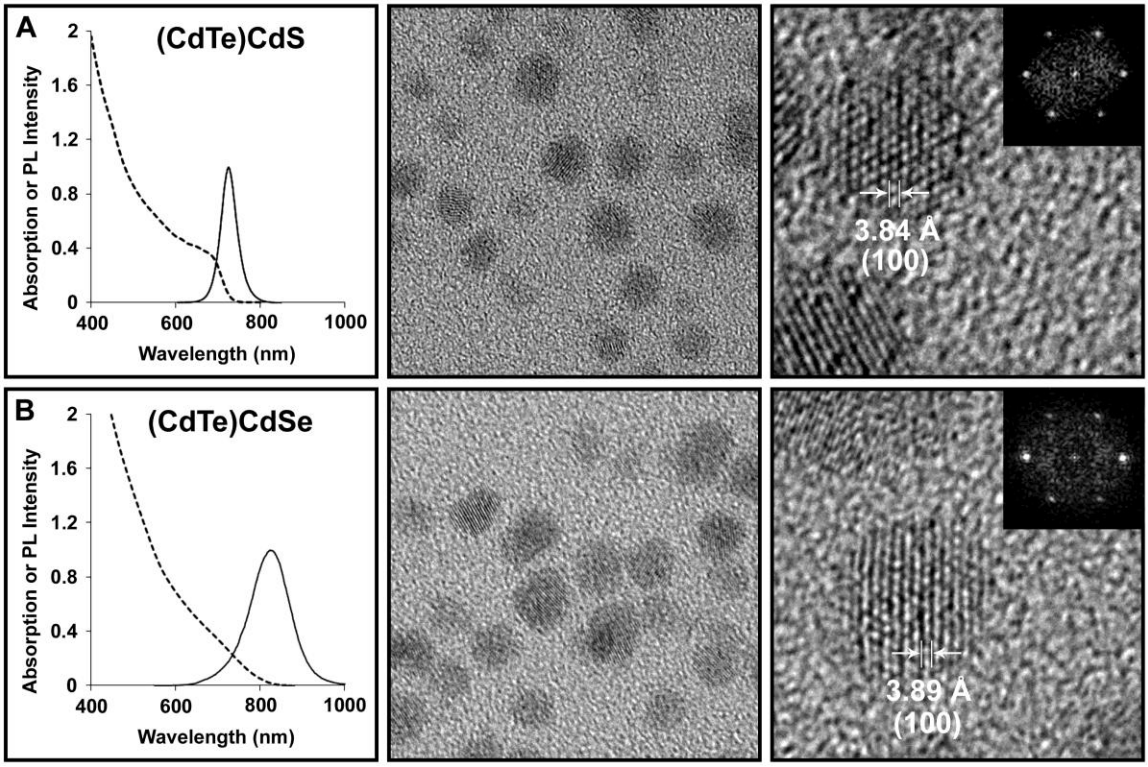

Figure 6.17: Characterization of (core)shell quantum dots prepared from CdTe nanocrystals with a multidentate ligand. (CdTe)CdS (A) and (CdTe)CdSe (B) nanocrystals are depicted. Left: Absorption (dotted line) and emission spectra (solid line) are plotted in arbitrary units. Middle: High-resolution transmission electron micrographs of the nanocrystals. The dimensions of each box are 50 nm x 50 nm. Right: Representative nanocrystal shown at high magnification with and inset showing a fast Fourier transform of the nanocrystal image. The dimensions of each box are 14 nm x 14 nm. Both nanocrystals are oriented with their zinc blende (111) planes parallel to the TEM grid.

It is likely that these heterostructure materials grew as shells, or as gradient-structures on the cores. This is because an alloying of the materials would generally result in a blue-shift in emission due to an increase in bandgap, as discussed in Chapter 4. Growth of a CdSe shell resulted in a dampening of absorption features and a decrease in band-edge oscillator strength, consistent with a type-II heterostructure. However the CdS nanocrystals maintained a strong band-edge and the degree of red-shift in the optical spectra was less than expected from previous studies (Chapter 4). This is a result of

incomplete deposition of the sulfur precursor. The reactivities of selenium and sulfur are significantly lower than that of Te, resulting in slow shell growth over the course of several hours and incomplete reactions. The ratio of Te:Se in (CdTe)CdSe quantum dots was found to be 1.8:1, and the ratio of Te:S in (CdTe)CdS was found to be 4:1. Indeed, the reactivity of sulfur toward the multidentate ligand-bound cadmium ions was so low that CdS nanocrystals could not independently nucleate in the presence of amphipol ligands. In addition, small cadmium selenide nanocrystallites could nucleate in the presence of amphipols but their strongly inhibited growth limited their size to less than ~2.5 nm. Because of the low reactivity of sulfur and selenium, (core)shell heterostructures could be produced through the simultaneous introduction of the core and shell precursors, without sequential additions of shell precursors. Although this is interesting from the perspective of synthetic ease on an industrial scale without the need for multiple high temperature injections, the resulting heterostructures are more difficult to characterize due to the lack of *a priori* knowledge of their sizes and extinction coefficients, compared to binary CdTe nanocrystals.

6.3.4 CdTe Fluorescence Stabilization. A drawback to the use of CdTe as a photoluminescent nanocrystal material is that its fluorescent intensity is known to be quickly quenched after exposure to air (Chapter 5).[14,16,37] This is also true for the quantum dots prepare here. Although these quantum dots generally had quantum yields of 40-60% immediately after synthesis, they quenched to just a few percent over the course of minutes to hours once exposed to air. This effect was found to occur in water even under oxygen-free conditions, and even if the solutions were protected from light. CdTe quantum dots that were prepared using traditional methods, and then transferred to water using amphipols instantly quenched upon resuspension in water, even though the original quantum dots were brightly fluorescent (Chapter 5). Although these quantum

dots were significantly more resistant to quenching in nonpolar solvents, they also eventually quenched under these conditions when exposed to air.

Because of this oxidative lability, it was presumed that CdS or CdSe shell growth would lead to an increase in photochemical stability. Instead shell growth led to a gradual and steady decline in quantum yield. As well, the resulting nanoparticles were not photostable, although they were more stable than the core nanocrystals alone. This is surprising, as the growth of (core)shell (CdTe)CdS and (CdTe)CdSe quantum dots generated highly stable and bright nanocrystals (Chapter 4) when using monovalent amine ligands. The mechanism for this shell-induced quenching likely arises from the carboxylic acid ligands on the amphipol ligands. When the monovalent amine ligands of the traditional (core)shell nanocrystals were exchanged with oleic acid, the emission intensity markedly dropped, suggesting that the carboxylic acid ligands are not ideal passivants for these heterostructures.

This problem of fluorescence instability has been overcome with the addition of a small amount of hydrophilic thiol ligand to the quantum dots in water (0.1 mM 1-thioglycerol). After incubation for several hours at room temperature, the fluorescence reappears, and remains following purification through FPLC or ultracentrifugation. A similar repair phenomenon can also improve the photochemical properties of CdTe-amphipol quantum dots prepared with multistep syntheses using molecular ligands. Although the mechanism of this photoluminescence restoration is not clear, it is likely that these strongly reducing ligands can repair oxidized defect sites on the quantum dot surface that arise when they are exposed to oxygen and other oxidizing species in aqueous solution. Indeed, CdTe nanocrystals can be synthesized in aqueous solution in the presence of thiolate ligands, with highly efficient photoluminescence.[38,39] These small

ligands do not displace the hydrophobic bilayer surrounding the amphibious quantum dots, as their elution times from size-exclusion chromatography columns did not change (data not shown). Instead, it is likely that these ligands can penetrated through the semiporous polymeric shell to interact with the quantum dot surface. A similar mechanism was postulated for the interaction of β-mercaptoethanol with CdSe/ZnS quantum dots coated with amphipols, which was found to modulate fluorescence quantum yield and blinking.[40,41]

Once stabilized by thiols, the quantum dots were strongly photoluminescent for several days after purification, but eventually bleached again if stored under room light. This is likely due to photochemical oxidation of the quantum dot-bound thiolate ligands.[18] In pursuit of a more permanent solution to this problem, we attempted to postsynthetically modify the nanocrystal surfaces with nonpolar ligands that would become permanently incorporated within the nanocrystal micelle shell once dispersed in water. Comparing alkyl phosphines, phosphine oxides, phosphonic acids, amines, carboxylic acids, and thiols, it was found that only phosphines were capable of maintaining the photoluminescence efficiency of these quantum dots in water. Typically, after the nanocrystals were synthesized in the amphipol-PEG mixture at 280ºC, the reaction temperature was decreased to 240ºC, trioctylphosphine (TOP) was added and ligand exchange was allowed to commence for 1 hour. The concentration of TOP was a critical parameter, as too little had no impact (less than 2:1 TOP:cadmium) and too much of this highly nonpolar ligand dramatically reduced the solubility of the resulting nanocrystals in water. It was found that an 8:4:1 ratio of carboxylic acid ligands:TOP:cadmium was ideal for most reactions. Quantum dots that were processed in this manner were optically stable for weeks to months in water after purification, and the same phenomenon was found to improve the properties of CdTe nanocrystals prepared with multistep syntheses

and amphipol encapsulations. In the future, the production of optically stable nanocrystals may be simplified with the addition of phosphine moieties to the amphipol backbone to create a locally reducing environment, or by using nanocrystalline materials that are less prone to oxidation, such as (CdSe)ZnS.

6.4 Outlook. The rationale for the use of multidentate ligands in the synthesis of nanocrystals was inspired by the need to retard the growth rate of nanocrystals in reactions that normally proceed uncontrollably. It was hypothesized that increasing the number of chelating moieties per ligand, and increasing its molecular weight would decrease the reactivity of the precursors, thereby slowing nucleation and growth of the nanocrystals. Indeed these multidentate ligands dramatically decrease the growth rates of nanocrystals in solution, and also yield novel reaction kinetics. These slow nucleation and growth processes will be particularly valuable for studying the nature of nucleation and growth in poorly understood nanocrystal reactions. In addition, the *in situ* coating of nanocrystals with flexible multidentate ligands will be useful for studying the interactions of strong multivalent binding on the highly curved and rigid surfaces of nanocrystals.

In future work, the amphibious nature of the nanocrystals produced in this work will be a great asset for a wide range of applications, however the structure of the polymeric coating may be even more important. A strong binding strength of the polymer is indicated by the exceptional colloidal stability of the resulting nanocrystals and their resistance to Ostwald ripening at high temperatures. Although this polymeric shell is strongly bound in polar and nonpolar solvents, it is also porous. This paradox is a direct result of the bulky, linear structure of the polymer. These nanocrystals are coated with a monolayer of bulky multidentate carboxylate ligands, which can strongly bind to metal atoms on the nanocrystal surface through polydentate interactions. However, this ligand

binds in a disordered fashion to the surface, likely leaving patchy holes in the monolayer that are too small to be filled in by large ligands, but large enough to provide a space for diffusion of solutes to the surface. When these nanocrystals are dispersed in a polar solvent, an additional layer of surfactant is coated on the surface, which forms a hydrophobic bilayer, providing an additional layer of stability through hydrophobic interactions. However this bilayer is fluid-like and disordered like its underlying monolayer, and thereby allowing access to the surface through pores in the organic shell. Combined with the high degree of surface faceting of the nanocrystals, this attribute immediately shows utility for the production of homogeneous catalytic nanocrystals, such as palladium. Colloidal stability of homogeneous catalysts has been a major limiting factor in utility, and the nanocrystals often entirely precipitate as bulk metal by the end one catalytic cycle.[42,43] The possibility of producing a variety of nanocrystals with a rare combination of surface accessibility and high stability will also be invaluable for the production of new biological probes, energy transfer and charge transfer devices, and for the study of nanocrystal faceting and surface reconstruction.

6.5 References

1. Smith, A. M. & Nie, S. M. Minimizing the hydrodynamic size of quantum dots with multifunctional multidentate polymer ligands. *J. Am. Chem. Soc.* **130,** 11278-11279 (2008).

2. Wang, M. F., Dykstra, T. E., Lou, X. D., Salvador, M. R., Scholes, G. D., & Winnik, M. A. Colloidal CdSe nanocrystals passivated by a dye-labeled multidentate polymer: Quantitative analysis by size-exclusion chromatography. *Angew. Chem. Int. Ed.* **45,** 2221-2224 (2006).

3. Wang, M. F., Felorzabihi, N., Guerin, G., Haley, J. C., Scholes, G. D., & Winnik, M. A. Water-soluble CdSe quantum dots passivated by a multidentate diblock copolymer. *Macromolecules* **40,** 6377-6384 (2007).

4. Duan, H. W. & Nie, S. M. Cell-penetrating quantum dots based on multivalent and endosome-disrupting surface coatings. *J. Am. Chem. Soc.* **129,** 3333-3338 (2007).

5. Querner, C., Reiss, P., Bleuse, J., & Pron, A. Chelating Ligands for nanocrystals' surface functionalization. *J. Am. Chem. Soc.* **126,** 11574-11582 (2004).

6. Susumu, K., Uyeda, H. T., Medintz, I. L., Pons, T., Delehanty, J. B., & Mattoussi, H. Enhancing the stability and biological functionalities of quantum dots via compact multifunctional ligands. *J. Am. Chem. Soc.* **129,** 13987-13996 (2007).

7. Kim, S. W., Kim, S., Tracy, J. B., Jasanoff, A., & Bawendi, M. G. Phosphine oxide polymer for water-soluble nanoparticles. *J. Am. Chem. Soc.* **127,** 4556-4557 (2005).

8. Kim, S. & Bawendi, M. Oligomeric ligands for luminescent and stable nanocrystal quantum dots. *J. Am. Chem. Soc.* **125,** 14652-14653 (2003).

9. Zhang, S. S., Leem, G., Srisombat, L. O., & Lee, T. R. Rationally designed ligands that inhibit the aggregation of large gold nanoparticles in solution. *J. Am. Chem. Soc.* **130,** 113-120 (2008).

10. Lauffenburger, D. A. & Linderman, J. J. *Receptors: Models for Binding, Trafficking, and Signaling*. Oxford University Press, New York, NY (1996).

11. Chakraborty, A. K. & Golumbfskie, A. J. Polymer adsorption-driven self-assembly of nanostructures. *Annu. Rev. Phys. Chem.* **52,** 537-573 (2001).

12. Wang, K. T., Iliopoulos, I., & Audebert, R. Viscometric behavior of hydrophobically modified poly(sodium acrylate). *Polym. Bull.* **20,** 577-582 (1988).

13. Gohon, Y., Pavlov, G., Timmins, P., Tribet, C., Popot, J. L., & Ebel, C. Partial specific volume and solvent interactions of amphipol A8-35. *Anal. Biochem.* **334,** 318-334 (2004).

14. Ma, J., Chen, J. Y., Guo, J., Wang, C. C., Yang, W. L., Xu, L., & Wang, P. N. Photostability of thiol-capped CdTe quantum dots in living cells: the effect of photo-oxidation. *Nanotechnology* **17,** 2083-2089 (2006).

15. Ma, J., Chen, J. Y., Zhang, Y., Wang, P. N., Guo, J., Yang, W. L., & Wang, C. C. Photochemical instability of thiol-capped CdTe quantum dots in aqueous solution and living cells: Process and mechanism. *J. Phys. Chem. B* **111,** 12012-12016 (2007).

16. Yu, W. W., Wang, Y. A., & Peng, X. G. Formation and stability of size-, shape-, and structure-controlled CdTe nanocrystals: Ligand effects on monomers and nanocrystals. *Chem. Mater.* **15,** 4300-4308 (2003).

17. Wiley, B., Sun, Y., Mayers, B., & Xia, Y. Shape-controlled synthesis of metal nanostructures: the case of silver. *Chem. Eur. J.* **11,** 454-463 (2005).

18. Aldana, J., Wang, Y., & Peng, X. Photochemical instability of CdSe nanocrystals coated by hydrophilic thiols. *J. Am. Chem. Soc.* **123,** 8844-8850 (2001).

19. Smith, A. M., Duan, H. W., Rhyner, M. N., Ruan, G., & Nie, S. M. A systematic examination of surface coatings on the optical and chemical properties of semiconductor quantum dots. *Phys. Chem. Chem. Phys.* **8,** 3895-3903 (2006).

20. Gaponik, N., Talapin, D. V., Rogach, A. L., Eychmuller, A., & Weller, H. Efficient phase transfer of luminescent thiol-capped nanocrystals: From water to nonpolar organic solvents. *Nano Lett.* **2,** 803-806 (2002).

21. Sanders, C. R., Hoffman, A. K., Gray, D. N., Keyes, M. H., & Ellis, C. D. French swimwear for membrane proteins. *ChemBioChem* **5,** 423-426 (2004).

22. Popot, J. L. et al. Amphipols: polymeric surfactants for membrane biology research. *Cell. Mol. Life Sci.* **60,** 1559-1574 (2003).

23. Yu, M. W. & Peng, X. G. Formation of high-quality CdS and other II-VI semiconductor nanocrystals in noncoordinating solvents: Tunable reactivity of monomers. *Angew. Chem. Int. Ed.* **41,** 2368-2371 (2002).

24. Murray, C. B., Sun, S. H., Gaschler, W., Doyle, H., Betley, T. A., & Kagan, C. R. Colloidal synthesis of nanocrystals and nanocrystal superlattices. *IBM J. Res. Dev.* **45,** 47-56 (2001).

25. Nann, T. Phase-transfer of CdSe@ZnS quantum dots using amphiphilic hyperbranched polyethylenimine. *Chem. Commun.*1735-1736 (2005).

26. Duan, H. W., Kuang, M., Wang, D. Y., Kurth, D. G., & Mohwald, H. Colloidally stable amphibious nanocrystals derived from poly {[2-(dimethylamino)ethyl] methaerylatel capping. *Angew. Chem. Int. Ed.* **44,** 1717-1720 (2005).

27. Yu, W. W., Qu, L. H., Guo, W. H., & Peng, X. G. Experimental determination of the extinction coefficient of CdTe, CdSe, and CdS nanocrystals. *Chem. Mater.* **15,** 2854-2860 (2003).

28. Pellegrino, T., Manna, L., Kudera, S., Liedl, T., Koktysh, D., Rogach, A. L., Keller, S., Radler, J., Natile, G., & Parak, W. J. Hydrophobic nanocrystals coated with an amphiphilic polymer shell: A general route to water soluble nanocrystals. *Nano Lett.* **4,** 703-707 (2004).

29. Wu, X. Y., Liu, H. J., Liu, J. Q., Haley, K. N., Treadway, J. A., Larson, J. P., Ge, N. F., Peale, F., & Bruchez, M. P. Immunofluorescent labeling of cancer marker Her2 and other cellular targets with semiconductor quantum dots. *Nat. Biotechnol.* **21,** 41-46 (2003).

30. Pons, T., Uyeda, H. T., Medintz, I. L., & Mattoussi, H. Hydrodynamic dimensions, electrophoretic mobility, and stability of hydrophilic quantum dots. *J. Phys. Chem. B* **110,** 20308-20316 (2006).

31. Zoonens, M., Giusti, F., Zito, F., & Popot, J. L. Dynamics of membrane protein/amphipol association studied by Forster resonance energy transfer: implications for in vitro studies of amphipol-stabilized membrane proteins. *Biochemistry* **46,** 10392-10404 (2007).

32. Murray, C. B., Norris, D. J., & Bawendi, M. G. Synthesis and characterization of nearly monodisperse CdE (E = S, Se, Te) semiconductor nanocrystallites. *J. Am. Chem. Soc.* **115,** 8706-8715 (1993).

33. Battaglia, D. & Peng, X. G. Formation of high quality InP and InAs nanocrystals in a noncoordinating solvent. *Nano Lett.* **2,** 1027-1030 (2002).

34. Hines, M. A. & Scholes, G. D. Colloidal PbS nanocrystals with size-tunable near-infrared emission: Observation of post-synthesis self-narrowing of the particle size distribution. *Adv. Mater.* **15,** 1844-1849 (2003).

35. LaMer, V. K. & Dinegar, R. H. Theory, production and mechanism of formation of monodispersed hydrosols. *J. Am. Chem. Soc.* **72,** 4847-4854 (1950).

36. Kwon, S. G., Piao, Y., Park, J., Angappane, S., Jo, Y., Hwang, N. M., Park, J. G., & Hyeon, T. Kinetics of monodisperse iron oxide nanocrystal formation by "heating-up" process. *J. Am. Chem. Soc.* **129,** 12571-12584 (2007).

37. Cho, S. J., Maysinger, D., Jain, M., Roder, B., Hackbarth, S., & Winnik, F. M. Long-term exposure to CdTe quantum dots causes functional impairments in live cells. *Langmuir* **23,** 1974-1980 (2007).

38. Rogach, A. L., Franzl, T., Klar, T. A., Feldmann, J., Gaponik, N., Lesnyak, V., Shavel, A., Eychmuller, A., Rakovich, Y. P., & Donegan, J. F. Aqueous synthesis of thiol-capped CdTe nanocrystals: State-of-the-art. *J. Phys. Chem. C* **111,** 14628-14637 (2007).

39. Gaponik, N., Talapin, D. V., Rogach, A. L., Hoppe, K., Shevchenko, E. V., Kornowski, A., Eychmuller, A., & Weller, H. Thiol-capping of CdTe nanocrystals: An alternative to organometallic synthetic routes. *J. Phys. Chem. B* **106,** 7177-7185 (2002).

40. Hohng, S. & Ha, T. Near-complete suppression of quantum dot blinking in ambient conditions. *J. Am. Chem. Soc.* **126,** 1324-1325 (2004).

41. Jeong, S., Achermann, M., Nanda, J., Lvanov, S., Klimov, V. I., & Hollingsworth, J. A. Effect of the thiol-thiolate equilibrium on the photophysical properties of aqueous CdSe/ZnS nanocrystal quantum dots. *J. Am. Chem. Soc.* **127,** 10126-10127 (2005).

42. Narayanan, R. & El-Sayed, M. A. Some aspects of colloidal nanoparticle stablity, catalytic activity, and recycling potential. *Top. Catal.* **47,** 15-21 (2008).

43. Narayanan, R. & El-Sayed, M. A. Catalysis with transition metal nanoparticles in colloidal solution: nanoparticle shape dependence and stability. *J. Phys. Chem. B* **109,** 12663-12676 (2005).

CHAPTER 7

Biocompatibility of Quantum Dots

Quantum dots have many highly desirable attributes for applications in biology and medicine, including intense single molecule fluorescence, a resistance to photobleaching, and spectral multiplexing capabilities (Chapter 2). These qualities are particularly relevant for applications in live cell imaging and for intraoperative fluorescence imaging, for which there is a dearth of suitable probes. However current state-of-the-art quantum dots are inadequate for these applications due to their large sizes, poor colloidal stability, propensity for nonspecific binding, inconvenient bioconjugation capacity, and possible cytotoxic effects. In this thesis, many of these shortcomings have been overcome through the optimization of semiconductor nanocrystal structure, optical properties, and colloidal attributes, and this chapter extends these concepts to improve the biocompatibility of quantum dots and to understand how nanoparticles interact with living cells and biomolecules.

In this chapter, a thorough experimental approach is undertaken to uncover the factors controlling the biocompatibility of semiconductor nanocrystals. Several major experimental findings are reported, along with many new concepts in nanocrystal biocompatibility. First, ultrasmall quantum dots (<6 nm) exhibit a vastly decreased propensity for nonspecific binding to serum components, compared to their larger counterparts (>6 nm). This observation has never been reported and could only be revealed through the development of the compact multidentate ligand (Chapter 5).

Second, the colloidal stability, propensity for protein adsorption, and cellular uptake of quantum dots in a biological environment is strongly dependent on the surface properties of the nanoparticle. Nonspecific binding of these quantum dots can be minimized by reducing the electrostatic charge of commonly used carboxylate coatings through surface modification with non-ionic polymers. Third, nanocrystals coated with a strongly bound multidentate polymer can spontaneously and specifically assemble with proteins terminated by a polyhistidine sequence, generating a basis for simple and efficient bioconjugation. Fourth, if these proteins contain energy accepting dyes, extremely high efficiencies of energy transfer can be attained due to the reduced distance between the nanocrystal and the dye. Finally, the cytotoxicity of quantum dots toward cells has been studied in depth, revealing atypical trends with chemical composition. The traditional paradigm of cadmium-dominated toxicity is challenged by the overwhelming toxicity of zinc- and selenium-based quantum dots, caused by a unique type of nanocrystal surface chemistry. These results provide great insight into the interactions between nanoparticles and biological systems and will help to facilitate the exploitation of the full capabilities of semiconductor nanocrystals.

7.1 Nonspecific Binding to Proteins

Biological fluids such as blood, cytosol, and lymph are complex saline solutions crowded with macromolecules that may either be reducing (e.g. cytosol) or oxidizing (peroxisomal contents), acidic (lysosomal fluid) or alkaline (bile). These conditions may be sufficiently harsh to disrupt the delicate balance of forces stabilizing colloidal suspensions of nanocrystals through electrostatic destabilization at high ionic strength (0.15 M) and nonspecific adsorption and aggregation induced by a large excess of biomacromolecules. Indeed the biocompatibility of semiconductor

quantum dots has been a major limiting factor for single molecule imaging studies in cells and for achieving a high level of specificity in biological fluids. Commonly used commercial quantum dots are coated with thick polymeric shells that are prone to protein adsorption, and quantum dots coated in small ligands aggregate unless they are in the presence of excess ligands, which are often intrinsically toxic and bioactive. For this reason, the use of a thin and stable multidentate ligand coating (Chapter 5) offers a unique opportunity to overcome these issues, study the interactions of small quantum dots with biological fluids and cells, and to advance the fields of quantum dot bioimaging and biosensing.

7.1.1 Quantum Dot Surface Coatings. In order to determine how semiconductor nanocrystals behave in complex biological fluids, the study of their properties in serum is an appropriate starting point. Serum contains nearly all of the components of blood plasma with a high concentration of a variety of biologically relevant proteins (~8% by weight), most abundantly albumin and immunoglobulins. Figure 7.1 shows the results of an experiment in which (CdSe)ZnS nanocrystals (3.5 nm nanocrystal diameter, 530 nm emission) were coated with 7 different surface coatings, incubated in serum for 1 hour at 37°C, and then subjected to agarose gel electrophoresis. Each pair of lanes contains quantum dots in a neutral buffer without serum (left lane) or quantum dots incubated with serum (right lane), showing that all of the nanocrystals have a different mobility after incubation with serum. Because the relative electrophoretic mobility is only dependent on the zeta potential of the particle, serum must modify either the nanocrystal size or charge. Either way, this must be due to an adsorption phenomenon, as electrophoresis is purification process in which weakly interacting species are separated from the quantum dots.

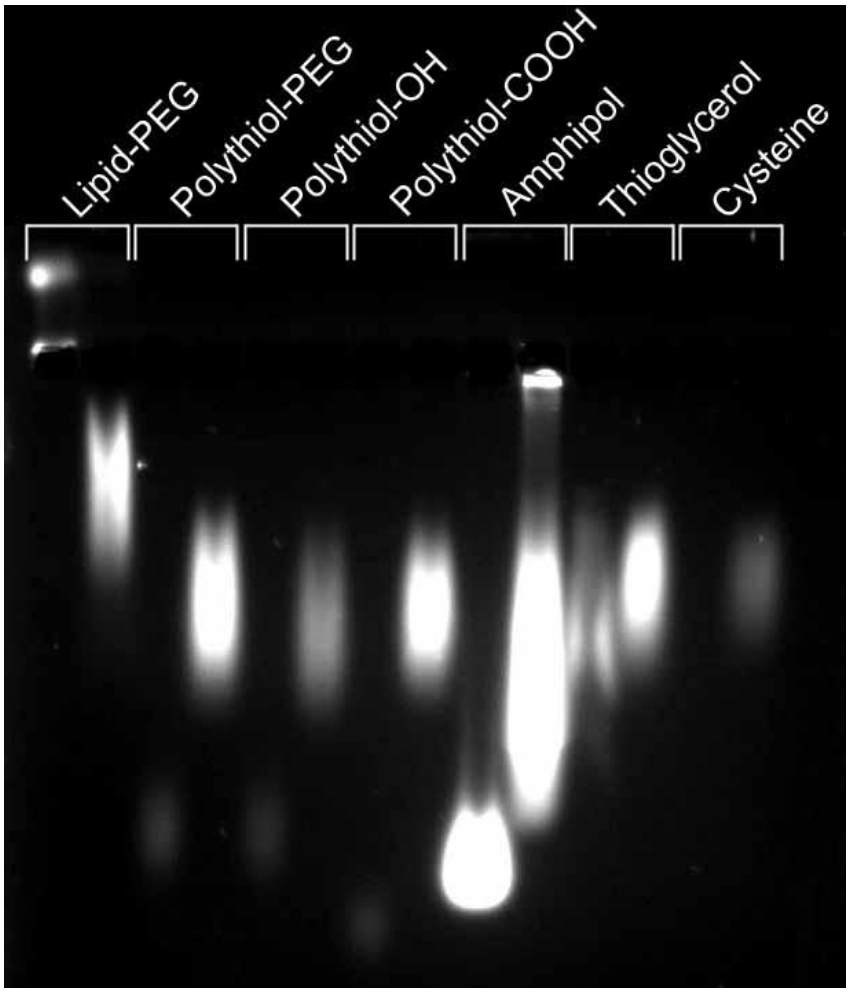

Figure 7.1: Nonspecific binding of serum by (CdSe)ZnS quantum dots with 7 different coatings. Agarose gel (0.7%) electrophoresis was performed in pH 8.5 sodium borate buffer. Each nanocrystal coating is labelled above two adjacent lanes, with the left lane containing nanocrystals in PBS, and the right lane containing nanocrystals in 50% (v/v) fetal bovine serum. Each sample was heated to 37°C for 1 hour. The inorganic nanocrystal diameter was 3.5 nm, and the hydrodynamic sizes ranged from ~4.5 nm (thioglycerol and cysteine) to ~22 nm (lipid-PEG). Polythiol refers to the multidentate ligand developed in Chapter 5, which was used in its native form (COOH) or with conjugated hydroxyl groups (OH) or short chain PEG (380 Da). This fluorescence image was obtained with ultraviolet illumination and a long-pass filter.

The surface coatings investigated here are chemically and colloidally diverse, including small molecules (cysteine and thioglycerol), multidentate ligands, and amphiphilic polymer coatings (amphipol and lipid-PEG), with neutral to negative

surface charges. Yet despite this broad range of physicochemical properties, all of these quantum dots had similar electrophoretic mobilities after protein adsorption, implicating similar interactions with serum components. It should be noted that lipid-PEG quantum dots adsorbed by serum had a lower mobility compared to the other types of surface coatings, likely due to their much larger hydrodynamic size. It is quite surprising that large, highly anionic, stable coatings like amphipol resulted in similar interactions with serum components as small, ionically neutral, unstable coatings like cysteine. It has previously been reported that cysteine coated quantum dots are naturally resistant to adsorption due to a nearly neutral zwitterionic surface.[1,2] However these nanocrystal were so labile that they entirely precipitated and quenched during electrophoresis and were strongly adsorbed by serum proteins. The identity of the adsorbing proteins cannot be directly inferred from this simple experiment, but albumin is the most prevalent plasma protein, it is negative in charge, and it has a propensity for binding 'sticky' epitopes, reflected in its common use as a blocking agent for *in vitro* assays. Therefore, this protein is likely to be an important contributor to adsorption (see below).

7.1.2 Quantum Dot Size and Charge. From the preceding section, it may seem that serum adsorption to quantum dot surfaces is inevitable and cannot be modulated through nanocrystal size or surface charge. However this conclusion is misleading, as each of these surface coatings resulted in different overall nanoparticle size, charge, colloidal stability, and chemical functionality. Independently altering these parameters will be necessary in order to understand the phenomena intrinsic to nonspecific protein adsorption and the ability to minimize this generally undesirable characteristic.

Figure 7.2 depicts the results of a nonspecific serum adsorption experiment using CdTe quantum dots coated with the multidentate polymer ligand (Chapter 5). The core size was either 2.5 nm, yielding a 5.5 nm hydrodynamic diameter, or 4.5 nm, yielding a 7.5 nm hydrodynamic diameter. The 2.5 nm quantum dots have essentially the same gel mobility in the presence or absence of serum, although a very small quantity of these nanocrystals form a small band with lower mobility after serum adsorption (left gel, compare lanes 0x-PBS and 0x-Serum). For the 4.5 nm quantum dots, the contrast is stark; the nanocrystals have a different mobility after serum adsorption, forming a new electrophoretic band, and the native band is completely eliminated (right gel, compare lanes 0x-PBS and 0x-Serum). This data demonstrates that nanoparticles with identical surface properties have a size-dependent propensity for protein adsorption, with smaller nanoparticles being considerably more resistant to nonspecific interactions.

.

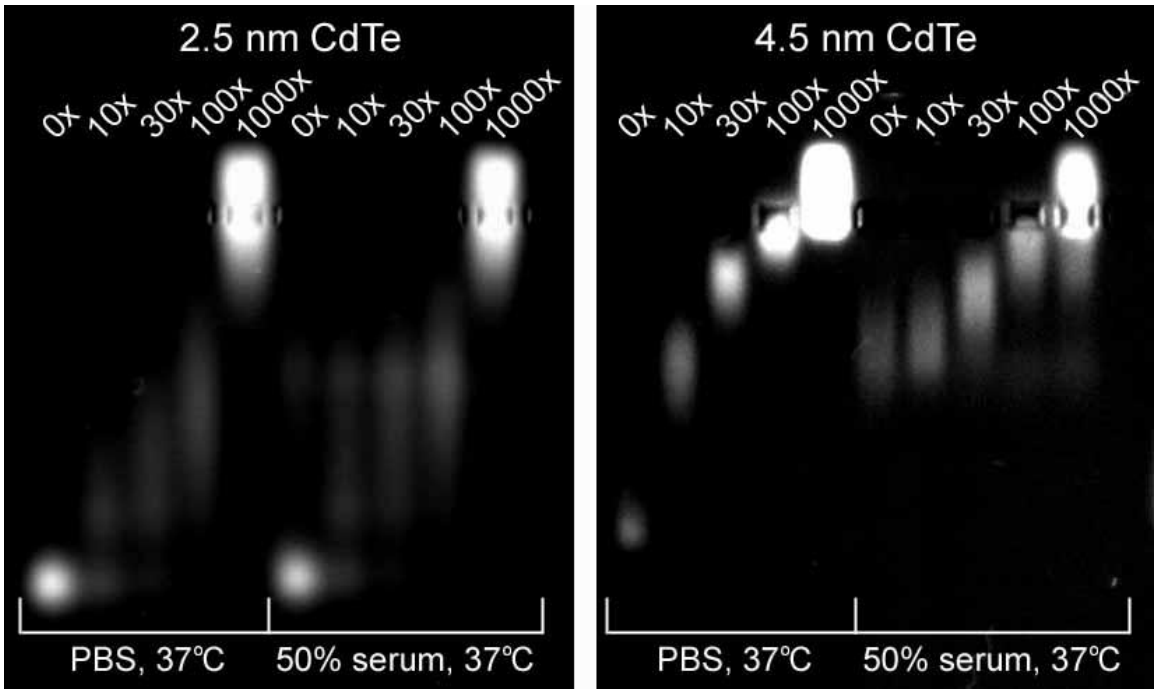

Figure 7.2: Nonspecific serum binding of CdTe nanocrystals with two core sizes (2.5 nm and 4.5 nm) and different surface charges. Agarose gel (0.7%) electrophoresis was performed in pH 8.5 sodium borate buffer. Quantum dots were coated with the multidentate polymer and diluted in PBS, resulting in a hydrodynamic size of 5.5 nm for the 2.5 nm cores and 7.5 nm for the 4.5 nm cores. Quantum dots were then mixed with fetal bovine serum (50%), incubated at 37C for 1 hour, and subjected to agarose gel electrophoresis. In addition, various amounts of PEG-thiol (2000 Da) were added, as indicated by the values above the lanes (0-1000 molar excess). The fluorescence image of this agarose gel was obtained with ultraviolet illumination and a long-pass filter, showing the ~530 nm emission and ~660 nm emission from the small and large quantum dots, respectively.

In order to determine if these binding characteristics can be altered through modulation of the surface charge, these same multidentate ligand-coated quantum dots were incubated for 24 hours with 2000 Da PEG-thiol in a 10x, 30x, 100x, or 1000x molar excess. This thiolated ligand is capable of binding directly to the nanocrystal surface to a yield shell of non-ionic PEG. Gel electrophoresis indicates that incubation of 2.5 nm or 4.5 nm CdTe quantum dots with this polymer can reduce the surface charge of the multidentate ligand coating through by this mechanism (left

gel, compare PBS lanes 0x-1000x; right gel, compare PBS lanes 0x-1000x). As more PEG was added to the quantum dots, their electrophoretic mobility was significantly reduced until the surface was completely neutralized. It is currently unclear if these ligands displaced the strongly bound multidentate ligand or it these ligands just adsorbed to empty patches on the crystal surface, reducing the surface charge by steric shielding.

When 2.5 nm quantum dots were completely PEGylated, they were roughly 14 nm in hydrodynamic diameter, as determined by dynamic light scattering, and neutral in surface charge with nearly zero electrophoretic mobility. After this surface modification, these nanocrystals were still completely resistant to protein adsorption, showing the same mobility in the presence and absence of serum (left gel, compare lanes 1000x-PBS and 1000x-Serum). A similar resistance to protein adsorption was obtained for the PEGylated 4.5 nm cores, although they did yield a small mobile band in the presence of serum (right gel, compare lanes 1000x-PBS and 1000x-Serum). In between the two extremes of anionic and neutral surface charge, 2.5 nm CdTe quantum dots with a partially PEGylated surface remained resistant to serum adsorption (left gel, compare lanes 10x-1000x-PBS and 10x-1000x-Serum), whereas a molar excess of at least 100x PEG-thiol was necessary to eliminate the majority of nonspecific serum adsorption for larger 4.5 nm cores (right gel, compare lanes 10x-1000x-PBS and 10x-1000x-Serum). Taken together, these data indicate that ultrasmall quantum dots (< ~6 nm) have an inherent capacity to resist nonspecific protein binding. However, larger particles may also be rendered non-stick through the adsorption of non-ionic polymers like PEG, but a high surface concentration is necessary in order to yield a uniform monolayer with repulsive brush-like polymer conformations.

These findings could not have been observed without the strongly bound multidentate polymer, allowing the production of extremely compact quantum dots with high colloidal stability. Many other compact quantum dots have been prepared with sizes smaller than 6 nm, but they are always coated with monovalent thiolated ligands which quickly desorb from the quantum dot surface, reducing their stability and increasing their propensity for nonspecific binding. In order to determine if nanocrystals coated with monovalent ligands show similar binding attributes as those coated with stable multidentate ligands, CdTe nanocrystals with sizes of 3.0 nm and 5.0 nm were coated with thioglycerol, resulting in hydrodynamic diameters of 4.0 and 6.5 nm, respectively. To preserve colloidal stability, these particles were maintained in a solution containing a large excess of ligand (10 mM). These nanocrystals were then diluted in PBS, serum, or PBS containing albumin (3% w/v) and incubated at 37°C for 1 hour. Agarose gel electrophoresis revealed that the small nanocrystals were strongly resistant to serum protein adsorption compared to their larger counterparts. That is, the electrophoretic mobilities of the 4.0 nm hydrodynamic diameter quantum dots were essentially unchanged with protein adsorption, but the 6.5 nm quantum dots were completely different in the presence of serum or pure protein. Although these results are inconclusive due to the presence of a large amount of reducing thioglycerol, they support the size-dependent adsorption findings obtained for pure CdTe quantum dots coated with multidentate ligands.

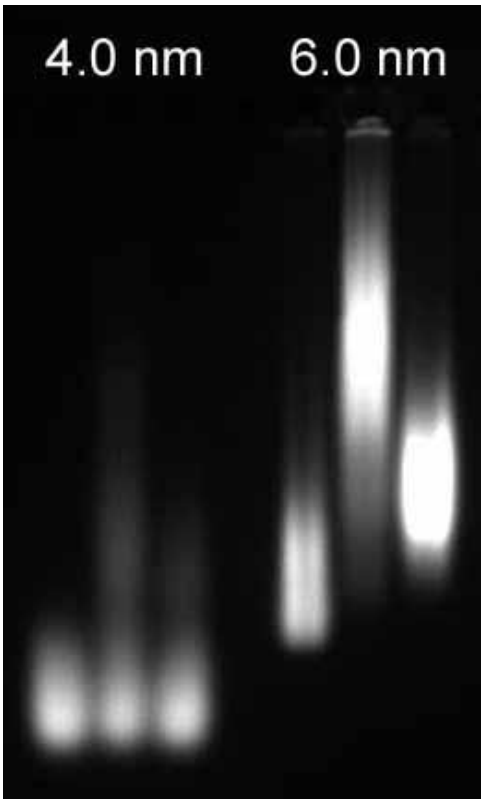

Figure 7.3: Nonspecific adsorption of serum and albumin to quantum dots coated with monovalent thiols. Agarose gel (0.7%) electrophoresis was performed in pH 8.5 sodium borate buffer. Thioglycerol-coated quantum dots (3.0 nm core/4.0 nm hydrodynamic diameter and 5.0 nm core/6.0 nm hydrodynamic diameter) were saturated with thioglycerol (10 mM) in order to maintain stability, and mixed with PBS (left lane), serum (middle lane, 50%), or bovine serum albumin (right lane, 3%). The fluorescence image of this agarose gel was obtained with ultraviolet illumination and a long-pass filter, simultaneously showing the ~570 nm emission and ~680 nm emission from the small and large quantum dots, respectively.

7.1.3 Mechanism of Size-Dependent Protein Adsorption. The resistance of small nanocrystals to serum adsorption is a new finding that has a multifaceted mechanism. Three attributes of nanoparticle interaction dominate on the ~6 nm scale and below: diffusivity (kinetics), surface curvature (enthalpy), and surface disorder (entropy). In the first case, as the size of a colloid decreases its diffusion coefficient (D) increases, as given by the Stokes-Einstein relation:

$$D = \frac{kT}{6\pi\eta r} \qquad \textbf{Equation 7.1}$$

where r is the radius of the particle, k is Boltzmann's constant, T is the temperature, and η is the solvent viscosity. Thereby, smaller particles have greater momentum in solution, which disrupts weak intermolecular interactions through entropic Brownian motion.

As the nanoparticle size decreases the probability of collisions between nanoparticles also decreases. The bimolecular association rate constant[3] for two spherical particles of radius r_A and r_B is

$$k_a = 4\pi D_A D_B (r_A + r_B) \qquad \textbf{Equation 7.2}$$

For a mixture of two nanoparticles with different sizes, the rate of collision increases as the difference in size increases, as the larger particle can act as a 'target' for more diffusive smaller particle to hit. This means that for colloidal nanocrystals interacting with proteins, diffusion-limited adsorption will be minimized for nanocrystals that are similar in size to the proteins. The rate of collisional interaction between nanocrystals and albumin is plotted in Figure 7.4, showing a minimum rate constant for nanocrystals with the same diameter as albumin. However serum contains proteins with a wide range of macromolecular size and shape, and the rate of adsorption will likely be more complex. Nevertheless, nearly all serum proteins are hydrodynamically between 3 and 10 nm, which means that nanocrystals within this size range should be more diffusionally resistant to adsorption.

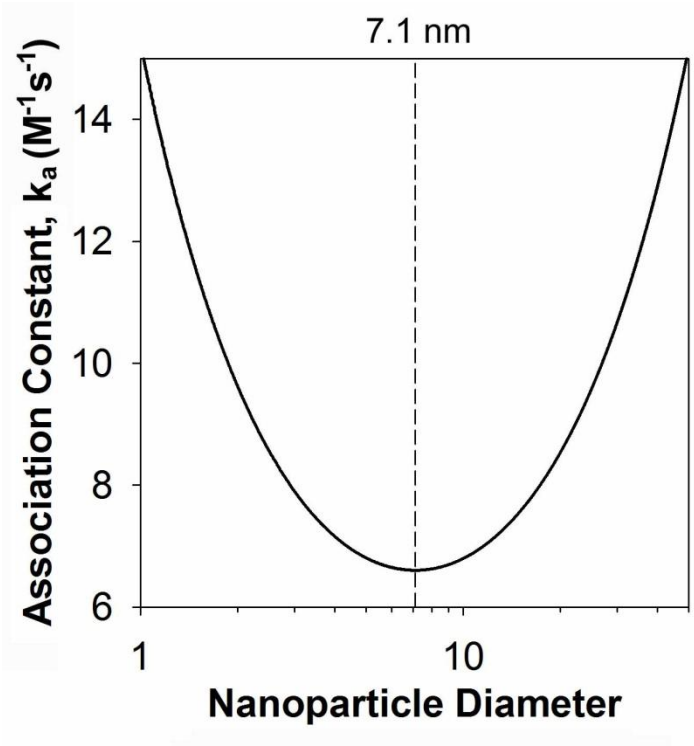

Figure 7.4: Calculated association constant for collision-limited adsorption between albumin and nanoparticles of different sizes at 1 μM concentration. The lowest probability of collision is for nanoparticles with the same hydrodynamic size as albumin, 7.1 nm diameter.

Diffusion rates and collisional frequencies can only control the kinetics of adsorption; attractive forces must be present for adsorption to be a thermodynamically favorable process. The nature of the chemical and physical interactions between nanocrystals and proteins cannot be elucidated without analyzing specific protein-nanoparticle combinations, but most adsorption events are likely due to a combination of ionic and van der Waals forces. Electrostatic forces are much more long-range than van der Waals forces, and therefore minimizing ionic charge is important for reducing electrostatic adsorption, as well as minimizing induced-dipole attractions. These forces may also be magnified through multivalency, as discussed in Chapters 5 and 6. Thereby, the maximum number of interactions possible between two like-sized particles

increases with the nanoparticle surface area. In addition, the number of geometrically allowable multivalent interactions is dictated by surface curvature. That is, a smaller nanoparticle has a greater surface curvature, and the distance separating individual chemically attractive moieties increases as the size decreases. For a very small nanocrystal, the surface curvature is so high that only a few adsorption events can occur between nanoparticles, and thus the total energy of attraction will be lower. A larger particle will have a flatter surface, allowing a larger number of multivalent interactions per particle. For the interaction of a quantum dot with a serum protein, such as albumin, the valency of interaction will decrease with decreasing nanoparticle size. At some size cutoff, there will be so few interactions that they will no longer be sufficient to immobilize proteins on the nanocrystal surface, and the nanocrystals will have a reduced binding propensity. This phenomenon is minimized when the nanocrystals are the same size, or smaller than the proteins to which they adsorb.

This rationale may help to establish why biological macromolecules such as globular proteins are naturally resistant to nonspecific intermolecular adsorption in biological fluids, resulting in serum protein circulation half-times of days to months. However a direct comparison between proteins and nanocrystals is unsatisfactory, as nanocrystals are physically dissimilar from organic proteins in many ways. Proteins have a high degree of ordered rigidity built into their secondary and tertiary structures, yet their surfaces are rich with hydrophilic residues that are flexible and entropic. The surface disorder associated with proteins may help to explain their inherent colloidal stability compared to colloidal nanocrystals. Nanocrystals are hard, ordered structures with nearly zero entropy at room temperature, and their surface atoms are immobile. An organic interface with a liquid medium is crucial for the stabilization of nanocrystals as colloids. However the volumetric proportion of the organic domain and its means of

adhesion to the nanocrystal surface dictate how entropic the surface is. For a specific organic surface coating thickness, the fraction of organic domain to crystalline domain increases as the size decreases. For example, CdTe nanocrystals coated with a monolayer of the multidentate polymer have an organic shell that is ~1.5 nm thick. This means that the total organic volume on a 2.5 nm core will be ~10 times the amount of crystal volume, compared to a ratio of ~1.5 for a 5.5 nm nanocrystal core (Figure 7.5). This high fraction of organic composition allows the total nanoparticle to behave more like an organic molecule than a hard sphere, with a higher degree of surface entropy. This will energetically favor thermal interaction with the solvent, rather than the formation of an ordered protein-adsorbed structure. Quantum dots coated with small monovalent ligands are especially prone to surface entropic ordering, as the orientation of ligands is dictated by the atoms of the underlying crystalline facets, and even 2.5 nm nanocrystals coated with thioglycerol have a higher fraction of crystalline domain than organic domain. In the opposite extreme, nanocrystals coated with linear PEG chains are extremely stable due to the high entropic energy of solubilization of PEG, yet such polymeric coatings necessarily yield large particles.

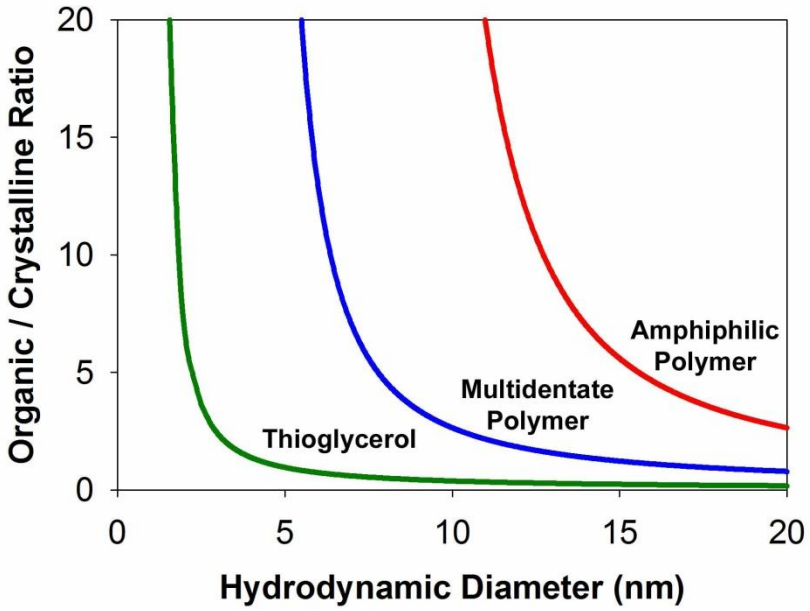

Figure 7.5: Ratio of organic shell to crystalline core domain size by volume. Ratios are calculated for small molecule ligands (thioglycerol, 0.5 nm thickness), multidentate ligands (1.5 nm thickness), and amphiphilic polymers (3.5 nm thickness).

Another important difference between proteins and nanocrystals is the role of surface domain curvature. As mentioned above, colloidal nanocrystals like quantum dots are essentially hard spheres coated with mobile organic surface domains. However geometrically spherical proteins do not really exist for direct comparison. Even large globular proteins have grooved surfaces with ridges rich with microdomains. These structures function to effectively increase the surface curvature, such that very few intermolecular binding events are possible. For instance, antibodies have a molecular weight of ~150 kDa, which would correlate to a 10 nm spherical globular protein. However, antibodies are far from spherical, containing three domains of ~50 kDa linked together through a Y-shaped hinge region. Globular proteins with a molecular weight of 50 kDa have a hydrodynamic size of ~6.5 nm, which is similar to that of albumin. Such surface intricacy is prevalent throughout biology, especially in giant protein structures,

like the ribosome and large macromolecular motors, and may be a natural evolutionary tendency for minimization of nonspecific interactions. These attributes point toward the use of nanocrystals with alternative architectures, such as nanorods or tetrapods, which can maintain a much higher surface curvature and diffusivity for larger sizes of particles compared to spherical quantum dots.

7.2 Cellular Binding and Uptake of Quantum Dots

For intracellular imaging of living cells and tracking membrane receptors with quantum dots, it is vital to understand the mechanisms of interaction between nanoparticles and living cells in culture. Most importantly, it is critical to eliminate nonspecific interactions with the plasma membrane, understand the mechanism of nanoparticle uptake, and minimize secondary effects of quantum dots, such as cytotoxicity or changes in osmotic pressure. In this section, the nanocrystal size and surface properties are correlated with their interaction with cultured cells and their fate within cells for the goal of generating quantum dots optimized for labelling of living cells.

7.2.1 Cell Culture and Assay Protocols. HeLa cells were cultured in ATCC-modified Eagle's Minimum Essential Medium (EMEM) with 10% fetal bovine serum at 37ºC (5% CO_2), and grown in 8-well LabTek chambers (Nalgene Nunc) to achieve 20% confluency. Twenty-four hours after seeding, cells were rinsed with serum-free medium and serum-free medium containing quantum dots (20 nM) was added. After 20 minutes at 37ºC, imaging was performed with a spinning disk confocal microscope (Ultraview, Perkin Elmer) using 488 nm laser excitation, a long pass filter, and a high sensitivity CCD camera (ORCA-ER, Hamamatsu).

A431 cells were cultured in Dulbecco's Modified Eagle's Medium (DMEM) with 10% fetal bovine serum at 37ºC (5% CO_2), and grown in 96-well plates. Twenty-four hours after seeding at 23,000 cells per well, cells were rinsed with serum-free medium, and a solution of quantum dots (1-100 nM) in serum-free Hank's Buffered Salt Solution (HBSS) was added. After 2 hours at 37ºC, the cells were stained with Hoechst nuclear dye (10 µL per well, 10 µg/mL) for 20 minutes at room temperature in the dark. The cells were then washed three times with HBSS and imaged with epifluorescence and brightfield microscopy.

7.2.2 Quantum Dot Charge Effects. The electrostatic charge associated with small molecules, macromolecules, and large colloids significantly impacts their association with biological molecules and cellular structures, and can modulate cellular internalization and subcellular distribution. To study this effect using quantum dots, 6.5 nm (CdSe)ZnS nanocrystals with 6 different surface coatings (see Chapter 5) were mixed with subconfluent monolayers of cultured HeLa cells for 20 minutes. Figure 7.6 shows fluorescence confocal micrographs overlaid on brightfield images, revealing the surface-dependence of the interactions between quantum dots and cells. Nanocrystals coated in neutral polyethylene glycol (amphiphilic diblock copolymer, A, and lipid-PEG, D) were highly stable in solution and showed very little interaction with the cells. This finding is in accord with the earlier observation of a reduction in nonspecific binding to serum proteins for neutralized surface coatings. The negatively charged colloids (mercaptopropionic acid, B, and amphipol, E) also showed very little cellular association, but their colloidal stability in saline solution at 37ºC was poor, producing large aggregates on the growth substrate. These conditions of relatively high ionic strength, high temperature, and a medium of salts and biomolecules most likely decreased the anionic stabilization of these two types

of carboxylated quantum dots and initiated their aggregation. This could be completely eliminated through PEGylation of the surface coatings (Figure 7.6F) prior to addition to the cells. Neutral and anionic surface coatings resist association with cells due to the intrinsic negative charge of plasma membrane phospholipids, and cationic surface coatings promote cellular adsorption, as verified with PEI-coated quantum dots (Figure 7.6C). These nanocrystals quickly associated with cells after addition to the medium and were highly toxic with limited active uptake unless they were also PEGylated.[4] Therefore, for the production of highly specific probes for molecular imaging on plasma membranes and inside of cells, it will be necessary to use anionic or neutral surface coatings, although it may be possible to harness nonspecific charge-induced uptake of cationic nanocrystals for imaging the process of endocytosis.

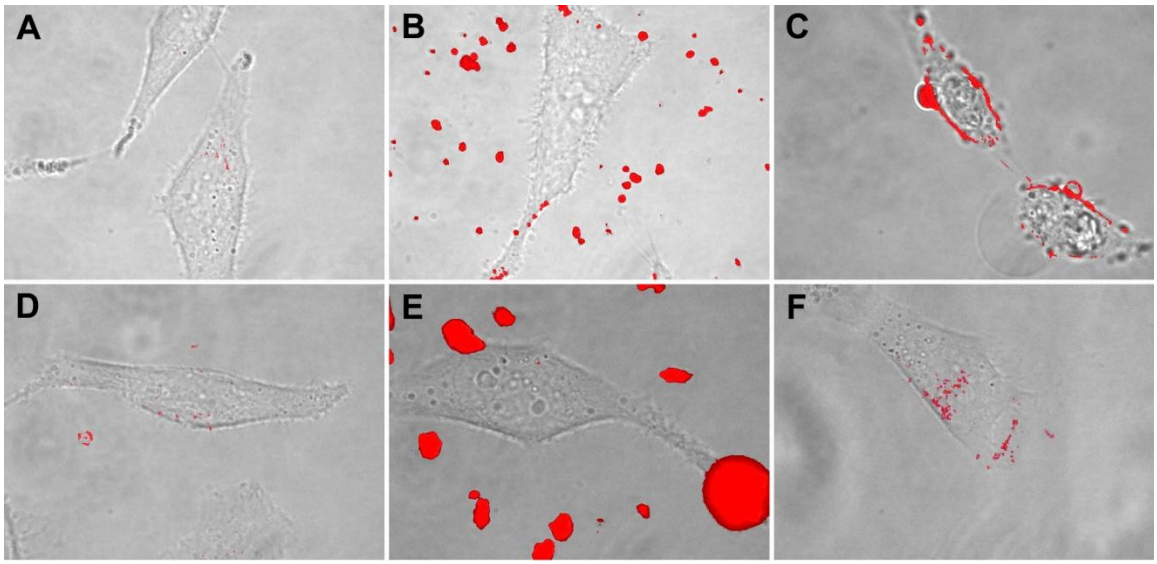

Figure 7.6: Quantum dots (20 nM) incubated with HeLa cells for 20 minutes at 37ºC in serum-free medium. Confocal fluorescence micrographs were focused near the cell centers. Fluorescence images were false-colored red before they were overlaid on bright-field images. (A) Quantum dots coated with the amphiphilic diblock copolymer have a nearly neutral surface of PEG and showed very little aggregation or association with cells. (B) Quantum dots coated with

mercaptopropionic acid are unstable and aggregated in solution, yielding insoluble precipitates. (C) Quantum dots coated with polyethylenimine are stable in solution and rapidly associate with cellular plasma membranes. (D) Lipid-PEG encapsulated nanocrystals show little aggregation or cellular uptake. (E) Quantum dots coated in amphipols aggregate and precipitate outside of cells. (F) Quantum dots coated in amphipols and then conjugated to PEG show similar behaviour as the other PEGylated quantum dots.

7.2.3 Quantum Dot Size Effects. The new discovery of a reduction in nonspecific interactions for protein-sized quantum dots may lead to the development of new types of specific cellular probes. To test the interaction between such small nanocrystals and cells, CdTe nanocrystals (2.5 nm) with green emission (530 nm) were coated with the multidentate polymer (Chapter 5), resulting in a hydrodynamic diameter of 5.5 nm. These nanocrystals were found to have markedly decreased adsorption to serum components in earlier studies. After incubation with A431 cells for 2 hours, these quantum dots also showed no visible fluorescence in cellular cytoplasms or nuclei (Figure 7.7). However, consistent fluorescence contrast was observed in cellular debris and dead cells. This suggests that these small nanocrystals can get trapped in the small pores of collapsed cellular structures and aggregated proteins, yet they cannot penetrate into living cells and they have very limited nonspecific uptake.

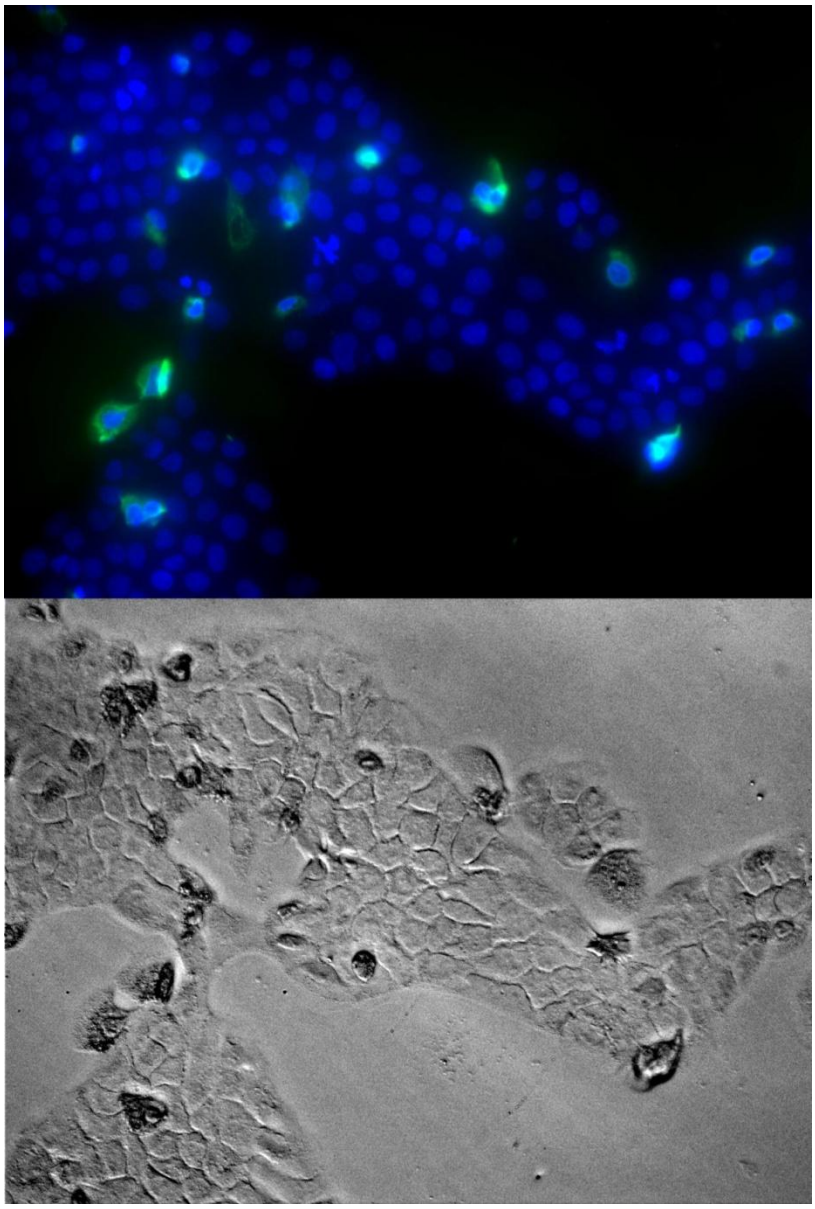

Figure 7.7: Uptake of 5.5 nm quantum dots by A431 cells. Cells were incubated with a 100 nM solution of quantum dots for 2 hours at 37ºC, washed three times, and imaged via epifluorescence microscopy (top) and brightfield microscopy (bottom). The top image shows an overlay of the blue (Hoechst dye) and green (quantum dot) channels, showing no internalization of the quantum dots inside living cells. Fluorescence is noted in cellular debris or dead cells, which was a rare event.

Previously it was shown that the addition of PEG-thiol to small CdTe quantum dots coated with the multidentate polymer resulted in neutralization of the surface charge as

well as a preservation of their resistance to nonspecific adsorption (Figure 7.2). Extending these findings to cellular interactions, quantum dots incubated with a 1000x excess of PEG-thiol were added to A431 cells under the same conditions used above (Figure 7.8). The quantum dots still did not enter living cells or adhere to their surfaces, but this modification essentially eliminated the interaction between the nanoparticles and dead cells and debris. It is likely that the increase in size due to PEGylation prevented the penetration of these quantum dots into the small pores in the plasma membranes of dead cells, and eliminated their association with large fibrous structures.

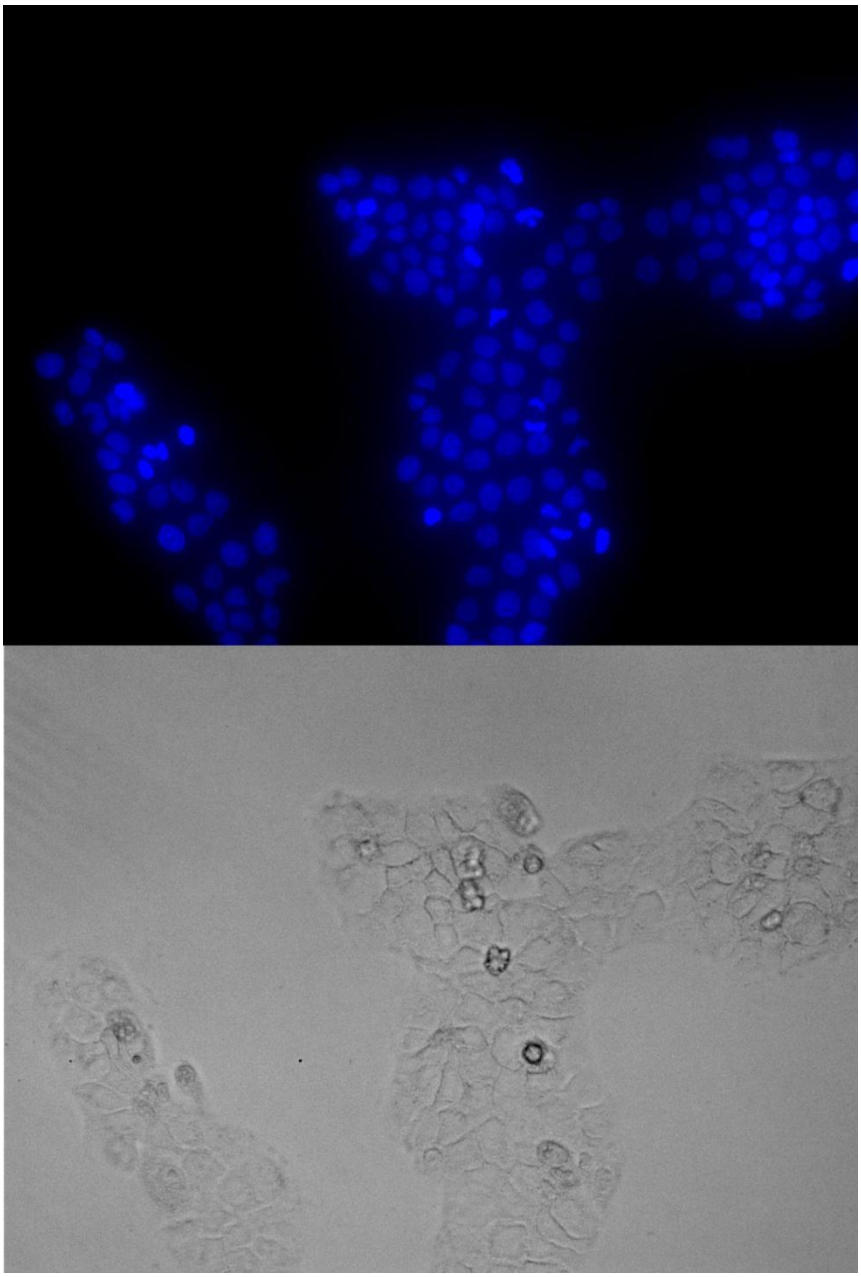

Figure 7.8: Uptake of PEGylated quantum dots by A431 cells. Quantum dots were incubated with a 1000x molar excess of 2000 Da PEG-thiol for 24 hours. Cells were incubated with a 100 nM solution of quantum dots for 2 hours at 37ºC, washed three times, and imaged via epifluorescence microscopy (top) and brightfield microscopy (bottom). The top image shows an overlay of the blue (Hoechst dye) and green (quantum dot) channels, showing no fluorescence contrast from quantum dots. Fluorescence was not found in cellular debris or dead cells.

Figure 7.2 demonstrates that larger quantum dots (4.5 nm core, 7.5 nm hydrodynamic diameter) are significantly more prone to nonspecific binding of serum proteins compared to smaller nanocrystals. To determine if this relationship similarly impacts their association with cells, these 7.5 nm nanoparticles were incubated with A431 cells under similar conditions as those used above. These nanocrystals were quickly internalized, staining internal regions of each cell as well as the cell periphery (Figure 7.9). The quantum dots accumulated in a brightly fluorescent spot near the center of each cell, which superficially suggests nuclear localization. However a Hoechst dye costain reveals that this stained region is actually outside of the cellular nucleus (Figure 7.10). This staining pattern is consistent with localization to the microtubule organizing center (MTOC), which is in accord with literature reports of an endocytotic mechanism of quantum dot internalization (Chapter 2).

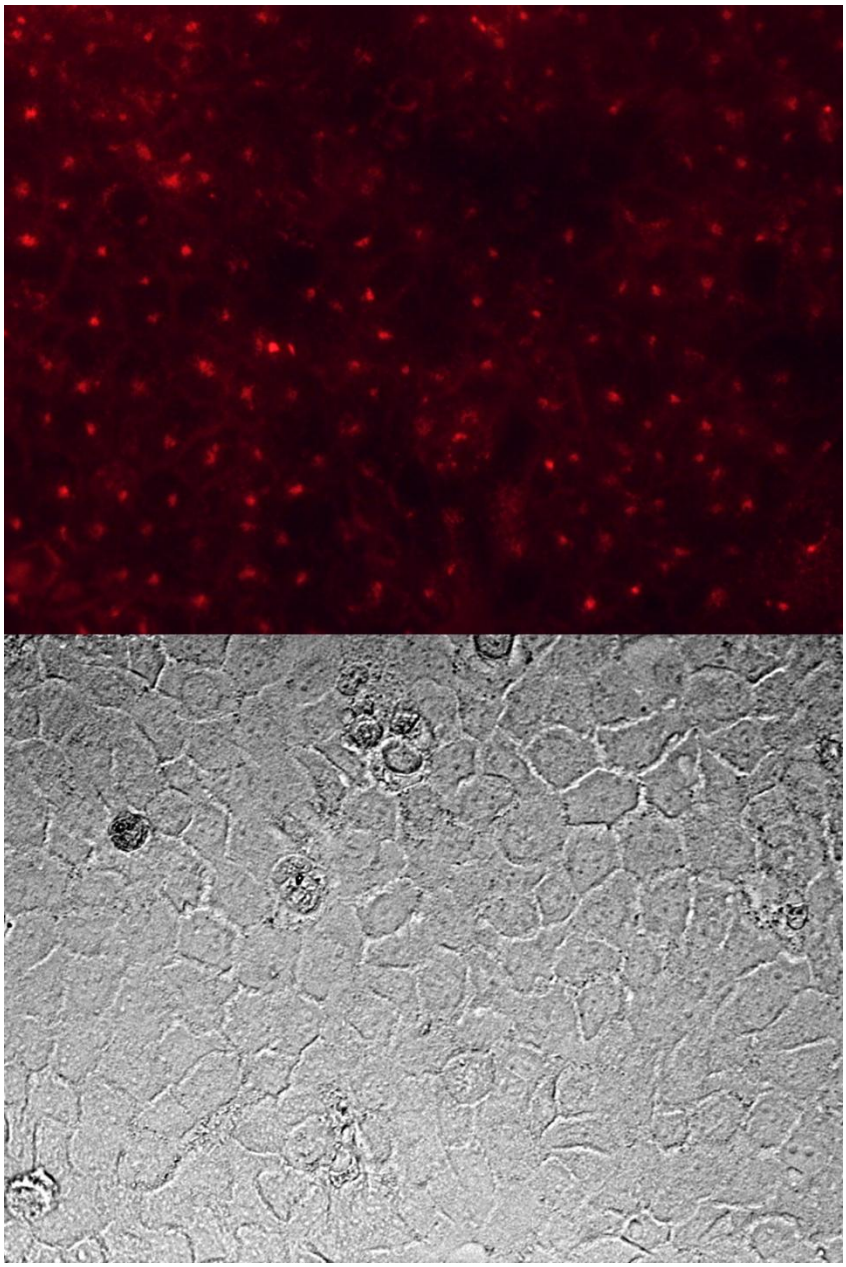

Figure 7.9: Uptake of 7.5 nm quantum dots by A431 cells. Cells were incubated with a 100 nM solution of quantum dots for 2 hours at 37ºC, washed three times, and imaged via epifluorescence microscopy (top) and brightfield microscopy (bottom), focusing near the centers of cells. The top image shows false color images of red quantum dot fluorescence, showing strong intracellular uptake. Fluorescence was not found in cellular debris or dead cells.

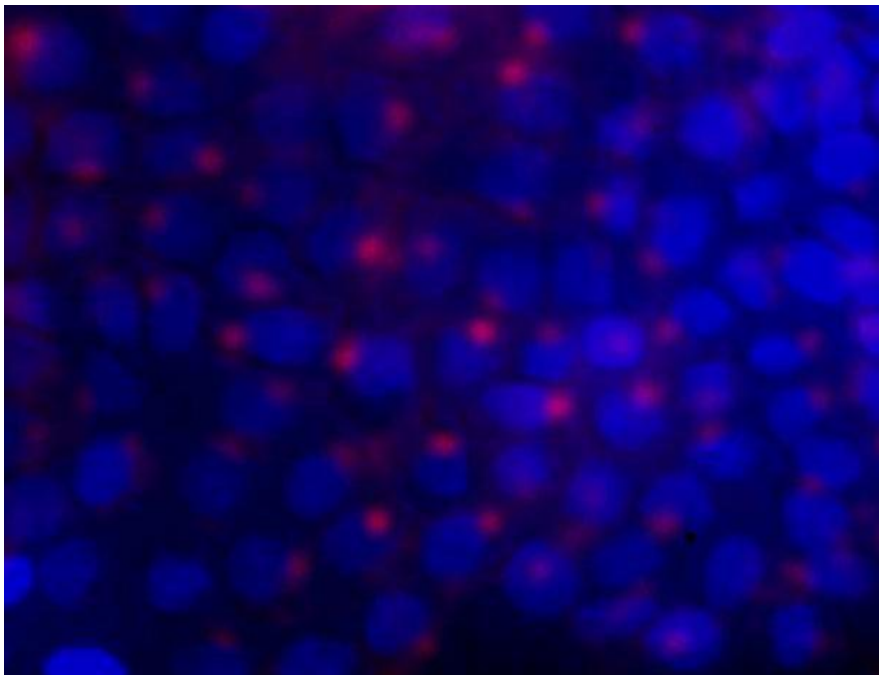

Figure 7.10: Costain of A431 cells with Hoechst nuclear stain and 7.5 nm CdTe quantum dots. Quantum dot contrast was found outside of the nucleus, except in some cells, in which the nanocrystals appear either on the top or bottom of the nucleus, out of focus. Quantum dot localization to the MTOC region is consistent with an endocytotic uptake mechanism.

In conclusion, quantum dots with a hydrodynamic diameter smaller than 6 nm exhibited a dramatic decrease in cellular internalization and binding compared to larger quantum dots. The forces at play are likely to be similar to those described earlier for nonspecific protein binding to quantum dots. That is, larger particles have a natural tendency to nonspecifically bind to cellular surface structures and plasma membrane proteins, inducing binding events that can initiate endocytosis. The MTOC localization of these quantum dots is consistent with an endocytotic mechanism of uptake, as endocytotic vesicles are transported to the MTOC region via active molecular machinery. The use of a thin multidentate ligand coating also precludes the widespread aggregation of traditional anionic polymeric coatings and monovalent ligands (Figure 7.11). In addition,

these cells did not show any signs of overt toxicity or abnormal behaviour in the presence of 100 nM quantum dots. Taken together, these results suggest that these compact quantum dots are significantly more useful for labelling of live cells compared to their larger counterparts coated with amphiphilic polymers.

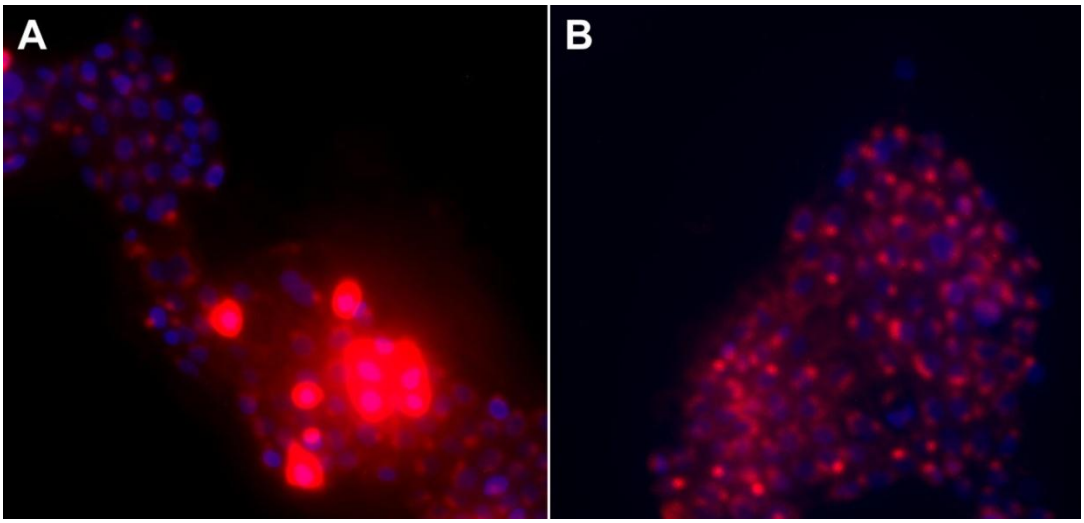

Figure 7.11: Staining comparison between CdTe quantum dots coated with an amphiphilic polymer (A) and the multidentate polymer (B). Cells are costained with a Hoechst dye for nuclear contrast. Homogeneous quantum dot samples were used for both experiments, but significant aggregation of quantum dots coated with the amphiphilic polymer resulted from a combination of cellular adhesion and colloidal destabilization under biological conditions.

7.3 Bioconjugation to Polyhistidine-Tagged Proteins

Minimizing nonspecific interactions is only half of the means to generating specific optical probes for biomedicine. Introducing a biorecognition capability is fundamental to modern molecular medicine, targeted therapy and imaging, and cell and tissue labeling. Many methods have been described for coupling colloidal particles to biomacromolecules like antibodies and nucleic acids, as well as small molecule ligands

and enzyme substrates (see section 2.3.4.4). Among these, covalent conjugation and streptavidin-biotin coupling have been the most commonly used, yet more recent recombinant protein strategies have made great strides in improving coupling efficiency and controlling the geometry of crosslinking.[5-13] Recombinant protein methods developed for high-yield purifications, such as terminal polyhistidine-labeling, have been used to induce spontaneous protein self-assembly on nanocrystals containing surface metal ions, resulting in a high efficacy of bio-specificity.[5,7,8] Such methods have been previously limited by the overall size and stability of the resulting probes, and this section aims to overcome these issues with the implementation of ultrasmall quantum dots prepared within this thesis (Chapter 5). The results demonstrate a high efficiency of self-assembly, high stability, as well as the capacity to prepare modular protein A-modified probes with affinity for nearly antibody.

7.3.1 Quantum Dot-Protein A Conjugation. Protein A is an exceptional candidate for constructing a modular biospecificity adaptor for quantum dots. This bacterial protein binds to the Fc region of immunoglobulins, leaving the antigen-binding $F(ab')_2$ domains directed away from the protein, and has a wide species specificity. Thereby, a Protein A-quantum dot conjugate would be capable of specifically binding a wide range of antibodies (K_d =10 pM to 100 nM)[14] with outward direction of the antigen binding units. Protein A is 42 kDa, or roughly 6 nm in hydrodynamic diameter, and contains 4 antibody binding domains, which could allow for the binding of multiple antibodies for a single quantum dot for increased multivalent affinity for antigens.

In order to couple Protein A to quantum dots, a recombinant version of the protein with an N-terminal his(6) sequence (Clontech) was tested for specific binding to (CdSe)ZnS quantum dots coated with the multidentate polymer. Semiconductor nanocrystals

coated with small monovalent ligands have previously been shown to specifically self-assemble with his-tagged proteins with a binding constant of ~1 nM.[15] Protein A was covalently linked to the fluorescent dye Alexa 546 (Molecular Probes) in order to monitor binding events. Small green quantum dots with a nanocrystal size of 3.65 nm and a hydrodynamic size of ~7.2 nm were mixed in different ratios with the dye-conjugated His-tagged protein, and allowed to equilibrate for at least 24 hours. Figure 7.12 shows color photographs of the results of agarose gel electrophoresis for these quantum dot-protein mixtures. On the left gel, the pure quantum dots without any protein, labeled '0', were anionic in borate buffer (pH 8.5) and migrated from the lanes toward the anode (downward). Pure Protein A (lane labeled 'Protein A') has a weaker negative charge and consequently it had a shorter migration distance. The gel labeled with yellow numbers depict quantum dots conjugated to his-tagged, dye-conjugated Protein A, with Protein A:quantum dot ratios of 0:1 to 4:1. With increasing amount of protein, the migration distance of the quantum dots decreased due to the increase in hydrodynamic size caused by conjugation. This size increase was verified by size-exclusion chromatography (data not shown). In addition, the nanoparticle band became yellow due to the fluorescent color of the dye (~2 dyes per Protein A). The same experiment was also performed using Protein A that was not labeled with a dye, depicted in the next lanes labeled with white numbers. These bands show essentially the same migration distances as those with the dye, suggesting that dye conjugation to the protein A does not impact the interaction between the protein and the nanocrystal.

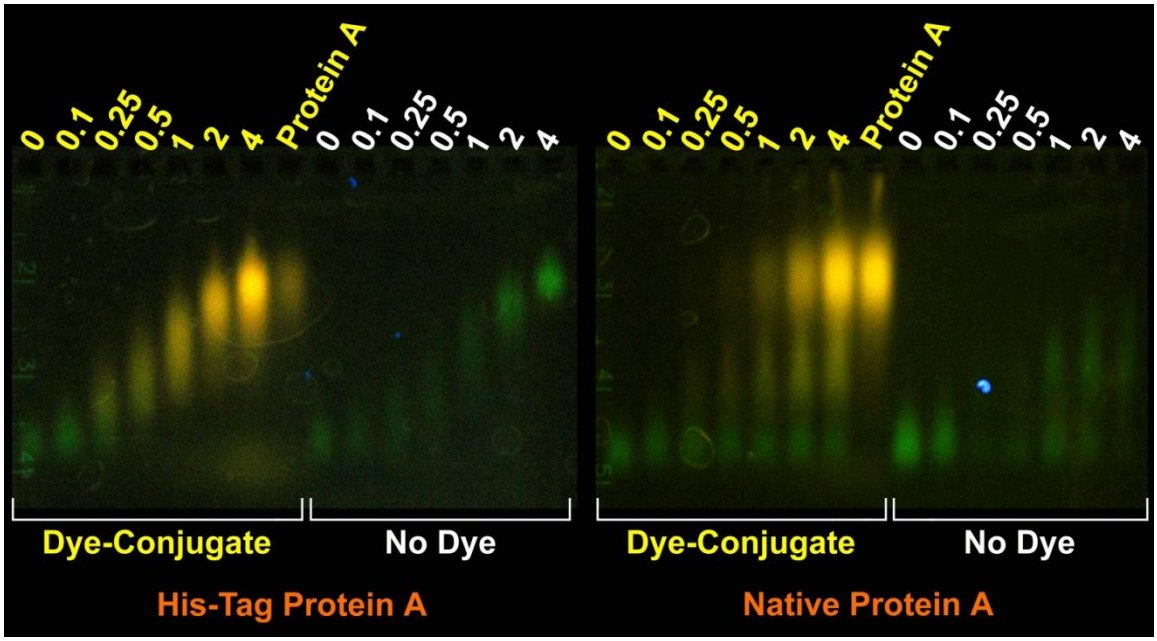

Figure 7.12: Color image of conjugates of Protein A and green quantum dots in an agarose gel following 45 minutes of electrophoresis at 100V. Wells are at the top of the image, and all particles and proteins ran toward the anode (bottom). The numbers at the tops of the lanes represent the Protein A:quantum dot ratio (e.g. '4' is 4 protein A per 1 quantum dot). The quanum dots are green and protein A was labeled with the yellow dye Alexa 546. The left gel depicts quantum dots mixed with recombinant protein A containing a His-tag, with or without dye conjugation. The right gel depicts quantum dots mixed with native protein A (no His-tag) with or without dye conjugation. See text for discussion. Pure protein A is included in the 8th lane for each gel. Blue haze from the image caused by the agarose gel was digitally removed with prudence to preserve the color and intensity of the green and yellow fluorescence.

The gel on the right of Figure 7.12 shows the same coupling reactions as those on the left, except that Protein A was a native nonrecombinant version that lacks a polyhistidine tail. The nanocrystals retained their original long migration distance bands, and were effectively purified from Protein A through electrophoresis. However, a small amount of green-yellow streaking arose between the quantum dot and Protein A bands at high protein concentrations (e.g. see band '4') which suggests a small degree of nonspecific adsorption between the nanocrystals and the protein. This is not unexpected, as these

particles are larger than the previously discussed ~6 nm threshold for limiting nonspecific adsorption to 6 nm Protein A, and no additional precautions were taken to reduce such effects (e.g. addition of albumin or surfactants). The lanes labeled with white numbers on the right gel confirm that these nonspecific binding events are due to protein-quantum dot adsorption and not due to the dye conjugation.

Figure 7.13 depicts larger quantum dots coupled to Protein A. These (CdSe)ZnS nanocrystals had a ~6.5 nm crystalline core and a hydrodynamic diameter of ~9.5 nm. These larger particles also specifically assembled with the his-tag on Protein A, as verified by the gradual decrease in migration distance with increasing protein:quantum dot ratio (see the first 5 lanes labeled with yellow numbers). However, in accord with previous findings in this chapter, these particles were much more prone to nonspecific adsorption than their smaller counterparts. A 4:1 ratio of protein:quanutm dot resulted in complete adsorption of the free quantum dots even when the protein had no polyhistidine sequence, as depicted in the 4(N) lanes. Again, the nonspecific interactions of larger particles preclude their use as sensitive and specific probes, although it is possible that these interactions may be overcome through surface modifications such as surface charge reduction via PEGylation, as discussed in section 7.2.

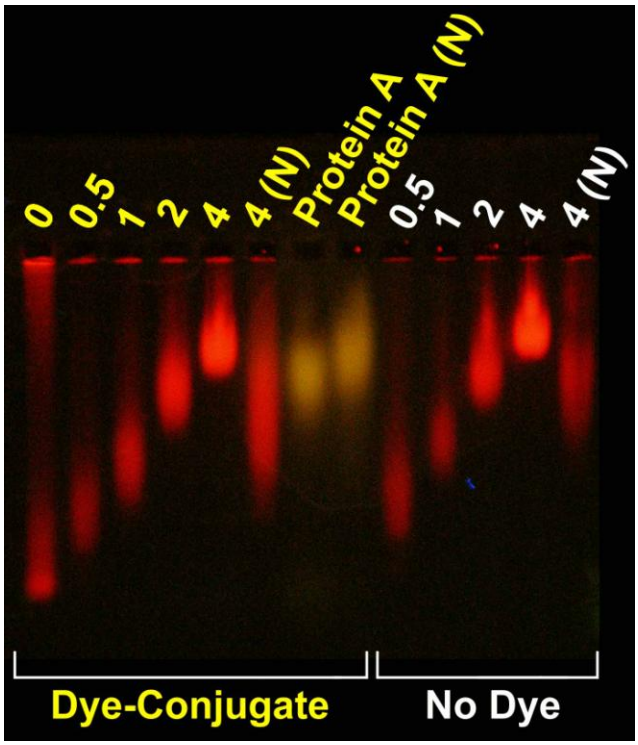

Figure 7.13: Real color image of Protein A-quantum dot conjugates in an agarose gel following 45 minutes of electrophoresis at 100V. Quantum dots were 6.5 nm in crystalline diameter and 9.5 nm in hydrodynamic diameter. Wells are at the top of the image, and all particles and proteins ran toward the anode (bottom). The labels at the tops of the lanes represent the Protein A:quantum dot ratio or pure Protein A. All mixtures used his-tagged recombinant Protein A, except for those labeled with 'N,' indicating the native protein with no polyhistidine sequence. The quanum dots are red and Protein A is labeled with the yellow dye Alexa 546. The intense brightness of the quantum dots obscures any yellow fluorescence from the protein conjugates. See text for further discussion.

It is interesting to note that these nanocrystal-protein conjugates do not form instantaneously. Instead, self-assembly requires hours to days to equilibrate, as determined by fluorescence spectroscopy (see section 7.3.3) and gel electrophoresis. In contrast, Mattoussi and coworkers have reported that the equilibration of his-tag proteins and quantum dots coated with small molecular ligands occurs in 10-15 minutes.[15] This finding is not surprising in light of the different surface coatings of these materials. Small molecule ligands such as hydrophilic thiols are known to desorb from the nanocrystal

surface, and have a relatively low affinity.[16,17] The multidentate polymer ligand significantly increases this affinity, and provides fewer available binding sites on the nanocrystal surface for the polyhistidine tail. In addition, the polymeric coating provides a steric barrier to association with the protein. Currently the mechanism of self-assembly is unclear and merits further study. If binding requires part of the polymer to briefly desorb from the surface, it may be possible to increase the speed of binding with mild heating. Alternatively, if the polyhistidine tag is capable of disrupting the polymeric coating, this process should be strongly dependent on the length and chemistry of the peptide tail. Finally, because the on-rate of the specific association is dramatically decreased, it may be possible that the off-rate will be altered as well. Studies on the effects of the multidentate polymer coating on the dissociation constants are ongoing.

7.3.2 Quantum Dot-Protein A-IgG Conjugation. In order to determine if the quantum dot-Protein A conjugates can be used as modular adaptors for IgG conjugation, green quantum dots with a 1:1 ratio of Protein A were prepared and mixed with various amounts of rabbit anti-goat IgG (Invitrogen). Each Protein A has 4 binding sites for IgG, but only 2 are simultaneously active, so it is possible that up to 2 IgG molecules can bind to each conjugate, although steric considerations may be limiting. Protein A was labeled with the fluorescent dye Alexa 594. Figure 7.14 depicts an agarose gel after electrophoresis of these conjugates. On the left, the first lane shows the original green quantum dots (labeled 'QD), and the second lane shows the quantum dots conjugated 1:1 with protein A (labeled 'QD-Protein A'), with a yellow color due to the Alexa dye on Protein A. The next 5 lanes labeled with red numbers show these conjugates after incubation with increasing amounts of IgG, labeled with a red dye. It can be seen that the migration distance of the quantum dots steadily decreases up to a ratio of 1:1 in association with red fluorescence, confirming an increase in size and association with

IgG. Increasing the amount of protein to 2:1 may further decrease the migration distance (see gel in Figure 7.15 with longer electrophoretic duration), which suggests that it may be possible to bind more than one IgG to each Protein A. In the second set of lanes labeled with red numbers, the same experiment was performed using Protein A that was not conjugated to a dye, confirming that the dye did not block the IgG-binding domain of Protein A, and did not disrupt its functionality. On the gel on the right (labeled $F(ab')_2$), the same experiment was performed again, except the antibody was first cleaved to remove the Protein-A-specific Fc domain, leaving the $F(ab')_2$ antigen binding domains. The nanocrystals were mixed with these antibody fragments in the same ratios, and no binding was observed, as the original yellow bands remained for all of the antibody:quantum dot ratios. This control verifies that the binding of the antibody to the nanoparticle construct was specific, and would be expected to yield directional orientation of the antibody on the nanocrystal surface for antigen binding. It is important to note that no purification steps were performed in any of the processes implemented herein. The self-assembly between these nanocrystals, polyhistidine-tagged proteins, and antibodies is highly specific and robust, and no significant dissociation has been observed. This asset is far reaching, as purification of nanoparticle constructs is often a limiting step in conjugation, especially for small sized particles, which are hydrodynamically similar to the molecules from which they must be separated.

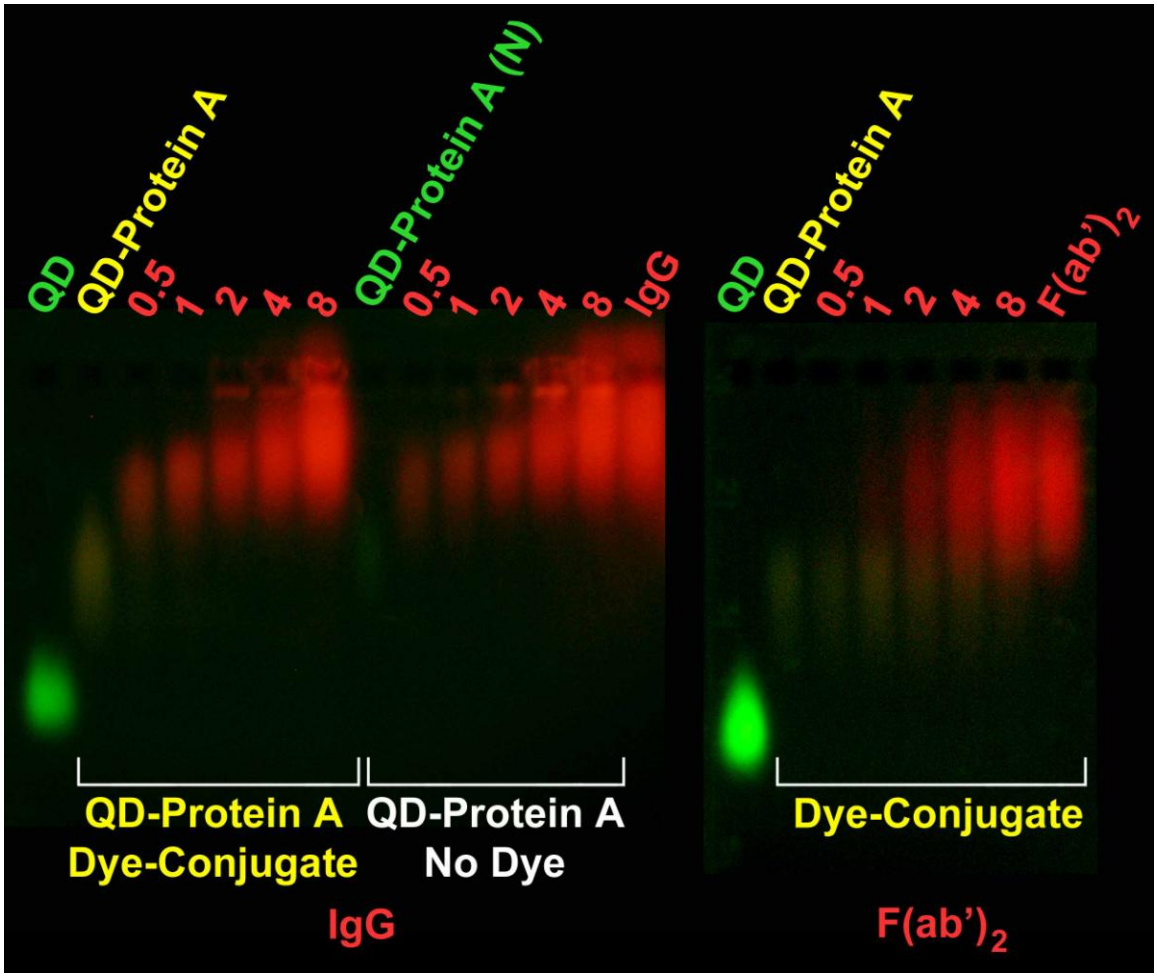

Figure 7.14: Real color image of Protein A-quantum dot conjugates mixed with varying amounts of antibodies in an agarose gel following 45 minutes of electrophoresis at 100V. Wells are at the top of the image, and the anode is at the bottom. Quantum dots (QDs) are shown with green fluorescence, in addition to quantum dots coupled 1:1 with his-tagged Protein A (QD-Protein A), which was labeled with Alexa 546 (yellow) or not labeled (green). The numbers at the tops of the lanes represent the antibody:quantum dot ratio (e.g. 4 is 4 IgG per 1 quantum dot-Protein A conjugate). On the left gel, the antibody is whole, and can bind to Protein A, whereas the Fc fragment is cleaved off on the right gel ($F(ab')_2$). An image for longer electrophoresis time is shown in Figure 7.15, corresponding to lanes 2-7 of the left gel (QD-Protein A, 0.5, 1, 2, 4, and 8).

Figure 7.15: Gel image after 90 minutes of electrophoresis, corresponding to lanes 2-7 (QD-Protein A, 0.5, 1, 2, 4, and 8) of the left gel in Figure 7.14.

7.3.3 Optical Properties of Protein-Quantum Dot Conjugates. It has been noted in the literature and verified in this work that the binding of his-tagged proteins to (CdSe)ZnS quantum dots increases the quantum efficiency of the nanocrystals.[5,8] Figure 7.16 shows spectra of green quantum dots in the presence of increasing amounts of recombinant his-tagged Protein A, demonstrating a nearly two-fold increase of quantum efficiency, from 31% to 58%. These nanocrystals were purposely prepared to be as small as possible, with a minimal shell thickness of ~1.5 monolayers of ZnS, which leads to lower quantum efficiency in water than nanocrystals with thicker shells.[1,18,19]

This is known to induce nonradiative surface-defects, which can be removed through surface modification or annealing.[20-22] The increase in photoluminescence efficiency with the binding of basic amine-containing polyhistidine peptides is likely the result of the passivation of surface defects. Indeed, in nonpolar solvents, adsorption of basic amine-containing ligands to (CdSe)ZnS quantum dots leads to an increase in quantum yield.[23-25] However, these nanocrystals also exhibit significant deep trap emission at longer wavelengths, which is a radiative form of surface related defects. Surprisingly his-tag binding did not modify this defect. Instead, the band-edge luminescence increased independently of the deep trap emission, suggesting that there are two independent types of surface related defects in these quantum dots

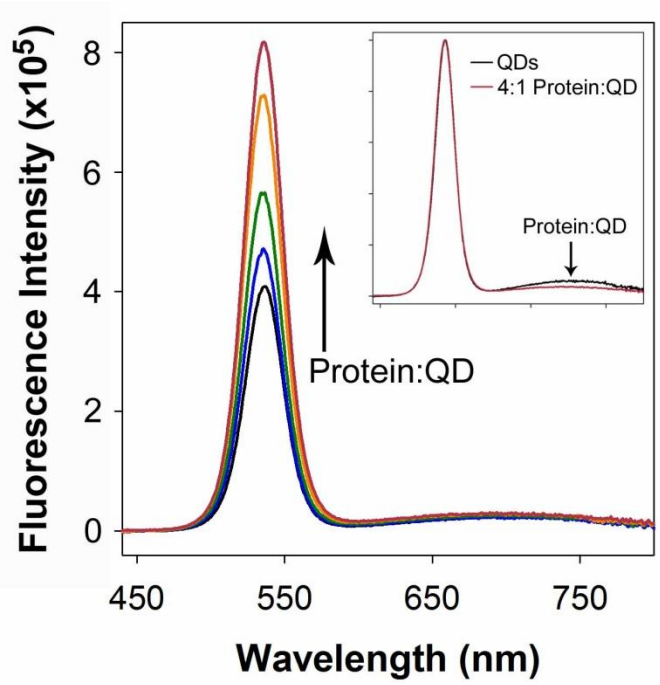

Figure 7.16: Fluorescence spectra of (CdSe)ZnS quantum dots mixed with different amounts of His-tagged protein. The spectrum of pure quantum dots is black, showing significant deep-trap emission. Adding His-tagged proteins increased the quantum efficiency of the bandgap emission (arrow indicates 0 to 4 proteins per quantum dot). In the inset, the spectra of 0:1 and 4:1 protein:quantum dot ratios are normalized to show the relative changes in the band-edge and deep trap emission. The band-edge emission changed independently from the deep trap emission, which did not significantly change.

In the preparation of the Protein A conjugates in section 7.3.1, the organic dye Alexa 546 was specifically chosen to match the spectral properties of the green quantum dots in order to generate an efficient energy transfer pair (Figure 7.17). Fluorescence resonance energy transfer (FRET) has been a highly successful means of modulating quantum dot fluorescence, monitoring binding events, and for preparing quantum dot-biosensors.[5,6,26-30] Energy from excited state quantum dots can be efficiently accepted by organic dyes and other quantum dots if they are in close proximity, yielding an excited state acceptor which can emit fluorescent light at a longer wavelength. The physics of this process have been rigorously described in the literature, and the resulting equations are given here.[6,31,32] The Forster radius, R_o, is the distance between the donor and acceptor that yields 50% energy transfer efficiency:

$$R_o = \left(I \frac{9000(\ln 10) Q_D \kappa_p^2}{128\pi^5 N_A n_D^4} \right)^{1/6} \qquad \textbf{Equation 7.3}$$

where I is the overlap integral between the fluorescence spectrum of the donor and the absorption spectrum of the acceptor (here I =3.86 x 10^{-13} M^{-1} cm^3), $\kappa_p$is the dipole orientation factor (usually $\sqrt{2/3}$), Q_D is the quantum efficiency of the donor, and n_D is the refractive index of the solvent. For the quantum dot-Alexa dye conjugates used herein, R_o was calculated to be 5.3 nm. The FRET efficiency, E, can be calculated as:

$$E = 1 - \frac{F_{DA}}{F_D} \qquad \textbf{Equation 7.4}$$

where F_D is the integrated fluorescence intensity of the donor alone and F_{DA} is the intensity in the presence of the acceptor. The distance between the donor and acceptor, r, can then be calculated as

$$r = R_o \left(\frac{n(1-E)}{E} \right)^{1/6} \qquad \textbf{Equation 7.5}$$

where n is the average number of acceptors per donor.

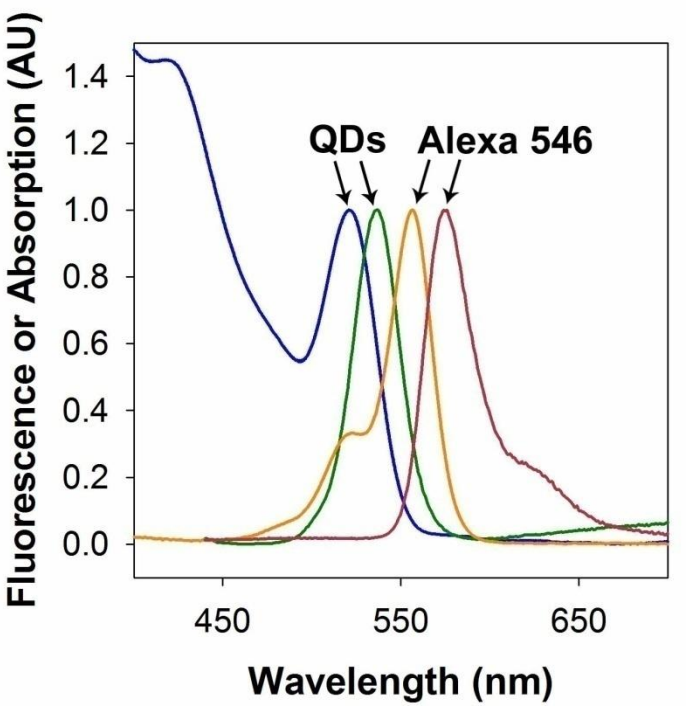

Figure 7.17: Fluorescence and absorption spectra of (CdSe)ZnS quantum dots and the Alexa 546 dye. Quantum dot absorption is depicted in blue and the fluorescence spectrum is green. Note the deep trap emission at longer wavelengths. The absorption spectrum of Alexa 546 is orange and the fluorescence spectrum is red.

Figure 7.18 depicts the fluorescence spectra of the green quantum dots conjugated to his-tagged Protein A with Alexa 546 acceptor dyes. An increase in the amount of conjugated protein substantially decreased the fluorescence quantum yield from the quantum dot, an expected characteristic for an increase in the number of acceptors on a single FRET donor. However, the acceptor dye fluorescence only increased proportionally for the addition of up to 0.5 proteins per quantum dot (~2 dyes per protein). The distance between the donor and acceptor was calculated to be 5.06 nm, which is close to the predicted value of 4.8 nm from the nanocrystal radius from TEM (1.83 nm) and the hydrodynamic radius of protein A (3.0 nm). The small discrepancy may be accounted for by the linker length of the polyhistidine sequence. Importantly,

this value is less than the Forster radius (5.3 nm), allowing highly efficient energy transfer. This level of quenching efficiency is not possible for larger nanocrystals, again validating the utility of small sized nanocrystals for biomedical applications.

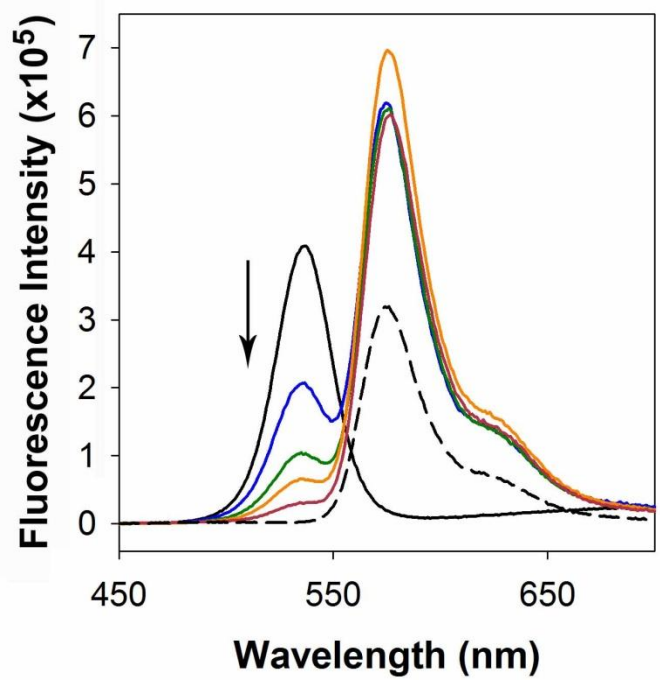

Figure 7.18: Fluorescence and absorption spectra of (CdSe)ZnS quantum dots self-assembled with polyhistidine-tagged Protein A conjugated to a FRET acceptor dye (Alexa 546). The arrow denotes increasing Protein A concentration, from 0 to 4 proteins per quantum dot. The quantum dot emission decreased markedly from its original value (black solid line), whereas the fluorescence efficiency of the dye only slightly increased above its original value (black dotted line).

For conjugations of 1 protein or more per quantum dot, the acceptor fluorescence did not increase substantially, indicating a quenching of the quantum dots by a non-FRET mechanism. Nevertheless, at a conjugation ratio of 4:1, the quantum dots were quenched by a surprising 97% of their original value. The nature of this quenching merits further study, and may relate to the deep-trap emission states of the quantum dot, or the interaction of the his-tag with regions of the CdSe that are not fully passivated with

a shell, inducing a short-lifetime surface defect state. Future studies will test the FRET efficiency in relation to the thickness of the insulating inorganic shell.

7.4 Quantum Dot Cytotoxicity

The potential toxicity of semiconductor quantum dots toward living cells and organisms is a subject of great concern. The frequently observed cytotoxic impact of cadmium-based quantum dots on cultured cells has typically been attributed to the release of toxic, carcinogenic cadmium ions, however this correlation is not yet convincing. Chapter 2 provides a detailed analysis of the cytotoxicity literature to date on semiconductor nanocrystals, and concludes that there is an overwhelming number of confounding factors that could have overshadowed the cytotoxic effects of cadmium in these studies. In this section, the role of cadmium in cellular cytotoxicity is studied using structurally and compositionally relevant controls, divulging new attributes of quantum dot toxicity. First, the cytotoxicity of cadmium is far overwhelmed by the cytotoxicity of selenium components. Second, reducing the composition of cadmium in quantum dots by increasing the zinc content may actually lead to an *increase* in cytotoxicity toward many cell types due to the higher acidity of zinc. Third, recently touted cadmium-free quantum dots composed of ZnSe are extremely toxic toward many cell types due to the unique surface chemistry of this material, resulting in the formation of highly toxic elemental selenium species. This work demonstrates that many of the proven toxicity rules for organic molecules and metal ions cannot be directly applied to nanoparticles, for which an entirely new toxicity paradigm must be developed.

7.4.1 Cell Culture Methods and Cytotoxicity Assays. For analysis of cellular toxicity of cadmium-containing and cadmium-free quantum dots, three types of cells were utilized, human liver carcinoma HepG2 cells, primary human umbilical vein endothelial cells (HUVECs), and immortalized mouse fibroblasts (NIH3T3s). HepG2s were cultured in MEM with 10% FBS, subcultured at a ratio of 1:4, and assayed at passage 4-9. HUVECs were cultured in EBM-2 media with EGM-2 supplements (Lonza), subcultured at a ratio of 1:4, and assayed at passage 6. NIH3T3s were cultured in DMEM with 10% bovine calf serum, subcultured at a ratio of 1:20, and assayed at passages 4-9. All cellular incubations were conducted at 37°C in 5% CO_2.

For proliferation assays, cells were plated in black, clear-bottom 96 well plates at densities of 5000 cells per well for HepG2s, 2000 cells per well for HUVECs, or 1000 cells per well for NIH3T3s. After 24 hours of seeding, the medium was replaced with fresh medium containing quantum dots (100 µL complete medium plus 100 µL quantum dots in PBS), and the cells were incubated for 5 or 6 days. After each 24 hour increment, including the initial time point, one redundant plate of cells was washed with HBSS or PBS, emptied, and frozen at -80°C to determine the number of cells. After completion of the 5 or 6 day experiment, all of the cell counts were obtained through DNA quantification using Hoechst 33258 dye. The cells were thawed to room temperature, 100 µL of distilled water was added to each well, and the plates were incubated at 37°C for 1 hour. The cells were then lysed by freezing the plates at -80°C for 3 hours. The cells were again thawed, 100 µL of Hoechst solution (FluoReporter Blue, Invitrogen) was added to each well, and calf thymus DNA (Sigma-Aldrich) in tris-EDTA buffer was used in control wells for calibration of DNA concentration. The

fluorescence intensity was determined in each well using a microplate reader with 360/40 nm excitation and 460/40 nm emission filters.

For determination of cellular viability, HepG2 cells were plated at 20,000 cells per well and HUVECs were plated at 10,000 cells per well in black, clear bottom 96 well plates. After 24 hours of seeding, the medium was replaced with fresh medium containing quantum dots (100 µL complete medium plus 100 µL quantum dots in HBSS). After 24 hours of incubation with the quantum dots, the metabolic activity was determined by measuring cellular respiration using a colorimetric redox assay based on a tetrazolium salt, WST-8, 2-(2-methoxy-4-nitrophenyl)-3-(4-nitrophenyl)-5-(2,4-disulfophenyl)-2H-tetrazolium monosodium salt. Cells were washed once with HBSS, and then 150 µL of WST-8 (Dojindo) was added to each well, followed by 2.5 hours of incubation at 37°C. The optical density at 450 nm was then determined using a microplate reader. Quantum dot uptake was too low to significantly impact the readings through optical absorption.

7.4.2 Cytotoxicity of Reduced-Cadmium Quantum Dots. Cadmium-rich and reduced-cadmium quantum dots were prepared in order to test the conventional notion that the fundamental cytotoxic feature of a quantum dot is the cadmium composition. In Chapter 4, strain-tunable (CdTe)ZnSe quantum dots were introduced, which can have extremely low cadmium content, with 4-20 times less cadmium than traditional quantum dots with a comparable size. CdTe cores (2.5 nm diameter) were synthesized and capped with 3 monolayers of either ZnSe or CdSe. Theoretically, the (CdTe)ZnSe quantum dots should have significantly lower cytotoxicity than (CdTe)CdSe quantum dots, because degradation would only initially release selenium and zinc atoms, both of which are biocompatible and micronutrients for cells. These nanocrystals were coated with PEG-

thiol and purified in aqueous solution, and their cytotoxicity was deduced from cellular proliferation assays.

HepG2 cells are a highly relevant hepatic cell line for use in toxicological evaluation of nanoparticles, as they express a large number of the degradative enzymes that are responsible for metabolism of exogenous substances *in vivo* (e.g. cytochrome P450s), and preliminary reports suggest that the liver will be the primary site of nanoparticle accumulation after intravenous administration (see Chapter 2). Quantum dot concentrations typically used for live cell imaging were selected (1 nM and 50 nM) for the (CdTe)CdSe and (CdTe)ZnSe materials. These nanoparticle levels did not significantly change the growth rate of HepG2 cells over the course of 5 days (Figure 7.19). It is surprising that both of these quantum dots showed no cytotoxic impact on these cells over the course of this assay, as a 50 nM dose of nanoparticles corresponds to 2.8 μM Cd^{2+} for the (CdTe)ZnSe quantum dots and 11.2 μM Cd^{2+} for the (CdTe)CdSe quantum dots, which is close to the reported IC_{50} dose of cadmium chloride in HepG2 cells (22 μM).[33] This suggests that these nanocrystals may be degraded at a slow rate, yielding a gradual release of cadmium that can be managed by the metabolic capacity of the cells.

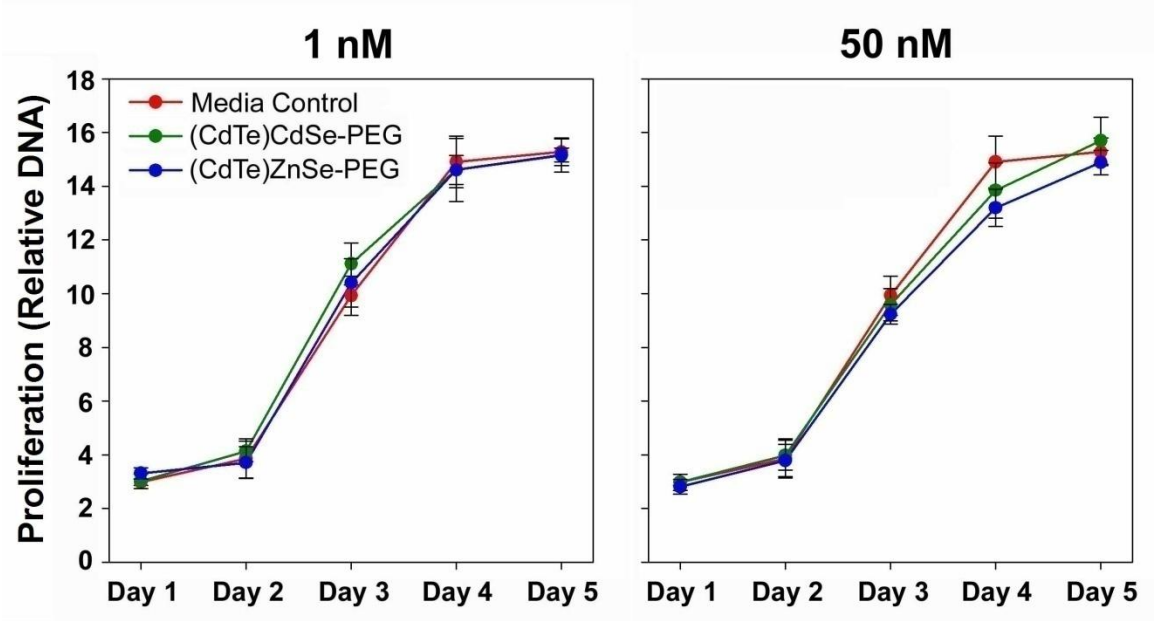

Figure 7.19: Proliferation assay on HepG2 cells in the presence of cadmium-rich and reduced-cadmium quantum dots. All of the proliferation values were within experimental error of the assay at all time points for both nanocrystal concentrations.

The same proliferation assay was performed on NIH3T3 cells. With this cell type, the presence of cadmium-rich (CdTe)CdSe quantum dots again did not significantly impact cell growth (Figure 7.20) at both high and low doses (1 nM and 50 nM). However, the reduced-cadmium (CdTe)ZnSe quantum dots surprisingly inhibited the growth of these cells over the course of 6 days at a 50 nM dose. This finding is unexpected and cannot be explained from the traditional perspective of cadmium-limiting toxicity of quantum dots.

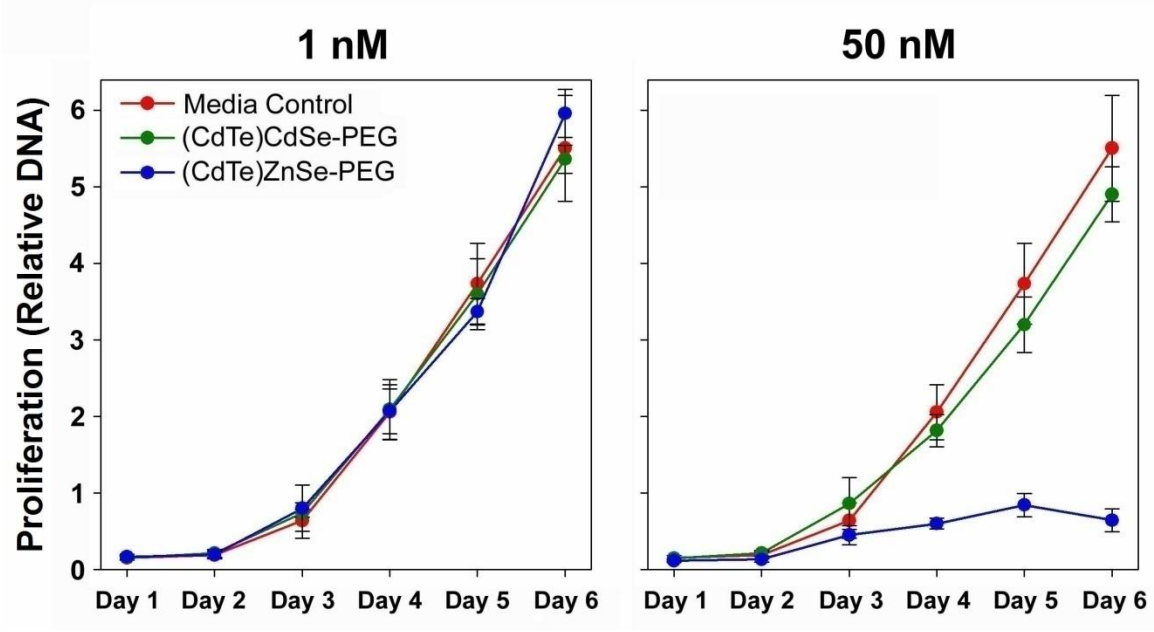

Figure 7.20: Proliferation assay on NIH3T3 cells in the presence of cadmium-rich and reduced-cadmium quantum dots. Proliferation values of cells exposed to 50 nM (CdTe)ZnSe at 4 days and beyond were significantly lower than the control and the cells exposed to cadmium-rich quantum dots. At all other time points for both nanocrystal concentrations, all of the cell counts were within the experimental error of the assay.

7.4.3 Cytotoxicity of Core Quantum Dots. The two (CdTe)CdSe and (CdTe)ZnSe quantum dots contained either 3 or 4 distinct elements, respectively, which complicates the evaluation of the unique cytotoxic effects of these particles. To this end, simple binary compounds were prepared to independently study the effects of individual elements and surface properties. CdSe and ZnSe quantum dots were synthesized with a diameter of 4 nm and with identical nonpolar ligand (a mixture of trioctylphosphine and hexadecylamine). It is important to emphasize that these quantum dots were identical in size and composition, except for the identity of the cation, which was either divalent zinc or cadmium. However, ZnSe naturally has a higher affinity for most basic ligands (Chapter 2), and so both of these quantum dots were encapsulated in 4 different hydrophilic surface coatings in order to independently distinguish colloidal effects due to

nanoparticle stability from compositional effects. The four different surface coatings were chosen to give a broad range of colloidal stabilities, from the most labile small molecule coatings (thioglycerol) to the most stable amphiphilic polymer coatings (lipid-PEG). Thiol-PEG and the multidentate polymer ligands were also used in order to generate nanocrystals with high solute access to the nanocrystal surface facets, with both neutral and anionic surfaces, respectively. Cell proliferation and cell viability assays were used to evaluate cytotoxicity.

Figure 7.21 shows the proliferation of HepG2 cells in the presence of CdSe or ZnSe binary quantum dots, with 4 different surface coatings. In line with the observations from cytotoxicity assays of (core)shell quantum dots, the CdSe quantum dots did not significantly alter cellular growth compared to cells not exposed to quantum dots. ZnSe quantum dots also showed no impact on cell growth, until the 5^{th} day of exposure, at which point the cells had significantly retarded growth compared to cells that were not exposed to cells, and compared to cells exposed to CdSe quantum dots. Interestingly, all of the four surface coatings yielded similar trends for each composition, showing that colloidal effects may be negligible for this specific type of assay and cell type.

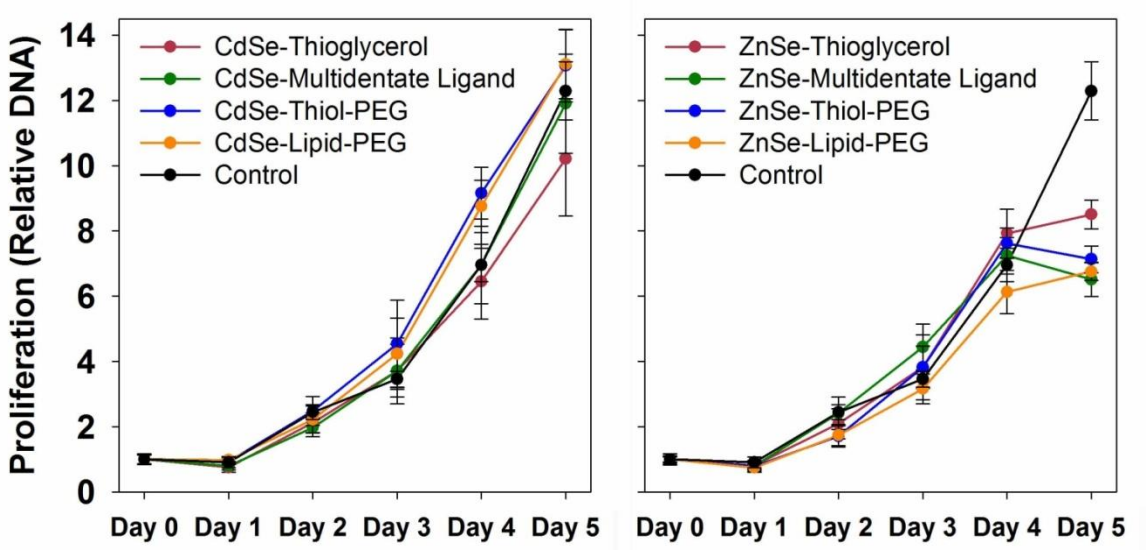

Figure 7.21: Proliferation of HepG2 cells in the presence of 50 nM quantum dots composed of CdSe or ZnSe. See text for descriptions of the 4 different surface coatings. Proliferation values for cells exposed to ZnSe at 5 days were significantly lower than the control and the cells exposed to CdSe quantum dots. At all other time points for both nanocrystal types, all of the cell counts were within the experimental error of the assay.

Figure 7.22 shows the proliferation of primary human umbilical vein endothelial cells in the presence of CdSe or ZnSe binary quantum dots, with 4 different surface coatings. In the presence of CdSe, the cells had a higher degree of growth rate variation, but they were all similar to the control cells that were not exposed to quantum dots. The only statistical exception was the lipid-PEG coated CdSe quantum dots, which significantly inhibited cell growth at the 5 day point. In stark contrast, all of the ZnSe quantum dots *strongly inhibited cell growth*, with statistical significance at 2 days and beyond. In fact, the DNA content for all of these cells markedly decreased, suggesting not only a ZnSe-induced decrease in proliferation rate, but also necrosis and/or apoptosis. The use of this more sensitive primary cell type may have been vital for revealing this phenomenon in comparison to the more hardy immortalized HepG2s.

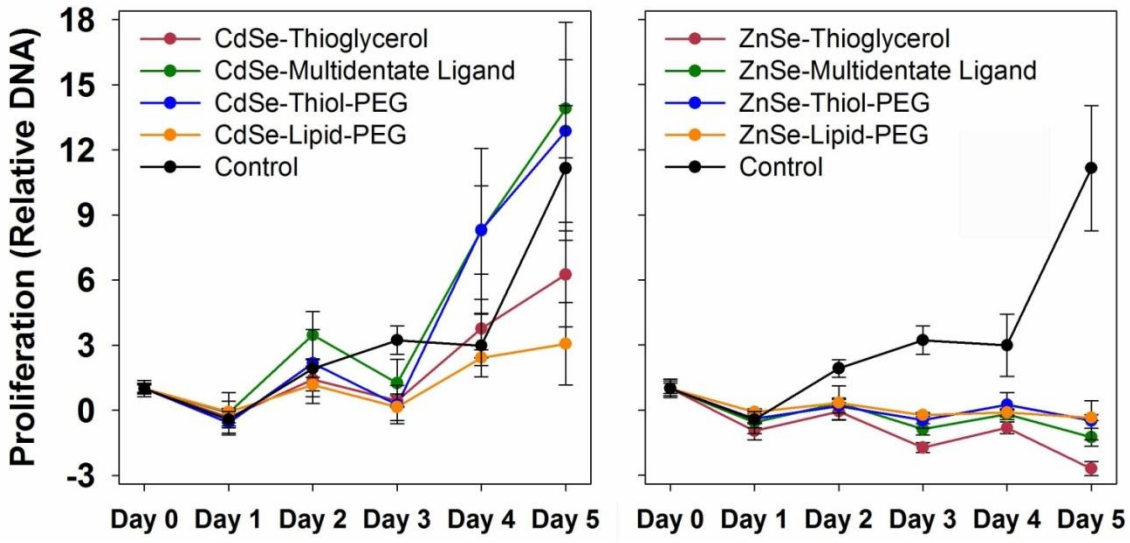

Figure 7.22: Proliferation of HUVECs in the presence of 50 nM quantum dots composed of CdSe or ZnSe. See text for descriptions of the 4 different surface coatings. Proliferation values for cells exposed to ZnSe at 2 days and beyond were significantly lower than the control.

Two unexpected findings have been reported so far. First, ZnSe quantum dots are markedly more cytotoxic than CdSe quantum dots, independent of the surface coating. The mechanism of this effect is the subject of sections 7.4.4 and 7.4.5. Second, the cytotoxic effect toward cells is dependent on the cell type. To gain greater insight into this finding, a cellular viability assay was implemented. This assay is a variation of the traditional MTT assay, which measures the activity of mitochondrial reductase enzymes with a colorimetric substrate. Thus viability correlates with the rate of cellular respiration and metabolic activity. Figure 7.23 shows the viability of HUVEC cells and HepG2 cells after 24 hours of exposure to different concentrations of lipid-PEG coated quantum dots composed of CdSe, ZnSe, or (ZnSe)ZnS. These latter (core)shell quantum dots were added to this study in order to determine if the high toxicity of the ZnSe quantum dots could be modulated through surface stabilization, as sulfides are more resistant to

oxidation than selenides. For the HUVEC cells, both CdSe and ZnSe quantum dots were found to strongly decrease cellular metabolism in a dose dependent manner. Although there was considerable statistical variability in the viability values, the ZnSe quantum dots were significantly more toxic, with an IC_{50} of 13.86 $\pm$ 4.13 nM, compared to 44.84 $\pm$ 11.67 nM for CdSe. As well, overcoating of a ZnS shell significantly decreased the toxicity of ZnSe quantum dots, increasing the IC_{50} to within standard deviation of the CdSe quantum dots (33.49 $\pm$ 8.12 nM), showing that the degradation rate of ZnSe impacts its toxicity. The impact of quantum dot composition on cellular metabolism was even more striking for the HepG2 cells, which showed a nearly 4-fold increase in metabolic rate after 24 hours of exposure to ZnSe quantum dots at concentrations over which CdSe quantum dots do not significantly alter cellular viability. This result demonstrates that moderate concentrations of ZnSe induced either a proliferative response in these cells by increasing the rate of cellular metabolism, or induced the overexpression of mitochondrial reductase enzymes. Addition of large amounts of either CdSe or ZnSe quantum dots (>100 nM) reduced cellular viability.

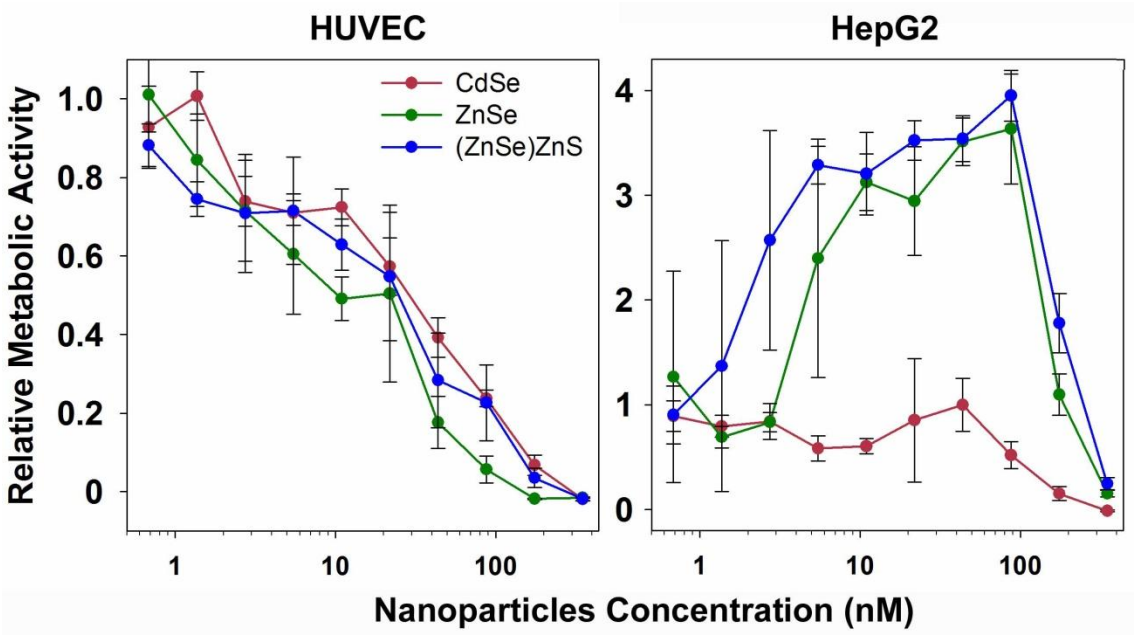

Figure 7.23: Metabolic activity of HUVEC and HepG2 cells after a 24 hour exposure to various concentrations of ZnSe, CdSe, and (ZnSe)ZnS quantum dots. All quantum dots were coated with lipid-PEG. HUVECs showed a dose-dependent decrease in respiration in response to all of the quantum dot compositions, whereas zinc-containing quantum dots induced an increase in viability in HepG2 cells.

7.4.4 Mechanism of Quantum Dot Cytotoxicity. The cytotoxicity results described in section 7.4.3 cast a considerable amount of doubt on the traditional understanding of quantum dot toxicity from the perspective of cadmium-poisoning. The fact that decreasing the content of cadmium in (core)shell quantum dots and the use of cadmium-free ZnSe quantum dots both result in reduced cellular proliferation and viability of primary endothelial cells and immortalized fibroblasts suggests that other factors are predominant. Colloidal impacts can be ruled out by the fact that all of the 4 surface coatings that were tested resulted in similar trends in proliferation in two cell types.

The stark difference between CdSe and ZnSe quantum dots is obvious instantly upon phase transfer to water. Aqueous ZnSe quantum dots immediately form a cloudy

residue in water, independent of the type of organic coating. This residue can be removed as a red pellet through filtration or centrifugation, however a new precipitate will form quickly thereafter. Over several months, the effect is striking (Figure 7.24), resulting in a completely opaque red-brick solution that began as a colorless, clear solution. Elemental analysis of the red-brick precipitate revealed a composition of selenium, and its appearance is consistent with that of amorphous elemental selenium in the 0-oxidation state.[34,35] This effect does not occur for CdSe quantum dots, which slowly oxidize over time to yield a clear, colorless solution.

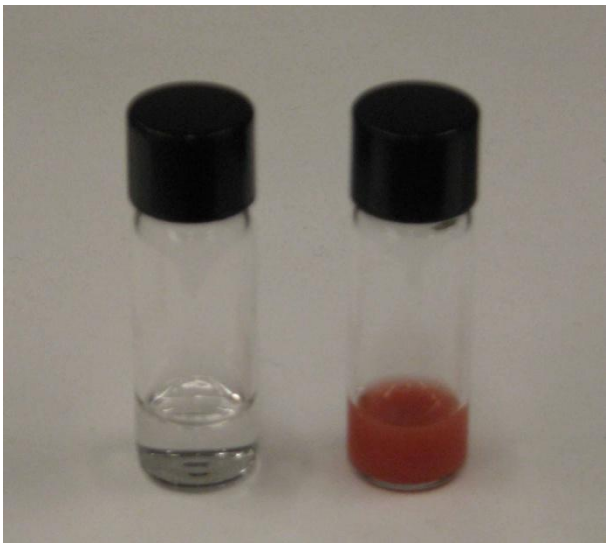

Figure 7.24: ZnSe quantum dots coated in lipid-PEG, prepared fresh (left) and after sitting at room temperature for 4 months (right).

Selenides such as ZnSe or CdSe are in the -2 oxidation state, whereas elemental selenium is in the 0-oxidation state. Therefore the release of elemental selenium from ZnSe must be due to an oxidative degradation mechanism. This effect can also be catalyzed by ultraviolet light, as shown in Figure 7.25. Photooxidation of CdSe quantum dots, in accord with results obtained in Chapter 5, resulted in a clear colorless solution,

whereas ZnSe quantum dots again yielded a precipitate. ZnSe quantum dots with a selenium-rich surface yielded more of the precipitate at a faster rate than ZnSe quantum dots with a zinc-terminated surface.

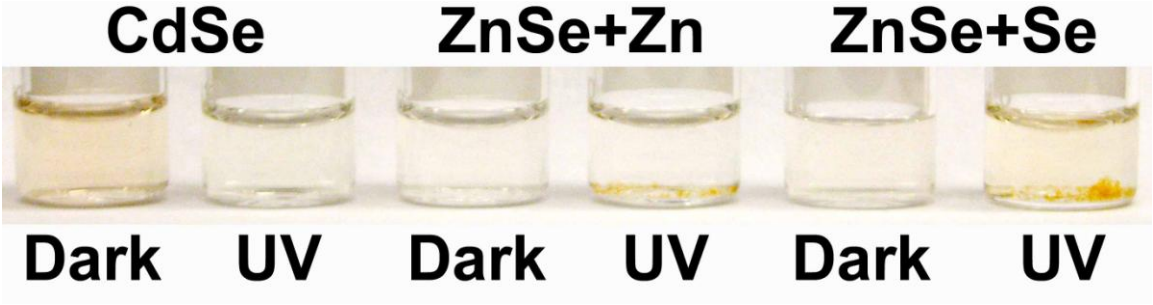

Figure 7.25: Photographs of vials containing lipid-PEG coated CdSe and ZnSe quantum dots stored in the dark or exposed to ultraviolet light for 48 hours. The visible absorption of CdSe quantum dots was completely eliminated through photooxidation due to a complete dissolution of the quantum dots, yielding soluble selenium oxides. The ZnSe quantum dots were synthesized to have surfaces rich with zinc (ZnSe+Zn) or selenium (ZnSe+Se). After photooxidation of solutions of these quantum dots at the same concentration, the quantum dots with a selenium rich surface generated more insoluble elemental selenium product (right).

Altogether these results show a correlation between the generation of elemental selenium and cytotoxicity of ZnSe quantum dots. Selenium species are unique in their cytotoxic impact, as selenium is actually a micronutrient, but there is only a small difference in concentration between nutritionally relevant levels and cytotoxic levels.[35,36] In addition, selenium forms chemically diverse organic and inorganic compounds in a wide range of oxidation states, as well as several allotropic elemental structures, including nano-selenium particles.[36,37] Elemental selenium is highly insoluble in water, and therefore it is difficult to compare its toxicity directly to its soluble inorganic and organic counterparts. However several reports have demonstrated a high level of cytotoxic effects caused by selenium species in the 0-oxidation state, such as nano-

selenium, although the toxicity is generally less than that of selenite ions due to differences in bioavailability and uptake.[35,38,39] The current understanding of the cytotoxic mechanisms of selenium compounds implicates the reduction of oxidized selenium compounds in the cytosol by glutathione, resulting in the formation of toxic reactive oxygen species (ROS) such as superoxide radicals. [36,37,40-43]

The unusual oxidative production of elemental selenium by ZnSe quantum dots is likely to be the cause of the unexpectedly high cytotoxicity of ZnSe compared to CdSe, which preferentially form soluble selenium oxy anions with higher oxidation states (selenates and selenites). In this proposed oxidation mechanism, ZnSe quantum dots and CdSe quantum dots can be engulfed by HUVEC and HepG2 cells through endocytotic mechanisms discussed in Chapter 2 and in Section 7.2. After endosomal internalization, the ZnSe quantum dots selectively produce elemental selenium in the cell, in contrast to CdSe, which generates ionic selenium species. Elemental selenium can bind to proteins to generate highly reactive and toxic substances,[38] and small selenium particles, such as Se_8 allotropes, may directly leak through the vesicle membrane due to their nonpolar nature. This will induce ROS formation and cause cytotoxic effects that abate cell growth and viability. The anionic selenium species of higher oxidation state generated by CdSe will remain in vesicles, reducing their bioavailability and oxidative capacity. HepG2 cells, on the other hand, produce a variety of oxidative enzymes and are more resistant to oxidative stress due to their hepatic biology and immortalization, compared to HUVECs. Therefore these cells have a greater propensity to upregulate antioxidant enzymes such as reductases to combat the hyperoxidative stress imposed by selenium. It has been widely reported that exposure of cells to oxidizing substances like selenium induces reductase enzyme overexpression in order to restore a cellular redox balance

and avert oxidative damage,[41,43-45] a finding that was confirmed herein (Figure 7.23). The increased metabolic rate of HepG2 cells after 24 hours of exposure to ZnSe may be interpreted as the induction of reductase enzymes to combat the intracellular oxidative state induced by selenium. The capacity of HepG2 cells to overcome this oxidative state explains why their growth rates were not significantly affected by ZnSe exposure, compared to the less hardy and less enzymatically equipped primary endothelial cells.

7.4.5 Mechanism of Oxidation of CdSe and ZnSe. The mechanisms that trigger the generation of elemental selenium from ZnSe and CdSe nanocrystals in aqueous solution can be understood from the perspective of the unique redox and acid/base chemistries of these materials.

7.4.5.1 Redox Chemistry of Selenium. The II-VI semiconductors are labile toward oxidation due to the high oxidation potential of reduced chalcogenides (S^{2-}, Se^{2-} and Te^{2-}).[46] The chemical reactions governing oxidation of CdS nanocrystals in aqueous solution have been thoroughly investigated,[47-49] but the degradation of CdSe and CdTe are less understood. However, the similar chemistry between these materials allows direct extrapolation. The stable inorganic selenium species are the selenides (Se^{2-}), elemental selenium (Se^0), the selenites (Se^{4+}), and the selenates (Se^{6+}). The oxidation of selenides (e.g. ZnSe or CdSe) by dissolved oxygen is described by the following set of equations and redox potentials.

$$Se^{2-} + 2O_2 \longrightarrow SeO_4^{2-} \qquad \Delta\varepsilon^o = 2.14\ V \qquad \textbf{Equation 7.6}$$

$$Se^{2-} + \tfrac{3}{2}O_2 \longrightarrow SeO_3^{2-} \qquad \Delta\varepsilon^o = 1.89\ V \qquad \textbf{Equation 7.7}$$

$$Se^{2-} + \tfrac{1}{2}O_2 + 2H^+ \longrightarrow Se^o + H_2O \qquad \Delta\varepsilon^o = 1.54\ V \qquad \textbf{Equation 7.8}$$

The positive redox potentials for these reactions indicate that oxidation of selenides (ZnSe or CdSe) is spontaneous under standard state conditions. This is also the case for the oxidation of sulfides to sulfur, sulfite, and sulfate, with redox potentials of 1.09, 1.18, and 2.28 V, respectively. The oxidation potential of tellurides is higher, with 1.76 V for oxidation to tellurium, 2.31 V to tellurite, and 2.45 V to tellurate. These chemical trends in oxidation potential are reflected in the trends in stability of the cadmium and zinc chalcogenides toward oxidation under oxygen-limiting conditions, with CdS > CdSe > CdTe.

When selenides are oxidized by molecular oxygen in solution, the corresponding rate constants are

$$K = \frac{[SeO_4^{2-}]}{[Se^{2-}][O_2]^2} \qquad \textbf{Equation 7.9}$$

$$K = \frac{[SeO_3^{2-}]}{[Se^{2-}][O_2]^{3/2}} \qquad \textbf{Equation 7.10}$$

$$K = \frac{[Se^{o}]}{[Se^{2-}][O_2]^{1/2}[H^+]^2} \qquad \textbf{Equation 7.11}$$

Equation 7.11 shows that the oxidation of selenide to elemental selenium is the only reaction among these that is pH-dependent. That is, direct oxidation to selenate or selenite ions is only dependent on the concentration of oxygen, whereas oxidation to selenium requires two protons. This equation could also be written for reactions in basic conditions, for which a water molecule would yield a hydroxide ion, but this reaction is less favorable ($\Delta\varepsilon^o = 1.33$), and acidic medium is more appropriate for the experimental conditions of this work, as discussed below.

It is important to note that photoillumination of semiconductor nanocrystals above the bandgap energy results in the formation of excited state electrons. These electrons have an even higher oxidation potential, which further increases the oxidation potential of the nanocrystal, resulting in faster degradation.

7.4.5.2 Surface-Limited and Proton-Limited Generation of Elemental Selenium.

Equations 7.6-7.11 demonstrate that it is thermodynamically favorable for selenides to oxidize completely to Se^{6+}. However, these reactions do not occur in solution under equilibrium conditions, but instead occur on the surfaces of nanocrystal facets, which causes kinetic factors do dominate. For the oxidation of a ZnSe or CdSe nanocrystal in solution, oxygen molecules must traverse an organic shell to reach the crystal surface facet, where they may oxidize selenide ions to yield various oxidation products. Under these conditions, oxygen diffusion is limiting. Because of this, the capacity to inhibit solute diffusion to the nanocrystal surface has been the predominant paradigm for preventing quantum dot oxidation and degradation.[17,50] Similar mechanisms limit the rates of electrochemical reactions on electrodes due to the presence of an electrical double layer.

Analysis of Equations 7.8 and 7.11 reveals that the limiting reagent for the oxidation of selenide to elemental selenium is the hydronium ion. Whereas oxygen is the only solute required to oxidize selenides to the 4+ and 6+ oxidation states, oxidation to elemental selenium requires both oxygen and a proton. At biological pH in an aerobic environment at standard temperature and pressure, the concentration of oxygen in solution (~0.5 mM) is more than 4 orders of magnitude greater than the concentration of hydronium ions (~25 nM). Even in acidic endosomal vesicles, the oxygen concentration would still be much higher ($[H^+]$ = ~0.01 mM). In addition, hydrophobic bilayers on quantum dots are

expected to have greater permeability toward neutral oxygen molecules, rather than cationic hydronium ions. Therefore, the kinetics of oxidation would favor the reactions for which only oxygen is required (Equations 7.6 and 7.7), which would yield purely selenate and selenite ions, rather than elemental selenium.

7.4.5.3 Generation of Surface Protons from Zinc Hydration. One way for the selenide nanocrystals to bypass the concentration- and diffusion-limited access of protons is through the self-generation of hydronium ions directly on the nanocrystal surface. Metal cations are almost always acidic in aqueous solution, due their capacity to deprotonate their hydration shells. The weak acidities of Zn^{2+} and Cd^{2+} ions are shown in the following two equations

$$Zn^{2+} + 2H_2O \longrightarrow Zn(OH)_2 + 2H^+ \qquad K_a = 3.33 \times 10^{-12} \qquad \textbf{Equation 7.12}$$

$$Cd^{2+} + 2H_2O \longrightarrow Cd(OH)_2 + 2H^+ \qquad K_a = 1.39 \times 10^{-14} \qquad \textbf{Equation 7.13}$$

Zn^{2+} is much more acidic than Cd^{2+} because it is a smaller ion and it is more soluble in water. Importantly, a comparison of Equations 7.12 and 7.13 shows the rate constant for Zn^{2+} is 240 times greater than Cd^{2+}. This realization can be immediately related back to Equation 7.11, which shows that oxidation of selenide to elemental selenium requires protons. These protons can be directly supplied through the hydration of zinc or cadmium ions that are released from the oxidative degradation of ZnSe or CdSe. Because these reactions take place on the *surface* of the nanocrystals, rather than as free solutes, the formation of hydrated zinc would be expected to yield a much higher local concentration of hydronium ions on the quantum dot surface. This compartmentalized surface reaction can then proceed at a much lower effective pH than that of the surrounding buffer. The high acidity of zinc compared to cadmium would then

be expected to favor the generation of elemental selenium over selenates and selenites by ZnSe quantum dots, which is in line with experimental observations (Section 7.4.4).

The overall oxidation reactions to elemental selenium can now be balanced as

$$ZnSe + \tfrac{1}{2}O_2 + H_2O \longrightarrow Zn(OH)_2 + Se^o \qquad \textbf{Equation 7.14}$$

$$CdSe + \tfrac{1}{2}O_2 + H_2O \longrightarrow Cd(OH)_2 + Se^o \qquad \textbf{Equation 7.15}$$

These equations are independent of the pH of the medium, and the only difference between the rate of generation of elemental selenium from ZnSe or CdSe is due to the differences in acidity of hydrated zinc ions and cadmium ions. The reactions still require the diffusion of oxygen and water to the surface. Because water is in excess to oxygen by a factor of ~10^5, the surface concentration of oxygen would be expected to be limiting. It is also noteworthy that although the acidity constant of Zn^{2+} is 240 times greater than that of Cd^{2+}, this is only accurate for the second proton dissociation (Equations 7.12 and 7.13). The dissociation rate constant for the first proton from hydrated Zn^{2+} is roughly 1250 times that of Cd^{2+}. A simple calculation shows this difference in acidity results in a local concentration of hydronium ions that is more than 10 times higher for ZnSe compared to CdSe. Although two hydronium ions are needed to balance the reaction with selenium oxidation, the release of single protons would be expected to push the reaction forward, in accord with Le Chatelier's principle.

The effect of zinc-induced acidification of the nanocrystal microenvironment will be amplified even if other oxidation mechanisms take place (e.g. Equations 7.6 and 7.7) due to the requisite release of divalent zinc. That is, for ZnSe,

$$ZnSe + \tfrac{3}{2}O_2 + H_2O \longrightarrow Zn(OH)_2 + SeO_3^{2-} + 2H^+ \qquad \textbf{Equation 7.16}$$

$$ZnSe + 2O_2 + H_2O \longrightarrow Zn(OH)_2 + SeO_4^{2-} + 2H^+ \qquad \textbf{Equation 7.17}$$

and for CdSe,

$$CdSe + 2O_2 + H_2O \longrightarrow Cd(OH)_2 + SeO_4^{2-} + 2H^+ \qquad \textbf{Equation 7.18}$$

$$CdSe + \tfrac{3}{2}O_2 + H_2O \longrightarrow Cd(OH)_2 + SeO_3^{2-} + 2H^+ \qquad \textbf{Equation 7.19}$$

Therefore all of the oxidation reactions that generate divalent zinc and cadmium will increase the local pH of the nanocrystals. Because of the aforementioned higher acidity of zinc hydrates, this effect of selenide oxidation to elemental selenium will be disproportionately amplified for ZnSe over CdSe.

7.4.5.4 Multistep and Single Step Oxidation Reactions. Equations 7.6-7.8 suggest that the oxidation of selenides can proceed as single reaction steps or as multistep reactions.

$$Se^{2-} \xrightarrow{1/2O_2} Se^0 \xrightarrow{O_2} SeO_3^{2-} \xrightarrow{1/2O_2} SeO_4^{2-} \qquad \textbf{Equation 7.20}$$

$$Se^{2-} \xrightarrow{2O_2} SeO_4^{2-} \qquad \textbf{Equation 7.21}$$

Equation 7.20 describes the mechanism of selenide oxidation as multiple oxidation steps leading to the final product of selenate ions in a 6+ oxidation state. Equation 7.21 describes the oxidation of selenide to selenate in a single reaction step. Both mechanisms have the same thermodynamic favorability, but the multistep reaction is strongly favored kinetically. This is because the reactions are oxygen-limited, and fewer oxygen molecules are needed per reaction. The single step reaction requires two oxygen molecules to react simultaneously with a single selenide to yield one selenate ion, which would be an improbable occurrence.

The multistep nature of these surface reactions is evident in the large disparity in oxidation propensity of cadmium chalcogenide nanocrystals. As stated previously, the oxidation propensity follows the trend CdTe > CdSe > CdS, with CdS nanocrystals being vastly more stable than CdTe nanocrystals under oxidizing conditions. However the

redox potentials for single step reactions (Equation 7.21) follow the trend CdTe > CdS > CdSe, and the potentials are very similar for CdTe (2.45 V) and CdS (2.28 V). These trends are only reflected accurately when considering the multistep oxidations, for which tellurides have a much higher oxidation potential (1.76 V) than the sulfides (1.09 V), and the selenides appropriately fall between these two extremes (1.54 V).

7.4.5.5 Surface Structure Effects. One major difference between ZnSe and CdSe crystals is the smaller bond length for ZnSe (5.668 Å) compared to CdSe (6.052 Å), which causes the planar density of atoms on the surface facets of ZnSe to be higher. The 12.2% higher surface density of atoms favors reactions between a single oxygen molecule and multiple selenium atoms. Equation 7.8 shows that the reaction stoichiometry for the oxidation of selenide to elemental selenium is 2:1 Se^{2-}:O^2. This suggests that the distance between adjacent selenium ions is a vital kinetic parameter for this oxidative mechanism, compared to the 1:1 stoichiometry of selenite formation (Equation 7.7). The closest distance between two selenide ions on any facet is ~4.3 Å for ZnSe and ~4.0 Å for CdSe. Factoring in atomic radii, this means that there is a minimum separation of ~1.7 Å between the electron clouds of surface selenides for ZnSe, compared to ~2.0 Å for CdSe. This distance range is remarkably similar to the length of the long axis of O_2 molecules (~2.4 Å), meaning that the probability of oxidation of two adjacent Se^{2-} ions by a single O_2 molecule should be much higher for ZnSe than for CdSe. In addition, because the surface atoms are more closely spaced on ZnSe, the density of organic surface ligands is also higher, thus increasing the steric hindrance on the nanocrystal surface. This results in a smaller diffusion space for solutes to reach the nanocrystal surface, decreasing the probability of multi-oxygen oxidation reactions.

7.4.5.6 Inhibition of the Oxidation of Elemental Selenium. Although the multistep oxidation process is expected to dominate, it is logical that elemental selenium, once formed on the nanocrystal surface, would be again oxidized to selenite or selenate. However a closer examination reveals that these reactions are inhibited by the local acidic environment of the nanocrystal surface.

$$Se^{o} + \tfrac{3}{2}O_2 + H_2O \longrightarrow SeO_4^{2-} + 2H^{+} \qquad \textbf{Equation 7.22}$$

$$Se^{o} + O_2 + H_2O \longrightarrow SeO_3^{2-} + 2H^{+} \qquad \textbf{Equation 7.23}$$

Again, Le Chatelier's principle maintains that the acidic local environment will inhibit the further oxidation of elemental selenium to higher oxidation states. This essentially introduces a dead-end to selenium oxidation, ending with elemental selenium. Selenium is highly insoluble in water, and therefore the selenium that is formed will remain adsorbed to the nanocrystal surface, eventually precipitating as large solids. This effect should be more prominent for ZnSe over CdSe, because of a larger steric barrier to diffusive release of selenium particles

7.4.5.7 Summary. The methodology outlined in this section shows that the formation of elemental selenium from ZnSe nanocrystals is a result of the unique redox chemistry of selenium on nanocrystal surfaces and the acidity of zinc hydrates. The generation of localized acidity on the nanocrystal surface causes an amplification of the generation of elemental selenium, which reaches an oxidative dead-end due to acidity of the microenvironment. This process is inhibited for CdSe nanocrystals due to the weaker acid strength of divalent cadmium and its lower solubility. These mechanisms underscore the fact that the overwhelming thermodynamic favorability of complete oxidation of selenium species can be controlled through compartmentalized steric control of the reaction and the associated byproducts. In terms of the biocompatibility of

these nanocrystals, the theory outlined herein suggests that it will be necessary to eliminate ZnSe domains from quantum dots due to unavoidable production of highly toxic elemental selenium. The use of ZnS should afford greater biocompatibility due to the low toxicity of elemental sulfur and its lower oxidation potential.

7.5 References

1. Liu, W. H., Choi, H. S., Zimmer, J. P., Tanaka, E., Frangioni, J. V., & Bawendi, M. Compact cysteine-coated CdSe(ZnCdS) quantum dots for in vivo applications. *J. Am. Chem. Soc.* **129,** 14530-14531 (2007).

2. Choi, H. S., Liu, W., Misra, P., Tanaka, E., Zimmer, J. P., Ipe, B. I., Bawendi, M. G., & Frangioni, J. V. Renal clearance of quantum dots. *Nat. Biotechnol.* **25,** 1165-1170 (2007).

3. Berg, O. G. & von Hippel, P. H. Diffusion-controlled macromolecular interactions. *Annu. Rev. Biophys. Chem.* **14,** 131-160 (1985).

4. Duan, H. W. & Nie, S. M. Cell-penetrating quantum dots based on multivalent and endosome-disrupting surface coatings. *J. Am. Chem. Soc.* **129,** 3333-3338 (2007).

5. Medintz, I. L., Clapp, A. R., Mattoussi, H., Goldman, E. R., Fisher, B., & Mauro, J. M. Self-assembled nanoscale biosensors based on quantum dot FRET donors. *Nat. Mater.* **2,** 630-638 (2003).

6. Clapp, A. R., Medintz, I. L., Mauro, J. M., Fisher, B. R., Bawendi, M. G., & Mattoussi, H. Fluorescence resonance energy transfer between quantum dot donors and dye-labeled protein acceptors. *J. Am. Chem. Soc.* **126,** 301-310 (2004).

7. Liu, W., Howarth, M., Greytak, A. B., Zheng, Y., Nocera, D. G., Ting, A. Y., & Bawendi, M. G. Compact biocompatible quantum dots functionalized for cellular imaging. *J. Am. Chem. Soc.* **130,** 1274-1284 (2008).

8. Howarth, M., Liu, W. H., Puthenveetil, S., Zheng, Y., Marshall, L. F., Schmidt, M. M., Wittrup, D. K., Bawendi, M., & Ting, A. Y. Monovalent, reduced-size quantum dots for imaging receptors on living cells. *Nat. Methods* **5,** 397-399 (2008).

9. So, M. K., Xu, C. J., Loening, A. M., Gambhir, S. S., & Rao, J. H. Self-illuminating quantum dot conjugates for in vivo imaging. *Nat. Biotechnol.* **24,** 339-343 (2006).

10. Fernandez-Suarez, M., Baruah, H., Martinez-Hernandez, L., Xie, K. T., Baskin, J. M., Bertozzi, C. R., & Ting, A. Y. Redirecting lipoic acid ligase for cell surface protein labeling with small-molecule probes. *Nat. Biotechnol.* **25,** 1483-1487 (2007).

11. Howarth, M., Takao, K., Hayashi, Y., & Ting, A. Y. Targeting quantum dots to surface proteins in living cells with biotin ligase. *Proc. Natl. Acad. Sci. U.S.A.* **102,** 7583-7588 (2005).

12. Zhang, Y., So, M. K., Loening, A. M., Yao, H. Q., Gambhir, S. S., & Rao, J. H. HaloTag protein-mediated site-specific conjugation of bioluminescent proteins to quantum dots. *Angew. Chem. Int. Ed.* **45,** 4936-4940 (2006).

13. Pinaud, F., King, D., Moore, H. P., & Weiss, S. Bioactivation and cell targeting of semiconductor CdSe/ZnS nanocrystals with phytochelatin-related peptides. *J. Am. Chem. Soc.* **126,** 6115-6123 (2004).

14. Ogi, H., Motohisa, K., Hatanaka, K., Ohmori, T., Hirao, M., & Nishiyama, M. Concentration dependence of IgG-protein A affinity studied by wireless-electrodeless QCM. *Biosens. Bioelectron.* **22,** 3238-3242 (2007).

15. Sapsford, K. E., Pons, T., Medintz, I. L., Higashiya, S., Brunel, F. M., Dawson, P. E., & Mattoussi, H. Kinetics of metal-affinity driven self-assembly between proteins or peptides and CdSe-ZnS quantum dots. *J. Phys. Chem. C* **111,** 11528-11538 (2007).

16. Aldana, J., Lavelle, N., Wang, Y. J., & Peng, X. G. Size-dependent dissociation pH of thiolate ligands from cadmium chalcogenide nanocrystals. *J. Am. Chem. Soc.* **127,** 2496-2504 (2005).

17. Aldana, J., Wang, Y., & Peng, X. Photochemical instability of CdSe nanocrystals coated by hydrophilic thiols. *J. Am. Chem. Soc.* **123,** 8844-8850 (2001).

18. Chen, Y. F., Vela, J., Htoon, H., Casson, J. L., Werder, D. J., Bussian, D. A., Klimov, V. I., & Hollingsworth, J. A. "Giant" multishell CdSe nanocrystal quantum dots with suppressed blinking. *J. Am. Chem. Soc.* **130,** 5026-5027 (2008).

19. Xie, R. G., Kolb, U., Li, J. X., Basche, T., & Mews, A. Synthesis and characterization of highly luminescent CdSe-Core $CdS/Zn_{0.5}Cd_{0.5}S/ZnS$ multishell nanocrystals. *J. Am. Chem. Soc.* **127,** 7480-7488 (2005).

20. Dabbousi, B. O., Rodriguez-Viejo, J., Mikulec, F. V., Heine, J. R., Mattoussi, H., Ober, R., Jensen, K. F., & Bawendi, M. G. (CdSe)ZnS core-shell quantum dots: Synthesis and characterization of a size series of highly luminescent nanocrystallites. *J. Phys. Chem. B* **101,** 9463-9475 (1997).

21. Cao, Y. & Wang, J. One-pot synthesis of high-quality zinc-blende CdS nanocrystals. *J. Am. Chem. Soc.* **126,** 14336-14337 (2004).

22. Talapin, D. V., Rogach, A. L., Kornowski, A., Haase, M., & Weller, H. Highly luminescent monodisperse CdSe and CdSe/ZnS nanocrystals synthesized in a hexadecylamine-trioctylphosphine oxide-trioctylphospine mixture. *Nano Lett.* **1,** 207-211 (2001).

23. Jasieniak, J. J. & Mulvaney, P. From Cd-rich to Se-rich - the manipulation of CdSe nanocrystal surface stoichiometry. *J. Am. Chem. Soc.* **129,** 2841-2848 (2007).

24. Yuan, C. T., Chou, W. C., Chen, Y. N., Chou, J. W., Chuuji, D. S., Lin, C. A. J., Li, J. K., Chang, W. H., & Shen, J. L. Study of fluorescence enhancement of colloidal CdSe/ZnS quantum dots bound to hexadecylamine by single-molecule measurements. *J. Phys. Chem. C* **111,** 15166-15172 (2007).

25. Qu, L. H. & Peng, X. G. Control of photoluminescence properties of CdSe nanocrystals in growth. *J. Am. Chem. Soc.* **124,** 2049-2055 (2002).

26. Anikeeva, N., Lebedeva, T., Clapp, A. R., Goldman, E. R., Dustin, M. L., Mattoussi, H., & Sykulev, Y. Quantum dot/peptide-MHC biosensors reveal strong CD8-dependent cooperation between self and viral antigens that augment the T cell response. *Proc. Natl. Acad. Sci. U.S.A.* **103,** 16846-16851 (2006).

27. Snee, P. T., Somers, R. C., Nair, G., Zimmer, J. P., Bawendi, M. G., & Nocera, D. G. A ratiometric CdSe/ZnS nanocrystal pH sensor. *J. Am. Chem. Soc.* **128,** 13320-13321 (2006).

28. Zhang, C. Y., Yeh, H. C., Kuroki, M. T., & Wang, T. H. Single-quantum-dot-based DNA nanosensor. *Nat. Mater.* **4,** 826-831 (2005).

29. Willard, D. M. & Van Orden, A. Quantum dots: resonant energy-transfer sensor. *Nat. Mater.* **2,** 575-576 (2003).

30. Dennis, A. M. & Bao, G. Quantum dot-fluorescent protein pairs as novel fluorescence resonance energy transfer probes. *Nano Lett.* **8,** 1439-1445 (2008).

31. Clapp, A. R., Medintz, I. L., & Mattoussi, H. Forster resonance energy transfer investigations using quantum-dot fluorophores. *ChemPhysChem* **7,** 47-57 (2006).

32. Clapp, A. R., Medintz, I. L., Fisher, B. R., Anderson, G. P., & Mattoussi, H. Can luminescent quantum dots be efficient energy acceptors with organic dye donors? *J. Am. Chem. Soc.* **127,** 1242-1250 (2005).

33. Urani, C., Melchioretto, P., Canevali, C., & Crosta, G. F. Cytotoxicity and induction of protective mechanisms in HepG2 cells exposed to cadmium. *Toxicology* **19,** 887-892 (2005).

34. Song, J. M., Zhu, J. H., & Yu, S. H. Crystallization and shape evolution of single crystalline selenium nanorods at liquid-liquid interface: from monodisperse amorphous Se nanospheres toward Se nanorods. *J. Phys. Chem. B* **110,** 23790-23795 (2006).

35. Zhang, J. S., Gao, X. Y., Zhang, L. D., & Bao, Y. P. Biological effects of a nano red elemental selenium. *Biofactors* **15,** 27-38 (2001).

36. Barceloux, D. G. Selenium. *Clin. Toxicol.* **37,** 145-172 (1999).

37. Letavoyova, L., Vlckova, V., & Brozmanova, J. Selenium: from cancer prevention to DNA damage. *Toxicology* **227,** 1-14 (2006).

38. Sieber, F., Daziano, J. P., Gunther, W. H. H., Krieg, M., Miyagi, K., Sampson, R. W., Ostrowski, M. D., Anderson, G. S., Tsujino, I., & Bula, R. J. Elemental selenium generated by the photobleaching of seleno-merocyanine photosensitizers forms conjugates with serum macro-molecules that are toxic to tumor cells. *Phosphorus Sulfur Silicon Relat. Elem.* **180,** 647-657 (2005).

39. Zhang, J., Wang, H., Yan, X., & Zhang, L. Comparison of short-term toxicity between Nano-Se and selenite in mice. *Life Sci.* **76,** 1099-1109 (2005).

40. Weiller, M., Latta, M., Kresse, M., Lucas, R., & Wendel, A. Toxicity of nutritionally availabel selenium compounds in primary and transformed hepatocytes. *Toxicology* **201,** (2004).

41. Peng, D., Zhang, J., Liu, Q., & Taylor, E. W. Size effect of elemental selenium nanoparticles (Nano-Se) at supranutritional levels on selenium accumulation and glutathione S-transferase activity. *J. Inorg. Biochem.* **101,** 1457-1463 (2007).

42. Kim, T. S., Yun, B. Y., & Kim, I. Y. Induction of the mitochondrial permeability transition by selenium compounds mediated by oxidation of the protein thiol groups and generation of the superoxide. *Biochem. Pharmacol.* **66,** 2301-2311 (2003).

43. Zhong, W. & Oberley, T. D. Redox-mediated effects of selenium on apoptosis and cell cycle in the LNCaP human prostate cancer cell line. *Cancer Res.* **61,** 7071-7078 (2001).

44. Eftekharpour, E., Holmgren, A., & Juurlink, B. H. J. Thioredoxin reductase and glutathione synthesis is upregulated by t-butylhydroquinone in cortical astrocytes but not in cortical neurons. *Glia* **31,** 241-248 (2000).

45. Nalvarte, I., Diamdimopoulos, A. E., Nystom, C., Nordman, T., Miranda-Vizuete, A., Olsson, J. M., Eriksson, L., Bjornstedt, M., Arner, E. S. J., & Spyrou, G. Overexpression of enzymatically active human cytosolic and mitochondrial thioredoxin reductase in HEK-293 cells. *J. Biol. Chem.* **279,** 54510-54517 (2004).

46. Bard, A. J. *Standard Potentials in Aqueous Solution*. CRC Press, Boca Raton, FL (1985).

47. Spanhel, L., Haase, M., Weller, H., & Henglein, A. Photochemistry of colloidal semiconductors. 20. Surface modification and stability of strong luminescing CdS particles. *J. Am. Chem. Soc.* **109,** 5649-5655 (1987).

48. Rossetti, R. & Brus, L. E. Electron-hole recombination emission as a probe of surface chemistry in aqueous CdS colloids. *J. Phys. Chem.* **86,** 4470-4472 (1982).

49. Kalyanasundaram, K., Borgarello, E., Duonghong, D., & Gratzel, M. Cleavage of water by visible-light irridiation of colloidal CdS solutions: inhibition of photocorrosion by RuO_2. *Angew. Chem. Int. Ed.* **20,** 987-988 (1981).

50. Smith, A. M., Duan, H. W., Rhyner, M. N., Ruan, G., & Nie, S. M. A systematic examination of surface coatings on the optical and chemical properties of semiconductor quantum dots. *Phys. Chem. Chem. Phys.* **8,** 3895-3903 (2006).

APPENDIX A

Supplementary Discussion for X-Ray Diffraction Simulations

Scattering of light from crystalline lattice planes can be accurately modeled using the Debye equation, which sums the intensity of scattering from atomic pairs across the entire crystal and averages the scattering over spherical orientations:

$$I(q) = \sum_i \sum_j f_i(q) f_j(q) \frac{\sin(qr_{ij})}{qr_{ij}} \qquad \textbf{Equation A1}$$

$$q = 4\pi \frac{\sin\theta}{\lambda} \qquad \textbf{Equation A2}$$

I is the coherent scattering intensity at angle θ, f is the atomic scattering factor for atom i or j, r_{ij} is the distance between the atoms i and j, and λ is the wavelength of light. This equation is tractable for small nanocrystals, and has previously shown great accuracy in verifying the structures of nanocrystals with one or more domains.[1-4]

In this work, a structure was generated by stacking ~20 nm (111) or (0001) planes of atoms in zinc blende or wurtzite orientations, respectively. These structures were then pared to the desired size and shape, with phase and stacking fault density dictated by the original structure. The Debye equation was then solved for this structure using the DISCUS software package,[5] incorporating thermal fluctuations of the atomic positions through temperature factors.[6] The differences in crystal structure for zinc blende and wurtzite are manifested in a few distinct reflections in the diffraction spectra, as depicted in Figure A1. For wurtzite (A), the (0002) reflection at ~27° is a convolution of three individual peaks, accounting for its broadened appearance compared to the equivalent

(111) reflection in the zinc blende spectrum (C). In addition, the zinc blende spectrum (C) lacks reflections equivalent to the wurtzite ($10\bar{1}2$) reflection at ~38° and the ($10\bar{1}3$) reflection at ~50°. By introducing polytypic defects via stacking faults, each structure gradually adds features resembling of the other structure. For example, adding one zinc blende stacking fault in the middle of the wurtzite structure (B) reduces the intensity and peak width of the (102) and (103) reflections, and decreases the width of the peak convolution at ~27°. Introducing one wurtzite stacking fault into the middle of the zinc blende nanocrystal (D) yields a small amount of scattering in the region of ($10\bar{1}3$) wurtzite reflection. The addition of 3 stacking faults to the zinc blende nanocrystal adds a significant wurtzite character to the spectrum (E), showing the development of a distinct ($10\bar{1}3$) peak. The (F) spectrum was generated by averaging 20 different nanocrystals to yield a frequency of 0.32 stacking faults per plane, which closely matches the experimentally observed spectrum of CdTe in Figure 4.18.

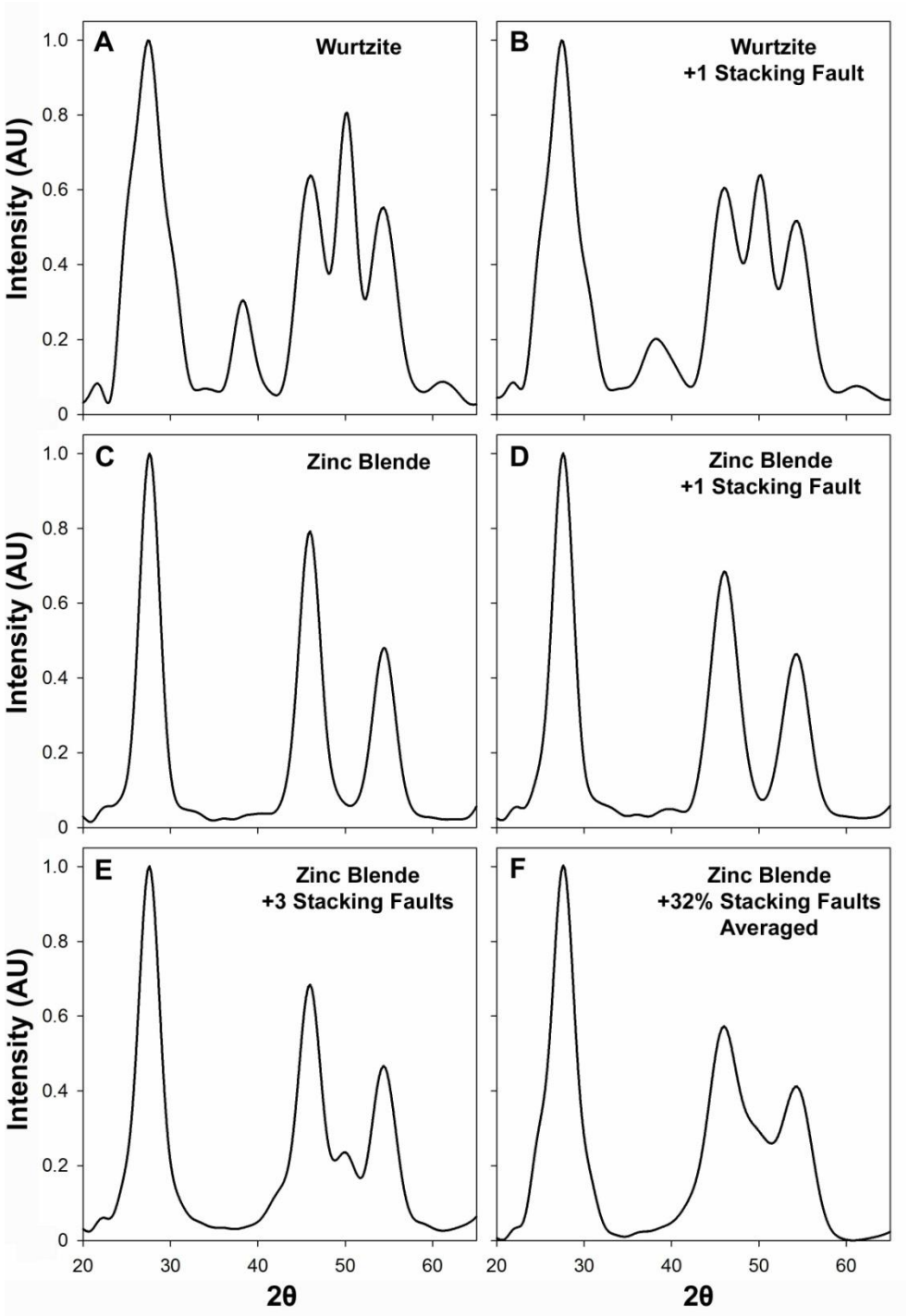

Figure A1: Simulations of diffraction spectra of CdTe nanocrystals with wurtzite, zinc blende, or polytypic structures. Nanocrystals were modeled as hexagonal prisms with 4.2 nm height and 3.0 nm width. Pure wurtzite nanocrystals are shown (A) as well as ones containing a single zinc blende single stacking fault (B). Pure zinc blende nanocrystals are shown (C) as well as ones containing a single wurtzite stacking fault (D). A single zinc blende nanocrystal with three wurtzite stacking faults is shown in (E). The last spectrum (F) is the average of 20 randomly stacked nanocrystals with a 0.32 frequency of wurtzite stacking faults, reproduced from Figure 4.18.

A.1 References

1. Bawendi, M. G., Kortan, A. R., Steigerwald, M. L., & Brus, L. E. X-ray structural characterization of larger CdSe semiconductor clusters. *J. Chem. Phys.* **91,** 7282-7290 (1989).

2. Murray, C. B., Norris, D. J., & Bawendi, M. G. Synthesis and characterization of nearly monodisperse CdE (E = S, Se, Te) semiconductor nanocrystallites. *J. Am. Chem. Soc.* **115,** 8706-8715 (1993).

3. Dabbousi, B. O., Rodriguez-Viejo, J., Mikulec, F. V., Heine, J. R., Mattoussi, H., Ober, R., Jensen, K. F., & Bawendi, M. G. (CdSe)ZnS core-shell quantum dots: Synthesis and characterization of a size series of highly luminescent nanocrystallites. *J. Phys. Chem. B* **101,** 9463-9475 (1997).

4. Cao, Y. W. & Banin, U. Growth and properties of semiconductor core/shell nanocrystals with InAs cores. *J. Am. Chem. Soc.* **122,** 9692-9702 (2000).

5. Proffen, T. & Neder, R. B. DISCUS: a program for diffuse scattering and defect-structure simulation. *J. Appl. Crystallogr.* **30,** (1997).

6. Butt, N. M., Bashir, J., & Knan, M. N. Compilation of temperature factors of cubic compounds. *Acta Crystallogr.* **A49,** 171-174 (1993).

APPENDIX B

Elasticity Model for Strain Engineering of Quantum Dots

A significant number of published studies have analyzed the effects of strain on the optical and electronic properties of lattice-mismatched semiconductor heterostructures,[1-8] as well as strained quantum dot 'inclusions' within pseudo-infinite bulk matrices.[9-17] However comparatively few studies have focused on the heteroepitaxial strain within free-standing nanocrystals, in which all domains share a significant portion of the strain.[18-20] Kolenbrander and coworkers developed the most rigorous and suitable strain model for the nanocrystals prepared in Chapter 4, based on elastic modeling of concentric spheres.[19] This approach is used to model heteroepitaxial strain in such systems in Chapter 4, and is described further in this appendix. The pressure across the interface between the two concentric spheres with inner radius r_c (core) and outer radius r_s (shell) is

$$p = \frac{\frac{3E_S}{3(1-\nu_S)}\epsilon\,(1 - r_c^3/\,r_s^3)}{1 - \frac{2m}{3}(1 - r_c^3/\,r_s^3)} \qquad \textbf{Equation B.1}$$

where the subscript 's' corresponds to the material of the shell and 'c' corresponds to the material of the core, E is Young's modulus, ν is Poison's ratio, ϵ is the constrained strain for concentric spheres:

$$\epsilon = \frac{3K_c}{3K_c + 4\mu_s} \times \frac{a_c - a_s}{a_s} \qquad \textbf{Equation B.2}$$

where K is the bulk modulus, μ is the shear modulus, a is the lattice constant, and m is the elastic mismatch parameter,

$$m = \frac{E_S}{(1 - \nu_S)} \times \left[\frac{(1 - 2\nu_S)}{E_S} - \frac{(1 - 2\nu_C)}{E_C} \right] \qquad \textbf{Equation B.3}$$

The hydrostatic stress on the core can then be expressed in spherical coordinates as

$$\sigma^c_{rr} = \sigma^c_{\theta\theta} = \sigma^c_{\varphi\varphi} = -p \qquad \textbf{Equation B.4}$$

The anisotropic stress on the shell is different in the radial and tangential directions, and depends on the distance from the particle center, r:

$$\sigma^s_{rr} = p \frac{r_c^3 / r_s^3}{(1 - r_c^3 / r_s^3)} \times \left[1 - \left(\frac{r_s}{r} \right)^3 \right] \qquad \textbf{Equation B.5}$$

$$\sigma^s_{\theta\theta} = \sigma^s_{\varphi\varphi} = p \frac{r_c^3 / r_s^3}{(1 - r_c^3 / r_s^3)} \times \left[1 + \frac{1}{2} \left(\frac{r_s}{r} \right)^3 \right] \qquad \textbf{Equation B.6}$$

The stress can then be used to directly calculate the strain in the radial and tangential directions for the core and shell materials using the bulk modulus and Young's modulus. We note that II-VI semiconductors are somewhat anisotropic materials, and Young's modulus is therefore different for different lattice directions. The selection of appropriate values for this parameter is crucial for accurate calculations, although these calculations are only accurate when assuming isotropic materials parameters.

The elastic strain energy for the core material is

$$E^c_E = \frac{1}{2} (3 \sigma^c_{rr} \varepsilon^c_{rr}) (\frac{4}{3} \pi r_c^3) \qquad \textbf{Equation B.7}$$

The strain energy for the shell is

$$E^s_E = \frac{1}{2} \int_{r_c}^{r_s} (\sigma^s_{rr} \varepsilon^s_{rr} + 2\sigma^s_{\theta\theta} \varepsilon^s_{\theta\theta}) (4 \pi r^2 \, dr) \qquad \textbf{Equation B.8}$$

Therefore the energy of elastic strain for the entire nanocrystal is

$$E_E = \pi r_c^3 p^2 \left[\frac{(1 - 2\nu_C)}{\mu_C (1 + \nu_C)} + \frac{(1 - 2\nu_S)}{\mu_S (1 + \nu_S)} \frac{r_c^3 / r_s^3}{(1 - r_c^3 / r_s^3)} + \frac{1}{2\mu_S (1 - r_c^3 / r_s^3)} \right] \qquad \textbf{Equation B.9}$$

The lowest energy coherency defect is predicted to be that of a single dislocation loop at the interface between the core and shell with the same radius as that of the core. The energy of the dislocation loop is

$$E_{DL} = 2\pi r_c \left[\frac{|b|^2\, 2\mu_s\mu_c/(\mu_s+\mu_c)}{4\pi(1-\nu_s)}\right] \ln\left(\frac{8\alpha r_c}{|b|}-1\right) \qquad \textbf{Equation B.10}$$

where α is the dislocation core parameter and $|b| = 1/2\langle 110\rangle_s$ is the burgers vector of the dislocation loop. The dislocation core parameter is typically given a value of 4 for tetrahedral semiconductors.[9,19,21,22] The elastic energy relieved by dislocation loop formation is the interaction energy:

$$E_{Interaction} = -\pi r_c^2\, p\, |b| \qquad \textbf{Equation B.11}$$

The critical radius for shell thickness is that which the elastic energy of the coherent state is equal to the energy of formation of the dislocation loop plus the residual elastic strain energy.

B.1 References

1. Romanov, A. E., Pompe, W., Mathis, S., Beltz, G. E., & Speck, J. S. Threading dislocation reduction in strained layers. *J. Appl. Phys.* **85,** 182-192 (1999).

2. Bolkhovityanov, Y. B., Pchelyakov, O. P., & Chikichev, S. I. Silicon-germanium epilayers: physical fundamentals of growing strained and fully relaxed heterostructures. *Phys. Usp.* **44,** 655-680 (2001).

3. Pinardi, K., Jain, U., Jain, S. C., Maes, H. E., Van Overstraeten, R., & Willander, M. Critical thickness and strain relaxation in lattice mismatched II-VI semiconductor layers. *J. Appl. Phys.* **83,** 4724-4733 (1998).

4. Jain, S. C., Willander, M., Pinardi, K., & Maes, H. E. A review of recent work on stresses and strains in semiconductor heterostructures. *Phys. Scr.* **T69,** 65-72 (1997).

5. Gendry, M., Drouot, V., Hollinger, G., & Mahajan, S. Effect of surface steps and nonstoichiometry on critical thickness of strained InGaAs layers grown by molecular-beam epitaxy on InAlAs/InP heterostructures. *Appl. Phys. Lett.* **66,** 40-42 (1995).

6. Tuchman, J. A. & Herman, I. P. General trends in changing epilayer strain through the application of hydrostatic pressure. *Phys. Rev. B* **45,** 11929-11935 (1992).

7. Brunner, K. Si/Ge nanostructures. *Rep. Prog. Phys.* **65,** 27-72 (2002).

8. Lamberti, C. The use of synchrotron radiation techniques in the characterization of strained semiconductor heterostructures and thin films. *Surf. Sci. Rep.* **53,** 1-197 (2004).

9. Kolesnikova, A. L. & Romanov, A. E. Misfit dislocation loops and critical parameters of quantum dots and wires. *Philos. Mag. Lett.* **84,** 501-506 (2004).

10. Yang, F. Q. Effect of interfacial stresses on the elastic behavior of nanocomposite materials. *J. Appl. Phys.* **99,** (2006).

11. Yang, M., Sturm, J. C., & Prevost, J. Calculation of band alignments and quantum confinement effects in zero- and one-dimensional pseudomorphic structures. *Phys. Rev. B* **56,** 1973-1980 (1997).

12. Persson, J., Hakanson, U., Johansson, M. K. J., Samuelson, L., & Pistol, M. E. Strain effects on individual quantum dots: Dependence of cap layer thickness. *Phys. Rev. B* **72,** 085302 (2005).

13. Pryor, C., Pistol, M. E., & Samuelson, L. Electronic structure of strained InP/$Ga_{0.51}In_{0.49}P$ quantum dots. *Phys. Rev. B* **56,** 10404-10411 (1997).

14. Williamson, A. J., Zunger, A., & Canning, A. Prediction of a strain-induced conduction-band minimum in embedded quantum dots. *Phys. Rev. B* **57,** R4253-R4256 (1998).

15. He, L. X., Bester, G., & Zunger, A. Strain-induced interfacial hole localization in self-assembled quantum dots: Compressive InAs/GaAs versus tensile InAs/InSb. *Phys. Rev. B* **70,** 235316 (2004).

16. Eshelby, J. D. The determination of the elastic field of an ellipsoidal inclusion, and related problems. *Proc. R. Soc. London, A* **241,** 376-396 (1957).

17. Duan, H. L., Karihaloo, B. L., Wang, J., & Yi, X. Compatible composition profiles and critical sizes of alloyed quantum dots. *Phys. Rev. B* **74,** (2006).

18. Duan, H. L., Karihaloo, B. L., Wang, J., & Yi, X. Strain distributions in nano-onions with uniform and non-uniform compositions. *Nanotechnology* **17,** 3380-3387 (2006).

19. Balasubramanian, S., Ceder, G., & Kolenbrander, K. D. Three-dimensional epitaxy: Thermodynamic stability range of coherent germanium nanocrystallites in silicon. *J. Appl. Phys.* **79,** 4132-4136 (1996).

20. Raychaudhuri, S. & Yu, E. T. Critical dimensions in coherently strained coaxial nanowire heterostructures. *J. Appl. Phys.* **99,** (2006).

21. Frank, F. C. & Vandermerwe, J. H. One-Dimensional Dislocations. 2. Misfitting Monolayers and Oriented Overgrowth. *Proc. R. Soc. London, A* **198,** 216-225 (1949).

22. Frank, F. C. & Vandermerwe, J. H. One-Dimensional Dislocations. 1. Static Theory. *Proc. R. Soc. London, A* **198,** 205-216 (1949).

APPENDIX C

Nanocrystal Characterization

Absorption spectra in the range of 300-900 nm were measured on a Shimadzu UV-2401PC scanning spectrophotometer with 1.0 nm slit widths. Absorption spectra from 850-1700 nm were measured using a NIR-512 spectrometer from Ocean Optics with a tungsten halogen lamp. Photoluminescence spectra were acquired using either a SPEX FluoroMax-2 spectrofluorometer or a spectrofluorometer from Photon Technology International. For the latter instrument, a xenon lamp was used for excitation, and the detector was a photomultiplier tube for the spectral range 400-850 nm, and an InGaAs detector was used for the range 850-1600 nm. Quantum yield was measured by comparison to Atto dyes (520, 565, 610, or 680) dissolved in ethanol. All samples and standards were diluted to an optical density of 0.05 at the excitation wavelength, the emission spectra were integrated, and quantum yield was calculated after correcting for solvent refractive indices.[1] Time-resolved fluorescence decay spectra were obtained with excitation from a 478 nm pulsed diode laser. A spectrometer was used to resolve the peak emission wavelength, detected using a photomultiplier tube.

Zeta potential measurements were recorded with a Malvern Zetasizer Nano ZS90, with all samples in pH 8.5 borate buffer or pH 7.4 phosphate nuffer. Dynamic light scattering data was obtained using a Brookhaven 90Plus Particle Size Analyzer. Before analysis, nanoparticle samples (1-100 μM, depending on the core size) were first centrifuged at 7000g for 10 minutes and then filtered through a 0.2 μm filter. Ultracentrifugal isolation of aqueous solutions of nanocrystals was performed on a Beckman Coulter Optima TLX

Ultracentrifuge, typically at 100,000 rpm for 1 hour. Gel filtration chromatography was performed on a Superose 6 10/300 GL column, with 280 nm absorption monitored on an AKTAprime plus system (GE Healthcare). The flow rate was 0.5 mL/min and the following protein standards were used for molecular weight determination: Ferritin (440 kDa), Aldolase (158 kDa), Ovalbumin (43 kDa), and carbonic anhydrase (29 kDa).

For transmission electron microscopy, 5 µL of sample was dropped onto formvar/carbon 200 mesh TEM grids. Basic transmission electron microscopy was performed by Dr. Hong Yi using a Hitachi H-7500 TEM at the Electron Microscopy Core Facility at Emory University. High resolution TEM was performed by Dr. Amar Kumbhar using a Hitachi H-9500 at the Clemson University Electron Microscopy Facility, or by Dr. Yong Ding using a JEOL 4000EX at Georgia Tech. X-ray diffraction spectra were measured using a Bruker SMART 1000 CCD/Hi-Star dual-detector diffractometer, with a cobalt X-ray source. Inductively-coupled plasma-mass spectrometry (ICP-MS) was performed with a PlasmaQuad 3 at the Center for Applied Isotope Studies at the University of Georgia.

C.1 References

1. Himel, C. M. & Mayer, R. T. 5-Dimethylaminonaphthalene-1-sulfonic acid (dans-acid) as a standard for quantum yield of fluorescence. *Anal. Chem.* **42,** 130-& (1970).

VITA **Andrew M. Smith**

Department of Biomedical Engineering
Emory University and Georgia Tech
Woodruff Memorial Building, Suite 2007
101 Woodruff Circle, Atlanta, GA 30322
[Tel]: 404-642-1303, [Fax]: 404-727-3567
[Email]: Andrew.Michael.Smith@gmail.com

EDUCATION

August 2008 **Ph.D. Bioengineering**
Georgia Institute of Technology, Atlanta, GA
Thesis Advisor: Professor Shuming Nie
Dissertation: Engineering Semiconductor Nanocrystals for Molecular, Cellular, and In Vivo Imaging
GPA: 3.77/4.00

August 2002 **B.S. Chemistry**
Georgia Institute of Technology, Atlanta, GA
GPA: 3.89/4.00, *with highest honor*

RESEARCH EXPERIENCE

2008-Present Distinguished CCNE Postdoctoral Fellowship
Location: Emory University Center for Cancer Nanotechnology Excellence
Advisor: Dr. Shuming Nie, Wallace H. Coulter Distinguished Chair in Biomedical Engineering and Director of Emory-Georgia Tech Cancer Nanotechnology Center
Advisor: Dr. Brian Leyland-Jones, Director of the Winship Cancer Institute, Associate Vice President for Health Affairs
- Development of nanoparticle probes for intraoperative imaging of cancer.
- Study of the interaction between nanoparticles and biological systems.
- Examination of cellular signaling pathways in living cells in real time using quantum dots.

2002-2008 Graduate Research in Biomedical Applications of Nanotechnology
Location: Georgia Institute of Technology and Emory University
Advisor: Dr. Shuming Nie, Wallace H. Coulter Distinguished Chair in Biomedical Engineering and Director of Emory-Georgia Tech Cancer Nanotechnology Center
- Synthesized new types of near-infrared semiconductor nanocrystals.
- Developed advanced synthesis techniques for nanocrystals.
- Generated novel colloidal surface modification strategies for stabilization of nanoparticles with high stability and small size.
- Used fluorescent quantum dots to image mouse models of cancer.
- Studied interactions of nanoparticles with blood, cells, and animals.
- Lab manager

2000-2002 Undergraduate Research Scholars (URS) Internship in Tissue Engineering
Location: Georgia Institute of Technology
Advisor: Dr. Athanassios Sambanis, Professor of Chemical Engineering
Advisor: Dr. Robert Nerem, Professor and Director of the Institute for Bioengineering and Bioscience
- URS Program of the Georgia Tech/Emory Center for the Engineering of Living Tissues (GTEC) is funded by the National Science Foundation.
- Developed a retroviral gene delivery system for therapeutic transduction of human cells.
- Genetically modified primary human cells for use in vascular grafts.
- Tested thrombotic characteristics of vascular cell linings in vitro.

2000-2001 Undergraduate Research in Biomechanical Engineering
Location: Georgia Institute of Technology
Advisor: Dr. Robert Cargill, Former Assistant Professor of Mechanical Engineering
- Mechanically strained neuronal cells to model traumatic brain injury, and for the intracellular delivery of transgenes.

2000 Undergraduate Research in Biochemistry
Location: Georgia Institute of Technology
Advisor: Dr. James Powers, Regents' Professor of Chemistry and Biochemistry
- Synthesized inhibitor of angiotensin converting enzyme I, conjugated to a technetium chelate, for use in scintigraphic molecular imaging of the lung and kidneys.

PUBLICATIONS

Peer-reviewed journal articles

Smith AM, Nie SM. Chemical analysis and cellular imaging with quantum dots. *Analyst*, 129: 672-677 (2004). (Cover article)

Bailey RE, Smith AM, Nie SM. Quantum dots in biology and medicine. *Physica E*, 25: 1-12 (2004).

Smith AM, Gao XH, Nie SM. Quantum dot nanocrystals for in vivo molecular and cellular imaging. *Photochemistry and Photobiology*, 80: 377-385 (2004). (Cover article)

Smith AM, Ruan G, Rhyner MN, Nie SM. Engineering luminescent quantum dots for in vivo molecular and cellular imaging. *Annals of Biomedical Engineering*, 34: 3-14 (2006).

Smith AM, Dave S, Nie SM, True L, Gao XH. Multicolor quantum dots for molecular diagnostics of cancer. *Expert Review of Molecular Diagnostics*, 6: 231-244 (2006).

Rhyner MN, Smith AM, Gao XH, Mao H, Yang L, Nie SM. Quantum dots and multifunctional nanoparticles: new contrast agents for tumor imaging. *Nanomedicine*, 1: 209-217 (2006).

Smith AM, Duan HW, Rhyner MN, Ruan G, Nie SM. A systematic examination of surface coatings on the optical and chemical properties of semiconductor quantum dots. *Physical Chemistry Chemical Physics*, 8: 3895-3903 (2006).

Xing Y, Smith AM, Agrawal A, Ruan G, Nie SM. Molecular profiling of single cancer cells and clinical tissue specimens with semiconductor quantum dots. *International Journal of Nanomedicine*, 1: 473-481 (2006).

Kairdolf BA, Mancini MC, Smith AM, Nie SM. Minimizing nonspecific cellular binding of quantum dots with hydroxyl-derivitized surface coatings. *Analytical Chemistry,* 80: 3029 (2008).

Smith AM, Duan HW, Mohs AM, Nie SM. Bioconjugated quantum dots for in vivo molecular and cellular imaging. *Advanced Drug Delivery Reviews,* 60: 1226-1240 (2008).

Mancini MC, Kairdolf BA, Smith AM, Nie SM. Oxidative quenching and degradation of polymer encapsulated quantum dots: new insights into the long term fate of semiconductor nanocrystals in vivo. *Journal of the American Chemical Society*,130: 10836-10837 (2008).

Smith AM, Nie SM. Minimizing the hydrodynamic size of quantum dots with multifunctional multidentate polymer ligands. *Journal of the American Chemical Society*, 130: 11278-11279 (2008).

Kairdolf BA, Smith AM, Nie SM. One-pot synthesis, encapsulation, and solubilization of size-tuned quantum dots with amphiphilic multidentate ligands. *Journal of the American Chemical Society,* 130: 12866-12867 (2008).

Smith AM, Mohs AM, Nie SM. Tuning the electronic and optical properties of quantum dots by lattice strain. *Nature Nanotechnology,* **in press**.

Smith AM, Nie SM. Nanocrystal synthesis in an amphibious bath: spontaneous generation of hydrophilic and hydrophobic surface coatings. *Angewandte Chemie,* **in press**.

Smith AM, Wen M, Nie SM. Advanced nanocrystal surface chemistry: Overcoming the tradeoff between size and stability. In preparation. Invited review for *Accounts of Chemical Research*, **in preparation**.

Smith AM, Nie SM. Emerging opportunities analysis with semiconductor quantum dots. *Annual Review of Analytical Chemistry*, **in preparation**.

Smith AM, Nie SM. Cation exchange of Hg(2+) with semiconductor nanocrystals as a mechanism for independent tuning of nanocrystal size and optical properties. *Journal of the American Chemical Society*, **in preparation**.

Smith AM, Mancini MC, Wen M, Liu J, and Nie SM. Nonspecific binding of semiconductor quantum dots: Dependence on size and surface coatings. *Nano Letters*, **in preparation**.

Smith AM and Nie SM. Tuning the sizes of semiconductor nanocrystals with a mixture of strong and weak ligands. *Journal of Physical Chemistry C*, **in preparation**.

Mohs AM, Smith AM, Mancini MC, Nie SM. Evaluating the independent contributions of material composition, size, and charge to the cytoxicity of semiconductor quantum dots. In preparation. *Nano Letters*, **in preparation**.

Book chapters

Smith AM and Nie SM. Semiconductor quantum dots for molecular and cellular imaging, chapter in *The Biomedical Engineering Handbook*, 3rd edition, CRC Press (2006).

Ruan G, Agrawal A, Smith AM, Gao XH, Nie SM. Quantum dots as fluorescent labels for molecular and cellular imaging, chapter in *Reviews in Fluorescence*, Springer (2006).

Rhyner MN, Smith AM, Gao XH, Mao H, Lily L, Nie SM. Quantum dots and targeted nanoparticle probes for in-vivo tumor imaging, chapter in *Nanoparticles in Biomedical Imaging*, Springer (in press, 2008).

CONFERENCE PRESENTATIONS

"Genetically engineered fibroblasts as a substitute for endothelial cells on vascular grafts," Biomedical Engineering Society Annual Fall Meeting, Durham, NC 2001. Oral contribution.

"Near-infrared quantum dot probes for biological detection," SPIE Optics East, Philadelphia, PA 2004. Invited talk.

"Bioconjugated quantum dot nanoparticles: molecular imaging, profiling, and in vivo imaging," BioJapan 2004, Tokyo, Japan, 2004. Invited Keynote Lecture.

"Bioconjugated quantum-dot nanocrystals for probing single molecules and single cells," American Chemical Society National Meeting, Washington, D.C. 2005. Oral contribution.

"Quantum dots: new probe development and applications in cancer profiling and imaging," Emory-Georgia Tech Frontiers of Cancer Nanotechnology Symposium, Braselton, GA 2006. Poster presentation.

"Bioconjugated quantum dots for molecular and cellular imaging: bandgap and surface engineering," Biomedical Engineering Society Annual Fall Meeting, Chicago, Il 2006. Invited talk.

"Bioconjugated quantum dots for molecular and cellular imaging: bandgap and surface engineering," AVS Symposium, Anaheim, CA 2006. Invited talk.

"Giant spectral shifts induced by lattice strain in semiconductor quantum dots," Emory-Georgia Tech Frontiers of Cancer Nanotechnology Symposium, Pine Mountain, GA 2007. Poster presentation.

"Strain-tunable, near-infrared quantum dots for in vivo molecular imaging of cancer," Joint Molecular Imaging Conference, Providence, RI 2007. Poster presentation.

"Strain-tunable quantum dots for nontoxic, near-infrared imaging of cancer in vivo," Biomedical Engineering Society Annual Fall Meeting, Los Angeles, CA 2007. Oral contribution.

"Acid-stable quantum dots using proton-repelling surface coatings: Implications in oral delivery of imaging and therapeutic nanoparticles," Emory-Georgia Tech Frontiers of Cancer Nanotechnology Symposium, Callaway Gardens, GA 2008. Poster presentation.

"Characterization of semiconductor quantum dots for use in biological imaging," Harvard Center for Nanoscale Systems, Cambridge, MA 2008. Invited seminar.

PATENTS

Rhyner MN, Nie SM, Smith AM. *Micellar Structures, Methods of Making Micellar Structures, Methods of Imaging, and Methods of Delivering Agents*. Provisional Patent in Preparation with Emory Office of Tech Transfer and the Law Firm Thomas, Kayden, Horstemeyer, and Risely.

Smith AM, Nie SM, Kairdolf, BA. *Quantum Dots, Methods of Making Quantum Dots, and Methods of Using Quantum Dots*. Provisional Patent in Preparation with Emory Office of Tech Transfer and the Law Firm Thomas, Kayden, Horstemeyer, and Risely.

AWARDS AND HONORS

1997-2002	Recipient of Georgia's HOPE Scholarship
2001	Biomedical Engineering Society Undergraduate Research Award
2002-2006	Whitaker Foundation Graduate Research Fellowship
2005	*Photochemistry and Photobiology* 2004 Best Review Paper of the Year
2006	Outstanding Poster Award, Emory-Georgia Tech Frontiers of Cancer Nanotechnology Symposium
2007	*Annals of Biomedical Engineering*'s 2006 Best Review Paper of the Year

REFERENCES

Furnished upon request.